List of Contributors

H. J. Andersen, *Department of Food Science, Danish Institute of Agricultural Sciences, Research Centre Foulum, P.O. Box 50, DK-8830 Tjele, Denmark*

N. Baril, *Magnetic Resonance Centre, CNRS-University Victor Segalen Bordeaux 2, Bordeaux, France*

H. C. Bertram, *Department of Food Science, Danish Institute of Agricultural Sciences, Research Centre Foulum, P.O. Box 50, DK-8830 Tjele, Denmark*

J. D. de Certaines, *Magnetic Resonance Centre, University of Rennes 1, France*

R. Y. Dong, *Department of Physics and Astronomy, Brandon University, Brandon, MB, Canada R7A 6A9, and Department of Physics and Astronomy, University of Manitoba, Winnipeg, MB, Canada R3T 2N2*

J.-M. Franconi, *Magnetic Resonance Centre, CNRS-University Victor Segalen Bordeaux 2, Bordeaux, France*

T. Hiraoki, *Department of Applied Physics, Graduate School of Engineering, Hokkaido University, Sapporo 060-8628, Japan*

S. Kitazawa, *Department of Applied Physics, Graduate School of Engineering, Hokkaido University, Sapporo 060-8628, Japan*

G. Madelin, *Magnetic Resonance Centre, CNRS-University Victor Segalen Bordeaux 2, Bordeaux, France*

P. Permi, *Institute of Biotechnology, Structural Biology and Biophysics Program, NMR Laboratory, P.O. Box 65, FIN-00014, University of Helsinki, Helsinki, Finland*

E. Thiaudière, *Résonance Magnétique des Systèmes Biologiques, UMR 5536 CNRS – Université Victor Segalen Bordeaux 2, Bordeaux, France*

A. Tsutsumi, *Department of Applied Physics, Graduate School of Engineering, Hokkaido University, Sapporo 060-8628, Japan*

S. Zhang, *Sealy Center for Structural Biology, Department of Human Biological Chemistry and Genetics, University of Texas Medical Branch, Galveston, Texas 77555-1157, USA*

Preface

It gives me great pleasure to introduce Volume 53 of Annual Reports on NMR Spectroscopy. As is customary with this series of reports, the power of NMR throughout science is reflected in the diverse nature of the topics contained in this volume.

The first account is on 'Phase Incremented Pulses in NMR with Applications' by S. Zhang, this is followed by 'Advances in NMR Studies of Liquid Crystals' by R. Y. Dong, H. C. Bertram and H. J. Anderson report on 'Applications of NMR in Meat Science', 'NMR Characterization of Mechanical Waves' is covered by G. Madelin, N. Baril, J. D. de Certaines, J.-M. Francone and E. Thiaudiere, the next account is on 'Aspects of Coherence Transfer in High Molecular Weight Proteins' by P. Permi, the final chapter is on 'Local Dynamics in Polypeptides studied by Solid State ^{2}H NMR' by T. Hiraoki, S. Kitazawa and A. Tsutsumi.

It is with gratitude that I offer my thanks to all of these reporters and to the production staff at Elsevier for their considerable help in the creation of this volume.

Royal Society of Chemistry
Burlington House
Piccadilly
London, UK

G. A. WEBB
January 2004

Contents

Local Dynamics in Polypeptides Studied by Solid State ^{2}H NMR: Side Chain Dynamics of Poly(γ-benzyl L-glutamate) and Racemic Poly(γ-benzyl glutamate)

Phase Incremented Pulses in NMR with Applications

SHANMIN ZHANG

Sealy Center for Structural Biology, Department of Human Biological Chemistry and Genetics, University of Texas Medical Branch, Galveston, Texas 77555-1157, USA
Tel.: 409-747-6821; Fax: 409-747-6850; E-mail: shanminz@hotmail.com

ANNUAL REPORTS ON NMR SPECTROSCOPY
VOLUME 53 ISSN 0066 4103
DOI 10.1016/S0066-4103(04)53001-6

Phase incremented pulse (PIP) in NMR was used around the early 1980s to achieve frequency-shifted excitation while preserving the phase coherence among the RF pulses applied before and after the PIP. At that time, the amount of frequency shift and the locations of all the effective RF fields were well-known. The strengths and phases, on the other hand, remained under explored until a theory about PIP was presented in 1996. It turned out that all the effective RF fields could be described by only two more terms: a scaling factor and a universal phase shift. Thereafter, the phase shifted unsymmetrical excitation bands by a PIP became apparent. Later, a procedure for establishing the phase coherence in PIPs was introduced. As a result, the Bloch vector model that was used almost solely in the conventional rotating frame is now applicable to multiple Eigenframes of PIPs as if it were still in the conventional rotating frame and a number of NMR experiments, such as the broadband inversion, Hahn spin echo, and offset modulated composite pulse, all composed of PIPs, were constructed systematically. In addition, some of the applications of the PIPs in decoupling and selective excitation were developed and the RF interference in the form of the Bloch-Siegert offset shift was addressed quantitatively by a near neighbour approximation.

1. INTRODUCTION

The successes of various NMR experiments rely utterly on the schemes of the radio frequency (RF) pulse sequences.[1–6] To accomplish a certain task, a spin system inside a strong magnet must be excited with a precise frequency, an appropriate phase, a desired flip-angle, and at a right time. It is a pertinent metaphor for composing a piece of harmonic music with notes, chords, dynamics, and rhythms, as analogized by Ernst at his hometown Winterthur shortly after he received the 1991 Nobel Prize in chemistry. To the experienced NMR 'composers' who design pulse sequences, these tones are well-known. However, what is often ignored is the phase coherence in RF pulses – the right phase relationship among the RF pulses applied at different times. The phase

coherence must be maintained within each scan and it is, fortunately, achieved by the NMR instruments themselves with a reference frequency that comes from the same source as that of the RF pulses. Therefore, human intervention is usually not required for keeping the phase coherence. It is no longer guaranteed whenever a frequency jump is executed in a pulse sequence. An arbitrary phase can be introduced, leading to a broken phase coherence. Unpredictable results may occur if the phase coherence, which is necessary in a pulse sequence, is not fulfilled (Fig. 1). The problem associated with the frequency jump can be solved by using a number of numerical controlled oscillates (NCO), each tracking a single frequency. A different NCO is used when a frequency jump is encountered. An alternative way is to use a frequency synthesizer that is capable of a phase memory. A compensation for an appropriate phase can be provided by the synthesizer each time the RF pulse returns to the carrier frequency from a frequency jump.

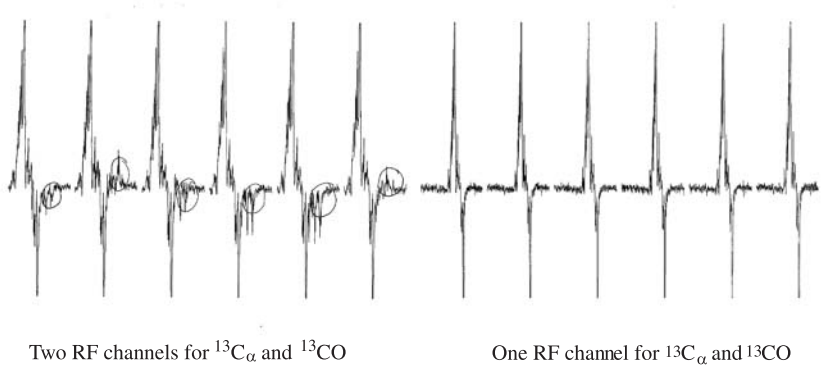

Fig. 1. Repeated first increment of a HCACO experiment using one and two RF channels for $^{13}C_\alpha$ and ^{13}CO pulses. Marked with circles are the artifacts with random phases due to the lack of phase consistency between the $^{13}C_\alpha$ and ^{13}CO RF pulses. Although the two ^{13}C RF channels used for the spectra on the left are derived from the same 10 MHz reference, the $^{13}C_\alpha$ and ^{13}CO RF channels are naturally set to different frequencies, and their respective RF pulses operate in different rotating frames, resulting in a random relative phase between the two channels from one scan to another. As the $^{13}C_\alpha$ and ^{13}CO RF pulses typically are not completely selective, the lack of phase consistency between the two frameworks leads to the observed artifacts of pseudo-random phase from spins affected by both pulses. When phase and amplitude modulation is used to derive the $^{13}C_\alpha$ and ^{13}CO pulses from a single RF channel, as can be seen with the spectra on the right, the phase relationships between the pulses and the receiver are stable and the artifacts are cancelled by phase cycling. This problem was first observed in the Kay laboratory in 1992. It was forwarded to Varian where the problem was recognized as the phase consistency between multiple RF channels as defined above. The advantage of using phase and amplitude modulations to derive pulse sequences of phase consistent pulses at a variety of frequencies applied equally to both sequential and simultaneous RF pulses. Courtesy of Steve H. Smallcombe, Varian NMR Instruments and Lewis E. Kay, University of Toronto.

The phase coherence can also be achieved simply by using a linearly phase incremented pulse (PIP) without resorting to additional hardware. Since all the RF pulses utilized for constructing a PIP have the same carrier, no frequency jump is involved. Consequently, phase coherence between the RF pulses applied before and after the PIP is reserved naturally.

In the early 1980s, phase modulated pulses,[7–12] for broadband decoupling for example, and PIPs,[13–17] for achieving mainly a frequency-shifted excitation, were used. Kay and Bax used a PIP to suppress the solvent peak that was not on-resonance[16] and the other to generate a PIP of multiple frequencies with only a single waveform generator.[17] Extensive use of PIPs appeared until the emergence of the triple-resonance and three dimensional experiments pioneered by Kay, Bax, Griesinger, Sørensen, Ernst, and many others.[18–24]

In spite of the frequency-shifted excitation, the quantized PIP inevitably excites multiple sidebands located at $n/\Delta\tau$ $(n = \pm 1, \pm 2, \ldots)$ from the centre band. An attempt was made[16] to calculate the excitation profile of multiple bands created by a PIP of a constant RF field strength, using an approximate method based on the Fourier analysis. The accuracy of the method relies partly on the linear response of the spin system, which is, unfortunately, not true in most cases except for a small angle excitation. In addition, the spins inside a magnet consitute a quantum system, which is sensitive not only to the strengths but also to the phases of the RF fields. Any classical description is doomed to failure if the quantum nature of the spin system emerges.

Due to the large number of steps in a PIP, each with a phase increment, it is quite discouraging to calculate directly the response of a PIP. This obstacle, however, can be lifted largely by introducing a new or the second rotating frame (in contrast to the conventional rotating frame), in which the phase of the PIP is periodic. As a result, all the strengths and phases of the effective RF fields, which are responsible to the excitation profile of multiple bands, can be derived analytically as discussed in Section 2.[25]

The excitation profile of multiple bands was also known for periodic RF pulses, such as the DANTE (delays alternating with nutation for tailored excitation) sequence.[26] Similar to the PIP, all the phases and strengths of the effective RF fields can be obtained by expanding the periodic pulse into a Fourier series and properly rearranging the terms afterwards.[27] Detailed calculation, comparison with the PIP, and the excitation profiles by a periodic pulse of $f_{1x}|\sin(\pi t/T)|I_x$ and a DANTE sequence are presented in Section 3.

Because of the coexistence of the multiple effective RF fields, the RF interference appears in each excitation band.[25] The interference may be neglected if the strengths of any two interacting RF fields are much weaker than the frequency separation between them. Otherwise, the RF interference is noticeable and needs to be taken into account in the calculation of the excitation profile.

The RF interference associated with an infinite number of effective RF fields is a typical problem addressed by the Floqute theory.[28–32] To solve the problem, one may, however, face the diagonalization of a matrix with infinite dimensions, which is often unlikely to be done analytically. Certain approximations, such as the perturbation method, may be used.[32]

In most cases, each excitation band is determined largely by its corresponding RF field and is perturbed by the neighbouring fields. Under such circumstances, the RF interference can be derived by the coherent averaging theory. This approach shows that each RF field contributes to an excitation profile, an offset shift that is termed the Bloch-Siegert offset shift (BSOS).[33] Since the BSOS is inversely proportional to the separation of the two interacting RF fields, only a few near neighbours need to be taken into account, resulting in a near neighbour approximation (NNA). The RF interference and NNA will be covered in Section 4.

PIPs are adopted in numerous HCN triple-resonance experiments for ^{13}C- and ^{15}N-double-labelled proteins, where $^{13}C_\alpha$ or ^{13}CO needs to be excited separately to achieve selective coherence transfer or homonuclear decoupling.[34–38] The ^{13}CO, centred at 174 ppm, and the $^{13}C_\alpha$, centred at 56 ppm, have approximate chemical-shift ranges of 20 and 30 ppm, respectively. In the excitation of one band, the other band is somewhat affected due to the off-resonance effects.[1,2] For instance, in the middle of the evolution time of the $^{13}C_\alpha$, a 180° ^{13}CO PIP, with a carrier located at the centre of the $^{13}C_\alpha$, is used for homonuclear decoupling. To minimize the disturbance to the $^{13}C_\alpha$, restriction on the strength of the PIP is often imposed. Nevertheless, a non-linear Bloch-Siegert phase shift (BSPS)[39–42] is introduced to all the $^{13}C_\alpha$ peaks, in addition to the losses of both the transverse and longitudinal magnetizations.[42]

The BSPS can be corrected by adding an additional $^{13}C_\alpha$ pulse at a later time.[34,43] However, the loss of magnetizations is usually unrecoverable by this method. It was also shown by McCoy and Mueller that the BSPS can be corrected by applying a compensating pulse on the other side of the peak of interest.[44] This idea was tested quite successfully for a long (1.6 ms) sech adiabatic inversion pulse, where the pulsewidth becomes less crucial in the BSPS compensation. It is, however, quite different to compensate the BSPS by a short PIP. An improper pulsewidth can create distortions to the longitudinal and transverse magnetizations so severely that the scheme of the BSPS compensation may not work at all. The compensation of BSPS with an additional PIP will be introduced in Section 5.

The idea of using the linear phase increments to achieve frequency-shifted excitation can be adopted almost to any pulses, such as hard (amplitude fixed) pulses, shaped pulses, and even adiabatic inversion pulses. Unlike any other pulses, the adiabatic pulses have already used non-linear phase increments for tilting the effective RF field slowly compared with the Larmor frequency of the spins in the rotating frame in order to fulfill the adiabatic condition.

Even under such a circumstance, the linear phase increments can still be implemented in a similar manner to any PIPs. The overall effect is to shift the whole adiabatic inversion band or decoupling range to a new location that is $\Delta f = \Delta\varphi/(2\pi\Delta\tau)$ away from the original one. It is also possible to create multiple adiabatic inversion bands with a single waveform generator[45] or to make an additional frequency-shifted adiabatic pulse for compensation of the Bloch-Siegert frequency shift[46] (BSFS) encountered in ^{13}C homonuclear adiabatic decoupling.[47,48] These are the subjects of Section 6.

Unlike the phase coherence in RF pulses, the phase coherence in PIPs is no longer maintained by the NMR instruments,[49] at least not by the current NMR instruments. In Section 7, a method is presented for establishing the phase coherence in PIPs for a spin system subjected to multiple PIPs in a pulse sequence. The calculation is done in a rotating frame with a speed of $2\pi\Delta f = \Delta\varphi/\Delta\tau$ relative to the rotating frame. This particular frame is defined as the Eigenframe, in which the phase of the centre band RF field of the PIP is stationary. More importantly, the phase differences between different Eigenframes can be attributed to the initial phases of the PIPs, making it possible to use the Bloch vector model even in different Eigenframes. As a result, a new way to construct composite pulses is provided with not only amplitude and phase modulations but also offset modulation.

Although at the time of preparing this chapter, most of the materials have been published as can be inferred from the references, it is a wonderful opportunity to present them here as an integrated piece of work with a broad focus, unified derivation, and logical order. To make it easier for the readers, most of the derivations, simple or complicated, are shown in great detail. For the majority of NMR readers, it is not difficult to understand, if not the theories, the concepts and ideas and to use them in constructing PIPs of their interest.

2. MULTIPLE EFFECTIVE RF FIELDS CREATED BY A PIP

2.1. The definition of a PIP

A PIP is composed of a series of back-to-back pulses of an equal width $\Delta\tau$ as shown in Fig. 2. In addition to an initial phase φ_0 assigned to all the steps, a phase increment $\Delta\varphi$ ($-180^\circ \le \Delta\varphi \le 180^\circ$) is implemented in the following way

$$\varphi(t) = \begin{cases} 0, & 0 \le t < \Delta\tau \\ \Delta\varphi, & \Delta\tau \le t < 2\Delta\tau \\ 2\Delta\varphi, & 2\Delta\tau \le t < 3\Delta\tau \\ \cdots & \cdots \\ (N-2)\Delta\varphi, & (N-2)\Delta\tau \le t < (N-1)\Delta\tau \\ (N-1)\Delta\varphi, & (N-1)\Delta\tau \le t \le N\Delta\tau \end{cases}, \tag{1}$$

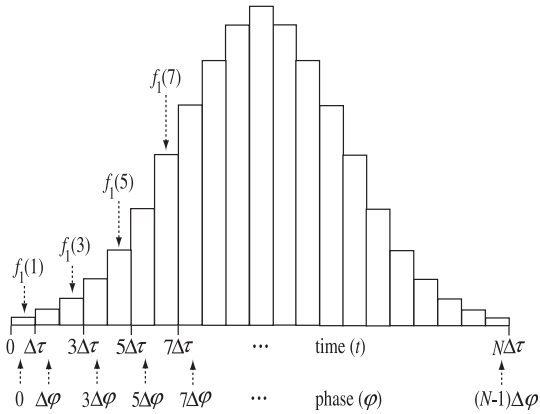

Fig. 2. A Gaussian shaped PIP with a phase increment $\Delta\varphi$, time increment $\Delta\tau$, total number of steps N, RF field strength $f_1(k)$ (for the kth step), and initial phase $\varphi_0 = 0$. Reprinted from Ref. 25 with permission from the American Institute of Physics publications.

where N is the total number of steps and $\tau = N\Delta\tau$ is the pulsewidth of the PIP. The RF field strength for each step is fixed and is denoted by $f_1(k)$, where k is an index of the step. In general, any PIP can be expressed as PIPΔf (φ_0, $\Delta\varphi$, $\Delta\tau$, $f_1(k)$, steps), where $\Delta f = (\Delta\varphi/2\pi\Delta\tau)$ is the frequency shift of the PIP in units of kHz.

2.2. Theory of PIP

For a non-interacting spin-1/2 system subjected to a PIP of an arbitrary shape, the Hamiltonian in the rotating frame with a RF carrier frequency f_{rf} can be written as[1,2]

$$\begin{aligned}\mathcal{H} &= (f_0 - f_{\mathrm{rf}})I_z + f_1(t)e^{-i[\varphi(t)+\varphi_0]I_z} I_x e^{i[\varphi(t)+\varphi_0]I_z} \\ &= \delta I_z + f_1(t)e^{-i[\varphi(t)+\varphi_0]I_z} I_x e^{i[\varphi(t)+\varphi_0]I_z} \qquad \text{(in Hz)},\end{aligned} \tag{2}$$

where $2\pi f_0 = \omega_0$ is the Larmor frequency of the spins in the external magnetic field, $f_1(t)$ is the RF field strength, and $\delta = f_0 - f_{\mathrm{rf}}$ is the offset in the rotating frame. The phase incremented part in the second term of Eq. (2) can be expressed as

$$\begin{aligned}&e^{-i[\varphi(t)+\varphi_0]I_z} I_x e^{i[\varphi(t)+\varphi_0]I_z} \\ &\quad = e^{-i(\omega_s t+\varphi_0)I_z}[e^{i[\omega_s t-\varphi(t)]I_z} I_x e^{-i[\omega_s t-\varphi(t)]I_z}]e^{i(\omega_s t+\varphi_0)I_z}\end{aligned}$$

$$= \frac{1}{2} e^{-i(\omega_s t + \varphi_0) I_z} [(I_x + iI_y) e^{i\alpha(t)} + (I_x - iI_y) e^{-i\alpha(t)}] e^{i(\omega_s t + \varphi_0) I_z}$$

$$= \frac{1}{2} e^{-i(\omega_s t + \varphi_0) I_z} [I_+ e^{i\alpha(t)} + I_- e^{-i\alpha(t)}] e^{i(\omega_s t + \varphi_0) I_z}, \tag{3}$$

where $\omega_s = \Delta\varphi/\Delta\tau = 2\pi\Delta f$, $\alpha(t) = \omega_s t - \varphi(t)$, and the ladder operators of $I_+ = I_x + iI_y$ and $I_- = I_x - iI_y$ with their properties under transformation[1,50]

$$e^{-i\varphi I_z} I_+ e^{i\varphi I_z} = I_+ e^{-i\varphi}, \tag{4a}$$

$$e^{-i\varphi I_z} I_- e^{i\varphi I_z} = I_- e^{i\varphi}. \tag{4b}$$

According to the definition, $\alpha(t)$ in Eq. (3) is a periodic function of t with a period of $\Delta\tau$ as shown in Fig. 3. Through the above procedure, the phase $\varphi(t)$, as it appeared in the exponential in Eq. (2), is now separated from the product of $\varphi(t)I_z$. Consequently, both terms of $e^{-i\alpha(t)}$ and $e^{i\alpha(t)}$, which are the function of $\varphi(t)$, can be expanded into a Fourier series of complex exponentials[51]

$$e^{-i\alpha(t)} = \sum_{n=-\infty}^{\infty} a_n e^{i(2n\pi/\Delta\tau)t}, \quad t \neq m\Delta\tau \quad (m \text{ integer}), \tag{5a}$$

$$e^{i\alpha(t)} = \sum_{n=-\infty}^{\infty} a_n^* e^{-i(2n\pi/\Delta\tau)t}, \quad t \neq m\Delta\tau, \tag{5b}$$

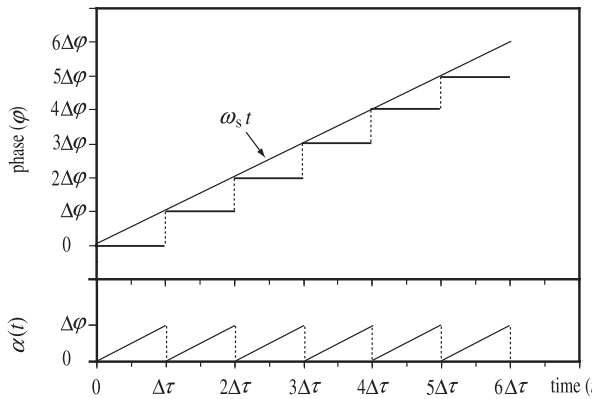

Fig. 3. The phase $\varphi(t)$ of a PIP (step function) and of a linearly increased phase $\omega_s t$ (straight line) in the rotating frame (top). The difference of the two phases $\alpha(t) = \omega_s t - \varphi(t)$ is periodic with a period of $\Delta\tau$ (bottom), where $-\alpha(t)$ is the phase in the second rotating frame with a speed of ω_s relative to the rotating frame.

with the expansion coefficients

$$a_n = \frac{1}{\Delta\tau}\int_0^{\Delta\tau} e^{-i\alpha(t)} e^{-i(2n\pi/\Delta\tau)t} dt, \tag{6}$$

where the expansion is performed over the first period, in which $\alpha(t) = \omega_s t$, due to the periodic nature of $e^{i\alpha(t)}$ and $e^{-i\alpha(t)}$. At $t = m\Delta\tau$, $e^{i\alpha(t)}$ and $e^{-i\alpha(t)}$ become non-continuous and at these jump points, the Fourier series in Eqs. (5a) and (5b), according to the Dirichlet theorem, converge to the arithmetic mean of the right-hand and left-hand limits of their own functions respectively

$$\sum_{n=-\infty}^{\infty} a_n = \frac{1 + e^{-i\Delta\varphi}}{2}, \tag{7a}$$

$$\sum_{n=-\infty}^{\infty} a_n^* = \frac{1 + e^{i\Delta\varphi}}{2}. \tag{7b}$$

These jump points, however, will not contribute to the evolution of the spin system since they have infinitesimal durations and therefore have no accumulative effects.

The expansion coefficients in Eq. (6) can be calculated straightforwardly

$$\begin{aligned} a_n &= \frac{1}{\Delta\tau}\int_0^{\Delta\tau} e^{-i\alpha(t)} e^{-i(2n\pi/\Delta\tau)t} dt = \frac{1}{\Delta\tau}\int_0^{\Delta\tau} e^{-i((2n\pi/\Delta\tau)+(\Delta\varphi/\Delta\tau))t} dt \\ &= \frac{i}{(2n\pi + \Delta\varphi)}\left[e^{-i\Delta\varphi} - 1\right] \\ &= \frac{2\sin(\Delta\varphi/2)}{(2n\pi + \Delta\varphi)}\, e^{-i(\Delta\varphi/2)} \\ &= \lambda_n e^{-i(\Delta\varphi/2)}, \end{aligned} \tag{8}$$

where

$$\lambda_n = \frac{2\sin(\Delta\varphi/2)}{(2n\pi + \Delta\varphi)} \tag{9}$$

is a scaling factor of the nth effective RF field and $e^{-i(\Delta\varphi/2)}$ introduces a phase shift of $-\Delta\varphi/2$ to all the effective RF fields.

It follows from Eqs. (5), (8), and (3), that

$$I_+e^{i\alpha(t)} + I_-e^{-i\alpha(t)} = \sum_{n=-\infty}^{\infty} \lambda_n \left[I_+ e^{-i((2n\pi/\Delta\tau)t - (\Delta\varphi/2))} + I_- e^{i((2n\pi/\Delta\tau)t - (\Delta\varphi/2))} \right]$$

$$= 2 \sum_{n=-\infty}^{\infty} \lambda_n e^{-i((2n\pi/\Delta\tau)t - (\Delta\varphi/2))I_z} I_x e^{i((2n\pi/\Delta\tau)t - (\Delta\varphi/2))I_z}, \quad (10)$$

where Eqs. (4a) and (4b) are used.

Substitution of Eqs. (3) and (10) into Eq. (2), the Hamiltonian becomes

$$\mathcal{H}(t) = \delta I_z + f_1(t) \sum_{n=-\infty}^{\infty} \lambda_n e^{-i[(2\pi\Delta f + \omega_n)t - (\Delta\varphi/2) + \varphi_0]I_z} I_x e^{i[(2\pi\Delta f + \omega_n)t - (\Delta\varphi/2) + \varphi_0]I_z}, \quad (11)$$

where $\omega_n = (2n\pi/\Delta\tau)$. The above equation shows that a PIP can be decomposed into an infinite number of effective RF fields applied simultaneously and separated equally in the frequency domain. The nth effective RF field, for example, is represented by

$$f_1(t)\lambda_n e^{-i[(2\pi\Delta f + \omega_n)t - (\Delta\varphi/2) + \varphi_0]I_z} I_x e^{i[(2\pi\Delta f + \omega_n)t - (\Delta\varphi/2) + \varphi_0]I_z}, \quad (12)$$

where the frequency of the nth field is shifted by $(\Delta f + \omega_n/2\pi)$ from the carrier, the field strength is scaled by λ_n, and the phase is subjected to a shift of $-\Delta\varphi/2$. Since this phase shift is introduced to all the effective RF fields it is termed the universal phase shift (UPS)

$$\text{UPS} = -\frac{\Delta\varphi}{2}. \quad (13)$$

According to Eqs. (8) and (9), the effective RF fields are scaled unsymmetrically (in respect to the sideband number n) by the scaling factor λ_n, in response to the unsymmetrical excitation profile. When $\lambda_n < 0$, the nth effective RF field becomes negative, which corresponds to a sign change of the operator I_x from positive to negative, or equivalently, a 180° phase shift is introduced to the nth effective RF field. Consequently, a phase inversion occurs in the transverse magnetization of the nth excitation band.

Even though all the effective RF fields have the same shape $f_1(t)$, the excitation profiles of different bands, strictly speaking, are not identical due to the different scaling factors and non-linear response of the spin system. They are, however, fairly close to each other, especially for those bands with comparable scaling factors.

2.3. Transformation between the rotating frame and the second rotating frame

All the effective RF fields created by a PIP are shifted from the carrier frequency f_{rf}. To calculate the nth excitation band for example, a transformation from the rotating frame to a new one (or the second rotating frame) is often needed, where the nth field plays the role of a new carrier. This transformation can be achieved by a unitary operator of[1]

$$U_n(t) = e^{-i(2\pi\Delta f + \omega_n)tI_z}. \tag{14}$$

After the calculation in the second rotating frame, a back transformation, in general, is needed to return to the conventional rotating frame

$$\sigma_R(\tau) = U_n(\tau)\sigma_{RR}(\tau)U_n^{-1}(\tau), \tag{15}$$

where $\sigma_{RR}(\tau)$ is the density matrix in the second rotating frame and it is the superposition of I_x, I_y, and I_z. The transformation corresponds to a rotation of $\sigma_{RR}(\tau)$ around I_z with a rotation angle

$$\zeta_n = (2\pi\Delta f + \omega_n)\tau = 2\pi\Delta f\tau, \tag{16}$$

leading to an additional phase shift. In the above equation, $(\tau/\Delta\tau) = N$ as an integer is used and $2\pi\Delta f\tau$ $(= (\Delta\varphi/\Delta\tau)\tau = \Delta\varphi \times N)$ can be considered as the total phase increment of the PIP (the actual phase is incremented up to $(N-1)\Delta\varphi$ as shown in Eq. (1) and Fig. 2 since the first step has a phase of 0°). The phase shift ζ_n in Eq. (16) is independent of the sideband number n and it vanishes if a PIP is designed with a total phase increment

$$2\pi\Delta f\tau = 2m\pi \quad (m \text{ integer}), \tag{17}$$

which corresponds to a coincidence of the two frames at time τ.

2.4. Energy conservation law in PIPs

As any RF pulse, each effective RF field created by a PIP dissipates power to the probe. The power by the nth effective field for the kth step,

for example, can be expressed as

$$P_n(k) \propto \frac{1}{\Delta\tau}\int_{(k-1)\Delta\tau}^{k\Delta\tau} \left(f_1(k)\lambda_n e^{-i[(2\pi\Delta f+\omega_n)t-(\Delta\varphi/2)+\varphi_0]}\right) \times \left(f_1(k)\lambda_n e^{-i[(2\pi\Delta f+\omega_n)t-(\Delta\varphi/2)+\varphi_0]}\right)^* dt = f_1^2(k)\lambda_n^2, \tag{18}$$

where both $f_1(k)$ and λ_n are real and time-independent. It can be easily shown that in the calculation of power dissipation, any interference term between two different effective RF fields, f_{1m} and f_{1n} $(m \neq n)$ for example, vanishes. Consequently, the total power dissipated by all the effective RF fields is then

$$\sum_{n=-\infty}^{\infty} P_n(k) \propto \sum_{n=-\infty}^{\infty} f_1^2(k)\lambda_n^2 = f_1^2(k)\sum_{n=-\infty}^{\infty}\lambda_n^2. \tag{19}$$

On the other hand, the total dissipated power by the PIP can be derived directly

$$P_{\mathrm{PIP}}(k) \propto \frac{1}{\Delta\tau}\int_{(k-1)\Delta\tau}^{k\Delta\tau} f_1^2(k)dt = f_1^2(k). \tag{20}$$

It follows from Eqs. (19) and (20) that the scaling factors of any PIP must satisfy the condition of

$$\sum_{n=-\infty}^{\infty}\lambda_n^2 = 1, \tag{21}$$

in order to observe the energy conservation law in PIPs.

Equation (21) can also be shown by the following property of the Fourier analysis[52]

$$\langle f|f\rangle = \sum_{n=-\infty}^{\infty} |a_n|^2\langle\psi_n|\psi_n\rangle, \tag{22}$$

where f is a continuous function, a_n are the coefficients of the Fourier expansion, and $\psi_n = e^{-i\omega_n t}$ are the orthogonal Eigenfunctions.

Because of the energy conservation law, the RF field strength of the centre band is scaled down to give up its energy to the effective RF fields of the

sidebands. To reduce the loss of the field strength of the centre band, the sideband excitations need to be minimized.

2.5. The symmetry of the scaling factors

The scaling factors of a PIP [Eq. (9)] as a function of $\Delta\varphi$ are plotted in Fig. 4 for $n = -2$ to 2, from which one can see that the scaling factor $\lambda_n(\Delta\varphi)$ is not equal to its counterpart

$$\lambda_n(\Delta\varphi) \neq \lambda_{-n}(\Delta\varphi). \tag{23}$$

It leads to unsymmetrical excitation bands in respect to the sideband number n. However, the scaling factor remains unchanged if both the side band number n and the phase increment $\Delta\varphi$ change sign

$$\lambda_n(\Delta\varphi) = \lambda_{-n}(-\Delta\varphi). \tag{24}$$

This symmetry implies that the RF field strengths for the sideband number n and its counterpart $-n$ exchange if $\Delta\varphi$ changes the sign, which can also be inferred from Fig. 4.

In the limiting case

$$\lim_{\Delta\varphi \longrightarrow 0^\circ} \lambda_n(\Delta\varphi) = \begin{cases} 1, & n = 0 \\ 0, & n \neq 0 \end{cases}. \tag{25}$$

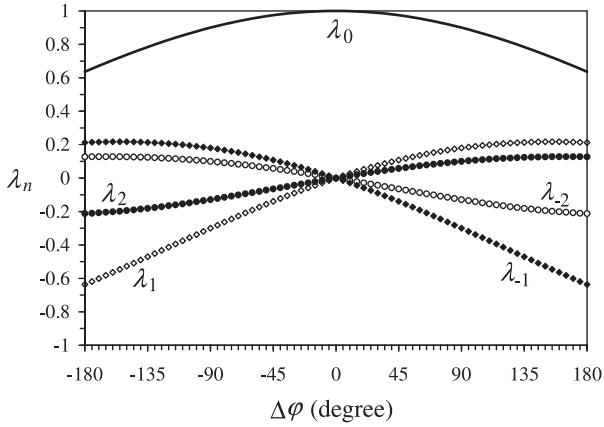

Fig. 4. The scaling factors λ_n ($n = -2$ to 2) of any PIPs as a function of the phase increment $\Delta\varphi$, where $\lambda_0(\Delta\varphi) = \lambda_0(-\Delta\varphi)$ and $\lambda_1(\Delta\varphi) = \lambda_{-1}(-\Delta\varphi)$, $\lambda_2(\Delta\varphi) = \lambda_{-2}(-\Delta\varphi)$.

This result is expected and in agreement with the energy conservation law in PIPs since under the above condition, the PIP reduces to a normal RF pulse with no phase increment. Consequently, the sideband excitations vanish and there is no scaling and UPS for the centre band.

From Eq. (9), it can also be shown that the minimum and maximum absolute values of $\lambda_n (n \neq 0)$ always occur at $\Delta\varphi \rightarrow \pm\pi$, i.e.,

$$|\lambda_n|_{\max} = \lim_{\Delta\varphi \longrightarrow -\pi} |\lambda_n(\Delta\varphi)| = \left|\frac{2}{(2n-1)\pi}\right|, \tag{26a}$$

$$|\lambda_n|_{\min} = \lim_{\Delta\varphi \longrightarrow \pi} |\lambda_n(\Delta\varphi)| = \left|\frac{2}{(2n+1)\pi}\right|, \tag{26b}$$

for $n > 0$, and

$$|\lambda_n|_{\max} = \lim_{\Delta\varphi \longrightarrow \pi} |\lambda_n(\Delta\varphi)| = \left|\frac{2}{(2n+1)\pi}\right|, \tag{26c}$$

$$|\lambda_n|_{\min} = \lim_{\Delta\varphi \longrightarrow -\pi} |\lambda_n(\Delta\varphi)| = \left|\frac{2}{(2n-1)\pi}\right|, \tag{26d}$$

for $n < 0$. It follows from the above four equations that

$$|\lambda_n|_{\max} = |\lambda_{-n}|_{\max} = \frac{2}{(2|n|-1)\pi}, \tag{27a}$$

$$|\lambda_n|_{\min} = |\lambda_{-n}|_{\min} = \frac{2}{(2|n|+1)\pi}, \tag{27b}$$

$$|\lambda_n|_{\min} = |\lambda_{|n|+1}|_{\max} = \frac{2}{(2|n|+1)\pi}. \tag{27c}$$

For the centre band, it can be shown that

$$\lambda_{0\max} = \lim_{\Delta\varphi \longrightarrow 0^\circ} \lambda_0(\Delta\varphi) = 1, \tag{28a}$$

$$\lambda_{0\min} = \lim_{\Delta\varphi \longrightarrow \pm\pi} \lambda_0(\Delta\varphi) = \frac{2}{\pi}. \tag{28b}$$

A conclusion can be drawn from Eqs. (26) to (28) that the greater the $|n|$, the weaker the effective RF field strength

$$|\lambda_0(\Delta\varphi)| \geq |\lambda_{\pm1}(\Delta\varphi)| \geq |\lambda_{\pm2}(\Delta\varphi)| \geq |\lambda_{\pm3}(\Delta\varphi)| \cdots, \tag{29}$$

for any $\Delta\varphi$.

2.6. The constrain on the phase increment

In Section 2.1, the phase increment is defined in the range of $-\pi \leq \Delta\varphi \leq \pi$ and it sets a boundary of the frequency shift (Fig. 5)

$$-\Delta f_{\max} \leq \Delta f \leq \Delta f_{\max}, \tag{30}$$

where $\Delta f_{\max} = (\Delta\varphi/2\pi\Delta\tau) = 1/(2\Delta\tau)$. These conditions, however, are not imposed upon the theory of PIPs. A phase increment $\Delta\varphi = \pi + \varepsilon\,(0 < \varepsilon < \pi)$ for instance is an eligible value to be used in the calculation of the effective RF fields. Correspondingly, the frequency shift of the centre band

$$\Delta f = \frac{\Delta\varphi}{2\pi\Delta\tau} = \Delta f_{\max} + \frac{\varepsilon}{2\pi\Delta\tau} = \Delta f_{\max} + \delta f, \tag{31}$$

which falls outside the boundary as shown in Fig. 5; the scaling factor

$$|\lambda_0| = \left|\frac{2\sin[(\pi+\varepsilon)/2]}{\pi+\varepsilon}\right| < |\lambda_{-1}| = \left|\frac{2\sin[(\pi+\varepsilon)/2]}{-\pi+\varepsilon}\right|; \tag{32}$$

and the location of the sideband for $n = -1$ falls into the boundary of the frequency shift, a territory designated for the centre bands.

All the above results, which are true but not desired, can be avoided by using a complementary phase increment

$$\Delta\varphi = (\pi + \varepsilon) - 2\pi = -\pi + \varepsilon. \tag{33}$$

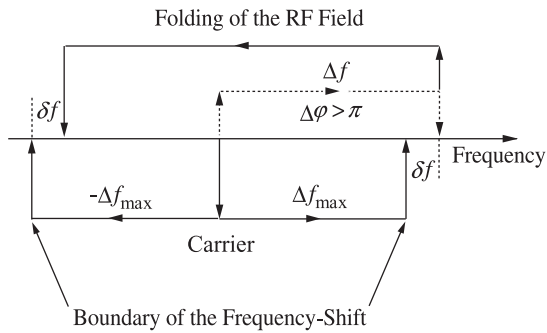

Fig. 5. The boundary of the frequency shift, $-\Delta f_{\max} \leq \Delta f \leq \Delta f_{\max}\ (=1/(2\Delta\tau))$, formed by any PIPs with a range of phase increment $-\pi \leq \Delta\varphi \leq \pi$. A phase increment $\Delta\varphi > \pi$ creates a frequency shift $\Delta f > \Delta f_{\max}$, but the strongest RF field ($n = -1$, in this case) is shifted to a negative position as if it were folded into the boundary from the centre band.

Under this condition, the frequency shift of the centre band becomes

$$\Delta f = \frac{\Delta\varphi}{2\pi\Delta\tau} = -\Delta f_{\max} + \frac{\varepsilon}{2\pi\Delta\tau} = -\Delta f_{\max} + \delta f, \tag{34}$$

which falls inside the boundary; the scaling factor

$$|\lambda_0| = \left|\frac{2\sin[(-\pi+\varepsilon)/2]}{-\pi+\varepsilon}\right| > |\lambda_1| = \left|\frac{2\sin[(-\pi+\varepsilon)/2]}{\pi+\varepsilon}\right|; \tag{35}$$

and the locations of the sideband RF fields fall outside the boundary. Except for the sideband number n and the sign of the scaling factors, the overall results of the two cases, including the frequencies, phases, and strengths of all the effective RF fields, are the same and they are summarized in Table 1.

As shown above, a phase increment $\Delta\varphi > \pi$ ($\Delta\varphi < 2\pi$) will not create a frequency shift Δf of the strongest RF field greater than $\Delta f_{\max} = 1/(2\Delta\tau)$. Rather, the strongest field is shifted to a negative position as if it were folded into the boundary of the frequency shift from the original centre band (Fig. 5), resembling the folding of NMR peaks into the spectral window caused by a slower sampling rate than the Nyquist frequency. The folded RF field can be derived with the complementary phase increment $\Delta\varphi - 2\pi$. However, the easiest way for avoiding the confusions is to define a range of the phase increment, $-\pi \le \Delta\varphi \le \pi$, as defined in Section 2.1. In this way, the centre band RF field of the strongest field strength falls inside the boundary while all the sideband RF fields of weaker field strengths fall outside the boundary.

Table 1. Comparison between the results by two PIPs, one with a phase increment of $\Delta\varphi = 234°$ and the other with a complementary phase increment of $\Delta\varphi = -126°$. For both PIPs, the time increment $\Delta\tau = 50$ μs and RF field strength $f_1 = 1.235$ kHz. The phase includes a UPS $= -(\Delta\varphi/2)$ and a 180° if $\lambda_n < 0$

Phase increment		$\Delta\varphi = 234°$				
Sideband number	n	−2	−1	0	1	2
Frequency (kHz)	f_n	−33	−13	13	33	53
Scaling factor	λ_n	−0.210	−0.810	0.436	0.172	0.107
Field strength (kHz)	f_{1n}	0.259	1.000	0.539	0.212	0.132
Phase	θ_n	63°	63°	−117°	−117°	−117°
Complementary phase increment		$\Delta\varphi = -126°$				
Sideband number	n	−1	0	1	2	3
Frequency (kHz)	f_n	−33	−13	13	33	53
Scaling factor	λ_n	0.210	0.810	−0.436	−0.172	−0.107
Field strength (kHz)	f_{1n}	0.259	1.000	0.539	0.212	0.132
Phase	θ_n	63°	63°	−117°	−117°	−117°

With Eqs. (9) and (11), the same effective RF fields are derived for $\Delta\varphi = \pi$ and $\Delta\varphi = -\pi$ since the two phase increments are indistinguishable.

2.7. Computer simulation of the excitation profiles

To verify the theory of PIP, a computer program using C language was developed. It can be used to directly calculate the excitation profiles by PIPs or any other RF pulses. The calculation is based on the Bloch vector model for a non-interacting spin-1/2 system, where the spin-lattice relaxation during the pulse is neglected. The basic idea of the program is discussed as follows.

The kth increment of a PIP creates a kth rotation around its effective RF field[1]

$$e^{-i(\beta_k \boldsymbol{n}_k \cdot \boldsymbol{I})} \sigma_{k-1} e^{i(\beta_k \boldsymbol{n}_k \cdot \boldsymbol{I})}, \tag{36}$$

where σ_{k-1} is the density operator just before the kth step of a PIP and $\boldsymbol{n}_k$ is a unit vector of the kth step defined in terms of the field strength $f_1(k)$, phase φ_k, and offset δ

$$n_{kx} = \frac{f_1(k)\cos(\varphi_k)}{\sqrt{f_1^2(k) + \delta^2}}, \tag{37a}$$

$$n_{ky} = \frac{f_1(k)\sin(\varphi_k)}{\sqrt{f_1^2(k) + \delta^2}}, \tag{37b}$$

$$n_{kz} = \frac{\delta}{\sqrt{f_1^2(k) + \delta^2}}, \tag{37c}$$

and the kth rotational angle is determined by

$$\beta_k = 2\pi\sqrt{f_1^2(k) + \delta^2}\,\Delta\tau, \tag{37d}$$

where all steps are assumed to have the same width $\Delta\tau$.

The rotation described by Eq. (36) can be expressed by a 2×2 matrix[50]

$$R_k = \begin{bmatrix} \cos\left(\frac{\beta_k}{2}\right) - i n_{kz}\sin\left(\frac{\beta_k}{2}\right) & (-i n_{kx} - n_{ky})\sin\left(\frac{\beta_k}{2}\right) \\ (-i n_{kx} + n_{ky})\sin\left(\frac{\beta_k}{2}\right) & \cos\left(\frac{\beta_k}{2}\right) + i n_{kz}\sin\left(\frac{\beta_k}{2}\right) \end{bmatrix}. \tag{38}$$

The overall rotation by a PIP is then

$$R = R_N \cdots R_2 R_1, \tag{39}$$

where R is also a 2×2 matrix. In the above representation, the three operators I_x, I_y, and I_z, are the well-known Pauli matrices[6]

$$I_x = \frac{1}{2}\begin{bmatrix} 0 & 1 \\ 1 & 0 \end{bmatrix}, \quad I_y = \frac{1}{2}\begin{bmatrix} 0 & -i \\ i & 0 \end{bmatrix}, \quad I_z = \frac{1}{2}\begin{bmatrix} 1 & 0 \\ 0 & -1 \end{bmatrix}. \tag{40}$$

The three components of the final magnetization, which are normalized and the function of the offset δ, can be obtained by

$$\langle I_\alpha \rangle(\delta) = 2\mathrm{Tr}[I_\alpha R \sigma_0 R^{-1}], \quad \alpha = x, y, z, \tag{41}$$

where σ_0 is the initial density matrix and is often represented by I_z. The phase of the excitation profile, which depends also on the offset δ, can be calculated by

$$\vartheta(\delta) = \cos^{-1}\left(\frac{\langle I_x \rangle(\delta)}{\sqrt{[\langle I_x \rangle(\delta)]^2 + [\langle I_y \rangle(\delta)]^2}}\right), \quad \text{if } \langle I_y \rangle(\delta) \geq 0, \tag{42a}$$

$$\vartheta(\delta) = -\cos^{-1}\left(\frac{\langle I_x \rangle(\delta)}{\sqrt{[\langle I_x \rangle(\delta)]^2 + [\langle I_y \rangle(\delta)]^2}}\right), \quad \text{if } \langle I_y \rangle(\delta) < 0. \tag{42b}$$

The overall rotation angle for a particular offset δ can also be obtained from the rotation matrix defined in Eqs. (38) and (39)

$$\beta(\delta) = 2\cos^{-1}\{\mathrm{Re}[R_{11}(\delta)]\}, \tag{43}$$

where $R_{11}(\delta)$ is the element of the rotation matrix of $R(\delta)$.

In a similar way, the overall rotation axis as a function of the offset can be derived from the rotation matrix

$$n_x(\delta) = \frac{-\mathrm{Im}[R_{12}(\delta)]}{\sin(\beta/2)}, \tag{44a}$$

$$n_y(\delta) = \frac{-\mathrm{Re}[R_{12}(\delta)]}{\sin(\beta/2)}, \tag{44b}$$

$$n_z(\delta) = \frac{-\mathrm{Im}[R_{11}(\delta)]}{\sin(\beta/2)}. \tag{44c}$$

From the above rotation axis, the phase of the effective RF field of a PIP can be calculated

$$\theta_n(\delta_n) = \cos^{-1}\left(\frac{n_x(\delta_n)}{\sqrt{n_x^2(\delta_n)+n_y^2(\delta_n)}}\right), \quad \text{if } n_y(\delta_n) \geq 0, \tag{45a}$$

$$\theta_n(\delta_n) = -\cos^{-1}\left(\frac{n_x(\delta_n)}{\sqrt{n_x^2(\delta_n)+n_y^2(\delta_n)}}\right), \quad \text{if } n_y(\delta_n) < 0, \tag{45b}$$

where $\delta_n = (\Delta f + \omega_n/2\pi)$ is the offset at which the nth effective RF field resides. Further, from the rotation angle $\beta_n(\delta_n)$ [Eq. (43)] and the axis [Eqs. (44a) to (44c)] it is straightforward to obtain the field strength f_{1n} and the scaling factor λ_n of the effective RF field.

It is worth mentioning that the phase $\theta_n(\delta_n)$ is computed in the rotating frame and the result is the same as in the second rotating frame with a speed of $2\pi\Delta f + \omega_n$ relative to the carrier frequency if the PIP satisfies the condition of $2\pi\Delta f\tau = 2m\pi$. Otherwise, the simulated phase may be different from the calculated one and may lose its physical meaning since there are numerous ways to rotate a magnetization from the initial position to the final destination. To avoid this problem, the PIP may be prolonged or shortened to meet the condition of $2\pi\Delta f\tau = 2m\pi$ and one can get the phase θ_n, which is independent of the length of the PIP as long as the condition is satisfied. The phase for the original PIP can then be obtained through a proper frame transformation discussed in Section 2.3.

2.8. The excitation profile by a PIP

A Gaussian shaped PIP10 (0°, 144°, 40 μs, $f_1(k)$, 125) is constructed with $f_1(k) = 0.1577\exp[-0.002(k-63)^2]$ kHz, $k = 1, 2, \ldots, 125$ and a pulsewidth $\tau = 5$ ms. Under those conditions, the frequency shift of the PIP $\Delta f = (\Delta\phi/2\pi\Delta\tau) = 10$ kHz, the frequency separation between the adjacent RF fields $\Delta = (1/\Delta\tau) = 25$ kHz, and the UPS $= -72°$. All the scaling factors λ_n can be calculated from Eq. (9). Disregarding the scaling factor λ_0, the RF field for the centre band is a 90° pulse and the amplitude of each band can be calculated in terms of

$$A_n = |\sin(\lambda_n 90°)|. \tag{46}$$

All the parameters of the PIP are listed in Table 2 for $n = -2$ to 2, together with the results obtained from the computer simulation discussed in Section 2.7.

Table 2. The frequencies f_n, phases θ_n, scaling factors λ_n of the effective RF fields and the amplitudes A_n of the excitation bands created by a Gaussian shaped PIP10 (0°, 144°, 40μs, $f_1(k)$, 125) with $f_1(k) = 0.1577 \exp[-0.002 \times (k-63)^2]$ kHz and a total phase increment $2\pi\Delta f\tau = 2m\pi$

Sideband number	n	−2	−1	0	1	2
Frequency	f_n (kHz)	−40	−15	10	35	60
Computer simulated						
Amplitude	A_n	0.293	0.712	0.928	0.333	0.197
Phase	θ_n	108.0°	108.0°	−72.0°	−72.0°	−72.0°
Scaling factor	λ_n	−0.189	−0.505	0.757	0.216	0.126
Calculated						
Amplitude	A_n	0.293	0.712	0.928	0.333	0.197
Phase	θ_n	108°	108°	−72°	−72°	−72°
Scaling factor	λ_n	−0.189	−0.505	0.757	0.216	0.126

Reprinted from Ref. 25 with permission from the American Institute of Physics publications.

For $n = -1$ and -2, the scaling factors $\lambda_n < 0$, a phase inversion occurs as discussed above. The phases of the effective RF fields ($n = -1, -2$) become $\theta_n = \mathrm{UPS} + 180° = -72° + 180° = 108°$. Since this PIP satisfies the condition of $2\pi\Delta f\tau = 100\pi$ [Eq. (17)], the transformation from the second rotating frame back to the rotating frame is not necessary. The computer simulated peaks are slightly shifted (several Hertz), due to the interference between the effective RF fields which will be discussed in Section 4. For comparison, the values of A_n and θ_n in Table 2 are taken at the calculated frequencies f_n. The calculated values of A_n and θ_n agree well with the computer simulated ones indicating the accuracy of the theory of PIP.

The excitation bands ($n = -2$ to 2) of the PIP are shown in Fig. 6. As expected, it appears to be unsymmetrical regarding the centre band at 10 kHz in response to the unsymmetrical scaling factors.

For comparison, another PIP is constructed with the same parameters as the previous one except for the phase increment $\Delta\varphi = 0.82\pi$. For this PIP, $2\pi\Delta f\tau = 102.5\pi$ and a back transformation from the second rotating frame to the conventional rotating frame is needed. It corresponds to adding 0.5π (90°) to the phase (RR) in the second rotating frame. The final phases θ_n of the effective RF fields in the rotating frame agree well with the computer simulated results as shown in Table 3.

In some cases only the frequency-shifted centre band is desired and the sideband excitations need to be minimized. This can be achieved by using a small $\Delta\varphi$. For instance, if $|\Delta\varphi| < 30°$, $|\lambda_0(\Delta\varphi)| > 0.9886$, and $|\lambda_n(\Delta\varphi)| < 0.0899$ for any n except for $n = 0$. In this case, the field strength of the centre band is only slightly affected and the field strengths of the sidebands are negligibly small. Furthermore, the sideband can be moved to outside the spectral width

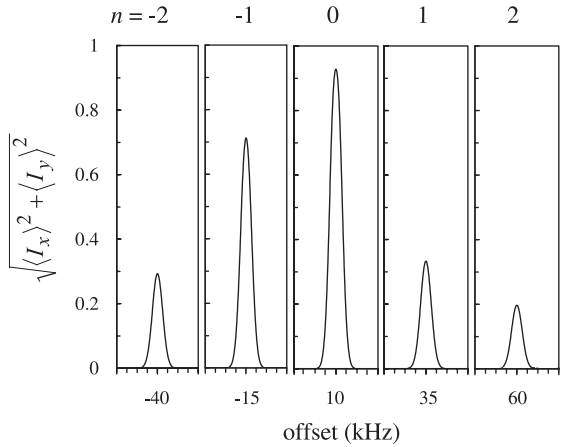

Fig. 6. Computer simulated excitation bands ($n = -2$ to 2) by a Gaussian shaped PIP (Table 2), where the centre band ($n = 0$) is shifted to 10 kHz and the spectral width of each band is 4 kHz. The amplitudes of the profiles are asymmetric in response to the asymmetric effective RF fields.

Table 3. The frequencies f_n, phases θ_n of the effective RF fields and the amplitudes A_n of the excitation bands created by a Gaussian shaped PIP with the same parameters as that in Table 2, except for a $\Delta\phi = 0.82\pi$ and $2\pi\Delta f\tau = (2m + 0.5)\pi$

Sideband number	n	-2	-1	0	1	2
Frequency	f_n(kHz)	-39.75	-14.75	10.25	35.25	60.25
Computer simulated						
Amplitude	A_n	0.297	0.727	0.921	0.334	0.198
Phase	θ_n	$-163.8°$	$-163.8°$	16.2°	16.2°	16.2°
Scaling factor	λ_n	-0.192	-0.518	0.746	0.217	0.127
Calculated						
Amplitude	A_n	0.297	0.727	0.921	0.334	0.198
Phase (RR)	θ_n	106.2°	106.2°	$-73.8°$	$-73.8°$	$-73.8°$
Phase	θ_n	$-163.8°$	$-163.8°$	16.2°	16.2°	16.2°
Scaling factor	λ_n	-0.192	-0.518	0.746	0.217	0.127

Reprinted from Ref. 25 with permission from the American Institute of Physics publications.

by using a small time increment $\Delta\tau$ so that $(1/\Delta\tau) >$ the spectral width. To obtain a frequency shift $\Delta f = 25$ kHz for example, one may choose $\Delta\varphi = \pi/10$ and $\Delta\tau = 2$ μs. The sidebands for $n = \pm 1$ are located at $(1/\Delta\tau) = 500$ kHz away from the centre band, which is usually far outside the spectral width. The UPS can be compensated by adding an initial phase $\varphi_0 = -\text{UPS} = \Delta\varphi/2$ to all the steps of the PIP or by anti-symmetrizing the PIP as discussed in Section 4.5.

3. MULTIPLE EFFECTIVE RF FIELDS CREATED BY A PERIODIC RF PULSE

3.1. Periodic pulse

It is well-known that the excitation profile by a periodic pulse also has a pattern of multiple bands in response to the multiple effective RF fields. The DANTE sequence,[26] for instance, was one of the most frequently used periodic pulse in the past for selective excitation of a narrow centre band. It is constructed by a long train of hard pulses with a certain delay between two adjacent pulses. The advantage of using the DANTE sequence over the weak, soft RF pulses relies on that it is not necessary to change the RF power level in the pulse sequence. Consequently, phase distortions and certain delays accompanied by the abrupt changes of the RF power level are avoided.

In general, a periodic pulse is composed of multiple identical shaped pulses and each shaped pulse is in turn composed of a number of back-to-back hard pulses with same or different strengths. The periodic pulse can be described by its x and y components of the RF field, i.e., $f_{1x}(t)$ and $f_{1y}(t)$ with a period of T and a pulsewidth τ. These two components satisfy the periodic conditions of $f_{1x}(t+T)=f_{1x}(t)$ and $f_{1y}(t+T)=f_{1y}(t)$, respectively.

3.2. Calculation of the effective RF fields by a periodic RF pulse

For a non-interacting spin-1/2 system subjected to a periodic RF irradiation, the Hamiltonian in the rotating frame can be expressed as[1,2]

$$\mathcal{H}(t) = \delta I_z + f_{1x}(t) I_x + f_{1y}(t)\, I_y \quad \text{(in Hz)}. \tag{47}$$

The x and y components of the RF field in the above equation can be expanded into a Fourier series of complex exponentials[51]

$$f_{1\alpha}(t) = \sum_{n=-\infty}^{\infty} a_{n\alpha} e^{i\omega_n t}, \quad \alpha = x, y, \tag{48}$$

where $\omega_n = 2n\pi/T$ and the complex expansion coefficients

$$a_{n\alpha} = \frac{1}{T}\int_0^T f_{1\alpha}(t) e^{-i\omega_n t} dt. \tag{49}$$

Here $a_{-n\alpha} = a^*_{n\alpha}$ since $f_{1\alpha}(t)$ is real. With the above expansion, the term $f_{1\alpha}(t)I_\alpha$ in Eq. (47) can be rearranged in the following way

$$\begin{aligned}(a_{n\alpha}e^{i\omega_n t} + a_{-n\alpha}e^{-i\omega_n t})I_\alpha &= 2|a_{n\alpha}|\left[\frac{\mathrm{Re}(a_{n\alpha})\cos(\omega_n t) - \mathrm{Im}(a_{n\alpha})\sin(\omega_n t)}{|a_{n\alpha}|}\right]I_\alpha \\ &= 2|a_{n\alpha}|[\cos(\theta_{n\alpha})\cos(\omega_n t) - \sin(\theta_{n\alpha})\sin(\omega_n t)]I_\alpha \\ &= 2|a_{n\alpha}|[\cos(\omega_n t + \theta_{n\alpha})]I_\alpha \\ &= |a_{n\alpha}|[e^{-i(\omega_{-n}t+\theta_{-n\alpha})I_z}I_\alpha e^{i(\omega_{-n}t+\theta_{-n\alpha})I_z} \\ &\quad + e^{-i(\omega_n t+\theta_{n\alpha})I_z}I_\alpha e^{i(\omega_n t+\theta_{n\alpha})I_z}], \end{aligned} \tag{50}$$

where $|a_{n\alpha}| = \sqrt{\mathrm{Re}(a_{n\alpha})^2 + \mathrm{Im}(a_{n\alpha})^2} = |a_{-n\alpha}|$, $\omega_n = (2n\pi/T) = -\omega_{-n}$, and the phase

$$\theta_{n\alpha} = \Theta\cos^{-1}(\mathrm{Re}(a_{n\alpha})/|a_{n\alpha}|), \tag{51a}$$

with

$$\Theta = \begin{cases} +1, & \text{if} \quad \mathrm{Im}(a_{n\alpha}) \geq 0 \\ -1, & \text{if} \quad \mathrm{Im}(a_{n\alpha}) < 0. \end{cases} \tag{51b}$$

Since $a_{-n\alpha} = a^*_{n\alpha}$ or $\mathrm{Re}(a_{-n\alpha}) = \mathrm{Re}(a_{n\alpha})$, $\mathrm{Im}(a_{-n\alpha}) = -\mathrm{Im}(a_{n\alpha})$, and $|a_{-n\alpha}| = |a^*_{n\alpha}|$, it follows from Eqs. (51a) and (51b) that

$$\theta_{-n\alpha} = -\theta_{n\alpha}. \tag{51c}$$

Substitution of Eqs. (48) and (50) into Eq. (47), one obtains

$$\begin{aligned}\mathcal{H} = \delta I_z + \sum_{n=-\infty}^{\infty}[&\bar{f}_{1x}\lambda_{nx}e^{-i(\omega_n t+\theta_{nx})I_z}I_x e^{i(\omega_n t+\theta_{nx})I_z} \\ &+ \bar{f}_{1y}\lambda_{ny}e^{-i(\omega_n t+\theta_{ny})I_z}I_y e^{i(\omega_n t+\theta_{ny})I_z}], \end{aligned} \tag{52a}$$

where

$$\bar{f}_{1\alpha} = (1/T)\int_0^T f_{1\alpha}(t)dt, \quad \alpha = x, y, \tag{52b}$$

are the average values of the effective RF fields, and

$$\lambda_{n\alpha} = |a_{n\alpha}|/\bar{f}_{1\alpha} \tag{52c}$$

and $\theta_{n\alpha}$ defined in Eq. (51a) are the scaling factors and phases of the nth effective RF field, respectively. In Eq. (52c), $\bar{f}_{1\alpha} \neq 0$ is assumed. In case of $\bar{f}_{1\alpha} = 0$, the effective RF field of the centre band vanishes (this may not be true for the sidebands), which is usually not a desired periodic pulse.

Similar to the PIP, the Hamiltonian [Eq. (52a)] of a periodic pulse shows an infinite number of effective RF fields with both x and y components of the scaling factors $\lambda_{n\alpha}$ and the phases $\theta_{n\alpha}$. The periodic pulse, however, acquires a different symmetry as that of the PIP. From Eq. (52c) and $a_{-n\alpha} = a^*_{n\alpha}$, it follows that the scaling factor $\lambda_{n\alpha}$ is symmetric in respect to the sideband number n, while the phase $\theta_{n\alpha}$ is anti-symmetric according to Eq. (51c). These symmetries seem to be a coincidence arising from the mathematical derivations. As a matter of fact, they are the intrinsic natures of the periodic pulse. Considering the term $f_{1x}(t)I_x$ for instance, any I_y component created by the rotating field denoted by ω_n must be compensated at any time t by its counter-component ω_{-n} in order to reserve the amplitude modulated RF field.

3.3. Energy conservation law in periodic pulses

As in the PIP, each effective RF field dissipates power to the probe. The total power over a period of T by all the effective RF fields can be described by

$$\sum_{n=-\infty}^{\infty} P_{n\alpha}(T) \propto \sum_{n=-\infty}^{\infty} \bar{f}_{1\alpha}^2 \lambda_{n\alpha}^2 = \bar{f}_{1\alpha}^2 \sum_{n=-\infty}^{\infty} \lambda_{n\alpha}^2. \tag{53}$$

The dissipated power can also be calculated directly from the periodic pulse

$$P_{\text{periodic pulse}}(T) \propto \frac{1}{T}\int_0^T f_{1\alpha}^2(t)dt = f_{1\alpha\text{rms}}^2, \tag{54}$$

where $f_{1\alpha\text{rms}}^2$ is the root-mean-square value of the RF field. To observe the energy conservation law in periodic pulses, the scaling factors must fulfill the condition of

$$\sum_{n=-\infty}^{\infty} \lambda_{n\alpha}^2 = \frac{f_{1\alpha\text{rms}}^2}{\bar{f}_{1\alpha}^2}. \tag{55}$$

Similar to the case of the PIP, the more power dissipated by the RF fields of the sidebands, the less the power of the centre band.

3.4. Excitation profiles by periodic pulses

A periodic 90° pulse is going to be discussed first and then a DANTE sequence follows. The periodic pulse is described by $f_{1x}|\sin(\pi t/T)|I_x$, with a period $T = 100$ μs, $f_{1x} = 0.025\pi$ kHz, and a pulsewidth $\tau = 5$ ms.

According to Eq. (49), the expansion coefficients of the pulse can be obtained conveniently

$$\begin{aligned} a_n &= \frac{1}{T}\int_0^T f_{1x}|\sin(\pi t/T)|e^{-i\omega_n t}dt \\ &= \frac{-2f_{1x}}{(4n^2-1)\pi}, \end{aligned} \tag{56}$$

from which the scaling factors and phases can be deduced using Eqs. (52b), (52c), and (51a) to (51c)

$$\lambda_n = \lambda_{-n} = \left|\frac{1}{(4n^2-1)}\right|, \tag{57}$$

and

$$\begin{cases} \theta_0 = 0^\circ \\ \theta_n = -\theta_{-n} = 180^\circ, \quad n \neq 0. \end{cases} \tag{58}$$

The Hamiltonian of this periodic pulse becomes [refer to Eq. (52a)]

$$\mathcal{H} = \delta I_z + \frac{2f_{1x}}{\pi}\sum_{n=-\infty}^{\infty} \lambda_n e^{-i(\omega_n t+\theta_n)I_z} I_x e^{i(\omega_n t+\theta_n)I_z}, \tag{59}$$

where $2f_{1x}/\pi$ is the average value of the pulse strength. The amplitude of each excitation band is determined by

$$A_n = |\sin(\lambda_n 90^\circ)|. \tag{60}$$

Since $\lambda_0 = 1$ and $\theta_0 = 0$, there is no scaling and phase shift for the centre band excitation which is created simply by the average RF field. All other

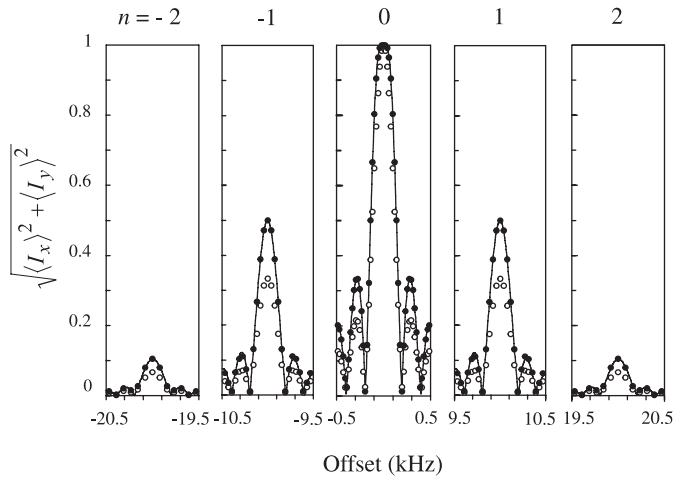

Fig. 7. The excitation profiles ($n = -2$ to 2) by a periodic pulse of $f_{1x}|\sin(\pi t/T)|I_x$, where the solid lines are computer simulated results, solid circles are calculated with the effective RF fields, and open circles are obtained from the Fourier transformation of the RF shape. In the computer simulation, the pulse is composed of 4001 steps and has a pulsewidth $\tau = 5$ ms. Reprinted from Ref. 27 with permission from Elsevier.

excitation bands are subjected to scaling in pulse strengths and shifts in phases. It is well-known that an analytical excitation profile can be obtained if one knows the pulse strength and phase of the RF field. Therefore, the excitation bands by the effective RF fields for $n = -2$ to 2 are derived as shown in Fig. 7 together with the results obtained directly from the computer simulation of the RF field $f_{1x}|\sin(\pi t/T)|I_x$. The results from the Fourier transformation method of the pulse shape are also shown, where the amplitude of the centre band is normalized to 1 for comparison. The calculated results agree well with the computer simulated ones, while the results from the Fourier transformation deviate substantially mainly due to the non-linearity and quantum nature of the spin system. For the same reason, the shapes of the excitation sidebands are different for different sideband numbers $|n|$. On the other hand, no matter what the sideband number n is, the Fourier transformation method creates a uniform shape, differing only in amplitudes. It is a unique trait arising from the method.

As shown in Table 4, the strengths of the effective RF fields are symmetrical while the phases are anti-symmetrical in terms of the sideband number n as expected for a periodic pulse (refer to Section 3.2). In addition, the calculated results agree well with the computer simulated ones.

As a second example, a DANTE sequence is taken into account with a period $T = 200$ μs, the pulsewidth of a single pulse $d = 10$ μs, pulse strength $f_{1x} = 1$ kHz, and pulsewidth $\tau = 5$ ms. As in the previous case, the expansion

Table 4. The frequencies f_n, phases θ_n, scaling factors λ_n of the effective RF fields, and the amplitudes A_n of the excitation bands created by a periodic pulse of $f_{1x}|\sin(\pi t/T)|I_x$, with 4001 steps and a pulsewidth $\tau = 5$ ms

Sideband number	n	-2	-1	0	1	2
Frequency	f_n(kHz)	-20	-10	0	10	20
Computer simulated						
Amplitude	A_n	0.105	0.500	1.000	0.500	0.105
Phase	θ_n	180.0°	180.0°	0.0°	180.0°	180.0°
Calculated						
Amplitude	A_n	0.105	0.500	1.000	0.500	0.105
Phase	θ_n	180°	180°	0°	180°	180°
Scaling factor	λ_n	1/15	1/3	1	1/3	1/15

Reprinted from Ref. 27 with permission from Elsevier.

coefficients, scaling factors, and phases can be obtained straightforwardly

$$a_n = \frac{1}{T}\int_0^T f_{1x}(t)e^{-i\omega_n t}dt$$

$$= \frac{f_{1x}}{T}\int_0^d e^{-i(2n\pi/T)t}dt$$

$$= \frac{f_{1x}}{2n\pi}\left\{\sin\left(\frac{2n\pi d}{T}\right) - i\left[1-\cos\left(\frac{2n\pi d}{T}\right)\right]\right\}, \quad n \neq 0, \tag{61a}$$

$$a_0 = \frac{d}{T}f_{1x}, \tag{61b}$$

and

$$\lambda_n = \left|\frac{T}{n\pi d}\sin\left(\frac{n\pi d}{T}\right)\right|, \quad n \neq 0, \tag{62a}$$

$$\lambda_0 = 1, \tag{62b}$$

and

$$\theta_n = -\frac{n}{|n|}\left[\left|\frac{n\pi d}{T}\right| \bmod \pi\right], \quad n \neq 0, \tag{63a}$$

$$\theta_0 = 0. \tag{63b}$$

Table 5. The frequencies f_n, phases θ_n, scaling factors λ_n of the effective RF fields, and the amplitudes A_n of the excitation bands created by a DANTE sequence

Sideband number	n	-10	-5	0	5	10
Frequency	f_n(kHz)	-50	-25	0	25	50
Computer simulated						
Amplitude	A_n	0.841	0.988	1.000	0.988	0.841
Phase	θ_n	90.0°	45.0°	0.0°	$-45.0°$	$-90.0°$
Calculated						
Amplitude	A_n	0.842	0.988	1.000	0.988	0.842
Phase	θ_n	90°	45°	0°	$-45°$	$-90°$
Scaling factor	λ_n	0.637	0.900	1.000	0.900	0.637

Reprinted from Ref. 27 with permission from Elsevier.

For $|n\pi d/T| < \pi$, a linear phase shift is introduced as a function of sideband number n

$$\theta_n = -\frac{n\pi d}{T}. \tag{64}$$

Since $\lambda_0 = 1$ and $\theta_0 = 0$, the excitation profile of the centre band is equivalent to that by a pulse with the same pulsewidth and the average pulse strength, in agreement with the earlier conclusion.[26]

The scaling factors, phases, and amplitudes for $n = -10, -5, 0, 5$, and 10 are shown in Table 5, along with the results from the computer simulation. As expected, the scaling factors λ_n are symmetric while the phases θ_n are anti-symmetric.

4. NEAR NEIGHBOUR APPROXIMATION

4.1. RF interference

In both PIPs and periodic pulses, the Hamiltonians [Eqs. (11) and (52a)] can be generally expressed as

$$\mathcal{H}(t) = \delta I_z + \sum_{n=-\infty}^{\infty} f_{1n} e^{-i(\omega_n t+\theta_n)I_z} I_x e^{i(\omega_n t+\theta_n)I_z}. \tag{65}$$

If the strengths of any two effective RF fields is much smaller than their frequency separation, the RF interference between them is small and may be ignored. The examples discussed in Sections 2 and 3 belong to this category. On the contrary, if the strengths of the effective fields are much

stronger than their separation, the corresponding excitation bands may be distorted so severely that it is hard to get an analytical solution. Otherwise, the RF interference can be considered as a perturbation that can be calculated with the coherent averaging theory.[33]

4.2. RF interference by two RF fields

The simplest way to explore the RF interference is to consider a Hamiltonian with only two RF fields, the *0*th and *1*st RF fields for example

$$\mathcal{H}(t) = \delta I_z + f_{10} e^{-i\theta_0 I_z} I_x e^{i\theta_0 I_z} + f_{11} e^{-i(\omega_1 t+\theta_1) I_z} I_x e^{i(\omega_1 t+\theta_1) I_z} \quad \text{(in Hz)}, \tag{66}$$

where f_{10}, f_{11} and θ_0, θ_1 are the strengths and phases of the *0*th and *1*st RF fields, respectively.

According to the coherent averaging theory,[3,4,53] the zero-order average Hamiltonian can be obtained straightforwardly

$$\overline{\mathcal{H}}^{(0)} = \frac{1}{T}\int_0^T \mathcal{H}(t)dt = \delta I_z + f_{10} e^{-i\theta_0 I_z} I_x e^{i\theta_0 I_z}, \tag{67}$$

where the contribution from the *1*st RF field in Eq. (66) is averaged to zero over a period $T\,(=2\pi/\omega_1)$ and the pulsewidth $\tau = mT$ (m integer) is assumed.

Similarly, the first-order average Hamiltonian can be derived

$$\begin{aligned}\overline{\mathcal{H}}^{(1)} &= \frac{-i\pi}{T}\int_0^T dt_2 \int_0^{t_2} [\mathcal{H}(t_2), \mathcal{H}(t_1)]dt_1 \\ &= -\frac{\delta f_{11}}{\Delta} e^{-i\theta_1 I_z} I_x e^{i\theta_1 I_z} - \frac{f_{11}^2}{2\Delta} I_z + \frac{f_{11} f_{10}}{\Delta} \cos(\theta_{10}) I_z,\end{aligned} \tag{68}$$

where $\Delta = (1/T)$ is the frequency separation and $\theta_{10} = \theta_1 - \theta_0$ is the relative phase between the two RF fields.

It can be shown that the second-order average Hamiltonian has the form of

$$\begin{aligned}\overline{\mathcal{H}}^{(2)} = \frac{-2\pi^2}{3T}\int_0^T dt_3 \int_0^{t_3} dt_2 \int_0^{t_2} \big\{ &[\mathcal{H}(t_3), [\mathcal{H}(t_2), \mathcal{H}(t_1)]] \\ &+ [\mathcal{H}(t_1), [\mathcal{H}(t_2), \mathcal{H}(t_3)]] \big\} dt_1 \\ = -\frac{f_{11}^2}{\Delta^2} \delta I_z + \frac{f_{11} f_{10}}{\Delta^2} &\cos(\theta_{10}) \delta I_z + \cdots,\end{aligned} \tag{69}$$

where only the I_z component is shown explicitly and all the I_x and I_y components, which cause a small phase shift and disturbance of the excitation profile, are ignored.

Up to the second order, the average Hamiltonian can be written as

$$\begin{aligned}\overline{\mathcal{H}} &= \overline{\mathcal{H}}^{(0)} + \overline{\mathcal{H}}^{(1)} + \overline{\mathcal{H}}^{(2)} \\ &= \delta I_z + f_{10} e^{-i\theta_0 I_z} I_x e^{i\theta_0 I_z} - \frac{\delta f_{11}}{\Delta} e^{-i\theta_1 I_z} I_x e^{i\theta_1 I_z} \\ &\quad - \frac{f_{11}^2}{2(\Delta-\delta)} I_z + \frac{f_{11} f_{10}}{\Delta-\delta}\cos(\theta_{10}) I_z - \frac{f_1^2}{2\Delta^2}\delta I_z + \cdots,\end{aligned} \tag{70}$$

where $1+(\delta/\Delta) \approx 1/[1-(\delta/\Delta)]$ has been used. Ignoring the sixth (high order) term in Eq. (70) and all the other terms that are not shown explicitly, the average Hamiltonian becomes

$$\begin{aligned}\overline{\mathcal{H}} &= \delta I_z + f_{10} e^{-i\theta_0 I_z} I_x e^{i\theta_0 I_z} - \frac{\delta f_{11}}{\Delta} e^{-i\theta_1 I_z} I_x e^{i\theta_1 I_z} \\ &\quad - \frac{f_{11}^2}{2(\Delta-\delta)} I_z + \frac{f_{11} f_{10}}{\Delta-\delta}\cos(\theta_{10}) I_z.\end{aligned} \tag{71}$$

In the above equation, the third term is introduced by the interference between the *1*st RF field and the offset term δI_z and it causes a small phase shift; the fourth term is simply the BSFS introduced by the *1*st RF field alone; and the fifth term is created by the interference between the two RF fields.

4.3. Bloch-Siegert offset shift

Due to the presence of the RF interference and the BSFS terms, $\delta = 0$ in the Hamiltonian [Eq. (71)] is no longer the on-resonance condition. According to the definition, the on-resonance occurs when the sum of all the I_z components in the Hamiltonian vanishes. This leads to the following equation

$$\delta - \frac{f_{11}^2}{2(\Delta-\delta)} + \frac{f_{11} f_{10}}{\Delta-\delta}\cos(\theta_{10}) = 0, \tag{72}$$

with a solution of

$$\delta = \frac{1}{2}\left(\Delta - \sqrt{\Delta^2 + 4 f_{11} f_{10}\cos(\theta_{10}) - 2 f_{11}^2}\right) = \text{BSOS}, \tag{73}$$

where the shift of the on-resonance is the BSOS. For $|\delta/\Delta| \ll 1$, the BSOS can be obtained straightforwardly from Eq. (72)

$$\mathrm{BSOS} = \frac{f_{11}^2}{2\Delta} - \frac{f_{11} f_{10}}{\Delta} \cos(\theta_{10}). \tag{74}$$

Unlike the BSFS[46–48,54] and BSPS,[34,38–44] where the precession of the magnetization is perturbed by a RF field during the evolution time, the BSOS is caused by the perturbation field f_{11} during the excitation by another field f_{10}.

4.4. RF Interference by multiple effective RF fields

Since the zero-order average Hamiltonian of each RF field $f_{1m}(m \neq 0)$ and the first-order average Hamiltonians between any two RF fields f_{1m}, f_{1n}, $(m, n \neq 0)$ are averaged to zero, the results in Eq. (71) can be extended to $2m$ (from $-m$ to m, $m \neq 0$) effective RF fields that interfere with the centre RF field f_{10} if the contribution from the second-order average Hamiltonian [Eq. (69)] is ignored or equivalently if $|\delta/\Delta| \ll 1$. Under these conditions, the average Hamiltonian for the centre RF field that interacts with $2m$ near neighbours can be expressed as

$$\begin{aligned} \overline{\mathcal{H}} = {} & \delta I_z + f_{10} e^{-i\theta_0 I_z} I_x e^{i\theta_0 I_z} - \sum_{n=-m, n\neq 0}^{n} \frac{\delta f_{1n}}{n\Delta} e^{-i\theta_n I_z} I_x e^{i\theta_n I_z} \\ & - \sum_{n=-m,\, n\neq 0}^{n} \left[\frac{f_{1n}^2}{2n\Delta} - \frac{f_{1n} f_{10}}{n\Delta} \cos(\theta_{n0}) \right] I_z. \end{aligned} \tag{75}$$

For the RF fields away from the centre or with a larger n, the effect of RF interference to the centre excitation band can be neglected since $n\Delta$ occurs in the denominator. In practice, it is often sufficient to consider only a few near neighbours in the calculation, i.e., the NNA. The nearest neighbour approximation, for example, takes only two neighbours with $n = \pm 1$, and it is denoted as NNA1. In general, an approximation that takes $2m$ neighbours, from $-m$ to m $(m \neq 0)$, is denoted as NNAm and the corresponding BSOS is expressed as (refer to Eqs. (74) and (75))

$$\mathrm{BSOS} = \sum_{n=-m,\, n\neq 0}^{n} \left[\frac{f_{1n}^2}{2n\Delta} - \frac{f_{1n} f_{10}}{n\Delta} \cos(\theta_{n0}) \right]. \tag{76}$$

Although the BSOS for NNAm in the above equation is derived for the centre band, they are suitable for any other bands, as long as the right relative phases and frequency separations are used.

4.5. Anti-symmetrization of a PIP

As mentioned in Section 2, a phase $= (1/2)\Delta\varphi$ can be added to all the steps of a PIP to compensate the UPS. Alternatively, the UPS can be compensated by splitting the first step of the PIP equally into two parts and moving the first part to the end of the PIP (Fig. 8). This process is called anti-symmetrization of a PIP since the phase of the final PIP is anti-symmetric. In general, an anti-symmetrized PIP can be denoted as PIP$\Delta f(\varphi_0, 0^\circ - \Delta\varphi - 0^\circ, \Delta\tau, f_1(k)$, steps) or PIP$\Delta f$as in short. Disregarding the initial phase φ_0, the PIPΔfas is anti-symmetric in the sense that the phase of any step fulfills the condition of $\phi_k = -\phi_{N+1-k}$, where k is the index of steps and N is now the total number of steps of the PIPΔfas. The PIPΔfas has one more step than the original PIP but its pulsewidth remains unchanged. It starts at $\phi_1 = 0^\circ$ and ends at $\phi_N = 0^\circ$, and the pulse satisfies $(N-1)\Delta\varphi = 2m\pi$, with an integer m. This condition is in fact assumed in the derivation of the BSOS and therefore is necessary for comparing the theoretical and simulated results.

Although the anti-symmetry process does not change the scaling factors of the effective RF fields, it compensates the UPS for all the RF fields. In addition, all the phases with an odd sideband number n are inverted, while the others remain the same. This property can be shown by the following analysis.

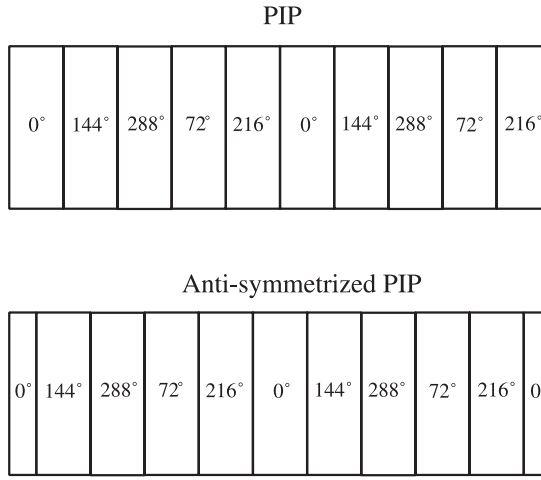

Fig. 8. The procedure for anti-symmetrizing a PIP. A PIP8(0°, 144°, 50 μs, 1.3214 kHz, 10) is shown on top and it is anti-symmetrized (bottom) by splitting the first step into two equal parts and moving the first part to the end of the PIP. The total number of steps ($N = 11$) of the anti-symmetrized PIP increases by one but the pulsewidth remains the same. The phase satisfies the condition of $\varphi_k = -\varphi_{N+1-k}$. Reprinted from Ref. 33 with permission from the American Institute of Physics publications.

Table 6. The frequencies f_n, field strengths f_{1n}, phases θ_n, and scaling factors λ_n of the effective RF fields created by a PIP8(0°,144°, 50 μs, 1.3214 kHz, 10) and its anti-symmetrized PIP8(0°, 0°–144°–0°, 50 μs, 1.3214 kHz, 11), respectively, where λ_n and f_n are the same for both PIPs

Sideband number	n	−2	−1	0	1	2
Frequency (kHz)	f_n	−32	−12	8	28	48
Calculated						
Scaling factor	λ_n	−0.1892	−0.5046	0.7568	0.2162	0.1261
RF strength (kHz)	f_{1n}	0.2500	0.6667	1.0000	0.2857	0.1667
Phase (PIP8)	θ_n	108°	108°	−72°	−72°	−72°
Phase (PIP8as)	θ_n	180°	0°	0°	180°	0°
Polarization	$\langle I_z\rangle_n$	0.707	−0.500	−1.000	0.624	0.866
Computer simulated						
Phase (PIP8)	θ_n	108.0°	108.0°	−72.0°	−72.0°	−72.0°
Phase (PIP8as)	θ_n	180.0°	0.0°	0.0°	180.0°	0.0°
Polarization	$\langle I_z\rangle_n$	0.706	−0.502	−1.000	0.622	0.866

The computer simulated polarization $\langle I_z\rangle_n$ is taken at the frequency where the BSOS is taken into account. For example, the BSOS for the centre band is 30.6 Hz and the value of $\langle I_z\rangle_n$ is taken at 8.0306 kHz. Reprinted from Ref. 33 with permission from the American Institute of Physics publications.

According to the theorem of Fourier analysis, a time shift of half a step ($\Delta\tau/2$) of a PIP will correspondingly cause a phase shift in the frequency domain[52]

$$\mathscr{F}\left[f\left(t+\frac{\Delta\tau}{2}\right)\right] = e^{i(2\pi\Delta f+\omega_n)\Delta\tau/2}F(2\pi\Delta f+\omega_n)$$
$$= e^{i\Delta\varphi/2}e^{in\pi}F(2\pi\Delta f+\omega_n), \tag{77}$$

which introduces a factor $e^{i\Delta\varphi/2}$ that compensates the UPS $= -(\Delta\varphi/2)$ for all bands and another one

$$e^{in\pi} = \begin{cases} 1 & \text{for even } n \\ e^{i\pi} & \text{for odd } n \end{cases}, \tag{78}$$

which creates a phase inversion if the sideband number n is odd (Table 6).

4.6. Simulation of BSOS by two RF fields

Assume two RF fields, both 90° pulses, are applied simultaneously with the same pulse strength $f_{10} = f_{11} = 0.5$ kHz and pulsewidth $\tau = 0.5$ ms, where f_{11} is

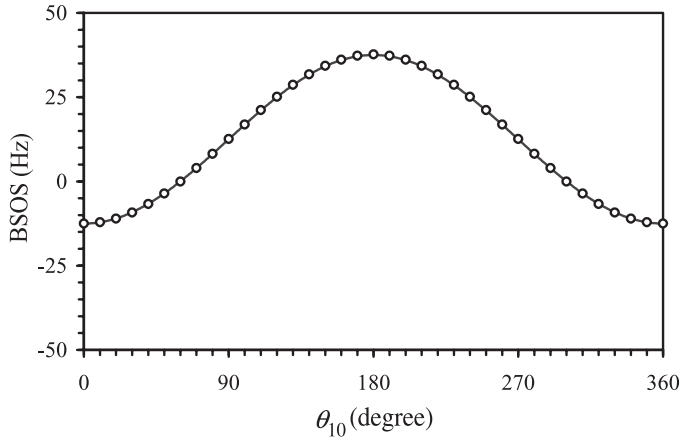

Fig. 9. The BSOS as a function of the relative phase $\theta_{10}(=\theta_1 - \theta_0)$ between the RF fields f_{10} and f_{11} where the solid line is a theoretical curve calculated with Eq. (74), while the open circles are computer simulated directly from the two PIPs. $f_{10}=0.5$ kHz and $\theta_0=0°$. f_{11} is created by a PIP10 (0°, 3.6°, 1.0 μs, 0.5 kHz, 500) that is anti-symmetrized according to the procedure discussed in Section 4.5. Reprinted from Ref. 33 with permission from the American Institute of Physics publications.

situated $\Delta=10$ kHz away from f_{10}. The phase for the centre RF field $\theta_0=0°$ is fixed, while the phase θ_1 for f_{11} is varied from 0° to 360° in 10° steps. For each value of θ_1, an excitation profile is generated using the computer program discussed in Section 2.7. The amount of the BSOS is determined by examining the shift of the on-resonance condition, where the z-component of the overall rotation axis is minimized.

The simulated result and the theoretical curve obtained from Eq. (74) are shown in Fig. 9, where both positive and negative BSOS appear as manifested by Eq. (74). In particular, when the relative phase $\theta_{10}=60°$ and 300°, respectively, the BSOS caused by the two terms in Eq. (74) cancel as predicted.

4.7. Calculation of BSOS using the NNA

The anti-symmetrized PIP8(0°, 0°–144°–0°, 50 μs, 1.3213 kHz, 10) (Fig. 8) is taken into account first. Figure 10 shows the inversion profile of the PIP8as and Table 6 lists the scaling factors, RF field strengths, phases, and polarizations for $n=-2$ to 2. For the PIP8as, the UPS $=-72°$ for all bands is compensated and a phase inversion occurs if n is odd (Table 6), in agreement with the previous conclusions. Another phase inversion appears for $\lambda_n<0$ ($n=-2$ and -1) as discussed in Section 2.2.

The BSOS for NNA1, NNA2, and NNA3 are calculated with Eq. (76) and the results are shown in Table 7 together with the computer simulated results.

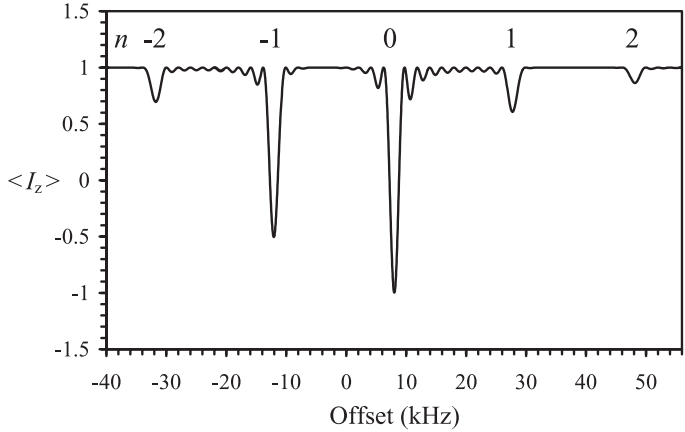

Fig. 10. The inversion profile ($n = -2$ to 2) created by an anti-symmetrized PIP8(0°, 0°–144°–0°, 50 μs, 1.3214 kHz, 11). Due to the RF interference, all the peaks are shifted slightly and the shifted amounts can be calculated with the NNA as shown in Table 7. Reprinted from Ref. 33 with permission from the American Institute of Physics publications.

Table 7. BSOS (Hz) for NNA1 to NNA3 calculated with Eq. (76), along with the computer simulated results from the anti-symmetrized PIP8(0°, 0°–144°–0°, 50 μs, 1.3214 kHz, 11)

Sideband number	n	−2	−1	0	1	2
Frequency (kHz)	f_n	−32	−12	8	28	48
NNA1		16.9	−18.2	38.6	−36.2	−3.1
NNA2		36.2	−10.2	27.7	−47.2	−11.7
NNA3		35.3	−13.1	32.1	−46.0	−13.3
Simulated (PIP8as)		36.1	−12.0	30.6	−46.8	−14.3

Reprinted from Ref. 33 with permission from the American Institute of Physics publications.

Compared with the simulated results, the percentage of error for the centre band is about 26% for NNA1 and it drops to 5% for NNA3, converging rapidly as the number of neighbours increases.

Next, a periodic pulse $f_{1x}|\sin(\pi t/T)|I_x$ is considered, with $f_{1x} = (\pi/2)$ kHz, $T = 50$ μs, the pulsewidth $\tau = 0.5$ ms, and a total number of steps $N = 1000$. According to the procedure illustrated in Fig. 8, the periodic pulse is symmetrized (not anti-symmetrized) since the phases are the same for all the steps. As a result, the strength of the symmetrized pulse satisfies the condition of $\mathrm{A}(t) = \mathrm{A}(T - t)$, $0 \le t \le T$.

The scaling factors, phases, and the strengths of the effective RF fields for $n = -2$ to 2 are shown in Table 8 and the BSOS for NNA1 to NNA3 is shown

Table 8. The frequencies f_n, field strengths f_{1n}, phases θ_n, and scaling factors λ_n of the effective RF fields created by a periodic pulse $f_{1x}|\sin(\pi t/T)|I_x$

Sideband number	n	-2	-1	0	1	2
Frequency (kHz)	f_n	-40	-20	0	20	40
Calculated						
Scaling factor	λ_n	1/15	1/3	1	1/3	1/15
RF strength (kHz)	f_{1n}	1/15	1/3	1	1/3	1/15
Phase	θ_n	$-180°$	$-180°$	0°	180°	180°
Polarization	$\langle I_z\rangle_n$	0.978	0.500	-1.000	0.500	0.978
Computer simulated						
Phase	θ_n	$-180.0°$	$-180.0°$	0.0°	180.0°	180.0°
Polarization	$\langle I_z\rangle_n$	0.978	0.500	-1.000	0.500	0.978

The computer simulated polarization $\langle I_z\rangle_n$ is taken at the frequency where the BSOS is taken into account. Reprinted from Ref. 33 with permission from the American Institute of Physics publications.

Table 9. BSOS (Hz) for NNA1 to NNA3 calculated with Eq. (76), together with the computer simulated results from the symmetrized pulse of $f_{1x}|\sin(\pi t/T)|I_x$

Sideband number	n	-2	-1	0	1	2
Frequency (kHz)	f_n	-40	-20	0	20	40
NNA1		1.7	42.7	0.0	-42.7	-1.7
NNA2		15.9	41.5	0.0	-41.5	-15.9
NNA3		16.5	41.3	0.0	-41.3	-16.5
Simulated		16.4	41.2	0.0	-41.2	-16.4

Reprinted from Ref. 33 with permission from the American Institute of Physics publications.

in Table 9. The BSOS is anti-symmetrical in respect to the sideband number n due to the symmetrical RF fields and anti-symmetrical frequency separation $n\Delta$. It is balanced for the centre band. The convergence of the BSOS from NNA1 to NNA3 is faster than the previous PIP because the strengths of the effective RF fields fall rapidly as the sideband number n increases.

5. BLOCH-SIEGERT PHASE SHIFT COMPENSATED PIPS

5.1. Bloch-Siegert phase shift

Bloch-Siegert phase shift is usually introduced in homonuclear nuclear decoupling with an inversion pulse that is far off-resonance to the spins in precession. To minimize the disturbance, the strength of the inversion pulse

is often restricted. For instance, to apply a 180° pulse on the ^{13}CO in the middle of the evolution time of the $^{13}C_\alpha$ for homonuclear decoupling, the pulse strength f_1 satisfies the relationships of[19]

$$2\pi f_1 \tau = \pi, \tag{79}$$

for the inversion of the ^{13}CO, and

$$2\pi\sqrt{\Delta f^2 + f_1^2}\,\tau = 2m\pi \quad (m \text{ integer}), \tag{80}$$

for the null of the centre of $^{13}C_\alpha$, where $f_{1\text{eff}} = \sqrt{\Delta f^2 + f_1^2}$ is the effective RF field, τ is the pulsewidth, and $\Delta f = 118$ ppm is the difference of the chemical shifts between the centres of the $^{13}C_\alpha$ and ^{13}CO. It follows from Eqs. (79) and (80) that

$$f_1 = \frac{\Delta f}{\sqrt{4m^2 - 1}}. \tag{81}$$

To have a proper excitation range or the RF field strength, usually only $m = 1$ or 2 is used, leading to $f_1 = \Delta f/\sqrt{3}$ and $f_1 = \Delta f/\sqrt{15}$, respectively.

The ^{13}CO inversion pulse can be achieved by a PIP with the carrier placed at the centre of the $^{13}C_\alpha$. This inversion PIP causes an additional procession of the $^{13}C_\alpha$ spins. The amount of the phase shift in the rotating frame of the ^{13}CO, where the centre of the ^{13}CO spins is on-resonance to the inversion PIP, can be calculated

$$\varphi_{CO} \approx -2\pi\sqrt{(\Delta f - \delta)^2 + f_1^2}\,\tau, \tag{82}$$

where δ is an offset of a $^{13}C_\alpha$ resonance measured from the carrier and the minus phase implies that the $^{13}C_\alpha$ has a lower Larmor frequency than that of the ^{13}CO. Since $(\Delta f - \delta) \gg f_1$ (far off-resonance condition), this precession is virtually around the z axis, otherwise uneven precession occurs in the x–y plane. This precession, however, must be evaluated in the rotating frame of $^{13}C_\alpha$ since the carrier frequency is placed at the centre of $^{13}C_\alpha$. A transformation of the rotating frame from the ^{13}CO to $^{13}C_\alpha$ frame is therefore necessary, resulting in another phase of $2\pi\Delta f\tau$. Consequently, the phase shift in the rotating (or $^{13}C_\alpha$) frame

$$\begin{aligned}\varphi_{C_\alpha} &\approx 2\pi\Delta f\tau - 2\pi\sqrt{(\Delta f - \delta)^2 + f_1^2}\,\tau \\ &\approx 2\pi\delta\tau - \frac{f_1^2}{\Delta f - \delta}\pi\tau,\end{aligned} \tag{83}$$

where the first term is caused by the free precession of a $^{13}C_\alpha$ spin with an offset δ and the second term is the BSPS caused by the ^{13}CO inversion pulse

$$\text{BSPS} = -\frac{f_1^2}{\Delta f - \delta}\pi\tau. \tag{84}$$

As shown in the above equation, the BSPS is non-linear in respect to the offset δ.

5.2. Compensation of BSPS by a pair of complementary PIPs

Assume a 180° PIP is applied at the centre of the ^{13}CO in the middle of the $^{13}C_\alpha$ evolution time for homonuclear decoupling and at the same time a compensating PIP is applied on the other side of the $^{13}C_\alpha$ (Fig. 11) to minimize the disturbance to the $^{13}C_\alpha$ that may have a transverse or longitudinal magnetization. The two simultaneous PIPs become an amplitude modulated pulse described by $2f_1\cos(2\pi\Delta ft)I_x$, where f_1 is the pulse strength of each 180° PIP and $t = 0$, $\Delta\tau$, $2\Delta\tau\ldots$. For any negative value of the amplitude, i.e., $2f_1\cos(2\pi\Delta ft) < 0$, the corresponding absolute value is used but the phase is shifted 180°. The carrier frequency is placed at the centre of $^{13}C_\alpha$.

To see the compensation effect by the pair of PIPs, the interaction exerted on the $^{13}C_\alpha$ spins needs to be known. For a $^{13}C_\alpha$ peak with an offset δ, the Hamiltonian of the system can be expressed as

$$\mathcal{H}(t) = 2f_1\cos(2\pi\Delta ft)I_x + \delta I_z \quad \text{(in Hz)}. \tag{85}$$

The Hamiltonian is now time-dependant and its overall effect on the spin density operator can be calculated using the coherent averaging theory.[3,4,53]

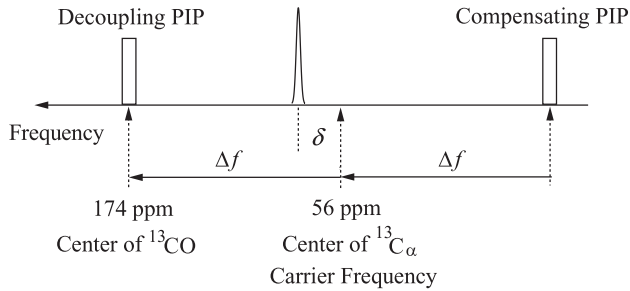

Fig. 11. The BSPS compensated PIPs, one applied at the centre of the ^{13}CO for decoupling and the other at the other side of $^{13}C_\alpha$ for compensating the BSPS. Reprinted from Ref. 42 with permission from Elsevier.

The zero-order average Hamiltonian can be obtained straightforwardly

$$\overline{\mathcal{H}}^{(0)} = \frac{1}{\tau}\int_0^\tau \mathcal{H}(t)dt = f_1\frac{\sin(2\pi\Delta f\tau)}{\pi\Delta f\tau}I_x + \delta I_z$$

$$= \delta I_z, \quad \text{if } 2\pi\Delta f\tau = m\pi \quad (m \text{ integer}). \tag{86}$$

Here $2\pi\Delta ft = m\pi$ is imposed to eliminate the effect by the zero-order interaction of the RF field, otherwise a term containing I_x will remain and it will distort the longitudinal magnetization, transverse magnetization, as well as the BSPS of the $^{13}C_\alpha$. For the on-resonance condition, $\delta = 0$, all the higher-order average Hamiltonians vanish since $[\mathcal{H}(t'), \mathcal{H}(t'')] = 0$ for arbitrary t' and t''. As a result, the centre of the $^{13}C_\alpha$ remains unexcited no matter how strong the pulse is.

The first- and second-order average Hamiltonians can be calculated similarly

$$\overline{\mathcal{H}}^{(1)} = \frac{-\pi i}{\tau}\int_0^\tau dt_2\int_0^{t_2}[\mathcal{H}(t_2), \mathcal{H}(t_1)]dt_1$$

$$= \frac{2f_1^2}{\pi\Delta f^2}[1 - \cos(2\pi\Delta f\tau)]\delta I_y, \tag{87}$$

and

$$\overline{\mathcal{H}}^{(2)} = \frac{-2\pi^2}{3\tau}\int_0^\tau dt_3\int_0^{t_3}dt_2\int_0^{t_2}\{[\mathcal{H}(t_3),[\mathcal{H}(t_2),\mathcal{H}(t_1)]] + [\mathcal{H}(t_1),[\mathcal{H}(t_2),\mathcal{H}(t_3)]]\}dt_1$$

$$= -\frac{f_1^2}{\Delta f^2}\delta I_z - \frac{f_1\delta}{\Delta f^2}[1 + \cos(2\pi\Delta f\tau)]\delta I_x, \tag{88}$$

where $2\pi\Delta ft = m\pi$ and $2\pi\Delta f_1\tau = \pi$ (required by the ^{13}CO 180° PIP) are used. From Eqs. (87) and (88) one can see that $\overline{\mathcal{H}}^{(1)} = 0$, if m is even and the term including I_x in $\overline{\mathcal{H}}^{(2)}$ becomes zero if m is odd. Only the linear phase shift term $-(f_1^2/\Delta f^2)\delta I_z$ in $\overline{\mathcal{H}}^{(2)}$ is independent of m and it introduces a linear phase shift.

The average Hamiltonian up to the second-order can be expressed as

$$\overline{\mathcal{H}} = -\frac{f_1\delta}{\Delta f^2}[1 + \cos(2\pi\Delta f\tau)]\delta I_x + \frac{2f_1^2}{\pi\Delta f^2}[1 - \cos(2\pi\Delta f\tau)]\delta I_y + \left(1 - \frac{f_1^2}{\Delta f^2}\right)\delta I_z. \tag{89}$$

Under the conditions of f_1 and $\delta \ll \Delta f$, the terms containing I_x and I_y in the above equation are small compared to the chemical-shift term δI_z. But they

can be in the same order as the linear phase shift term $-(f_1^2/\Delta f^2)\delta I_z$ for certain m values. In contrast to the linear phase shift term, these two terms only have a second-order effect on the BSPS since they are orthogonal to the dominating chemical-shift term.[42]

Neglecting the two terms with I_x and I_y, the Hamiltonian in Eq. (89) becomes $\overline{\mathcal{H}} = (1 - f_1^2/\Delta f^2)\delta I_z$, which causes a phase shift of

$$\varphi_{\mathrm{PIPs}} = 2\pi\delta\tau - 2\pi\frac{f_1^2}{\Delta f^2}\delta\tau, \tag{90}$$

where the first term $2\pi\delta\tau$ is caused by the free precession of the spins with an offset δ, and the second term is caused by the pair of PIPs. The additional phase shift, by definition, is

$$\mathrm{BSPS} = -2\pi\frac{f_1^2}{\Delta f^2}\delta\tau. \tag{91}$$

Compared with the BSPS by a single PIP [Eq. (84)], the BSPS by a pair of complementary PIPs is reduced significantly and more importantly, it is now linearly proportional to the offset δ, making it possible to be eliminated completely. The minus sign in Eq. (91) implies that the actual phase evolution during the pulse is scaled by a factor of

$$\lambda = 1 - \frac{f_1^2}{\Delta f^2}. \tag{92}$$

Equivalently, one may think that the evolution does not change but the effective pulsewidth τ_{eff} is scaled by the same factor

$$\tau_{\mathrm{eff}} = \lambda\tau. \tag{93}$$

By taking into account the scaling factor in the pulse sequence, the linear BSPS can be effectively removed. Additionally, this linear BSPS can also be corrected by a first-order phase correction.

5.3. Computer simulations

For comparison, the disturbance to the transverse and longitudinal magnetizations and the BSPS of the $^{13}C_\alpha$ introduced by a single 180° PIP and by the simultaneous PIPs are shown in Fig. 12. The pulse strength f_1 for the single PIP is 5.75 kHz ($\approx \Delta f/\sqrt{15}$), where $\Delta f = 22.22$ kHz is approximately the frequency separation between the centres of the $^{13}C_\alpha$ and ^{13}CO for a 750 MHz instrument (Fig. 11). For the PIPs, the field strength

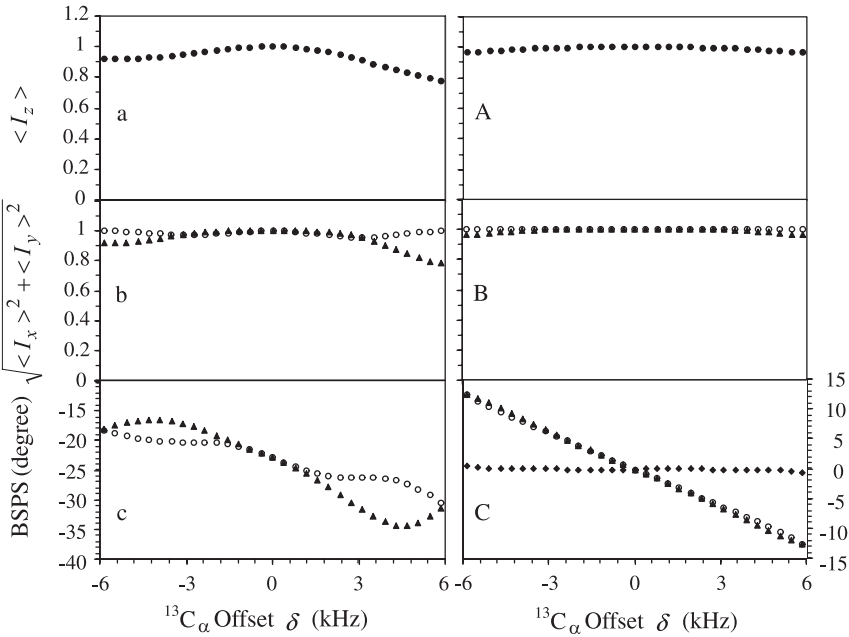

Fig. 12. The influences of the longitudinal magnetization, transverse magnetization, and the BSPS of the $^{13}C_\alpha$ caused by a single 180° PIP (a, b, c) and by the BSPS compensated PIPs (A, B, C). The solid triangles and open circles (b, B and c, C) represent the results with an initial transverse magnetization along the x and y axis, respectively. The BSPS (solid triangles) is compensated (solid diamonds in C) when the scaling factor of the pulsewidth, $\lambda = [1 - (f_1^2/\Delta f^2)]$, is taken into account. The single 180° PIP applied at the centre of the ^{13}CO is denoted by PIP22.22(2°, 4°, 0.5 μs, 5.75 kHz, 174). An initial phase $\varphi_0 = 2°$ is used to compensate the UPS of the PIP. The BSPS compensated PIPs is then represented by PIP22.22(0°, 0°, 0.5 μs, $2f_1\cos(2\pi\Delta f t + \varphi_0)$, 180), where $2f_1 = 11.12$ kHz, $\varphi_0 = 2°$, and $t = 0$, $\Delta\tau$, $2\Delta\tau$, ... Reprinted from Ref. 42 with permission from Elsevier.

is $f_1 = 5.56$ kHz ($2\pi\Delta f = 4\pi$, $m = 4$), which leads to a zero coefficient of I_y in the average Hamiltonian [Eq. (89)]. As shown in Fig. 12, the disturbance to the longitudinal (A) and transverse (B) magnetizations and the BSPS (C) of the $^{13}C_\alpha$ caused by the simultaneous PIPs are much smaller than that by the single PIP (a, b, c) because of the compensating effects. In addition, the BSPS is effectively linear as predicted by Eq. (91). Application of the scaling factor to the pulsewidth [Eqs. (92) and (93)] leads to an almost complete self-compensation of the BSPS (Fig. 12C) and no phase correction is required for the $^{13}C_\alpha$ spectrum.

Similar results were observed for a pair of complementary PIPs with a condition of $2\pi\Delta f\tau = 3\pi$ ($m = 3$), where the term including I_y is maximized and the term including I_x becomes zero in the average Hamiltonian

[Eq. (89)],[42] further manifesting that both terms in Eq. (89) with I_x and I_y can be eligibly ignored.

Unlike the compensation of the BSPS for a long pulse,[44] the pulsewidth τ for short PIPs is crucial. Away from the condition of $2\pi\Delta f\tau = m\pi$, a significant zero-order term will arise and the longitudinal magnetization, the transverse magnetization, and the BSPS can be distorted so severely that the BSPS compensation scheme does not work at all.[42]

Similar compensation effects were also found for a pulse strength of $f_1 = 11.11$ kHz and $2\pi\Delta f\tau = 2\pi$ ($m = 2$). The inversion profile of the pulse is shown in Fig. 13b, together with the inversion profile by a single PIP (a). The null region of the $^{13}C_\alpha$ is broadened significantly by the simultaneous PIPs in addition to the compensation of the BSPS.

Due to the BSOS discussed in Section 4.3, the inversion profiles are shifted by 1.38 kHz to the left and right side, respectively (Fig. 13b). The amount of the shift compared to the bandwidth of the inversion profile is significant. To have a right position of inversion, the effect of the BSOS needs to be taken

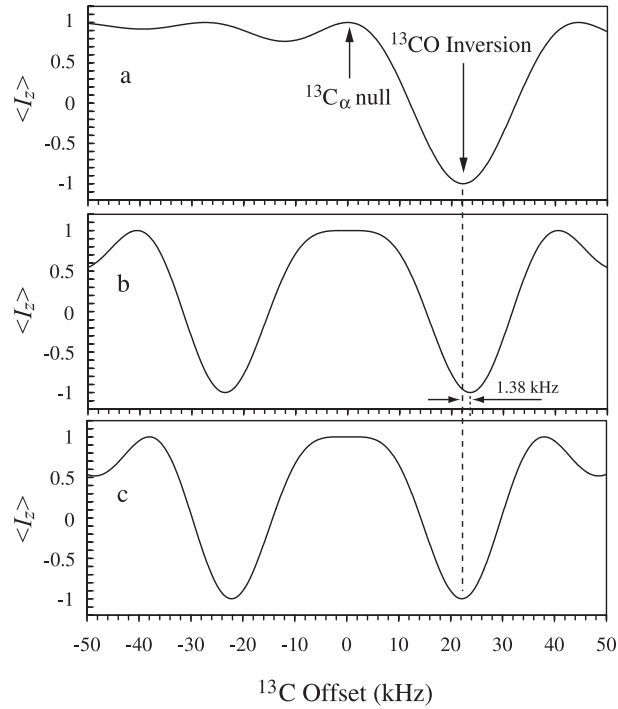

Fig 13. Inversion profiles by a single PIP22.22(0°, 4°, 0.5 μs, 12.83 kHz, 78) (a), satisfying the condition of $f_1 = \Delta f/\sqrt{3}$, by a simultaneous PIP22.22(0°, 0°, 0.5 μs, $2f_1\cos(2\pi\Delta ft)$, 90) (b), satisfying the condition of $2\pi\Delta f\tau = 2\pi$ or $2f_1 = 22.22$ kHz, and by a modified simultaneous PIP20.91(0°, 0°, 0.5 μs, $2f_1\cos(2\pi\Delta ft)$, 96) (c) with $\Delta f = 2f_1 = 20.91$ kHz. Both of the simultaneous PIPs are symmetrized.

into account and the frequency shift Δf, field strength f_1, and the pulsewidth τ of the pair of complementary PIPs needs to be modified. The frequency separation between the centres of the $^{13}C_\alpha$ and ^{13}CO should fulfill the condition of (refer to Eq. (74))

$$\Delta f - \frac{f_1^2}{4\Delta f} + \frac{f_1^2}{2\Delta f}\cos(\theta_{10}) = 22.22 \text{ kHz}, \tag{94}$$

where Δf is now the frequency shift of the PIPs (that needs to be determined) and the relative phase $\theta_{10} = 0^\circ$. Using the relationship of $2\pi f_1 \tau = \pi$ [Eq. (79)] and the condition of $2\pi\Delta f\tau = 2\pi$, it is easy to solve Eq. (94) and to obtain $\Delta f = 20.91$ kHz and $2f_1 = 20.91$ kHz. Based on these results, a new pair of complementary PIPs is formed, PIP20.91 (0°, 0°, 0.5 μs, 2 $f_1$cos($2\pi\Delta f\tau$), 96), which is also symmetrized. As shown in Fig. 13c the inversion profile at the centre of the ^{13}CO matches well with the one by the single PIP (Fig. 13a) yet it still reserves all the other characteristics of the complementary PIPs.

If the pulse strength of the simultaneous PIPs is further increased to $2f_1 = 44.48$ kHz and $2\pi\Delta f\tau = \tau$ ($m = 1$), ($f_1/\Delta f$) in Eq. (89) is no longer a small value and the Magnus-expansion in the coherent averaging theory may not converge. Consequently, the compensation in the null region vanishes almost completely.

In a similar way, an adiabatic inversion pulse can also be used to compensate the BSPS,[44] where the condition $\Delta f\tau \gg 1$ is usually fulfilled due to a long pulsewidth in order to meet the adiabatic condition. Consequently, all the terms in the average Hamiltonian containing the cos($2\pi\Delta ft$) and sin($2\pi\Delta ft$) functions approach zero over a long time τ and the condition, $2\pi\Delta f\tau = m\pi$ imposed for a short pulse, becomes less crucial in the BSPS compensation. Only the linear phase shift term[47]

$$\mathcal{H} = -\frac{f_{1\text{rms}}^2}{\Delta f^2}\delta I_z \tag{95}$$

remains, where $f_{1\text{rms}}^2 = (1/\tau)\int_0^\tau f_1^2(t)dt$ is the mean-square value of the time-dependent RF field $f_1(t)$. Similar to the PIPs, the remaining linear BSPS can be corrected by taking into account a scaling factor, $\lambda = [1 - (f_{1\text{rms}}^2/\Delta f^2)]$, of the pulsewidth.

6. PHASE INCREMENTED ADIABATIC PULSES

6.1. Implementation of phase increment to adiabatic pulses

Adiabatic pulses are usually composed of a number of back-to-back pulses of equal width $\Delta\tau$. The amplitude adopts a certain shape that is normally

symmetric in respect to the centre, while the phase has a non-linear increment. To achieve a frequency-shifted adiabatic inversion, a linear phase increment can be added to the adiabatic pulse as shown below.

$$\{\varphi(t), A(t)\} = \begin{cases} \text{Original} & & \text{Phase incremented} & & \\ \text{Phase} & \text{Amplitude} & \text{Phase} & \text{Amplitude} & \text{Time} \\ \varphi_1 & A_1 & \varphi_1 + 0 & A_1 & 0 \le t < \Delta\tau \\ \varphi_2 & A_2 & \varphi_2 + \Delta\varphi & A_2 & \Delta\tau \le t < 2\Delta\tau \\ \varphi_3 & A_3 & \varphi_3 + 2\Delta\varphi & A_3 & 2\Delta\tau \le t < 3\Delta\tau \\ \cdots & \cdots & \cdots & \cdots & \cdots \end{cases}, \tag{96}$$

where the first two columns on the right side define the original adiabatic pulse and the next two columns represent the phase incremented adiabatic pulse. φ_1, φ_2, φ_3, and A_1, A_2, A_3 in Eq. (96) are the phases and amplitudes of the first, second, and third steps, respectively, while $\Delta\varphi$ is the phase increment. As in any PIPs, the amount of the frequency shift is determined by $\Delta f = \Delta\varphi/(2\pi\Delta\tau)$.

6.2. Phase incremented double adiabatic decoupling for ^{13}C- and ^{15}N-labelled proteins

For ^{13}C- and ^{15}N-labelled proteins, the ^{13}CO and $^{13}C_\alpha$, with chemical shift ranges of 20 and 30 ppm, respectively, need to be decoupled simultaneously in some NMR experiments. Since there is a 93 ppm gap between these two regions, where there are no protein backbone resonances, decoupling the entire ^{13}C chemical shift range (143 ppm) is not only inefficient but also causes sample heating, especially for protein samples with a high salt concentration at high magnetic fields.

An efficient way is to decouple these two regions separately, one centred at the ^{13}CO frequency and the other at the $^{13}C_\alpha$ frequency. To achieve this goal, an adiabatic decoupling sequence is used to decouple the ^{13}CO while another phase incremented adiabatic decoupling, with the same carrier frequency as the ^{13}CO, is used to decouple the $^{13}C_\alpha$ as shown in Fig. 14. The two decoupling sequences can be combined to form a double-band adiabatic decoupling with only a single waveform generator.

The procedure to combine any two phase modulated pulses is straightforward and is going to be discussed below. For the kth step of the two pulses (denoted by the two indices a and b), their amplitudes and phases can be described by A_{ka}, φ_{ka} and A_{kb}, φ_{kb}, respectively. The vector sum (denoted

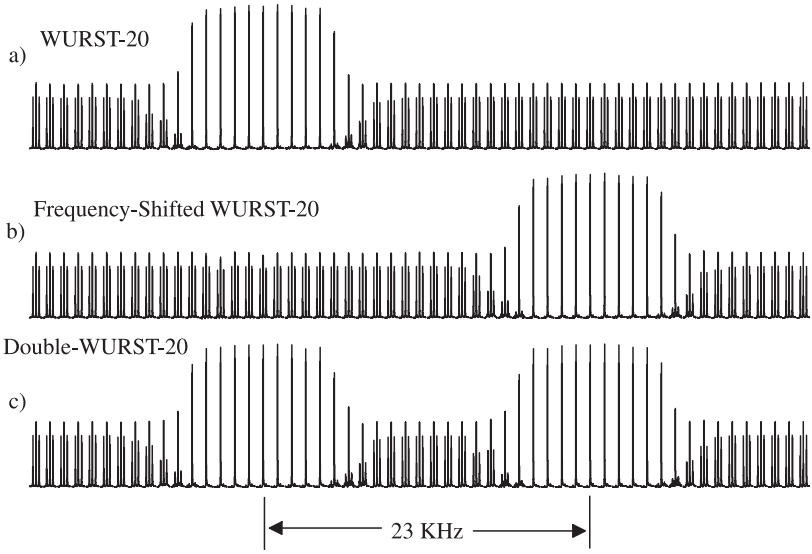

Fig. 14. Arrays of ^{1}H spectra from a sample of ^{13}C ($\sim 64\%$) labelled CH_3I with a WURST-20 adiabatic decoupling (a), a frequency-shifted WURST-20 decoupling (b), and a Double-WURST-20 decoupling (c). For the WURST-20, $f_{1\max} = 1.39$ kHz and $f_{1\mathrm{rms}} = 0.88 f_{1\max} = 1.22$ kHz and for the Double-WURST-20, $f_{1\max} = 2.78$ kHz and $f_{1\mathrm{rms}} = 0.62 f_{1\max} = 1.72$ kHz. Reprinted from Ref. 45 with permission from Elsevier.

by an index s) of the x and y components of the two pulses is

$$A_{ksx} = A_{ka}\cos(\varphi_{ka}) + A_{kb}\cos(\varphi_{kb}) \tag{97a}$$

and

$$A_{ksy} = A_{ka}\sin(\varphi_{ka}) + A_{kb}\sin(\varphi_{kb}). \tag{97b}$$

The kth amplitude and phase of the combined field are then

$$A_{ks} = \sqrt{A_{ksx}^2 + A_{ksy}^2} \tag{98a}$$

and

$$\varphi_{ks} = \cos^{-1}\left(\frac{A_{ksx}}{\sqrt{A_{ksx}^2 + A_{ksy}^2}}\right), \quad \text{if } A_{ksy} \geq 0, \tag{98b}$$

$$\varphi_{ks} = -\cos^{-1}\left(\frac{A_{ksx}}{\sqrt{A_{ksx}^2 + A_{ksy}^2}}\right), \quad \text{if } A_{ksy} < 0. \tag{98c}$$

The experimental result by the double adiabatic decoupling pulse is shown in Fig. 14c, where the ^{13}CO and C_α bands are decoupled separately as expected. To run the experiment using the double adiabatic decoupling with the same decoupling range, the RF field strength $f_{1\max}$ has to be increased by 6 dB, which corresponds to doubling the amplitude of the pulse. Importantly, the rms value of the pulse strength, however, increases only by a factor of $\sqrt{2}$ due to the interference between the two pulses. Therefore, the power dissipated to the probe, which is proportional to the square of the rms value of the pulse strength, is only doubled. It can be shown that with the same decoupling scheme, roughly three times the power is required to decouple the entire region (143 ppm).[45]

6.3. Phase incremented double adiabatic decoupling for compensation of the Bloch-Siegert frequency shift

In triple-resonance multidimensional NMR, homonuclear ^{13}CO (or $^{13}C_\alpha$) decoupling, during the $^{13}C_\alpha$ (or ^{13}CO) evolution time, is often required for ^{13}C- and ^{15}N-labelled proteins.[47,55,56] It may be accomplished either by a selective 180° inversion pulse in the middle of the evolution time as discussed in Section 5, or by a selective decoupling pulse applied entirely during the evolution time, such as the SEDUCE (selective decoupling using crafted excitation) sequence,[41] one of the more widely used homonuclear decoupling sequences. The SEDUCE decoupling was recently replaced by adiabatic decoupling. The advantage of using adiabatic decoupling, over any other schemes, is that it has the highest decoupling efficiency,[45] a well-defined decoupling region, and its tolerance to the RF field strength or consequently the RF inhomogeneous, as long as the frequency sweep satisfies the adiabatic condition.[11,12,57–63]

As with any other homonuclear decoupling, the transverse magnetization of the $^{13}C_\alpha$, for example in the evolution time, is perturbed by the decoupling pulse, resulting in an additional precession virtually around the z axis. Since the adiabatic decoupling is applied during the entire evolution time of the $^{13}C_\alpha$, a non-linear frequency shift rather than a phase shift appears in the spectrum. This is termed the Bloch-Siegert (frequency) shift in the NMR literature in honour of their discovery of the phenomenon.

The BSFS by a single adiabatic decoupling can be obtained as follows. For a period of an adiabatic decoupling T, the phase accumulated by the

additional precession in the rotating frame of the ^{13}CO, where the decoupling pulse is applied, can be calculated

$$\varphi_{\mathrm{CO}}(T) \approx -2\pi \int_0^T \sqrt{(\Delta f-\delta)^2+f_1^2(t)}dt$$
$$\approx -2\pi\Delta f T + 2\pi\delta T - \pi\frac{f_{1\mathrm{rms}}^2}{\Delta f-\delta}T, \tag{99}$$

where $f_{1\mathrm{rms}}^2 = (1/T)\int_0^T f_1^2(t)dt$ is the mean-square value of the decoupling field strength $f_1(t)$ and the condition of $f_1(t)/\Delta f) \ll 1$ for any t is assumed. After a transformation from the rotating frame of the ^{13}CO to $^{13}\mathrm{C}_\alpha$, the phase accumulation in the $^{13}\mathrm{C}_\alpha$ frame can be obtained

$$\varphi_{\mathrm{C}_\alpha}(T) \approx 2\pi\delta T - \pi\frac{f_{1\mathrm{rms}}^2}{\Delta f-\delta}T, \tag{100}$$

where the first term is caused by the free precession of the $^{13}\mathrm{C}_\alpha$ spins with an offset δ, and the second term is introduced by the decoupling field, leading to a

$$\mathrm{BSFS} = -\frac{f_{1\mathrm{rms}}^2}{2(\Delta f-\delta)}. \tag{101}$$

The minus sign in the above equation implies that the NMR peaks are always pushed away by the decoupling field as illustrated in Fig. 15.

As demonstrated by McCoy and Mueller,[54] the BSFS can be reduced significantly by using a compensating pulse applied on the other side of the $^{13}\mathrm{C}_\alpha$. It is easy to see from Eq. (101) that the BSFS by the two phase

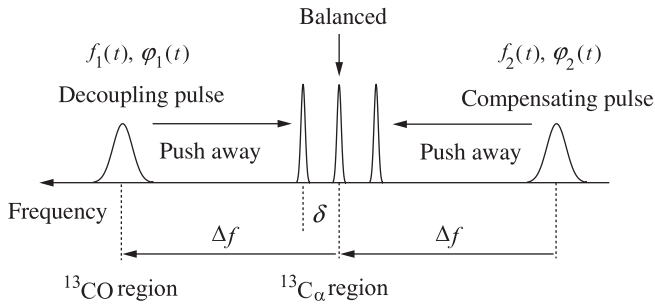

Fig. 15. Adiabatic decoupling of ^{13}CO from $^{13}\mathrm{C}_\alpha$ with a compensating pulse applied on the other side of the peaks. The compensating and decoupling pulses have the same shape but opposite frequency sweep. Due to the Bloch-Siegert effects, both the left and the right peaks are pushed towards the center while the centre peak is balanced and remains in its position. Reprinted from Ref. 47 with permission from Elsevier.

incremented adiabatic decoupling pulses applied on the opposite side of the $^{13}C_{\alpha}$ becomes

$$\begin{aligned} \text{BSFS} &= -\frac{f_{1\text{rms}}^2}{2(\Delta f - \delta)} + \frac{f_{1\text{rms}}^2}{2(\Delta f + \delta)} \\ &\approx -\frac{f_{1\text{rms}}^2}{\Delta f^2}\delta, \end{aligned} \tag{102}$$

where the interference term by the two decoupling fields is averaged out over a relatively long decoupling time. The above equation tells us that the compensating pulse, in theory, gets rid of the BSFS only for the centre point ($\delta = 0$). A reduced offset dependent BSFS still remains. It is scaled approximately by a factor of ($2\delta/\Delta f$) for the double adiabatic decoupling. For, $\delta = 0$, the BSFS vanishes; for $\delta > 0$, it is negative; and for $\delta < 0$, it is positive. The whole spectrum is therefore contracted by a factor of

$$\lambda = [1 - (f_{1\text{rms}}/\Delta f)^2]. \tag{103}$$

To compensate for the contracting effect, a dilated evolution time

$$t_1' = \frac{t_1}{\lambda} \approx [1 + (f_{1\text{rms}}/\Delta f)^2]t_1 \tag{104}$$

can be used in the experiment, leading to a complete compensation of the BSFS.[47,48]

6.4. Experimental

In the $^{13}C_{\alpha}$–^{13}CO homonuclear decoupling experiments, the double adiabatic decoupling uses a non-linear frequency sweep that is created in a certain way that the adiabatic inversion is offset independent.[60,61,63] It leads to a superb decoupling profile with quite a broad range and very sharp edges, particularly suitable for homonuclear decoupling. The double adiabatic decoupling is constructed with a single waveform generator using the method discussed in Section 6.2. To use the BSFS compensated double adiabatic decoupling, the RF field strength needs to be increased 6 dB, which corresponds to double the amplitude. The $f_{1\text{rms}}$ and the RF power, however, are increased only by a factor of $\sqrt{2}$ and 2, respectively. Here, sample heating is not an important issue since the required decoupling range and the decoupling time or the evolution time, in the indirectly detected dimension, are rather limited. In addition, adiabatic decoupling is the most efficient decoupling scheme in NMR.[45]

The offset independent adiabatic decoupling used in the experiments has a Gaussian shape, $A(t) = f_{1\max}\exp[-\alpha(t - T/2)^2]$ ($\alpha = 2.55$ (kHz)^2, $T = 2.8$ ms), and a phase cycle of (0°, 150°, 60°, 150°, 0°).[64,65] The pulse has a maximum RF field strength of $f_{1\max} = 2.38$ kHz and a root-mean-square value of $f_{1\mathrm{rms}} = 1.26$ kHz. A non-linear frequency sweep is constructed according to Ref. 60. The entire sweep is 8 kHz, which produces a slightly smaller decoupling range.

A HSQC sequence[66] with water suppression is used in the experiments with a sample of ^{15}N- and ^{13}C-labelled (–COOH is unlabelled) N-acetylglycine. The ^{13}C carrier frequency is applied at the methyl $^{13}CH_3$ at 26.07 ppm. A frequency shifted decoupling is applied to the ^{13}CO,[45] with a phase increment of $\Delta\varphi = 23.4°$ and time increment of $\Delta t = 2.8$ μs, corresponding to a frequency shift $\Delta f = 23.2$ kHz. A compensating decoupling sequence is applied at -23.2 kHz with the same RF amplitude modulation but with an opposite frequency sweep. All the experiments were performed on a Varian Unity-Plus 600 MHz NMR instrument with a 5 mm HCN triple-resonance probe.

Figure 16 shows the ^{13}C spectra of N-acetylglycine obtained from the traces of the indirectly detected dimension of the HSQC experiment. The spectrum

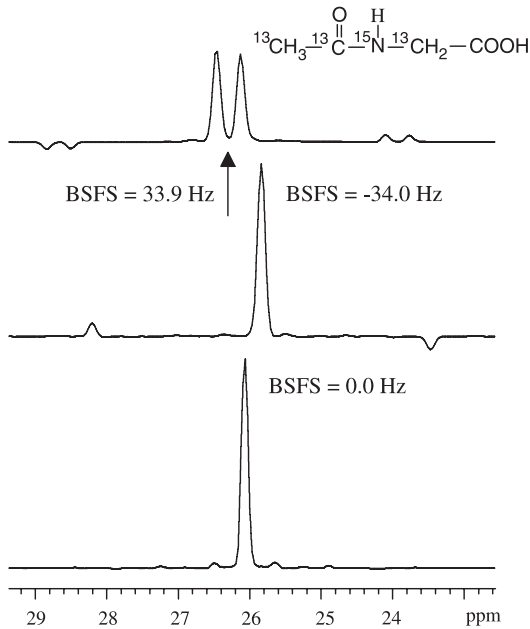

Fig. 16. $^{13}CH_3$ spectra obtained from the traces of two dimensional HSQC spectra with a partially labeled sample of N-acetylglycine. The spectra are acquired with a single adiabatic decoupling (middle), with a compensating decoupling (top), and with a double adiabatic decoupling (bottom). Reprinted from Ref. 47 with permission from Elsevier.

in the middle is obtained with a single adiabatic decoupling $f_1(t)$ (Fig. 15), which causes a BSFS of -34.0 Hz and cyclic irradiation sidebands at $\pm 1/T$ (opposite phase) from the centre peak.[47,48] Unlike the heteronuclear decoupling, where the sidebands are introduced by the modulation of heteronuclear coupling by the decoupling pulse and one usually sees the same phase for all the sidebands,[67,68] the ^{13}C sidebands, in this case, are introduced by direct irradiation of the decoupling pulse.[47,48] The intensities and phases of these sidebands are therefore determined by the amplitude and phase modulations of the decoupling pulse.

The spectrum at the top of Fig. 16 is obtained with the compensating decoupling pulse alone. Since it is located 46.4 kHz away from the ^{13}CO, there is no decoupling effect and the $^{13}CH_3$ peak is split into two with a separation of the ^{13}CO–$^{13}CH_3$ J coupling constant. Also, because the compensating pulse is applied on the other side of the peak, which changes the sign of the BSFS [Eq. (101)], the peaks are shifted to the left side almost the same amount and the spectrum has negative sidebands (also split into two) relative to the spectrum in the middle as expected.[47,48]

The spectrum at the bottom of Fig. 16 is obtained with the double adiabatic decoupling pulse, one located at -23.2 kHz and the other at 23.2 kHz. The BSFS is compensated and sidebands are eliminated by the compensating pulse. In addition, the amplitude of the peak is higher than that in the middle, showing a better decoupling effect. Similar results were obtained for ^{13}C off-resonance δ ranging from -3 to 3 kHz, where $|\delta|/\Delta f < 0.13$ can be treated as close to on-resonance.

As shown in Fig. 17, the BSFS, by a double adiabatic decoupling, is not only significantly reduced compared with that by a single adiabatic decoupling but it also becomes linear as a function of the offset as predicted by Eq. (102). This linear BSFS is corrected by the application of a dilated evolution time $t_1' = [1 + (f_{1\mathrm{rms}}/\Delta f)^2]t_1$.

7. COHERENT EXCITATION WITH PIPS

7.1. Phase coherence in PIPs

As in the phase coherence in RF pulses, the phase coherence in PIPs – the right phase relationship among the PIPs applied at different times, and the relevant offsets, must be taken care of cautiously when multiple PIPs, with the same or different frequency shifts (Δf), are encountered in a pulse sequence. Under such circumstances, the evolution of a spin system has to be calculated in different rotating frames defined by the corresponding PIPs and a special case may arise, where a spin experiences an on-resonance excitation but off-resonance evolution in the conventional rotating frame. Unpredictable results may occur if the phase coherence in PIPs fails. Unfortunately, to date, no

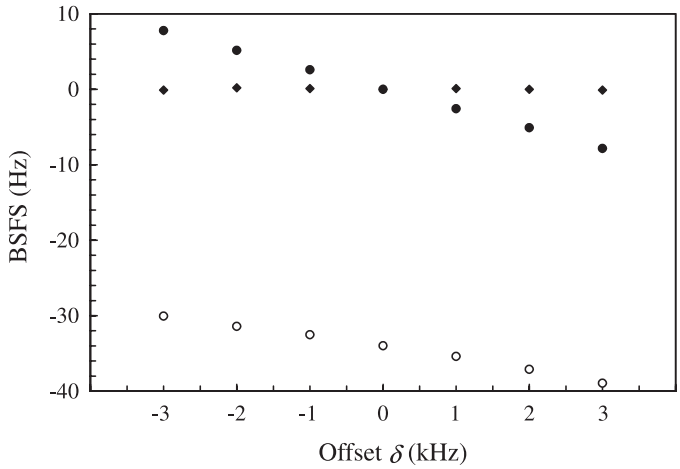

Fig. 17. The BSFS versus the offset δ for a single (open circles) and a double adiabatic (filled circles) decoupling, respectively. By application of a dilated evolution time $t_1' = 1.00223t_1$, the remaining BSFS, which is linearly proportional to the offset, is eliminated (filled diamonds). Reprinted from Ref. 47 with permission from Elsevier.

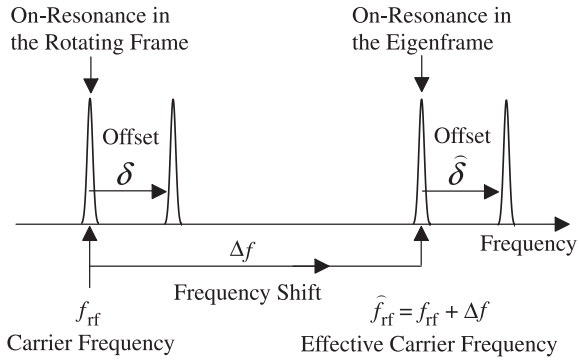

Fig. 18. The relationship between the excitations in the rotating frame by a RF pulse and in the Eigenframe by a PIP. The offset in the Eigenframe $\hat{\delta}$ is measured from the effective carrier $\hat{f}_{rf} = \Delta f + f_{rf}$, where the frequency shift is $\Delta f = \Delta\varphi/2\pi\Delta\tau$. Reprinted from Ref. 49 with permission from Elsevier.

NMR instruments take care of this phase coherence in PIPs and therefore human intervention becomes inevitable.

7.2. The Eigenframe of a PIP

To understand the concept of phase coherence in PIPs it is quite helpful to define an Eigenframe of a PIP as shown in Fig. 18. For a frequency-shifted

excitation by a PIP, the effective carrier frequency $\widehat{f}_{\mathrm{rf}}$ or the on-resonance is shifted to $\Delta f + f_{\mathrm{rf}}$. Therefore, the phase of the centre band RF field of the PIP should be defined in a rotating frame with a speed of $2\pi\Delta f$ relative to the rotating frame since only in this frame is the phase stationary. This particular rotating frame is defined as the Eigenframe of the PIP, where the evolution of the density operator can be calculated similar to that in the conventional rotating frame.

7.3. The phase inheritance

The phase coherence in RF pulses is maintained through a reference signal that provides a phase reference for all the pulses applied at any time as shown in Fig. 19. For example, if the first pulse, described by $A_{\max}\sin(\omega_{\mathrm{rf}}t)$, is applied at a time $t=0$, the second pulse, applied at a time t_s from the beginning of the pulse sequence, must have the form of

$$A_{\max}\sin[\omega_{\mathrm{rf}}(t-t_s)+\varphi_s], \quad t \geq t_s, \tag{105}$$

in order to keep the same phase as the first one. In Eq. (105), $\varphi_s = \omega_{\mathrm{rf}}t_s$ is a phase inherited from the reference signal (Fig. 19). Little attention has been paid to the phase inheritance in NMR experiments since NMR instruments take care of this automatically for users.

When multiple PIPs are encountered, the phase inheritance must also be taken into account as in the case of the RF pulses. For a most simplified phase inheritance with only two consecutive PIPs (Fig. 20), the phase of the first increment of the PIP_2 must have a value that is one increment $\Delta\varphi$ greater than the phase of the last step of the PIP_1 in order to keep the same phase of

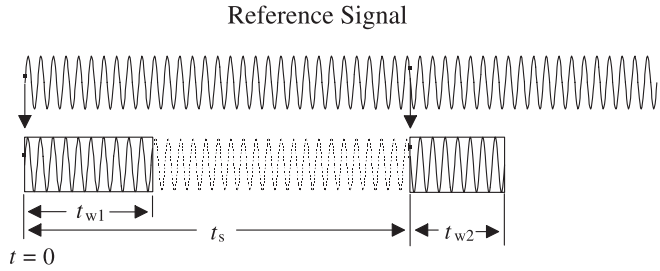

Fig. 19. A reference signal (top) which is served as a phase reference for RF pulses (bottom) applied at any time. The initial phases of the first and second pulse are inherited from the reference signal at time $t=0$ and $t=t_s$, respectively. Consequently, both pulses have the same phase in the rotating frame. Reprinted from Ref. 49 with permission from Elsevier.

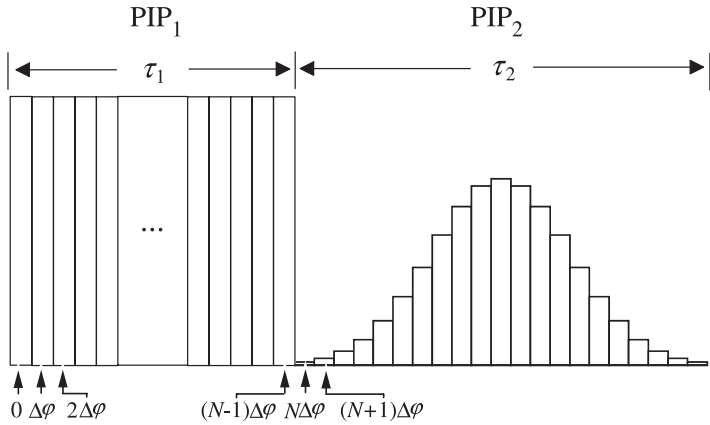

Fig. 20. Schematic representation of the phase inheritance for two PIPs applied consecutively with the same phase increment $\Delta\varphi$ and time increment $\Delta\tau$. Reprinted from Ref. 49 with permission from Elsevier.

the two PIPs, where $N\Delta\varphi$ is an inherited phase from the PIP_1. A more general definition of the phase inheritance will be defined in the following section.

7.4. Theory of coherent excitation with PIPs

A spin system, initially in thermal equilibrium, can be described by a density operator $\sigma(0)$ which is proportional to I_z under the high temperature approximation.[3] After a 90° pulse, the system will evolve under the Hamiltonian and the density operator $\sigma(t)$ in the rotating frame with a speed $\omega_{rf} = 2\pi f_{rf}$ can be written as[3,4]

$$\sigma(t) = L(t)\sigma(0)L^{-1}(t), \tag{106}$$

where the unitary propagator is defined as

$$L(t) = Te^{-i\int_0^t \mathcal{H}(t')dt'}, \tag{107}$$

and T is the Dyson time ordering operator. The Hamiltonian of the system in the rotating frame can be expressed as

$$\mathcal{H}(t) = \delta I_z + \mathcal{H}_{in} + \boldsymbol{f}_1(t)\cdot\boldsymbol{I} \quad \text{(in Hz)}, \tag{108}$$

where the truncated time-independent Hamiltonian $\mathcal{H}_{in}$ is included for generality and it contains all the other spin interactions, J coupling for instance.

For a PIP, the last term in Eq. (108) can be expressed as

$$\boldsymbol{f}_1(t)\cdot\boldsymbol{I} = f_1(t)e^{-i[\varphi_0+\varphi(t)]I_z}I_x e^{i[\varphi_0+\varphi(t)]I_z}, \tag{109}$$

where φ_0 is the initial phase and $\varphi(t)$ is the phase that increments.

As discussed in Section 7.2, it is convenient and intuitive to introduce a new rotating frame with a speed of

$$\widehat{\omega} = 2\pi\Delta f = \frac{\Delta\varphi}{\Delta\tau} \tag{110}$$

relative to the rotating frame since only in this Eigenframe (denoted by the symbol $\frown$) is the phase of the centre band of the PIP a constant.

The Hamiltonian in Eq. (108) can be transformed into the Eigenframe with a unitary operator $U = e^{-i\widehat{\omega}tI_z}$ [1,25]

$$\begin{aligned}\widehat{\mathcal{H}}(t) &= U^{-1}\mathcal{H}U - i(U^{-1}\dot{U}/2\pi)\\ &= (\delta-\Delta f)I_z + \widehat{\mathcal{H}}_{in} + f_1(t)e^{i\widehat{\omega}tI_z}[e^{-i[\varphi_0+\varphi(t)]I_z}I_x e^{i[\varphi_0+\varphi(t)]I_z}]e^{-i\widehat{\omega}tI_z}\\ &\approx \widehat{\delta}I_z + \mathcal{H}_{in} + \lambda_0 f_1(t)e^{-i\left(\varphi_0-\frac{\Delta\varphi}{2}\right)I_z}I_x e^{i\left(\varphi_0-\frac{\Delta\varphi}{2}\right)I_z},\end{aligned} \tag{111}$$

where δ is the offset in the rotating frame, $\widehat{\delta} = \delta - \Delta f = f_0 - (f_{\mathrm{rf}} + \Delta f)$ is the offset in the Eigenframe (Fig. 18), λ_0 is a scaling factor of the RF field strength of the centre band [Eq. (9)], and $-\Delta\varphi/2$ is the UPS. In Eq. (111), $\widehat{\mathcal{H}}_{in} = \mathcal{H}_{in}$ since the truncated internal interaction commutes with I_z, i.e., $[\mathcal{H}_{in}, I_z] = 0$. Here, $\Delta \gg f_{1n}$ is assumed and all the sideband excitations are ignored.

The evolution of the density operator can be calculated in the Eigenframe first and the result is then transformed to the rotating frame. For simplicity, a pulse sequence with two PIPs (refer to Fig. 20) is taken into account first. The calculation is then extended to a general case with any number of PIPs.

At the end of the PIP_1, the density operator in the Eigenframe of the PIP_1 can be expressed as

$$\widehat{\sigma}(\tau_1) = \widehat{L}_1(\tau_1)\,\widehat{\sigma}(0)\,\widehat{L}_1^{-1}(\tau_1). \tag{112}$$

The above density operator needs to be transformed to the rotating frame before calculating the evolution of the density operator by the PIP_2. It can be done by a frame transformation of

$$\sigma(\tau_1) = U_1(\widehat{\omega}_1\tau_1)\,\widehat{L}_1(\tau_1)\,\widehat{\sigma}(0)\,\widehat{L}_1^{-1}(\tau_1)U_1^{-1}(\widehat{\omega}_1\tau_1). \tag{113}$$

The Eigenframe of the PIP_2 starts at the end of τ_1 and at this particular moment this Eigenframe and the rotating frame coincide. Consequently, the

density operator $\sigma(\tau_1)$ is the same as $\widehat{\sigma}(\tau_1)$ in the Eigenframe of the PIP_2. Without a frame transformation, $\sigma(\tau_1)$ serves directly as an initial density operator in the Eigenframe of PIP_2. Therefore, at the end of τ_2 the density operator in the Eigenframe of the PIP_2 is

$$\begin{aligned}\widehat{\sigma}(\tau_1+\tau_2) &= \widehat{L}_2(\tau_2)\sigma(\tau_1)\widehat{L}_2^{-1}(\tau_2)\\ &= \widehat{L}_2(\tau_2)U_1(\widehat{\omega}_1\tau_1)\widehat{L}_1(\tau_1)\widehat{\sigma}(0)\widehat{L}_1^{-1}(\tau_1)U_1^{-1}(\widehat{\omega}_1\tau_1)\widehat{L}_2^{-1}(\tau_2), \qquad (114)\end{aligned}$$

and after a frame transformation, the density operator in the rotating frame becomes

$$\begin{aligned}\sigma(\tau_1+\tau_2) &= U_2\widehat{L}_2(\tau_2)U_1\widehat{L}_1(\tau_1)\widehat{\sigma}(0)\widehat{L}_1^{-1}(\tau_1)U_1^{-1}\widehat{L}_2^{-1}(\tau_2)U_2^{-1}\\ &= U_2U_1U_1^{-1}\widehat{L}_2(\tau_2)U_1\widehat{L}_1(\tau_1)\widehat{\sigma}(0)\widehat{L}_1^{-1}(\tau_1)U_1^{-1}\widehat{L}_2^{-1}(\tau_2)U_1U_1^{-1}U_2^{-1}\\ &= U_2U_1\widehat{\boldsymbol{L}}_2(\tau_2)\widehat{L}_1(\tau_1)\widehat{\sigma}(0)\widehat{L}_1^{-1}(\tau_1)\widehat{\boldsymbol{L}}_2^{-1}(\tau_2)U_1^{-1}U_2^{-1}, \qquad (115)\end{aligned}$$

where the arguments $\widehat{\omega}_1\tau_1$ and $\widehat{\omega}_2\tau_2$ of U_1 and U_2 are omitted for simplicity. The operator U_1, introduced to transform $\widehat{\sigma}(\tau_1)$ back into the rotating frame, acts now on the propagator of the PIP_2. It rotates $\widehat{L}_2(t)$ around the $-I_z$ axis with an angle of $\phi_1 = \widehat{\omega}_1\tau_1$, i.e.,

$$U_1^{-1}\widehat{L}_2(\tau_2)U_1 = \widehat{\boldsymbol{L}}_2(\tau_2) = Te^{-i\int_{\tau_1}^{\tau_1+\tau_2}\widehat{\mathcal{H}}_2(t')dt'} \qquad (116)$$

and

$$\begin{aligned}\hat{\mathcal{H}}_2(t) &= U_1^{-1}\hat{\mathcal{H}}_2U_1\\ &= \widehat{\delta}_2I_z + \mathcal{H}_{in} + \lambda_{02}f_{12}(t)e^{-i(\varphi_{02}+\mathrm{UPS}_2-\phi_1)I_z}I_xe^{i(\varphi_{02}+\mathrm{UPS}_2-\phi_1)I_z}, \qquad (117)\end{aligned}$$

where $\widehat{\boldsymbol{L}}_2(\tau_2)$ and $\widehat{\boldsymbol{\mathcal{H}}}_2(t)$, both in bold phase, are termed the shifted-propagator and Hamiltonian in the Eigenframe of the PIP_2, respectively, with an additional phase shift $\phi_1 = \widehat{\omega}_1\tau_1$ introduced by the frame transformation.

In general, for a pulse sequence of any number of PIPs, the density operator is described by

$$\begin{aligned}\sigma(\tau_1+\tau_2+\cdots+\tau_n) = U_n\cdots U_2U_1\widehat{\boldsymbol{L}}_n(\tau_n)\cdots\widehat{\boldsymbol{L}}_2(\tau_2)\widehat{L}_1(\tau_1)\sigma(0)\\ \times\widehat{L}_1(\tau_1)\widehat{\boldsymbol{L}}_2^{-1}(\tau_2)\cdots\widehat{\boldsymbol{L}}_n^{-1}(\tau_n)U_1^{-1}U_2^{-1}\cdots U_n^{-1}, \qquad (118)\end{aligned}$$

where the shifted-propagator $\widehat{\boldsymbol{L}}_k(\tau_k)$ in the Eigenframe is defined as

$$\begin{aligned}\widehat{\boldsymbol{L}}_k(\tau_k) &= U_1^{-1}U_2^{-1}\cdots U_{k-1}^{-1}\widehat{L}_k(\tau_k)U_{k-1}\cdots U_2U_1\\ &= Te^{-i\int_{\tau_1+\cdots+\tau_{k-1}}^{\tau_1+\cdots+\tau_{k-1}+\tau_k} U_1^{-1}U_2^{-1}\cdots U_{k-1}^{-1}\widehat{\mathcal{H}}_k(t')U_{k-1}\cdots U_2U_1dt'}\\ &= Te^{-i\int_{\tau_1+\cdots+\tau_{k-1}}^{\tau_1+\cdots+\tau_{k-1}+\tau_k}\widehat{\boldsymbol{\mathcal{H}}}_k(t')\,dt'},\end{aligned} \tag{119}$$

where

$$\begin{aligned}\widehat{\boldsymbol{\mathcal{H}}}_k(t) &= \widehat{\delta}_kI_z+\mathcal{H}_{in}\\ &\quad+\lambda_{0k}f_{1k}(t)e^{-i(\varphi_{0k}+\mathrm{UPS}_k-\phi_{k-1})I_z}I_xe^{i(\varphi_{0k}+\mathrm{UPS}_k-\phi_{k-1})I_z}\end{aligned} \tag{120}$$

is the shifted-Hamiltonian of the PIP_k in the Eigenframe, and

$$\phi_{k-1}=\widehat{\omega}_1\tau_1+\widehat{\omega}_2\tau_2+\cdots+\widehat{\omega}_{k-1}\tau_{k-1} \tag{121}$$

is the sum of all the phases accumulated through the changes of the Eigenframes before the PIP_k.

The phase of the PIP_k in Eq. (120)

$$\varphi_k=\varphi_{0k}+\mathrm{UPS}_k-\phi_{k-1} \tag{122}$$

is determined not only by its own initial phase φ_{0k} and UPS_k but also by an inherited phase ϕ_{k-1} from all the previous PIPs. Equation (122) is a more general expression of the phase inheritance for any PIP. Unlike the normal RF pulses, this phase inheritance must be taken care of by the user rather than by the NMR instrument. To have a desired phase φ_k of the PIP_k, the initial phase φ_{0k} can be adjusted.

Equation (118) allows us to calculate the response of a spin system by any number of PIPs. The unitary operators $U_1^{-1}U_2^{-1}\cdots U_{k-1}^{-1}$ act on the propagator $\widehat{L}_k$ causing only a phase shift of the PIP_k. And the shifted-propagators, $\widehat{\boldsymbol{L}}_k\cdots\widehat{\boldsymbol{L}}_2\widehat{L}_1$, act consecutively on the density operator without the frame transformation as if it were still in the rotating frame with a single carrier. The offset, however, must be calculated in the Eigenframe of each PIP, i.e., $\widehat{\delta}_k=(f_0-f_{\mathrm{rf}}-\widehat{\omega}_k/2\pi)$.

It is worth mentioning that Eq. (118), derived from the PIPs, is actually rather general and can be used for any pulse sequences with or without PIPs. If $\Delta\varphi$ of a PIP equals zero, the PIP$\Delta f(\varphi_0,\ \Delta\varphi=0,\ \Delta\tau,\ f_1(k),$ steps) reduces to a normal shaped pulse. If, on the other hand, $f_1=0$ (correspondingly, $\varphi_0=0$

and $\Delta\varphi = 0$), the PIP reduces to a delay with a delay time equal to the pulsewidth.

7.5. Applications

In this section, three experiments are going to be discussed. Two of them, a broadband inversion and a Hahn spin echo, are well-known in the rotating frame. They need to meet the requirement of the phase coherence in PIPs in order to work properly in the Eigenframe. The third is a composite pulse with offset modulation.

Assume a broadband inversion pulse ($90^\circ_x 180^\circ_y 90^\circ_x$)[69] is adopted to excite a region 50 kHz away from the carrier frequency. To this end, the three RF pulses need to be replaced by three PIPs. PIP_1 is composed of 50 steps, a time increment $\Delta\tau = 0.5$ μs, and a phase increment $\Delta\varphi = 9^\circ$. It can be represented by $PIP_1 50(4.5^\circ, 9^\circ, 0.5\ \mu s, 10.01\ kHz, 50)$, where the RF field strength 10.01 kHz is calculated from the 90° pulsewidth (25 μs) and the scaling factor λ_{01} ($= 0.99897$). An initial phase $\varphi_{01} = 4.5^\circ$ is used in the PIP_1 to compensate the $UPS_1 = -(1/2)\Delta\varphi = -4.5^\circ$, otherwise the PIP_1 would have a phase of -4.5° rather than 0° (or the x phase).

To achieve the same frequency shift as the PIP_1, the PIP_2 and PIP_3 have the same $\Delta\tau$, $\Delta\varphi$, and the pulse strength as the PIP_1. The PIP_2 has 100 steps since it is a 180° PIP. In addition to its own UPS_2 ($= -4.5^\circ$), the PIP_2 is also subjected to an inherited phase $\phi_1 (= \widehat{\omega}_1 \tau_1 = 450^\circ)$ from the PIP_1. According to Eq. (122), the PIP_2 with a 90° (or y) phase must obey the following equation in order to satisfy the phase coherence in PIPs

$$\varphi_2 = \varphi_{02} + UPS_2 - \phi_1 = 90^\circ, \tag{123}$$

from which $\varphi_{02} = 184.5^\circ$ or -175.5° is determined. The PIP_2 can be written as $PIP_2 50(-175.5^\circ, 9^\circ, 0.5\ \mu s, 10.01\ kHz, 100)$. Similarly, PIP_3 can be determined as $PIP_3 50(-85.5^\circ, 9^\circ, 0.5\,\mu s, 10.01\,kHz, 50)$. Here the final frame transformation to the rotating frame using $U_3 U_2 U_1$ is not necessary since only the inversion profile (or the z component of the magnetization) is of interest.

As shown in Fig. 21a, the simulated broadband inversion profile by the three PIPs resembles the profile by the composite pulse $90^\circ_x 180^\circ_y 90^\circ_x$ except for a different excitation region. The inversion profile is severely distorted (Fig. 21b) if the three initial phases, $\varphi_{01} = 0^\circ$, $\varphi_{02} = 90^\circ$, and $\varphi_{03} = 0^\circ$ are used, indicating that the right phase relationship in the rotating frame is the wrong one in the Eigenframe. The phase coherence in PIPs needs to be considered even for PIPs with the same frequency shift, $\Delta f = 50$ kHz in this case.

For a Hahn spin echo sequence,[70] $90^\circ_y - \tau - 180^\circ_x - \tau'$, the magnetization in the rotating frame will be refocused to the x axis at the end of the sequence.

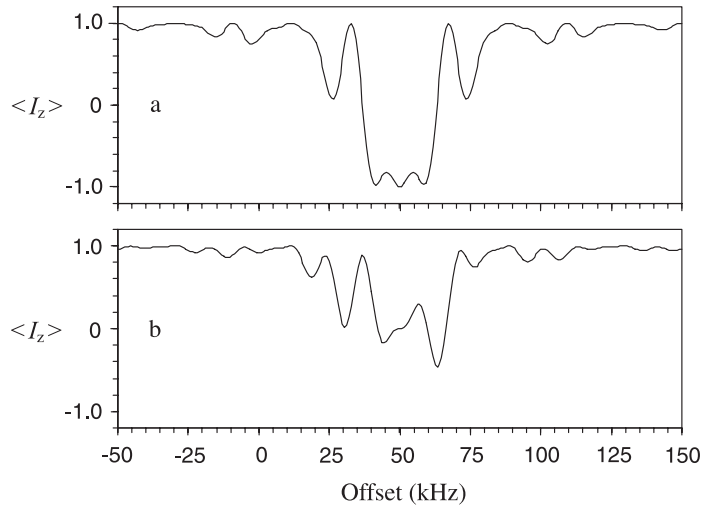

Fig. 21. Simulated broadband inversion profiles by a composite (180°) PIP (a), $PIP_3 50(-85.5°, 9°, 0.5\ \mu s, 10.01\ kHz, 50)$ $PIP_2 50(-175.5°, 9°, 0.5\ \mu s, 10.01\ kHz, 100)$, $PIP_1 50(4.5°, 9°, 0.5\ \mu s, 10.01\ kHz, 50)$, and by the same PIPs but different initial phases (b), $\varphi_{01} = 0°$, $\varphi_{02} = 90°$, and $\varphi_{03} = 0°$. Reprinted from Ref. 49 with permission from Elsevier.

To create a spin echo 50 kHz away from the carrier frequency, two PIPs are required. The first 90°_y pulse can be replaced by $PIP_1 50(94.5°, 9°, 0.5\ \mu s, 10.01\ kHz, 50)$ with a pulsewidth $t_w = 25\ \mu s$, where the same parameters as the previous case are used. A 4.5° phase is included in the initial phase to compensate the UPS ($= -(1/2)\Delta\varphi = -4.5°$). After the PIP_1 there is a delay τ, during which the evolution of the density operator can still be considered in the Eigenframe, as if the PIP_1 were extended to the entire τ with zero pulse strength. To meet the phase coherence in PIPs, the phase of the PIP_2 should obey the equation of $\varphi_2 = \varphi_{02} + UPS_2 - \phi_1 = 0°$, where $\phi_1 = \widehat{\omega}_1(t_w + \tau)$ is the inherited phase. Therefore, ϕ_{02} can be derived and from which the PIP_2 can be constructed. However, this frequency-shifted Hahn spin echo will refocus the magnetization to the x axis in the Eigenframe rather than in the conventional rotating frame. To refocus the final magnetization to the x axis in the rotating frame, the density operator in the Eigenframe needs to be transformed back to the rotating frame, which introduces an additional phase shift of $\widehat{\omega}(3t_w + \tau + \tau')$ [Eq. (15)]. For compensating this phase shift, the magnetization should be refocused to an axis with a phase of $-\widehat{\omega}(3t_w + \tau + \tau')$ in the Eigenframe. This can be accomplished by adding a phase of $-\widehat{\omega}(3t_w + \tau + \tau')/2$ to φ_2 of the PIP_2

$$\varphi_2 = \varphi_{02} + UPS_2 - \phi_1 = -\widehat{\omega}(3t_w + \tau + \tau')/2, \tag{124}$$

or

$$\varphi_{02} = \widehat{\omega}(t_w + \tau) + \frac{\Delta\varphi}{2} - \frac{\widehat{\omega}}{2}(3t_w + \tau + \tau')$$

$$= \frac{\Delta\varphi}{2} - \frac{\widehat{\omega}}{2}(\tau' - \tau + t_w). \tag{125}$$

For $\tau' = \tau$,

$$\varphi_{02} = \frac{\Delta\varphi}{2} - \frac{\widehat{\omega}}{2} t_w, \tag{126}$$

where the delay and the pulsewidth of the PIP_2 disappear due to the refocusing effect of the 180° pulse. Only the UPS ($= -\Delta\varphi/2$) and the phase $-\widehat{\omega} t_w/2$ (partially refocused) need to be taken into account. From Eq. (125), the initial phase of the PIP_2 can be determined $\varphi_{02} = -220.5°$ or 139.5°. The PIP_2 is then $PIP_2$50(139.5°, 9°, 0.5 μs, 10.01 kHz, 100).

For $\tau' = \tau - t_w$, however,

$$\varphi_{02} = \frac{\Delta\varphi}{2}, \tag{127}$$

which is now independent both of the pulsewidth t_w and delay τ. In this situation, a $PIP_2$50(4.5°, 9°, 0.5 μs, 10.01 kHz, 100) can be used. Except for a 4.5°(−UPS), the phase relationships of the two pulses, in the rotating frame and in the Eigenframe, become the same.

In both of the above cases, $\tau' = \tau = 1$ ms and $\tau' = \tau - t_w = 0.975$ ms, the computer simulations show that the phases of the magnetization $\theta = 0.0°$ in the rotating frame, in agreement with the theoretical prediction.

In many triple-resonance experiments, HNCO for instance, coherence needs to be transferred from the amide ^{15}N to the adjacent ^{13}CO but not to the $^{13}C_\alpha$. To this end, a selective ^{13}CO 180° pulse is used in the INEPT segment. It inverts the ^{13}CO region centred at 174 ppm but nulls the $^{13}C_\alpha$ region centred at 56 ppm. Similar to the homonuclear decoupling discussed in Section 5, the RF field strength must satisfy the relationships of[19]

$$2\pi f_1 \tau = \pi, \tag{128}$$

for inversion of the ^{13}CO, and

$$2\pi\sqrt{f_1^2 + \Delta f^2}\,\tau = 2m\pi \quad (m \text{ integer}), \tag{129}$$

for null of the $^{13}C_{\alpha}$, which leads to

$$f_1 = \frac{\Delta f}{\sqrt{4m^2 - 1}}, \tag{130}$$

where Δf ($= 118$ ppm) is the difference of chemical shifts between the centers of the ^{13}CO and $^{13}C_{\alpha}$. For $m = 1$, which corresponds to a 2π rotation of $^{13}C_{\alpha}$, Eq. (130) reduces to

$$f_1 = \frac{\Delta f}{\sqrt{3}}. \tag{131}$$

Figure 22a shows the inversion and null profile of this scheme. It has a narrow inversion and null bandwidths and in addition, the null point moves when the RF field strength f_1 varies.

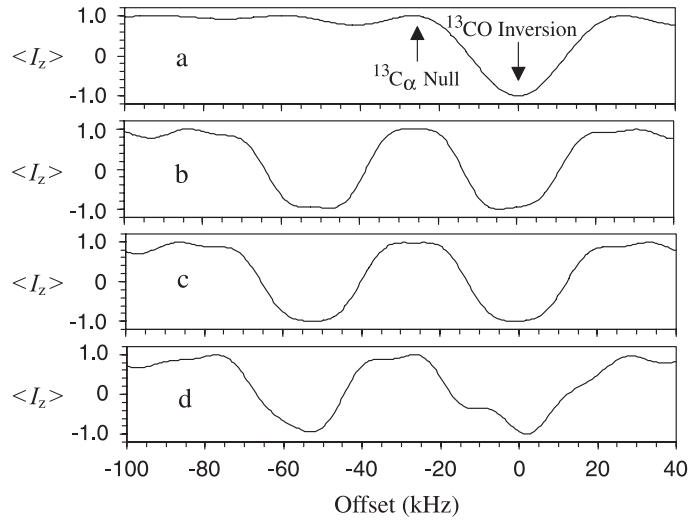

Fig. 22. Simulated excitation profiles of selective inversion and null by a single RF pulse (a) and by two consecutive PIPs (b, c, and d). The single pulse is applied on-resonance to the centre of the ^{13}CO (at 174 ppm which is assigned to 0 kHz) with a pulse strength $f_1 = 15.42$ kHz and pulsewidth $\tau = 32.4$ μs. Under this condition, the centre of the $^{13}C_{\alpha}$ (at 56 ppm, corresponding to -26.7 kHz for a 900 MHz instrument) is subjected to a 2π rotation, resulting in a null excitation as shown in (a). For (b), two consecutive PIPs, $PIP_1 0(0°,0°$, 0.6 μs, 15.42 kHz, 54) and PIP_2-53.4($-5.77°$, $-11.54°$, 0.6 μs, 15.42 kHz, 54), are used with the $PIP_1 0$ being the same as the RF pulse used in (a) and the PIP_2-53.4 being a compensating pulse. (c) is obtained by slightly adjusting the centre of inversion and the overall rotation angle. The two PIPs used are $PIP_1 1.57(0.17°$, $0.34°$, 0.6 μs, 18.34 kHz, 51) and PIP_2-54.95($11.36°$, $-11.87°$, 0.6 μs, 18.34 kHz, 51). The compensation becomes rather poor (d) by exchanging the order of the two PIPs used in (b) due to the failure of the phase coherence in PIPs. Reprinted from Ref. 49 with permission from Elsevier.

To overcome these problems, a compensating PIP can be applied on the other side of the $^{13}C_\alpha$ region immediately after the first inversion pulse. The first pulse is a 180° pulse with a x phase and is on-resonance to the centre of the ^{13}CO. As mentioned above, it can still be denoted as a $PIP_1 0(0°, 0°, 0.6\ \mu s, 15.42\ kHz, 54)$ with a $\Delta f = 0$ and $\Delta\varphi = 0$. The PIP_2 needs to be applied on the other side of the $^{13}C_\alpha$, with also a x phase as the $PIP_1 0$. According to Eq. (122), the initial phase of the PIP_2 must satisfy the equation of

$$\varphi_2 = \varphi_{02} + UPS_2 - \phi_1 = 0°, \tag{132}$$

where the inherited phase from the $PIP_1 0$, $\phi_1 = 0°$, since no phase increment is used in the $PIP_1 0$ or $\widehat{\omega}_1 = 0$. Therefore only the UPS_2 of the PIP needs to be taken into account in determining the initial phase of $\varphi_{02} = -UPS_2$. The second PIP can be expressed as $PIP_2\text{-}53.4(-5.77°, -11.54°, 0.6\ \mu s, 15.42\ kHz, 54)$.

The two PIPs constitute an offset modulated composite pulse for use with a 900 MHz NMR instrument. As a result, the centre of $^{13}C_\alpha$ is subjected to two consecutive 2π rotations of opposite offsets, one positive and the other negative, but of the same (x) phases in the two different Eigenframes as shown in Fig. 23. In the vicinity of the centre of the $^{13}C_\alpha$, the sum of the two rotation angles can be expressed as

$$\varphi = 2\pi\sqrt{f_1^2 + (\Delta f - \delta)^2}\,\tau + 2\pi\sqrt{f_1^2 + (\Delta f + \delta)^2}\,\tau, \tag{133}$$

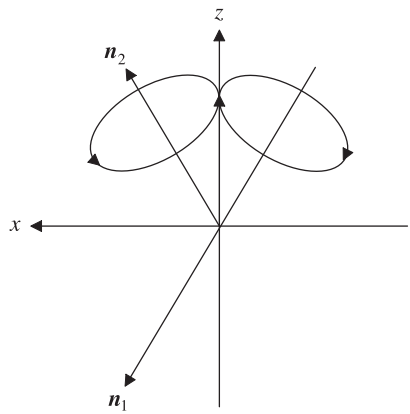

Fig. 23. Offset compensated two consecutive 2π rotations by two consecutive PIPs around $\boldsymbol{n}_1$ in the Eigenframe of the PIP_1 with a negative offset $-\Delta f$ and around $\boldsymbol{n}_2$ in the Eigenframe of the PIP_2 with a positive offset Δf. Both pulses have a x phase but in different Eigenframes. Reprinted from Ref. 49 with permission from Elsevier.

where δ is an offset measured from the centre of the $^{13}C_\alpha$ and τ is the pulsewidth. For small δ , the rotation angle can be expanded into a series of δ

$$\begin{aligned}\varphi &= 2\pi\sqrt{f_1^2+\Delta f^2}\tau - 2\pi\frac{\Delta f\tau}{\sqrt{f_1^2+\Delta f^2}}\delta + \cdots \\ &\quad + 2\pi\sqrt{f_1^2+\Delta f^2}\tau + 2\pi\frac{\Delta f\tau}{\sqrt{f_1^2+\Delta f^2}}\delta + \cdots \\ &= 4\pi\sqrt{f_1^2+\Delta f^2}\tau + \cdots \\ &\approx 4\pi. \end{aligned} \tag{134}$$

In the above equation, the first-order terms in δ cancel, which implies that the deviation from a 360° rotation by PIP_1 due to a small δ is compensated by the deviation from PIP_2. To the first order of δ, the rotation angle $\varphi \approx 4\pi$ leading to a remarkable compensation. As a consequence, the null point at the $^{13}C_\alpha$ region is broadened significantly (Fig. 22b). It is important to note that the inversion region of the ^{13}CO is broadened as well by the compensating PIP_2 since the overall rotation angle and axis by the two PIPs become quite insensitive to the offsets. It can be shown that the overall rotation angle at the centre of the ^{13}CO is about 161.46° rather than 180° but the rotation axis is approximately in the x–y plane, causing an incomplete inversion. Also, the centre of inversion is slightly shifted to the upfield region. These effects are caused by the interference between the two bands. The overall rotation becomes 179.97° if the RF field strength is increased to $2\pi f_1\tau = 202°$. And the small shift of the inversion centre can be corrected by adding a small phase increment to the PIP_1. The final result by the modified pulses is shown in Fig. 22c.

The compensating effect becomes quite poor when the order of the two PIPs is changed (Fig. 22d). The distorted excitation profile can be corrected if an inherited phase $\phi = \widehat{\omega}\tau = 96.84°$ from the first PIP (PIP_2-53.4 in this case) is added to the second PIP ($PIP_1$0) to form two consecutive PIPs of $PIP_2$0(96.84°, 0°, 0.6 μs, 15.42 kHz, 54) and PIP_1-53.4(−5.77°, −11.54°, 0.6 μs, 15.42 kHz, 54). The change of the order of PIPs will affect the inherited phases and therefore it may ruin the phase coherence in PIPs.

8. CONCLUSIONS

A PIP is equivalent to an infinite number of asymmetrically amplitude scaled and phase shifted RF fields that are applied simultaneously and are separated equally in the frequency space. In addition to their locations, all

the RF fields are subjected to a scaling factor $\lambda_n = 2\sin(\Delta\varphi/2)/(2n\pi + \Delta\varphi)$ and a UPS ($= -(1/2)\Delta\varphi$). They are scaled in such a way that under any circumstance, the greater the sideband number $|n|$, the weaker the RF field strength. The UPS can be compensated either by adding a phase of $\Delta\varphi/2$ to the initial phase φ_0 of the PIP or by anti-symmetrizing the PIP. The phase increment should be confined in the range of $-\pi \le \Delta\varphi \le \pi$. Otherwise, a $\Delta\varphi > \pi$ ($\Delta\varphi < 2\pi$) will cause a folding of the strongest RF field into the boundary of the frequency shift, $-\Delta f_{\max} \le \Delta f \le f_{\max}$, with a negative frequency shift.

In order to observe the energy conservation law in PIPs, the scaling factors of any PIP are constrained by the equation of $\sum_{n=-\infty}^{\infty} \lambda_n^2 = 1$. Since $\lim_{\Delta\varphi \to 0^\circ} \lambda_0^2 = 1$, the RF fields of the sidebands acquire energy at the expanse of a reduced field strength of the centre band. However, the centre band only gives up to 59.5% of its energy since a minimum of 40.5% ($= \lim_{\Delta\varphi \to \pm\pi} \lambda_0^2 = (2/\pi)^2$) of the energy remains.

The centre band RF field of a PIP is usually used to achieve a frequency-shifted excitation while preserving the phase coherence among the RF pulses applied before and after the PIP. The phase coherence in RF pulses is crucial in some of the multidimensional NMR experiments, especially in the ^{13}C dimension where the ^{13}CO and $^{13}C_\alpha$ need to be excited separately. Unpredictable results may occur if the phase coherence in RF pulses fails in some NMR experiments.

A periodic pulse also introduces multiple effective RF fields that are symmetric in amplitude and anti-symmetric in phase. For the centre band RF field, the phase is not shifted and the strength is equal to the average value of the periodic pulse. Similar to the case of the PIP, all the phases and scaling factors of the RF fields can be obtained analytically and to fulfill the energy conservation law in periodic pulses, the scaling factors obey the equation of $\sum_{n=-\infty}^{\infty} \lambda_n^2 = (f_{1\text{rms}}^2/\bar{f}_1^2)$.

As a result of the RF interference, a BSOS is introduced to the excitation profile. Unlike the BSFS and BSPS, where the precession of the magnetization is perturbed by nearby RF fields, the BSOS is caused by nearby RF fields during the excitation of a desired RF field. Consequently, the BSOS depends not only on the strengths and locations of the perturbing fields but also on the relative phases between the desired and perturbing RF fields. The NNA provides an accurate measure of the BSOS caused by multiple RF fields, which is otherwise hard to deal with in NMR.

The idea of using phase increment to achieve frequency-shifted excitation can be extended virtually to any sort of RF pulses, including the most complicated adiabatic inversion pulses where a non-linear phase increment has already been applied. Using the phase increment, double or multiple pulses can be constructed with only a single waveform generator in order to excite different regions of a NMR spectrum or to compensate the BSFS, BSPS, as well as BSOS.

One of the ultimate goals for using the PIPs is to achieve the phase coherence in PIPs with the same or different frequency shifts. Unlike the phase coherence in RF pulses that is achieved automatically by NMR instruments, the phase coherence in PIPs is no longer taken care of by machines. Human intervention is therefore inevitable. By analogy to what the NMR instrument does to preserve the phase coherence in RF pulses, the inherited phase accumulated from all the previous PIPs needs to be taken into account in determining the correct phase of each PIP. By doing so, the Bloch vector model, which is so helpful in understanding the NMR concepts and is used almost solely in the conventional rotating frame, is now applicable to the environments of multiple PIPs or multiple Eigenframes as if it were still in the rotating frame of a single carrier frequency. In this way, the scope of the Bloch vector model is extended so significantly that new pulse schemes, such as the offset modulated composite pulses, which were conceptually difficult to discern in the past and are now perceivable and sometimes apparent.

ACKNOWLEDGEMENTS

This work was supported in part by the Sealy Center for Structural Biology, University of Texas Medical Branch at Galveston. Valuable comments by Mr. Zhenjie Yan and Dr. Steve H. Smallcombe, Varian NMR Instruments and dedicated work by Cynthia J. Orlea in the preparation of this manuscript are highly appreciated. Figure 1 was generously provided by Drs. Steve H. Smallcombe and Lewis E. Kay, University of Toronto. Long term cooperation with Dr. David G. Gorenstein on a number of research projects forms the basis of this chapter. The author would also like to take this opportunity to acknowledge Dr. Graham A. Webb, the Royal Society of Chemistry, for the invitation to contribute a chapter on 'Phase Incremental Pulses in NMR'.

REFERENCES

1. A. Abragam, *Principles of Nuclear Magnetism*, Oxford University Press, Oxford, 1961, 19–27.
2. R. R. Ernst, G. Bodenhausen and A. Wokaun, *Principles of Nuclear Magnetic Resonance in One and Two Dimensions*, Oxford University Press, Oxford, 1987, 44–49, 116–124.
3. M. Mehring, *High Resolution NMR Spectroscopy in Solids*, Springer, Berlin, 1976, 63–64, 83–87.
4. U. Haeberlen, High Resolution NMR in Solids: Selective Averaging, *Advances in Magnetic Resonance, Suppl. 1*, Academic Press, New York, 1976, 64–69.
5. C. P. Slichter, *Principles of Magnetic Resonance*, 3rd edn, Springer-Verlag, Berlin, 1990, 1–50.
6. M. Goldman, *Quantum Description of High-Resolution NMR in Liquids*, Oxford University Press, Oxford, 1988, 54–69.
7. M. H. Levitt, *J. Magn. Reson.*, 1982, **50**, 95.

8. W. S. Warren and A. H. Zewail, *J. Chem. Phys.*, 1983, **78**, 2279.
9. J. Baum, R. Tyko and A. Pines, *J. Chem. Phys.*, 1983, **79**, 4643.
10. R. Tyko, *Phys. Rev. Lett.*, 1983, **51**, 775.
11. J. Baum, R. Tyko and A. Pines, *Phys. Rev.*, 1985, **A 32**, 3435.
12. M. S. Silver, R. I. Joseph, C. N. Chen, V. J. Sank and D. I. Hoult, *Nature*, 1984, **310**, 681.
13. G. Drobny, A. Pines, S. Sinton, D. Weitekamp and D. Wemmer, *Faraday Div. Chem. Soc. Symp.*, 1979, **13**, 49.
14. A. A. Bothner-By and J. Dadok, *J. Magn. Reson.*, 1987, **72**, 540.
15. H. Geen, X. Wu, P. Xu, J. Friedrich and R. Freeman, *J. Magn. Reson.*, 1989, **81**, 646.
16. L. E. Kay, D. Marion and A. Bax, *J. Magn. Reson.*, 1989, **84**, 72.
17. S. L. Patt, *J. Magn. Reson.*, 1992, **96**, 94.
18. L. E. Kay, G. M. Clore, A. Bax and A. M. Gronenborn, *Science*, 1990, **249**, 411.
19. L. E. Kay, M. Ikura, R. Tschudin and A. Bax, *J. Magn. Reson.*, 1990, **89**, 496.
20. M. Ikura, L. E. Kay and A. Bax, *Biochemistry*, 1990, **29**, 4659.
21. C. Griesinger, O. W. Sørensen and R. R. Ernst, *J. Magn. Reson.*, 1987, **73**, 574.
22. C. Griesinger, O. W. Sørensen and R. R. Ernst, *J. Magn. Reson.*, 1989, **84**, 14.
23. R. R. Ernst, *Angew. Chem.*, 1992, **104**, 817.
24. G. W. Vuister, R. Boelens and R. Kaptein, *J. Magn. Reson.*, 1988, **80**, 176.
25. S. Zhang and D. G. Gorenstein, *J. Chem. Phys.*, 1996, **105**, 5659.
26. G. A. Morris and R. Freeman, *J. Magn. Reson.*, 1978, **29**, 433.
27. S. Zhang and D. G. Gorenstein, *Chem. Phys. Lett.*, 1999, **303**, 587.
28. J. H. Shirley, *Phys. Rev.*, 1965, **B 138**, 979.
29. M. M. Maricq, *Phys. Rev.*, 1982, **B 25**, 6622.
30. Y. Zur, M. H. Levitt and S. Vega, *J. Chem. Phys.*, 1983, **78**, 5293.
31. D. B. Zax, G. Goelman, D. Abraamovich and S. Vega, *Advances in Magnetic Resonance*, Vol. 14, W. S. Warren, ed., Academic Press, San Diego, CA, 1990.
32. T. Nakai and C. A. McDowell, *J. Chem. Phys.*, 1992, **95**, 3452.
33. S. Zhang, *J. Chem. Phys.*, 2004, **120**, 1886.
34. S. Grzesiek and A. Bax, *J. Magn. Reson.*, 1992, **96**, 432.
35. D. R. Muhandiram and L. E. Kay, *J. Magn. Reson.*, 1994, **B 103**, 203.
36. A. L. Davis, R. Boelens and R. Kaptein, *J. Biomol. NMR*, 1992, **2**, 395.
37. T. Szyperski, D. Braun, C. Fernandez, C. Bartels and K. Wüthrich, *J. Magn. Reson.*, 1995, **B 108**, 197.
38. M. Sattler, J. Schleucher and C. Griesinger, *Prog. NMR Spectrosc.*, 1999, **34**, 93.
39. R. Freeman, *A Handbook of Nuclear Magnetic Resonance*, Wiley, New York, 1988, 14–16.
40. L. Emsley and G. Bodenhausen, *Chem. Phys. Lett.*, 1990, **168**, 297.
41. M. A. McCoy and L. Mueller, *J. Am. Chem. Soc.*, 1992, **114**, 2108.
42. S. Zhang and D. G. Gorenstein, *Chem. Phys. Lett.*, 2002, **362**, 278.
43. G. W. Vuister and A. Bax, *J. Magn. Reson.*, 1992, **98**, 428.
44. M. A. McCoy and L. Mueller, *J. Magn. Reson.*, 1992, **99**, 18.
45. S. Zhang, J. Wu and D. G. Gorenstein, *J. Magn. Reson.*, 1996, **A 123**, 181.
46. F. Bloch and A. Siegert, *Phys. Rev.*, 1940, **57**, 552.
47. S. Zhang and D. G. Gorenstein, *J. Magn. Reson.*, 1998, **132**, 81.
48. S. Zhang and D. G. Gorenstein, *J. Magn. Reson.*, 1999, **138**, 281.
49. S. Zhang and D. G. Gorenstein, *J. Magn. Reson.*, 2002, **154**, 73.
50. J. J. Sakurai, *Modern Quantum Mechanics*, Addison-Wesley, California, 1985, 26–29, 163–168.
51. P. R. Wallace, *Mathematical Analysis of Physical Problems*, Dover Publications, Inc., New York, 1984, 153–156.
52. K. B. Howell, *Principles of Fourier Analysis*, Chapman & Hall/CRC, Boca Raton, 2001, 129–141, 311–316.
53. U. Haeberlen and J. S. Waugh, *Phys. Rev.*, 1968, **175**, 453.
54. M. A. McCoy and L. Mueller, *J. Magn. Reson.*, 1992, **98**, 674.

55. D. R. Muhandiram and L. E. Kay, *J. Magn. Reson*., 1994, **B 103**, 203.
56. L. E. Kay, G. Y. Xu and T. Yamazaki, *J. Magn. Reson*., 1994, **A109**, 129.
57. M. R. Bendall, *J. Magn. Reson*., 1995, **A 112**, 126.
58. E. Kupče and R. Freeman, *J. Magn. Reson*., 1995, **A 115**, 273.
59. R. Fu and G. Bodenhausen, *J. Magn. Reson*., 1995, **A 117**, 324.
60. A. Tannús and M. Garwood, *J. Magn. Reson*., 1996, **A 120**, 133.
61. E. Kupče and G. Wagner, *J. Magn. Reson*., 1995, **B 109**, 329.
62. H. Matsuo, E. Kupče, H. Li and G. Wagner, *J. Magn. Reson*., 1995, **B 113**, 91.
63. E. Kupče and R. Freeman, *J. Magn. Reson*., 1996, **A 118**, 299.
64. R. Tycko, A. Pines and R. Gluckenheimer, *J. Chem. Phys*., 1985, **83**, 2775.
65. T. Fujiwara and K. Nagayama, *J. Magn. Reson*., 1988, **77**, 53.
66. G. Bodenhausen and D. J. Reuben, *Chem. Phys. Lett*., 1980, **69**, 185.
67. S. Zhang and D. G. Gorenstein, *J. Magn. Reson*., 2000, **144**, 316.
68. S. Zhang and D. G. Gorenstein, *J. Magn. Reson*., 2000, **147**, 110.
69. M. H. Levitt and R. Freman, *J. Magn. Reson*., 1979, **33**, 473.
70. E. L. Hahn, *Phys. Rev*., 1950, **80**, 580.

Advances in NMR Studies of Liquid Crystals

RONALD Y. DONG

Department of Physics and Astronomy, Brandon University, Brandon, MB, Canada R7A 6A9, and Department of Physics and Astronomy, University of Manitoba, Winnipeg, MB, Canada R3T 2N2

ANNUAL REPORTS ON NMR SPECTROSCOPY
VOLUME 53 ISSN 0066 4103
DOI 10.1016/S0066-4103(04)53002-8

Recent solid state NMR studies of liquid crystalline materials are surveyed. The review deals first with some background information in order to facilitate discussions on various NMR (^{13}C, ^{1}H, ^{2}H, ^{19}F etc.) works to be followed. This includes the following: spin Hamiltonians, spin relaxation theory, and a survey of recent solid state NMR methods (mainly ^{13}C) for liquid crystals on the one hand, while on the other hand molecular ordering of mesogens and motional models for liquid crystals. NMR studies done since 1997 on both solutes and solvent molecules are discussed. For the latter, thermotropic and lyotropic liquid crystals are included with an emphasis on newly discovered liquid crystalline materials. For the solute studies, both small molecules and weakly ordered biomolecules are briefly surveyed.

1. INTRODUCTION

Liquid crystals (LC)[1–4] represent a class of materials that form intermediate anisotropic phases between the solid and isotropic liquid phases. Their constituent molecules are organic compounds, which possess certain shape anisotropy (e.g., rod-like, disk-like, banana-like) and give several types of thermotropic LC such as calamitics, discotics, metallomesogens, and bent-core (banana) mesogens. Thermotropics exhibit one or more mesomorphic phases or simply mesophases (e.g., nematic, smectic, columnar, chiral, and banana B phases) upon changing the temperature of the material. Additionally, these monomeric units of various shapes can be incorporated into main-chain and/or side-chain polymers to give liquid crystallinity.[5,6] There is another class of LC known as lyotropics, which are formed by dissolving amphiphilic molecules into a selective solvent (and co-solvent) to form a two or more components system and can exhibit mesophases like micellar, nematic, hexagonal, lamellar, and/or cubic phases by varying the temperature, the solute concentration or both of these. The phenomenon of 'double melting' was discovered in several esters of cholesterol by F. Reinitzer[7] in 1888. These substances melt into an isotropic clear liquid only after passing through an intermediate stable phase in the form of an opaque liquid. Many fundamental advances in understanding LC phases were made before the mid 1960s. These included the model of long stiff rods by Onsager[8] which showed the role of repulsive forces, the Maier-Saupe statistical model[9] which pointed to the role of dispersion forces, and the model by Gelbart and Cotter[10] which united these two approaches in the Van der Waals theories. But the real push in LC research came only after the first application of these materials in electro-optical technology.[11] Indeed, new liquid crystalline materials are being discovered at an alarming rate because of their applied and fundamental nature.

One of the characteristic properties of LC mesophases is the existence of a unique symmetry axis denoted by a unit vector called the director $\underset{\sim}{\mathbf{n}}$. On the

average, mesogenic molecules tend to point more or less along the director. For instance, nematics are optically uniaxial and apolar, i.e., $\underset{\sim}{\mathbf{n}}$ and $-\underset{\sim}{\mathbf{n}}$ are equivalent. A quantitative measure of the parallelity of molecules in mesophases is the (orientational) order parameter $S = \frac{1}{2}\langle 3\cos^2\theta - 1\rangle$, where θ is the angle between the long axis of a molecule and $\underset{\sim}{\mathbf{n}}$, and brackets denote the thermal average. The order parameter can be measured using one of many anisotropic properties of LC. In addition to the orientational ordering, positional order may also occur in layered structures shown by different smectic phases[12] and lamellar phases. For biaxial smectic phases (e.g., smectic C), besides the layer structure the orientation of molecules within each layer is specified by two directors. Now the structures of various mesophases are described in standard texts,[1–4] and the readers can refer to them for further information. However, it may be useful to recall here some remarkable features of LC. It is well known that LC show unusual optical properties. For instance, the chiral nematic (cholesteric) phase shows selective Bragg reflections at certain optical wavelengths. This is caused by the periodic structures in this phase, whose pitch length is temperature sensitive. Applications of cholesterics range from detecting hot spots in human tumours, and microelectronics to locating fractures. Twisted-nematic display has been well received in the watch, calculator and personal computer industry. For molecules containing lateral electric dipole(s) with or without chiral centre(s), their tilted smectic phases and chiral subphases exhibit ferro- and/or antiferroelectric properties. Non-linear optics and electro-optical properties can be observed in chiral smectic C (SmC*) phases of LC monomers and polymers. More recently, antiferro-electricity and ferro-electricity have also been found in smectic phases formed by achiral bent-core (banana) molecules.[13] Smectics have become progressively more competitive in display applications. Metallomesogens have shown light induced optical non-linearities.[14] Remarkable mesophases can be formed by detergents. The so-called 'neat' phase exhibits sucessive sheets of lipid and water molecules. Biological membranes formed by lipids and proteins play a crucial role in many living processes. Model membranes formed with lipids and water have been used to mimic biological systems. Insertion of proteins in model membranes is also possible. Lyotropic phases of certain rod-like molecules with enough water to perserve biological functions have been used to study weakly oriented proteins or nuclei acids.[15,16] The non-zero average of certain nuclear interactions can then be used to gain structure information of biomolecules.

Nuclear Magnetic Resonance (NMR) spectroscopy has been shown to be a powerful technique for studying both the structure and dynamics of liquid crystals.[17–19] In general, NMR of solids and partially ordered systems show three different dynamical ranges: extreme fast motion regime, intermediate motion regime, and ultraslow motion regime. In the extreme fast motion limit, the reciprocal of the characteristic time τ for the motional process (e.g., exchange) is of the order of the Larmor frequency ($\omega_0/2\pi$), i.e., $1/\tau \geq 10^8\ \mathrm{s}^{-1}$,

and the NMR spectrum reflects an average spin Hamiltonian. For example, deuterium NMR spectrum of deuterated LC shows resolved quadrupolar doublets in nematic phases, which give the non-zero average quadrupolar interaction at each deuterium site(s). Dynamics of molecules can be followed by measuring nuclear spin relaxation rate(s). The ultraslow motion regime is characterized by $1/T_1 < 1/\tau < 1/T_2$, where T_1 and T_2 are the spin–lattice and spin–spin relaxation times, respectively. Here $1/\tau \simeq 10^3\ s^{-1}$ is too slow to affect the NMR lineshape, and motions can be studied by two-dimensional (2D) exchange experiments or some sort of magnetization transfer methods. The intermediate motion regime is characterized by $1/\tau$ of the order of the strength of spin interaction, which gives the observed NMR spectral pattern. Here τ (30–100 μs) is still larger than T_2 and dynamical information can be derived from simulations of NMR spectral patterns. These three different motional regimes have been realized in various mesophases. Proton spin–lattice relaxation studies of thermotropic LC in the late 1960s[20–23] played a crucial role in identifying the unique collective dynamics known as order director fluctuations (DF).[24] Later, DF involving two-dimensional or three-dimensional thermal excitations were found to be important in lipid bilayer dynamics.[25–27] Besides DF, it was soon realized[28] that translational and rotational diffusions of mesogenic molecules also induce nuclear spin relaxation as in normal liquids, although with certain motional restrictions. Furthermore, spin relaxation due to internal bond rotations in non-rigid molecules must also be taken into account. Deuterium NMR relaxometry has been applied successfully to assess internal correlated motions.[18]

The present report is organized as follows: Section 2 provides a brief overview of spin Hamiltonians and spin relaxation theory[29] encountered in LC studies; Section 3 gives a description of molecular ordering in LC, while Section 4 outlines NMR techniques which have recently been used in the LC field; Models for different molecular processes: DF, molecular rotations (MR), translational self-diffusion (TD), and internal motions are surveyed in Section 5; Section 6 describes NMR studies of oriented solutes (mainly small molecules) in LC; Section 7 focuses on NMR studies of thermotropics; Section 8 briefly surveys the corresponding advances in lyotropics and weakly ordered biological molecules in lyotropics; Section 9 mentions a few other NMR studies, and the final section provides a brief summary and outlook. It is not our aim to provide an exhaustive survey of NMR literature of LC since 1996, but to highlight some recent advances in the application of pulse NMR techniques to LC and to put a particular emphasis on information obtained by NMR from newer and exotic LC materials. The author will undoubtedly miss some interesting and useful papers in this survey and would therefore express his regret on such oversights. The reader is referred to many existing books[17,30–33] for a more complete coverage of the literature.

2. SPIN HAMILTONIAN AND RELAXATION THEORY

Molecules in ordinary liquids average out all anisotropic spin interactions due to isotropic Brownian motions, and their NMR spectra are governed by the Hamiltonian in units of Hz due to the Zeeman interaction, the isotropic chemical shift (σ) and the isotropic indirect spin–spin coupling (J)

$$H = -\frac{B_0}{2\pi}\sum_i \gamma_i(1-\sigma_i^{\mathrm{iso}})I_{iZ} + \sum_{i<j} J_{ij}^{\mathrm{iso}}\underset{\sim}{\mathbf{I}}_i \cdot \underset{\sim}{\mathbf{I}}_j \tag{1}$$

where the external magnetic field B_0 is along the laboratory z axis and the superscript iso denotes the isotropic part of the tensorial quantities $\underset{\approx}{\sigma}$ and $\underset{\approx}{\mathbf{J}}$. The above Hamiltonian is not a true representation in LC due to the fact that molecules do not tumble isotropically and are partially oriented by an intermolecular potential of mean torque as a result of their shape anisotropy. Although molecules in ordinary liquids may be orientationally ordered by an applied electric or magnetic field, such an effect is usually small in comparison with that in a mesophase. Three main types of spin interactions of interest in LC are: dipole–dipole, nuclear electric quadrupole, and chemical shielding interactions. Nuclear quadrupolar interactions exist for spin $I > 1/2$. The indirect spin–spin coupling is usually small in comparison to the direct dipole–dipole interactions, but may be important in some solute studies.

2.1. Spin Hamiltonian

The spin interactions, dipole–dipole (D), nuclear electric quadrupole (Q) and chemical shielding (CS), may be formally written in terms of irreducible tensors of rank l[34] in Hz:

$$H_\lambda = C_\lambda \sum_l \sum_{m=-l}^{l} (-1)^m T_m^{l,\lambda} R_{-m}^{l,\lambda} \tag{2}$$

where the rank $l = 0$, 1, and 2 and the scalar factor C_λ is an appropriate constant for the spin interaction labelled by λ ($C_D = -\mu_0\gamma_1\gamma_S\hbar/4\pi^2$, $C_Q = eQ/[h2I(2I-1)]$, and $C_{CS} = \gamma_1/2\pi$). The spin operators T_m^l with order m for $\lambda = D$ or Q in the laboratory (X, Y, Z) frame are

$$T_0^0 = -\frac{1}{\sqrt{3}}\underset{\sim}{\mathbf{I}} \cdot \underset{\approx}{\mathbf{S}}$$

$$T_0^2 = \sqrt{\frac{1}{6}}\left(3I_Z S_Z - \underset{\sim}{\mathbf{I}} \cdot \underset{\approx}{\mathbf{S}}\right)$$

$$T^2_{\pm 1} = \mp\frac{1}{2}(I_Z S_\pm + I_\pm S_Z)$$
$$T^2_{\pm 2} = \frac{1}{2} I_\pm S_\pm \tag{3}$$

For the heteronuclear dipole–dipole interaction, the spin $\underset{\sim}{\mathbf{I}} \neq \underset{\sim}{\mathbf{S}}$ whereas for the homonuclear dipolar or electric quadrupole interaction, $\underset{\sim}{\mathbf{I}} = \underset{\sim}{\mathbf{S}}$. For the anisotropic chemical shielding interaction, the spin operators are

$$T^0_0 = -I_Z B_0/\sqrt{3}$$
$$T^2_0 = \sqrt{2/3} I_Z B_0$$
$$T^2_{\pm 1} = \mp I_Z B_0/2$$
$$T^2_{\pm 2} = 0$$

The coupling tensor R^l_m in the laboratory frame is time dependent due to the motions of spin-bearing molecules. It can be expressed in terms of the rotational transformation of the corresponding irreducible components ρ^l_n in the principal axis system (PAS) to the laboratory frame by

$$R^l_m = \sum_n D^{l*}_{m,n}(\Omega_{PL}) \rho^l_n \tag{4}$$

where $D^l_{m,n}(\Omega_{PL})$ denotes the Wigner rotation matrices and Ω_{PL} denotes the Euler angles by which the laboratory frame is brought into coincidence with the PAS. Now

$$\rho^2_0 = \sqrt{3/2}\Delta_\lambda$$
$$\rho^2_{\pm 1} = 0$$
$$\rho^2_{\pm 2} = \frac{1}{2}\Delta_\lambda \eta_\lambda$$

where Δ_λ and η_λ can be obtained from V_{ii}, the principal values of the coupling tensor $\underset{\approx}{V}$. For the quadrupolar case, $\Delta_Q = V_{ZZ} = eq$, the electric field gradient (*efg*) and $\eta_Q = (V_{YY} - V_{XX})/V_{ZZ}$, the asymmetry parameter of the *efg* tensor, while for the dipolar case, $\eta_D = 0$ and $\Delta_D = \langle 1/r^3_{IS} \rangle$, where r_{IS} is the internuclear distance and the brackets denote a vibrational average. For both these cases, $\rho^0_0 = 0$, while for the chemical shielding interaction, $\rho^0_0 = -(\sigma_{11} + \sigma_{22} + \sigma_{33})/\sqrt{2} = -(\mathrm{Tr}\ \underset{\approx}{\sigma})/\sqrt{2}$, $\Delta_{CS} = \sigma_{33} - \frac{1}{3}\ \mathrm{Tr}\ \underset{\approx}{\sigma}$ and $\eta_{\mathrm{CS}} = (\sigma_{22} - \sigma_{11})/\Delta_{\mathrm{CS}}$ where $\sigma_{\alpha\beta}$ are the chemical shielding tensor elements. For other spin interactions like spin-rotation and indirect spin–spin coupling, Eq. (2) still applies (see Ref. 34).

In the high-field limit, the dominant term in the overall Hamiltonian $H = H_Z + H_D + H_Q + H_J$ is the Zeeman contribution. For a typical spectrometer operating at a moderate field (100 MHz), the Zeeman energy is $\approx 10^8$ Hz, while dipolar and quadrupolar interactions are rarely larger than 10^5 Hz, and indirect spin–spin couplings are no bigger than 10^2 Hz. Thus, the off diagonal matrix elements of $H_D + H_Q + H_J$ which couple different $I_Z = \sum_i I_{iZ}$ can be neglected to a good approximation. The implication of the high-field approximation is that certain simplifications can be made in the above tensorial spin interactions. As a result, the total Hamiltonian in the (X, Y, Z) frame can be written as[35]

$$\begin{aligned} H = & -\frac{B_0}{2\pi}\sum_i \gamma_i(1-\sigma_{iZZ})I_{iZ} + \sum_{i<j} J_{ij}^{\text{iso}}\underset{\sim}{\mathbf{I}}_i \cdot \underset{\sim}{\mathbf{I}}_j \\ & + \sum_{i<j}(2D_{ij}^{\text{aniso}} + J_{ij}^{\text{aniso}})[I_{iZ}I_{jZ} - \frac{1}{4}\{I_{i+}I_{j-} + I_{i-}I_{j+}\}] \\ & + \sum_i \frac{q_i^{\text{aniso}}}{4I_i(2I_i-1)}(3I_{iZ}^2 - \underset{\sim}{\mathbf{I}}_i \cdot \underset{\sim}{\mathbf{I}}_i) \end{aligned} \tag{5}$$

where

$$J_{ij}^{\text{iso}} = \frac{1}{3}\text{Tr}\,\underset{\approx}{\mathbf{J}} \tag{6}$$

$$J_{ij}^{\text{aniso}} = J_{ij,ZZ} - J_{ij}^{\text{iso}} \tag{7}$$

$$D_{ij}^{\text{aniso}} = -\frac{\mu_0\gamma_i\gamma_j h}{4\pi^2\langle r_{ij}^3\rangle}P_2(\cos\theta_{ij}) \tag{8}$$

$$q_i^{\text{aniso}} = \frac{eQ_iV_{iZZ}}{h} \tag{9}$$

and θ_{ij} is the polar angle of the internuclear vector between the i–j spin pair in the (X, Y, Z) frame.

2.2. Density matrix and relaxation theory

Nuclear spin relaxation is considered here using a semi-classical approach, i.e., the relaxing spin system is treated quantum mechanically, while the thermal bath or lattice is treated classically. Relaxation is a process by which a spin system is restored to its equilibrium state, and the return to equilibrium can be monitored by its relaxation rates, which determine how the NMR signals detected from the spin system evolve as a function of time. The Redfield relaxation theory[36] based on a density matrix formalism can provide

analytical expressions for both the spin–lattice and spin–spin relaxation rates. The ensemble averaged state of the spin system is specified by the spin density matrix $\underset{\approx}{\rho}$ and its evolution is governed by:

$$\frac{\partial \rho}{\partial t} = -i[H, \rho] \tag{10}$$

Consider a spin system whose spin Hamiltonian consists of a time-independent Hamiltonian H_0 and a stochastic perturbation Hamiltonian $H_\lambda(t)$ due to a small spin–lattice coupling,

$$H = H_0 + H_\lambda(t) \tag{11}$$

where the time averaged $H_\lambda(t)$ is non-zero and the fluctuations in $H_\lambda(t)$ are treated as a stationary random function. The spin–lattice coupling $H_\lambda(t)$ can be isolated by removing the static Hamiltonian H_0 (i.e., Zeeman interaction) in the so-called interaction picture. The evolution of the density matrix in the interaction frame $\tilde{\rho}$ is given by

$$\frac{\partial \tilde{\rho}}{\partial t} = -i\left[\tilde{H}_\lambda(t) - \langle \tilde{H}_\lambda(t)\rangle, \tilde{\rho}\right] \tag{12}$$

where the superscript tilde represents the corresponding operator in the interaction representation, the angular brackets denote the time average, and the square brackets denote the commutator.[29,37,38] The Hamiltonian $\tilde{H}_\lambda(t)$ has double time dependences, one from its random character and the other from being in the interaction representation, and

$$\tilde{H}_\lambda(t) = \exp(iH_0 t) H_\lambda(t) \exp(-iH_0 t) \tag{13}$$

Equation (12) can be integrated formally to give

$$\tilde{\rho}(t) = \tilde{\rho}(0) - i\int_0^t [\tilde{H}_\lambda(t') - \langle \tilde{H}_\lambda(t')\rangle,\ \tilde{\rho}(t')]\, dt' \tag{14}$$

Substituting Eq. (14) into Eq. (12), and neglecting any correlation between the density matrix and the spin–lattice coupling Hamiltonian, one obtains to first order

$$\frac{\partial \tilde{\rho}(t)}{\partial t} = -\int_0^\infty \left\langle \left[\tilde{H}_\lambda(t) - \left\langle \tilde{H}_\lambda \right\rangle, \left[\tilde{H}_\lambda(t-\tau) - \left\langle \tilde{H}_\lambda \right\rangle, \tilde{\rho}(t) - \tilde{\rho}_{eq}\right]\right]\right\rangle d\tau \tag{15}$$

where $\tilde{\rho}(t)$ on the right side of the above equation has been replaced by $\tilde{\rho}(t) - \tilde{\rho}_{eq}$ with $\tilde{\rho}_{eq}$ being the thermal equilibrium density matrix determined

by H_0, i.e.,

$$\rho_{eq} = \frac{e^{-H_0/kT}}{\mathrm{Tr}\{e^{-H_0/kT}\}}$$

with k being the Boltzmann constant, and the angular brackets over the double commutator denote an average over all the molecules in the sample. The time t has to be chosen within the limits $\tau_c < t < \tau$, where τ_c is the correlation time of the random process, and $1/\tau$ gives the rate of change in $\tilde{\rho}(t)$. In the laboratory frame, T^l_p is time independent and given in terms of basis operators by $\sum_q T^l_{p,q}$, while in the interaction representation, it can be shown that[29]

$$\tilde{T}^l_p(t) = \sum_q T^l_{p,q} e^{-i\omega_{p,q}t} \tag{16}$$

where $\omega_{p,q}$ are the characteristic frequencies arising through transforming to the interaction picture and can be expressed in terms of a linear combination of the resonant frequencies of the relaxing spin(s). Using Eqs. (2), (13) in Eq. (15) and the secular approximation, i.e., neglecting contributions from rapidly oscillating terms, as well as the fact that $H_\lambda(t)$ is Hermitian, one obtains[29]

$$\frac{\partial\tilde{\rho}(t)}{\partial t} = -(C_\lambda)^2 \sum_l \sum_{p,q} \left[T^l_{-p,q}, \left[T^l_{p,q}, \tilde{\rho}(t) - \tilde{\rho}_{eq}\right]\right] \times \int_0^\infty \left\langle \left(R^{l*}_p(t+\tau) - \left\langle R^{l*}_p \right\rangle\right)\left(R^l_p(t) - \left\langle R^l_p \right\rangle\right)\right\rangle e^{-i\omega_{p,q}\tau} d\tau \tag{17}$$

At this point, only one type of H_λ is considered. To account for possible interference effects or cross correlations among two different relaxation interactions λ and λ' with ranks l and l', respectively, the above equation is modified to give[39]

$$\frac{\partial\tilde{\rho}(t)}{\partial t} = -\sum_{l,l'} \sum_{p,p',q} C_\lambda C_{\lambda'} \left[T^{l'}_{-p',q}, \left[T^l_{p,q}, \tilde{\rho}(t) - \tilde{\rho}_{eq}\right]\right] \times \int_0^\infty \left\langle \left(R^{l'*}_p(t+\tau) - \left\langle R^{l'*}_p \right\rangle\right)\left(R^l_p(t) - \left\langle R^l_p \right\rangle\right)\right\rangle e^{-i\omega_{p,q}\tau} d\tau \tag{18}$$

where $\delta_{p'p}$ has been used for the random spatial coupling tensors inside the angle brackets, and the operators are subjected to the conditions of same rank, opposite orders and the same frequency. One can introduce a general

definition for the correlation functions:

$$G_m^{l',l}(\tau) = \left\langle \left(R_m^{l'*}(t+\tau) - \left\langle R_m^{l'*}\right\rangle\right)\left(R_m^{l}(t) - \left\langle R_m^{l}\right\rangle\right)\right\rangle \Big/ \left(\rho_0^{l'}\rho_0^{l}\right) \tag{19}$$

When $l \neq l'$, the above gives the so-called cross-correlation functions and the associated cross-correlation rates (longitudinal and transverse). Cross-correlation functions arise from the interference between two relaxation mechanisms (e.g., between the dipole–dipole and the chemical shielding anisotropy interactions, or between the anisotropies of chemical shieldings of two nuclei, etc.).[40] When $l' = l = 2$, one has the autocorrelation functions $G_m^2(\tau)$ or simply

$$G_m(\tau) = \left\langle \left(R_m^{2*}(t+\tau) - \left\langle R_m^{2*}\right\rangle\right)\left(R_m^{2}(t) - \left\langle R_m^{2}\right\rangle\right)\right\rangle \Big/ \left(\rho_0^{2}\right)^2 \tag{20}$$

These describe the dynamics of a unique interaction component Δ_λ, and can be used to simplify Eq. (17). For the special case of $\eta_\lambda = 0$, $R_{-m}^2 = (-1)^m D_{m0}^2(\Omega_{PL})\rho_0^2$ and $G_m(\tau)$ reduces to a familiar form:

$$G_m(\tau) = \left\langle \left(D_{m0}^{2*}(\Omega_{PL}, t+\tau) - \left\langle D_{m0}^{2*}\right\rangle\right)\left(D_{m0}^{2}(\Omega_{PL}, t) - \left\langle D_{m0}^{2}\right\rangle\right)\right\rangle \tag{21}$$

Using the irreducible spectral densities of motion $J_m(\omega_{m,q})$ as the Fourier transform (F.T.) of $G_m(\tau)$, one can rewrite Eq. (17) as

$$\frac{\partial \tilde{\rho}(t)}{\partial t} = -\left(C_\lambda \rho_0^2\right)^2 \sum_m \sum_q J_m\left(\omega_{m,q}\right)\left[T_{-m,q}^2, \left[T_{m,q}^2, \tilde{\rho}(t) - \tilde{\rho}_{eq}\right]\right] \tag{22}$$

where

$$J_m\left(\omega_{m,q}\right) = \int_0^\infty G_m(\tau) e^{-i\omega_{m,q}\tau} d\tau \tag{23}$$

Similarly, for the case of cross-correlations one has

$$\frac{\partial \tilde{\rho}(t)}{\partial t} = -\sum_{l',l} \sum_{p',p,q} a_{l'l} J_{l',l}\left(\omega_{p,q}\right)\left[T_{-p',q}^{l'}, \left[T_{p,q}^{l}, \tilde{\rho}(t) - \tilde{\rho}_{eq}\right]\right] \tag{24}$$

where $a_{l'l} = C_{\lambda'} C_\lambda \rho_0^{l'} \rho_0^{l}$ and the spectral densities $J_{l'l}(\omega_{p,q})$ are defined in terms of the cross-correlation functions as in Eq. (23). The evolution of density matrix in the laboratory frame is simply given by

$$\frac{\partial \rho(t)}{\partial t} = -i[H_0, \rho(t)] - \sum_{l',l} \sum_{p',p,q} a_{l'l} J_{l',l}\left(\omega_{p,q}\right)\left[T_{-p',q}^{l'}, \left[T_{p,q}^{l}, \rho(t) - \rho_{eq}\right]\right] \tag{25}$$

Now the expectation (mean) value of any physical observable $\langle A(t)\rangle = \mathrm{Tr}\{A\rho(t)\}$ can be calculated using Eq. (22) for the auto-correlation case ($l' = l$). For instance, A can be one of the relaxation observables for a spin system. Thus, the relaxation rate can be written as a linear combination of irreducible spectral densities and the coefficients of expansion are obtained by evaluating the double commutators for a specific spin–lattice interaction λ in the auto-correlation case. In working out $G_m(\tau)$ [e.g., Eq. (21)], one can use successive transformations from the PAS to the (X, Y, Z) frame, and the closure property of the rotation group to rewrite $D^2_{m0}(\Omega_{PL})$ so as to include the effects of local segmental, molecular, and/or collective motions for molecules in LC. The calculated irreducible spectral densities contain, therefore, all the frequency and orientational information pertaining to the studied molecular system.

2.3. Cross-relaxation and auto-relaxation rates

Using Eq. (25) and applying the following trace property twice

$$\mathrm{Tr}\{A[B, C]\} = \mathrm{Tr}\{[A, B]C\},$$

viz.

$$\begin{aligned}\mathrm{Tr}\left\{Q\left[T^{l'}_{-p',q}, \left[T^{l}_{p,q}, \rho(t) - \rho_{eq}\right]\right]\right\} &= \mathrm{Tr}\left\{\left[Q, T^{l'}_{-p',q}\right]\left[T^{l}_{p,q}, \rho(t) - \rho_{eq}\right]\right\} \\ &= \mathrm{Tr}\left\{\left[\left[Q, T^{l'}_{-p',q}\right], T^{l}_{p,q}\right]\left(\rho(t) - \rho_{eq}\right)\right\}\end{aligned}$$

the time evolution of a NMR observable Q is[37,39]

$$\begin{aligned}\frac{\partial}{\partial t}\langle Q(t)\rangle = &-i\langle[Q, H_0]\rangle t - \sum_{l',l}\sum_{p',p,q} a_{l'l}J_{l',l}(\omega_{p,q}) \\ &\times\left\{\left\langle\left[\left[Q, T^{l'}_{-p',q}\right], T^{l}_{p,q}\right]\right\rangle(t) - \left\langle\left[\left[Q, T^{l'}_{-p',q}\right], T^{l}_{p,q}\right]_{eq}\right\rangle\right\}\end{aligned} \tag{26}$$

The double commutator $[[Q, T^{l'}_{-p',q}], T^{l}_{p,q}]$ may form new operators different from Q, and some of these new operators may not even be physical observables. When the double commutator conserves the operator Q, one speaks of the auto-correlation mechanism. Otherwise, one speaks of the cross-relaxation process. In other words, cross-relaxation is independent of the nature of the relaxation mechanism, but involves the interconversion between different operators. To facilitate such a possibility, it is desirable to write the density operator in terms of a complete set of orthogonal basis

operators B_j:[38]

$$\rho(t) = \sum_{i=1}^{N} b_j(t) B_j \tag{27}$$

where $N = 2^n$ for a n spin system, and the expansion coefficients $b_j = \langle B_j | \rho(t) \rangle$. Now Eq. (25) can be rewritten in a matrix form as:

$$\frac{\partial}{\partial t} b_r(t) = \sum_s \left\{ i\Omega_{rs} b_s(t) - R_{rs}\left[b_s(t) - b_s^{eq} \right] \right\} \tag{28}$$

where the frequency Ω_{rs} is given by

$$\Omega_{rs} = \frac{\langle B_r | [H_0, B_s] \rangle}{\langle B_r | B_r \rangle}$$

and the relaxation matrix element R_{rs} is

$$R_{rs} = \sum_{l',l} \sum_{p',p,q} a_{l'l} J_{l'l}(\omega_{p,q}) \frac{\left\langle B_r \left| \left[T^{l'}_{-p',q'}, \left[T^{l}_{p,q}, B_s \right] \right] \right\rangle}{\langle B_r | B_r \rangle}$$

When $r \neq s$, one has interconversion between operators B_r and B_s, and R_{rs} is a cross-relaxation rate. Note that the cross-relaxation may or may not contain interference effects depending on the indices l' and l, which keep track of interactions $C_{\lambda'}$ and C_{λ}. Cross-correlation rates and cross-relaxation rates have not been fully utilized in LC. However, there is a recent report[41] on this subject using both the ^{13}C chemical shielding anisotropy and C–H dipolar coupling relaxation mechanisms to study a nematic, and this may be a fruitful arena in gaining dynamic information for LC. We summarize below some well known (auto-)relaxation rates for various spin interactions commonly encountered in LC studies.

2.3.1. *Dipole–dipole relaxation*

To study dipole–dipole relaxation, one must distinguish between homonuclear and heteronuclear (unlike) spin-$\frac{1}{2}$ pairs. The latter gives rise to the so-called 3/2 effect.[29] For an isolated pair of like spin-$\frac{1}{2}$ nuclei ($I = 1$) separated by an internuclear distance r, the treatment of spin relaxation is identical to that for a spin-1 quadrupole system. The Zeeman spin–lattice relaxation time T_{1Z} and spin–spin relaxation time T_2 are given, respectively, by

$$T_{1Z}^{-1} = K_D[J_1(\omega_0) + 4J_2(2\omega_0)] \tag{29}$$

$$T_2^{-1} = K_D\left[\frac{3}{2}J_0(0) + \frac{5}{2}J_1(\omega_0) + J_2(2\omega_0)\right] \tag{30}$$

where in the SI units $K_D = (3/2)(\mu_0\gamma^2\hbar/4\pi r^3)^2$. The dipolar spin–lattice relaxation time T_{1D} accounts for the energy transfer from the dipolar order to the lattice, and can be determined using the Jeener-Broekaert (JB) sequence $90^0_x - \tau - 45^0_y - \tau - 45^0_y$.[42] In LC, relatively fast diffusive motions of neighbouring molecules average out the intermolecular dipolar interactions. The proton system may sometimes be treated as an ensemble of isolated spin pairs. In this limit and under the high spin-temperature approximation[29]

$$T_{1D}^{-1} = K_D\left[3J_1(\omega_0)_{intra}\right] \tag{31}$$

where the subscript *intra* in $J_1(\omega_0)$ is to emphasize the contribution from an isolated spin-$\frac{1}{2}$ pair within a molecule (and only the first nearest neighbouring spin yields a major contribution). The validity of Eq. (31) is questioned,[43] as the prediction of $T_{1Z}/T_{1D} = 3$ in the limit of negligible $J_2(2\omega_0)$ is seldom observed in proton relaxation experiments on LC. Thus, possible contributions to T_{1D} from multi-spin interactions and correlations have been examined,[44] but found to be negligible. Equation (31) has recently been modified by removing the short correlation time approximation, i.e., the secular dipolar Hamiltonian is now combined with the Zeeman Hamiltonian to work out the time dependences of the spin operators in the Redfield high temperature theory.[45] The complex problem of spin correlations and dipolar relaxation without the high spin-temperature approximation has also been addressed, i.e., including second (and higher) order in $\hbar\omega/kT$.[46]

For heteronuclear dipolar relaxation, the dipole–dipole coupling between two unlike spin-$\frac{1}{2}$ nuclei I and S (e.g., ^{13}C–H pair) separated by an internuclear distance r_{IS} is considered. The Zeeman spin–lattice (T_{1Z}) and spin–spin (T_2) relaxation times for the I spin are given, respectively, by

$$T_{1Z}^{-1} = \frac{1}{3}K'_D[J_0(\omega_I - \omega_S) + 3J_1(\omega_I) + 6J_2(\omega_I + \omega_S)] \tag{32}$$

$$T_2^{-1} = \frac{1}{6}K'_D[4J_0(0) + J_0(\omega_I - \omega_S) + 3J_1(\omega_I) + 6J_1(\omega_S) + 6J_2(\omega_I + \omega_S)] \tag{33}$$

where $K'_D = (3/2)(\mu_0\gamma_I\gamma_S\hbar/4\pi r_{IS}^3)^2$.

2.3.2. *Quadrupolar relaxation ($I = 1$)*

The spin–lattice relaxation rate of the Zeeman order, i.e., $\langle I_Z\rangle$ and of the quadrupolar order, i.e., $\langle 3I_Z^2 - 2\rangle$, can be shown to follow respective expressions in terms of $J_m(m\omega)$[47]

$$T_{1Z}^{-1} = K_Q[J_1(\omega_0) + 4J_2(2\omega_0)] \tag{34}$$

$$T_{1Q}^{-1} = K_Q[3J_1(2\omega_0)] \tag{35}$$

where $K_Q = (3\pi^2/2)(e^2qQ/h)^2$ with e^2qQ/h being the quadrupolar coupling constant, and the asymmetry parameter η for the quadrupolar coupling is assumed to be zero. For deuteron or nitrogen-14, there are three spin eigenstates $|1\rangle$, $|0\rangle$ and $|-1\rangle$ for the static Hamiltonian, whose corresponding populations are P_1, P_0, and P_{-1}. While the Zeeman order is given by the population difference $P_1 - P_{-1}$, the quadrupolar order involves a linear combination of all populations $2P_0 - P_1 - P_{-1}$. The T_{1Z} and T_{1Q} can be simultaneously measured using the JB pulse sequence or its broadband version given by the Wimperis sequence.[48] Note that the secular ($m = 0$) spectral density, which contains information about molecular motions on all time scales (within the motional narrowing limit), is not involved in T_1. The non-secular ($m = 1, 2$) spectral densities are affected by motions on a time scale faster than the reciprocal Larmor frequency (typically $< 10^{-7}$ s). To investigate slow motions (typically $> 10^{-3}$ s), one can do field cycling experiments at low Larmor frequencies, or measure the spin–spin relaxation rates T_2. Three independent spin–spin relaxation times can be measured for deuteron(s)[49]

$$T_{2a}^{-1} = K_Q\left[\frac{3}{2}J_0(0) + \frac{5}{2}J_1(\omega_0) + J_2(2\omega_0)\right] \tag{36}$$

$$T_{2b}^{-1} = K_Q\left[\frac{3}{2}J_0(0) + \frac{1}{2}J_1(\omega_0) + J_2(2\omega_0)\right] \tag{37}$$

$$T_{2D}^{-1} = K_Q[J_1(\omega_0) + 2J_2(2\omega_0)] \tag{38}$$

The spin–spin relaxation time T_{2a} can be measured by a quadrupolar echo pulse train $90^\circ_x - \tau - 90^\circ_y - (2\tau - 90^\circ_y)_n$ if the pulse spacing $\tau \ll 2/\Delta\nu$ is satisfied (i.e., the deuteron spin relaxes as if the quadrupolar splitting $\Delta\nu$ is absent or if a non-selective excitation is achieved). Due to the large quadrupolar splitting often encountered in LC, the above condition for τ cannot be fulfilled experimentally and the two lines relax independently (i.e., $\tau > 2/\Delta\nu$ or selective excitation of half of the doublet exists). The quadrupolar echo pulse train then measures[50]

$$T_2^{-1} = K_Q\left[\frac{3}{2}J_0(0) + \frac{3}{2}J_1(\omega_0) + J_2(2\omega_0)\right] \tag{39}$$

Finally, the double quantum (DQ) spin–spin relaxation time T_{2D} can be determined using the pulse sequence $90^\circ_x - \tau - 45^\circ_y - 90^\circ_x - t - 45^\circ_y$.[51] The first three pulses create the DQ coherence, and the last read pulse converts the DQ to a single quantum coherence for detection.

2.3.3. *Chemical shielding anisotropy relaxation*

The magnetic field at a resonant nucleus depends on the applied external B_0 field, as well as the screening of the applied field at the nucleus by its

surrounding electrons. As the shielding (or chemical shift) tensor $\underset{\approx}{\sigma}$ is anisotropic, its principal components σ_{XX}, σ_{YY}, and σ_{ZZ} are different. The relaxation rates due to the chemical shielding anisotropy (CSA) depend on the square of the applied B_0 field. Hence the chemical shielding tends to dominate at high fields and for nuclei exhibiting large chemical shifts. Suppose $\underset{\approx}{\sigma}$ is axially symmetric, i.e., $\sigma_{ZZ} = \sigma_{\parallel}$ and $\sigma_{XX} = \sigma_{YY} = \sigma_{\perp}$. The fluctuating magnetic field due to CSA $\Delta\sigma = \sigma_{\parallel} - \sigma_{\perp}$ at a nucleus can cause spin–lattice and spin–spin relaxation, giving

$$T_{1Z}^{-1} = c^2 6J_1(\omega_0) \tag{40}$$

$$T_2^{-1} = c^2[4J_0(0) + 3J_1(\omega_0)] \tag{41}$$

where $c^2 = (\gamma B_0 \Delta\sigma)^2/9$. In the case of non-axial CSA tensor, the Zeeman spin–lattice and spin–spin relaxation time rates are given, respectively, by Eqs. (40) and (41) except the prefactor c^2 is replaced by

$$c^2 = \frac{1}{9}(\gamma B_0 \Delta\sigma)^2 \left(1 + \frac{\eta_{cs}^2}{3}\right) \tag{42}$$

where $\Delta\sigma = \sigma_{33} - (\sigma_{22} + \sigma_{11})/2$. In the fast motion limit, both spin–lattice and spin–spin relaxation rates show a quadratic field dependence, while in the slow motion regime, the spin–lattice relaxation rate becomes independent of the magnetic field and the spin–spin relaxation rate still retains a quadratic field dependence.

3. MOLECULAR ORDERING IN LC

One of the characteristic features of mesogenic molecules in uniaxial mesophases is their orientational order specified by a set of order parameters, which forms a symmetric and traceless order matrix $\underset{\approx}{S}$. For rigid molecules, the elements of order matrix $S_{\alpha\beta}$, defined by Saupe,[52] $\underset{\approx}{S}$ are given by

$$S_{\alpha\beta} = \frac{1}{2}\left\langle 3\cos\theta_{z,\alpha}\theta_{z,\beta} - \delta_{\alpha\beta}\right\rangle \tag{43}$$

where $\theta_{z,\alpha}$ is the angle between the Z axis (along $\underset{\sim}{\mathbf{n}}$) and α axis, $\alpha, \beta = x, y$ or z of a molecule-fixed frame, and the ensemble average is carried out by a time average of individual molecules over their tumbling motions in the same domain of the sample. In a magnetic or electric field of sufficient field strength, different domains of nematic and some smectic LC can align macroscopically to give a single domain sample. Since $S_{\alpha\beta} = S_{\beta\alpha}$ and $\sum_{\alpha} S_{\alpha\alpha} = 0$,

there are five independent order parameters:

$$\begin{aligned} S_{zz} &= \langle 3\cos^2\theta - 1\rangle/2 \\ S_{xx} - S_{yy} &= 3\langle \sin^2\theta \cos^2\phi\rangle/2 \\ S_{xy} &= 3\langle \sin^2\theta \sin^2\phi\rangle/4 \\ S_{xz} &= 3\langle \sin\theta\cos\theta\cos\phi\rangle/2 \\ S_{yz} &= 3\langle \sin\theta\cos\theta\sin\phi\rangle/2 \end{aligned} \tag{44}$$

where the polar angles (θ, ϕ) specify the Z axis (the director) in the molecular (x, y, z) frame. The number of non-zero, independent elements of $S_{\alpha\beta}$ depends on the point group symmetry of the molecule. For molecules with C_1 and C_i symmetry, all 5 order parameters are non-zero. On the other extreme, one has one order parameter $S = S_{zz}$ for rigid ellipsoids of axial symmetry (C_3 and higher symmetry). Two order parameters S_{zz}, and $S_{xx} - S_{yy}$ exist for molecules with C_{2v}, D_2, and D_{2h} symmetry, while S_{zz}, $S_{xx} - S_{yy}$ and S_{xy} are non-zero for molecules with C_2, C_{2h}, and C_s symmetry. For non-rigid molecules, order parameters can be defined for individual molecular segments. Alternatively, one needs to consider all possible conformers available to the molecule and to apply statistical models.[17,33] For any secondrank tensor element A_{ij}, the partial average of its component along the director ($\underset{\sim}{\mathbf{n}} \| Z$ axis) in uniaxial mesophases can easily be shown to give

$$\langle A_{ZZ}\rangle = A_0 + \frac{2}{3}\sum_{\alpha,\beta} S_{\alpha\beta} A_{\alpha\beta} \tag{45}$$

where $A_0 = \frac{1}{3}\mathrm{Tr}\,\underset{\approx}{\mathbf{A}}$ and is independent of the axis system chosen. For the chemical shielding tensor and the indirect spin–spin interaction $A_0 = \sigma^{\mathrm{iso}}$ and $\mathrm{A}_0 = J_{ij}^{\mathrm{iso}}$, respectively, while A_0 vanishes for the dipole–dipole and quadrupolar interactions. Equation (45) is a result of tensor transformation from the (X, Y, Z) frame to the molecular (x, y, z) frame. To express the molecular properties in the spin Hamiltonian using $S_{\alpha\beta}$, one can write for the chemical shielding

$$\sigma_{i,zz} = \sigma_i^{\mathrm{iso}} + \sigma_i^{\mathrm{aniso}} \tag{46}$$

$$\sigma_i^{\mathrm{aniso}} = \frac{2}{3}\sum_{\alpha,\beta} S_{\alpha\beta}\sigma_{i,\alpha\beta} \tag{47}$$

Similarly, one obtains for the indirect spin–spin interaction

$$J_{ij}^{\mathrm{iso}} = \frac{1}{3}\left(J_{ij,xx} + J_{ij,yy} + J_{ij,zz}\right) \tag{48}$$

$$J_{ij}^{\mathrm{aniso}} = \frac{2}{3}\sum_{\alpha,\beta} S_{\alpha\beta} J_{ij,\alpha\beta} \tag{49}$$

for the dipole–dipole interaction

$$D_{ij}^{\text{aniso}} = \frac{2}{3}\sum_{\alpha,\beta} S_{\alpha\beta} D_{ij,\alpha\beta} \tag{50}$$

and for the quadrupolar interaction

$$q_{ij}^{\text{aniso}} = \frac{2}{3}\sum_{\alpha,\beta} S_{\alpha\beta} q_{i,\alpha\beta} \tag{51}$$

Eqs. (46)–(51) can be used in Eq. (5) to give the average Hamiltonian in the laboratory frame in terms of the order parameter tensor. The NMR spectrum arising from Eq. (5) can provide a means to determine the orientational ordering of molecules in uniaxial LC.

To consider the effect of tilting the director away from the magnetic field, let the director $\underset{\sim}{\mathbf{n}}$ tilt at an angle β w.r.t. the B_0 field(Z axis). Equation (45) is modified due to an additional coordinate transformation (i.e., $(X, Y, Z) \rightarrow$ director frame $\rightarrow (x, y, z)$) to give[53]

$$\langle A_{ZZ} \rangle = A_0 + \left[\frac{1}{2}\left(3\cos^2\beta - 1\right)\right]\frac{2}{3}\sum_{\alpha,\beta} S_{\alpha\beta} A_{\alpha\beta} \tag{52}$$

This equation indicates that the average anisotropic part of A along the magnetic field is now scaled by a reduction factor $P_2(\cos\beta)$. As a consequence of the director tilt, the total Hamiltonian becomes

$$\begin{aligned} H = &-\frac{B_0}{2\pi}\sum_i \gamma_i I_{iZ}\left(1 - \sigma_i^{\text{iso}} - P_2(\cos\beta)\sigma_i^{\text{aniso}}\right) + \sum_{i<j} J_{ij}^{\text{iso}}\, \underset{\sim}{\mathbf{I}}_i \cdot \underset{\sim}{\mathbf{I}}_j \\ &+ \sum_{i<j} P_2(\cos\beta)\left(2D_{ij}^{\text{aniso}} + J_{ij}^{\text{aniso}}\right)\left[I_{iZ}I_{jZ} - \frac{1}{4}\left\{I_{i+}I_{j-} + I_{i-}I_{j+}\right\}\right] \\ &+ \sum_i P_2(\cos\beta)\frac{q_i^{\text{aniso}}}{4I_i(2I_i-1)}\left(3I_{iZ}^2 - \underset{\sim}{\mathbf{I}}_i \cdot \underset{\sim}{\mathbf{I}}_j\right) \end{aligned} \tag{53}$$

In applying Eq. (53), one must keep in mind the following conditions: (1) rotational motions of molecules are fast on the NMR time scale, (2) the director dynamics are governed by the magnetic torque and the mechanical motion of the sample if any, and (3) the magnetic field is sufficient to quantize the nuclear spin. Under mechanical spinning of the sample about a spinning axis $\underset{\sim}{\Omega}$ which is tilted at an angle η w.r.t. B_0 (Fig. 1), the behaviour of the director is governed by the anisotropy in the diamagnetic susceptibility $\Delta\chi$, the magnetic and viscous torques, and the spinning speed ω_r of the sample. This is because the potential energy of the director alignment depends on $P_2(\cos\beta)$

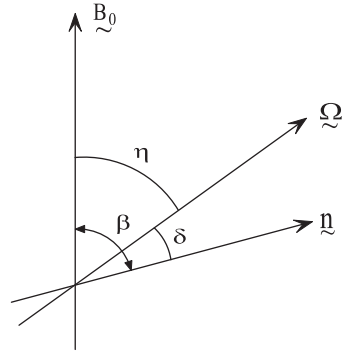

Fig. 1. Plot of the orientations of director and spinning axis of a rotating sample w.r.t. the external magnetic field.

and $\Delta\chi$ (see below). When the sample with $\Delta\chi > 0$ is spun at $\omega_r > \omega_c$ ($\omega_c = \Delta\chi B_0^2/\gamma_1$ is a characteristic frequency and γ_1 is the Leslie rotational twist coefficient), the director has no time to orient parallel to B_0, but would orient to minimize the average potential energy (or $\cos^2\beta$) over one cycle of the rotation. Suppose the director has polar angles δ and φ in the principal frame of the bulk liquid crystal, defined by the spinning axis $\underset{\sim}{\Omega}$ (see Fig. 1). It can be shown that

$$\cos\beta = \cos\eta\cos\delta + \sin\eta\sin\delta\cos(\omega_r t + \varphi)$$

and

$$P_2(\cos\beta) = \left(\frac{3\cos^2\eta - 1}{2}\right)\left(\frac{3\cos^2\delta - 1}{2}\right) \tag{54}$$

For nematics with $\Delta\chi > 0$ and spun at $\omega_r > \omega_c$, the director tends to align along $\underset{\sim}{\Omega}$ ($\delta = 0$) when $\eta < \theta_m$ (magic angle θ_m is 54.7°), or the directors are distributed in a plane perpendicular to $\underset{\sim}{\Omega}$ ($\delta = 90°$) when $\eta > \theta_m$. If $\Delta\chi < 0$, the above conditions for η would reverse. When doing off-magic-angle-spinning (OMAS)[53,54] in the case $\delta = 0$, substitution of Eq. (54) into Eq. (53) shows that all anisotropic interactions (e.g., D_i^{aniso}) will be scaled down by a factor $(3\cos^2\eta - 1)/2$. When $\eta = \theta_m$, the LC directors have no preferred orientation, and the sample behaves like a powder. In the limit of $\eta = \theta_m$, only the isotropic interactions σ_i^{iso} and J_{ij}^{iso} survive in Eq. (53). For example, the ^{13}C NMR spectrum obtained from mesophases using magic-angle-spinning (MAS) shows only the isotropic chemical shifts.

To end this section, let us mention a particular case of Eq. (53) when there is no quadrupolar interaction. In the simple case of the chemical shift difference being larger than the average dipolar coupling, i.e., $\sigma_i - \sigma_j \gg D_{ij}$, the

truncated dipolar interaction, which has only the $I_{iZ}I_{jZ}$ term, is termed the first-order dipolar coupling.[38] The corresponding NMR spectrum is called a first-order spectrum. When the average dipolar couplings D_{ij} exceed the chemical shift differences, the dipolar interaction must now include the $I_{i+}I_{j-}$ and $I_{i-}I_{j+}$ terms leading to more complex second-order spectra. A technique to simply second-order spectra is the proton-detected local field (PDLF) spectroscopy.[55–58] It can yield high-resolution ^{13}C–^{1}H couplings by detecting the dipolar local field produced by the ^{13}C spins at different proton sites in the indirect dimension of a 2D experiment.

4. SURVEY OF NMR METHODS

Here some recent applications of solid state NMR multi-pulse techniques to LC are highlighted. Specifically, ^{13}C NMR is surveyed as it has increasingly become the method of choice to investigate newer liquid crystalline materials. Apart from mentioning some recent 2D NMR techniques using the deuterium probe, the NMR methods using either the deuteron or proton spin can be found in the literature.[17,18,31–33,59] To achieve spectral resolution of different ^{13}C chemical shifts in solids, mechanical rotation of the sample is needed to reduce anisotropic spin interactions even though the ^{13}C chemical shifts cover a relatively large range (>200 ppm). If the sample is spun about an axis oriented at θ w.r.t. B_0 field and at a spinning rate ω_r considerably larger than the coupling constants Δ_λ, the orientational dependent nuclear spin interactions are scaled down by a factor of $\frac{1}{2}(3\cos^2\theta - 1)$. This fact is used in the technique of magic-angle-spinning (MAS) where $\theta = \theta_m$.[60,61] Modern spectrometer can now routinely provide a spinning rate of 20 kHz and higher. Soon after the introduction of MAS, cross-polarization (CP)[62] was found to enhance signals of rare spins like ^{13}C and ^{15}N under the Hartmann–Hahn (H.–H.) condition. Thus CP and MAS have significantly increased the sensitivity of ^{13}C NMR spectroscopy. CP/MAS together with multiple-pulse proton decoupling can now achieve highly resolved ^{13}C spectra in solids. The idea behind the coherent averaging of the anisotropic spin interactions involves either manipulating the spins in the spin space or spatially averaging them through mechanical rotation of the sample. These will now be discussed separately.

4.1. Spatial averaging techniques

Among spatial reorientation techniques, one can find MAS, OMAS, variable angle spinning (VAS) and switched angle spinning (SAS) techniques. Mechanical spinning of LC materials, which has dated back to the early seventies,[63,64] can control the averaging of anisotropic spin interactions

beyond what the static LC samples can provide. The potential energy U of the director under mechanical sample rotation (see Fig. 1) is given using Eq. (54) for $P_2(\cos\beta)$

$$U = -\frac{1}{3}\Delta\chi B_0^2\left(\frac{3\cos^2\eta - 1}{2}\right)\left(\frac{3\cos^2\delta - 1}{2}\right). \tag{55}$$

For OMAS, the director can be aligned either parallel or perpendicular to the rotor axis $\tilde{\Omega}$. When the director alignment is parallel to the $\tilde{\Omega}$ axis ($\delta = 0$), OMAS has been used to scale the dipolar coupling,[64] the CSA[53] and the quadrupolar coupling[65] by the factor $(3\cos^2\eta - 1)/2$. For the case of ^{13}C NMR, the overlap of ^{13}C peaks in the proton-coupled ^{13}C spectra is still too severe to give useful information. To alleviate this difficulty, OMAS in combination with 2D separated local field (SLF) spectroscopy[66–68] has been extensively used to recover ^{13}C–^{1}H dipolar coupling constants in LC.[53,54,69] In the 2D SLF spectroscopy, the pulse sequence contains an evolution (t_1) period and a detection (t_2) period. The NMR data set is collected as a function of both t_1 and t_2. During the t_1 period, a pulse sequence is applied that removes the ^{1}H–^{1}H dipolar couplings and reduces the ^{13}C–^{1}H dipolar couplings by a factor r, while broadband ^{13}C–$\{H_1\}$ decoupling is used during the t_2 period. Using double F.T., the spectrum in the F_2 dimension shows the normal proton-decoupled ^{13}C peaks, while the slices in the F_1 dimension show the individual ^{13}C nuclei with ^{13}C–^{1}H couplings. Each set of the splitting is given by[53]

$$\Delta\nu = r\left[(3\cos^2\eta - 1)D_{ij}^{\text{aniso}} + J_{ij}\right] \tag{56}$$

where $J_{ij} = J_{ij}^{\text{iso}} + J_{ij}^{\text{aniso}}$ can be obtained from the isotropic spectrum as $J_{ij}^{\text{aniso}} \simeq 0$ and the value of r is determined by the ^{1}H–^{1}H homonuclear decoupling sequence used. Now the diploar coupling constant D_{ij}^{aniso} for each molecular segment can be readily determined. The D_{ij}^{aniso} values contain the same information as those in quadrupolar splittings observed from a corresponding deuterated liquid crystal. When the directors are oriented normal to the spinning axis of the rotor, the β angle w.r.t. the magnetic field has a distribution, resulting in the appearance of spinning sidebands. This can be understood by examining the time dependence of the β angle:[70]

$$\begin{aligned}\frac{3\cos^2\beta(t) - 1}{2} = \frac{1}{4}[&(3\cos^2\eta - 1)(3\cos^2\delta - 1) + 3\sin(2\eta)\sin(2\delta)\\ &\times\cos(\omega_r t + \varphi) + 3\sin^2\eta\sin^2\delta\cos(2\omega_r t + 2\varphi)]\end{aligned} \tag{57}$$

Since $\delta = 90^\circ$, only the $\cos(2\omega_r t + 2\varphi)$ term contributes, giving sidebands at even multiples of the spinning frequencies.

For polymeric LC or LC with relatively high viscosity, the director's reorientation time in the magnetic field can be sufficiently long so that dynamic director experiments[71] can be carried out. Using a non-spinning polymeric LC sample, a 2D dynamic director experiment has recently been used[72] to correlate ^{13}C CSA at two different director orientations (0° and 90°) w.r.t. the B_0 field. The experiment is done with the director oriented first at 0° during the evolution t_1 period, then the director is positioned (by rotating the sample) at 90° during the detection t_2 period. The CSA cross-peaks at 0° and 90° orientations can improve the spectral resolution in comparison with the 1D spectrum, and allow the determination of σ^{iso} and σ^{aniso}. The SAS technique has recently been employed[73] to correlate the first-order dipolar spectrum of a solute molecule dissolved in a LC solvent with its isotropic spectrum in a 2D dynamic director experiment. In this 2D experiment, the pulse sequence $90° - t_1 - 45° - t_m - 45° - t_2$ was used, in which during the t_1 period the rotor axis of a dynamic angle spinning probe was at 25° and during the t_2 period it was at the magic angle. A 2D spectrum was obtained, which reveals the dipolar couplings in the form of clearly separated cross-peaks.

4.2. Spin averaging techniques

The presence of ^1H–^1H and ^1H–^{13}C dipolar couplings makes the observation of well-resolved ^{13}C spectra in LC a non-trivial matter. When OMAS is used, the proton dipolar coupling is significantly reduced, and further application of multiple-pulse homonuclear decoupling can remove the residual dipolar couplings. Also the ^{13}C signal must be acquired with efficient heteronuclear ^{13}C–$\{^1H\}$ decoupling. Heteronuclear and homonuclear decoupling schemes, which were designed for liquids and solids, may need modifications when applying to LC.

4.2.1. *Heteronuclear ^{13}C–$\{^1H\}$ proton decoupling*

The aim of heteronuclear decoupling is to observe well-resolved ^{13}C spectra in LC through removing spin interactions (i.e., dipolar and J couplings) between the abundant (^1H) and rare (^{13}C) spins. A brute-force method is to apply an on resonance continuous wave (CW) radiofrequency (*r.f.*) irradiation. Since high *r.f.* power is often required to suppress the rather large ^{13}C–^1H dipolar couplings in a non-spinning LC sample, the CW method can cause severe heating and create large temperature gradients inside the sample.[74] This produces an undesired perturbation on the order parameter of the sample and deteriorates the spectral resolution. To avoid the *r.f.* heating, low power decoupling (ca. 20 kHz or less) and a long recycling time (≥ 30 s) are typical for high-resolution ^{13}C NMR studies of LC. One possible alternative to CW decoupling is to produce low power decoupling by modulating the *r.f.*

irradiation as done in liquids. Furthermore, the aquisition time should not be made unnecessarily long. Low power heteronuclear decoupling schemes, such as the well-known Waltz-16 sequence[75] for liquid-state NMR, do not work in LC since they fail to account for the presence of proton–proton and proton–carbon dipolar couplings. Other alternative is to borrow decoupling schemes from the solid-state, e.g., the two pulse phase modulation (TPPM) technique.[76] The decoupling schemes for solids often work well with MAS, which average all anisotropic interactions to the zeroth order. Since liquid crystalline samples are usually not spun at the magic angle in order to preserve the director alignment by the magnetic field, heteronuclear decoupling sequences designed for rotating solids are generally inappropriate. Thus, the decoupling schemes for LC must consider a non-zero average static Hamiltonian, containing all the spin interactions, along the director. In the past, many special decoupling sequences have been designed for LC.[77,78] Recent developments in LC decoupling schemes include the small phase angle rapid cycling (SPARC)[78] and the small phase incremental alternation (SPINAL).[79] The SPARC-16 decoupling sequence is based on a 16-step phase cycling of the two-step ($P\overline{P}$) TPPM technique to give

$$\text{SPARC-16} = P\overline{P}P\overline{P}P\overline{P}P\overline{P}P\overline{P}P\overline{P}P\overline{P}P\overline{P} \tag{58}$$

where the square pulse width P is $180 \pm 30^\circ$, and the phase shift is $\pm(10^\circ - 12^\circ)$ ($-$ sign is for $\overline{P}$). The SPINAL-64 is a series of 64 phase-alternating *r.f.* pulses:

$$\text{SPINAL-64} = Q\overline{Q}Q\overline{Q}Q\overline{Q}Q\overline{Q} \tag{59}$$

where

$$Q = P(10^\circ)P(-10^\circ)P(15^\circ)P(-15^\circ)P(20^\circ)P(-20^\circ)P(15^\circ)P(-15^\circ)$$

and

$$\overline{Q} = P(-10^\circ)P(10^\circ)P(-15^\circ)P(15^\circ)P(-20^\circ)P(20^\circ)P(-15^\circ)P(15^\circ)$$

with the square pulse $P(\varepsilon)$ being 165° and ε being the phase angle. It is noted that SPINAL-64 has a nominal rotation angle cycle of 64π. As seen in Fig. 2, SPINAL-64 seems to give the best ^{13}C NMR spectrum in the nematic pentylcyanobiphenyl (5CB) with a decoupling power of 18 kHz. The superiority of SPINAL-64 decoupling sequence has recently been demonstrated in a ^{13}C spectrum of a fluorinated liquid crystal,[80] in which dipolar couplings between the fluorine and ring carbons can be readily seen. SPINAL-64 sequence has also been used in our recent ^{13}C studies of bent-core mesogens. Heteronuclear decoupling schemes (e.g., DROOPY-1, SDROOPY-1) with continuously phase modulated *r.f.* pulses have recently been designed for LC

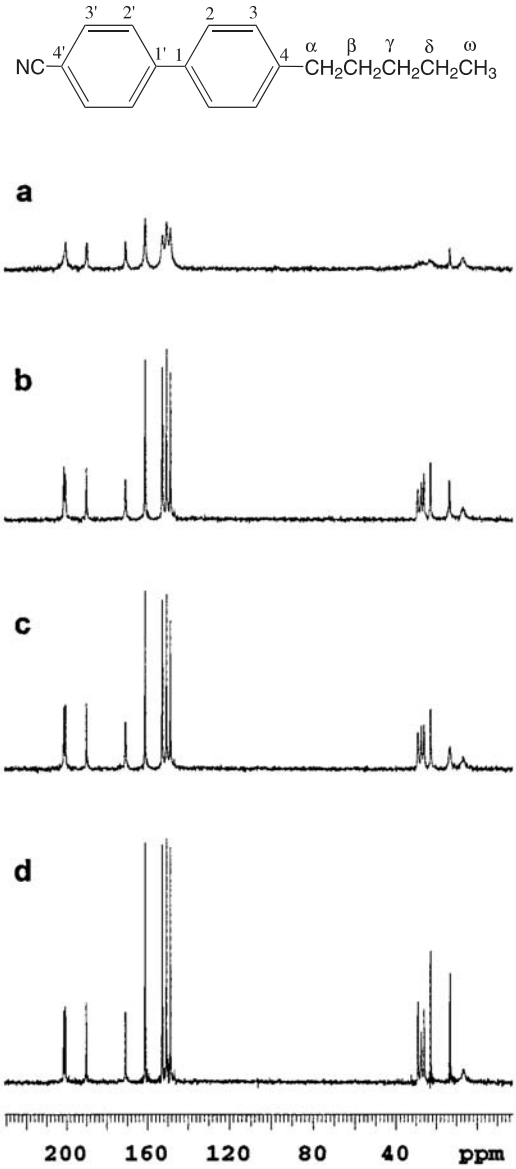

Fig. 2. ^{13}C NMR spectra in its nematic phase (at ambient temperature) of 5CB and its structure. The decoupling power was 18 kHz. The decoupling sequences were (a) Waltz-16, (b) TPPM, (c) SPARC-16, and (d) SPINAL-64. The peak assignment is (from left to right for decreasing chemical shifts): 4, 1′, 1, 4′, 3′, 3, 2′, 2, γ, α, β, δ, ω, and -CN. (Reproduced by permission of Elsevier Science.)

using a numerical optimization technique.[81] DROOPY has only a 6π rotation angle cycle, but seems to give comparable performance as SPINAL-64 in 5CB. Furthermore, SDROOPY-1 was found to be very robust with respect to the proton *r.f.* power setting, and sufficiently broadband in the proton transmitter offset, and consequently gave good decoupling for both the aromatic and aliphatic protons.

4.2.2. *Homonuclear decoupling*

Homonuclear decoupling is used to remove dipolar couplings among the abundant spins such as ^{1}H. Both MAS and cyclic multiple-pulse sequences have been used. The former acts on the space part of the spin Hamiltonian, while the latter acts on its spin part. Both approaches involve rotation, one in the real space and the other in the spin space. The similarity of these approaches is particularly obvious in the case of dipolar interaction. For CSA, the spin part is different from the space part, which allows one to discriminate it from the dipolar broadening by means of suitable pulse sequences. The earliest method of homonuclear dipolar decoupling was demonstrated by the off-resonance 'magic angle CW' irradiation, proposed by Lee and Goldburg (LG).[82] In the LG method, a strong *r.f.* B_1 field is applied off-resonance at $\omega_0 \pm \Delta\omega$, satisfying the condition $\gamma B_1/\Delta\omega = \sqrt{2}$, so that in the rotating frame the spins would precess about an axis (along the effective field) forming the magic angle θ_m w.r.t. the B_0 field. Consequently the homonuclear dipolar coupling term vanishes in the effective spin Hamiltonian. Since the LG method can only eliminate the dipolar interaction to the zeroth order, it is not very effective. Later on, the multiple-pulse WAHUHA sequence was proposed by Waugh and co-workers.[83,84] This four pulse cyclic sequence was more effective, because it removed the dipolar terms in the average spin Hamiltonian to the first order. It has become the building block of many subsequent decoupling sequences, e.g., MREV-8,[85] BR-24,[86] BLEW-48,[87] TREV-8,[88] and MSHOT-3.[89] It is noted that BLEW-48 is windowless, since during continuous *r.f.* irradiation the phases of π/2 pulses are switched. The TREV-8 method involves the use of time-reversal spin echoes, while the MSHOT-3 (magic sandwich high order truncation) method is specially designed to remove higher order dipolar terms. The theoretical scaling factors for MREV-8, BLEW-48 and MSHOT-3 are 0.536, 0.424 and 0.354, respectively.

Later the LG method has been improved to give the frequency-switched Lee–Goldburg (FSLG-2) decoupling scheme, in which the CW *r.f.* irradiation frequency is switched between the two LG conditions $\pm\gamma B_1/\sqrt{2}$ for each 2π rotation of the proton magnetization about the effective field.[90–92] The scaling factor for FSLG-2 is 0.577. Another variant of the LG method is the phase-modulated Lee–Goldburg (PMLG) decoupling.[93] The new scheme produces line narrowing not by switching the frequency as in FSLG-2, but by a multi-pulse sequence which consists of a series of *r.f.* pulses with the phase sequentially varying from one pulse to another. Both FSLG-2 and PMLG

suppress the zero- and first-order dipolar terms in the average spin Hamiltonian. Fung and co-workers have compared in two recent studies the efficiencies of some of the homonuclear decoupling sequences in LC.[94,95] At the time of this review, the BLEW-48 appears to be best in decoupling proton spins in ^{13}C NMR studies of LC.

4.3. Two-dimensional techniques

As mentioned previously, 2D NMR and SLF or PDLF spectroscopy have been applied to LC, allowing the dispersion of carbon chemical shifts to be utilized for the measurement of ^{13}C–^{1}H dipolar couplings and the determination of local orders. Multi-dimensional techniques use the homonuclear and heteronuclear decoupling sequences as building blocks. The 2D SLF spectroscopy has been mentioned in Section 4.1. The F_1 dimension in the 2D spectrum contains slices, each showing 2^m lines with m being the number of coupled protons, for the different ^{13}C atoms. After the scaling factor r of the homonuclear decoupling sequence is taken into account, the splittings in each multiplet are related to the ^{13}C–^{1}H dipolar coupling. Further improvement in the resolution has been achieved by PDLF spectroscopy developed by Pines and co-workers,[55–58] and the 3D version of PDLF spectroscopy in which the proton chemical shift is introduced as the third dimension.[96] The PDLF spectroscopy of a stationary 5CB sample is demonstrated in Fig. 3.[58] As seen in this figure, ^{13}C–^{1}H dipolar couplings of various molecular segments can be readily determined. The pulse sequence for the PDLF method is shown in Fig. 4. The BLEW-48 sequence is used for proton–proton dipolar decoupling and the two $\pi/2$ pulses of the S spin act as a 'z-filter'. In the PDLF spectroscopy, the homonuclear dipolar decoupling information is encoded into the magnetization of the abundant (proton) spin and then is transferred to the rare (carbon) spin by CP. The name PDLF arises from the fact that NMR signal is observed by detecting the proton. A later version of PDLF detects ^{13}C signal instead.[57,58,95,96] The PDLF spectra are governed by simple two-spin ^{1}H–^{13}C couplings, while in the SLF experiment the ^{13}C magnetization evolves under the local fields of all the neighbouring protons. By combining with OMAS at $\eta = 48.2^\circ$, the superior performance of PDLF over SLF is clearly demonstrated in Fig. 5.[95] Also a 10-fold increase in sensitivity is observed in the PDLF spectrum over the SLF spectrum. The 3D version of PDLF spectroscopy has been used to obtain long-range ^{13}C–^{1}H dipolar couplings.[96] To identify dipolar coupling between two non-bonded ^{13}C and ^{1}H nuclei, the ^{13}C–^{1}H dipolar couplings must be correlated with both ^{13}C and ^{1}H chemical shifts. Hence an additional dimension is introduced for the ^{1}H chemical shift.

Proton–carbon 'HETCOR' experiment has recently been done on a liquid crystal[97] to observe long-range proton–carbon correlations. In this

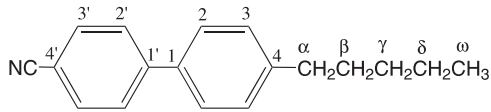

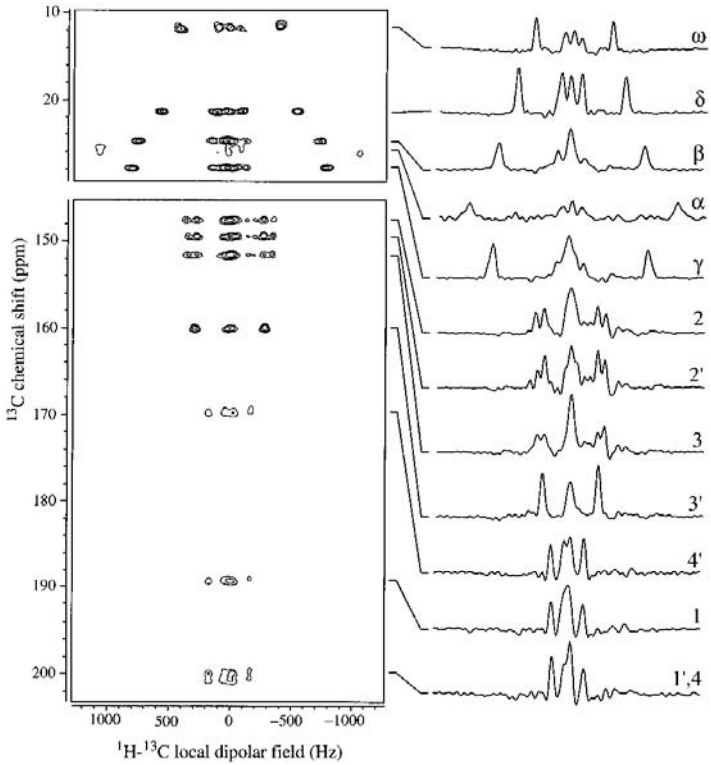

Fig. 3. Contour plot of the proton-detected local field (PDLF) spectrum of a static 5CB sample. The traces taken parallel to ω_1 for each carbon site show distinct doublets that are related to individual C–H couplings. (Reproduced by permission of American Chemical Society.)

experiment, both homonuclear and heteronuclear couplings are removed while retaining only the proton chemical shifts during the evolution period. This is achieved by the FSLG-2 homonuclear decoupling together with a carbon π pulse at the middle of the evolution period. CP is then used to transfer the proton polarization to carbons for signal detection under heteronuclear decoupling. The contact time has been varied to distinguish direct and long-range correlations between the protons and carbons. ^{13}C–^{1}H dipolar couplings in LC can also be estimated by means of a variant of the 2D SLF experiment in which transient dipolar oscillations are observed as a function of the contact time during CP.[98] Now the dipolar oscillations are highly damped due to

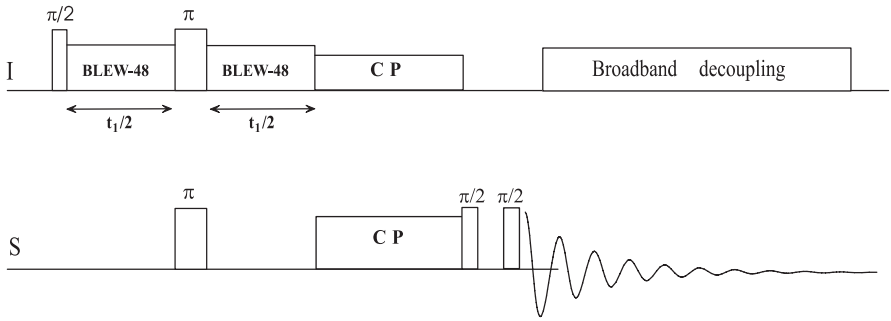

Fig. 4. A schematic diagram of the 2D PDLF (PELF) method using the BLEW-48 sequence for ^{1}H–^{1}H dipolar decoupling. CP denotes cross polarization. The last two $\pi/2$ pulses of the S spin act as a '*Z*' filter. (Reproduced by permission of Elsevier Sicence.)

couplings among the proton spins. As a result, the peaks in the 2D spectrum are broad. To alleviate this, the following experiment was devised for the liquid crystal EBBA.[99] After initial CP, the proton r.f. is switched off to destroy the remaining proton magnetization, while the ^{13}C magnetization remains spin-locked for this period. During the oscillatory transfer between protons and carbons, the proton offset and carbon power level are changed to satisfy both LG and H–H conditions such that the transfer of magnetization between proton and carbon takes place under the homonuclear proton spin decoupling, leading to a reduction in the line width along the dipolar (F_1) axis. Homonuclear LG decoupling of protons and polarization inversion (PI)[100] have been used in 2D SLF experiments. Beside the dipolar oscillations, there exists also a non-oscillatory part. F.T. along F_1 of the former gives the cross-peaks, while of the latter a zero frequency peak. For small dipolar couplings, the cross-peaks are closer and may overlap substantially with the zero frequency peak, making their determination difficult. Fortunately, PI can be used to suppress the zero frequency peak. It was demonstrated[101] in MBBA that PI leads to a doubling in the amplitude of the dipolar oscillations, and a reduction in the initial value of the non-oscillatory part. By means of SLF spectroscopy, the 2D spectra in the nematic phase of MBBA using CP and PI, respectively are shown in Fig. 6. It is noted that not only short range dipolar couplings of carbons with attached protons can be found, but also those of quaternary carbons (C_4, C_4', and C_1') coupled to remote protons are resolved. A recent 2D PDLF experiment[102] uses a pulse sequence containing low power PMLG decoupling during the evolution (t_1) period, in which the ^{1}H magnetization evolves under the effect of the chemical shifts, ^{19}F–^{1}H dipolar and scalar interactions. The proton signal is then recorded in the detection period (t_2). Double F.T. yields ^{19}F–^{1}H dipolar doublets in the indirect (F_1) dimension, and in the direct (F_2) dimension, the normal ^{1}H spectrum. In this work, a number of mono- and di-fluorinated

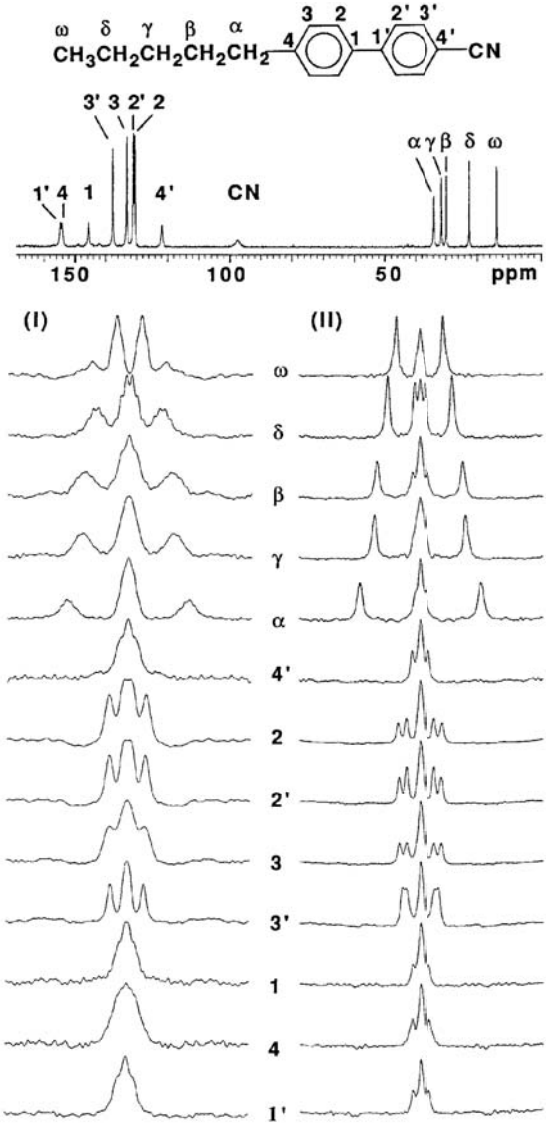

Fig. 5. ^{13}C NMR spectrum (top) of 5CB at 21°C and 9.4 T, spinning at 1.1 kHz and $\eta = 48.5°$. Column I: 2D SLF slices in the F_1 dimension, while Column II: 2D PDLF slices in the F_1 dimension. The pulse sequence used is shown in Fig. 4. (Reproduced by permission of Elsevier Science.)

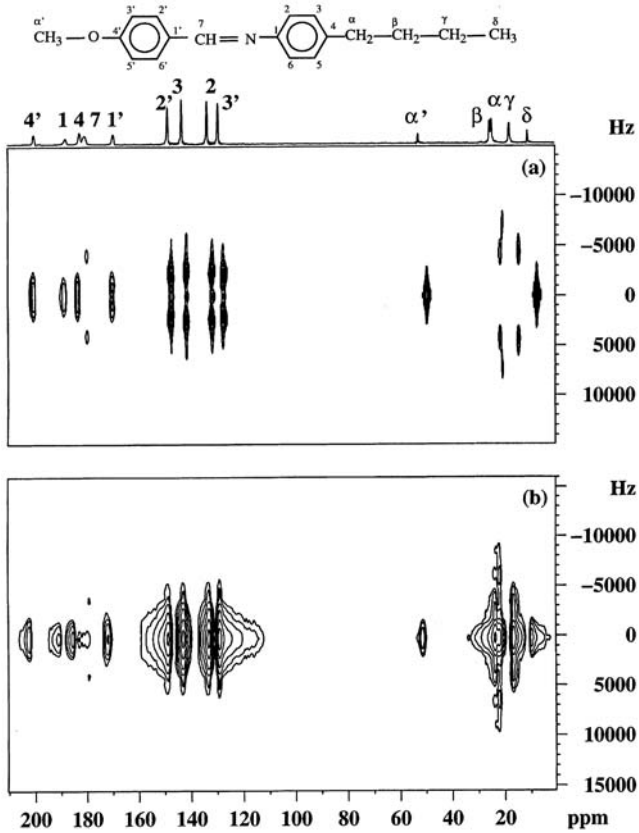

Fig. 6. ^{13}C 2D SLF spectrum of MBBA in its nematic phase at 298 K obtained with polarization inversion (a) and without polarization inversion (b). The F_2-axis corresponds to ^{13}C chemical shifts, and the F_1-axis corresponds to the dipolar oscillation frequencies. (Reproduced by permission of Elsevier Science.)

molecules dissolved in nematic solvents were studied to give the ^{19}F–^{1}H dipolar couplings. Figure 7 shows a 2D PDLF spectrum of a solute 2-fluorotoluene dissolved in the nematic solvent ZLI1695. The top projection shows the completely coupled ^{1}H spectrum and the right projection shows the PDLF spectrum obtained under PMLG decoupling at a decoupling field of 17 kHz. The polarization inversion spin exchange at the magic angle (PISEMA) experiment[100,103] combines FSLG homonuclear decoupling with CP in the t_1 period, and the carbon signal is detected in the t_2 period under TPPM heteronuclear decoupling. The ^{1}H–^{13}C dipolar couplings are monitored through the transient oscillations, which take place during the CP process. 2D PISEMA spectroscopy has recently been employed to study polypeptides in oriented membrane samples.[104] Comparison between various ^{1}H–^{13}C SLF

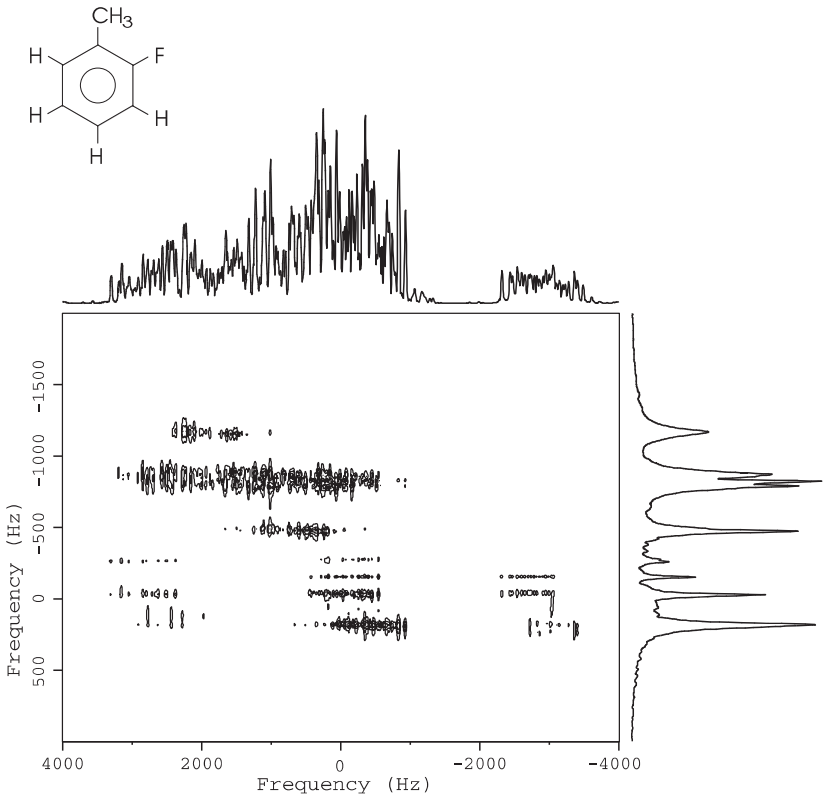

Fig. 7. Contour plot of the 2D PDLF experiment performed on a sample of 2-fluorotoluene dissolved in the nematic solvent ZLI1695. The right projection shows the PDLF spectrum obtained under 17 kHz decoupling with PMLG. (Reproduced by permission of Elsevier Science.)

experiments, viz., SLF, PDLF, and PISEMA has also been carried out in columnar and nematic LC.[105] A modified PISEMA sequence has recently been proposed to recouple ^{1}H–^{13}C dipolar coupling under MAS condition and applied to a singly ^{13}C-labelled discotic liquid crystal.[106] The dynamic effects in ^{13}C MAS spectra show up in a similar way as in high-resolution spectra of liquids, i.e., one can see that lines can broaden, then coalesce etc. in the dynamic spectra. The power of ^{13}C MAS NMR has been demonstrated in a study of dynamic processes in a discotic liquid crystal.[107] In particular, the dynamic range of ^{13}C MAS is pushed down to slower rates due to the natural line width of ^{13}C peaks being smaller than the deuterium line width. For a general discussion of dynamic NMR in LC, the reader is referred to a recent review by Luz.[108] In particular, the complementary ^{2}H techniques of dynamic quadrupole echo and 2D exchange experiment play an important role in the dynamic NMR of LC.

Several techniques have been developed to correlate the ^{13}C spectrum with the deuterium spectrum in order to assign and measure deuterium quadrupolar splittings in oriented materials. One of these is the deuterium correlation experiment known as DECOR.[109] In the DECOR sequence, a CP step is required to uniformly transfer magnetization from deuterons to carbons. Since the deuterium resonances are split by the quadrupolar interactions in LC, it is necessary to use a ramp CP (by sweeping the ^{2}H frequency) to satisfy the Hartmann–Hahn (H.–H.) condition. To avoid the need of a ramp CP, a heteronuclear multiple quantum coherence (HMQC) experiment has been used to correlate shifts in ^{13}C and ^{2}H spectra of a fully deuterated 5CB sample.[110] This experiment requires decoupling the deuteria from the carbons, which could present a problem when the sum of ^{13}C–^{2}H scalar and dipolar couplings is large in oriented materials. A new 2D heteronuclear correlation experiment, in which ^{1}H chemical shifts and ^{1}H–^{2}H dipolar interactions in the first dimension are correlated with ^{13}C chemical shifts and ^{13}C–^{2}H dipolar interactions in the second dimension, has been demonstated in a columnar discotic.[111]

A deuterium 2D Q-COSY experiment has recently been proposed,[112] using a $\pi/2 - t_1 - \pi - t_2$ pulse sequence (Fig. 8(a)), to study weakly oriented systems. The 1D deuterium NMR spectrum obtained in a simple one-pulse experiment

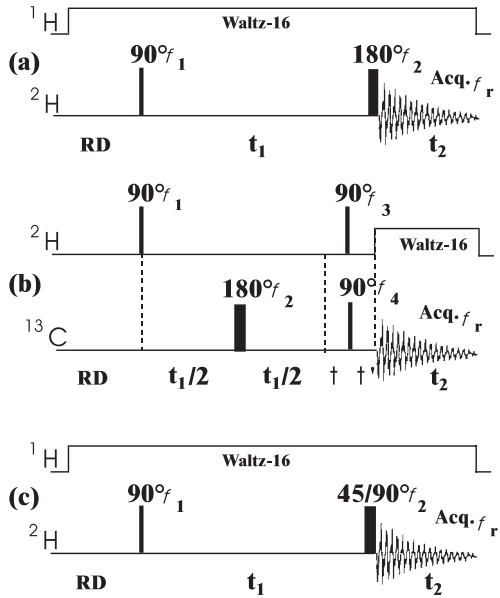

Fig. 8. Pulse schemes for ^{2}H 2D NMR spectroscopy of weakly ordered, deuterated solutes: (a) ^{2}H Q-COSY, (b) ^{2}H–^{13}C HETCOR experiment with ^{13}C decoupling, (c) ^{2}H–^{2}H COSY 2D experiment. (Reproduced by permission of American Chemical Society.)

does not show symmetrical quadrupolar doublets, since the magnitude of quadrupolar splittings is comparable to the ^2H chemical shift dispersion. Thus, it is difficult to identify various doublets in a crowded 1D spectrum. The 2D Q-COSY spectrum shows only the quadrupolar doublets along the main 45° diagonal and no diagonal peaks. After tilting the data as done in the 2D J-resolved experiment, all the quadrupolar doublets line up parallel to the F_1 axis with a scaling factor of 2 for the chemical shift along the F_2 dimension. Hence, one can extract signals of all the inequivalent deuterons in the molecule by correlating the ^2H chemical shifts with the corresponding quadrupolar doublets. Figure 9 shows a 2D Q-COSY spectrum of

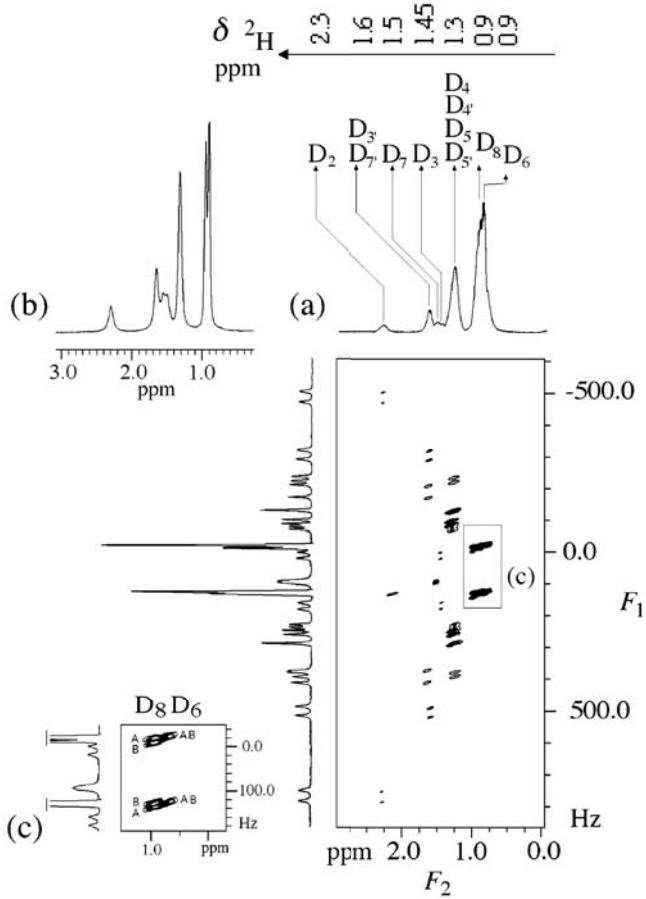

Fig. 9. (a) Tilted ^2H Q-COSY 2D map obtained for the (±)-EHA. The spectrum was symmetrized prior to the tilt procedure. In the F1 and F_2 dimensions are displayed the ^2H–$\{^1H\}$ 1D spectrum; (b) isotropic ^2H–$\{^1H\}$ spectrum of (±)-EHA recorded in $CDCl_3$; (c) expansion of the region of methyl groups. (Reproduced by permission of American Chemical Society.)

perdeuterated (±)-2-ethylhexanoic acid dissolved in a chiral nematic solvent (PBLG/CH_3Cl).[112] Instead of the HMQC experiment of Sandström, one can consider a HETCOR experiment for correlating ^2H and ^{13}C signals. In this experiment, quadrupolar modulated single quantum coherences are produced by a ^2H $\pi/2$ pulse and these evolve in the t_1 period in which the ^{13}C–^2H couplings are refocused by a ^{13}C π pulse at the middle of the t_1 period (see Fig. 8(b)). The single quantum coherences are then transfered into ^{13}C magnetization by CP through simultaneuos application of $\pi/2$ pulses for the deuteria and carbons. During the detection (t_2) period, the carbons are detected under the broadband deuterium decoupling. In the 2D map, the ^{13}C chemical shifts in the F_2 dimension are correlated to the ^2H quadrupolar splittings centred on their respective chemical shifts in the F_1 dimension. Because of the larger ^{13}C chemical shift dispersion, the HETCOR spectrum offers a better reading of quadrupolar doublets when comparing to a tilted 2D Q-COSY spectrum. Finally, deuterium–deuterium correlation spectroscopy was first demonstrated in a liquid crystal by Emsley and Turner[113] using a spin-echo method. The observation of cross-peaks due to the dipolar coupling between adjacent deuterons allows the assignment of quadrupolar doublets. This method has been adopted for natural abundant deuterium studies of chiral solute dissolved in chiral LC solvents to separate the quadrupolar splittings into two coherent data set, one for each enantiomer. The so-called 2D COSY-90 spectrum is obtained by a $\pi/2 - t_1 - \pi/2 - t_2$ pulse sequence (Fig. 8(c)) and shows a ^2H spectrum on the diagonal and auto-correlation peaks which are displaced from the other diagonal by the chemical shifts.[114]

5. DYNAMICAL PROCESSES: MOTIONAL MODELS

Several dynamical processes are known to contribute simultaneously to the nuclear spin relaxation in LC. The task of achieving a composite model for all the relevant motional processes in different mesophases (particularly in biaxial and tilted chiral phases) is daunting. This is further complicated by the coupling effects among them when the time scales of the motional processes become comparable. In practice, arguments of different time scales are often used to simplify the complexity of the model. However, there is no unique way to carry out different levels of approximations, and the composite models used by different authors simply depend on the taste of the author. In LC, one encounters both non-collective (individual) motions and collective motions known as DF, which involve many molecules within a domain. These slow collective motions can be treated as hydrodynamic modes arising from thermal deformations in LC. Either two-dimensional excitations as seen in smectic and lamellar phases[26,115] or three-dimensional excitations in nematics[24,116] can occur. Due to the different dimensionality, they show quite different frequency dependences. NMR field cycling experiments are

instrumental in demonstrating that the DF mechanism is responsible for the frequency dispersion of the proton spin–lattice relaxation rate in LC, especially below 1 MHz.[117]

The non-collective motions include the rotational and translational self-diffusion of molecules as in normal liquids. Molecular reorientations under the influence of a potential of mean torque set up by the neighbours have been described by the small step rotational diffusion model.[118–124] The roto-translational diffusion of molecules in uniaxial smectic phases has also been theoretically treated.[125,126] This theory has only been tested by a spin relaxation study of a solute in a smectic phase.[127] Translational self-diffusion (TD)[29] is an intermolecular relaxation mechanism, and is important when proton is used to probe spin relaxation in LC. TD also enters indirectly in the treatment of spin relaxation by DF. Theories for TD in isotropic liquids and cubic solids[128–130] have been extended to LC in the nematic (N),[131] smectic A (SmA),[132] and smectic B (SmB)[133] phases. In addition to the overall motion of the molecule, internal bond rotations within the flexible chain(s) of a mesogenic molecule can also cause spin relaxation. The conformational transitions in the side chain are usually much faster than the rotational diffusive motion of the molecular core.

There are different approaches to incorporate internal rotations within molecules: the segmental diffusion model,[134,135] the superimposed rotations model,[136] and the decoupled model.[137,138] In the segmental diffusion model, local segmental motions are considered first to average the quadrupolar coupling in an intermediate frame for each deuteron along the labelled lipid acyl chain in a lipid membrane system. The intermediate frame at each carbon site is chosen so that the residual quadrupolar coupling tensor is diagonal and specified by two unknown model parameters χ_Q^{eff} and η_Q^{eff}. Here η_Q^{eff} is a motionally induced asymmetry parameter of the quadrupolar interaction. Additional model parameters are the Euler angles needed to transform from each intermediate frame to the molecular frame (e.g., the principal frame of the rotation diffusion tensor for the lipid molecule). In practice, this approach involves up to three adjustable parameters to model the internal dynamics at each carbon site along the acyl chain. Although the above model needs a substantial number of fitting parameters, it does not assume that the rotational diffusive motion of the entire molecule is independent of the fast conformational changes in the flexible chain. In the superimposed rotations model, the rotations of carbon–carbon bonds in the chain are assumed to be free (i.e., free rotational diffusion), independent of each other and uncoupled from the overall molecular rotation. For each $C_i - C_{i+1}$ bond, the superimposed rotations model must introduce an additional correlation time τ_i to account for its rotation w.r.t. its previous bond in the chain. The predictions of this model are consistent with the experimental observations that the deuteron spin–lattice relaxation rates $R^{(i)}$ decrease monotonically along the chain[136,139–141] in LC. The same trend has also been observed in ^{13}C

spin–lattice relaxation rates.[142] However, the presence of the potential of mean torque in LC has made the assumption of independent bond rotations questionable. Later, correlated internal motions are considered explicitly by generating all possible conformations for a mesogenic molecule using the Flory's isomeric model.[143] These conformations are weighted by their equilibrium probabilities, which can be calculated from the potential of mean torque. This approach leads to the decoupled model proposed independently by us[137] and Nordio.[138] Here we will summarize some formulae of spectral densities for various relaxation mechanisms.

5.1. Director fluctuations

It is well-known[17] that DF contribute only to $J_1(\omega)$ in the small angle (θ) approximation, where θ is the angle between the instantaneous director and its equilibrium orientation. When θ is not small, contributions to $J_0(\omega)$ and $J_2(2\omega)$ become non-zero. Indeed, there is a small correction to $J_1(\omega)$ due to the second-order ($\propto\theta^2$) contribution. Since DF involve a distribution of correlation times or long wavelength modes, the spectral densities show characteristic frequency behaviours. When the principal component of the spin interaction (e.g., C–D bond) makes an angle $\beta_{M,Q}$ with the long axis of the molecule, the spectral densities are given to second-order in θ for nematics by[116,144,145]

$$J_0(\omega) = A^2 \frac{S_0^2}{(1-3\alpha)^2}[d_{00}^2(\beta_{M,Q})]^2 \frac{1}{\pi}\ln\left[1+\left(\frac{\omega_c}{\omega}\right)^2\right] \tag{60}$$

$$J_1(\omega) = A \frac{S_0^2}{(1-3\alpha)^2}\left[d_{00}^2(\beta_{M,Q})\right]^2(1-4\alpha)U\left(\frac{\omega_c}{\omega}\right)\omega^{-1/2} \tag{61}$$

$$J_2(2\omega) = A^2 \frac{S_0^2}{(1-3\alpha)^2}\left[d_{00}^2(\beta_{M,Q})\right]^2 \frac{1}{3\pi}\ln\left[1+\left(\frac{\omega_c}{2\omega}\right)^2\right] \tag{62}$$

where S_0 is the nematic order parameter, the cutoff function $U(\omega_c/\omega)$

$$U(x) = \frac{1}{2\pi}\ln\left[\frac{x-\sqrt{2x}+1}{x+\sqrt{2x}+1}\right] + \frac{1}{\pi}\left[\tan^{-1}\left(\sqrt{2x}-1\right)+\tan^{-1}\left(\sqrt{2x}-1\right)\right] \tag{63}$$

accounts for the cutoff of coherence modes at high frequencies, the prefactor A is given by

$$A = \frac{3kT}{4\sqrt{2}\pi}\left(\frac{\eta}{K^3}\right)^{1/2} = \frac{3\pi\alpha}{2\sqrt{2}\omega_c} \tag{64}$$

with ω_c being the high frequency cutoff, K is the average elastic constant, η is the average viscosity, and the parameter α, defined by Eq. (64), is a measure of the magnitude of DF ($\alpha \ll 1$).

The above spectral densities can be modified for the occurence of chain flexibility, and for the director being oriented at θ_{LD} w.r.t. the external B_0 field in the L frame. For C–D bonds located in the flexible chain, the effect of DF is reduced due to an additional averaging of the time dependent factor $d^2_{00}(\beta_{M,Q})$ by conformational transitions in the chain. Consequently, the spectral densities given in Eqs. (60)–(62) are modified by replacing $S_0 d^2_{00}(\beta_{M,Q})$ by the segmental order parameter S_{CD} of the C–D bond at a particular carbon site on the chain.[146,147] As observed experimentally,[148,149] the spectral densities in a flexible chain show a S^2_{CD} dependence when DF dominate the relaxation rates. The general expression of $J_m(\omega;\, \theta_{LD})$ due to DF in uniaxial nematic phases is given by

$$\begin{aligned} J_m(\omega;\theta_{\mathrm{LD}}) = \frac{3\pi}{8}\frac{S^2_{\mathrm{CD}}}{(1-3\alpha)^2}\Bigg\{ & \frac{3\alpha^2}{\omega_c}\ln(1+x)^2\left[d^2_{m0}(\theta_{\mathrm{LD}})\right]^2 \\ & + \frac{4\alpha}{\sqrt{2\omega_c}}\frac{(1-4\alpha)}{\sqrt{\omega}}U(x)\left(\left[d^2_{m1}(\theta_{\mathrm{LD}})\right]^2 + \left[d^2_{m-1}(\theta_{\mathrm{LD}})\right]^2\right) \\ & + \frac{\alpha^2}{\omega_c}\ln(1+x^2)\left(\left[d^2_{m2}(\theta_{\mathrm{LD}})\right]^2 + \left[d^2_{m-2}(\theta_{\mathrm{LD}})\right]^2\right)\Bigg\} \end{aligned} \tag{65}$$

where $x = \omega_c/\omega$. There is an alternative treatment, also up to second-order in θ,[150] in which the long molecular axis samples the collective hydrodynamic modes while the molecule still reorients about this long axis with a diffusion constant $D_{\|}$. With the assumption that these two motions are not coupled to each other, the spectral densities J_0, J_1, and J_2 are all non-zero and differ from those given above. Specifically, they contain terms that are proportional to $\langle\theta^2\rangle/D_{||}$. This theory was used to account for ^{13}C spin–lattice relaxation rates in a liquid crystal.

In SmA and lamellar phases, all twist modes are forbidden due to the relatively large values of twist elastic constant (K_{22}), resulting in a different frequency dependence for 2-dimensional DF. Thus, the spectral density $J_1(\omega)$ due to 2-dimensional DF (or layer undulations) is given ($K_{33} \ll K_{22} = K_{11}$)[115]

$$J_1^{\mathrm{DF}}(\omega) = \frac{3k_BT}{2K_{11}\xi_Z}\omega^{-1} \tag{66}$$

where ξ_Z is a coherence length along the Z direction (the layer normal) in the part of sample where the layers are parallel to each other. The proton T_1 due to DF in a SmA phase is found as

$$\frac{1}{T_{1\mathrm{DF}}} = B_{\mathrm{DF}}\omega^{-1}, \tag{67}$$

where

$$B_{\mathrm{DF}} = \frac{9}{4}\left(\frac{\mu_0\gamma^2\hbar}{4\pi r^3}\right)^2 \frac{k_B T S_0^2}{K_{11}\xi_z}\left[d_{00}^2(\beta)\right]^2. \tag{68}$$

The above result is true if ξ_Z is independent of $q_\perp$ (i.e., constant). If, however, this coherence length is wave vector dependent[1]

$$\varepsilon = \frac{1}{\lambda q_\perp^2},$$

where λ is a constant of the order of the molecular length, a logarithmic dependence in the spin–lattice relaxation rate is obtained

$$T_1^{-1} \propto \ln\left[1 + (\omega_{\perp c}/\omega)^2\right].$$

This equation only accounts for the high cutoff frequency $\omega_{\perp c}$ ($\omega_{\perp c} = K_{11}q_{\perp c}^2/\eta$), and diverges as $\omega \to 0$. When the high- (ω_c) and low-frequency (ω_l) cutoffs are taken into account, one obtains for smectogens

$$J_1^{\mathrm{DF}}(\omega) = \frac{3k_B T}{2K_{11}\xi_Z\omega}\left(\frac{2}{\pi}\tan^{-1}\frac{\omega_c}{\omega} - \frac{2}{\pi}\tan^{-1}\frac{\omega_t}{\omega}\right); \tag{69}$$

where $\omega_c = K_{11}q_c^2/\eta$ and $\omega_l = K_{11}q_l^2/\eta$. In terms of the coherence lengths ξ_Z and $\xi_\perp$ (perpendicular to the layer normal), $q_c = 2\pi/\xi_Z$ and $q_l = 2\pi/\xi_\perp$. Now B_{DF} in Eq. (67) is given by

$$B_{\mathrm{DF}} = \frac{9}{4}\left(\frac{\mu_0\gamma^2\hbar}{4\pi r^3}\right)^2 \frac{k_B T S_0^2}{K_{11}\xi_Z}\left(d_{00}^2(\beta)\right]^2\left[\frac{2}{\pi}\tan^{-1}\frac{\omega_c}{\omega} - \frac{2}{\pi}\tan^{-1}\frac{\omega_l}{\omega}\right]. \tag{70}$$

In treating 2D director fluctuations (due to layer undulations) in lamellar phases of biomembranes, Halle[27] found a different expression (for $\omega \ll \omega_p$) when couplings among bilayers were included:

$$T_1^{-1} \propto \ln\left[\left(\frac{d}{L_z} + \frac{\omega}{\omega_P}\right)^{-1}\left(1 + \frac{\omega}{\omega_p}\right)\right],$$

where L_z is the sample thickness along the layer normal, d the average layer distance and ω_p, the 'patch' frequency, is

$$\omega_p = \frac{\pi}{d^2}\left(\frac{K_{11}}{\eta} + D_{\perp}^{t}\right).$$

5.2. Anisotropic rotational diffusion

A small step rotational diffusion model has been used to describe molecular rotations (MR) of rigid molecules in the presence of a potential of mean torque.[118–120,151] To calculate the orientation correlation functions, the rotational diffusion equation must be solved to give the conditional probability for the molecule in a certain orientation at time t given that it has a different orientation at $t=0$, and the equilibrium probability for finding the molecule with a certain orientation. These orientation correlation functions were found as a sum of decaying exponentials.[120] In the notation of Tarroni and Zannoni,[123] the spectral denisities ($m=0$, 1, 2) for a deuteron fixed on a reorienting symmetric top molecule are:

$$J_m^{\mathrm{MR}}(m\omega) = \sum_n \left[d_{n0}^2(\beta_{M,Q})\right]^2 \sum_k \frac{(A_{mn}^2)_k (B_{mn}^2)_k}{(m\omega)^2 + (B_{mn}^2)_k} \tag{71}$$

where m and n represent the projection indices of a rank 2 tensor in the L and molecular (M) frames, respectively, $(B_{mn}^2)_k/D_{\perp}$, the decay constants, are the eigenvalues of the rotational diffusion (Γ) operator and $(A_{mn}^2)_k$, the relative weights of the exponentials, are the corresponding eigenvectors. In this model, the rotational diffusion tensor is diagonalized in the M frame with principal components $D_{\parallel}$ and $D_{\perp}$. $D_{\parallel}$ and $D_{\perp}$ specify the diffusion of the molecule about its long axis (the axis of assumed cylindrical symmetry) and about its short axis, respectively. These rotational diffusion constants enter into the decay constants. In the notation of Vold and Vold,[122] the spectral densities using only three exponentials ($j=1$, 2, 3) take the form of

$$J_m^{\mathrm{MR}}(m\omega) = \sum_n \left[d_{n0}^2(\beta_{M,Q})\right]^2 c_{mn} \sum_j \frac{a_{mn}^{(j)}\left(\tau_{mn}^{(j)}\right)^{-1}}{(m\omega)^2 + \left(\tau_{mn}^{(j)}\right)^{-2}} \tag{72}$$

where c_{mn}, the mean square average of the Wigner rotation matrices, are the initial amplitudes of the orientation correlation functions

$$c_{mn} = \left\langle |D_{mn}^2(\Omega)|^2 \right\rangle - \left(\overline{D_{00}^2}\right)^2 \tag{73}$$

and $a_{mn}^{(j)}$ represent the normalized weight of each exponential whose time constant is

$$\left[\tau_{mn}^{(j)}\right]^{-1} = \frac{6D_{\perp}}{b_{mn}^{(j)}} + n^2(D_{||} - D_{\perp}) \tag{74}$$

The $a_{mn}^{(j)}$, $b_{mn}^{(j)}$, and c_{mn} coefficients are given numerically as polynomials of S_0 and their expansion coefficients are tabulated in Table 1 of Volds for the Maier-Saupe potential. In the single exponential approximation for $g_{mn}(t)$,[119] the spectral densities simplify to

$$J_m^{\mathrm{MR}}(m\omega) = \sum_n \left[d_{n0}^2(\beta_{M,Q})\right]^2 c_{mn} \frac{a_{mn}(\tau_{mn})^{-1}}{(m\omega)^2 + (\tau_{mn})^{-2}} \tag{75}$$

where the superscript $j = 1$ has been dropped for simplicity. Different approaches have been used to tackle the existence of a cross-term between the molecular reorientation and DF.[152–154] In particular, they produce different cross-terms with opposite signs. The small cross-term of Freed is negative.

Another rotational diffusion model known as the anisotropic viscosity model[156,157] is very similar to the above model, and its main feature is to diagonalize the rotational diffusion tensor in the L frame defined by the director. A similar (but not the same) expression as Eq. (71) is $J_n^{\mathrm{MR}}(\eta\omega)$

$$J_n^{\mathrm{MR}}(n\omega) = \sum_m \left[d_{m0}^2(\beta_{M,Q})\right]^2 \sum_k \frac{(A_{mn}^2)_k (B_{mn}^2)_k}{(n\omega)^2 + (B_{mn}^2)_k} \tag{76}$$

where the rotational diffusion constants D_α, D_β are used in place of $D_{||}$ and $D_\perp$, and they denote, respectively, the precessional and tumbling motions of the long molecular axis w.r.t. the director. In the Volds notation, the spectral densities are still given by Eq. (72), but the correlation times given in Eq. (74) now contain $m^2(D_\alpha - D_\beta)$ instead of $n^2(D_{||} - D_\perp)$. An extension to the anisotropic viscosity model is given by Vold and Vold[122] in which rotations of the molecule about its long axis (γ-motion) are included, and assumed to be independent of the α- and β- motions with a diffusion constant D_γ. This so called 'third rate' model uses correlation times in the form of

$$\left[\tau_{mn}^{(j)}\right]^{-1} = \frac{6D_{\beta}}{b_{mn}^{(j)}} + m^2(D_\alpha - D_\beta) + \zeta(n)D_\gamma \tag{77}$$

where the function $\zeta(n)$ is $(1 - \delta_{n,0})$ or n^2 if the γ-motion is described by the strong collision[155] or small step diffusion limit,[136] respectively.

A simple composite model of slow motions and molecular reorientations is the so-called 'slowly relaxing local structure model' by Freed.[156,157] This

model is good for nearly isotropic solutions that show locally ordered clusters, and the spectral densities are written in terms of three Lorentzians to account for the reorientation with a correlation time $\tau_0^{-1} = 6D(D_\perp = D_\parallel = D)$ and a correlation time τ_x for the slowly fluctuating component of the mean potential:

$$J_m(\omega) = \left[d^2_{00}(\beta_{M,Q})\right]^2 \left\{ c_{m0} \frac{a_{m0} b_{m0} \tau_0}{1 + \omega^2 (b_{m0}\tau_0)^2} + \frac{1}{5}(a_{m0})^2 (b_{m0})^2 S_l^2 \left[\frac{\tau_x}{1 + \omega^2 \tau_x^2} - \frac{\tau_0'}{1 + (\omega \tau_0')^2} \right] \right\} \tag{78}$$

Here $S_l = \langle D^2_{00} \rangle$ is the order parameter of the local structure and $(\tau_0')^{-1} = (\tau_x)^{-1} + (\tau_0)^{-1}$. Now $\tau_0' \simeq \tau_0$ as the correlation time τ_x for the slowly fluctuating mean potential is much longer than τ_0. When the spectral densities are independent of the projection index m (i.e., nearly 'isotropic' fluid), $a_{m0} = b_{m0} = 1$ and $c_{m0} = 1/5$, the above equation reduces to sum of two Lorentzians:

$$J(\omega) = \frac{1}{5}\left[d^2_{00}(\beta_{M,Q})\right]^2 \left[(1 - S_l^2) \frac{\tau_0}{1 + \omega^2 \tau_0^2} + S_l^2 \frac{\tau_x}{1 + \omega^2 \tau_x^2} \right] \tag{79}$$

The same result has been obtained by Lipari and Szabo in their 'model-free' approach.[158] The first term in the above equation accounts for the effect of local order on the isotropic rotation through the factor $1 - S_l^2$, and the second term is due to the slower fluctuations in the local ordered clusters. This model-free approach has become popular among workers in the area of lyotropics and biomembranes.

5.3. Anisotropic translational diffusion

For spin-$\frac{1}{2}$ nuclei, dipolar interactions may be modulated by intramolecular (DF, reorientation etc.) and/or intermolecular (TD) processes. In general, the intra- and inter-molecular processes can produce quite different T_1 frequency dispersion curves. In practice, NMR field cycling experiments are often needed to extend the frequency domain from those employed in conventional spectrometers to a lower frequency range (i.e., the kHz regime) for unambiguous separation (and identification) of different relaxation mechanisms. The proton spin relaxation by anisotropic TD in various mesophases has been considered by Žumer and Vilfan.[131–133,159] In the nematic phase, Žumer and Vilfan found the following expression for T_1

$$T_1^{-1}(\omega) = \frac{9}{8}\left(\frac{\mu_0 \gamma^2 \hbar}{4\pi}\right)^2 \frac{n\tau_\perp}{d^3} Q\left(\omega\tau_\perp, \frac{\langle r_\perp^2 \rangle}{d^2}, \frac{D^0_{\parallel}}{D^0_{\perp}}\right) \tag{80}$$

where n is the number of spins per unit volume, $\langle r_\perp^2 \rangle$ is the mean square jump length in the direction perpendicular to the long molecule axis, d is the distance of closest approach of two proton spins on neighbouring molecules, $\tau_\perp$ is the correlation time for two successive jumps in the direction along $r_\perp$, Q is a dimensionless function which depends on the details of the TD process and on the spatial arrangement of molecules, and $D_{||}^0/D_\perp^0$, representing the translational diffusion anisotropy for a system with perfect order (i.e., $S_0 = 1$), is given in terms of the principal components of translational diffusion tensor $D_{||}^t$ and $D_\perp^t$[160]

$$\frac{D_{||}^0}{D_\perp^0} = \frac{D_{||}^t - \overline{D^0}(1 - S_0)}{D_\perp^t - \overline{D^0}(1 - S_0)} \tag{81}$$

with $\overline{D^0} = (D_{||}^0 + 2D_\perp^0)/3$. In the limit $\omega\tau_\perp << 1$, Eq. (80) reduces to

$$T_1^{-1}(\omega) \propto C - (\omega\tau_\perp)^{1/2} \tag{82}$$

where C is a constant, in accordance with the Torrey's theory of translational diffusion in isotropic liquids.[128,161] Indeed Torrey's isotropic approximation has been used in the past to account for spin relaxation due to TD in nematics.[162] Equation (61) and Equation (69) for smectic phases have recently been used to account for proton spin relaxation in LC.[163] Although the T_1 relaxation by translational diffusions of molecules in N and SmA phases are quite similar,[131,132] the particular structure of the twist grain boundary smectic A (TGB_A) presents a unique situation for molecules exhibiting translational diffusion.[164] TGB_A is a kind of frustrated SmA phase. Molecules crossing the grain boundary region from one smectic block to an adjacent one along the helical axis need to rotate by an angle $\Delta\alpha$ (the angle between adjacent blocks). This kind of roto-translation relaxation of spin-$\frac{1}{2}$ nuclei on neighbouring molecules has been detected by a proton T_1 dispersion study in the compound $18FBTCO_1M_7$.[165]

5.4. Correlated internal bond rotations

It is well-known that deuterium NMR spectra found in aligned LC show well-resolved quadrupolar doublets for different sites. Deuterium quadrupolar splittings for a molecule exhibiting many conformational states cannot be described by a single order matrix as in a rigid molecule. Thus, all possible conformations must first be generated using, for example, the rotational isomeric state (RIS) model of Flory.[143] Each conformer has its own order matrix describing its orientational tendency in the nematic mean field. The task of modelling the quadrupolar splittings becomes rather complex, because

a large number of order matrices is needed to evaluate the splittings of all possible conformers. These must be properly averaged to give the observed quadrupolar splittings $\Delta\nu_i$ for the C_i deuterons, i.e.,

$$\Delta\nu_i = \frac{3}{2}\left(\frac{e^2qQ}{h}\right)\sum_{n=1}^{N} p_n S_{bb}^{n,i} \tag{83}$$

where p_n is the equilibrium probability for finding the molecule in the n conformer, $S_{bb}^{n,i}$ is the segmental order parameter for the C_i–D bond (along the b axis) of the molecule in the conformation n, is given by

$$S_{bb}^{n,i} = \sum_{\alpha}^{x,y,z} S_{\alpha\alpha}^{n}\cos^2\theta_{\alpha b}^{n,i} \tag{84}$$

with $S_{\alpha\alpha}^{n}$ denote the principal components of the order matrix for the nth conformer, and $\theta_{\alpha b}^{n,i}$ denotes the angle between the C_i–D bond of the nth conformer and the principal α axis of the potential of mean torque $U_{\text{ext}}(n,\Omega)$ for the nth conformer having an orientation Ω w.r.t. the director. In the PAS of the potential of mean torque, $S_{\alpha\alpha}^{n}$ can be evaluated in a manner described for a rigid biaxial particle.[166] To construct the potential of mean torque $U_{\text{ext}}(n,\Omega)$, the additive potential (AP) method pioneered by Marcelja[167] and later refined by Emsley *et al.*[168] can be used. It is assumed that the molecule can be divided into a small number of rigid segments. Each segment has an interaction tensor that is independent of the conformation. The interaction tensor $U_{\text{ext}}(n,\Omega)$ for the molecule in conformation n is calculated by transforming the segmental interaction tensors from their local frames into a common molecular frame and then adding them together. The total anisotropic potential energy $U(n,\Omega)$ for the molecule in conformation n is given by

$$U(n,\Omega) = U_{\text{int}}(n) + U_{\text{ext}}(n,\Omega) \tag{85}$$

where $U_{\text{int}}(n)$, the internal energy, can usually be approximated by $U_{\text{int}}(n) = N_gE_{tg}$ with N_g being the number of *gauche* linkages in the chain, and E_{tg} the energy difference between the *gauche* linkage and the *trans*. The equilibrium probability for the nth conformer is given by the Boltzmann statistics

$$p_n = \frac{1}{Z}\exp\left[-\frac{U_{\text{int}}(n)}{kT}\right]Q_n \tag{86}$$

where the conformation-orientational partition function Z is

$$Z = \sum_{n}\exp\left[-U_{\text{int}}(n)/kT\right]Q_n$$

and the orientational partition function Q_n is

$$Q_n = \int \exp\left[-U_{\text{ext}}(n, \Omega)/kT\right] d\Omega$$

The potential of mean torque, parameterized by the local interaction tensors X_a and X_c (assume to be cylindrical) for the aromatic core and the C–C segment, respectively, can be mapped out at each temperature by fitting the observed quadrupolar splittings in the mesophase. Furthermore, the order matrix of an 'average' conformer of the molecule can also be calculated.[17] Now p_n is needed to describe the internal dynamics.

The decoupled model using the master rate equation method is described here to account for the correlated internal motion in a flexible chain. The conformational changes in the chain are assumed to be much faster than the overall motion. These two motional processes are therefore independent of each other as they occur on different time scales. To account for the internal motion of the molecule, one needs to transform from the PAS of the spin interaction to the L frame (via Ω_{QL}) through successive coordinates (Ω_{QI}, Ω_{IM}, Ω_{ML}): the intermediate (I) frame, chosen to describe various conformations in the chain, is fixed with respect to the M frame. The original decoupled model[137] uses three phenomenological jump constants k_1, k_2, and k_3 to describe transitions among different conformations and to construct the transition rate matrix $\underset{\sim}{\mathbf{R}}$. Suppose the carbon–carbon backbone of a pentyl chain is in a configuration characterized by $\{ijklm\}$. The one-bond (k_1) motion is given by $\{ijklm\} \rightarrow \{ijklm'\}$, and the two-bond ($k_2$) motion is for $\{ijklm\} \rightarrow \{ijkl'm\}$ and $\{ijkl'm'\}$. One-bond and two-bond motions occur at the end of the chain. The three-bond (k_3) motion involves the interchanging of two alternate (next-nearest-neighbour) bonds, viz., $\{ijklm\} \rightarrow \{ilkjm\}$. The latter motion produces no net translation of the attached chain, and has been thought to be a favourable process in ordered phases. In general, there can be several jump constants for each type of bond motion. For simplicity, we adopt only one jump constant for each type of bond rotation. The spectral densities for the C_i deuterons on the chain of an asymmetric top molecule for the case of the I frame being coincident with the M frame are given by ($m = 0, 1, 2$)

$$J_m^{(i)}(m\omega) = \sum_n \sum_{n'} \sum_{j=1}^{N} \left(\sum_{l=1}^{N} d_{n0}^2\left(\beta_{MQ}^{(i)l}\right) \exp\left[-in\alpha_{MQ}^{(i)l}\right] x_l^{(1)} x_l^{(j)} \right)$$

$$\times \left(\sum_{l'=1}^{N} d_{n'0}^2\left(\beta_{MQ}^{(i)l'}\right) \exp\left[-in'\alpha_{MQ}^{(i)l'}\right] x_{l'}^{(1)} x_{l'}^{(j)} \right)$$

$$\times \sum_k \frac{(A^2_{mnn'})_k\left[\left(B^2_{mnn'}\right)_k+|\lambda_j|\right]}{m^2\omega^2+\left[\left(B^2_{mnn'}\right)_k+|\lambda_j|\right]^2}$$

$$+\delta_{m,0}S_0^2\sum_{j=1}^{N}\left|\sum_{l=1}^{N} d^2_{00}(\beta^{(i)l}_{MQ})x^{(1)}_l x^{(j)}_l\right|^2 \Big/ |\lambda_j| \tag{87}$$

where $\beta^{(i)l}_{MQ}$ and $\alpha^{(i)l}_{MQ}$ are the polar angles for the C_i–D bond of the lth conformer in the M frame fixed on the molecular core, $|\lambda_j|$ and $\underset{\sim}{\mathbf{x}}^{(j)}$ are the eigenvalues and eigenvectors from diagonalizing $N \times N$ $\underset{\approx}{\mathbf{R}}$ matrix with N being the number of possible conformations in the chain. One of the N real and negative eigenvalues is zero and the corresponding eigenvector $\underset{\sim}{\mathbf{x}}^{(1)}$ is given by $x^{(1)}_n = (p_n)^{1/2}$. The A and B coefficients are those shown in Eq. (71) except they are now generalized to describe the molecular reorientation for an asymmetric top.[123] The decoupled model has successfully been used to understand the internal dynamics of flexible chain(s) in many different LC studied by proton[169] and deuteron[170–181] spin relaxation. Some of these studies have shown rather high values of k_3 (about 10^{17}–10^{18} s^{-1}), especially in materials containing alkyloxy side chain(s). In addition, one or more jump constants do not seem to show thermally activated behaviours in some LC. Now the k_3 (or type I motion of Helfand[182]) motion should call for a high activation energy[183,184] because several bonds must be activated almost simultaneously, and thus should produce a low k_3 value. Helfand has classified conformational transitions in the chain into three types: besides the type I motion, type III motion consists of one- and two-bond motions described above, and type II motion also consists of two kinds, viz., $t\ t\ t\ t \rightarrow g^{\pm}tg^{\mp}t$ is a *gauche* pair production or a kink formation, and $t\ t\ g\ t \rightarrow g\ t\ t\ t$ is a *gauche* migration.[182] The type II motion does not swing the chain but the chain does translate. Given that Helfand has discarded the type I motion[183,184] and in view of the observed high k_3 rates, the original decoupled model has recently been modified[185,186] by replacing the k_3 motion by the type II motion of Helfand. The jump rates k_g and k'_g are for the *gauche* migration and *gauche* pair formation, respectively. The modified decoupled model inevitably introduces an additional jump constant in describing internal chain dynamics. The $\underset{\approx}{\mathbf{R}}$ matrix is now different, but the expression given by Eq. (87) for spectral densities remains. We note that the modified decoupled model would not work well for molecules with alkyl side chains.

To describe quadrupolar splittings and internal dynamics, the following geometry has been adopted: for an alkyloxy chain, the O–C_α bond is taken to be fixed on the phenyl ring plane with $\angle C_{ar}OC_\alpha = 126.4^\circ$; $\angle CCC$, $\angle CCH$, and $\angle HCH$ are assumed to be 113.5°, 107.5°, and 113.6°, respectively. In constructing $U_{\text{ext}}(n, \Omega)$, the O–C bond is treated as a C–C bond, and $\angle OCC = \angle CCC$ is assumed. The dihedral angles $\phi = 0,\ \pm 112^\circ$ are for rotation about each C–C bond or the O–C bond to generate the three RIS.

For the modified decoupled model, the number of conformations has been limited to those with relatively high probabilities. For instance, a hexyloxy chain which contains four or more *gauche* C–C bonds can be safely ignored, because they are energetically unfavourable. Even the conformations with two consecutive *gauche* C–C bonds (i.e., $g^{\pm}g^{\pm}$ and $g^{\pm}g^{\mp}$) can be ignored. Going to an octyloxy chain, conformations with four *gauche* C–C bonds are allowed, while for a decyloxy chain conformations with up to five *gauche* C–C bonds are allowed. With these assumptions, $N = 43$, 171, and 683 for molecules containing a hexyloxy, octyloxy, and decyloxy[187] chain, respectively. In setting up the $\mathbf{R}$ matrix among the N conformations, the following conditions are imposed:[185] (i) direct transition between g^+ and g^- states is disallowed as this costs too much energy; (ii) transitions between *gtgtt* and *tgtgt* cannot proceed directly as these also cost too much energy (however, $gtgtt \rightleftharpoons ttttt \rightleftharpoons tgtgt$ are possible); and (iii) no three-bond (k_3) motion is allowed. For example, there is a total of 584 transitions for $\mathbf{R}$ in the case of 8OCB.[188] Among the 292 forward transitions, there are 86 type III motions about the C_6–C_7 bond (k_1 motion), 42 type III motions about the C_5–C_6 bond (k_2 motion), and 164 type II motions. For the latter type, 82 transitions are for the *gauche* migration and 82 transitions are for the kink formation.

5.5. Total spin relaxation rate

Since different molecular processes may simultaneously contribute to the spin relaxation in LC, the relaxation rates due to various relaxation mechanisms are additive if the motions can be decoupled on the basis of sufficiently different correlation times:[30]

$$T_1^{-1} = T_{1\mathrm{TD}}^{-1} + T_{1\mathrm{DF}}^{-1} + T_{1\mathrm{MR}}^{-1} + T_{1X}^{-1} \tag{88}$$

where $T_{1\mathrm{TD}}^{-1}$ denotes the relaxation rate due to TD, $T_{1\mathrm{MR}}^{-1}$, the relaxation rate due to MR and/or internal motions, and T_{1X}^{-1}, the cross term contribution between MR and DF. For deuterons, $T_{1\mathrm{TD}}^{-1}$ is zero because of the intramolecular nature of quadrupolar interaction. When the time scale argument for superimposing different relaxation mechanisms becomes untenable, the treatment of spin relaxation becomes more complex. There is one model[189] which does not use the time scale separation when the molecular reorientation has slowed down to be comparable to the correlation times of DF.

6. STUDIES OF ORIENTED SOLUTES

Liquid crystals have been used as an ordered medium for small solutes since the first observation of ^{1}H NMR spectrum of benzene in a nematic phase by Saupe and Englert.[190] The NMR spectra of solutes disolved in thermotropics

or lyotropics contain a wealth of information about the structure, conformation and orientational order of the solute, as well as the interaction between the solute and the mean field potential of the liquid crystalline solvent. Since the solvent molecules are usually complex, non-rigid and show low molecular symmetry, study of these molecules may often be a formidable task. Hence an important role of oriented solutes is their usage as a probe to study LC solvents. Oriented solutes of known symmetry can, therefore, provide a useful route to gain information on LC as long as the orientational properties of the solute can mimic those of the solvent. Furthermore, NMR studies of oriented solutes have ranged from the determination of the solute geometry to the possible discrimination of chiral (pro-chiral) solutes in chiral LC solvents. In recent years, anisotropic spin interactions (e.g., dipolar couplings) of weakly aligned biomolecules such as proteins have been used[15,16,191] to determine protein structures. The direction of a dipolar coupling between a I–S spin pair in one fragment of the protein may be related to the direction of another dipolar coupling in a distant fragment simply because these fragments share the same orientational order tensor. A survey of this subfield is deferred to Section 8.2.

6.1. NMR of small solutes

Various NMR-active nuclei (e.g., ^{1}H, ^{13}C, ^{19}F, and ^{2}H) have been used to give high resolution NMR spectra[35] of small solutes dissolved in LC. It is common to use solute concentrations of 5% by weight in nematic phases, but concentrations of 15% by wt. or higher are sometimes possible without destroying the liquid crystalline properties of the solvent. Although proton NMR has high sensitivity, the one-quantum NMR spectrum of a compound can become intractable when the number (N) of interacting spins ($I = 1/2$) in the spin system becomes larger than 6 or 7. The maximum number of single quantum transitions is $(2N)!/[(N-1)!(N+1)!]$. This number can be reduced by the symmetry of the spin-bearing molecule. For instance, a six-spin system should have 792 single quantum transitions. A more symmetrical molecule like benzene, C_6H_6, has only 72 transitions in the one-quantum proton spectrum. For larger spin systems, a way to reduce the complexity of the solute spectrum is to employ multiple quantum (MQ) NMR.[38] MQ spectra are typically obtained by 2D NMR methods.[192] The maximum number of m-quantum transitions in a MQ spectrum for N interacting spins ($I = 1/2$) is now given by $(2N)!/[(N-m)!(N+m)!]$. For example, there are 1.1×10^4 one-quantum ($m = 1$) transitions for $N = 8$, but only one transition for the 8-quantum spectrum. The corresponding number of transitions is 16 for 7-quantum, 120 for 6-quantum, and 560 for 5-quantum transitions. In principle, the $N-1$ and $N-2$ quantum spectra can be more easily analyzed and have enough transitions to completely solve all the spectral parameters for most spin

systems. In using MQ spectra, one should realize that the intensities cannot be used in the spectral analysis since they depend on both spectral and experimental parameters in a complex manner. Furthermore, the sparseness of lines in MQ spectra may lead to an incorrect 'fit'. More accurate spectral parameters can only be derived by analyzing the one-quantum spectrum as it is recorded with higher digital resolution leading to sharper resonances. Thus, the spectral parameters derived from high-order spectra are usually used as input parameters to simulate more complex single quantum spectra when higher resolution is desired. As an example, Fig. 10 shows 300 MHz experimental and simulated single quantum spectra of an 8-spin system biphenylene (BPLN) dissolved in three nematic LC solvents, one of which is a 'magic' mixture.[194] The dipolar couplings D_{ij} of BPLN were determined from the simulations.

In studying ^{13}C NMR of non-enriched solute molecules, the interference of the solvent ^{13}C peaks is more serious than that for ^{1}H NMR particularly when proton decoupling is employed. The coupled ^{13}C NMR spectra of small solutes such as chloroform show only a few peaks due to the first-order ^{13}C–^{1}H coupling. Now the ^{1}H–^{1}H dipolar interaction increases rapidly with increasing solute size making the analyses of coupled ^{13}C spectra more and more difficult. Thus, the use of coupled ^{13}C NMR spectra to obtain structural information of oriented solute molecules encounters a somewhat limited scope. HMQC (coherence between different spins such as $^{1}H/^{2}H$, $^{1}H/^{13}C$, $^{1}H/^{15}N$) has been used to study solute molecules in LC solvents. A recent natural abundance ^{13}C NMR study has shown that large ^{1}H–^{1}H dipolar couplings can be estimated with inverse detect ^{13}C–^{1}H heteronuclear single quantum coherence (HSQC) or HMQC experiment.[193] Figure 11 shows a 500 MHz HSQC spectrum of 1,1-difluoro-1,2-dibromoethane oriented in the nematic solvent ZLI1132 and the corresponding HMQC is reproduced in Fig. 12. The combination of HMQC and HSQC experiments can aid the analyses of the proton spectra and proton spectra selectively detected for individual carbons. Field *et al.*[195] have used the spectral widths of MQ spectra to extract the Saupe order parameters by doing simulation for an 8-spin system (indene) dissolved in a nematic LC solvent. This is possible because the spectral widths of higher-order spectra depend on the molecular orientation and only a small set of orientation order parameters can satisfy the spectral widths of two or more MQ spectra.

Specifically deuterated solute can be used to aid the analysis of a complex proton spectrum. With the development of high field and high sensitivity NMR instrumentation, it is now possible to routinely obtain natural abundance ^{2}H NMR spectra of LC[196] and solute molecules[197] in a reasonable time. Indeed, one interesting application is the demonstration of chiral discrimination using proton decoupled natural abundance ^{2}H NMR of chiral solute molecules dissolved in non-aqueous solutions of poly(γ-benzyl-L-glutamate) (PBLG).[198] The chiral LC solvent formed by a chiral polymer

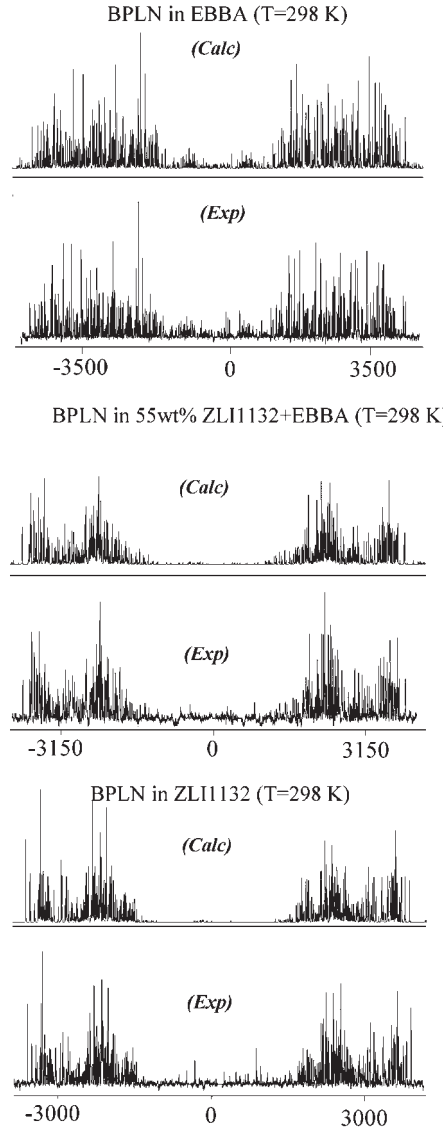

Fig. 10. Experimental and calculated ^{1}H NMR spectra of PBLN in three different nematic solvents at room temperature. (Reproduced by permission of American Chemical Society.)

PBLG or poly-ε-carbobenzyloxy-L-lysine (PCBLL) and an organic solvent such as $CHCl_3$, CH_2Cl_2, DMF . . .[199,200] can produce a difference in interactions for different enantiomers of a solute molecule.[112,201] Hence enantiomers can produce different NMR spectra as a consequence of differential

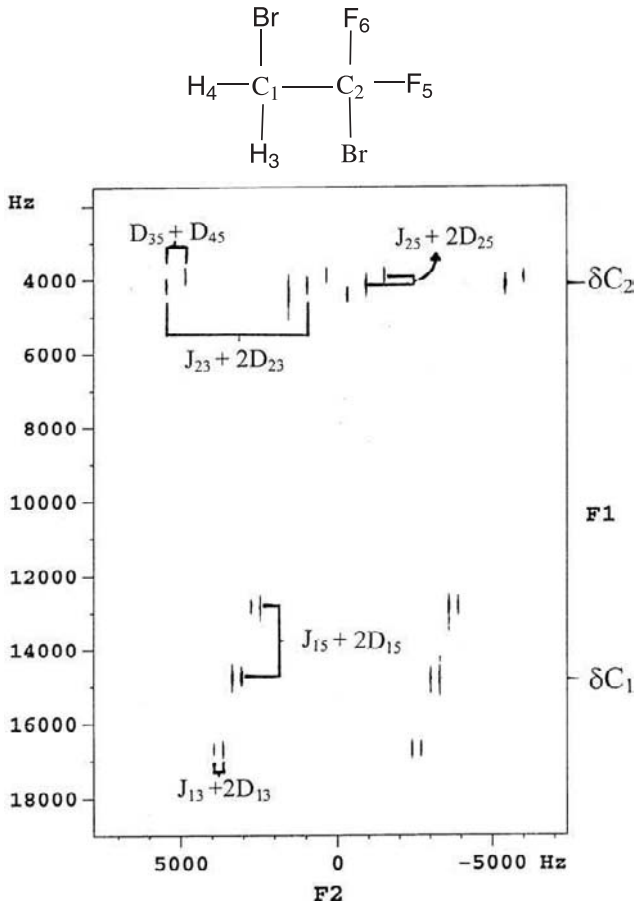

Fig. 11. 500 MHz HSQC spectrum of 1,1-difluoro-1,2-dibromoethane dissolved in the nematic solvent ZLI-1132. (Reproduced by permission of Elsevier Science.)

ordering effect. Figure 13 shows a tilted 2D natural abundance Q-COSY spectrum of (±)-1-pentyn-3-ol.[112] Note that the chiral carbon shows two distinct quadrupolar doublets for the C* deuteron. In the PBLG, cosolvent and solute mixtures, one usually observes liquid-like molecular motions and T_1, T_2 values. Consequently, residual couplings (or order parameters) are smaller by at least two or more orders of magnitude than those found in thermotropic LC solvents. Proton 2D selective refocusing experiment (SERF) was used to measure proton–proton dipolar couplings from unresolved lines of (±1)-1,2-dibromopropane in PBLG/$CHCl_3$.[202] The selective (shaped) pulses in the SERF experiment, which centre on the methyl resonance, simplify considerably the signal of the methyl group, as all the couplings

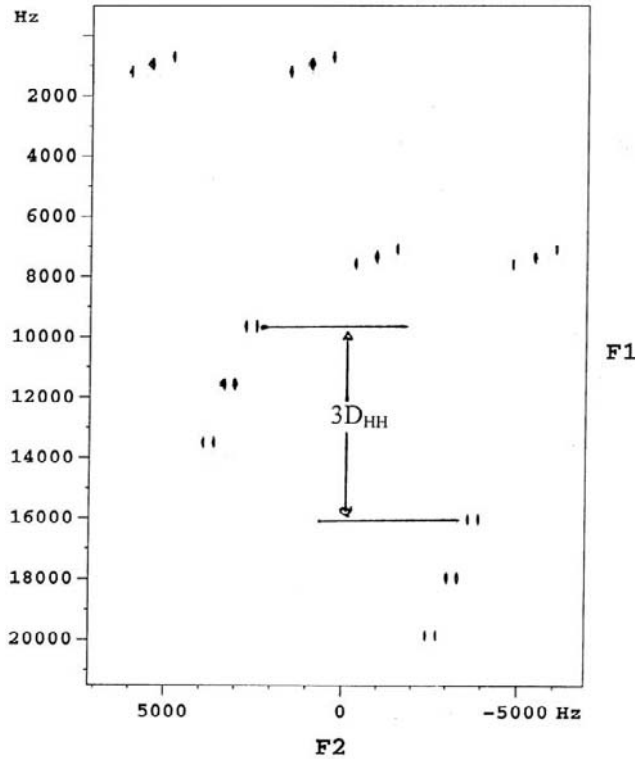

Fig. 12. 500 MHz HMQC spectrum of 1,1-difluoro-1,2-dibromoethane in ZLI-1132. (Reproduced by permission of Elsevier Science.)

are refocussed except the dipole–dipole coupling between the methyl protons. The presence of two proton–proton geminal couplings in the F_1 dimension provides evidence of R- and S-enantiomers. It is also possible to use proton-decoupled ^{13}C NMR spectra to observe a difference in the chemical shielding anisotropies of the two enantiomers.[199,203] Even some achiral molecules act like prochiral when they are placed in a chiral LC solvent.[198] The approach has also been applied to study chiral alkanes.[204]

Sample spinning of an oriented solute, iodotrifluoro-ethylene, in a LC solvent was used to resolve homonuclear dipolar couplings between fluorines based on their isotropic chemical shifts.[73] This is achieved by a ^{19}F SAS-COSY correlation experiment to obtain a first-order spectrum. Sample spinning in this experiment allows the nematic director to align at two different angles w.r.t. the external magnetic field. When a LC mixture with vanishing $\Delta\chi$ is spun, the director orientation can switch between along and perpendicular to the spinning axis depending on the angle between the rotor

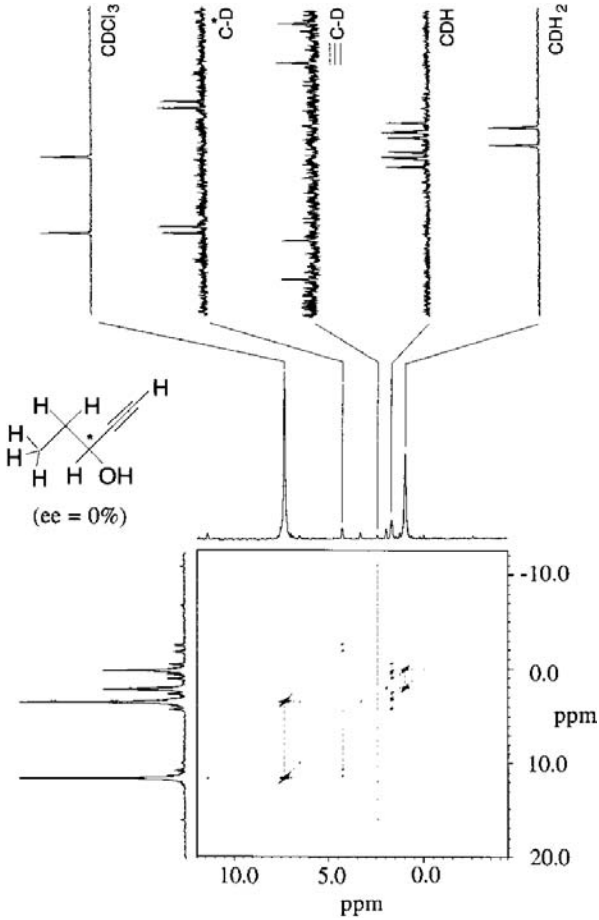

Fig. 13. Tilted 2D spectrum of natural abundance ^{2}H Q-COSY experiment of (±)-1-pentyn-ol dissolved in PBLG/chloroform chiral nematic liquid crystal. The spectrum was symmetrized prior to the tilting procedure. Note that all isotopomers of the mixture are clearly visualized. (Reproduced by permission of American Chemical Society.)

axis and the external field, as well as the rotor spinning speed.[205] The field dependence of fluorine T_1 for C_6F_6 dissolved in the nematic phase of MBBA has been studied by means of NMR field cycling method.[206] The solute spectral densities were interpreted using contributions from the anisotropic rotation diffusion and director fluctuations of the solvent molecules. The ^{13}C and ^{1}H NMR relaxation of chloroform dissolved in a smectic LC have been used to investigate the roto-translation motion of the solute molecule.[127,207]

6.2. Quantum computing

NMR quantum computing[208,209] has been discussed in several recent reviews.[210–212] The requirement for a spin system to act as a quantum processor is the ability to address its qubit(s) or quantum bit(s). This can be achieved in spin-1/2 systems by the nuclei having different Larmor frequencies and unequal mutual couplings among all the spins. For example, a 2-qubit ^{13}C–^{1}H system has four pseudo-pure states $|00\rangle$, $|01\rangle$, $|10\rangle$, and $|11\rangle$, each of them has all but one of the four energy levels being populated equally. The four pseudo-pure states show distinct ^{1}H and ^{13}C spectra. Since scalar J couplings are small and become zero between nuclei few bonds away, dipolar couplings among spin-1/2 nuclei, and quadrupolar couplings of spin $I \geq 1$ systems are preferred. However, these couplings are averaged out to zero in liquids and become too large and too many in solids. Hence NMR of solute molecules partially oriented in LC appears to be a suitable avenue to explore quantum information processing.[213] Kumar and co-workers have recently reported the creation of pseudo-pure states in quadrupolar spin systems like ^{137}Cs ($I = 7/2$)[214] and ^{7}Li ($I = 3/2$).[215] Other workers on quadrupolar systems include 2-qubit $I = 3/2$ systems[216–218] and 3-qubit $I = 7/2$ systems.[219–221] For non-identical spin-1/2 systems with either scalar or dipolar coupling, the number of qubits is equal to the number (n) of spins. ^{13}C-enriched solutes, including $^{13}CH_3CN$[222,223] and $^{13}CHCl_3$,[224,225] utilize dipolar couplings to give pseudo-pure states for quantum computing. Besides the ^{13}C–^{1}H dipolar coupling, other dipolar-coupled systems (e.g., ^{1}H–^{19}F)[226] can also be used. Recently, the spin cluster of strongly coupled protons ($n = 19$) in a 5CB molecule has been manipulated using multifrequency irradiation with low amplitude to give a spectrum of many sharp peaks with controllable frequencies and amplitudes.[227,228] An algorithm for parallel search by means of ^{1}H NMR in 5CB has also been proposed.[229]

7. STUDIES OF THERMOTROPICS

The application of solid state NMR spectroscopy to provide insights on the structure and dynamics of thermotropic LC remains a vibrant field of research. The most common spin probes are ^{13}C, ^{1}H, and ^{2}H. The choice of a suitable spin probe depends on the studied LC material and/or the availability of its labelled compound(s). Recent studies of thermotropics are surveyed by loosely grouping them based on their molecular shape and/or chemical structure. The survey is not intended to be exhaustive and is biased by the author's interests.

7.1. Calamitics

Here we concentrate on rodlike molecules, but recent interest on bent-core (banana) mesogens will also be included even though only a few NMR studies have so far been reported. One important prediction in the study of soft condensed matter in the past 10 years is that fluid smectic phases formed from molecules without asymmetric (chiral) carbons, due to symmetry breaking, could show a spontaneous polarization in the layer plane.[230–232] Indeed the spontaneous breaking of mirror symmetry in 'liquids' has gained much interest even outside the LC community. When found in soft matter, particularly in biology and biochemistry, it may be important for chiral recognition and self-assembling of supermolecular structure and functions.

7.1.1. *Classical type*

For the development of certain NMR methods, classical materials like 4-cyano-4′-*n*-pentyl biphenyl (5CB) are still used as model compounds. First several recent proton works are mentioned. Translation self-diffusion and its anisotropy in LC[233] can shed light on various aspects of molecular packing in mesophases. Pulse-field-gradient spin-echo (PGSE) was used in conjunction with multi-pulse homonuclear dipolar decoupling to provide accurate translational diffusion coefficients (D^t) in LC. It has been shown[234] that in the nematic phase of 5CB, the temperature dependences of $D^t_{\|}$, $D^t_{\perp}$, and the isotropic average $\langle D^t \rangle$ do not follow simple Arrhenius relations. The reorientation dynamics of director has continuously attracted attention from various workers.[235–237] The determination of director orientation is even possible in specific fragments of mesogens.[238] It is well-known that a nematic LC has an isotropic orientational distribution of the local directors unless under an external aligning field. Thus a nematic monodomain under an external magnetic field will suffer a mesoscopic disorder when the field is switched off. The director orientation dynamics of 8CB has been studied in the off-field state by following the proton lineshape in a fast field cycling NMR experiment.[239] The ordering and disordering were followed at several magnetic field strengths. As expected, the magnetic torque is much larger than thermal fluctuations of the director at high fields, while the reverse is true at low field strengths (i.e., thermal fluctuations dominate the orientation dynamics). Thermal hystereses have been observed for the proton second moments and spin relaxation times in the nematic phase (over a narrow 6° range) of trans-4(4-propylcyclohexy) benzonitrile.[240] Substantial differences in these measurements upon heating and cooling seem to indicate that the nematic order and molecular dynamics depend on the thermal history of the sample. The interaction between a monochromatic ultrasound energy and DF has also been studied in 5CB, 8CB, and *p*-azoxyanisole using the proton field cycling

technique.[241,242] A new free energy term representing the coupling between the ultrasonic waves and DF was added in order to derive T_1 due to DF under sonication. This explains the change in the T_1 relaxation dispersion due to an acoustic-induced enhancement of the DF modes in the whole frequency range.

Proton decoupled ^{13}C NMR resonances of weakly fluorinated organic molecules are often broad, thus degrading the spectral resolution and the ability to observe the splittings due to the C–F dipolar and *J* couplings. The ^{13}C–$\{^1H\}$ NMR spectra from two monofluorinated LC I35 and I52 have enabled the determination of dipolar couplings between individual carbons to the fluorine nucleus in these molecules.[243] These LC molecules contain a fluorine atom on one of its phenyl rings. The AP method was used to determine the shape of the potential which governs rotation about the inter-ring bond in the biphenyl fragment. Later ^{13}C work was carried out in I35 using a better proton decoupling sequence, i.e., SPINAL-64, to clearly observe C–F splittings in its ^{13}C spectrum.[80] The line broadening was ascribed to off-resonance effects in the proton frequency due to the contribution of effective coupling between ^1H and ^{19}F ($\sim$ 5.2 kHz). CP is needed to observe ^{13}C spectra of non-enriched LC. The effect of r.f. induced heating during the CP period may be non-negligible, and has been studied in 8CB as a function of the CP time.[244] This problem is similar to the sample heating by the proton decoupling power mentioned earlier. SLF and PDLF spectroscopy are useful for the measurement of 1-bond and 2-bond ^{13}C–^1H dipolar couplings in LC. For the determination of long range dipolar couplings, other methods have been used. These dipolar coupling constants are important for the study of conformational equilibria of flexible chain(s) in LC. Long range ^2H–^{13}C dipolar coupling constants have been obtained from 1D ^{13}C spectra of monodeuterated LC.[69,245,246] For example, the proton-decoupled ^{13}C NMR spectrum of a monodeuterated 4′-(1-deuteropentyloxy)-4-biphenylcarbonitrile (5OCB-d_1) gives nine ^2H–^{13}C dipolar coupling constants for carbon ranging from one to six bonds from the deuterium nucleus.[247] Long range ^{13}C–^{13}C dipolar coupling constants have been obtained from the proton decoupled ^{13}C spectrum of a ^{13}C-labelled 4′-cyano-4-biphenyl hexanoate-1-^{13}C. Eleven ^{13}C–^{13}C dipolar couplings were found[248] for carbon nuclei ranging from one to seven bonds away from the singly labelled carbon. Detailed analysis of long range dipolar couplings of these molecules in terms of the chain conformation equilibria remains to be carried out.

1D and 2D ^{13}C NMR were carried out in a series of novel nematogens by Bayle and co-workers to study the effects on the conformation and order due to the addition of lateral and/or terminal substituents.[249–251] For example, lateral flexible substituents are found to adopt a mean conformation more or less parallel to the mesogenic core. As a result, lateral chains are less disordered than terminal chains. Nematogens containing polyoxyethylene ether (POE) chain as a lateral crown ether and terminal chain(s) have been

studied.[252,253] These materials are good candidates for ionic conduction.[254] The orientational orders for some fragments of LC containing the 2-phenyl-indazole core were recently estimated by means of 1D and 2D ^{13}C NMR techniques.[255] Various CP schemes to enhance ^{13}C signals used in these LC studies of ordering have recently been reviewed.[256] Also CP to transfer magnetization from the proton dipolar reservoir to the carbons was achieved in the liquid crystal EBBA under the mismatched H.–H. condition.[257] As noted before, the ^{13}C chemical shifts in LC depend on the orientation β between the director and the external magnetic field through $P_2(\cos\beta)$, i.e., $\sigma_{obs} = \sigma_{iso} + \sigma_{aniso}\, P_2(\cos\beta)$. Even when the distribution of orientations in the sample is broad (which is identical for all angles), the ^{13}C line broadening is minimum at 0° and 90° giving relatively sharp lines.[72] 2D dynamic director experiment described in Section 4.1 has been carried out to take advantage of this fact on moderately viscous monomeric and polymeric LC (e.g., 8OCB, PBA, etc.). The 2D spectrum shows spectra at 0° and 90° orientations. The ^{13}C peak positions at 0° and 90° have coordinates at $\sigma_{iso} + \sigma_{aniso}$ and $\sigma_{iso} - \sigma_{aniso}/2$, respectively. These allow the determination of σ_{iso} and σ_{aniso} for a particular carbon. ^{13}C NMR relaxation studies of LC are, thus far, limited to a more qualitative approach when compared to deuteron spin relaxation studies. However, a recent study has demonstrated how cross-correlations between the relaxation processes originating from the CSA of ^{13}C and its dipolar coupling with the attached proton for various carbons can be used to extract motional parameters in MBBA.[41] The MBBA sample was spun at 6 kHz under MAS, and its ^{13}C spectrum (without proton decoupling) showed doublets for carbons with directly bonded protons that arose from the J coupling. The authors stated that while the ^{13}C–^{1}H couplings are removed by MAS, the relaxation mechanisms remain unaltered. The spectral densities, derived from self-relaxation, cross-relaxation and cross-correlation rates, were interpreted using the Lipari-Szabo model-free approach. Rotational diffusion coefficients $D_{\|}$ and $D_{\perp}$ were determined in the nematic phase of MBBA at one temperature from the ortho and methine carbons. This work appears to show that ^{13}C relaxation can turn out to be a powerful mean to extract dynamical information in LC.

Among the different approaches to study anisotropic rotational diffusions in LC, deuterium spin relaxation measurements are most interesting and popular.[17,18,188] In particular, correlated internal rotations within a flexible end chain(s) of LC can be studied by ^{2}H NMR due to the site specificity of the deuteron(s). The theory needed to interpret the quadrupolar splittings and spectral densities of motion in a self-consistent manner has been outlined in Section 5.4. Here we highlight the decoupled model[137,186] by examining two examples, one is 5CB whose ring and alkyl chain are deuteriated and the other is 1-methylheptyl 4′-(4-*n*-decyloxy-benzoyloxy)biphenyl-4-carboxy-late (10B1M7),[187] a chiral LC with its achiral decyloxy chain deuterated. For an alkyl chain, the original decoupled model using three jump constants

k_1, k_2, and k_3 is good, while for an alkyloxy chain, the modified decoupled model in which the k_3-motion is replaced by the *gauche* migration (k_g) and *gauche* pair formation (k'_g) seems more appropriate. Since the deuterium T_{1Z} and T_{1Q} were measured at 15.1 and 46 MHz, the spectral densities $J_1(\omega)$ and $J_2(2\omega)$ will have a negligible contribution from DF. However, DF have been studied through measurements of deuteron spin–spin relaxation time T_2.[180] As seen in Eq. (39), $J_0(0)$ in the T_2 expression can be sensitive to DF in second order [see Eq. (60)]. Figure 14 shows plots of spectral densities for the ring, C_α, C_β, C_γ, and C_δ deuterons versus the temperature in the nematic phase of 5CB-d_{15}. The smoothed $J_1(\omega)$ and $J_2(2\omega)$ are reproduced from Ref. 181, while the $J_0(0)$ from Ref. 180. The number of conformations in the pentyl chain is 81 and the size of transition rate matrix is 81×81. For the deuteron(s) on each carbon site, the spectral densities are calculated according to

$$\begin{aligned} J_1(\omega) &= J_1^{\mathrm{MR}}(\omega) \\ J_2(2\omega) &= J_2^{\mathrm{MR}}(2\omega) \\ J_0(0) &= J_0^{\mathrm{MR}}(0) + J_0^{\mathrm{DF}}(0) \end{aligned} \tag{89}$$

where $J_0^{\mathrm{DF}}(0)$ is given by Eq. (60) and $J_i^{\mathrm{MR}}(\omega)$ is given by Eq. (87) for the case of a symmetric top ($n = n'$). A global target analysis was carried out to fit the experimental spectral densities, resulting in a quality (Q) factor for the 'fits' of 1%. The high frequency cutoff was set at 1 MHz for DF and the calculated spectral densities are also shown in Fig. 14 as solid and dashed curves. The prefactor A in Eq. (64) was found to be slightly temperature dependent and k_2 was temperature independent at 7×10^{14} s^{-1}. The remaining motional parameters found at 22°C[180] are $k_1 = 8 \times 10^{10}$ s^{-1}, $k_3 = 5.3 \times 10^{12}$ s^{-1}, $D_\perp = 4.2 \times 10^7$ s^{-1}, $D_R = 1.3 \times 10^9$ s^{-1}, $D_\parallel = 9.5 \times 10^8$ s^{-1}, and $A = 2.4 \times 10^{-5}$ s$^{1/2}$. The activation energies of molecular reorientations are $E_a(D_\perp) =$ 37.3 kJ/mol and $E_a(D_\parallel) = 42.6$ kJ/mol. It is common to see that in NMR relaxation study of LC, $E_a(D_\perp) \lesssim E_a(D_\parallel)$, and the reason for this apparent unphysical picture is its inability to nail down the tumbling motion with good precision. At 22°C, the molecular reorientation contributions to the $J_0(0)$ for various methylene deuterons along the chain amount to between 21 and 30%. Their remaining contributions are attributed to the second order DF. We now turn to the application of the modified decoupled model to study the chain dynamics of a decyloxy chain in a chiral mesogen 10B1M7.[187] This study, however, does not involve the chiral chain and was restricted to its SmA phase since the deuterium signals of the achiral chain were severely broadening in the chiral phases below the SmA phase. Figure 15 reproduces the spectral densities at 15.1 and 46 MHz versus the temperature in the SmA phase of 10B1M7-d_{21}. As mentioned in Section 5.4, certain assumptions were made to reduce the number of significant conformations ($N = 683$) in the flexible achiral chain of 10B1M7. The simplifying assumptions used in setting

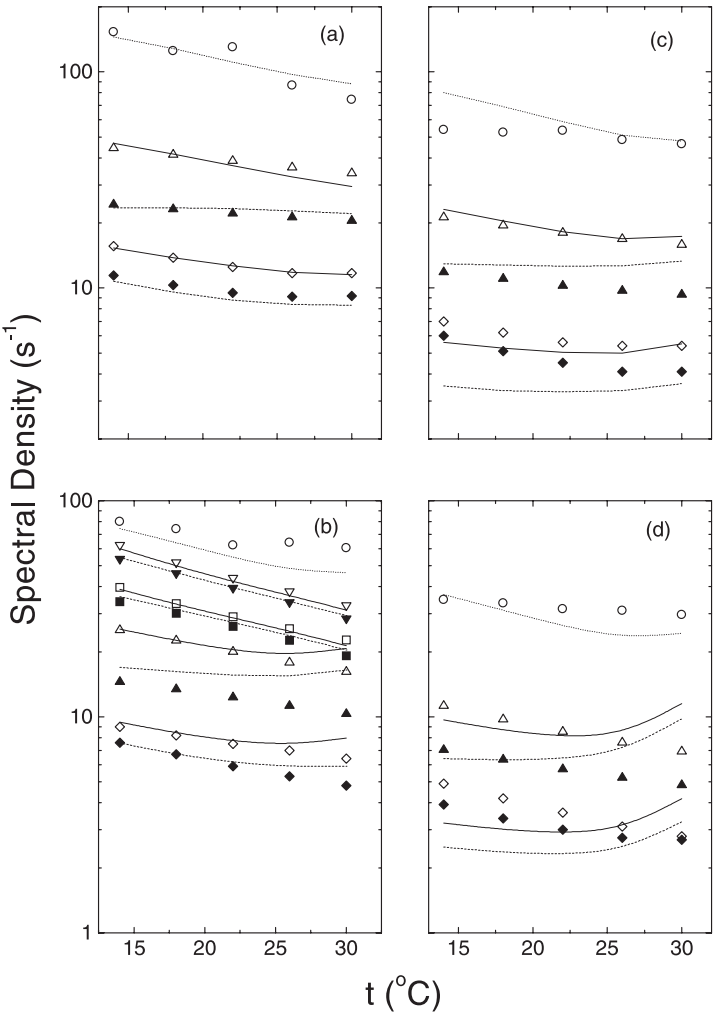

Fig. 14. Experimental (symbols) and fitted (lines) spectral densities of 5CB-d_{15}. J_1 and J_2 data are smoothed experimental values. (a), (b), (c), and (d) contain C_1, C_2, C_3, and C_4 data, respectively. In addition, the C_0 (ring) data are also shown in (b). For the aliphatic deuterons, circles, uptriangles, and diamonds denote $J_0(0)$, $J_1(\omega)$, and $J_2(2\omega)$, while for the ring deuterons, downtriangles and squares denote $J_1(\omega)$ and $J_2(2\omega)$, respectively. Closed symbols are for 46 MHz and open symbols are for 15.1 MHz. Solid and dashed curves are fitted spectral densities. (Adapted from Ref. 180.)

up the $\underset{\approx}{\mathbf{R}}$ matrix are given above, and there are 1388 forward conformational transitions in the achiral chain. Among them, there are 342 k_1-motions, 170 k_2-motions, 438 transitions for the *gauche* migration and 438 transitions for the *gauche* pair production. The quadrupolar splittings were first modelled using the AP method to give the nematic order parameter $S_0(= \langle S_{zz} \rangle)$ and the

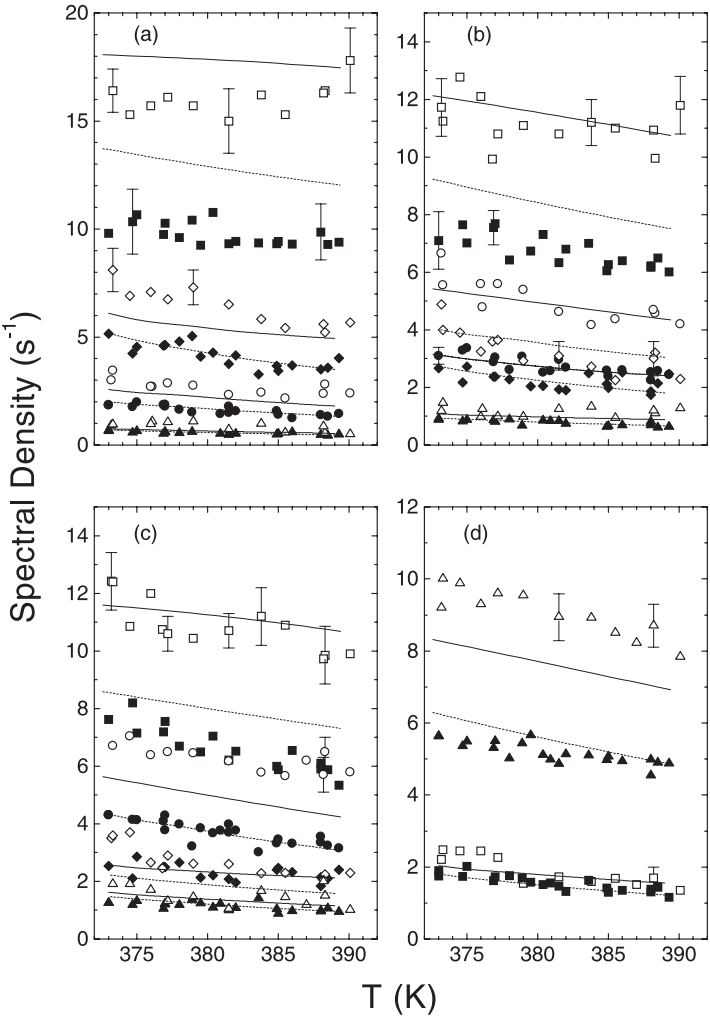

Fig. 15. Plots of spectral densities versus the temperature in 10B1M7-d_{21}. Open and closed symbols denote data at 15.1 and 46 MHz, respectively. (a) Squares and diamonds denote $J_1(\omega)$ and $J_2(2\omega)$ of $C_{1,2}$, while circles and triangles denote $J_1(\omega)$ and $J_2(2\omega)$ of C9, respectively, (b) squares and diamonds denote $J_1(\omega)$ and $J_2(2\omega)$ of C_3, while circles and triangles denote $J_1(\omega)$ and $J_2(2\omega)$ of C_8; (c) squares and diamonds denote $J_1(\omega)$ and $J_2(2\omega)$ of C_4, while circles and triangles denote $J_1(\omega)$ and $J_2(2\omega)$ of C_7; (d) traingles and squares denote $J_1(\omega)$ and $J_2(2\omega)$ of $C_{5,6}$. Solid and dashed curves are fitted spectral densities. (Adapted from Ref. 187.)

molecular biaxiality $\langle S_{xx} - S_{yy} \rangle$ of an 'average' conformer. The S_0 was found to range between 0.68 and 0.76 in the SmA phase. Using Eq. (87), a global target analysis was carried out to minimize the mean-squared percent deviation by varying the model parameters $D_{\parallel}$, $D_{\perp}$, k_1, k_2, k_g, and k'_g. This yielded

a Q factor of 2.8%. The calculated spectral densities are also shown in Fig. 15 as solid and dashed curves. As an example, the following model parameters were obtained at 377 K: $D_{\|} = 7.6 \times 10^9\ s^{-1}$, $D_{\perp} = 3.4 \times 10^7\ s^{-1}$, $k_1 = 1.2 \times 10^{13}\ s^{-1}$, $k_2 = 2.8 \times 10^{14}\ s^{-1}$, $k_g = 2.85 \times 10^{13}\ s^{-1}$, and $k'_g = 2.9 \times 10^{12}\ s^{-1}$. All motional parameters followed an Arrhenius temperature behaviour. To end this section, we mention the application of deuterium NMR spectroscopy to study the influence of photosensitive diheptylazobenzene (7AB) in the SmA phase of 8CB.[258] By irradiating 7AB with a UV light, cis-isomers of 7AB were formed in the mixture of 8CB/7AB. As a consequence, the highly bent 7AB cis molecules acted as a disordering factor and the reduction in the overall orientational order of the system could be followed using the quadrupolar splittings of the labelled 8CB and 7AB. The authors suggested that the photo-induced changes in the layer spacing are a consequence of changing S_0.

7.1.2. *Chiral and achiral mesogens*

Chirality (or a lack of mirror symmetry) plays an important role in the LC field. Molecular chirality, due to one or more chiral carbon site(s), can lead to a reduction in the phase symmetry, and yield a large variety of novel mesophases that possess unique structures and optical properties. One important consequence of chirality is polar order when molecules contain lateral electric dipoles. Electric polarization is obtained in tilted smectic phases. The reduced symmetry in the phase yields an in-layer polarization and the tilt sense of each layer can change synclinically (chiral SmC*) or anticlinically (SmC^*_A) to form a helical superstructure perpendicular to the layer planes. Hence helical distributions of the molecules in the superstructure can result in a ferro- (SmC*), antiferro- (SmC^*_A), and ferri-electric phases. Other chiral subphases (e.g., C^*_α) can also exist. In the SmC^*_A phase, the directions of the tilt alternate from one layer to the next, and the in-plane spontaneous polarization reverses by 180° between two neighbouring layers. The structures of the C^*_α and C^*_γ phases are less certain. The ferrielectric C^*_γ shows two interdigitated helices as in the SmC^*_A phase, but here the molecules are rotated by an angle different from 180° w.r.t. the helix axis between two neighbouring layers.

^{13}C T_1 relaxation and line width measurements have been used to study the structure and dynamics of ferro- and antiferro-electric liquid crystals.[259–263] In some cases, a marked line broadening of ^{13}C line widths was observed in a static sample for the aromatic carbons upon cooling into the ferroelectric SmC* phase, and not so for the aliphatic carbons. It was also found that ^{13}C spectra collected under MAS and high power decoupling show much sharper lines than without MAS.[261] Apart from spin relaxation by the dipolar interaction with the directly bonded proton, the contribution from CSA (especially at high magnetic fields) to ^{13}C spin relaxation (in particular for non-protonated carbons) can be drastically reduced when the sample spinning rate is sufficiently high. Both static and rotating samples under proton dipolar

decoupling were used to study the SmA–SmC* transition of S-MONBIC.[261] There are definite jumps in the T_1 values for the non-protonated carbons at the SmA–SmC* transition, indicating a discontinuous change in the dynamics of the molecular core at the transition. In the antiferroelectric LC 4-[(1-methylheptyloxy)carbonyl]penyl 4-[4-(octyloxy)biphenyl]carboxylate (S-MHPOBC), ^{13}C T_1 measurements under MAS for various carbon sites do not show discontinuity at the SmA–SmC$^*_A$ transition. However, a change in the slope of the ln T_1 versus the reciprocal temperature was seen in the SmC$^*_A$ phase for the lone chiral centre. The ^{13}C chemical shift is affected by the orientational properties in the mesophases, and large chemical shifts are observed for the aromatic carbons from the isotropic to a smectic (or nematic) phase of aligned samples. These shifts can be used to extract orientational order parameters for the LC molecule. According to Eqs. (46)–(47), the ^{13}C chemical shift of an aligned sample is

$$\delta_i = \delta_i^{\mathrm{iso}} + \frac{2}{3} S_{zz}\{\delta_{zz} - (\delta_{xx} + \delta_{yy})/2\} + \frac{1}{3}(\delta_{xx} - \delta_{yy})(S_{xx} - S_{yy}) + \frac{2}{3}(S_{yz}\delta_{yz} + S_{xz}\delta_{xz} + S_{xy}\delta_{xy}) \tag{90}$$

When rapid rotations exist, S_{xy}, S_{yz}, and S_{xz} vanish, and $S_{xx} - S_{yy}$ is usually small, thereby giving

$$\delta_i = \delta_i^{\mathrm{iso}} + \frac{2}{3} S_{zz}(\delta_{\|} - \delta_{\perp}) \tag{91}$$

where $\delta_{\|}$ is the chemical shift component along the direction of the long molecular axis (z), and $\delta_{\perp} = (\delta_{xx} + \delta_{yy})/2$ is the average chemical shift component along a short molecular axis. Both $\delta_{\|}$ and $\delta_{\perp}$ can be expressed in terms of the principal values (δ_{ii}) of the chemical shift tensor and the polar angles (α, β) denote the orientation of the $\underset{\approx}{\delta}$ tensor in the molecular (x, y, z) frame. In order to get S_{zz} from the chemical shifts, the principal components of chemical shielding tensor $\underset{\approx}{\sigma}$ have to be known (it is noted that $\underset{\approx}{\delta}$ and $\underset{\approx}{\sigma}$ in ppm are related by $\underset{\approx}{\delta} = \sigma_{\mathrm{ref}} - \underset{\approx}{\sigma}$, where σ_{ref} is from a reference such as TMS). The determination of these for each carbon nucleus in the solid state can be carried out by means of MAS and the 2D TOSS-deTOSS[264] or PASS2D experiment,[265] which gives a spinning sideband pattern for each resolved carbon resonance in the isotropic ^{13}C spectrum. The TOSS-deTOSS experiment has been used to obtain σ_{ii} for seven carbon nuclei in MHPOBC, and S_{zz} of 0.73 was determined at 403 K in its SmA phase.[266] Molecular structural information, such as that the chiral chain in MHPOBC is substantially bent from the long molecular axis (by as much at 43°)[263,267] or that the core of some ferroelectric LC has a bent structure,[268] can be derived using ^{13}C or ^{2}H NMR spectroscopy. The intramolecular motion of the chiral chain in MHPOBC was found to be frozen in the SmC$^*_A$ phase based on the transient oscillations

in the ^{13}C–^{1}H cross polarization dynamics.[269] ^{19}F NMR has also been used to study the orientational change of a trifluoromethyl group at the SmC*–SmC$^*_A$ transition in an antiferroelectric LC.[270]

Varacini and co-workers have employed deuterium spin–lattice relaxation times to study dynamics of several chiral mesogens.[187,268,271–274] No particular changes in T_{1Z} and T_{1Q} were observed[271] at the SmA–SmC* or SmC*–SmC$^*_A$ transition for deuterium nuclei on the aromatic core in good agreement with the above ^{13}C T_1 observations. The relaxation data can be understood in the SmA phase by fast molecular and internal rotations using Nordio model. The lack of a suitable relaxation model for chiral smectic phases has prevented a detailed analysis of their relaxation data. The chiral smectogen (S)-[4-(2-methylbutyl-d_{11}) phenyl-d_4]-4′-octylbiphenyl carboxylate (8BEF5-d_{15}) exhibits a very rich variety of chiral smectic phases. The order parameter S_{zz} of the phenyl ring fragment is found to be higher than the S_{zz} of the 'average' molecular conformer obtained by modelling all the quadrupolar splittings of 8BEF5-d_{15} with the AP method.[273] Since the order obtained with the AP method is influenced by the chiral chain deuterons, the result seems to suggest that the chiral chain must tilt w.r.t. the para axis in the molecule. This observation has been noted in ^{13}C NMR studies.[263,267]

Niori *et al*. first detected ferroelectricity in a smectic phase formed by bent-core or banana molecules in 1996.[13] When the achiral molecule has a C_{2v} symmetry, the in-layer polarization vector $\widehat{b}$, the director $\widehat{n}$ and the normal $\widehat{m}$ to the molecular plane are mutually perpendicular. Chirality occurs in tilted polar phases (the so-called B phases) formed by banana molecules due to the reduced symmetry. The tilt angle ϑ is measured by $\widehat{n} \times \widehat{k} = \sin\vartheta = |\vec{\xi}|$ where $\widehat{k}$ is the layer planar normal. The tilt direction $\vec{\xi}$ of the molecular planes, and the polar order axis are two independent symmetry breaking factors. Electro-optical switching has been observed in B_2 and B_5 phases. Phase structures and dynamics of B phases are the subject of intense research. ^{1}H, ^{19}F, and ^{13}C NMR have been reported in an antiferroelectric B_5 phase,[275] and ^{13}C NMR has been used to give order parameter in a B_2 phase.[276,277] Most of the banana molecules reported in the literature contain a 1,3-phenylene fragment as the central ring to create a bending angle of about 120°.[278] Introduction of substituents is possible at the central resorcinol unit at the 4- and/or 6-position. Substituents at the central phenyl ring can change the conformation of the whole molecule. While the bending angle is about 120° for 1,3-phenylene compounds, this angle is increased to 131° in the related derivative 4-chloro-resorcinol. The bending angle is even larger (ca. 156°) in a 4,6-dichloro-resorcinol derivative. ^{13}C NMR spectra of aligned banana samples can provide orientational and conformational information, as well as the bending angle. The methodology of extracting S_{zz} from the chemical shift anisotropies is exactly the same as in chiral mesogens. A recent work on a banana-shaped mesogen 4-chloro-1,3-phenylene bis[4-4′-(11-undecenyloxy)-benzoyloxy] benzoate has combined ^{2}H and ^{13}C NMR to study S_{zz} and the

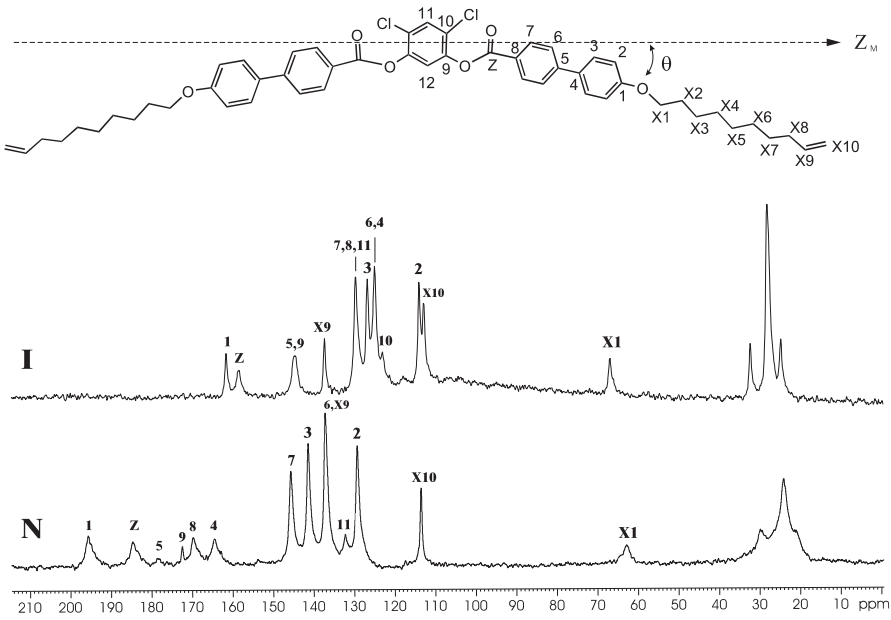

Fig. 16. Structure of a banana molecule 4,6-dichloro-1,3-phenylene bis[4′-(9-decenyloxy)biphenyl] carboxylate and ^{13}C NMR spectra in the nematic (top) and isotropic (bottom) phase.

bending angle in its nematic phase.[279] The bending angle was estimated to be ca. 141°. Figure 16 shows the molecular structure of a banana molecule (4,6-dichloro-1,3-phenylene bis[4′-(9-decenyloxy)biphenyl]carboxylate and two of its typical ^{13}C NMR spectra obtained at 100.6 MHz in an aligned sample, one of which is taken in the nematic phase and the other in the isotropic phase. The isotropic spectrum was obtained using a single carbon pulse to produce the FID which was acquired under the Waltz-16 proton decoupling. The nematic spectrum was collected using the standard CP (2 ms) after the proton 90° pulse and the carbon FID was acquired under the SPINAL-64 decoupling. It is obvious that upon entering the N phase, the aliphatic ^{13}C chemical shifts become slightly more shielded, while the aromatic ^{13}C chemical shifts become a lot less shielded. It is noted that the chemical shift anisotropy δ–δ^{iso} from the ring adjacent to the central ring can only give the best product $S_{zz}P_2(\cos\theta)$ at each temperature, where θ is the angle between the para axis of the 'lateral' ring with the long molecular z_m axis. Hence an independent means of getting S_{zz} or θ at one temperature (e.g., T_c) is necessary. The bending angle for the dichloro-substituted compound is given by $180° - 2\theta$. A ^{19}F NMR study in the B_2 phase of 5-fluoro-1,3-phenyl bis[4-(3-fluoro-4-*n*-dodecyloxyphenyliminomethyl)]benzoate gave spectra that showed a triplet representing the dipolar interactions between the ^{19}F atom on the central ring and its two

neighbouring protons, as well as a doublet splitting caused by ^{19}F atom on the outer side rings. The triplet separation observed from the central ring was used to determine S_{zz} directly, while the doublet separation gave $S_{zz}P_2(\cos\theta)$. The bending angle was found to be ca. 117° for this banana mesogen.[275]

Blue phases are shown by highly chiral materials and occur above the cholesteric phase and often exist for a few degrees just before the isotropic phase. There are three blue phases: BPI, BPII, and BPIII. Upon heating, one can observe the following sequence: BPI, BPII, and BPIII. To the author's knowledge, there is no recent NMR report on these blue phases. The reason is probably due to their small temperature range and complex cubic structures. Both BPI and BPII show long range orientational order and form a 3D body-centred cubic and a simple cubic structure, respectively. BPIII is isotropic and only appears in highly chiral compounds. Blue phases are frustrated phases as a result of the competition between chiral forces and packing topology.[281] There is evidence even for a smectic blue phase.[282] All these esoteric mesophases still await investigations by NMR.

7.1.3. *Metallomesogens*

There has been considerable interest in metal-containing LC (metallomesogens), but the use of NMR to study them is rather limited thus far. Metallomesogens combine the physical characteristics shown by a metal coordination complex with the liquid crystalline properties of organic molecule(s). The scope of metallomesogens is great, since there are some 60 metals which can in principle be coordinated to organic ligands. However, metallomesogens suffer from high transition temperatures, poor thermal stability, and high viscosity. Ghedini and coworkers have pioneered the mesomorphic orthopalladated azo complexes.[283] In particular, the cyclopalladated 4,4′-bis(hexyloxy) azoxybenzene (Azpac) is an exception, showing a nematic phase below 100°C and is a good candidate for NMR studies. Recently, deuterium NMR spectra were recorded by Veracini and co-workers[284,285] in the nematic phase of two isotopomers of Azpac: one deuterated in the positions 3 and 5 of both phenyl rings (Azpac-d_4) and the other deuterated in the hexyloxy chains (Azpac-d_{26}). Also their deuterium T_{1Z} and T_{1Q} were reported.[285] From the molecular structure of Azpac shown in Fig. 17, the acetylacetonate ligand and the phenyl ring A form a rigid planar fragment, whose dihedral angle w.r.t. the phenyl ring B is about 41°. The angle θ between the ring para axes is about 7°. A quantitative analysis of both the quadrupolar splittings and spectral densities at 46 MHz of both isotopomers was carried out[179] using the AP method for modelling the splittings from both chains (A and B) and the original decoupling model for interpreting the relaxation data. The two chains were treated identically and independent of each other in the AP method, while in writing down the transition rate matrix (243×243), only one chain (chain A or B) was explicitly considered. The spectral densities given by Eq. (71) were used for sites 3 and 5 of ring A as it involved only molecular reorientations,

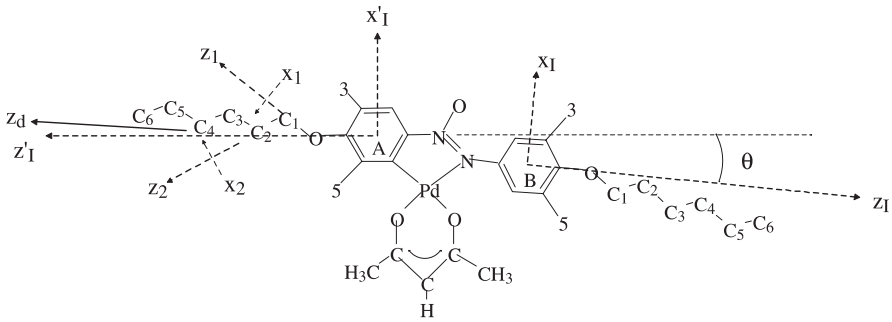

Fig. 17. Molecular structure of Azpac showing various coordinate systems used. Sites 3 and 5 on rings A and B are deuterated in Azpac-d_4. The long z_d axis makes a 1° angle with the z_I' axis.

while for ring B, due to additional internal ring rotation with a diffusive constant D_R, the equation was modified to give

$$J_m^{\mathrm{MR}}(m\omega) = \sum_n \left[d^2_{m_R 0}(\beta_{R,Q})\right]^2 \left[d^2_{nm_R}(\theta')\right]^2 \sum_k \frac{(A^2_{mn})_k \left[(B^2_{mn})_k + m_R^2 D_R\right]}{(m\omega)^2 + \left[(B^2_{mn})_k + m_R^2 D_R\right]^2} \quad (92)$$

where $\theta' = \theta - 1°$. Since the I frame was not identical to the M frame, Eq. (87) was modified for the chain deuterons (chain A or B) to give ($n = n'$)

$$J_m^{(i)}(m\omega) = \sum_n \sum_{j=1}^{243} \left| \sum_{j=1}^{243} \sum_{m_l} d^2_{nm_l}(\gamma) d^2_{m_l 0}(\beta_{lQ}^{(i)l}) \exp\left[-i m_l \alpha_{lQ}^{(i)l}\right] x_l^{(i)} x_l^{(j)} \right|^2$$

$$\times \sum_k \frac{(A^2_{mn})_k \left[(B^2_{mn})_k + |\lambda_j|\right]}{(m\omega)^2 + \left[(B^2_{mn})_k + |\lambda_j|\right]^2} \quad (93)$$

where the angle γ (between the z axes of I and M frames) depended on chain A or B, $\beta_{\mathrm{IQ}}^{(i)l}$ and $\alpha_{\mathrm{IQ}}^{(i)l}$ were the polar angles for the C_i–D bond of the conformer l in the I frame. $\gamma = 185°$ for chain B, and $\gamma = 1°$ for chain A. At each temperature, the six model parameters $D_{\|}$, $D_{\perp}$, D_R, k_1, k_2, and k_3 were derived by fitting the experimental to calculated spectral densities. These are summarized in Fig. 18 (k_3 is not shown as it is more or less constant at 6×10^{16} s^{-1}). It is interesting to note that the tumbling rate $D_{\perp}$ is at least an order of magnitude smaller than those of conventional calamitic LC. Finally to illustrate the fits at various deuteron sites, the spectral densities at 6.3° below T_c are shown in Fig. 19 for chain (ring) A and chain (ring) B.

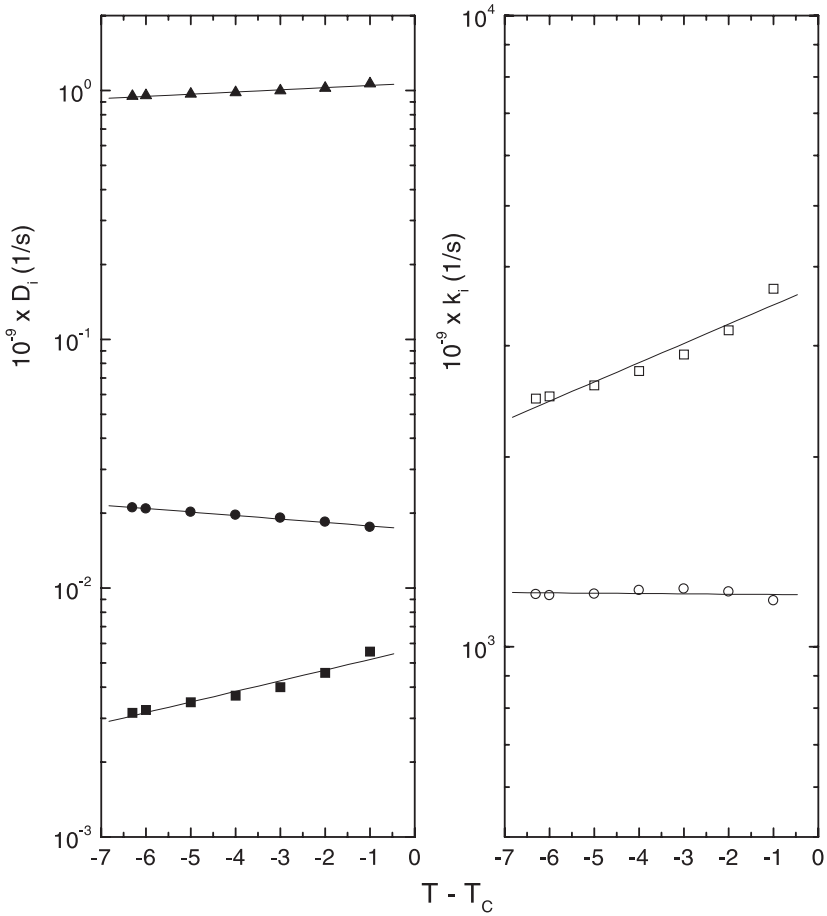

Fig. 18. Plots of rotational diffusion constants $D_\perp$ (closed squares), $D_\parallel$ (closed circles), and D_R (closed triangles), as well as jump constants k_1 (open squares) and k_2 (open circles) versus the temperature in the nematic phase of Azpac. Solid lines are to guide the eyes only. (Adapted from Ref. 179.)

7.2. Discotics

Discotic LC are formed by disk-like molecules with aromatic cores and side chains that are either hydrophobic (i.e., thermotropic) or hydrophilic (i.e., lyotropic). The discotic nematic (N_D) phase behaves like a normal nematic phase formed by rod-like molecules, and the disk-like molecules are oriented with their short molecular axes parallel to the director but show no positional order. More ordered columnar phases are commonly formed by thermotropic discotics. The two-dimensional structure can pack the columns into a hexagonal or rectangular columnar phase, while within the columns, disks can be

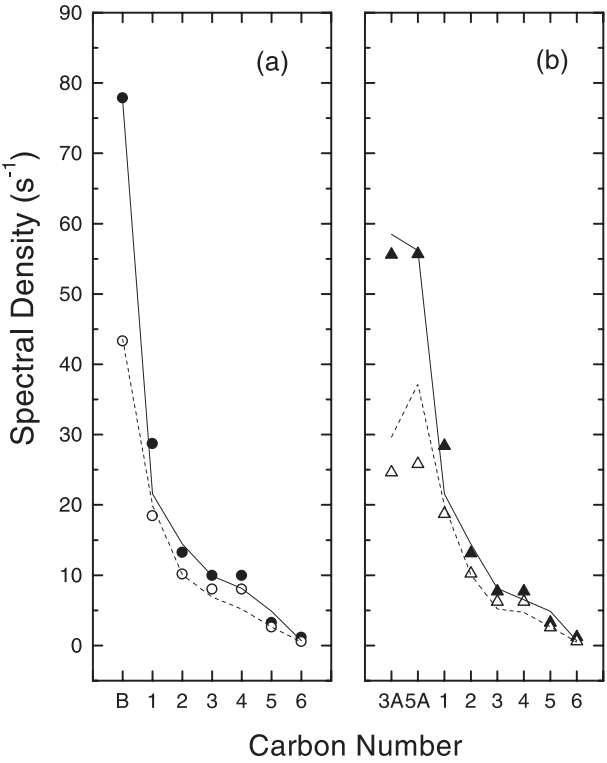

Fig. 19. Variation of the spectral densities $J_1(\omega)$ (closed symbols) and $J_2(2\omega)$ (open symbols) with the deuteron position in the nematic phase of Azpac ($T = 361.7$ K). (a) Ring B and chain B, (b) ring A and chain A. Solid and dashed lines are calculated spectral densities.

disordered (D_{hd}), ordered (D_{ho}), plastic (D_{hp}), or helical (H). The possible application of discotic materials as conducting layers in molecular electronic devices has attracted much interest. The columnar stacks with aromatic macrocyclic cores surrounded by insulating side chains can lead to a one-dimensional transport of charge and energy within the core region. Triphenylene based LC (e.g., HAT6) have served as model compounds for NMR studies of dynamics and structure.[175,286,287] HAT6 has also been studied by quasielastic neutron scattering,[288] which is sensitive to dynamics on a time scale (femtosecond to 10^2 ns) much shorter than that of NMR. Deuteron spin relaxation in the D_{ho} phase of HAT6, based on the anisotropic viscosity model, gave a tumbling rate of 3.8×10^7 s^{-1} and a spinning rate about the disk normal of 1.1×10^8 s^{-1} (at 351 K).[175] As charge-transfer processes occur on a picosecond time scale, the slow dynamics (ca. 10^8 s^{-1}) observed by NMR can only interfere with the charge transfer on longer length scales, e.g., to limit the long-range conductivity. The separation (d) between

neighbouring columns ranges between 1.6 and 2.7 nm. Translational self-diffusion between columns in D_{ho} phase of HAT5 has recently been measured[287] by means of deuterium stimulated-echo PGSE method. At 351 K, $D^t = 4 \times 10^{-14}$ m^2/s and its activation energy is quite high, indicating a solid-like jump behaviour. To estimate the column–column exchange rate (W) for disk molecules from $D^t = Wd^2$, using the above D^t value and $d = 2$ nm, one has $W = 10^4$ s^{-1}. Hence discotic mesogens can in principle form a one-dimensional molecular conducting wire. The effect of adding a lateral dipole in a fluorinated HAT6 (F-HAT6) has also been studied by deuteron spin relaxation,[289] and the analysis of experimental spectral densities at two Larmor frequencies based on the anisotropic viscosity model indicated that the activation energies for the spinning and tumbling motions w.r.t. the director are considerably higher for F-HAT6. At 351 K, $D_\alpha = 5.1 \times 10^7$ s^{-1} and $D_\beta = 2.8 \times 10^7$ s^{-1}. These values are also lower than those for HAT6 at the same temperature. The original decoupled model was used to derive the jump constants k_1, k_2, and k_3 of internal dynamics based on the chain spectral densities of HAT6.[175] It is not certain why the k_1 values (5×10^{17} s^{-1} at 351 K) seem to be rather high when comparing with those obtained in calamitic LC. Hexaoctyloxyrufigallol has been studied by deuterium NMR using two isotopomers, one deuterated in the aromatic core (rufigallol-d_2)[290] and the other deuterated at the C_α positions of all 6 chains (rufigallol-d_{12}).[291] While the molecular reorientation is modelled by the anisotropic viscosity model as in HAT6, a libration model is used to describe the wagging motions in two different types ('inner' vs. 'outer') of side chains by allowing the first CD bonds to diffuse in a circular arc within a defined apex angle. The 'inner' chains (3, 8) have two neighbouring side chains, while the 'outer' chains (2, 4, 7, 9) are more free to move due to only one neighbouring side chain. At 350 K, $D_\alpha = 3.2 \times 10^8$ s^{-1} and $D_\beta = 1.2 \times 10^7$ s^{-1}. For the 'outer' chains, both the diffusive rate ($D_{\phi 1}$) and the apex angle (ϕ_1) increase with decreasing temperature, while the diffusive rate ($D_{\phi 2} = 5.6 \times 10^9$ s^{-1}) and the apex angle ($\phi_2 = 138°$) for the 'inner' chains remain insensitive to temperature. At 350 K, $D_{\phi 1} = 2 \times 10^9$ s^{-1} and $\phi_1 \simeq 144°$. Recently, rufigallol has also been studied by ^{13}C SLF NMR spectroscopy.[292] By using various ^{2}H- and ^{13}C-labelled isotopomers, ^{13}C chemical shift tensor elements were found in order to study side chain conformations.[293] These authors have measured ^{1}H–^{13}C and ^{2}H–^{13}C dipolar couplings, from which the molecular order and conformation could be obtained. They concluded that in contrast to many other discotic LC, the conformation and mobility differ for the three non-equivalent side chains in rufigallol both in the solid and liquid crystalline phases. The estimated molecular structure in the mesophase is roughly in agreement with the conclusions of ^{2}H NMR study of rufigallol-d$_{12}$,[294] except for a different chain assignment, i.e., (3, 4, 8, 9) chains prefer out-of-plane conformations, while (2, 7) chains adopt in-plane conformations. Incidentally, PASS2D has been employed in this study to extract principal values of CSA tensors for the core

carbons in the solid and columar phases of rufigallol. The carbon CSA values in the solid state allowed the determination of the core order parameter. A new series of pyramidic LC formed by nona-alkanoyloxy tribenzocyclononene (CTV-n) has recently been studied by ^{13}C MAS spectroscopy.[107] The CTV-n homologues exhibit two isomeric forms, crown and saddle. Both isomers are mesogenic when substituted with sufficiently long side chains. NMR measurements indicate that molecules in the crown mesophase reorient about the column axes, whereas they are static in the saddle mesophase. This study has demonstrated the power of ^{13}C MAS NMR for studying dynamic processes in the discotic LC. Finally, hexa-peri-hexabenzocoronene (HBC), dodecyl-substituted HBC (HBC-C_{12}), and dodecylphenyl-substituted HBC (HBCPhC_{12}) have been studied using solid-state NMR techniques and X-ray diffraction by Spiess and co-workers.[295–297] Two-dimensional rotor-synchronized proton double quantum MAS spectra were recorded in HBC-C_{12}.[295] The π–π interactions of the aromatic cores in a herringbone structure, which existed in the solid state, were found to persist even in the LC phase. This accounts for the high one-dimensional charge carrier mobilities in HBC-C_{12} and HBC-PhC_{12}. The addition of phenyl ring in the side chain of HBC-PhC_{12} has, however, lowered the optimal π–π packing, and consequently slow axial motions of the disks around the column axes were seen.[297]

7.3. Polymeric liquid crystals

A brief survey of recent ^{2}H and ^{13}C NMR studies of thermotropic liquid crystalline polymers and copolymers is given. ^{13}C CP/MAS NMR spectra have been obtained as a function of temperature in a main-chain polyether (HMS-9) to probe the structure and chain conformation in its crystalline and nematic phases.[298] ^{13}C T_1 of the unresolved methylene carbon peaks shows a non-exponential decay which can be decomposed into 3 components. The shortest T_1 component is ascribed to all the C–C bonds of the methylene sequence undergoing rapid *trans-gauche* exchange, which is feasible in the nematic or supercooled LC phase. The other two components with longer T_1s reflect somewhat more ordered chain conformation in the methylene sequences, and the longest T_1 component arises from the crystalline phase. A ^{13}C MAS study of a main chain PB-18 polyester composed of 4,4′-dihydroxybiphenyl and octadecanedioic acid has been reported in its smectic H and crystalline phases.[299] Detailed information on the conformation of the mesogenic and aliphatic spacers is obtained in different phases by analyzing the carbon chemical shifts in ^{13}C CP/MAS spectra. The odd–even effect of flexible spacer units on the chain dynamics has been investigated recently in two main-chain LC polymers by two different groups using high resolution ^{13}C NMR techniques.[300,301] The molecular dynamics of poly-[(phenylsulfonyl)-p-phenylenealkylenebis(4-oxybenzoate)] (PSHQ-n) is monitored using

NMR spectra and T_1 measurements at different temperatures. The local polymer chain motion varies over a frequency range of 10^4–10^6 Hz in the nematic phase. The activation energy of this motion is found to increase with decreasing number (n) of methylene units in the spacer, and exhibits odd–even fluctuations. In a study of a homologous series of main-chain LC polyesters, ^{13}C CP/MAS and variable-temperature experiments reveal a conformationally more homogeneous and a less dynamic nature for the even-chained than for the odd-chained polymer structures.[300]

There are several recent deuteron spin relaxation studies of LC polymers and copolymers.[302–304] These studies involve deuterated phenyl rings, located in a main-chain LC polymer or side-chain LC copolymers, to probe the order and dynamics of the mesogenic groups. In one study, the LC copolymers are characterized by the same mesogenic side groups based on phenyl benzoate fragment and various contents of the acrylic and methacrylic units in the main chain polymer structure. Here differences in the order and dynamics of the mesogenic units bounded to the acrylic and the methacrylic monomers were found. It would appear that the mesogenic side groups are not completely decoupled from the main-chain skeleton due to the spacer having too few CH_2 units. The other LC copolymers are characterized by a mesogenic side group that has a chiral chain, and show a SmA and SmC* phase upon cooling from the isotropic liquid. In a magnetic field of 7T, the mesogen long axes are aligned by the magnetic field in the SmC* phase giving helical unwinding (i.e., a uSmC* phase). Deuterium T_{1Z} and T_{1Q} were measured in both mesophases to give $J_m(m\omega)$. To model these spectral densities, the overall motion of the copolymer was described by the anisotropic viscosity model, while the internal ring rotation was described by a small step diffusive process about the para axis. The activation energy for the internal ring rotation has a Gaussian distribution, indicating a degree of dynamic heterogeneity in this LC copolymer.

The anchoring conditions at the polymer-liquid crystal bounding interface are important in developing LC display devices. When the LC compound is confined either to porous inorganic materials (e.g., nucleopore membranes, porous glasses, or aerosils) or to polymer matrices (e.g., polymer-dispersed LC (PDLC), or polymer-stabilized LC), the geometry of the LC phase is strongly influenced by the shape and size of the cavity.[305] When a liquid crystal is confined in Anopore cavities, the spectrum consists of a doublet even above the clearing temperature. However, only a single line is observed in PDLC. This is owing to the distribution of surface directors in the cavity being isotropic and translational diffusion of molecules 'blurs' the splitting. The line width is larger than that found in the bulk isotropic phase. If the motional narrowing is incomplete, the residual static quadrupole interaction of deuterons in the surface layer would cause the line broadening to be inhomogeneous. On the other hand, if the broadening is dynamic in nature (i.e., homogeneous) due to slow time modulation of the quadrupolar interaction,

the line width is related to the spin–spin relaxation rate. Vilfan and co-workers have tackled this problem by carrying out deuteron T_1 and T_2 measurements.[306,307] These measurements can provide information on the effect of spatial constraints on the molecular mobility, and surface induced order. The spin–spin relaxation rate of the confined LC was found to be larger than that for the bulk by at least a factor of 2. It was assumed that the slow dynamical process is translational diffusion of molecules among surface sites with different local director orientations. This relaxation mechanism has been termed as 'reorientation mediated by translational displacement' (RMTD).[306,308] The director-field configuration within the cavity is closely related to the order parameter of the confined LC phase. Recently, ^{13}C NMR spectroscopy has been used to probe the orientational ordering of a confined LC in a homopolyacrylate matrix.[309] This study has also been extended to LC droplets confined in cross-linked polymer networks in order to examine different anchoring conditions at the polymer–LC interface.[310] The reorientational dynamics and orientational ordering in LC droplets were found to strongly depend on the alignment (homeotropic versus planar alignment) inside the LC droplets, which could be varied by using acrylate polymers with appropriate side chains. Higher order parameters were found for samples with LC droplets exhibiting planar anchoring. It is noted that relaxation mechanisms similar to those seen in confined thermotropic LC appear in lyotropic LC with a spatially modulated structure, albeit in somewhat modified form. Some recent works include the ripple phase[311] and lipid vesicles.[312,313]

8. STUDIES OF LYOTROPICS

Lyotropic surfactant liquid crystals have been reviewed by Tiddy and co-workers.[314] Another recent review focuses on NMR determination of translational diffusion of water and lipids in macroscopically aligned lyotropic LC.[315] In the past, NMR methods have successfully been employed to study phase equilibria and structures (e.g., hexagonal, lamellar, cubic phase) of lyotropics. Furthermore, orientation of various component molecules and their dynamics can be easily obtained. A brief survey of recent works is given in the next section. The methodology of using aqueous lyotropic LC (e.g., bicelle, phage) to weakly orient proteins for their structural information has aroused much interest, and the drive to higher magnetic field (>900 MHz) to gain better sensitivity is continuing. The reason why biomolecules must only be aligned weakly is because in most cases, increasing the molecular alignment produces greater number of coupled spins, thereby sharply degrading the resolution, sensitivity, and simplicity of the spectrum. The beauty of bicelles is that biomolecules are oriented in it so slightly that the spin system remains weakly coupled. Bicelles are aggregates of lipid molecules in aqueous solutions

(e.g., water). For certain mixtures of lipids, the bilayers form disc-like aggregates which move around freely in the aqueous solution. Because of their anisotropic magnetic susceptibility ($\Delta\chi$), the bicelles can be oriented spontaneously in a strong magnetic field. These serve to weakly order the dissolved biomolecules. The largest dipolar couplings act only as weak perturbations on the J couplings, and the huge number of remaining dipolar couplings produces only a slight line broadening. Biomolecular applications of lyotropics will also be discussed.

8.1. Lyotropic mesophases

Furó and co-workers have recently studied the counterion (Cl^- or Br^-) diffusion on oppositely charged micellar solutions of hexadecyltrimethylammonium chloride/water ($C_{16}TACl/D_2O$)[316] and ($C_{16}TABr/D_2O$)[317] by means of field-dependent T_1 and T_2 measurements of quadrupolar nuclei ^{35}Cl and ^{81}Br (both $I = 3/2$). In general, $I = 3/2$ nuclei show multiexponential T_1 and T_2.[318] However, the relaxation decays of ^{35}Cl and ^{81}Br in these micellar solutions were found to be effectively exponential. These studies reported that the counterion surface diffusion coefficient is about 10^{-9} m^2/s and the counterion diffuses faster than the surfactant molecule such that these two entities do not associate closely on a time scale greater than ca. 100 ps. Two distinct biaxial nematic phases have recently been identified in the $C_{14}TABr/n$-decanol/H_2O system using ^2H NMR spectroscopy and optical microscopy.[319] By increasing the decanol content, the phase sequence: hexagonal-N_C(calamitic nematic)-biaxial N_{BX}^+–biaxial N_{BX}^-–N_D(discotic nematic)–lamellar was found. Biaxial nematic phases N_{BX}^+ and N_{BX}^- are phases in which the largest component of the diamagnetic susceptibility is aligned parallel and perpendicular to the magnetic field, respectively. Based on the quadrupolar splittings, the $N_{BX}^+ - N_{BX}^-$ transition is first order, while the $N_C - N_{BX}^+$ and $N_{BX}^- - N_D$ transitions are second order. The cubic (I_1) phase of $C_{12}TACl/$water has been studied by ^2H NMR relaxation of the α-deuteriated surfactant.[320] The cubic phase is formed by arranging a number of aggregates on a cubic lattice in a certain way. The order of the surfactant is small (~ 0.06) due to both surface diffusions and aggregate rotations. The deuterium T_{1Z} dispersion curve (0.5–76.8 MHz) shows a three-step character, and can be explained by the Lorentzian three-step model.[321] Nitrogen (^{14}N) T_{1Z} and T_{1Q} measurements have also been carried out in the hexagonal phase of this lyotropic system (70 wt% $C_{12}TACl/D_2O$).[322] A Pake powder pattern was observed in the haxagonal phase, and the spectral densities $J_1(\omega, 90^\circ)$ and $J_2(2\omega, 90^\circ)$ were measured from the 90° edges. The relaxation data were interpreted using a simple model of 'classical' aggregate, in which fast local motions of the surfactant and its slow surface diffusions about the cylindrical aggregate axis were used.[323]

Lyotropic polymeric LC, formed by dissolving two aromatic polyamides in concentrated sulphuric acid, have been studied using variable-director ^{13}C NMR experiments.[324] The experimental line shapes at different angles w.r.t the external field were used to extract macromolecular order and dynamic in these ordered fluids. An interesting application of lyotropic LC is for the chiral discrimination of R- and S-enantiomers, and has recently been demonstrated by Courtieu and co-workers.[325] The idea was to include a chiral compound 1-deutero-1-phenylethanol in a chiral cage (e.g., β-cyclodextrin) which was dissolved and oriented by the nematic mean field in a cromolyn–water system. Proton-decoupled ^{2}H NMR spectrum clearly showed the quadrupolar splittings of the R- and S-enantiomers. The technique is applicable to water-soluble solutes.

NMR studies of phospholipids/water in the lamellar phase and gel phase can provide structure and dynamics of lipids and water at the lipid/water interface. Brown and co-workers have carried out numerous relaxation studies of 1,2-dimyristoyl-sn-glycero-3-phosphocholine (DMPC) in the LC state using ^{2}H and ^{13}C NMR spectroscopy.[135,154,326,327] ^{2}H and ^{14}N lineshape and relaxation analyses have recently been reported for the liquid crystalline L_α, the intermediate ripple $P_{\beta'}$ and the gel $L_{\beta'}$ phases of dipalmitoylphosphatidylcholine (DPPC)/water system[328]. The work aims at using ^{2}H NMR powder lineshapes and relaxation times T_1 and T_2 of water at different water contents and temperatures to address the observed narrow line in the $P_{\beta'}$ phase. The lateral diffusion along the curved interface is apparently insufficient to give the extremely narrow, almost isotropic, water line in the ripple phase. While the quadrupolar splitting of D_2O in the $L_{\beta'}$ phase decreases with increasing temperature, it increases with increasing temperature in the L_α phase. The behaviour in the L_α phase is explained by the fact that (a) the total order parameter of bound or interfacial water is negative,[329] and (b) the hydration of the choline groups contributes to a positive order parameter, while the water located deeper in the membrane contributes a negative order parameter. At higher temperatures, the sites deeper in the interface become accessible to water to a larger extent, and the quadrupolar splitting increases. By extrapolating the quadrupolar splitting of water to the $P_{\beta'}$ phase, plus the additional average due to lateral diffusions along the rippled surface, the narrow isotropic-like line appears to be reasonably understood. By combining ^{2}H NMR order parameter ($S_{CD}^{(i)}$) measurements with relaxation ($R_{1Z}^{(i)}$) studies of deuteriated saturated lipids (e.g., DMPC-d_{54}, DPPC-d_{62}) in the L_α phase, a comprehensive picture of the lipid bilayer organization was recently obtained.[327] Indeed, the viscoelastic properties of membrane lipids in the MHz region are modulated by the lipid acyl chain length (bilayer thickness), the interfacial area per molecule (polar head group), and the inclusion of non-ionic detergent (e.g., octaethyleneglycol-mon-n-dodecyl ether, $C_{12}E_8$) and/or cholesterol. It was shown that NMR relaxation of fluid bilayers (L_α phase) is governed by a broad distribution of thermal membrane fluctuations.

These fluctuations arise from tethering of the lipids at the aqueous interface via their polar head groups. The relatively slow motions consist of DF (2D and/or 3D) on a length scale of about the bilayer thickness or less, together with effective rotations of the flexible lipid molecules.[295] Brown and co-workers stated that the R_{1Z} is sensitive to the small-amplitude, collective DF modes in the L_α phase, since the local segmental motions of the lipids are too fast ($\tau_c \sim 10^{-11}$ s), thus affecting the spectral densities only at high frequencies. The visoelastic behaviour of lipid membranes in terms of the lipid composition can be inferred from the slopes of linear plots of $R_{1Z}^{(i)}$ versus $|S_{CD}^{(i)}|^2$ (see Fig. 20). A softer bilayer has a larger slope in such a plot. Based on

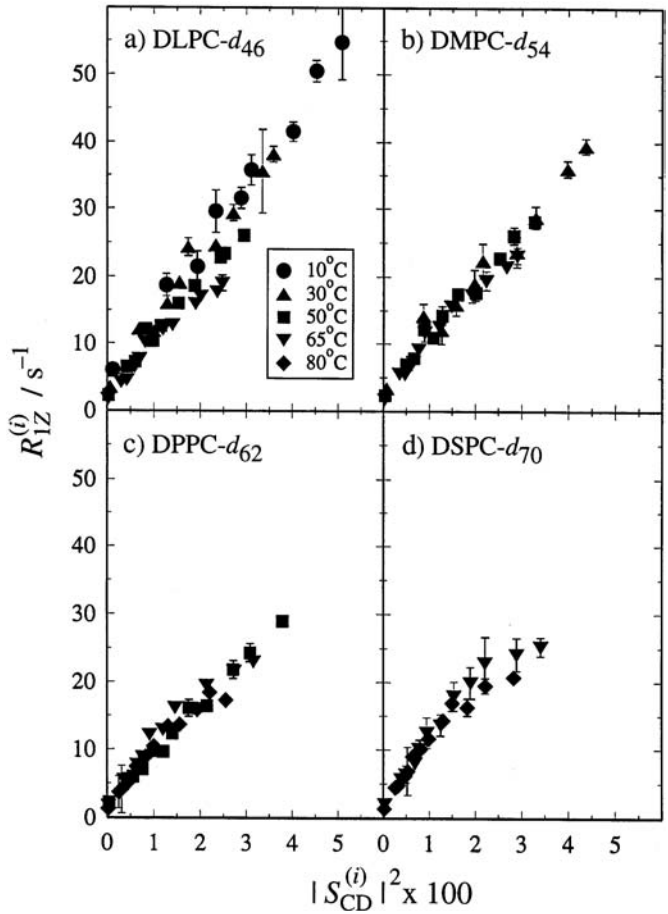

Fig. 20. Square-law functional dependence of spin–lattice relaxation rates $R_{1Z}^{(i)}$ on segmental order parameters $|S_{CD}^{(i)}|$, for a homologous series of disaturated phosphatidylcholines in the L_α state at a particular temperature. (a) DLPC-d_{46}, (b) DMPC-d_{54}, (c) DPPC-d_{62}, and (d) DSPC-d_{70}. (Reproduced by permission of Elsevier Science.)

the NMR relaxation analyses and the bilayer bending rigidity κ of the DMPC bilayer as a reference, the κ values for the other members of the homologous series of phosphocholines were estimated and compared favourably to other biophysical studies, which involved macroscopic deformations of thin membrane lipid films.

MAS has been applied to a highly viscous cubic phase of a lyotropic LC formed by 1-monooleolyl-rac-glycerol and water in order to obtain liquid-like ^{1}H and ^{13}C spectra.[330] Deuterium, sodium, and fluorine NMR spectroscopy have been applied to study the phase behaviour of several dilute lamellar systems formed by low concentrations of an *n*-hexadecylpyridinium salt, a sodium salt (e.g., NaBr, NaCl, or sodium trifluoroacetate), 1-hexanol, and D_2O.[331] The ^{2}H, ^{19}F, and ^{23}Na splittings were used to monitor the phase equilibria. The last two studies are motivated by the search of new lyotropic LC for the alignment of biomolecules.

8.2. NMR of larger solutes

Biological molecules such as lipids, proteins, nuclei acids, and carbohydrates are found to exist in various LC phases under certain conditions. Their LC structures are believed to play a crucial role in their biological functions and self assembly processes. Structure determination of biomolecules[15,332–336] in partially oriented media such as bicelles,[337] phages,[338,339] the tobacco mosaic virus[339] or dilute (swollen) lamellar phase,[340,341] has become very popular in recent years, and is made possible by measuring residual dipolar couplings (RDC) and/or anisotropic chemical shifts.[342] For certain mixtures of lipids, the bilayers formed by disc-shaped aggregates called bicelles (bilayered micelles) can swim around freely in the aqueous solution (e.g., water). The bicelles can orient spontaneously in a strong magnetic field due to their non-zero $\Delta\chi$ and become an oriented liquid. The spacing between individual bicelles in such a dilute LC phase is far greater than the size of the biomolecule typically studied by NMR. As molecules are ordered weakly and can diffuse freely in the aqueous solvent, the largest dipolar couplings act as weak perturbations on the *J* couplings (see below). Isotopically labelled molecules containing ^{13}C–^{1}H or ^{15}N–^{1}H pairs are usually used for better sensitivity. The spin Hamiltonian for a ^{13}C–^{1}H pair is given by

$$H = -B_0\left[\gamma_I\left(1+\overline{\delta^I_{zz}(\Theta)}\right)+\gamma_S\left(1+\overline{\delta^S_{zz}(\Theta)}\right)\right]+(2D^{\text{aniso}}_{IS}+J^{\text{iso}}_{IS})I_zS_z \qquad (94)$$

where J^{aniso}_{JS} is taken to be negligible,

$$\overline{\delta^j_{zz}(\Theta)} = \int \delta^j_{zz}(\Theta)P(\Theta)\,d\Theta \qquad (95)$$

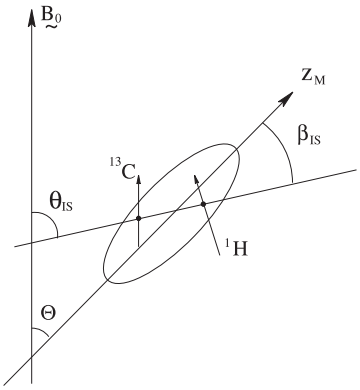

Fig. 21. Schematic diagram of a two-spin pair I–S in a molecule having a long molecular z_m axis making an angle Θ with the external magnetic field $\underset{\sim}{B_o}$. The internuclear vector makes an angle β_{IS} with respect to the z_m axis, and θ_{IS} w.r.t. the $\underset{\sim}{B_o}$.

with $P(\Theta)\,d\Theta$ being the probability of the molecule having an orientation between Θ and $\Theta + d\Theta$, $\delta^j_{zz}(\Theta)$ is the secular part of the chemical shift tensor of the jth nucleus, and D^{aniso}_{IS}, given in Eq. (8), now contains the Legendre $\overline{P_2(\cos\theta_{IS})}$. The angle Θ is between the long molecular (z_m) axis and the magnetic field, while θ_{IS} is between the magnetic field and the heteronuclear axis (see Fig. 21). The average $\delta^j_{zz}(\Theta)$ in the mesophase is not equal to the δ^{iso} of the jth nucleus. The β_{IS} angle describes the heteronuclear vector w.r.t. the z_m axis, and can be found from the residual dipolar interaction D^{aniso}_{IS}. The ^{13}C NMR spectrum for a ^{13}C–^{1}H pair consists of a doublet with a splitting $(2D^{\text{aniso}}_{IS} + J^{\text{iso}}_{IS})$. Note that D_{IS} is negative and the doublet splitting can either be larger or less than the J coupling observed in the isotropic phase depending on the orientation (β_{IS}) of the ^{13}C–^{1}H vector in the molecule. As biomolecules are aligned by the bicelle plane, θ_{IS} can sample with equal probability between 0 and 2π. For the ^{13}C–^{1}H vector parallel to z_m axis ($\beta_{IS} = 0$), $\overline{P_2(\cos\theta_{IS})} = 1/4$ and the splitting is given by $J^{\text{iso}}_{IS} + a/4$ where $a = -\mu_0\gamma_I\gamma_S h/4\pi^2 r^2_{IS}$. If the ^{13}C–^{1}H vector is perpendicular to the z_m axis, it has two degrees of freedom, one due to the molecule rotating around its long z_m axis and the other due to the z_m axis sampling between 0 and 2π. The $\overline{P_2(\cos\theta_{IS})}$ is now given by $-1/8$, and the splitting is $J^{\text{iso}}_{IS} - a/8$. For directly bonded ^{15}N–^{1}H pairs, the a value is positive and J^{iso}_{IS} is negative. A few years ago, Bax *et al.*[16,343] found that the dilute bicelle solutions can be tuned to yield favourable RDC through adjusting the concentration of the bicelles (as low as 3% w/v) in aqueous solutions. For example, one-bond ^{15}N–^{1}H, ^{13}C–^{1}H, ^{13}C–^{13}C, ^{13}C–^{15}N, and two bond ^{13}C–^{1}H dipolar couplings have been accurately measured in ^{13}C/^{15}N enriched ubiquitin dissolved in a bicelle solution.[344] Indirect ^{1}H detection, such as HSQC or HMQC, has been used to measure ^{13}C–^{1}H (or ^{15}N–^{1}H) dipolar couplings. Distance restraints from nuclear Overhauser effect (NOE)

spectroscopy have long been used for the structure determination of biomolecules. It has recently been demonstrated that the combination of NOE and RDC data provides the best structural parameters.[345]

Phospholipid bicelles can be aligned with their normal (the nematic director) either perpendicular ($\Delta\chi < 0$)[337,346] or parallel ($\Delta\chi > 0$)[347,348] to the magnetic field. It is noted that for bicelles with $\Delta\chi < 0$, membrane-bound proteins which do not have axial symmetry would not have a unique alignment w.r.t. the magnetic field. As a consequence, the NMR peaks show cylindrically symmetric powder patterns rather than sharp peaks unless the molecule undergoes fast axial motion. These tend to make the spectral analysis more difficult. To alleviate this, sample spinning[349,350] can be used. In any case, study of membrane-bound and membrane-soluble species in phospholipid bicelles with $\Delta\chi > 0$ can be advantageous. Now the interpretation of RDC in terms of molecular properties is complicated[351] by the fact that it is difficult to separate the structural and dynamic effects as well as to determine the alignment tensor parameters. Recent works have indicated that multiple alignment media can be used to determine precise 3D structures of proteins (e.g., Ubiquitin).[336,352,353] The limiting assumptions are: (i) internal motions are uncorrelated with the overall alignment and (ii) the structure and dynamics of the macromolecule is the same in different alignment media. It is noted that the alignment mechanism of proteins depend on the chosen ordering medium. Both the solute's shape and electrostatic interaction can play a role. A simple steric model has recently been proposed to quantitatively describe the relation between the solute's shape and its alignment in lyotropic LC (e.g., bicelles).[354,355] When comparing the predicted (using an alignment tensor given by the simple steric model) and observed ^{15}N–^{1}H dipolar couplings measured for the IgG-binding domain of Streptoccal protein G, the agreement is only good for the bicelle medium but not for the phage medium.[354] This demonstrates the important role of electrostatic terms in obtaining the alignment tensor in the phage medium. The fear that LC can skew the average distribution is unwarranted as demonstrated in a recent study of T4 lysozyme in solution using either bicelle or phage medium.[356] Now LC NMR can provide relative domian orientations of flexibly connected multidomain proteins. The use of different alignment media can provide not only the structural parameters, but also allow the extraction of dynamic information. A large set of protein backbone one-bond (heteronuclear) dipolar couplings has been obtained to refine the structure of the 56-residual third IgG-binding domain of Protein G (GB3).[336] The alignment media include bicelle, PEG (poly(ethylene) glycol), phage, and charged (positive or negative) stretched acryamide gels. The inclusion of experimental dipolar couplings for C^{α}–C' and N–C' increases the agreement between observed N–H or C^{α}–H^{α} dipolar couplings and values predicted from X-ray crystal structure of GB3. The study also indicates the amplitude of internal dynamics along GB3's backbone is far more homogeneous than previously seen in other proteins. However, a

small subset of GB3 residues seems to have internal dynamics. It is noted that protein backbone fluctuations of a moderate amplitude are not easily detected by dipolar couplings. Hence when small inconsistencies between different types of backbone dipolar coupling measurements being ascribed to dynamics, the estimated amplitudes of motion are far larger than expected.[357,358]

Vold and co-workers have employed solid state deuterium NMR spectroscopy to study properties of phospholipid bicelle systems[359,360] and a deuterated transmembrane peptide (P/6) in a bicelle solution formed by dilauryl phosphatidylcholine (DLPC) and dipalmitoyl phosphatidylcholine (DPPC).[361] In the latter work, structural orientations of transmembrane domains have been obtained and interactions between the membrane and transmembrane domain were studied. Residual ^{2}H quadrupolar couplings have been determined by a 2D NMR experiment using ^{1}H-detected ^{2}H in isotopically ^{13}C, ^{2}H-enriched carbohydrates in a LC medium comprised of 20% (w/v) DHPC : DMPC (1:3) in D_2O.[362] The effect of ceramide (Cer) N-palmitoyl-sphingosine in aqueous dispersions of 1-palmitoyl-2-oleoyl-sn-glycero-3-phosphocholine (POPC) has recently been studied by ^{2}H NMR.[363] In the study, the palmitoyl chain of each lipid was deuterated and the analysis of deuterium spectra as functions of temperature and composition (to a maximum concentration of 25% Cer) allowed the determination of a partial phase diagram of POPC/Cer. In the LC phase, it was found that both lipids POPC and Cer mix well, and the Cer chains are more ordered than POPC chains. The proton–proton 2D COSY experiment has been used to study an oligosaccharide dissolved in a bicelle solution[364] and an adenosine in 7.5% (w/v) DMPC/DHPC bicelles.[365] In the latter study, 2D SERF sequence[366] has been employed to selectively give absolute values of the spin–spin interactions. High-resolution ^{1}H MAS experiment has been carried out using CP in a ^{15}N-labelled polypetide Gramicidin A dispersed in DMPC/phosphate buffer.[367,104] Because of the strong ^{15}N–^{1}H dipolar coupling and the large range in ^{15}N chemical shifts, 2D PISEMA experiment[100] has also been applied to study polypetides (e.g., transmembrane domain) in oriented membrane systems.[104] By means of solid state NMR, one can measure orientational restraints and distance restraints. As average or residual second rank tensor couplings are being measured, the raw NMR data must contain the effect of motions. Simulations of NMR data must, therefore, take into account structural variability and dynamic effects in order to achieve a high resolution protein structure. Finally, a low-spin Fe(III) protein (cytochrome *c*) has been dissolved in a solution with synthetic surfactant lyotropic aggregates for partial alignment. This paramagnetic protein was chosen to obtain hyperfine-shifted proton signals in the lyotropic nematic phase, whose splittings in multiplets and variations in the peak position could be measured accurately and unambiguously.[368] These splittings are due to residual dipolar coupling of neighbouring geminal protons and are interpreted in terms of an orientational order tensor.

9. OTHER NMR STUDIES

Two recent NMR studies, both use a noble gas ^{129}Xe as a solute to probe phase transitions and dynamics of LC, are mentioned.[369,370] In the study of nematic reentrance in LC, ^{129}Xe chemical shifts, spin–spin (T_2) and spin–lattice (T_1) relaxation times were measured across the N-SmA and SmA-RN (reentrant nematic) phase transitions. The spin relaxation times are found to be much more sensitive to these phase transitions than the chemical shifts. As an example, Fig. 22 reproduces plots of T_1 and T_2 versus the reciprocal temperature for ^{129}Xe dissolved in a 27.16 wt% 6OCB/8OCB binary mixture.[369] This particular mixture had been previously studied by ^{1}H, ^{2}H, and ^{13}C NMR relaxation. It is clear from the graph that both T_1 and T_2 show a distinct change in the slope across a phase transition. The difference in the T_1 and T_2 values is interpreted as an indication of the presence of slow motional modes. The activation energies (measured from the slopes in Fig. 22) are higher in N and RN phases, and smaller in the isotropic and SmA phase. The higher activation energy in the RN phase than in the N phase of the 6OCB/8OCB system is not observed in another liquid crystal studied by these

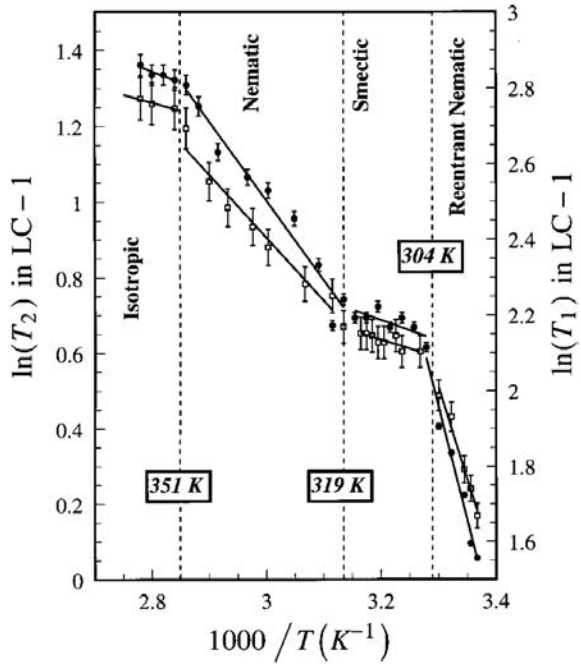

Fig. 22. Plots of T_1 and T_2 versus the reciprocal temperature for ^{129}Xe dissolved in 6OCB/8OCB at 11.7 T. (Reproduced by permission of American Chemical Society.)

authors,[369] and is accounted for by the presence of microcrystallites in this particular RN phase. The ^{129}Xe relaxation in LC is thought to be dominated by heteronuclear dipolar coupling between the dissolved ^{129}Xe and ^{1}H nuclei residing on the mesogenic molecules. This was checked by measuring T_1 at a different Larmor frequency. However, the details of xenon relaxation in LC remain to be further studied. The other study involves dissolving ^{129}Xe gas in a commercial ferroelectric LC, FELIX-R&D, which is composed of mostly phenylpyrimidine derivatives, and measuring ^{129}Xe translational diffusion constants parallel ($D^t_{||}$) and perpendicular ($D^t_{\perp}$) to the external magnetic field using the PGSE method.[370] The experiments reveal all the phase transitions (I-N-SmA-SmC*) in this FLC, and a continuous decrease in $D^t_{||}$ from the isotropic to the SmC* phase. The detection of phase transitions in this work is similar to what is seen for the ^{129}Xe T_1 and T_2 in Fig. 22. A redistribution of xenon atoms towards the interlayer spacing of smectic phases has also been inferred in this study.

10. SUMMARY AND OUTLOOK

It is clear that modern NMR spectroscopy has been successfully applied to provide valuable information in many and diverse partially ordered mesomorphic phases of LC. New and important pulse techniques are being developed to aid the spectral discrimination and/or structural determination of large and small molecules. With the latest development of high magnetic field and spectrometer hardware, multi-dimensional NMR and samples with low concentrations (and in natural abundance) of active NMR nuclei can be used for various LC investigations, ranging from the structural elucidation of large biomolecules in bicelles to new materials showing switchable B phases. One of the driving forces in LC research is their applications in LC displays, memory and detection devices. Another driving force is the recent interests in using weakly ordered lyotropic materials for the alignment of proteins, lipids, etc., to do high resolution NMR analyses. New and fundamental physical phenomena are being uncovered by studying new and unusual LC materials.

The review aims to highlight some recent studies that involve liquid crystals and show the utility of newer pulse NMR techniques in LC. They may involve solutes dissolved in ordered phases and their applications, or may involve the molecular ordering, rotational and/or translational diffusion of solvent molecules. Deuterium NMR spectroscopy has demonstrated many advantages over other nuclei like ^{1}H and ^{13}C, but the need to specifically deuteriate mesogens is sometimes a major drawback. ^{13}C NMR spectroscopy seems to be useful since non-enriched samples can often be used. However, the use of ^{13}C NMR in semi-solids like LC often requires more sophisticated NMR techniques and instrumentation. There are indeed many uncharted

territories in NMR of LC, both from a theoretical viewpoint and in experimentations. It is a unrealistic task for the present author to predict all those remaining challenges in this field. Nuclear spin relaxation is certainly not yet understood in biaxial smectic phases (in particular those involving chiral and non-chiral molecules), both experimentally and theoretically. The extraction of molecular dynamics (internal and overall rotations) in LC using ^{13}C spin auto-relaxation, cross-relaxation, and cross-correlation is still just beginning. In principle, the ^{13}C probe can be as good as deuterium to provide dynamical information once the methodology and theory are more developed. Chiral recognition in ordered systems may have a far reaching effect even outside the domain of LC community. Finally, quantum computing using NMR of LC may not seem to lead to any practical application soon. Such 'exotic' excursion may not only give fundamental understanding of spin dynamics, but may also provide unforseen discoveries.

ACKNOWLEDGEMENTS

The financial supports of the Natural Sciences and Engineering Council of Canada and Canada Foundation for Innovation are gratefully acknowledged.

REFERENCES

1. P. G. de Gennes and J. Prost, *Physics of Liquid Crystals*, Clarendon Press, Oxford, 1993.
2. P. J. Collings and M. Hird, *Introduction to Liquid Crystals*, Taylor & Francis, London, 1997.
3. S. Chandrasekhar, *Liquid Crystals*, Cambridge University Press, Cambridge, 1992.
4. G. Vertogen and W. H. de Jeu, *Thermotropic Liquid Crystals, Fundamentals*, Springer-Verlag, Berlin, Heidelberg, 1988.
5. C. B. McArdle, *Side Chain Liquid Crystal Polymers*, Blackie and Son, Glasgow, 1989.
6. R. A. Weiss and C. K. Ober, *Liquid-Crystalline Polymers*, Amer. Chem. Soc., Washington, 1990.
7. F. Reinitzer, *Monatsh Chem*., 1988, **9**, 421.
8. L. Onsager, *Ann. NY Acad. Sci*., 1949, **51**, 627.
9. W. Maier and A. Saupe, *Z. Naturforsch*., 1958, **13a**, 564.
10. M. A. Cotter, *J. Chem. Phys*., 1977, **66**, 1098; W. M. Gelbart and A. Gelbart, *Mol. Phys*., 1977, **23**, 1387.
11. G. H. Heilmeier and W. Helfrich, *Appl. Phys. Lett*., 1968, **13**, 91.
12. W. L. McMillan, *Phys. Rev. A*, 1971, **4**, 1238; 1972, **6**, 936.
13. T. Niori, F. Sekine, J. Watanabe, T. Furukawa and H. Takezoe, *J. Mater. Chem*., 1996, **6**, 1231.
14. G. Cipparrone, C. Verace, D. Duca, D. Pucci, M. Ghedini and C. Umeton, *Mol. Cryst. Liq. Cryst*., 1992, **212**, 217.
15. E. Alba and N. Tjandra, *Prog. Nucl. Magn. Reson. Spectrosc*., 2002, **40**, 175.
16. N. Tjandra and A. Bax, *Science*, 1997, **278**, 1111.
17. R. Y. Dong, *Nuclear Magnetic Resonance of Liquid Crystals*, 2nd edn., Springer-Verlag, New York, 1997.

18. R. Y. Dong, *Prog. Nucl. Magn. Reson. Spectrosc.*, 2002, **41**, 115.
19. R. Y. Dong, *Encyclopedia Spectroscopy and Spectrometry*, J. C. Lindon, ed., Academic Press, London, 1999, 1568.
20. J. W. Doane and J. J. Visintainer, *Phys. Rev. Lett.*, 1969, **23**, 1421; M. Weger and B. Cabane, *J. Phys. Colloq.*, 1969, **30**, C4–72.
21. R. Blinc, D. L. Hogenbloom, D. E. O'Reilly and E. M. Peterson, *Phys. Rev. Lett.*, 1969, **23**, 969.
22. C. E. Tarr, M. A. Nickerson and C. W. Smith, *Appl. Phys. Lett.*, 1970, **17**, 318.
23. R. Y. Dong and C. F. Schwerdtfeger, *Solid State Commun.*, 1970, **9**, 707.
24. P. Pincus, *Solid State Commun.*, 1969, **7**, 415.
25. M. F. Brown, *J. Chem. Phys.*, 1982, **77**, 1576.
26. J. A. Marqusee, M. Warner and K. A. Dill, *J. Chem. Phys.*, 1984, **81**, 6404.
27. B. Halle, *Phys. Rev. E*, 1994, **50**, 2415.
28. R. Blinc, M. Vilfan and V. Rutar, *Solid State Commun.*, 1975, **17**, 171.
29. A. Abragam, *The Principles of Nuclear Magnetism*, Clarendon Press, Oxford, 1961.
30. C. G. Wade, *Ann. Rev. Phys. Chem.*, 1977, **28**, 47.
31. J. W. Emsley, ed., *Nuclear Magnetic Resonance of Liquid Crystals*, D. Reidel, Dordrecht, Holland, 1985.
32. G. R. Luckhurst and C. A. Veracini, eds., *The Molecular Dynamics of Liquid Crystals*, Kluwer Academic, Dordrecht, 1994.
33. E. E. Burnell and C. de Lange, eds., *NMR of Orientationally Ordered Liquids*, Kluwer Academic, Dordrecht, 2003.
34. H. W. Spiess, P. Diehl, E. Fluck and R. Kosfeld, eds., *NMR Basic Principles and Progress*, Vol. 15, Springer-Verlag, Heidelberg, 1978, 55.
35. J. W. Emsley and J. C. Lindon, *NMR Spectroscopy using Liquid Crystal Solvents*, Pergamon Press, Oxford, 1975.
36. A. G. Redfield, *Adv. Magn. Reson.*, 1965, **1**, 1.
37. M. Goldman, *J. Magn. Reson.*, 2001, **149**, 160.
38. R. R. Ernst, G. Bodenhausen and A. Wokaun, *Principles of Nuclear Magnetic Resonance in One and Two Dimensions*, Clarendon Press, Oxford, 1987.
39. D. Frueh, *Prog. Nucl. Magn. Reson. Spectrosc.*, 2002, **41**, 305.
40. M. W. F. Fischer, A. Majumdar and E. R. P. Zuiderweg, *Prog. Nucl. Magn. Reson. Spectrosc.*, 1998, **33**, 207.
41. R. Bhattacharyya and A. Kumar, *Chem. Phys. Lett.*, 2003, **372**, 35.
42. J. Jeener and P. Broekaert, *Phys. Rev.*, 1967, **157**, 232.
43. R. C. Zamar, D. J. Pusiol and F. Noack, *J. Chem. Phys.*, 1998, **109**, 1128.
44. O. Mensio, R. C. Zamar, D. J. Pusiol and S. Becker, *J. Chem. Phys.*, 1999, **110**, 8155.
45. O. Mensio, C. E. González and R. C. Zamar, *J. Chem. Phys.*, 2002, **116**, 1530.
46. J. Jeener, A. Vlassenbroek and P. Broekaert, *J. Chem. Phys.*, 1995, **103**, 1309.
47. R. R. Vold, *Nuclear Magnetic Resonance of Liquid Crystals*, J. W. Emsley, ed., D. Reidel, Dordrecht, Holland, 1985, 253.
48. S. Wimperis and G. Bodenhausen, *Chem. Phys. Lett.*, 1986, **132**, 194; S. Wimperis, *J. Magn. Reson.*, 1989, **83**, 509.
49. H. Bildsøe, J. P. Jacobsen and K. Schaumberg, *J. Magn. Reson.*, 1976, **23**, 137; J. P. Jacobsen, H. Bildsøe and K. Schaumberg, *J. Magn. Reson.*, 1976, **23**, 153.
50. S. B. Ahmad, K. J. Packer and J. M. Ramsden, *Mol. Phys.*, 1977, **33**, 857.
51. K. J. Jeffrey, *Bull. Magn, Reson.*, 1981, **3**, 69.
52. A. Saupe, *Z. Naturforsch.*, 1964, **19a**, 161.
53. J. Courtieu, J. P. Bayle and B. M. Fung, *Prog. Nucl. Magn. Reson. Spectrosc.*, 1994, **26**, 141.
54. B. M. Fung, *Encyclopedia of Nuclear Magentic Resonance*, D. M. Grant and R. K. Harris, eds., Wiley, Chichester, 1996.
55. K. Schmidt-Rohr, D. Nanz, L. Emsley and A. Pines, *J. Phys. Chem.*, 1994, **98**, 6668.

56. M. Hong, K. Schmidt-Rohr and A. Pines, *J. Am. Chem. Soc*., 1995, **117**, 3310.
57. M. Hong, A. Pines and S. Caldarelli, *J. Phys. Chem*., 1996, **100**, 14815.
58. S. Caldarelli, M. Hong, L. Emsley and A. Pines, *J. Phys. Chem*., 1996, **100**, 18696.
59. F. Noack, *Prog. Nucl. Magn. Reson. Spectrosc*., 1986, **18**, 171.
60. E. R. Andrew and R. G. Eades, *Proc. R. Soc. London*, 1953, **A216**, 398.
61. I. Lowe, *Phys. Rev. Lett*., 1959, **2**, 285.
62. R. R. Hartmann and E. L. Hahn, *Phys. Rev*., 1962, **128**, 2042.
63. J. W. Emsley, J. C. Lindon, G. R. Luckhurst and D. Shaw, *Chem. Phys. Lett*., 1973, **19**, 345.
64. J. Courtieu, D. W. Alderman, D. M. Grant and J. P. Bayle, *J. Chem. Phys*., 1982, **77**, 723.
65. B. S. A. Kumar, N. Suryaprakash, K. V. Ramanathan and C. L. Khetrapal, *Chem. Phys. Lett*., 1987, **136**, 227.
66. J. S. Waugh, *Proc. Natl. Acad. Sci. USA*, 1976, **73**, 1394.
67. R. K. Hester, J. L. Ackerman, B. L. Neff and J. S. Waugh, *Phys. Rev. Lett*., 1976, **36**, 1081.
68. S. J. Opella and J. S. Waugh, *J. Chem. Phys*., 1977, **66**, 4919.
69. A. Höhener, A. Muller and R. R. Ernst, *Mol. Phys*., 1979, **38**, 909.
70. B. S. A. Kumar, K. V. Ramanathan and C. L. Khetrapal, *Chem. Phys. Lett*., 1988, **149**, 306.
71. M. Zhou, V. Frydman and L. Frydman, *J. Am. Chem. Soc*., 1998, **120**, 2178.
72. D. McElheny, M. Zhou and L. Frydman, *J. Magn. Reson*., 2001, **148**, 436.
73. R. H. Havlin, G. H. J. Park and A. Pines, *J. Magn. Reson*., 2002, **157**, 103.
74. B. M. Fung, *J. Magn. Reson*., 1990, **86**, 1371.
75. A. J. Shaka, J. Keeler, T. Frenkiel and R. Freeman, *J. Magn. Reson*., 1983, **52**, 335.
76. A. E. Bennett, C. M. Rienstra, M. Anger, K. V. Lakshmi and R. G. Griffin, *J. Chem. Phys*., 1995, **103**, 6951.
77. B. M. Fung, D. S. Mui, I. R. Bonnel and E. L. Enwall, *J. Magn. Reson*., 1984, **58**, 254.
78. Y. Yu and B. M. Fung, *J. Magn. Reson*., 1998, **130**, 317.
79. B. M. Fung, A. K. Khitrin and K. Ermolaev, *J. Magn. Reson*., 2000, **142**, 97.
80. G. Antonioli, D. E. McMillan and P. Hodgkinson, *Chem. Phys. Lett*., 2001, **344**, 68.
81. G. De Paëpe, D. Sakellariou, P. Hodgkinson, S. Hediger and L. Emsley, *Chem. Phys Lett*., 2003, **368**, 511.
82. M. Lee and W. Goldburg, *Phys. Rev*., 1965, **140**, 1261.
83. J. S. Waugh, L. M. Huber and U. Haeberlen, *Phys. Rev. Lett*., 1968, **20**, 180.
84. U. Haeberlen and J. S. Waugh, *Phys. Rev*., 1968, **175**, 453.
85. W. K. Rhim, D. D. Elleman and R. W. Vaughan, *J. Chem. Phys*., 1973, **59**, 3740.
86. D. P. Rhim and W. K. Rhim, *J. Chem. Phys*., 1979, **71**, 944.
87. D. P. Burum, N. Linder and R. R. Ernst, *J. Magn. Reson*., 1981, **44**, 173.
88. K. Takegoshi and C. A. McDowell, *Chem. Phys. Lett*., 1985, **116**, 100.
89. M. Howhy, P. V. Bower, H. J. Jakobsen and N. C. Nielsen, *Chem. Phys. Lett*., 1997, **273**, 297.
90. M. Mehring and J. S. Waugh, *Phys. Rev. B*, 1972, **5**, 3459.
91. A. Bielecki, A. C. Kolbert and M. H. Levitt, *Chem. Phys. Lett*., 1989, **155**, 341.
92. A. Bielecki, A. C. Kolbert, H. J. M. deGroot, R. G. Griffin and M. H. Levitt, *Adv. Magn. Reson*., 1990, **14**, 111.
93. E. Vinogradov, P. K. Madhu and S. Vega, *Chem. Phys. Lett*., 1999, **314**, 443.
94. B. M. Fung, *J. Magn. Reson*., 1987, **72**, 353.
95. B. M. Fung, K. Ermolaev and Y. Yu, *J. Magn. Reson*., 1999, **138**, 28.
96. S. A. Caldarelli, A. Lesage and L. Emsley, *J. Am. Chem. Soc*., 1996, **118**, 1224.
97. N. Sinha, R. Bhattacharyya and K. V. Ramanathan, *ENC Conf*., 2003, PJ426.
98. R. Pratima and K. V. Ramanathan, *J. Magn. Reson. A*, 1996, **118**, 7.
99. C. S. Nagaraja and K. V. Ramanathan, *Liq. Cryst*., 1999, **26**, 17.
100. C. H. Wu, A. Ramamorthy and S. J. Opella, *J. Magn. Reson. A*, 1994, **109**, 270.
101. N. Sinha and K. V. Ramanathan, *Chem. Phys. Lett*., 2000, **332**, 125.
102. M. Marjanska, F. Castiglione, J. D. Walls and A. Pines, *J. Magn. Reson*., 2002, **158**, 52.
103. P. Palmas, P. Tekely and D. Canet, *J. Magn. Reson*., 1993, **A104**, 26.

104. C. Farès and J. Davis, *NMR of Orientationally Ordered Liquids*, E. E. Burnell and C. de Lange, eds., Chap. 9, Kluwer Academic, Dordrecht, 2003.
105. S. V. Dvinskikh, H. Zimmermann, A. Maliniak and D. Sandström, *J. Magn. Reson.*, 2003, **163**, 46.
106. S. V. Dvinskikh, H. Zimmermann, A. Maliniak and D. Sandström, *J. Magn. Reson.*, 2003, **164**, 165.
107. H. Zimmermann, V. Bader, R. Poupko, E. J. Wachtel and Z. Luz, *J. Am. Chem. Soc.*, 2002, **124**, 15286.
108. Z. Luz, *NMR of Orientationally Ordered Liquids*, Chap. 19, E. E. Burnell and C. de Lange, eds., Kluwer Academic, Dordrecht, 2003.
109. C. Auger, A. Lesage, S. Caldarelli, P. Hodgkinson and L. Emsley, *J. Am. Chem. Soc.*, 1997, **112**, 112000.
110. D. Sandström and H. Zimmermann, *J. Phys. Chem. B*, 2000, **104**, 1490.
111. S. V. Dvinskikh, D. Sandström, H. Zimmermann and A. Maliniak, *Chem. Phys. Lett.*, 2003, **382**, 410.
112. D. Merlet, B. Ancian, J. P. Courtieu and P. Lesot, *J. Am. Chem. Soc.*, 1999, **121**, 5249.
113. J. W. Emsley and D. L. Turner, *Chem. Phys. Lett.*, 1981, **82**, 447.
114. P. Lesot, M. Sarfati, D. Merlot, B. Ancian, J. W. Emsley and B. A. Timimi, *J. Am. Chem. Soc.*, 2003, **125**, 7689.
115. R. Blinc, M. Luzar, M. Vilfan and M. Burgar, *J. Chem. Phys.*, 1975, **63**, 3445.
116. R. L. Vold, R. R. Vold and M. Warner, *J. Chem. Soc. Faraday Trans. II*, 1988, **84**, 997.
117. W. Wölfel, F. Noack and M. Stohrer, *Z. Naturforsch.*, 1975, **30a**, 437.
118. E. Berggren, R. Tarroni and C. Zannoni, *J. Chem. Phys.*, 1993, **99**, 6180; E. Berggren and C. Zannoni, *Mol. Phys.*, 1995, **85**, 299.
119. P. L. Nordio and P. Busolin, *J. Chem. Phys.*, 1971, **55**, 5485.
120. P. L. Nordio and U. Segre, *The Molecular Physics of Liquid Crystals*, G. R. Luckhurst and G. W. Gray, eds., Academic Press, New York, 1979, 411.
121. J. M. Bernassau, E. P. Black and D. M. Grant, *J. Chem. Phys.*, 1982, **79**, 253.
122. R. R. Vold and R. L. Vold, *J. Chem. Phys.*, 1988, **88**, 1443.
123. R. Tarroni and C. Zannoni, *J. Chem. Phys.*, 1991, **95**, 4550.
124. T. P. Trouard, T. M. Alam and M. F. Brown, *J. Chem. Phys.*, 1994, **101**, 5229.
125. G. J. Moro and P. L. Nordio, *J. Chem. Phys.*, 1985, **89**, 997.
126. A. Brognara, P. Pasini and C. Zannoni, *J. Chem. Phys.*, 2000, **112**, 4836.
127. M. Ishiwata and T. Ono, *J. Phys. Soc. Japan*, 1995, **64**, 3993.
128. H. C. Torrey, *Phys. Rev.*, 1953, **92**, 962, 1954, **96**, 690.
129. H. A. Resing and H. C. Torrey, *Phys. Rev.*, 1963, **131**, 1102.
130. G. J. Krüger, *Z. Naturforsch., Teil A*, 1969, **24**, 560.
131. S. Žumer and M. Vilfan, *Phys. Rev. A*, 1978, **17**, 424.
132. M. Vilfan and S. Žumer, *Phys. Rev. A*, 1980, **21**, 672.
133. S. Žumer and M. Vilfan, *Phys. Rev. A*, 1983, **28**, 3070.
134. T. P. Trouard, T. M. Alam, J. Zajicek and M. F. Brown, *Chem. Phys. Lett.*, 1992, **189**, 67.
135. T. P. Trouard, A. A. Nevzorov, T. M. Alam, C. Job, J. Zajicek and M. F. Brown, *J. Chem. Phys.*, 1999, **110**, 8802.
136. P. A. Beckmann, J. W. Emsley, G. R. Luckhurst and D. L. Turner, *Mol. Phys.*, 1986, **54**, 97.
137. R. Y. Dong and G. M. Richards, *Chem. Phys. Lett.*, 1990, **171**, 389; R. Y. Dong, *Phys. Rev. A*, 1991, **43**, 4310.
138. A. Ferrarini, G. J. Moro and P. L. Nordio, *Liq. Cryst.*, 1990, **8**, 593.
139. R. Y. Dong, J. Lewis, E. Tomchuk and E. Bock, *J. Chem. Phys.*, 1978, **69**, 5314.
140. T. M. Barbara, R. R. Vold and R. L. Vold, *J. Chem. Phys.*, 1983, **79**, 6338; T. M. Barbara, R. R. Vold, R. L. Vold and M. E. Neubert, *J. Chem. Phys.*, 1985, **82**, 1612.
141. D. Goldfarb, R. Y. Dong, Z. Luz and H. Zimmermann, *Mol. Phys.*, 1985, **54**, 1185.

142. J. S. Lewis, E. Tomchuk, H. M. Hutton and E. Bock, *J. Chem. Phys*., 1983, **78**, 632; J. S. Lewis, J. Peeling, E. Tomchuk, W. Danchura, J. Bozek, H. M. Hutton and E. Bock, *Mol. Cryst. Liq. Cryst*., 1987, **144**, 57.
143. P. J. Flory, *Statistical Mechanics of Chain Molecules*, Interscience, New York, 1969.
144. G. Van der Zwan and L. Plomp, *Liq. Cryst*., 1989, **4**, 133.
145. E. A. Joghems and G. Van der Zwan, *J. Phys. II*, 1996, **6**, 845.
146. R. Y. Dong and X. Shen, *J. Phys. Chem. A*, 1997, **101**, 4673.
147. A. A. Nevzorov and M. F. Brown, *J. Chem. Phys*., 1997, **107**, 10288.
148. R. Y. Dong, J. Lewis, E. Tomchuk and E. Bock, *J. Chem. Phys*., 1978, **69**, 5314.
149. G. D. Williams, J. M. Beach, S. W. Dodd and M. F. Brown, *J. Am. Chem. Soc*., 1985, **107**, 6868.
150. R. J. Wittebort, R. Subramanian, N. P. Kulshreshtha and D. B. DuPré, *J. Chem. Phys*., 1985, **83**, 2457.
151. A. Szabo, *J. Chem. Phys*., 1984, **81**, 150.
152. P. Ukleja, J. Pirš and J. W. Doane, *Phys. Rev*., 1976, **14**, 414.
153. J. H. Freed, *J. Chem. Phys*., 1977, **66**, 4183.
154. A. A. Nevzorov, T. P. Trouard and M. F. Brown, *Phys. Rev. E*, 1998, **58**, 2259.
155. R. Y. Dong, *Mol. Cryst. Liq. Cryst*., 1986, **141**, 349; D. E. Woessner, *J. Chem. Phys*., 1962, **36**, 1.
156. C. F. Polnaszek, G. V. Bruno and J. H. Freed, *J. Chem. Phys*., 1973, **58**, 3185.
157. C. F. Polnaszek and J. H. Freed, *J. Phys. Chem*., 1975, **79**, 2283.
158. G. Lipari and A. Szabo, *J. Am. Chem. Soc*., 1982, **104**, 4546.
159. S. Žumer and M. Vilfan, *Mol. Cryst. Liq. Cryst*., 1981, **70**, 39.
160. R. Blinc, M. Burgar, M. Luzar, J. Pirš, I. Zupančič and S. Žumer, *Phys. Rev. Lett*., 1974, **33**, 1192.
161. J. F. Harmon and B. H. Muller, *Phys. Rev*., 1969, **182**, 400.
162. K. H. Schweikert and F. Noack, *Z. Naturforsch. Teil A*, 1989, **44**, 597.
163. A. Carvalho, P. J. Sebastiào, A. C. Ribeiro, H. T. Nguyen and M. Vilfan, *J. Chem. Phys*., 2001, **115**, 10484.
164. S. Renn and T. Lubensky, *Phys. Rev. A*, 1998, **38**, 2132.
165. J. L. Figueirinhas, A. Ferraz, A. C. Ribeiro, H. T. Nguyen and F. Noack, *J. Phys. II France*, 1997, **7**, 79.
166. G. R. Luckhurst, C. Zannoni, P. L. Nordio and U. Segre, *Mol. Phys*., 1975, **30**, 1345.
167. S. Marcelja, *J. Chem. Phys*., 1974, **60**, 3599.
168. J. W. Emsley, G. R. Luckhurst and C. P. Stockley, *Proc. R. Soc. London Ser. A*, 1982, **381**, 117.
169. J. Struppe and F. Noack, *Liq. Cryst*., 1996, **20**, 595.
170. R. Y. Dong and G. M. Richards, *J. Chem. Soc. Faraday Trans*., 1992, **88**, 1885.
171. R. Y. Dong, L. Friesen and G. M. Richards, *Mol. Phys*., 1994, **81**, 10117.
172. R. Y. Dong, *Mol. Phys*., 1996, **88**, 979.
173. L. Geppi, M. Calucci, C. A. Veracini and R. Y. Dong, *Chem. Phys. Lett*., 1998, **296**, 357.
174. X. Shen and R. Y. Dong, *J. Chem. Phys*., 1998, **108**, 9177.
175. X. Shen, R. Y. Dong, N. Boden, R. J. Bushby, P. S. Martin and A. Wood, *J. Chem. Phys*., 1998, **108**, 4324.
176. R. Y. Dong, *Phys. Rev. E*, 1999, **60**, 5631.
177. R. Y. Dong, A. Carvalho, P. J. Sebastiào and H. T. Nguyen, *Phys. Rev. E*, 2000, **62**, 3679.
178. R. Y. Dong and M. Cheng, *J. Chem. Phys*., 2000, **113**, 3466.
179. R. Y. Dong, C. R. Morcombe, L. Geppi, M. Calucci and C. A. Veracini, *Phys. Rev. E*, 2000, **61**, 3466.
180. R. Y. Dong, *Phys. Rev. E*, 1998, **57**, 4316.
181. R. Y. Dong and G. M. Richards, *Mol. Cryst. Liq. Cryst. Sci. Technol. Sect. A*, 1995, **262**, 339.
182. E. Helfand, *J. Chem. Phys*., 1971, **54**, 4651.

183. E. Helfand, E. R. Wasserman and T. A. Weber, *Macromolecules*, 1980, **13**, 526.
184. J. Skolnick and E. Helfand, *J. Chem. Phys.*, 1980, **72**, 5489.
185. R. Y. Dong, *Chem. Phys. Lett.*, 2000, **329**, 92.
186. R. Y. Dong, *J. Chem. Phys.*, 2001, **114**, 5897.
187. R. Y. Dong, L. Chiezzi and C. A. Veracini, *Phys. Rev. E*, 2002, **65**, 041716.
188. R. Y. Dong, *NMR of Orientationally Ordered Liquids*, Chap. 16, E. E. Burnell and C. de Lange, eds., Kluwer Academic, Dordrecht, 2003.
189. B. J. Gertner and K. Lindenberg, *J. Chem. Phys.*, 1991, **94**, 5143.
190. A. Saupe and G. Englert, *Phys. Rev. Lett.*, 1963, **11**, 462.
191. J. H. Prestegard, *Nat. Struct. Biol.*, 1998, **5**, 517, (NMR Suppl.).
192. L. D. Field, E. E. Burnell and C. de Lange, eds., *NMR of Orientationally Ordered Liquids*, Kluwer Academic, Dordrecht, 2003, 67.
193. S. Vivekanandan and N. Suryaprakash, *Chem. Phys. Lett.*, 2001, **338**, 247.
194. G. Celebre and G. DeLuca, *J. Phys. Chem. B*, 2003, **107**, 3243.
195. L. D. Field, S. A. Ramadan and G. K. Pierens, *J. Magn. Reson.*, 2002, **156**, 64; *Mol. Phys.*, 2003, **101**, 2813.
196. K. Tabayashi and K. Akasaka, *J. Phys. Chem. B*, 1997, **101**, 5108; *Liq. Cryst.*, 1999, **26**, 127.
197. C. L. Khetrapal, K. V. Ramanathan, N. Suryaprakash and S. Vivekanandan, *J. Magn. Reson.*, 1998, **135**, 265.
198. P. Lesot, D. Merlet, A. Loewenstein and J. Courtieu, *Tetrahedron Assym.*, 1998, **9**, 1871.
199. M. Sarfati, P. Lesot, D. Merlet and J. Courtieu, *Chem. Soc. Chem. Commun.*, 2000, 2069.
200. C. Aroulanda, M. Sarfati, J. Courtieu and P. Lesot, *Enantiomer*, 2001, **6**, 281.
201. D. Merlet, M. Sarfati, B. Ancian, J. Courtieu and P. Lesot, *Phys. Chem. Chem. Phys.*, 2000, **2**, 2283.
202. J. Farjon, D. Merlet, P. Lesot and J. Courtieu, *J. Magn. Reson.*, 2002, **158**, 169.
203. A. Meddour, P. Berdague, A. Hedli, J. Courtieu and P. Lesot, *J. Am. Chem. Soc.*, 1997, **119**, 4502.
204. M. Sarfati, J. Courtieu and P. Lesot, *Chem. Soc. Chem. Commun.*, 2000, 1113.
205. S. Vivekanandan, H. S. Vinay Deepack, G. A. Nagana, K. V. Ramanathan and C. L. Khetrapal, *J. Mol. Struct.*, 2002, **602–603**, 485.
206. T. R. J. Dinesen, C.-L. Teng, S. Wagner and R. G. Bryant, *Chem. Phys. Lett.*, 1999, **310**, 155.
207. M. Ishiwata and T. Ono, *J. Phys. Soc. Jpn.*, 1995, **64**, 636.
208. D. G. Cory, A. F. Fahmy and T. F. Havel, *Proc. Natl. Acad. Sci. USA*, 1997, **94**, 1634.
209. N. A. Gershenfeld and I. L. Chuang, *Science*, 1997, **275**, 350.
210. I. L. Chuang, N. Gershenfeld, M. G. Kubinec and D. W. Leung, *Proc. R. Soc. Lond. Ser. A*, 1998, **454**, 447.
211. D. G. Cory, R. Laflamme, E. Knill, L. Viola, T. F. Havel, N. Boulant, G. Boutis, E. Fortunato, S. Lloyd, R. Martinez, C. Negrevergne, M. Pravia, Y. Sharf, G. Teklemariam, Y. S. Weinstein and W. H. Zurek, *Fortschr. Phys.*, 2000, **48**, 875.
212. J. A. Jones, *Prog. Nucl. Magn. Reson. Spectrosc.*, 2001, **38**, 325.
213. A. Kumar, K. V. Ramanathan, T. S. Mahesh, N. Sinha and K. V. R. M. Murali, *Pramana*, 2002, **59**, 243.
214. K. V. R. M. Murali, N. Sinha, T. S. Mahesh, M. H. Levitt, K. V. Ramanathan and A. Kumar, *Phys. Rev. A*, 2002, **66**, 022313.
215. N. Sinha, T. S. Mahesh, K. V. Ramanathan and A. Kumar, *J. Chem. Phys.*, 2001, **114**, 4415.
216. A. R. Kessel and V. L. Ermakov, *JETP Lett.*, 1999, **70**, 61.
217. A. K. Khitrin and B. M. Fung, *J. Chem. Phys.*, 2000, **112**, 6963.
218. V. L. Ermakov and B. M. Fung, *Phys. Rev. A*, 2002, **68**, 042310.
219. A. R. Kessel and V. L. Ermakov, *JETP Lett.*, 2000, **71**, 307.
220. A. K. Khitrin, H. Sun and B. M. Fung, *Phys. Rev. A*, 2001, **63**, 020301(R).
221. A. K. Khitrin and B. M. Fung, *Phys. Rev. A*, 2001, **64**, 032306.
222. B. M. Fung, *Phys. Rev. A*, 2001, **63**, 022304.

223. T. S. Mahesh, N. Sinha, K. V. Ramanathan and A. Kumar, *Phys. Rev. A*, 2002, **65**, 022312.
224. C. S. Yannoni, M. H. Sherwood, D. C. Miller, I. L. Chuang, L. M. K. Vandersypen and M. G. Kubinec, *Appl. Phys. Lett*., 1999, **75**, 3563.
225. M. Marjanska, I. L. Chuang and M. G. Kubinec, *J. Chem. Phys*., 2000, **112**, 5095.
226. B. M. Fung, *J. Chem. Phys*., 2001, **115**, 8044.
227. A. K. Khitrin, V. L. Ermakov and B. M. Fung, *Chem. Phys. Lett*., 2002, **360**, 161.
228. A. K. Khitrin, V. L. Ermakov and B. M. Fung, *J. Chem. Phys*., 2002, **117**, 6903.
229. A. K. Khitrin, V. L. Ermakov and B. M. Fung, *Phys. Rev. Lett*., 2002, **89**, 277902.
230. J. Prost and P. Barois, *J. Chem. Phys*., 1983, **80**, 65.
231. R. G. Petschek and K. M. Wiefling, *Phys. Rev. Lett*., 1987, **59**, 343.
232. F. Tournilhac, L. M. Blinov, J. Simon and S. V. Yablonski, *Nature*, 1992, **359**, 621.
233. F. Noack, *Handbook of Liquid Crystals*, Vol. 1, D. Demus, J. Goodby, G. W. Gray, H. W. Spiess and V. Vill eds., Wiley-VCH, Weinheim, 1998, 582.
234. S. V. Dvinskikh and I. Furó, *J. Chem. Phys*., 2001, **115**, 1946, and references therein.
235. J. W. Emsley, J. E. Long, G. R. Luckhurst and P. Pedrielli, *Phys. Rev. E*, 1999, **60**, 1831.
236. E. Ciampi, J. W. Emsley, G. R. Luckhurst, B. A. Timimi, G. Kothe and M. Tittelbach, *J. Chem. Phys*., 1997, **107**, 5907.
237. H. Gotzig, S. Grunenberg-Hassanein and F. Noack, *Z. Naturforsch. A*, 1994, **49**, 1179.
238. G. R. Luckhurst, T. Miyamoto, A. Sugimura and B. A. Timimi, *J. Chem. Phys*., 2002, **116**, 5099.
239. R. H. Acosta and D. J. Pusiol, *J. Chem. Phys*., 2003, **119**, 3461.
240. K. W. Lee, C. H. Lee, S. H. Yang, J. K. Cha, C. E. Lee and J. Kim, *Curr. Appl. Phys*., 2001, **1**, 529.
241. F. Bonetto, E. Anoardo and R. Kimmich, *Chem. Phys. Lett*., 2002, **361**, 237.
242. F. Bonetto, E. Anoardo and R. Kimmich, *J. Chem. Phys*., 2003, **188**, 9037.
243. E. Ciampi, M. I. C. Furby, L. Brennan, J. W. Emsley, A. Lesage and L. Emsley, *Liq. Cryst*., 1999, **26**, 109.
244. A. K. Chattah, F. M. Cucchietti, M. Hologne, J. Raya and P. Levstein, *Magn. Reson. Chem*., 2002, **40**, 772.
245. C. Canlet and B. M. Fung, *J. Phys. Chem. B*, 2000, **104**, 6181.
246. C. Canlet and B. M. Fung, *Liq. Cryst*., 2001, **28**, 1863.
247. C. Tan, C. Canlet and B. M. Fung, *Liq. Cryst*., 2003, **30**, 611.
248. C. Tan and B. M. Fung, *J. Phys. Chem. A*, 2003, **107**, 3966.
249. V. Rayssac, P. Lesot, J.-P. Bayle and S. Miyajima, *J. Chim. Phys*., 1998, **95**, 973.
250. B. Berdagué, J.-P. Bayle, H. Fujimori and S. Miyajima, *New J. Chem*., 1998, 1005.
251. P. Berdagué, M. Munier, P. Judeinstein, J.-P. Bayle, C. S. Nagaraja and K. V. Ramanathan, *Liq. Cryst*., 1999, **26**, 211.
252. P. Judeinstein, P. Berdagué, J.-P. Bayle, N. Sinha and K. V. Ramanathan, *Liq. Cryst*., 2001, **28**, 1691.
253. N. Sinha, K. V. Ramanathan, K. Leblanc, P. Judeinstein and J.-P. Bayle, *Liq. Cryst*., 2002, **29**, 449.
254. W. H. Meyer, *Adv. Mater*., 1998, **10**, 439.
255. P. Berdagué, P. Judeinstein, J.-P. Bayle, C. S. Nagaraja, N. Sinha and K. V. Ramanathan, *Liq. Cryst*., 2001, **28**, 197.
256. K. V. Ramanathan and N. Sinha, *Monatshefte für Chimie*, 2002, **133**, 1535.
257. T. N. Venkatraman, N. Sinha and K. V. Ramanathan, *J. Magn. Reson*., 2002, **157**, 137.
258. B. Zalar, O. D. Laurentovich, H. Zeng and D. Finotello, *Phys. Rev. E*, 2000, **62**, 2252.
259. A. Chen, C.-D. Poon, T. J. Dingemans and E. T. Samulski, *Liq. Cryst*., 1998, **24**, 255.
260. A. Yoshizawa, A. Yokoyama, H. Kikuzaki and T. Hirai, *Liq. Cryst*., 1993, **14**, 513.
261. A. Yoshizawa, H. Kikuzaki and M. Fukumasa, *Liq. Cryst*., 1995, **18**, 351.
262. K. Tokumaru, B. Jin, S. Yoshida, Y. Takanishi, K. Ishikawa, H. Takazoe, A. Fukuda, T. Nakai and S. Miyajima, *Jpn. J. Appl. Phys*., 1999, **38**, 147.

263. T. Nakai, S. Miyajima, Y. Takanishi, S. Yoshida and A. Fukuda, *J. Phys. Chem. B*, 1999, **103**, 406.
264. A. C. Kolbert and R. G. Griffin, *Chem. Phys. Lett*., 1990, **166**, 87.
265. O. N. Antzutkin, S. C. Shekar and M. H. Levitt, *J. Magn. Reson. A*, 1995, **115**, 7.
266. T. Nakai, H. Fujimori, D. Kuwahara and S. Miyajima, *J. Phys. Chem. B*, 1999, **103**, 417.
267. S. Yoshida, B. Jin, Y. Takanishi, K. Tokumaru, K. Ishikawa, H. Takezoe, A. Fukuda, T. Kusumoto, T. Nakai and S. Miyajima, *J. Phys. Soc. Jpn*., 1999, **68**, 9.
268. D. Catalano, M. Cavazza, L. Chiezzi, M. Geppi and C. A. Veracini, *Liq. Cryst*., 2000, **27**, 621.
269. H. Fujimori, J.-P. Bayle and S. Miyajima, *J. Phys. Soc. Jpn*., 2000, **69**, 3000.
270. S. Yoshida, B. Jin, Y. Takanishi, K. Ishikawa, H. Takezoe, A. Fukuda, T. Nakai and S. Miyajima, *Mol. Cryst. Liq. Cryst*., 1997, **301**, 203.
271. D. Catalano, M. Cifelli, M. Geppi and C. A. Veracini, *J. Phys. Chem. A*, 2001, **105**, 34.
272. L. Chiezzi, V. Domenici, M. Geppi, C. A. Veracini and R. Y. Dong, *Chem. Phys. Lett*., 2002, **358**, 257.
273. D. Catalano, L. Chiezzi, V. Domenici, M. Geppi, C. A. Veracini, R. Y. Dong and K. Fodor-Csorba, *Macromol. Chem. Phys*., 2002, **203**, 1594.
274. D. Catalano, M. Cifelli, M. Geppi, C. A. Veracini, A. Jakli, K. Fodor-Csorba and E. Gacs-Baitz, *Mol. Cryt. Liq. Cryst*., 2000, **351**, 245.
275. H. Nádasi, W. Weissflog, A. Eremin, G. Pelzl, S. Diele, B. Das and S. Grande, *J. Mater. Chem*., 2002, **12**, 1.
276. G. Pelzl, S. Diele, S. Grande, A. Jákli, Ch. Lischka, H. Kresse, H. Schmalfuss, I. Wirth and W. Weissflog, *Liq. Cryst*., 199, **26**, 401.
277. H. Dehne, M. Pötter, S. Sokolowski, W. Weissflog, S. Diele, G. Pelzl, I. Wirth, H. Kresse, H. Schmalfuss and S. Grande, *Liq. Cryst*., 2001, **28**, 1269.
278. T. Sekine, T. Niori, M. Sone, J. Watanabe, S.-W. Choi, Y. Takanishi and H. Takezoe, *Jpn. J. Appl. Phys*., 1997, **36**, 6455.
279. R. Y. Dong, J. Xu, K. Fodor-Csorba, V. Domenici, G. Prampolini and C. A. Veracini, *J. Phys. Chem. B*, in press.
280. R. Y. Dong, J. Xu, G. Benyei and K. Fodor-Csorba, to be published.
281. S. Kumar, *Liquid Crystals, Experimental Study of Physical Properties and Phase Transitions*, CUP, Cambridge, 2001.
282. B. Pansu, E. Grelet, M. H. Li and H. T. Nguyen, *Phys. Rev. E*, 2000, **62**, 658.
283. C. Versace, G. Cipparrone, D. Lucchetta, D. Pucci and M. Ghedini, *Mol. Cryst. Liq. Cryst. Sci. Tech., Sect. A*, 1992, **212**, 313.
284. L. Calucci, D. Catalono, M. Ghedini, N. L. Jones, D. Pucci and C. A. Veracini, *Mol. Cryst. Liq. Cryst. Sci. Tech., Sect. A*, 1996, **290**, 87.
285. L. Calucci, C. Forte, M. Geppi and C. A. Veracini, *Z. Naturforsch. A: Phys. Sci*., 1998, **53**, 427.
286. S. P. Brown and H. W. Spiess, *Chem. Rev*., 2001, **101**, 4125.
287. S. V. Dvinskikh, I. Furó, H. Zimmermann and A. Maliniak, *Phys. Rev. E*, 2002, **65**, 050702 (R).
288. F. M. Mulder, J. Stride, S. J. Picken, P. H. J. Kouwer, M. P. de Hass, L. D. A. Siebbeles and G. J. Kearley, *J. Am. Chem. Soc*., 2003, **125**, 3860.
289. R. Y. Dong, N. Boden, R. J. Bushby and P. S. Martin, *Mol. Phys*., 1999, **97**, 1165.
290. R. Y. Dong and C. R. Morcombe, *Liq. Cryst*., 2000, **27**, 897.
291. R. Y. Dong and R. Shearer, *Chem. Phys. Lett*., 2003, **375**, 463.
292. S. V. Dvinskikh, Z. Luz, H. Zimmermann, A. Maliniak and D. Sandström, *J. Phys. Chem. B*, 2003, **107**, 1969.
293. S. V. Dvinskikh, D. Sandström, Z. Luz, H. Zimmermann and A. Maliniak, *J. Chem. Phys*., 2003, **119**, 413.
294. M. Wirth, J. Leisen, C. Boeffel, R. Y. Dong and H. W. Spiess, *J. Phys. II*, 1993, **3**, 53.

295. S. P. Brown, I. Schnell, J. D. Brand, K. Müllen and H. W. Spiess, *J. Am. Chem. Soc*., 1999, **121**, 6712.
296. A. Fechtenkötter, K. Saalwächter, M. A. Harbison, K. Müllen and H. W. Spiess, *Angew. Chem. Int. Ed. Engl*., 1999, **38**, 3039.
297. I. Fishcbach, T. Pakula, P. Minkin, A. Fechtenkötter, K. Müllen, H. W. Spiess and K. Saalwächter, *J. Phys. Chem. B*, 2002, **106**, 6408.
298. H. Ishida and F. Horii, *Polymer*, 1999, **40**, 3781.
299. M. Tokita, M. Sone, H. Kurosu, I. Ando and J. Watanabe, *J. Mol. Struct*., 1998, **446**, 215.
300. D. McElheny, J. Grinshtein, V. Frydman and L. Frydman, *Macromolecules*, 2002, **35**, 3544.
301. M. Mizuno, A. Hirai, H. Matsuzawa, K. Endo, M. Suhara, M. Kenmotsu and C. D. Han, *Macromolecules*, 2002, **35**, 2595.
302. N. J. Heaton and G. Kothe, *J. Chem. Phys*., 1998, **108**, 8199.
303. M. Geppi, S. Pizzanelli and C. A. Veracini, *Chem. Phys. Lett*., 2001, **343**, 513.
304. E. Barmatov, L. Chiezzi, S. Pizzanelli and C. A. Veracini, *Macromolecules*, 2002, **35**, 3076.
305. G. P. Crawford and S. Žumer, *Liquid Crystals in Complex Geometries*, Taylor and Francis, London, 1996.
306. M. Vilfan, N. Vrbančič-Kopač, P. Ziherl and G. P. Crawford, *Appl. Magn. Reson*., 1999, **17**, 329.
307. M. Vilfan, T. Apih, A. Gregorovič, B. Zalar, G. Lahajnar, S. Žumer, G. Hinzec, R. Böhmer and G. Altho, *Magn. Reson. Imaging*, 2001, **19**, 433.
308. S. Stapf, R. Kimmich and R.-O. Seitter, *Phys. Rev. Lett*., 1995, **75**, 2855.
309. F. Roussel, C. Canet and B. M. Fung, *Phys. Rev. E*, 2002, **65**, 021701.
310. F. Roussel and B. M. Fung, *Phys. Rev. E*, 2003, **67**, 041709.
311. R.-O. Seitter, T. Link, R. Kimmich, A. Kobelkov, P. Wolfangel and K. Müller, *J. Chem. Phys*., 2000, **112**, 8715.
312. M. Vilfan, G. Althoff, I. Vilfan and G. Kothe, *Phys. Rev. E*, 2001, **64**, 022902.
313. G. Althoff, D. Frezzato, M. Vilfan, O. Stauch, R. Schubert, I. Vilfan, G. J. Moro and G. Kothe, *J. Phys. Chem. B*, 2002, **106**, 5506; 5517.
314. G. Fairhurst, S. Fuller, J. Gray, M. C. Holmes and G. J. T. Tiddy, *Handbook of Liquid Crystals*, Vol. 3, D. Demus, J. Goodby, G. W. Gray, H. W. Spiess and V. Vill eds., Wiley-VCH, Weinheim, 1998, 341.
315. G. Orädd and G. Lindblom, *NMR of Orientationally Ordered Liquids*, Chap. 18, E. E. Burnell and C. de Lange, eds., Kluwer Academic, Dordrecht, 2003.
316. N. Hedin, I. Furó and P. O. Eriksson, *J. Phys. Chem. B*, 2000, **104**, 8544.
317. N. Hedin and I. Furó, *J. Phys. Chem. B*, 1999, **103**, 9640.
318. L. G. Werbelow, *Encyclopedia of Nuclear Magnetic Resonance*, Vol. 6, D. M. Grant and R. K. Harris, eds., Wiley, Chichester, 1997, 4092.
319. A. A. de Melo Filho, A. Laverde and F. Y. Fujiwara, *Langmuir*, 2003, **19**, 1127.
320. M. Törnblom, R. Sitnikov and U. Henriksson, *Liq. Cryst*., 2000, **7**, 943.
321. H. Nery, O. Söderman, D. Canet, H. Walderhaug and B. Lindman, *J. Phys. Chem*., 1986, **90**, 5802.
322. R. Y. Dong, *Mol. Phys*., 2001, **99**, 637.
323. P.-O. Quist, B. Halle and I. Furó, *J. Chem. Phys*., 1991, **95**, 6945.
324. J. Grinshtein, D. McElheny, V. Frydman and L. Frydman, *J. Chem. Phys*., 2001, **114**, 5415.
325. J.-M. Péchiné, A meddour and J. Courtieu, *Chem. Commun*., 2002, 1734.
326. M. F. Brown and A. A. Nevzorov, *Colloids Surf. A*, 1999, **158**, 281.
327. M. F. Brown, R. L. Thurmond, S. W. Dodd, D. Otten and K. Beyer, *J. Am. Chem. Soc*., 2002, **124**, 8471.
328. T. Sparrman and P.-O. Westlund, *Phys. Chem. Chem. Phys*., 2003, **5**, 2114.
329. K. Aman, E. Lindahl, O. Edholm, P. Hakansson and P.-O. Westlund, *Biophys. J*., 2003, **84**, 102.
330. A. Pampel, E. Standberg, G. Lindblom and F. Volke, *Chem. Phys. Lett*., 1998, **287**, 468.

331. V. B. Reddy and B. M. Fung, *Langmuir*, 2001, **17**, 3563.
332. J. H. Prestegard, H. M. Al-Hashimi and J. R. Tolman, *Quart. Rev. Biophys.*, 2002, **33**, 371.
333. B. Simon and M. Sattler, *Angew. Chem. Int. Ed.*, 2002, **41**, 437.
334. J. R. Tolman, *Curr. Opin. Struct. Biol.*, 2001, **11**, 532.
335. M. Zweckstetter and A. Bax, *J. Am. Chem. Soc.*, 2001, **123**, 9490.
336. T. S. Ramirez, B. E. Ulmer, F. Delaglio and A. Bax, *J. Am. Chem. Soc.*, 2003, **125**, 9179.
337. C. R. Sanders II and J. P. Schwonek, *Biochemistry*, 1992, **31**, 8898.
338. M. R. Hansen, L. Mueller and A. Pardi, *Nat. Struct. Biol.*, 1988, **5**, 1065; M. R. Hansen, M. Rance and A. Pardi, *J. Am. Chem. Soc.*, 1998, **120**, 11210.
339. G. M. Clore, M. R. Starich and A. M. Gronenborn, *J. Am. Chem. Soc.*, 1998, **120**, 10571.
340. R. S. Prosser, J. A. Losonczi and I. V. Shiyanovskaya, *J. Am. Chem. Soc.*, 1998, **120**, 11010.
341. M. Rückert and G. Otting, *J. Am. Chem. Soc.*, 2000, **122**, 7793.
342. G. Cornilescu, J. L. Marquardt, M. Ottiger and A. Bax, *J. Am. Chem. Soc.*, 1998, **120**, 6836.
343. A. Bax and N. Tjandra, *J. Biomol. NMR*, 1997, **10**, 289.
344. M. Ottiger and A. Bax, *J. Am. Chem. Soc.*, 1999, **121**, 4690.
345. B. Stevensson, C. Landersjö, G. Widmalm and A. Maliniak, *J. Am. Chem. Soc.*, 2002, **124**, 5946.
346. R. R. Vold and R. S. Prosser, *J. Magn. Reson. B*, 1996, **113**, 267.
347. G. Cho, B. M. Fung and V. B. Reddy, *J. Am. Chem. Soc.*, 2001, **123**, 1537.
348. C. Tan, B. M. Fung and G. Cho, *J. Am. Chem. Soc.*, 2002, **124**, 11827.
349. G. Zandomeneghi, M. Tomaselli, J. D. van Beek and B. Meier, *J. Am. Chem. Soc.*, 2001, **123**, 910.
350. G. Zandomeneghi, M. Tomaselli, P. T. F. Williamson and B. H. Meier, *J. Biomol. NMR*, 2003, **25**, 113.
351. J.-C. Hus, D. Marion and M. Blackledge, *J. Am. Chem. Soc.*, 2001, **123**, 1541.
352. K. Nomura and M. Kainosho, *J. Mag. Reson.*, 2002, **154**, 146.
353. J. R. Tolman, *J. Am. Chem. Soc.*, 2002, **124**, 12020.
354. M. Zweckstetter and A. Bax, *J. Am. Chem. Soc.*, 2000, **122**, 3791.
355. M. Zweckstetter and A. Bax, *J. Biomol. NMR*, 2001, **20**, 365.
356. N. K. Goto, N. R. Skrynnikov, F. W. Dahlquist and L. E. Kay, *J. Mol. Biol.*, 2001, **308**, 745.
357. J. R. Tolman, J. M. Flanagan, M. A. Kennedy and J. H. Prestegard, *Nat. Struct. Biol.*, 1997, **4**, 292.
358. W. Peti, J. Meiler, R. Bruschweiler and C. Griesinger, *J. Am. Chem. Soc.*, 2002, **124**, 5822.
359. J. Struppe and R. R. Vold, *J. Magn. Reson.*, 1998, **135**, 541.
360. J. Struppe, J. A. Whiles and R. R. Vold, *Biophys. J.*, 2000, **78**, 281.
361. J. A. Whiles, K. J. Glover, R. R. Vold and E. A. Komives, *J. Magn. Reson.*, 2002, **158**, 149.
362. A. Kjellberg and S. W. Homans, *J. Magn, Reson.*, 2001, **151**, 90.
363. Y.-W. Hsueh, R. Giles, N. Kitson and J. Thewalt, *Biophys. J.*, 2002, **82**, 3089.
364. P. J. Bolon and J. H. Prestegard, *J. Am. Chem. Soc.*, 1998, **120**, 9366.
365. P. Krajewski and M. Bardet, *Magn. Reson. Chem.*, 2002, **40**, 225.
366. T. Fäcke and S. Berger, *J. Magn. Reson. A*, 1995, **113**, 114.
367. C. Farès, J. F. Sharom and J. H. Davis, *J. Am. Chem. Soc.*, 2002, **124**, 11232.
368. I. Bertini, F. Castellani, L. Luchinat, G. Martini, G. Parigi and S. Ristori, *J. Phys. Chem. B*, 2000, **104**, 10653.
369. J. Bharatam and C. R. Bowers, *J. Phys. Chem. B*, 1999, **103**, 2510.
370. J. Ruohonen, M. Ylihautala and J. Jokisaari, *Mol. Phys.*, 2001, **99**, 711.

Applications of NMR in Meat Science

HANNE CHRISTINE BERTRAM* AND HENRIK J. ANDERSEN

Department of Food Science, Danish Institute of Agricultural Sciences, Research Centre Foulum, P.O. Box 50, DK-8830 Tjele, Denmark
**Tel.: +45 89 99 15 06; Fax: +45 89 99 15 64; E-mail: Hannec.Bertram@agrsci.dk*

ANNUAL REPORTS ON NMR SPECTROSCOPY
VOLUME 53 ISSN 0066 4103
DOI 10.1016/S0066-4103(04)53003-X

This review presents the status of NMR applications in meat science. The potential and relevance of relaxation, imaging, and spectroscopic methodologies are covered within the different topics of importance for meat science and related muscle biology. The most widely explored area of NMR in meat science is ^{1}H relaxometry. The use of relaxometry has been highly successful due to its potential in characterising water and structural features in heterogeneous systems like muscle/meat. Focus is especially given to the area of determining water-holding capacity (WHC) and other meat quality traits controlled by water distribution and mobility, together with dynamic studies of physical changes during conversion of muscle to meat. Moreover, the elucidation of the observed relaxation characteristics in muscle and meat is discussed. NMR imaging studies have mostly been applied in the elucidation of structural changes and brine dynamic during processing of meat, i.e., freezing, curing and high pressure treatment, which are reviewed and put into perspective in relation to applications together with a description of the potential of the method in the authentication of fresh meat. Within NMR spectroscopy, studies on the ^{31}P nucleus have been dominating, and ^{31}P NMR spectroscopy has been applied to investigate the effect of genetic, feeding, and slaughter factors on meat quality through their action on phosphorous metabolism post mortem*, and these studies are considered and discussed in relation to their contribution to fundamental meat science. Finally, the present applications and potentials of ^{1}H NMR and ^{13}C NMR spectroscopy within meat science are considered together with the related technical problems using these methodologies.*

1. INTRODUCTION

The physical basis of nuclear magnetic resonance (NMR), a spectroscopic technique based on the fact that certain nuclei possess an angular magnetic moment, was first described by the groups of Bloch[1] and Purcell,[2] for which they were awarded the 1952 Nobel Prize in physics. Despite being initially discovered in physics, NMR has subsequently developed in chemistry in particular as a tool for elucidation of molecular structures of organic compounds (for a review, see for example Wider[3]). However, also in biological tissues, potential applications of the technique were soon demonstrated,[4–7] and improvements in instrumentation through development of pulsed-field equipment and high-field superconducting magnets have further enhanced the use of the NMR technique for biological applications. The multiplicity of information that can be obtained from NMR makes the technique novel and appreciated in biological sciences. NMR spectroscopy allows identification of the presence of particular molecules within a sample, a method that is widely used for studying metabolites in tissues (the discipline metabonomic). Due to the non-destructive and potential non-invasive character of the NMR technique, NMR spectroscopy not only allows detection of particular metabolites in intact tissue, but it also enables monitoring the kinetics of

these metabolites through changes in intensities of their spectral lines. Supplementary, NMR relaxometry provides information about the physical/chemical nature of certain nuclei in terms of mobility and compartmentalisation. Proton relaxometry is widely exploited for studies of the behaviour of water, the most abundant substance in many biological materials. Also in this aspect, the advantage of the non-destructiveness and potential non-invasiveness can be used to follow a certain progress. A third approach involves the use of magnetic field gradients to make images of biological tissues available and thereby provide information about spatial distribution of molecules within a sample.

This review aims at giving an overview of the NMR applications in meat science. This may be an idealistic scope, as meat science is not a strictly delimited area. In studies of the conversion of muscle to meat, initialised early *post mortem*, the limits to *in vivo* muscle physiology are vague, and therefore the differentiation of which studies belong to which discipline is subjective, and consequently studies have been included where we found it natural. Overall, the review attempts to demonstrate and discuss the different NMR methodologies (relaxometry, imaging, spectroscopy) and their potential applications within meat science based on the existing literature. In the end, conclusions will be drawn, and future perspectives are considered.

1.1. The muscle

The muscle is a highly organized tissue, built up of individual cells known as fibres, which are held together by connective tissue. Each muscle fibre consists of a high number of single strands of myofibrils. The myofibrils are again comprised of myofilaments. The myofilaments are divided into thin and thick filaments, which mainly contain two filamentary proteins, actin and myosin, respectively. The myofibrils occupy approximately 80% of the muscle cell volume, and the majority of the water, which makes up about 75% of the muscle, is located in the spaces between thin and thick filaments. A schematic drawing of muscle structure is shown in Fig. 1.

2. NMR PROTON RELAXOMETRY IN MEAT SCIENCE

An interesting feature of the relaxation is that it is not a spontaneous incident, but governed by molecular motion and interactions between nuclei. Consequently, it provides valuable information about the physical and chemical environments in which the nuclei are embedded. As mentioned above, meat contains approximately 75% water, organised within different structures, which is of fundamental significance for the quality of

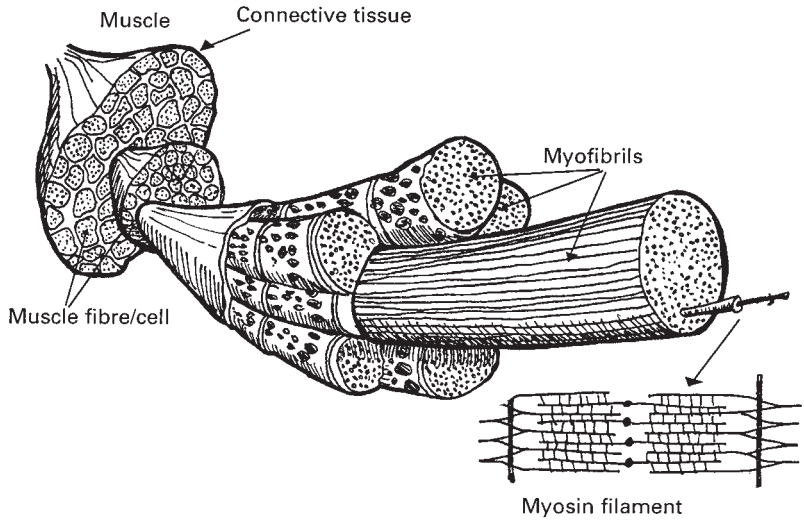

Fig. 1. Schematic view of muscle fibre structure and fibre sub-units.

the meat. Accordingly, as it will be discussed in the following, NMR proton relaxometry is a unique technique for studying meat quality, because it gives direct information about the physical (distribution, compartmentalisation) and chemical (mobility, interactions with macromolecules) water properties.

2.1. Interpretation of transverse relaxation in meat

Upon the introduction of NMR proton relaxometry in muscle studies, it was early recognised that a model based only on dipolar interactions is far too simple,[8–14] as:

- The T_2 relaxation of protons and deuterium in muscle water is much faster than T_2 relaxation of pure water.
- The T_2 relaxation of protons in muscle tissue is non-mono-exponential.

An explanation of these observations was attempted in terms of the *existence of different states/compartmentalisation* inspired by the model proposed by Zimmerman and Brittin,[15] suggesting that a spin system can be made up of a fixed number of phases with each phase characterised by an inherent relaxation rate. The relaxation observed will then depend on the rate of exchange between phases, and three situations can be outlined: (*i*) fast, (*ii*) slow, and (*iii*) intermediate exchange.

In case of fast exchange, the observed relaxation will be mono-exponential with the relaxation rate being an averaging of the individual inherent relaxation rates:

$$\frac{1}{T} = \sum_{i=1}^{n} \frac{P_i}{T_i}$$

where T is the relaxation time, P_i is the fraction of spins in the ith phase, and T_i is the relaxation time of the ith phase.

In case of slow exchange between phases, the relaxation decay becomes the sum of relaxation of the various phases and thereby multi-exponential:

$$M(t) = \sum_{i=1}^{n} M_i \exp\left(\frac{-t}{T_i}\right)$$

where $M(t)$ is the intensity of magnetisation at time t, M_i is the original relaxation of the phase i, and T_i the corresponding relaxation time.

In the category of intermediate exchange the expressions become more complex and the prediction of the relaxation less trivial as e.g., demonstrated by Belton and Hills.[16] It should be noted that the rate of exchange depends on the relaxation time scale, i.e., fast and slow exchange correspond to a short and long interchange time, respectively, in comparison to the inherent relaxation times.

The fact that an increased relaxation rate of protons and deuterons is found in muscle tissue compared with pure water has been explained by fast exchange between protons exhibiting rapid relaxation, e.g., spins in hydration layers and in bulk water.[8,12,17,18] However, another mechanism which involves cross-relaxation between water protons and protons in proteins was later proposed,[19] while Diegel and Pintar[14] suggested a mechanism including exchange of water to and from the hydration layer by slow diffusion. Efforts have been made to estimate the contribution from the different relaxation mechanisms in protein systems, which, however, is complex and dependent on magnetic field strength.[20–21]

The non-mono-exponentiality of the transverse relaxation in muscle and meat has most often been solved by decomposing the relaxation decay into two or three exponential components.[11,12,22–27] In general, this has resulted in the detection of a major relaxation component characterised by a time constant around 35–50 ms, which corresponds to approximately 80–95% of the relaxation, and a slower relaxing component characterised by a time constant around 100–250 ms, which represents approximately 5–15% of the relaxation. In addition, a fast relaxing component with a time constant between 0 and 10 ms, which corresponds to about 5% of the relaxation, has been observed.[9,11] The presence of three relaxation components in the

transverse relaxation of meat has been supported by continuous distributed exponential fitting of the transverse relaxation data, which has revealed equivalent relaxation components.[28] The focal point has been the major and the slower relaxing component. A widely used explanation of the fact that the T_2 relaxation in muscle tissue is non-mono-exponential is that slow exchange takes place between intra- and extra-cellular water pools, and accordingly the two components have been ascribed to intra- and extra-cellular water, respectively.[9,11,12] However, this is still a controversial matter giving rise to a lot of dispute in the literature. Fung and McGaughy[29] raised questions about the decomposition of the relaxation decay into a definite number of exponentials, as they argued that the non-mono-exponential behaviour is a likely consequence of hydrogen exchange, and therefore no evidence for the existence of different compartments. Moreover, Fung and Puon[30] observed that upon bi-exponential fitting of the transverse relaxation decay, the fraction of relaxation described by the two components differed between proton and deuterium, which was used as a further argument against the intra-/extra-cellular model. Subsequently, different approaches have been attempted in order to prove or disprove the intra-/extra-cellular model. These can be summarised into the following approaches:

(1) Theoretical considerations including calculations based on the knowledge of anatomical features.
(2) Use of extra-cellular markers (Gd-DTPA).
(3) Manipulation of intra-/extra-cellular ratio.
(4) Alteration of anatomical features:
    (i) Disintegration of membranes.
    (ii) Disruption of overall structural organisation.

Ad. 1. *Theoretical considerations including calculations based on the knowledge of anatomical features*. While considering whether or not it is reasonable to believe that the non-mono-exponential transverse relaxation reflects an intra- and extra-cellular compartmentalisation, it should be questioned if the slow-exchange assumption is reasonable taking into account the macroscopic features of a muscle cell from a theoretical point of view. The NMR-timescale criterion for exchange limit is comparison of the quantity $(\tau_i^{-1} + \tau_o^{-1})$, where τ_i and τ_o are the average lifetime of a water molecule inside and outside the cell, respectively, with $|R_i - R_o|$, which is the absolute difference in the intrinsic relaxation rates. If $|R_i - R_o| > (\tau_i^{-1} + \tau_o^{-1})$, the exchange is in the slow regime. Landis *et al.*[31] calculated the average lifetime of a water molecule in a muscle cell to 1.1 s. The assumption that the fraction of water in the extra-cellular space is 0.1,[32] results in $(\tau_i^{-1} + \tau_o^{-1}) = 10.8\ \mathrm{s}^{-1}$ (as $p_i + p_o = 1$ and $p_0/\tau_0 = p_i\tau_i$ must be fulfilled). If the relaxation rate inside the cell is set to $12\ \mathrm{s}^{-1}$ as measured in a protein gel,[33] and the extra-cellular water is assumed to have a relaxation rate similar to pure water ($2\ \mathrm{s}^{-1}$), $|R_i - R_o|$ becomes $10\ \mathrm{s}^{-1}$. Several assumptions are made in this simple

calculation, but it seems that the exchange between the intra- and the extra-cellular space should be described as either slow or intermediate as also concluded by Saab *et al.*[34]

Brownstein and Tarr[35] considered if the size of a muscle cell could give rise to non-mono-exponential transverse relaxation by assuming simple diffusion and planar geometry, and found that under these conditions and in the slow diffusion range, multi-exponential transverse relaxation could be expected when the sample size is between 1 and 30 μm. Accordingly, as muscle cells have a diameter of 10–100 μm,[36] the calculations performed by Brownstein and Tarr[35] indicate that the anatomical features of muscle cells are consistent with the expectation of multi-exponential transverse relaxation.

Ad. 2. *Use of extra-cellular markers (Gd-DTPA)*. Studies involving the paramagnetic agent, Gadolinium DTPA, known to remain extra-cellular and reduce the relaxation rate of protons,[37,38] have given opposing results regarding the intra-/extra-cellular hypothesis. Upon bi-exponential fitting of the transverse relaxation decay, Le Rumear *et al.*[24] showed that the use of Gd-DTPA decreased to a great extent the relaxation rate of the slow component and only to a small extent the fast component. Accordingly, the result indicates that the fast component should be ascribed to intra-cellular water, while the slow component should be ascribed to extra-cellular water. In contrast, using the same procedure, Adzamli *et al.*[39] found almost equal effects of Gd-DTPA on the two relaxation components, which, however, may be due to exchange over the membrane resulting in an effect on both the two relaxation components. Accordingly, no final conclusion regarding the ascription of the two relaxation components to intra-and extra-cellular water can be drawn from the present GD-DTPA studies.

Ad. 3. *Manipulation of intra-/extra-cellular ration*. Le Rumear *et al.*[24] manipulated intra-/extra-cellular ratios and showed that an increase in vascular volume induced by nerve stimulation increased the fraction of the slow relaxation component, while reduced intra-cellular/interstitial volume induced by osmotic diuresis decreased the fraction of the fast relaxing component and increased the fraction of the slow relaxing component, which indicates that the fast and slow relaxing component can be ascribed to the intra- and extra-cellular space, respectively.

Ad. 4. *Alteration of anatomical features*. Finally, several studies have attempted to manipulate the macroscopic features of muscle/meat tissue in order to verify or disprove the intra-/extra-cellular model. Efforts have been made to disrupt cell membranes by glycerination and DMSO treatment in order to make assessment of the potential role of membranes possible.[30,40,41] All these studies showed unaltered relaxation behaviour upon membrane disintegration, which suggests that intact cell membranes in themselves are not necessary for a non-mono-exponential relaxation. Irrelevance of membranes

has also been demonstrated in preparations of red blood cell ghosts mixed with variable 'extra-cellular' fluid composed of an aqueous protein solution. This showed that membrane transmission is too fast to give observable two-component relaxation. However, it was also demonstrated that if the red blood cell ghosts were packed into a region of which the dimensions were larger than the path length of a water molecule during the pulse spacing, then the transverse relaxation decay could be separated into two components, thus revealing that compartmentalisation can cause multiple components in the transverse relaxation.[42] Influence of disruption of the overall structure of the muscle tissue/meat by homogenisation on transverse relaxation decay has also been investigated.[12,40–41] Pearson *et al.*[12] and Cole *et al.*[40] observed a clear shift towards more mono-exponential relaxation with a time constant intermediate between the two relaxation components observed in intact tissue upon homogenisation, whereas Bertram *et al.*[41] merely observed a significant decrease in the fraction of the slowest component together with a minor decrease in the relaxation rate of the fastest component. The differences should probably be ascribed to the degree of disintegration of the overall structural organisation obtained in the different studies, and altogether the studies therefore strongly indicate that the overall structural organisation of the meat is responsible for the observation of a major relaxation component around 35–50 ms and a slower relaxing component around 100–250 ms. In addition, as the studies involving disintegration of membranes reveal that the detection of these two relaxation components is not affected by alterations in membrane properties, it can be concluded that it is the structure itself that is responsible for the anatomical separation of compartments with slow exchange, and which explains the observation of the two relaxation components, while the mechanism of separation of intra- and extra-cellular spaces by membranes is insignificant. In summary, it seems reasonable to propose that in meat:[41]

- The major relaxation component, characterised by a time constant of approximately 35–50 ms, accounting for 80–95% of the relaxation, and in the following referred to as T_{21}, represents water trapped within the protein-dense myofibrillar network.
- The slower relaxing component, characterised by a time constant of approximately 100–250 ms, accounting for 5–15% of the relaxation, and in the following referred to as T_{22}, represents water located outside the myofibrillar protein network, i.e., extra-myofibrillar water.
- The fastest relaxing component sometimes reported, characterised by a time constant between 0 and 10 ms,[9,11,28,41] and in the following referred to as T_{2B}, is ascribed to water tightly associated with macromolecules.

While this can be considered to be the situation in the meat, other circumstances could be expected in the *in vivo* muscle as well as during the

conversion of muscle to meat. The rationale for this is that in the *in vivo* muscle an active membrane system is present to ensure homeostasis, while a destabilisation and disruption of cell membranes is taking place during the conversion of muscle to meat, resulting in changed membrane properties, in particular permeability.[43] In addition, severe changes in the structure occur during the conversion of muscle, resulting in alterations both at the micro-[44,45] and macroscopic level.[46,47] The influence of meat structure on transverse relaxation will be considered further in the following.

2.2. Structural attributes and transverse relaxation

Back in 1980, Lillford *et al.*[48] suggested that transverse relaxation reflects structural features of the material investigated, as the relaxation rate will depend on the probability of a water molecule to meet a surface and thereby also the anatomical features. Later, Yamada[49] noticed that the transverse relaxation became faster in stretched, skinned muscle fibres compared with relaxed, skinned fibres, and it was concluded that intra-cellular water changes its properties associated with the actin and myosin interaction and thereby structural organisation of the muscle. A recent study investigated the relationship between transverse relaxation and well-characterised structural features of meat with emphasis on the relationship between myofilament lattice spacing and the T_2 relaxation parameters.[50] Correlations between the relaxation rate of T_{21} and sarcomere length/myofilament lattice were demonstrated, and it was suggested that the ratio between the I- and the A-band determines the relaxation rate of T_{21} (myofibrillar water), which was found to be consistent with quantitative considerations on the spatial distances in the myofilmentous matrix.[50]

During muscle growth, the composition of the muscle changes.[51,52] In particular, proteins accumulate, and therefore the myofibrillar protein density increases, suggesting that T_{21}, representing myofibrillar water, should be sensitive to the changes in composition taking place during muscle growth. This was confirmed in a study where transverse relaxation was measured 24 h *post mortem* in muscle samples from pigs slaughtered at various weights (between 25 and 150 kg), which revealed a close relationship between the changes in the relaxation time of T_{21} and protein content during growth.[53] Consequently, the findings support that the T_{21} component reflects water trapped within the myofibrils, and that the T_{22} component corresponds to water outside the myofibrillar lattice, i.e., extra-myofibrillar water.

X-ray studies have demonstrated that pH affects the myofilament lattice due to electrostatic repulsion.[45] Accordingly, the shown relationship between myofilament lattice and the T_{21} time constant[50] reveals that a correlation between the T_{21} time constant and pH should be expected, as it was also

demonstrated in meat.[22,27,54] In addition, the combination of pH decrease *post mortem* and high temperature is known to cause muscle protein denaturation as demonstrated by decreased protein solubility.[55–57] However, the understanding of how this protein denaturation is accompanied by changes in the structural organisation and the water distribution is very limited at present. Upon bi-exponential fitting of transverse relaxation decays measured in beef muscles, Tornberg *et al.*[54] showed that the *post mortem* progression in the T_{21} time constant was dependent on the pH decrease *post mortem*. Tornberg *et al.*[54] thereby demonstrated that transverse relaxation implies information about pH-induced structural changes *post mortem*. The significance of pH progression on the structural organisation and distribution of water has been further demonstrated on *post mortem* rabbit muscles exposed to high temperature (32°C), known to promote protein denaturation. This study showed that each T_2 population is not simply characterized by a single, discrete relaxation time, but rather by a continuous spectrum of relaxation times, and that denaturation of proteins results in a broader distribution of relaxation times.[58] This clearly demonstrates that transverse relaxation implies information about microstructural changes in meat upon protein denaturation.

In summary, the above studies on the relationship between meat structure, composition, and transverse relaxation are consistent with the ascription assignment of the T_{21} relaxation component to water located in the myofibrillar protein matrix. In addition, the studies confirm that transverse relaxation is an excellent tool for obtaining information about structural features in meat.

2.3. Water-holding capacity and transverse relaxation

Water-holding capacity (WHC), i.e., the ability of fresh meat to retain its own water, is an important meat quality trait due to its economic and sensory consequences. Consequently, measurement of WHC in meat is of interest. Renou *et al.*[22] were the first to show that both T_1 and T_2 relaxation correlate with WHC. Later, Tornberg *et al.*[25] demonstrated that T_2 relaxation differed significantly between meat classified as PSE (pale, soft, exudative, i.e., low WHC), normal and DFD (dark, firm, dry, i.e., high WHC), respectively, and recent studies have elaborated these observations and demonstrated that T_2 relaxation correlates with WHC over a wide range of WHC in pork.[26–28,59] A correlation between T_2 relaxation and WHC has also been demonstrated in fish flesh.[60] Table 1 shows the findings of different studies where the use of relaxation for determination of WHC in meat has been studied. In some of these studies, correlations were carried out using the whole transverse relaxation decay curve in a multivariate regression analysis,[26,59] and accordingly no information was obtained about the

Table 1. Results from studies of the relationship between proton relaxation and WHC in pork

Study	Relaxation parameter	Method for determination of WHC	N^a	Correlation coefficient
Renou *et al.*[22]	T_1	Imbibition method	98	0.59
Renou *et al.*[22]	T_2	Imbibition method	98	0.54
Tornberg *et al.*[25]	T_2	Honikel's bag method	40	0.60
Brøndum *et al.*[26]	T_1	Honikel's bag method	78	0.74
Brøndum *et al.*[26]	T_1	Filter paper press	78	0.46
Brøndum *et al.*[26]	T_2	Honikel's bag method	78	0.75
Brøndum *et al.*[26]	T_2	Filter paper press	78	0.53
Brown *et al.*[59]	T_2	Honikel's bag method	44	0.74
Brown *et al.*[59]	T_2	Filter paper press	44	0.71
Bertram *et al.*[27]	T_2	Honikel's bag method	74	0.77
Bertram *et al.*[27]	T_2	Centrifugation	74	0.77

[a]Number of samples included in the study.

specific relaxation parameters to which the correlation could be ascribed. However, when performing discrete exponential fitting on the transverse relaxation, the highest correlation to WHC was obtained on the T_{22} time constant,[25,27] or the relative fraction of amplitude ascribed to the T_{22} component.[22] This indicates that water represented by T_{22}, i.e., extra-myofibrillar water, is most critical for the amount of drip loss and thereby WHC. This was further supported in a study which showed that during loss of water from meat by centrifugation, the amplitude of the T_{22} component decreased proportionally with the amount of expelled water, thus revealing that transverse relaxation provides a unique, direct measure of the amount of mobile water that can be expected to be lost as drip.[28] Moreover, this explains the observed increases in the fraction of relaxation ascribed to the T_{22} component in meat from pigs carrying the halothane gene carriers,[23,61] which is known to give rise to a reduced WHC.[62–68] Further analysis of the *post mortem* progress in transverse relaxation was recently investigated in porcine muscle samples from carriers and non-carriers of the halothane gene exposed to two different cooling profiles.[69] A dramatic effect of the halothane gene on the development in the T_{22} population *post mortem*, which was most pronounced for muscle samples exposed to a slow cooling profile, was found. These findings imply that the increase in the T_{22} population in pork of halothane gene carriers is due to an acceleration in the *post mortem* reorganisation of water in intra-myofibrillar spaces and a subsequent increased formation of mobile extra-myofibrillar water, which partly elucidates the physical mechanism for reduced WHC in meat from halothane gene carriers.

2.4. The relation between transverse relaxation and *post mortem* events

During the *post mortem* period, several physical and biochemical processes that are characteristic for the conversion of muscles to meat are taking place. Superficially, the biochemical processes involve formation of lactate as a consequence of glycolysis under anaerobic conditions, whereas the physical processes on the structural level involve muscle contraction and on the biophysical level involve alterations in membrane properties. Offer and Knight[46] showed by microscopy that during the conversion of muscles to meat, 'gaps' appeared between muscle fibres and also between muscle fibre bundles, and the formation of drip was ascribed to the formation of water channels. Despite the fact that the findings of Offer and co-workers[46,47] form the basis for the present understanding of the underlying mechanisms of WHC, the microscopic method is associated with several disadvantages in sample preparation and allows only static pictures. In contrast, transverse relaxation provides an excellent tool for supplementary investigations as the method is non-destructive, which allows repeated measurements on the same sample, and provides a direct measure of the amount of mobile, extra-myofibrillar water.[28] Consequently, transverse relaxometry is a tool for dynamic visualization of changes in the water distribution in muscles *post mortem* simultaneously with the physical processes taking place, e.g., changes in membrane properties and muscle contraction leading to *rigor mortis*. By combining measurements of transverse relaxation, impedance and muscle contraction during the early *post mortem* period in porcine *m. longissmus dorsi*, simultaneous information about water mobility and distribution, membrane properties and physical events have been obtained.[70] Based on the results, the following hypothesis for the formation of drip has been proposed: immediately after exsanguination the muscle cells swell with a resultant increase in the T_{21} time constant, which is followed by expulsion of water from the cellular space into the extra-myofibrillar space with a resultant increase in the T_{22} water population and thereby the formation of extra-myofibrillar water compartments with mobile water found to reflect potential drip loss. Comparison of changes in the T_{22} water population and impedance characteristics (measurement of membrane properties) showed that the *post mortem* reorganisation of water is closely associated with membrane properties. Changes in the T_{21} attributes implied alterations in the structural organisation of the cellular water in the muscle simultaneous with *rigor* development, which is in agreement with a relationship between myofilament lattice spacing and transverse relaxation in pork.[50] In summary, this NMR approach has for the first time made it possible to suggest that a reorganisation of water in the muscles during their conversion to meat is taking place, and that this reorganization of water is related with physical processes taking place *post mortem*, i.e., contraction and membrane

destabilisation, hereby bringing further understanding of principal mechanisms in the formation of drip in meat.

Transverse relaxation measurements have also made it possible to further elucidate the effects of the cooling profile during the conversion of muscle to meat,[69] which is known to affect WHC of pork.[71–78] Accordingly, the chilling regime has been shown to affect the progress in the relaxation rate of the T_{21} population, probably due to differences in both conformational changes of the myofibrillar proteins, and differences in the structural organisation of cellular water *post mortem*. In addition, a pronounced effect on the progression in the T_{22} population as a function of cooling was also established, which corresponds to a difference in the balance of cellular and extra-cellular water early *post mortem*, and accordingly reflects differences in membrane integrity as a function of the cooling profile. These are interesting findings, as the biophysical effects of the *post mortem* temperature profile are poorly understood at present.

2.5. Longitudinal relaxation measurements in *post mortem* muscle and meat

In contrast to transverse relaxation, longitudinal relaxation in *post mortem* muscle and meat is in most studies reported to be mono-exponential.[17–18,29,49,79–83] This implies that exchange rates are fast on the time scale of longitudinal relaxation. However, with the use of two-dimensional relaxation techniques to evaluate longitudinal and transverse relaxation simultaneously, English *et al.*[84] and Saab *et al.*[34] have succeeded in demonstrating distinct T_1 values in spin groups characterised by longer and shorter T_2 values, respectively, which implies that despite being more complicated to measure, longitudinal relaxation also contains valuable information about structural organisation of different water populations. The use of T_1 measurement in meat science is scarce. Currie *et al.*[82] measured longitudinal relaxation continuously on rat muscle samples during *rigor* development and noticed a sudden change in the relaxation rate *post mortem*, which was suggested to reflect *rigor* development. Cameron *et al.*[85] likewise measured longitudinal relaxation continuously on rat muscles early *post mortem*, but did not observe any change in the relaxation time during the measuring period. Using the same approach, Farouk and Swan[86] measured longitudinal relaxation in beef samples, which had been incubated *pre rigor* at various temperatures in the range of 0 to 35°C, and showed that T_1 decreased with increasing incubation temperature. The result was explained in terms of increased protein denaturation with increasing incubation temperature, but as the moisture content in samples was almost inversely proportional to T_1, the relaxation results might as well express the total water content. Li *et al.*[87] studied the effect of marination with various phosphates

by measurement of T_1 relaxation in uncooked and cooked meat. A range of T_1 values was observed with the different phosphates, which could be ascribed to different moisture content. T_1 was markedly lower in cooked samples, which was explained by water loss during cooking. Dawkins *et al.*[88] investigated the effect of additives in meat batters by measurement of longitudinal relaxation, and thereby succeeded in demonstrating that oat gum and otrium have different water-binding properties, as relaxation times in batters with added otrium were lower compared with batters with added oat gum. In general, a decrease in relaxation times was observed with increasing concentration of additive (0–2%), which could be ascribed to lower moisture content.

In conclusion, compared with transverse relaxation, no impressive results regarding longitudinal relaxation measurements in meat science have been demonstrated at present, as it has mainly been shown that T_1 expresses differences in water content. Taking into consideration the faster acquisition of transverse relaxation times compared with longitudinal relaxation, and the more 'hidden' features in the longitudinal relaxation, it can be speculated if longitudinal relaxation will ever gain same attraction in meat science as transverse relaxation.

2.6. Studies on cooking and processing

The temperature profile during cooking is known to affect the amount of fluid loss from the meat.[89–90] Considering the possibilities of NMR relaxometry, this technique provides a tool for studying how the temperature is accompanied by shifts in water characteristics during cooking. Measuring T_2 relaxation in pork cooked to various temperatures in the range of 40°C to 90°C Tornberg and Larsson[91] showed that the amount of free water, i.e., water with a relaxation time of more than 1 s, increased steadily with increasing temperature, which corresponds to water being expelled with increasing temperature. Later, continuous relaxation measurements during the cooking process have provided further insight into the topic. Borisova and Oreshkin[92] studied transverse relaxation during cooking of meat aged at various periods and analysed the CPMG decay by decomposing it into five components. It was found that both before and during cooking the percentage of relaxation described by T_{21} (time constant of approximately 40 ms) was highest in pork aged for 48 h. It is worth noting that protein intrinsic fluorescence showed that pork aged for 48 h had the highest temperature at the onset of coagulative rearrangement in myofibrillar proteins, which implies that the amount of water located in the myofibrillar protein matrix upon cooking depends on the structural reorganisation of the myofibrillar network during cooking. In addition, it was observed that the T_{21} component splits into two components during cooking, which results in the formation of a relaxation component with a relaxation time of approximately

10–20 ms. At which temperature the splitting occurred depended on the length of the ageing period before cooking. Micklander *et al.*[93] studied transverse relaxation during cooking of meat using a more realistic cooking temperature profile, and reported appearance of a new water population around 40°C, which was hypothesised to reflect either expulsion of water from the myofibrillar lattice or the formation of a porous myosin gel. A more extensive transverse relaxation study[94] following the water distribution during cooking in a considerable number of pork samples of two qualities, of which one was known to give rise to higher cooking loss and lower technological yield,[56,95–101] revealed major changes in transverse relaxation characteristics at 43°C and 56°C, with the shift around 43°C being significantly affected by fresh meat quality.[102] The severe shift in water properties around 43°C was suggested to reflect myosin denaturation, hereby showing an effect of fresh meat quality on myosin denaturation characteristics and related water properties during cooking. Future studies relating the observed relaxation characteristics to the sensory attributes of the meat may give further insight into the relationship between fresh meat quality and juiciness.

It has long been recognised that the ability of meat to bind water increases upon addition of salt,[103] which can be explained by a swelling of the myofibrils.[104] Tornberg and Nerbrink[105] measured T_2 relaxation in isolated myofibrils, which had been placed in either an isotonic solution, a 0.4 M or a 0.8 M NaCl solution. In the isotonic solution, the relaxation decay was described by two relaxation times of approximately 35 and 120 ms, in the 0.4 NaCl solution the relaxation was dominated by the relaxation time of 120 ms, and in the 0.8 NaCl solution the relaxation was described by time constants of approximately 150 ms and 350–650 ms, and the differences were ascribed to different degrees of swelling. In the above-mentioned studies by Borisova and Oreshkin[92] and Bertram *et al.*[102] using continuous measurements during cooking, the effects of curing were also investigated. Both studies found that curing affected the different relaxation components. In contrast to uncured meat, Borisova and Oreshkin[92] found that meat aged for 96 h had the highest percentage of relaxation described by the T_{21} component, whereas the ability to retain this component was lower for meat aged for 48 h. A recent investigation showed that a major change in transverse relaxation characteristics taking place at 56°C in uncured meat was delayed to 63°C in the presence of salt.[102] The change was suggested to reflect the onset of collagen shrinkage and the subsequent longitudinal shrinkage of the meat, and accordingly the result implies an effect of curing on the structural changes taking place during cooking. The knowledge of biophysical effects of curing is very limited at present, and the results obtained using NMR relaxometry must be considered to be novel in relation to obtaining a better understanding of water organisation and structural effects of curing.[102]

Incorporation of non-meat ingredients, such as gums or proteins, into processed meats has been shown to stabilize emulsions and increase fat and

water retention.[106–110] Dawkins *et al.*[88] investigated the influence of addition of oat gum and oatrim to meat batters by measurement of transverse relaxation. In general, a decrease in relaxation times was observed with an increasing concentration of additive (0–2%), but while the transverse relaxation in samples with added otrium was directly inversely proportional to the otrium concentration, the response to oat gum concentration on relaxation was more complex, suggesting that besides affecting the total moisture content, addition of gum also affects the mobility of water in meat batters. The study by Dawkins *et al.*[88] demonstrates that relaxation studies can reveal valuable information about water properties in meat batters in relation to e.g., additives, and accordingly the area deserves further attention in the future in relation to obtaining a better understanding of optimization of water-binding in processed meats and meat batters.

Freezing is very a common way of preserving and storing meat. Recently NMR relaxometry was used to study changes in water mobility upon frozen storage of beef, and bi-exponential fitting of the transverse relaxation measured in the thawed meat showed decreases in the T_{21} population with increasing period of frozen storage.[111] This result is consistent with increases in squeezable drip and decreases in the intercellular water fraction. Accordingly, it was demonstrated that information regarding structural changes and reorganisation of water during frozen storage could be obtained using NMR relaxometry.

2.7. NMR relaxometry to predict/assess meat quality traits

Assessment of meat quality is of great interest both for the meat industry and consumers, as it enables differentiation among different qualities, may potentially increase yields and guarantees a specific quality. Assessment of WHC using NMR relaxometry is mentioned above. Beside the use of transverse relaxation measurements to obtain a further understanding of the factors and changes during cooking/processing, transverse relaxation measurements have also been applied to predict technological meat quality parameters such as cooking loss, Napole Yield and frying loss. Table 2 gives an overview of the correlations obtained between transverse relaxation measurements performed on fresh meat and technological quality traits. The correlations with cooking loss are not as high as those reported for WHC in fresh meat (Tables 1 and 2); however, compared with alternative measurements in fresh meat, e.g., pH and WHC, T_2 relaxation has been shown to be superior.[120] Overall, the results demonstrate the novelty of relaxation measurement for characterising water characteristics in meat. The results summarized in Table 2 include both correlations obtained using the whole transverse relaxation decay curve in a multivariate regression analysis,[59,112] and using specific information from discrete exponential fitting on the transverse

Table 2. Results from studies of the correlation between proton relaxation in fresh meat and subsequent technological traits

Study	Relaxation parameter	Parameter	N^a	Correlation coefficient
Renou *et al.*[22]	T_1	Cooking loss	98	0.35
Renou *et al.*[22]	T_2	Cooking loss	98	0.55
Fjelkner-Modig and Tornberg[113]	T_2	Frying loss	6	0.85
Brown *et al.*[59]	T_2	Cooking loss	44	0.43
Bertram *et al.*[112]	T_2	Cooking loss	102	0.64
Bertram *et al.*[112]	T_2	Napole Yield	102	0.58

[a]Number of samples included in the study.

relaxation.[22,113] Using the latter approach, the highest correlation was obtained with the fraction of relaxation described to the T_{22} time constant, which corresponds to the finding that the lowest cooking loss is obtained when a high amount of the water is located in the myofibrillar protein matrix.

At present, studies of correlations between NMR relaxation and sensory attributes of the meat are very limited. However, Fjelkner-Modig and Tornberg[113] found high correlations between T_2 relaxation and both juiciness and toughness of pork, even though the correlations were based on data from only six animals. Brøndum *et al.*[114] investigated the use of NMR relaxation for prediction of sensory attributes of pork stored at various periods in order to facilitate warmed-over flavour, and found high correlations between both T_1 and T_2 data and sensory parameters such as astringent, monosodium, salt and sour. Further studies are indeed needed to evaluate if NMR relaxation can be used to predict the sensory quality of meat.

Finally, NMR relaxometry has also been used in the determination of composition of meat and meat products. Correlations between relaxation parameters and fat content in minced meat and meat emulsions,[115–117] protein content in fresh meat[115,118] and moisture content in sausages[119] have been demonstrated; results from fat determinations are summarised in Table 3.

3. APPLICATIONS OF NMR IMAGING IN MEAT SCIENCE

Since its introduction in the early 1980s, NMR imaging has gained widespread use as a diagnostic tool in medicine. The possibilities for using the technique to obtain two- and three-dimensional images without damaging the investigated object also make the technique interesting in meat science and food science in general. Within meat science, NMR imaging has been applied for studying composition (fat and water content, connective tissue, fibre

Table 3. Results from studies of the correlation between proton relaxation in meat/meat products and fat content

Study	Product	Range of fat content (%)	Pulse sequence	N^a	Correlation coefficient
Renou *et al.*[115]	Minced meat	5–37	Spin-echo	11	0.999
Renou *et al.*[115]	Emulsion	25–38	Spin-echo	21	0.957
Pedersen *et al.*[116]	Minced meat	2–14	Spin-echo	47	0.61
Pedersen *et al.*[116]	Minced meat	2–14	CPMG	47	0.98
Pedersen *et al.*[116]	Minced meat	2–14	Diff-CPMG	47	0.99
Pedersen *et al.*[116]	Minced meat	2–14	Diff-CPMG	47	0.99
Sørland *et al.*[117]	Minced meat	1–14	m-PFGSE	42	0.98

[a]Number of samples included in the study.

types), curing and freezing. The status of NMR imaging in meat science is described briefly in the following.

3.1. Composition and size

Quantity and distribution of fat in the carcass and in the meat is a major issue for the meat industry. Whereas subcutaneous fat on the carcass is undesirable, the presence of intra-muscular fat may be considered a quality attribute as it affects the sensory attributes of the meat. Mitchell *et al.*[120] demonstrated how NMR imaging can provide information about the relative amount of fat within an animal using NMR imaging. Their approach can be used to estimate fat and meat content at species level. However, within muscles and in meat products where fat and meat are far less distinguishable, other methodologies are necessary. Duce *et al.*[121] attempted to determine water and fat quantitatively in meat/fat emulsions by a so-called modified Dixon-experiment, in which the chemical shift difference between fat and water is used to differentiate between the two compounds in the images. The technique involves the acquisition of two data sets where the contribution from a particular compound is eliminated in one image by adjusting the 180° pulse. From the water images, water intensities were determined, and a high correlation to water content determined by subsequent oven drying was demonstrated. In contrast, fat content could not be determined from the images, which most probably can be explained by too fast transverse relaxation times of the saturated fat, hence it did not contribute to signal intensity. Sophisticated image processing may improve the determination of composition from NMR images, as demonstrated by Ballerini *et al.*,[122] who presented a segmentation technique for determination of fat content in NMR images of beef.

Beside fat, the content and distribution of connective tissue in the meat is also considered to be of importance as these contribute to meat toughness. Based on differences in magnetic susceptibility compared with the surrounding muscle tissue, Bonny *et al.*[123] succeeded in visualizing the distribution of connective tissue in beef muscles. Clear differences in the organisation of connective tissue were demonstrated between two different muscle types.

A characteristic of muscles is their diversity, which among other factors is due to their different composition of fibre types. Bonny *et al.*[124] investigated NMR attributes of different muscles by ^{1}H NMR imaging on legs of anaesthetized rabbits, which allowed characterisation of five different muscles with various fibre type composition. T_1 and T_2 values were calculated from the obtained images, and the effects of muscle type on relaxation times were observed: a high content of oxidative fibres resulted in general in longer T_1 and T_2 values. The exact reason for this remains unknown, but it has been suggested to reflect a larger extra-cellular volume in these fibres.[125] However, within the same muscle, the opposite has also been found:[126] longer T_1 and T_2 values with increasing content of glycolytic fibres, and therefore other factors such as fat content, and characteristics of muscle proteins, e.g., myosin isoforms/hydrophobicity, probably also contribute to differences between different muscle types. In addition, total protein content probably also plays a role as indicated in a relaxation study on *post mortem* muscle.[53]

During growth, the size of muscles increases, and therefore determination of muscle size is of interest in order both to evaluate growth performance and in the classification of carcasses. Mitchell *et al.*[120] determined the size of the muscle *pectoralis* by ^{1}H NMR imaging on anaesthetized chickens. The volume of the muscle was determined using a three-dimensional reconstruction programme on images of cross-sections of *m. pectoralis*, and subsequent comparison with the value obtained upon dissection and weighing revealed a high correlation between the two methods ($r = 0.99$). Moreover, Scholz *et al.*[127] determined the volume of *m. longissimus dorsi* and overlaying fat by ^{1}H imaging on anaesthetized pigs of known halothane genotype, and showed significantly larger *longissimus* muscle in halothane gene carriers compared with non-carriers at 10 kg body weight, hereby confirming the improved growth performance in pigs carrying the halothane gene.[61–63,65] The ability of NMR imaging to show significant differences in the muscle size in 10 kg pigs demonstrates that NMR imaging can determine muscle size with fine accuracy, and the method can probably compete with dissection, which is time-consuming, labour-intensive and partly subjective, which makes it hard to standardize.

In conclusion, the studies reporting NMR imaging for determining factors such as composition and size demonstrate the feasibility for using NMR imaging to determine these parameters. However, all studies are of preliminary character, and further studies and development of less expensive NMR

imaging equipment are necessary before the technology eventually can be implemented as a routine method in these areas.

3.2. Curing

Curing increases the ability of meat to take up additional water.[103] Foucat *et al.*[128] studied the effect of brine injection in *pre rigor* rabbit muscles by continuous ^{1}H NMR imaging before and during *rigor* development. From T_2-weighted images, T_2 maps were constructed, and the progression in T_2 relaxation times in different regions was calculated. The diffusion of brine into the muscle was found to be depicted in a decrease in T_2. Histograms showing distribution of pixels in different T_2 intervals were also created, which revealed a more heterogeneous distribution of T_2 relaxation times in brine-injected muscles compared with control muscles. Diffusion imaging revealed larger standard deviation on diffusion coefficients in brine-injected muscles compared with control muscle, indicating heterogeneity in diffusion times. The heterogeneity reported probably reflects an incomplete diffusion of NaCl and is of no further interest in itself; however, the study showed that NMR imaging can be used to follow the progression in curing through a decrease in T_2. Guiheneuf *et al.*[129] performed ^{1}H NMR imaging on pork cured in brine solutions of various strengths (50, 100, and 190 mg NaCl per gram solution). From obtained images, T_1, T_2, proton density, and magnetization transfer rate were calculated and compared with water content and NaCl concentration in the samples. The parameters T_1, T_2, and the proton density decreased and the magnetization transfer rate increased with decreasing water content and higher NaCl concentration. It was concluded that the effect of curing on T_1 could be related to swelling, and that the effect on magnetization transfer rate could be ascribed to structural changes in the proteins. In contrast, the situation for T_2 was considered to be more complex, as sodium chloride may increase magnetic susceptibility, and because T_2 is affected by diffusion through the magnetic field. Curing of pork with and without mechanical tumbling was recently studied using NMR imaging and increases in calculated T_2 relaxation times were observed after both brine injection and tumbling.[130] In addition, a more evenly distribution of T_2 relaxation times was observed when comparing images acquired in the beginning and at the end of the tumbling process, resembling a more homogeneous distribution of the brine after 6 h tumbling.[132] Using a different approach, Guiheneuf *et al.*[131] have also added manganese ions to meat in an NMR imaging study of pork curing. Manganese ions are paramagnetic and therefore enhance the relaxation of water protons. The effect of manganese on the water proton relaxation was found to depend on sodium chloride concentration, and therefore it was concluded that manganese ions could be used as a sensitive probe to study the progress of curing. However, the fact that the relaxation of water protons

depends on both the degree of swelling and the manganese ion concentration complicates the situation and an eventual quantification.

In conclusion, the studies reported at present show that NMR imaging is a promising technique for obtaining further insight into the curing process in a non-invasive way, which is an area where the knowledge is scarce.

3.3. Pressure treatment

The tenderness of meat is an important quality trait.[132] Accordingly, methods for upgrading tough meat are of interest. The combination of heat treatment and pressurization has been found to have a beneficial effect on the mechanically determined toughness of meat,[133] however, with the major drawback that the meat is perceived as less juicy.[134] Therefore, a further exploitation of this method requires a better understanding of the process. Using ^{1}H NMR imaging on pressured and non-pressured cooked beef the combination of heat and pressure treatment was investigated in detail.[135] T_2 maps were constructed from the obtained NMR images, and a difference in transverse relaxation revealed alterations in water characteristics of pressured, cooked meat compared with cooked meat, which probably can explain the altered juiciness of pressured meat. A simultaneous investigation of ageing (1, 3, 8, and 16 days) prior to the pressure treatment and cooking showed decreasing transverse relaxation times with increasing length of the ageing period independent of treatment, hereby implying altered interactions between muscle proteins and water as a consequence of ageing. However, further investigations are needed to explore the potential of NMR imaging in obtaining a basic understanding of water characteristics of importance for meat quality.

3.4. Freezing

Freezing is an important preservation technology. During freezing, formation of ice crystals takes place, which causes damage of cell membranes.[136,137] This alters the structure of meat, which again has been found to affect the water-holding capacity of the meat.[138] ^{1}H NMR imaging has been applied to elucidate the effect of freezing of meat. Guiheneuf *et al.*[139] and Hall *et al.*[140] showed that NMR imaging could determine if meat has been frozen or not due to increases in magnetization transfer rate and decreases in T_1 upon freezing and thawing. The increase in magnetization transfer rate is presumably a result of protein denaturation, and the decrease in T_1 upon freezing/thawing probably reflects reduced mobility of proteins due to aggregation and thereby enhanced cross-relaxation, resulting in a reduction in T_1. The effect of water loss during thawing was not discussed in this study,

but could also be expected to contribute to a decrease in T_1 upon freezing/thawing. Effects of freezing/thawing on NMR imaging properties have also been investigated in fish muscles.[141,142] In conclusion, the studies reveal that NMR imaging, eventually relaxometry, can be used to determine if meat has been frozen or not, hereby making this approach a potential future tool in authentication.

In the study by Guiheneuf *et al.*,[139] no increase in the magnetisation transfer rate was observed during freezing storage (from 2 weeks to 2 months at $-18^{\circ}C$), implying that length of freezing period has no impact on the degree of denaturation. In contrast, Lee *et al.*[142] found decreases in signal intensity from 1 day to 30 days upon frozen storage of beef at $-20^{\circ}C$, which was ascribed to further ice and/or fat crystallization during frozen storage. Accordingly, although the properties of the proteins are not severely affected, alterations in physical water properties may still continue during frozen storage.

Kerr *et al.*[145] demonstrated the advantage of the non-invasive character of NMR imaging to follow the progression of freezing in whole chicken legs, as freezing was detected by decrease in signal intensity. No further quantification of the freezing profile was attempted, but a novel method for studying the intrinsic freezing process non-invasively on a heterogeneous material was demonstrated.

3.5. ^{1}H imaging for studying structural organisation of water

As discussed previously, NMR relaxometry has been proven to be an excellent technique to obtain knowledge regarding the structural organisation of water in muscle/meat, which is highly related to important meat quality traits. Transverse relaxation visualizes mobile, extra-myofibrillar water that can be considered potential drip loss,[28] which is consistent with the observation of water channels between fibres and fibre bundles by microscopy.[46,47] These water channels containing mobile water have been reported to be approximately 20–50 microns,[47] and accordingly it is expected that they can be visualized using NMR imaging. However, at present only one study aiming at visualizing these water channels by NMR imaging has been reported.[144] Bonny and Renou[144] characterised two different bovine muscles using diffusion tensor imaging, which provides information about diffusion in all dimensions. Hereby the degree of anisotropy of the diffusion is also obtained, and areas in muscles with water reservoirs characterised by longer T_2 values and more isotropically and free diffusion were observed, which probably reflects extra-myofibrillar water channels. The results are promising, and future studies aiming at studying the *post mortem* development and progression in these water reservoirs could be of interest in order to improve

the understanding of the significance of this structural reorganisation of water within the muscle.

3.6. ^{23}Na imaging

Elucidation of the progressive changes in NaCl distribution in meat during curing is important in order to ensure a rapid and homogeneous distribution of NaCl in the final product. A non-destructive and non-invasive method that traces the NaCl concentration at different positions in the meat is required in order to follow this progress. ^{23}Na NMR imaging has the potential to measure sodium concentrations as a function of both position and time. Renou *et al.*[145] followed the effect of brine injection in *pre rigor* rabbit muscles by subsequent continuous ^{23}Na NMR imaging. High signal intensity in the areas close (approx. 7 mm in diameter) to the artery was observed early after NaCl injection, and even after 6 h, the distribution of sodium was heterogeneous. ^{23}Na NMR imaging was also carried out after 24 h brining in tumbled and non-tumbled hams, which still displayed a heterogeneous distribution of sodium, in particular in the non-tumbled hams. However, independent of processing method, the distribution of sodium became much more homogeneous after cooking. One-dimensional ^{23}Na NMR imaging has also been carried out on pork samples during brining.[146] This allows the diffusion of sodium ions to be visualised in space and time. Calibration of sodium concentration provided possibilities for both qualitative and quantitative information regarding the diffusion of sodium in the meat during brining. The diffusion coefficient was found to decrease exponentially with increasing sodium concentration, which was suggested to reflect increased protein–ion interactions with increasing NaCl concentration. Accordingly, the study demonstrated the potential use of NMR imaging as a quantitative approach to understand the curing process, and thereby that the method is a potential tool to optimize an important technology in the meat industry.

4. APPLICATIONS OF NMR SPECTROSCOPY IN MEAT SCIENCE

Within meat science, NMR spectroscopy has mainly been carried out on ^{1}H, ^{13}C and ^{31}P, which all are nuclei with a nuclear spin of $I = 1/2$. Most relevant data on each nucleus will be reviewed in the following.

5. ^{31}P NMR SPECTROSCOPY

The most widely used nucleus in biological NMR spectroscopic studies is the ^{31}P nucleus. The reason is that its natural abundance is 100%, and its

relatively high sensitivity. Moreover, the nucleus plays an essential role in muscle energy metabolism. Burt *et al.*[148] first demonstrated that ^{31}P NMR spectroscopy enables detection of the various nucleoside phosphates and phosphocreatine (PCr), and the *post mortem* breakdown of these metabolites to inorganic phosphate can be followed in intact muscles as demonstrated early in frog,[148] rabbit,[149] and rat,[150] and in bovine muscle.[151] In addition, intra-cellular pH can be estimated from the chemical shifts of ATP, inorganic phosphate and sugar phosphates,[148,150,152,153] the chemical shift of inorganic phosphate being the most applied in muscles, because its pK-value allows determination of pH within the physiological range. ^{31}P NMR spectroscopy has also been applied within other areas of meat science, e.g., on different species and fibre types, studying the effect of dietary supplementation, the halothane genotype, slaughter factors in terms of electrical stimulation, stunning and chilling, different meat qualities, processing and finally perfusion studies. These will be described in detail in the following.

5.1. Species and fibre type

The first attempts to introduce ^{31}P NMR methodology in meat science involved qualitative studies comparing rates of metabolism 15 min[154] and 1 h[155] *post mortem* in porcine, ovine, and bovine muscles. These concluded that rates varied as follows: porcine muscle > ovine muscle > bovine muscle. However, as no detailed information is mentioned on *peri mortem* factors such as pre slaughter stress, stunning method, cooling procedure etc., which are all known to have strong influence on *post mortem* metabolism,[156] these preliminary reports appear to be non-conclusive although they demonstrate the potential of NMR spectroscopy in meat science.

Renou *et al.*[157] performed the first crucial ^{31}P NMR experiments with relevance for meat science by intensely following *post mortem* metabolism in three different rabbit muscles, an oxidative (*internal conoidal bundle*), a glycolytic (*m. psoas major*) and finally a muscle with intermediate fibre composition (*m. gastocnemius caput medialis*). The concentrations of metabolites were estimated using an internal standard followed by estimation of areas of signals. Kinetics showed that the rates of ATP and PCr degradation were highest in the purely oxidative muscle and lowest in the purely glycolytic muscle. Likewise, kinetics of pH-decrease, determined from the chemical shift of inorganic phosphate, demonstrated that the highest decrease rate in pH took place in the glycolytic muscle, whereas the lowest decrease rate in pH was observed in the oxidative muscle. In addition, the effect of varying the temperature between 15, 20, and 25°C on kinetics of metabolism and decrease in pH was studied, and as expected, rates increased with increasing temperature, and it is worth noting that the temperature effect was more pronounced in the oxidative muscle than in the glycolytic muscle.

Muscles with different fibre type composition have also been compared 15 min *post mortem* in chicken and pigeons.[153] Moreover, Azuma *et al.*[158,159] followed phosphorus metabolism *post mortem* in oxidative and glycolytic muscles of rat and goat. All these studies were in agreement with the study by Renou *et al.*,[157] who found lower initial levels of ATP and PCr and faster *post mortem* degradation rates in the oxidative muscle compared with the glycolytic muscles. However, in contrast to Renou *et al.*,[157] the decrease in pH was found to be fastest in the oxidative muscles in both rat and goat. This is surprising considering that glycogen levels are higher in glycolytic muscles, and furthermore, it is also in contrast to what has been reported in *in vivo* on muscles during exercise using ^{31}P NMR spectroscopy.[160] The explanation could be differences in buffering capacity between muscles.

In conclusion, ^{31}P NMR spectroscopy has already displayed metabolic differences between the muscle types, which could contribute to a better understanding of observed variations in properties among different muscle types and the significance of muscle type for meat quality.

5.2. Metabolic studies of importance for meat quality

Genetic[63–69] and management factors such as feeding[161–166] and slaughter procedures[75,77,78,80,167–172] are all known to affect meat quality due to their action on the *post mortem* processes. Over the years ^{31}P NMR spectroscopy has been a valuable tool to obtain a basic understanding of several of these factors' significance for *post mortem* metabolism. In the following, ^{31}P NMR spectroscopic studies within this area are reviewed.

Pork is often classified in three different qualities: Normal, PSE (pale soft exudative) meat, characterised by a low WHC, DFD (dark firm dry) meat, characterised by a high ultimate pH and a high WHC. PSE develops in particular as a result of short-term stress immediately before slaughter, which increases the *post mortem* rate of glycolysis and temperature, whereas DFD is often a result of long-term stress before slaughter causing depletion of glycogen stores.[156,169,173,174] Miri *et al.*[175] showed that a ^{31}P NMR spectrum acquired 30 min *post mortem* on porcine muscles could differentiate between meat classified as either PSE, DFD, or normal. Firstly, this result demonstrates the importance of *post mortem* energy metabolism on final meat quality, and secondly, it demonstrates that ^{31}P NMR spectroscopy early *post mortem* can provide information, which can be used in the prediction of the final meat quality.

An area where ^{31}P NMR spectroscopy has been widely used is in the studies on the phenomenon of malignant hyperthermia. The syndrome is initiated by halothane and therefore also referred to as halothane susceptibility, and the gene associated with the defect is named the halothane

gene.[176] In pigs, the syndrome is also called porcine stress syndrome, and it is associated with increased stress susceptibility, high incidences of death during transport and inferior meat quality.[63–69] Using ^{31}P NMR spectroscopy, the response to halothane has been examined *in vivo* in anaesthetised pigs of known halothane genotype, and it was found that after exposure to halothane, PCr and pH decreased in muscles from pigs carrying the halothane gene.[127,177–181] If the pigs were killed after exposure to halothane, the rate of the PCr and pH decrease *post mortem* was accelerated in muscles from halothane gene carriers compared with non-carriers,[127,179,182] revealing a strong metabolic response on halothane exposure both *in vivo* and *post mortem*. Also in the absence of halothane exposure, altered metabolic characteristics have been demonstrated in muscle biopsies of halothane gene carriers by ^{31}P NMR spectroscopy, as accelerated decreases in ATP, PCr, and pH were found compared with non-carriers.[69,182] Moreover, *in vivo* measurements have revealed different levels of phosphomonoesters muscles from the different genotypes.[177] ^{31}P NMR spectroscopy has also been performed on muscle strips from halothane gene carriers and non-carriers incubated in Krebs' solution.[183] During mechanical stimulation, pH and PCr fell severely, whereas ATP remained constant in muscle strips from halothane gene carriers.[183] In summary, ^{31}P NMR spectroscopy has verified differences in metabolic response to halothane between halothane gene carriers and non-carriers. One of the questions that still needs to be answered is whether the halothane response found in these ^{31}P NMR spectroscopic studies can be compared with the stress situation experienced by pigs in connection with slaughter. However, no such investigations have been reported in literature.

Dietary supplementation of vitamin E has been claimed to improve fresh pork quality, in particular water-holding capacity[161–163] and colour stability.[161,184,185] However, other studies have not been able to confirm this effect on water-holding capacity[164–166,186,187] or colour stability.[186,188–190] The effect of vitamin E has been suggested to contribute to the preservation of muscle cell membrane integrity by preventing the oxidation of membrane phospholipids during storage.[161,162,191] However, effects on muscle glycogen stores have also been reported,[166] and the exact action of vitamin E in relation to meat quality is still unknown. Lahucky *et al.*[187] investigated *post mortem* energy metabolism in the muscles of pigs fed a diet supplemented with vitamin E using ^{31}P NMR spectroscopy, and found increased levels of PCr 15 min *post mortem*, hereby revealing a possible effect of vitamin E supplementation on phosphorus metabolism, which can contribute to clarifying the action of vitamin E.

Dietary magnesium supplementation prior to slaughter has been reported to have a positive effect on meat quality,[192–198] which can be explained by the ability of magnesium to counteract the effects of catecholamine in stress situations.[199–200] Moesgaard *et al.*[201] investigated how dietary

magnesium supplementation affected *post mortem* energy metabolism using ^{31}P NMR spectroscopy and found a significantly reduced rate of PCr degradation in muscles from three of the four investigated magnesium-fed pigs. This explains the positive effect of magnesium supplementation on meat quality.

Despite much effort to determine the most preferable stunning method from an ethical point of view, this subject is still a matter of dispute.[202–205] Moreover, a basic understanding of the effect of stunning on metabolic processes of importance for meat quality is hardly available. The effect of stunning method on *post mortem* metabolism in muscles from pigs, which had been either CO_2-stunned, electrically stunned, stunned by captive bolt pistol followed by pithing or killed under anaesthesia, was recently investigated using ^{31}P NMR spectroscopy.[206] Significant differences in both the rate of energy metabolism and the pH decrease *post mortem* between the different stunning methods were demonstrated. The differences in rate of *post mortem* metabolism as a consequence of stunning method could be linked to differences in meat quality assessed as water-holding capacity. A noticeable result of the study is that the CO_2-stunning was found to be more stressful than anaesthesia, revealing that despite the fact that it can be considered to be moderate compared with other stunning methods, killing under CO_2-stunning is still not the most gentle method, which should be considered in connection with optimising stunning from both a meat quality and an ethical point of view.

Electrical stimulation of carcasses, which originally was introduced in lamb slaughter in New Zealand and Australia back in the 1950s, is to a great extent used in sheep and cattle slaughter in order to accelerate *post mortem* glycolysis and thereby prevent cold shortening if rapid chilling is applied.[161,167,168] Vogel *et al.*[151] used ^{31}P NMR spectroscopy to compare *post mortem* metabolism and pH development in stimulated and non-stimulated beef muscles and demonstrated qualitatively increased rates of metabolism in stimulated compared with non-stimulated muscles.

Several studies have reported improved WHC of pork upon tunnel chilling compared with batch chilling[75,77,78,80] without any further elucidation of the mechanisms behind this positive effect on WHC. *Post mortem* energy metabolism and pH development in porcine muscles exposed to a cooling profile similar to either a commercial batch or a tunnel chilling were studied by ^{31}P NMR spectroscopy.[207] Minor differences in *post mortem* rates of PCr and ATP degradation between cooling profiles were found. However, the pH progression was strikingly different in muscle samples exposed to different cooling profiles: a difference of up to 0.25 units in pH was observed. Noteworthy, theoretical considerations revealed that the difference in pH could almost entirely be ascribed to a temperature effect on muscle buffering capacity, while any contribution from an effect on rate of lactate formation was diminishing. It should be noted that the pigs used in the study were

anaesthetised before killing, and consequently the decrease in pH was much slower than what is observed when pigs are slaughtered under commercial conditions. Since the temperature effect on muscle buffering capacity has only been investigated in the pH range between 6.9 and 7.1,[208] it can therefore be questioned if the use of anaesthesia reflects the commercial situation where other temperature effects might be dominating. However, the results indicate the importance of temperature effect on muscle buffering capacity, which is a subject that has otherwise not been given much attention and which cannot be understood in further details without the use of NMR spectroscopy. Therefore, this area should be paid attention in the future.

Hot boning involves cutting of carcasses prior to *rigor* development, and is sometimes used because it saves energy and reduces the need for cold room capacity, as only muscles are frozen. Lundberg *et al.*[155] studied energy metabolism using ^{31}P NMR spectroscopy during and after thawing of *pre rigor* frozen bovine samples, and it was estimated that the course of *post mortem* metabolism in thawing meat that had been frozen *pre rigor* was similar to that of fresh meat. Nevertheless, when the sample reached 0°C, the changes took place in less than 1 h, which was about a factor 10 times faster than what is observed in fresh meat. The result thereby reveals strong effects on phosphorous metabolism of small temperature fluctuations around the freezing point, which is a finding that should be considered in the handling of hot-boned meat.

Using a different approach, and inspired by a technique developed by Meyer *et al.*,[209] Miri *et al.*[210] studied metabolism by ^{31}P NMR spectroscopy on isolated, perfused rabbit muscles. Metabolism could be kept constant during 2 h, and accordingly it was possible to compare the *in vivo* situation with the *post mortem* situation, as death was simulated by stopping perfusion. The effects of adrenaline administration and electrical stimulation were investigated. Hereby it was demonstrated how ^{31}P NMR spectroscopy can be used on isolated, perfused muscles to investigate how different factors/treatments affect metabolism both *in vivo*, *ante mortem*, and *post mortem*.[210] This must be considered interesting and promising, as it allows quantification of the effects of various pre-slaughter factors on metabolism, which otherwise is difficult with existing methods. Recently the metabolic effect of increased blood potassium levels, which are known to occur after heavy exercise, was also investigated in perfused muscles using ^{31}P NMR spectroscopy.[211] The study found no effects of increased [K^+] in the perfusate on the level of phoshorus metabolites in the muscles, implying that hyperkalemia can be excluded as a contributor to variations in metabolic rates *post mortem*.[211] ^{31}P NMR and ^{1}H NMR spectroscopic measurements have also been combined on isolated, perfused rabbit muscles, which enabled comparison of progression in lactate and pH *ante mortem* and *post mortem*.[212]

5.3. pH determination by ^{31}P NMR spectroscopy

Measurement of pH, both early *post mortem* and 24 h *post mortem*, is widely used as an indicator of meat quality (for a review, see Bendall and Swatland[213]), as it has been demonstrated to correlate with the water-holding capacity.[214,215] The pH in meat is traditionally determined by electrodes, which mainly measure the activity of H^+ ions in the extra-cellular space. However, this method is associated with certain problems. The invasive character by direct measurement with an electrode causes damage to the muscle cells and membranes, which may accelerate biochemical reactions such as glycolysis. In addition, the calibration of the electrode can also result in errors.[216] An alternative approach is to measure pH on homogenised meat samples in KCl/iodoacetate to stop glycolysis, which gives higher repeatability than probe measurements on intact muscles.[213] However, beside the drawback that measurements cannot be repeated on same tissue, this method also often compromises the temperature of the carcass, and therefore it does not reflect the actual situation, as pH is temperature-dependent.[217] Determination of pH by ^{31}P NMR spectroscopy, which is possible because chemical shifts of various compounds such as inorganic phosphate and ATP are pH-dependent, is a superior alternative due to the non-invasive nature of the technique. The principle behind pH determination by ^{31}P NMR spectroscopy is that the chemical shifts follow the so-called Henderson–Hesselbach equation:

$$\mathrm{pH} = \mathrm{pK} + \log\left(\frac{\delta - \delta_1}{\delta_2 - \delta}\right)$$

where for example for inorganic phosphate δ is the observed chemical shift of inorganic phosphate, and δ_1 and δ_2 are the chemical shifts for $H_2PO_4^{2-}$ and HPO_4^{3-}, respectively, which are determined by titration. A weakness of pH determination on *post mortem* muscles by NMR spectroscopy is that pK values depend on temperature and ionic strength. The temperature dependence is relatively easy to determine, and for inorganic phosphate it has been examined.[218] The dependence on ionic strength has also been analysed,[219] but in *post mortem* muscles it is more difficult to compensate for this effect, as the ionic strength at various points in time *post mortem* is not exactly known. Nevertheless, determination of pH by ^{31}P NMR spectroscopy is both highly advantageous as it is non-invasive/non-destructive, which makes repeated measurements on the exact same tissue location possible, and in addition, pH is determined at muscle temperature. The advantage of these features was demonstrated by continuous pH measurements by ^{31}P NMR spectroscopy on muscle samples exposed to two different cooling profiles.[207] The comprehensive pH profiles obtained made it possible to determine the effect of cooling profile on lactate formation and muscle buffering capacity, hereby

giving new basic knowledge regarding the progression in *post mortem* glycolysis, which could not have been obtained through traditional methods.

It is notable that pH determination by NMR spectroscopy in muscles has indicated pH heterogeneity as revealed by a broad resonance from inorganic phosphate.[149,151,153,157,175,220–222] This pH heterogeneity has been suggested to result from the presence of different fibre types.[151,160,220–222] However, the pH heterogeneity has also been suggested to reflect an intra-cellular compartmentalisation,[150–152,175] which is supported by the fact that Renou *et al.*[157] also found indications of pH heterogeneity in muscles consisting of only one fibre type. The topic is still controversial.

The pH determination by ^{31}P NMR spectroscopy mainly reflects intracellular pH, as the phosphorus compounds and metabolites essentially are located in the intra-cellular space.[223] However, NMR spectroscopy also provides possibilities for measuring extra-cellular pH using a pH-sensitive probe that remains extra-cellular. This has for example been demonstrated by Ojugo *et al.*,[224] who used the ^{31}P probe 3-aminopropyl phosphonate and the ^{19}F probe 3-[*N*-(4-fluoro-2-triflourmethylphenyl)-sulphamoyl]-propionic acid to determine extra-cellular pH in tumours.

5.4. Processing

Only a few ^{31}P NMR spectroscopic studies with the aim of obtaining a fundamental understanding of physical/chemical events through processing of meat have been reported. *Pre rigor* salting of meat is sometimes applied due to its positive effect on water-holding capacity,[225] and Bielicki *et al.*[226] investigated how arterial brine injection affected *post mortem* energy metabolism in rabbit muscles using ^{31}P NMR spectroscopy. *Post mortem* rates of PCr and ATP degradation were found to be enhanced by brine injection, and brine injection also caused pH heterogeneity as revealed by a broad resonance from inorganic phosphate.

Phosphate in combination with NaCl has a beneficial effect on the water-binding capacity of processed meat products; for a detailed description, see Schmidt.[227] The effect of phosphates is suggested to be alterations in pH or ionic strength, sequestration of metal ions, dissociation of actomyosin and depolymerisation of myosin.[103,104,228,229] However, before action, added phosphates must be hydrolysed by muscle phosphatases or non-enzymatically. Belton *et al.*[230] studied the hydrolysis of pyrophosphate and tripolyphosphate in comminuted chicken meat using ^{31}P NMR spectroscopy, and found that the rate of hydrolysis was dependent on the length of ageing period of the muscle as well as the presence of NaCl. Li *et al.*[231] studied the hydrolysis of various types of phosphates in intact chicken muscle with a similar approach by ^{31}P NMR spectroscopy and thereby demonstrated differences in rate of hydrolysis of various phosphates. The findings of these studies

are of interest in the optimisation of processing involving phosphate and NaCl addition and clearly show that ^{31}P NMR spectroscopy is a potential tool in this area.

6. ^{1}H NMR SPECTROSCOPY

In contrast to the numerous studies involving ^{31}P NMR spectroscopy, the number of studies in meat science including ^{1}H NMR spectroscopy is quite limited. ^{1}H NMR spectroscopy has the advantage of high sensitivity and high natural abundance of protons in biological tissue. However, a major disadvantage is the interaction from the large amount of water in biological tissue, which causes problems in the separation of single resonances. ^{1}H NMR spectroscopy has been applied to study the progression in metabolites *post mortem*, mainly lactate, and in attempts to determine meat composition, i.e., fat and water content. In addition, a kinetic study on extracted muscle pigment has been reported.

6.1. Metabolic studies of importance for meat quality

Formation and accumulation of lactate as a consequence of glycogen degradation under anaerobic conditions is the prime cause of the decrease in pH taking place *post mortem*. Taking into consideration the influence of the pH development on meat quality, methodologies for measuring formation of lactate are of great interest. A potential method is ^{1}H NMR spectroscopy, which can detect lactate; however, as mentioned above, problems arise because the signal from water hides signals from e.g., lactate. Using a water suppression technique, Lundberg *et al.*[232] demonstrated the feasibility of ^{1}H NMR spectroscopy to determine lactate concentrations in *post mortem* bovine muscles from the amplitude of the lactate methyl resonance ($\sim$1.3 ppm). Simultaneously, pH in the muscles was determined from the chemical shift of the histidine C_4 proton, which showed good agreement with lactate contents. Recently the first ^{1}H magic angle spinning (MAS) NMR spectroscopic study was performed to determine lactate in *post mortem* muscle samples.[233] In liquids, linewidths of resonances are relatively narrow because contribution from dipolar coupling and chemical shift anisotropy, the latter arising due to slow or restricted molecular motion, is averaged to zero because of rapid isotropic molecular motion. Contrary, in solids or semisolids including muscle/meat, molecular motion is restricted or anisotropic, and therefore this averaging does not occur, resulting in broader linewidths of the resonances. However, spinning at a high frequency at an angle of 54.44° (the magic angle) relative to the magnetic field reduces the effect of dipolar coupling to the signal linewidths markedly. Performing ^{1}H MAS NMR

spectroscopy (4 KHz spinning) continuously on rabbit muscle biopsies, the formation of lactate *post mortem* was followed and pH was determined from the chemical shift of the histidine C_4 proton.[233] Considering the possibilities in ^{1}H MAS NMR spectroscopy, this method might be a promising tool in the basic study of lactate formation in muscles exposed to different environmental stressors of importance in meat science. However, the effect of spinning at high frequencies on the muscle tissue needs to be investigated before conclusions on *post mortem* processes can be drawn. Consequently, further studies of the effects of spinning should attempt to elucidate the potential of the method.

6.2. Composition

Composition of the meat, i.e., water and fat content, is of major interest to the meat industry as it is used in classification and as a criterion in the payment to pig producers. In addition, consumers' increasing demand for low fat and the significance of intra-muscular fat on sensory attributes of meat make determination of composition a central topic. *In vivo* ^{1}H NMR spectroscopy has been performed on turkeys, and using the lipid methylene resonance ($\sim$1.3 ppm) and the water resonance ($\sim$4.8 ppm) for determination of fat and water content resulted in good agreement between this approach and chemical determinations.[120] However, only six animals were included in the study, and therefore the results must be considered preliminary. A similar approach on a localised volume of *m. biceps femoris* in pigs resulted in a lower fat content compared with fat determined by extraction and infrared spectroscopy on extracted fat,[234] which was ascribed to the fact that phospholipids were not measured by ^{1}H NMR spectroscopy. Ville *et al.*[235] likewise performed *in vivo* ^{1}H NMR spectroscopy on anaesthetised pigs on a localised volume of *m. longissimus dorsi*. Using the methylene protons relative to the resonance from water protons to estimate the fat content, no convincing correlation between ^{1}H NMR spectroscopic estimations and determinations by extraction procedures was obtained, which was suggested to be due to errors from body movement due to e.g., respiration. In contrast, high correlations between the area of the lipid methylene resonance, measured by ^{1}H NMR spectroscopy, and fat content determined by extraction ($r = 0.99$) has been obtained on dead control and obese mice and on mixtures of fresh pork and lard.[236] Finally, Renou *et al.*[237] have also demonstrated a high correlation ($r = 0.998$) between fat–water ratio in meat batters (fat content from 2 to 50% w/w) determined by ^{1}H NMR spectroscopy using peak intensities of the water and lipid methylene resonance and determination of fat and water by extraction and drying, respectively. In summary, the preliminary studies reported at present indicate that ^{1}H NMR spectroscopy may potentially be used to determine water and lipid content in intact carcasses.

However, taking into account the cost of the equipment, the complexity of the complicated measurements and the degree of information obtained, is it doubtful if the method will become widespread. In contrast, its use on meat products seems more applicable.

6.3. Processing

During cooking, meat shrinks and water is expelled. Walton and McCarthy[238] demonstrated that ^{1}H NMR spectroscopy could be used to determine water–fat ratio in hamburger, sausage and various chicken cuts during cooking. The water–fat ratio was determined as relative peak heights of the water resonance and the lipid methylene resonance, respectively, and it was shown that the ratio decreases 4–5-fold during cooking. Measurement of internal temperature in meat products during cooking is of interest in order to ensure food product safety and eventually uniformity, and Walton and McCarthy[238] also demonstrated that internal temperature during cooking could be estimated from the difference in the chemical shift of the water and fat resonance, respectively. The precision of temperature determination was highest in hamburger and sausage ($\sim 1^{\circ}$C) and lowest in chicken ($\sim 5^{\circ}$C) due to the lower fat content in the latter. However, the application must be considered of interest for on-line process control in the meat industry, if it becomes commercially applicable.

6.4. Colour stability

The appearance of meat is of substantial importance in modern marketing as consumers 'buy by the eye',[239] and meat colour is assumed to be an indicator of quality and freshness.[240] Meat colour is determined by the relative amount of the three different chemical states of myoglobin (for a review, see Renerre[241]). The different derivates are: (*i*) reduced myoglobin or deoxymyoglobin, which is the purple pigment of the deep muscle, (*ii*) oxymoglobin, formed on exposure to air, which is responsible for the attractive cherry-red appearance of meat, and (*iii*) oxidised myoglobin or metmyoglobin, which gives the meat a grey-brown appearance and therefore is undesirable. ^{1}H NMR spectroscopy has been used to study the kinetics of auto-oxidation of myoglobin extracted from two different bovine muscles.[242] The peak intensity of a methyl group in myoglobin was used as indicator of oxidation. Marked differences in the rate of auto-oxidation between the two muscle types were demonstrated, and also an effect of 8 days of storage prior to extraction was shown to affect the rate of auto-oxidation. This work on a model system seems interesting even though its relevance from a practical perspective only is evident the day where

such measurements can be made on whole cuts, which at present is quite uncertain.

7. ^{13}C NMR SPECTROSCOPY

The natural abundance of ^{13}C is low ($\sim$1%), which makes ^{13}C NMR spectroscopy less sensitive compared with e.g., ^{1}H and ^{31}P NMR spectroscopy. Only very few applications of ^{13}C NMR spectroscopy are reported in meat science. However, an interesting feature of ^{13}C NMR spectroscopy is its potential use for studies on muscle glycogen, which is of importance because of its crucial role in *post mortem* anaerobic glycolysis and lactate formation. Lundberg *et al.*[232] demonstrated that the *post mortem* course in degradation of glycogen and the simultaneous formation of lactate could be followed in bovine muscle by ^{13}C NMR spectroscopy using proton decoupling. A method for obtaining enhanced sensitivity of the ^{13}C nuclei in an NMR experiment is to perform cross polarisation (CP), which involves transfer of magnetisation from other nuclei, e.g., from protons to the ^{13}C nuclei. ^{13}C CP MAS NMR spectroscopy was recently for the first time carried out on frozen porcine muscle biopsies taken *in vivo*, early *post mortem* (1 and 45 min) and 24 h *post mortem*, and the amount of glycogen residues was estimated from the spectra.[243] A reasonable correlation between ^{13}C CP MAS NMR estimations of glycogen and biochemical determinations was demonstrated ($r = 0.74$). The efficiency of cross polarisation depends on the mobility of molecules, and thereby CP- and MAS-combined techniques can provide information about characteristics of larger molecules in biological systems. This was used in the above study where the resonance from methylene chains in fatty acids ($\sim$30 ppm) was greatly reduced in muscle samples from pigs that had been exposed to pre-slaughter-stress and subsequently were electrically stunned. The observed reduction in signal amplitude was probably caused by reduced efficiency of cross polarisation due to changes in mobility, and thereby reveals altered membrane properties in muscles of the pre-slaughter stressed/electrically stunned pig. At present the knowledge about effects of pre-slaughter stress and stunning method on muscle membrane properties is limited, and accordingly the described observation is of interest for further understanding of the physiological effects of stress known to result in inferior meat quality.

8. CONCLUSIONS

Even though NMR studies carried out within the area of meat science still appear somehow scattered, the present review demonstrates that NMR can be considered a method of high potential, which, despite its relatively recent

introduction, has already contributed successfully to basic knowledge within many essential areas of meat science. Even though the number of applications of NMR in meat science has increased strikingly in recent years, the area is still far from fully exploited. The insight and knowledge gained today continuously disclose new, interesting topics of relevance for the area and future studies. Table 4 summarises present and potential future applications of different NMR techniques within meat science.

With regard to relaxation, it can be concluded that the technique has proven successful in determination of WHC in fresh meat, and promising results with regard to other meat quality traits involving water properties such as cooking loss and technological quality are presently achieved. A problem when assessing a new method for determination of WHC is that it can only be compared with existing methods, and accordingly a better result than the inter-correlation coefficient of this method can never be obtained. Consequently, it is difficult to demonstrate the superiority of a new method compared with existing methods. However, it has been established that NMR relaxation of fresh meat reflects information that is partly decisive for subsequent heat-induced changes of importance for the distribution of water within the cooked meat and also seems to contain information about the inherent water of importance for the technological characteristics of the meat. The fact that LF-NMR relaxometry gives superior information compared with existing methods must be considered a strong argument in favour of this method in the characterisation of water-holding-associated issues in meat. Continuous relaxation measurement during the *post mortem* conversion of muscle to meat has proven a strong potential tool for improving the understanding of changes in water distribution and structure taking place *post mortem* and the relation of these events to the final WHC. Recent studies performing relaxation measurements during cooking of meat indicate that also during processing, relaxometry can provide valuable information about dynamic changes taking place.

The fact that NMR data contain information about important meat quality parameters and are capable of predicting these meat quality parameters is novel. However, for acknowledgement of its potential in the meat industry, implementation as an on-line technique for meat quality control is required. Taking into consideration some of the characteristics of the NMR technique – it is rapid, non-invasive and non-destructive and involves no health hazards – the technique should be expected to have a potential for on-line implementation, which preliminarily has been demonstrated for quality control of pitting fruit (for a detailed description, see Hills[244]). However, despite fulfilling the basic requirements for on-line implementation, many practical concerns still need to be solved – for example, on a commercial slaughter line, where 400 pigs typically are slaughtered per hour: the construction of appropriate magnets (which can polarise the sampling location within an appropriate time scale and with satisfactory magnet homogeneity),

Table 4. The different NMR techniques and their applications in meat science

Technique	Present applications	Potential future applications	Advantages	Disadvantages
LF-NMR relaxation	Determination of WHC[22,25–27,59]	Prediction of technological meat quality	Rapid Non-destructive	Equipment required Limited size of probe
	Determination of fat content[115–117]	On-line use for assessment of meat quality	Repeated measurements possible	Quantification of fat/water content requires calibration
	Dynamic investigations of: - Conversion of muscle to meat[72,73] - Cooking[96,97]	Elucidation of the effects of handling and processing on the technological meat quality	Water properties are studied within the meat matrix	
	Freezing/thawing studies[111]			
Imaging	Estimation of: - carcass composition[120,127] -muscle/meat composition[121–123]	Monitoring of changes during conversion of muscle to meat and during processing of meat	Information on properties of specific regions within a sample can be obtained	Expensive equipment required
	Curing studies[128–131]	Optimisation of curing processes	Repeated measurements possible	
	Freezing/thawing studies[139,140,143]	Temperature profiling during cooking, freezing etc. Detection of interior defects in products		
Spectroscopy	Dynamic studies on phosphorous metabolism[69,127,151,155,157,175,177–183,187,201,206,207]	Complete monitoring of the influence of peri-mortal factors on metabolism *post mortem*	Non-destructive	Expensive equipment required
			Repeated measurements possible	Absolute quantification of metabolites complicated (relaxation effects, baseline correction, etc.)

	Dynamic measurement of pH[207]		Laborious extraction procedures not necessary Intact muscles can be studied	Possibly 'NMR non-invisible pools' present in the meat
Solid-state MAS NMR spectroscopy	Determination of glycogen[243]	Dynamic studies on *post mortem* metabolism: - Degradation of glycogen - Formation of lactate	Laborious extraction procedures not necessary	Expensive equipment required
	Studies on mobilities of macromolecules (membrane constituents)[243]	Elucidation of the role of pro- and macro-glycogen in metabolism *post mortem*	Intact muscle/meat is studied	Limited sample size
			Measurement on frozen samples possible	MAS potentially causing physical damage to the sample Absolute quantification of metabolites complicated, in particular in CP experiments

equipment for signal excitation and rapid methods for data collection and analysis. On-line control of a paste, which does not require spatial resolution, is less problematic and at-line monitoring of fat content in meat emulsions has been demonstrated.[245] Preliminary results using an NMR mobile surface device (the so-called NMR-mouse) in food analysis[246] indicate that with further development on the hardware part the introduction as an on-line method may be a reality in the future.[247] In general, implementation of NMR techniques in meat industry must be considered a challenge in the future.

Present literature reveals that NMR imaging mainly has been applied in studies aiming at understanding processing factors such as curing, freezing and pressure treatment, where the usefulness of the technique has been demonstrated, particularly its potential in characterisation of changes over time. Contrary to NMR relaxation, NMR imaging with the focus of understanding basic mechanisms behind structural organisation of water and water properties are very limited.[143] In summary, a satisfactory quantification of changes and elucidation of causes for observed changes in relaxation characteristics/signal intensity are still lacking, and in general the area must still be considered to be far from fully explored. In addition, reported applications of imaging techniques for determination of composition must all be considered being of preliminary nature, and much more work within this field is needed before any conclusions about the potential of the approach within this area can be drawn.

The reports on NMR spectroscopy in meat science reveal that ^{31}P NMR spectroscopy has been widely applied within many different areas and has provided valuable information about metabolic response to various genetic and *peri mortem* factors, which has improved the understanding of the role of these factors in relation to meat quality considerably. Unfortunately the detection and quantification of lactate, which is a key metabolite in relation to meat quality, by ^{1}H NMR spectroscopy is associated with difficulties due to the dominating signal from water and overlapping signal from methylene in lipid. In addition, lactate shows anisotropic features due to dipolar coupling interactions originating from incomplete motional averaging of molecules, which otherwise occurs in aqueous solutions where molecules rotate freely and isotropically.[248] The last-mentioned problem can be overcome by magic angle spinning (MAS), where the contribution from dipolar coupling and anisotropy is eliminated,[249] and use of ^{1}H MAS NMR spectroscopy to estimate lactate in *post mortem* rabbit muscles has been demonstrated.[233] However, spinning at high frequencies may affect the muscle tissue, causing disintegration and damage of cell structures, and therefore this problem needs to be solved, which was also pointed out in connection with measurements on other tissues and cell cultures.[250–253] Consequently, further attention should be paid to techniques based on much lower spinning rates,[254,255] as it makes continuous measurements on *post*

mortem samples feasible without introducing any harmful effects from spinning. With regard to ^{13}C NMR spectroscopy, the finding that ^{13}C cross-polarisation (CP) MAS NMR spectroscopy appears to be sensitive to changes in cell membrane properties[242] must be considered extremely informative due to the potential role of membrane disintegration on meat quality, and ^{13}C CP MAS NMR spectroscopy seems to be a promising tool for advanced studies on alterations in membrane properties *post mortem* and may complement details obtained from relaxation studies.

In conclusion, NMR methodologies have already proven successful within meat science with applications in many different areas. However, many unexplored areas still exist where the potential of NMR can be expected to reveal useful and valuable information. The inspiration that can be obtained from NMR studies within other disciplines, e.g., medical areas, material science, physical/chemical sciences and food science in general, should be rewarded with great attention in future in order to continue development of the use of NMR in meat science.

REFERENCES

1. F. Bloch, W. W. Hansen and M. Packard, *Phys. Rev*., 1946, **69**, 127.
2. E. M. Purcell, H. C. Torrey and R. V. Pound, *Phys. Rev*., 1946, **69**, 37.
3. G. Wider, *Biotechniques*, 2000, **29**, 1278.
4. T. M. Shaw and R. H. Elsken, *J. Chem. Phys*., 1959, **18**, 1113.
5. E. Odeblad and G. Lindström, *Acta Radiol*., 1955, **43**, 469.
6. J. R. Singer, *Science*, 1959, **130**, 1652.
7. C. B. Bratton, A. L. Hopkins and J. W. Weinberg, *Science*, 1965, **147**, 138.
8. F. W. Cope, *Biophys. J*., 1969, **9**, 303.
9. C. F. Hazlewood, D. C. Chang, B. L. Nichols and D. E. Woessner, *Biophys. J*., 1974, **14**, 583.
10. J. R. Hansen, *Biochem. Biophys. Acta*, 1971, **230**, 482.
11. P. S. Belton, R. R. Jackson and K. J. Packer, *Biochim. Biophys. Acta*, 1972, **286**, 16–25.
12. R. T. Pearson, I. D. Duff, W. Derbyshire and J. M. V. Blanshard, *Biochim. Biophys. Acta*, 1974, **362**, 188.
13. B. M. Fung, *Biophys. J*., 1977, **19**, 315.
14. J. G. Diegel and M. M. Pintar, *Biophys. J*., 1975, **15**, 855.
15. J. R. Zimmerman and W. E. Brittin, *J. Phys. Chem*., 1957, **61**, 1328.
16. P. S. Belton and B. P. Hills, *Mol. Phys*., 1987, **61**, 999.
17. E. D. Finch and L. D. Homer, *Biophys. J*., 1974, **14**, 907.
18. B. M. Fung, D. L. Durham and D. A. Wassil, *Biochim. Biophys. Acta*, 1975, **399**, 191.
19. H. T. Edzes and E. T. Samulski, *J. Magn. Reson*., 1978, **31**, 207.
20. B. P. Hills, S. F. Takacs and P. S. Belton, *Mol. Phys*., 1989, **67**, 903.
21. J. Zhong, J. C. Gore and I. M. Armitage, *Magn. Reson. Med*., 1989, **21**, 295.
22. J. P. Renou, G. Monin and P. Sellier, *Meat Sci*., 1985, **15**, 225.
23. J. P. Renou, J. Kopp, P. Gatellier, G. Monin and G. Kozak-Reiss, *Meat Sci*., 1989, **26**, 101.
24. E. Le Rumear, J. de ertaines, P. Toulouse and P. Rochcongar, *Magn. Reson. Imaging*, 1987, **5**, 267.
25. E. Tornberg, A. Andersson, Å. Göransson and G. von Seth, *Pork Quality: Genetic and Metabolic Factors*, CAB International, UK, 239.

26. J. Brøndum, L. Munck, P. Henckel, A. Karlsson, E. Tornberg and S. B. Engelsen, *Meat Sci.*, 2000, **55**, 177.
27. H. C. Bertram, A. H. Karlsson and H. J. Andersen, *Meat Sci.*, 2001, **57**, 125.
28. H. C. Bertram, S. Dønstrup, A. H. Karlsson and H. J. Andersen, *Meat Sci.*, 2002, **60**, 279.
29. B. M. Fung and T. W. McGaughy, *Biophys. J.*, 1979, **28**, 293.
30. B. M. Fung and P. S. Puon, *Biophys. J.*, 1981, **3**, 27.
31. C. S. Landis, X. Li, F. W. Telang, P. E. Molina, I. Palyka, G. Vetek and C. S. Springer, *Magn. Reson. Med.*, 1999, **42**, 467.
32. K. M. Donahue, R. M. Wiesskoff, D. J. Parmelee, R. J. Callahan, R. A. Wilkinson, J. B. Mandeville and B. R. Rosen, *Magn. Reson. Med.*, 1995, **34**, 423.
33. B. P. Hills, S. F. Takacs and P. S. Belton, *Mol. Physics*, 1989, **67**, 919.
34. G. Saab, R. T. Thompson, G. D. Marsh, P. A. Picot and G. R. Moran, *Magn. Reson. Med.*, 2001, **46**, 1093.
35. K. R. Brownstein and C. E. Tarr, *Phys. Rev. A.*, 1979, **19**, 2446.
36. H. E. Huxley, *Sci. Am.*, 1965, **213**, 18.
37. H.-J. Weinmann, R. C. Brasch, W. R. Press and G. E. Wesbey, *Am. J. Roentgenol.*, 1984, **142**, 619.
38. E. J. Goldstein, K. R. Burnett, J. R. Hansell, J. Casaia, B. Farrar, D. Gelblum and G. L. Wolf, *Physiol. Chem. Phys. Med. NMR*, 1984, **16**, 97–104.
39. K. Adzamli, F. A. Jolesz, A. R. Bleier, R. V. Mulkern and T. Sandor, *Magn. Reson. Med.*, 1989, **11**, 172.
40. W. C. Cole, A. D. LeBlanC and S. G. Jhingran, *Magn. Reson. Med.*, 1993, **29**, 19.
41. H. C. Bertram, A. H. Karlsson, M. Rasmussen, S. Dønstrup, O. D. Petersen and H. J. Andersen, *J. Agric. Food. Chem.*, 2001, **49**, 3092.
42. R. S. Menon, M. S. Rusinko and P. S. Allen, *Magn. Reson. Med.*, 1991, **20**, 196.
43. F. Feldhusen, D. Königsmann, F.-J. Kaup, W. Drommer and S. Wenzel, *Meat Sci.*, 1992, **31**, 367.
44. H. J. Swatland and S. Belfry, *Mikroskopie*, 1985, **42**, 26.
45. L. Diesbourg, H. J. Swatland and B. M. Millman, *J. Anim. Sci.*, 1988, **66**, 1048.
46. G. Offer and P. Knight, *Developments in Meat Science*, Elsevier Applied Science, London, 1988, 172.
47. G. Offer and T. Cousins, *J. Sci. Food Agric.*, 1992, **58**, 107.
48. P. Lillford, A. H. Clark and D. V. Jones, *Water in Polymers*, ACS Symposium Series, American Chemical Society, Washington, D.C., 1980, 177.
49. T. Yamada, *Mechanisms of Work Production and Work Absorption in Muscle*, Plenum Press, New York, 1998, 145.
50. H. C. Bertram, P. P. Purslow and H. J. Andersen, *J. Agric. Food Chem.*, 2002, **50**, 824.
51. J. W. T. Dickerson and E. M. Widdowson, *Biochem. J.*, 1960, **74**, 247.
52. J. D. Sink and M. D. Judge, *Growth*, 1971, **35**, 349.
53. H. C. Bertram, M. Rasmussen, H. Busk, N. Oksbjerg, A. H. Karlsson and H. J. Andersen, *J. Magn. Reson.*, 2002, **157**, 267.
54. E. Tornberg, M. Wahlgren, J. Brøndum and S. B. Engelsen, *Food Chem.*, 2000, **69**, 407.
55. J. R. Bendall and J. Wismer-Pedersen, *J. Food Sci.*, 1962, **27**, 144.
56. R. N. Sayre, E. J. Briskey and W. G. Hoekstra, *J. Anim. Sci.*, 1963, **22**, 1012.
57. I. F. Penny, *Biochem. J.*, 1967, **104**, 609.
58. H. C. Bertram, A. K. Whittaker, A. H. Karlsson and H. J. Andersen, *J. Agric. Food Chem.*, 2003, **51**, 4072.
59. R. J. S. Brown, F. Capozzi, C. Cavani, M. A. Cremonini, M. Petracci and G. Placucci, *J. Magn. Reson.*, 2000, **147**, 89.
60. S. M. Jepsen, H. T. Pedersen and S. B. Engelsen, *J. Sci. Food Agric.*, 1999, **79**, 1793.
61. P. Bogner, E. Berenyi, A. Miseta, P. Horn, M. Kellermayer, D. N. Wheatley and F. A. Jolesz, *Acad. Radiol.*, 1996, **3**, 26.

62. K. Lundström, B. Essen-Gustavsson, M. Rundgren, I. Edfors-Lilja and G. Malmfors, *Meat Sci.*, 1989, **25**, 251.
63. S. M. De Smet, H. Pauwels, S. De Bie, D. I. Demeyer, J. Callewier and W. Eeckhout, *J. Anim. Sci.*, 1996, **75**, 1854.
64. C. Larzul, P. Le roy, R. Guéblez, A. Talmant, J. Gougué, P. Sellier and G. Monin, *J. Anim. Breed Genet.*, 1997, **114**, 309.
65. K. J. Stalder, L. L. Christian, M. F. Rothschild and E.-C. Lin, *J. Anim. Sci.*, 1997, **12**, 3114–3118.
66. K. J. Stalder, J. Maya, L. L. Christian, S. J. Moeller and K. J. Prusa, *J. Anim. Sci.*, 1998, **76**, 2435.
67. H. Busk, A. Karlsson and S. H. Hertel, *Quality of Meat and Fat in Pigs as Affected by Genetics and Nutrition*, EAAP Publication No. 100, Zürich, Switzerland, 2000, 129.
68. R. Lahucky, U. Baulain, M. Hennig, P. Demo, P. Krska and T. Liptaj, *Meat Sci.*, 2002, **61**, 233.
69. H. C. Bertram, A. H. Karlsson and H. J. Andersen, *Meat Sci.*, 2003, **65**, 1281.
70. H. C. Bertram, K. Rosenvold, A. Schäfer and H. J. Andersen, *Meat Sci.*, 2004, **66**, 915.
71. A. A. Taylor, *Proceedings from 17th European Meeting of Meat Research Workers*, Bristol, UK, 1971, 357.
72. A. A. Taylor and S. J. Dant, *J. Food Technol.*, 1971, **6**, 131.
73. A. Gigiel, *Proceedings from the 30th European Meeting of Meat Research Workers*, Bristol, UK, 1984, 63.
74. A. Gigiel, F. Butler and B. Hudson, *Meat Sci.*, 1989, **26**, 67.
75. S. D. M. Jones, L. E. Jeremiah and W. M. Robertson, *Meat Sci.*, 1993, **34**, 351.
76. M. D. Garrido, J. Pedauye, S. Banon, F. Marques and J. Laencina, *Lebensm. Wiss. U. Technol.*, 1994, **27**, 173.
77. P. G. van der Wal, B. Engel, G. van Beek and C. H. Veerkamp, *Meat Sci.*, 1995, **40**, 193.
78. P. Barton-Gade, *Proceedings from 44th Int. Congress of Meat Science and Technology*, Spain, 1998, 1066.
79. P. S. Belton, R. R. Jackson and K. J. Packer, *Biochim. Biophys. Acta*, 1973, **304**, 56.
80. B. M. Fung and T. W. McGaughy, *Biochim. Biophys. Acta*, 1974, **343**, 663.
81. D. C. Chang, C. F. Hazlewood and D. E. Woessner, *Biochim. Biophys. Acta*, 1976, **437**, 253.
82. R. W. Currie, R. Jordan and F. H. Wolfe, *J. Food Sci.*, 1981, **46**, 822.
83. V. Dedieu, F. Finat-Duclos, F. Joffre and D. Vincensini, *Invest. Radiol.*, 1999, **34**, 185.
84. A. E. English, M. L. G. Roy and R. M. Henkelman, *Magn. Reson. Med.*, 1991, **21**, 264.
85. I. L. Cameron, M. F. Finnie and G. D. Fullerton, *Physiol. Chem. Phys. Med. NMR*, 1984, **16**, 351.
86. M. M. Farouk and J. E. Swan, *Meat Sci.*, 1998, **49**, 233.
87. R. Li, W. L. Kerr, R. T. Toledo and J. A. Carpenter, *J. Food Sci.*, 2000, **65**, 575.
88. N. L. Dawkins, N. L. Gager, J. P. Cornillon, Y. Kim and O. Phelps, *J. Food Sci.*, 2001, **66**, 1276.
89. H. Heymann, H. B. Hedrick, M. A. Karrasch, M. K. Eggeman and M. R. Ellersieck, *J. Food Sci.*, 1990, **55**, 613.
90. M. D. Aaslyng, C. Bejerholm, P. Ertbjerg, H. C. Bertram and H. J. Andersen, *Food Quality and Preference*, 2003, **14**, 277.
91. E. Tornberg and G. Larsson, *Proceedings from 32nd European Meeting of Meat Research Workers*, Ghent, Belgien, 1986, 437.
92. M. A. Borisova and E. F. Oreshkin, *Meat Sci.*, 1992, **31**, 257.
93. E. Micklander, B. Peshlov, P. P. Purslow and S. B. Engelsen, *Trends Food Sci. Technol.*, 2002, **13**, 341.
94. J. Naveau, *Journees de la Recherche Porcine En France*, 1986, **18**, 265.
95. G. Monin and P. Sellier, *Meat Sci.*, 1985, **13**, 49.
96. M. Estrade, X. Vignon and G. Monin, *Meat Sci.*, 1993, **35**, 313.

97. K. Lundström, A. Andersson and I. Hansson, *Meat Sci.*, 1996, **20**, 145.
98. A.-C. Enfält, K. Lundström, A. Karlsson and I. Hansson, *J. Anim. Sci.*, 1997, **75**, 2924.
99. K. Lundström, A.-C. Enfält, E. Tornberg and H. Agerhem, *Meat Sci.*, 1998, **48**, 115.
100. C. Gariepy, D. Godbout, X. Fernandez, A. Talmant and A. Houde, *Meat Sci.*, 1999, **52**, 57.
101. A. Jonsäll, L. Johannsson and K. Lundström, *Meat Sci.*, 2001, **57**, 245.
102. H. C. Bertram, S. B. Engelsen, H. Busk, A. H. Karlsson and H. J. Andersen, *Meat Sci.*, 2004, **66**, 437.
103. R. Hamm, *Adv. Food Res.*, 1960, **10**, 355.
104. G. Offer and J. Trinick, *Meat Sci.*, 1983, **8**, 245.
105. E. Tornberg and O. Nerbrink, *Proceedings from the 30th European Meeting of Meat Research Workers*, Bristol, UK, 1984, 112.
106. E. A. Foegeding and S. R. Ramsey, *J. Sci. Food.*, 1986, **51**, 33.
107. S. A. Ensor, R. W. Mandigo, C. R. Calkins and L. N. Quint, *J. Food Sci.*, 1987, **52**, 1155.
108. N. B. Lecomte, J. F. Zayas and C. L. Kastner, *J. Food Sci.*, 1993, **58**, 464.
109. J. G. Bloukas, E. D. Paneras and S. Papadima, *J. Muscle Foods*, 1997, **8**, 63.
110. K.-W. Lin and M.-Y. Mei, *J. Food Sci.*, 2000, **65**, 48.
111. S. Yano, M. Tanaka, N. Suzuki and Y. Kanzaki, *Food Sci. Technol. Res.*, 2002, **8**, 137.
112. H. C. Bertram, H. J. Andersen, A. H. Karlsson, P. Horn, J. Hedegaard, L. Nørgaard and S. B. Engelsen, *Meat Sci.*, 2003, **65**, 707.
113. S. Fjelkner-Modig and E. Tornberg, *Meat Sci.*, 1986, **17**, 213.
114. J. Brøndum, D. V. Byrne, L. S. Bak, G. Bertelsen and S. B. Engelsen, *Meat Sci.*, 2000, **54**, 83.
115. J. P. Renou, J. Kopp and C. Valin, *J. Food Technol.*, 1985, **20**, 23.
116. H. T. Pedersen, H. Berg, F. Lundby and S. B. Engelsen, *Inn. Food Sci. Emerging Technol.*, 2001, **2**, 87.
117. G. H. Sørland, P. M. Larsen, F. Lundby, A-P. Rudy and T. Guiheneuf, *Meat Sci.*, 2004, **66**, 543–550.
118. L. R. H. Tipping, *Meat Sci.*, 1982, **7**, 279.
119. A. Gerbanowski, D. N. Rutledge, M. H. Feinberg and C. J. Ducauze, *Sciences des Alimentents*, 1997, **17**, 309.
120. A. D. Mitchell, P. C. Wang, R. W. Rosebrough, T. H. Elsasser and W. F. Schmidt, *Poultry Sci.*, 1991, **70**, 2494.
121. S. L. Duce, S. Ablett, T. M. Guiheneuf, M. A. Horsfield and L. D. Hall, *J. Food Sci.*, 1994, **59**, 808.
122. L. Ballerini, A. Högberg, G. Borgefors, A.-C. Bylund, A. Lindgård, K. Lunström, O. Rakotonirainy and B. Soussi, *IEEE Trans. Nuclear Sci.*, 2002, **49**, 195.
123. J.-M. Bonny, W. Laurent, R. Labas, R. Taylor, P. Berge and J.-P. Renou, *J. Sci. Food Agric.*, 2000, **81**, 337.
124. J.-M. Bonny, M. Zanca, O. Boespflug-Tanguy, V. Dedieu, S. Joandel and J.-P. Renou, *Magn. Reson. Imaging*, 1998, **16**, 167.
125. J. F. Polak, F. A. Jolesz and D. F. Adams, *Invest. Radiol.*, 1988, **23**, 107.
126. S.-Y. Kuno, S. Katsuta, T. Inouye, I. Anno, K. Matsumoto and M. Akisada, *Radiology*, 1988, **169**, 567.
127. A. Scholz, A. D. Mitchell, P. C. Wang, H. Song and Z. Yan, *Arch. Tierzucht.*, 1995, **38**, 539.
128. L. Foucat, S. Benderbous, G. Bielicki, M. Zanca and J.-P. Renou, *Magn. Reson. Imaging*, 1995, **13**, 259.
129. T. M. Guiheneuf, J.-J. Tessier, N. J. Herrod and L. D. Hall, *J. Sci. Food Agric.*, 1996, **71**, 163.
130. W. Dolata, E. Piotrowska, J. Wajdzik and J. Tritt-Goc, *Meat Sci.*, 2004, **67**, 25.
131. T. M. Guiheneuf, S. L. Duce, S. J. Gibbs and L. D. Hall, *Int. J. Food Sci. Technol.*, 1995, **30**, 447.
132. K. G. Grunert, *Food Qual. Preferences*, 1997, **8**, 157–174.
133. P. E. Bouton, P. V. Harris, J. J. Macfarlane and J. M. O'Shea, *Meat Sci.*, 1977, **1**, 307.
134. D. Ratcliff, P. E. Bouton, A. L. Ford, P. V. Harris, J. J. Macfarlane and J. M. O'Shea, *J. Food Sci.*, 1977, **42**, 857–859.

135. H. C. Bertram, A. K. Whittaker, R. W. Shorthose, A. H. Karlsson and H. J. Andersen, *Meat Sci.*, 2004, **66**, 301.
136. P. Mazur, *J. Gen. Physiol.*, 1963, **47**, 347.
137. W. F. Rall, D. S. Reid and C. Polge, *Cryobiology*, 1984, **21**, 106.
138. T. M. Ngapo, I. H. Babare, J. Reynolds and R. F. Mawson, *Meat Sci.*, 1999, **53**, 149.
139. T. M. Guiheneuf, A. D. Parker, J. J. Tessier and L. D. Hall, *Magn Reson. Chem.*, 1997, **35**, s112.
140. L. D. Hall, S. D. Evans and K. P. Nott, *Magn. Reson. Imaging*, 1998, **16**, 485.
141. L. Foucat, R. G. Taylor, R. Labas and J. P. Renou, *Am. Lab.*, 2001, **33**, 38.
142. S. Lee, P. Cornillon and Y. R. Kim, *J. Food Sci.*, 2002, **67**, 2251.
143. W. L. Kerr, D. S. Reid, R. J. Kauten and M. J. McCarthy, *Lebensm. Wiss. Technol.*, 1998, **31**, 215.
144. J.-M. Bonny and J.-P. Renou, *Magn. Reson. Imaging*, 2002, **20**, 395.
145. J.-P. Renou, S. Benderbous, G. Bielicki, L. Foucat and J.-P. Donnat, *Magn. Reson. Imaging*, 1994, **12**, 131.
146. T. M. Guiheneuf, S. J. Gibbs and L. D. Hall, *J. Food Eng.*, 1997, **31**, 457.
147. D. I. Hoult, S. J. W. Busby, D. G. Gadian, G. K. Radda, R. E. Richards and P. J. Seeley, *Nature London*, 1974, **252**, 285.
148. C. T. Burt, T. Glonek and M. Barany, *J. Biol. Chem.*, 1976, **251**, 2584.
149. P. J. Seeley, S. J. W. Busby, D. G. Gadian, G. K. Radda and R. E. Richards, *Biochem. Soc. Trans.*, 1976, **4**, 62.
150. S. J. W. Busby, D. G. Gadian, G. Radda, R. E. Richards and P. J. Seeley, *Biochem. J.*, 1978, **170**, 103.
151. H. J. Vogel, P. Lundberg, S. Fabiansson, H. Ruderus and E. Tornberg, *Meat Sci.*, 1985, **13**, 1.
152. R. B. Moon and J. H. Richards, *J. Biol. Chem.*, 1973, **248**, 7276.
153. K. Yoshizaki, H. Nishikawa, S. Yamada, T. Morimoto and H. Watari, *Jap. J. Physiol.*, 1979, **29**, 211.
154. P. Uhrin and T. Liptaj, *Gen. Physiol. Biophys.*, 1991, **10**, 83.
155. P. Lundberg, H. J. Vogel, S. Fabiansson and H. Ruderus, *Meat Sci.*, 1987, **19**, 1.
156. R.G. Cassens, D.N. Marple and G. Eikelenboom, *Adv. Food Res.*, 1975, **21**, 71.
157. J.-P. Renou, P. Canoni, P. Gatelier, C. Valin and P. J. Cozzone, *Biochemie*, 1986, **68**, 543.
158. Y. Azuma, N. Manabe, F. Kawai, M. Kanamori and H. Miyamoto, *J. Anim. Sci.*, 1994, **72**, 103.
159. Y. Azuma, N. Manabe, F. Kawai, M. Kanamori and H. Miyamoto, *Anim. Sci. Technol.*, 1994, **4**, 416.
160. M. Mizuno, N. H. Secher and B. Quistorff, *J. Appl. Physiol*, 1994, **76**, 531.
161. A. Asghar and N. T. Yeates, *Crit. Rev. Food Sci. Nutri.*, 1978, **10**, 115.
162. F. J. Monahan, J. I. Gray, A. Asghar, A. Haug, G. M. Strasburg, D. J. Buckley and P. A. Morrissey, *J. Agric. Food Chem.*, 1994, **42**, 59.
163. C. Jensen, C. Lauritsen and G. Bertelsen, *Trends Food Sci. Technol.*, 1998, **9**, 62.
164. P.-A. Dufey, *Agrarforschung*, 1998, **5**, 417.
165. K. O. Honikel, H. Rosenbauer, K. Fisher, W. D. Müller and J. Przytulla, *Fleishwirtschaft*, 1998, **78**, 1205.
166. K. Rosenvold, H. N. Lærke, S. K. Jensen, A. H. Karlsson, K. Lundström and H. J. Andersen, *Meat Sci.*, 2002, **62**, 48.
167. C. L. Davey, K. V. Gilbert and W. A. Carse, *N.Z. J. Agric. Res.*, 1976, **19**, 13.
168. B. B. Chrystall and C. E. Devine, *Meat Sci.*, 1978, **2**, 49.
169. P. V. Tarrant, *J. Food Sci. Technol.*, 1989, **13**, 79.
170. L. Christensen and P. Barton-Gade, *Fleishwirtschaft*, 1997, **77**, 604.
171. P. Barton-Gade and L. Christensen, *Meat Sci.*, 1998, **48**, 237.
172. H. A. Channon, A. M. Payne and R. D. Warner, *Meat Sci.*, 2000, **56**, 291.
173. E. J. Briskey, R. W. Bray, W. G. Hoekstra, R. H. Grummer and P. H. Phillips, *J. Anim. Sci.*, 1959, **18**, 153.

174. B. W. Moos, *J. Sci. Food Agric*., 1980, **31**, 308.
175. A. Miri, A. Talmant, J. P. Renou and G. Monin, *Meat Sci*., 1992, **31**, 165.
176. D. H. MacLennan and M. S. Phillips, *Sci*., 1992, **256**, 789.
177. R. Geers, C. Decanniere, H. Villé, P. van Hecke, V. Goedseels, F. Vanstapel, L. Bosschaerts, J. D. Ley, W. Zhang and S. Janssens, *Am. J. Res*., 1992, **53**, 613.
178. C. Decanninere, P. van Hecke, F. Vanstapel, H. Villé and R. Geers, *J. Appl. Physiol*., 1993, **75**, 955.
179. B. Moesgaard, B. Quistorff, V. G. Christensen, I. Therkelsen and P. F. Jørgensen, *Meat Sci*., 1995, **39**, 43.
180. A. M. Scholz, A. D. Mitchell, H. Song and P. C. Wang, *Proceedings from 6th World Congress on Genetics Applied to Livestock Production*, Australia, 1998.
181. G. Kohn, U. Baulain, M. Henning, R. Lahucky, D. Leibfritz and E. Kallweit, *Arch. Tierz*., 1998, **41**, 299.
182. R. Lahucky, J. Mojto and J. Poltarsky, *Meat Sci*., 1993, **33**, 373.
183. G. Kozak-Reiss, F. Desmoulin, C. F. Martin, G. Monin, J. P. Renou, P. Canioni and P. J. Cozzone, *Arch. Biochem. Biophys*., 1991, **287**, 312.
184. F. J. Monahan, A. Asghar, D. J. Gray, D. J. Buckley and P. A. Morrissey, *Proceedings of 38th Int. Congress of Meat Science and Technology*, Clermont-Ferrand, France, 1992, 543.
185. R. N. Arnold, S. C. Arp, K. K. Scheller, S. N. Williams and D. M. Shaefer, *Meat Sci*., 1993, **71**, 105.
186. C. Jensen, J. Guidera, I. M. Skovgaard, H. Staun, L. H. Skibsted, S. K. Jensen, A. J. Møller, J. Buckley and G. Bertelsen, *Meat Sci*., 1997, **45**, 491.
187. R. Lahucky, P. Krska, U. Küchenmeister, K. Nürnberg, T. Liptaj, G. Nürnberg, I. Bahelka, P. Demo, G. Kuhn and K. Ender, *Arch. Tierzucht*., 2000, **43**, 487.
188. J. E. Cannon, J. B. Morgan, G. R. Schmidt, J. D. Tatum, J. N. Sofos, G. C. Schmidt, R. J. Delmore and S. N. Williams, *J. Anim. Sci*., 1996, **74**, 98.
189. E. Zanardi, E. Novelli, G. P. Ghiretti, V. Dorigoni and R. Chizzolini, *Food Chem*., 1999, **67**, 163.
190. A. L. Phillips, C. Faustman, P. B. Lynch, K. E. Govoni, T. A. Hoagland and S. A. Zinn, *Meat Sci*., 2001, **58**, 289.
191. K. S. Cheah, A. M. Cheah and D. I. Krausgrill, *Meat Sci*., 1995, **39**, 255.
192. F. von Scmitten, H. Jüngst, K.-H. Schepers and A. Festerling, *Dtsch. Tierärtzl. Wschr*., 1984, **91**, 149.
193. W. Otten, A. Berrer, S. Hartmann, T. Bergerhoff and H. M. Eichinger, *Proceedings of 38th Int. Congress of Meat Science and Technology*, Clermont-Ferrand, France, 1992, 117.
194. A. L. Schaefer, A. C. Murray, A. K. W. Tong, S. D. M. Jones and A. P. Sather, *Can. J. Anim. Sci*., 1993, **73**, 231.
195. D. N. D'Souza, R. D. Warner, B. J. Leury and F. R. Dunshea, *Meat Sci*., 1998, **76**, 104.
196. D. N. D'Souza, R. D. Warner, F. R. Dunshea and B. J. Leury, *Meat Sci*., 1999, **51**, 221.
197. D. N. D'Souza, R. D. Warner, B. J. Leury and F. R. Dunshea, *Austr. J. Agric. Res*., 2000, **51**, 185.
198. J. K. Apple, C. V. Maxwell, B. deRodas, H. B. Watson and Z. B. Johnson, *J. Anim. Sci*., 2000, **78**, 2135.
199. E. A. Niemack, F. Stockli, E. Husmann, J. Sanderegger, H. G. Classens and J. Helbig, *Magnesium Bull*., 1979, **3**, 195.
200. V. M. Kietzmann and H. Jablonski, *Prakt. Tierarzt*, 1985, **661**, 328.
201. B. Moesgaard, E. Larsen, B. Quistorff, I. Therkelsen, V. Grøsfeld Christensen and P. Fogd Jørgensen, *Acta Vet. Scand*., 1993, **34**, 397.
202. A. M. Laursen, *Curr. Top. Vet. Med. Anim. Sci*., 1983, **25**, 64.
203. R. Lambooy, *Fleischwirtschaft*, 1990, **70**, 1173.
204. N. G. Gregory, *Meat Sci*., 1994, **36**, 45.
205. P. Barton-Gade, *Meat Quality and Meat Packaging*, ECCEAMST, Utrecht, The Netherlands, 1996, 25.

206. H. C. Bertram, H. Stødkilde-Jørgensen, A. H. Karlsson and H. J. Andersen, *Meat Sci.*, 2002, **62**, 113.
207. H. C. Bertram, S. Dønstrup, A. H. Karlsson, H. J. Andersen and H. Stødkilde-Jørgensen, *Magn. Reson. Imaging*, 2001, **19**, 993.
208. B. M. Hitzig, W.-C. Perng, T. Burt, P. Okunieff and D. C. Johnson, *Am. J. Physiol.*, 1994, **35**, 1008.
209. R. A. Meyer, T. R. Brown and M. J. Kushmerick, *Am. J. Physiol.*, 1985, **248**, C279.
210. A. Miri, L. Foucat, J. P. Renou, L. Rodet, A. Talmant and G. Monin, *Meat Sci.*, 1991, **30**, 327.
211. T. Astruc, G. Bielicki, J.P. Donnat, J.P. Renou, X. Fernandez and G. Monin, *Meat Sci.*, 2004, in press.
212. B. Mercier, P. Granier, J. Mercier, L. Foucat, G. Bielicki, J. Pradere, J.-P. Renou and C. Prefaut, *Eur. J. Appl. Physiol.*, 1998, **78**, 20.
213. J. R. Bendall and H. J. Swatland, *Meat Sci.*, 1988, **24**, 85.
214. A. Schäfer, K. Rosenvold, P. P. Purslow, H. J. Andersen and P. Henckel, *Proceedings 47th nt. Congress of Meat Science and Technology*, Krakow, Poland, 2001, 206.
215. R. L. J. M. van Laack, R. G. Kauffman and M. L. Greaser, *Proceedings 47th Int. Congress of Meat Science and Technology*, Krakow, Poland, 2001, 22.
216. A. H. Karlsson and K. Rosenvold, *Meat Sci.*, 2002, **62**, 497.
217. S. P. L. Sørensen and K. Linderstrom-Lang, *Comtes-Rendus des travaux du Laboratoire de Carlsberg*, 1924, **15**, 40.
218. G. J. Kost, *Magn. Reson. Med.*, 1990, **14**, 496.
219. Y. Seo, M. Murakami, H. Watari, Y. Imai, K. Yoshizaki, H. Nishikawa and T. Morimoto, *J. Biochem*, 1983, **94**, 729.
220. D. J. Taylor, P. J. Bore, P. Styles, D. G. Gadian and G. K. Radda, *Mol. Biol. Med.*, 1983, **1**, 77.
221. K. Vandenborne, G. Walter, J. S. Leigh and G. Goelman, *Am. J. Appl. Physiol.*, 1993, **265**, C1332.
222. S. Sunoo, K. Asano and F. Mitsumori, *Eur. J. Appl. Physiol.*, 1996, **74**, 2221.
223. M. Stubbs, Z. M. Bhujwalla, G. M. Tozer, L. M. Rodrigues, R. J. Maxwell, R. Morgan, F. A. Howe and J. R. Griffiths, *NMR Biomed.*, 1992, **5**, 351.
224. A. S. E. Ojugo, P. M. J. McSheehy, D. J. O. McIntyre, C. McCoy, M. Stubbs, M. O. Leach, I. R. Judson and J. R. Griffiths, *NMR Biomed.*, 1999, **12**, 495.
225. R. Hamm, *Meat Sci.*, 1977, **1**, 15.
226. G. Bielicki, G. S. Benderbous, L. Foucat, J.-P. Donnat and J.-P. Renou, *J. Food Sci.*, 1994, **59**, 1271.
227. G. R. Schmidt, *Muscle as Food*, Academic Press, Orlando, FL, 1986, 201.
228. G. R. Trout and G. R. Schmidt, *J. Food Sci.*, 1984, **49**, 687.
229. D. F. Lewis, K. H. M. Groves and J. H. Holgate, *Food Microstructure*, 1986, **5**, 53.
230. P. S. Belton, K. J. Packer and T. E. Southon, *J. Sci. Food Agric.*, 1987, **40**, 283.
231. R. Li, W. L. Kerr, R. T. Toledo and Q. Teng, *J. Sci. Food Agric.*, 2001, **81**, 576.
232. P. Lundberg, H. J. Vogel and H. Ruderus, *Meat Sci.*, 1986, **18**, 133.
233. H. C. Bertram, A. K. Whittaker, A. H. Karlsson and H. J. Andersen, *Int. J. Food Sci. Technol.*, 2004, in press.
234. R. Geers, C. Decanniere, H. Ville, P. van Hecke and L. Boddchaerts, *Meat Sci.*, 1995, **40**, 373.
235. H. Ville, G. Rambouts, P. van Hecke, S. Peremans, G. Maes, G. Spincemaille and R. Geers, *J. Anim. Sci.*, 1997, **75**, 2942.
236. A. D. Mitchell, P. C. Wang and T. H. Elsasser, *J. Sci. Food Agric.*, 1991, **56**, 265.
237. J. P. Renou, A. Briguet, P. Gatellier and J. Kopp, *Int. J. Food Sci Technol.*, 1987, **22**, 169.
238. J. H. Walton and M. J. McCarthy, *J. Food Process Eng.*, 1999, **22**, 319.
239. E. Schulz, *Proceedings 35th Int. Congress of Meat Science and Technology*, Copenhagen, Denmark, 1989, 9.

240. H. D. Naumann, V. J. Rhodes, D. E. Brady and E. R. Kiehl, *Food Technol*., 1957, **2**, 123.
241. M. Renerre, *Int. J. Food Sci. Technol*., 1990, **25**, 613.
242. L. Foucat, M. Renerre, P. Gatellier and M. Anton, *Int. J. Food Sci. Technol*., 1994, **29**, 1.
243. H. C. Bertram, H. J. Jakobsen, A. H. Karlsson, H. J. Andersen and S. B. Engelsen, *J. Agric. Food Chem*., 2003, **51**, 2064.
244. B. P Hills, *Magnetic Resonance Imaging in Food Science*, John Wiley & Sons, Inc., New York, 1998, 152.
245. J. P. Donnat, C. Beauvallet, L. Foucat, F. Veyres, G. Martin and J. P. Renou, *Abstracts from 3rd Int. Conf. NMR in Foods*, Portugal, 1995.
246. H. T. Pedersen, S. Ablett, D. R. Martin, M. J. D. Mallett and S. B. Engelsen, *J. Magn. Reson*., 2003, **165**, 49.
247. D. R. Martin, S. Martin, H. T. Pedersen and M. J. D. Mallett, *Abstracts from 6th Int. Conf. NMR in Foods*, France, Paris, 2002, 47.
248. A. C. Hsu and M. J. Dawson, *Magn. Reson. Med*., 2000, **44**, 418.
249. E. R. Andrew and R. G. Eades, *Nature*, 1959, **183**, 1820.
250. L. L. Cheng, M. J. Ma, L. Becerra, T. Hale, I. Tracey, A. Lackner and R. G. Gonzalez, *Proc. Natl. Acad. Sci. USA*, 1997, **94**, 6408.
251. P. Weybright, K. Millis, N. Campbell, D. G. Cory and S. Singer, *Magn. Reson. Med*., 1998, **39**, 337.
252. J. L. Griffin, M. Bollard, J. Nicholson and K. Bhakoo, *NMR Biomed*., 2002, **15**, 375.
253. J. L. Taylor, C.-L. Wu, D. Cory, R. G. Gonzalez, A. Bielecki and L. L. Cheng, *Magn. Reson. Med*., 2003, **50**, 627.
254. R. A. Wind, J. Z. Hu and D. N. Rommereim, *Magn. Reson. Med*., 2001, **46**, 213.
255. J. Z. Hu, D. N. Rommereim and R. A. Wind, *Magn. Reson. Med*., 2002, **47**, 829.

NMR Characterization of Mechanical Waves

GUILLAUME MADELIN[1], NATHALIE BARIL[1], JACQUES DONALD DE CERTAINES[2], JEAN-MICHEL FRANCONI[1] AND ERIC THIAUDIÈRE[3]

[1]*Magnetic Resonance Centre, CNRS-University Victor Segalen Bordeaux 2, Bordeaux, France;* [2]*Magnetic Resonance Centre, University of Rennes 1, France;* [3]*Résonance Magnétique des Systèmes Biologiques, UMR 5536 CNRS – Université Victor Segalen Bordeaux 2, 146 rue Léo Saignat, Case 93 F33076 Bordeaux, Cedex; E-mail: Eric.Thiaudiere@rmsb.u-bordeaux2.fr*

NMR characterization of biological tissues or materials (MR elastography) is a challenging and promising area of research. A review of ongoing progress in acoustic wave detection and characterization using NMR is given. After recalling some basic physical principles of acoustics (strain–stress relationship, viscoelasticity), NMR methods for shear or longitudinal wave detection are described, emphasizing pioneer works. Both spectroscopic and imaging methods are summarized, as well as a variety of procedures that allow reconstruction of (visco)elastic properties from NMR data. Emergent MR elastography (MRE) techniques were applied on inert materials for validation purposes. Relevant results were obtained on biological samples

ANNUAL REPORTS ON NMR SPECTROSCOPY
VOLUME 53 ISSN 0066 4103
DOI 10.1016/S0066-4103(04)53004-1

and in humans in vivo. *The clinical use of MRE dedicated to virtual palpation is nowadays clearly envisaged. MR elastography is also compared to another developing approach, namely ultrasonic elastography which exhibits complementary advantages and drawbacks.*

1. INTRODUCTION

The emergence of a new scientific research area often results from the unexpected convergence of new technology potentialities with the holding circuit of unresolved scientific questions, or conversely. Regarding works presently in progress on NMR characterization of mechanical waves, a useful starting point is probably both the growing use of static or oscillating NMR field gradients and the need, for various emergent reasons, of a better characterization of the mechanical properties of biological tissues.

Pathologies most often induce histological changes (such as inflammation and resulting edema, fibrosis, increase in oncotic pressure, variation of extracellular space, etc...) and then local variations of their bio-mechanical properties. This is why manual palpation has been for several thousand years one of the most traditional ways of medical diagnosis, though bearing two main limitations: the inaccessibility of embedded lesions and the highly subjective (or, at least, operator-dependent) result. Recently, cancer treatment individualization has increased the need for a better tissue characterization, based upon a new class of parameters among which the biomechanical properties of soft tissues. Clinical strategies for the design of patient-specific cancer treatments presently suffer from a lack of accurate tumor grading in terms of prognosis and forecast treatment efficiency; molecular biology (i.e., genomics and proteomics)[1,2] and more recently functional imaging (e.g., perfusion imaging, diffusion imaging, capillary permeability imaging, image texture analysis, metabolic chemical shift imaging, etc...) or even a convergence of both approaches have opened new exciting ways of investigation.[3]

As well, an important role of Magnetic Resonance Elastography (MRE) in tumour functional imaging can be expected. Another promising field of biomedical application of MRE will undoubtedly be computer-assisted surgery. The computed handling of surgical resection tools, in place of the surgeon hands, requires either to have a force back joystick, and/or to develop realistic modeling of elastic deformation of soft tissues during surgery.[4] It is well established that the models developed from *ex vivo* biomechanical data are not realistic enough to characterize soft tissues, due to the variation of oncotic pressure between *in vivo* and *post mortem* states. This is why real-time measurements of tissue visco-elasticity or, at least, *in vivo* measurement of accurate biomechanical parameters for modelling, is presently

a challenge. Similar biomechanical problems occur with the development of new materials and personalized designs of bio-implants.

The early concept of static field gradient (initially applied to NMR measurement of translational diffusion coefficients) was developed in the 1970s to space-encode the NMR signal with the beginning of MRI. In the early 1990s D. Rugar, J. A. Sidles and co-workers performed a surprising historical flash-back in revisiting the early famous experiment of O. Stern (Nobel prize in 1943) and W. Gerlach. They proposed a brilliant method for non-inductive detection of Magnetic Resonance.[5,6] The resulting huge improvement in NMR sensitivity was due to the use of strong oscillating magnetic field gradients. The theoretical basis of a similar method, applicable to NMR spectroscopy, was later proposed by C. J. Lewa.[7] In parallel and concomitantly to the pioneering work of J. A. Sidles, the use of oscillating gradients was first proposed by C. J. Lewa for NMR characterization of mechanical waves in biological tissues and, consequently, to the determination of their visco-elastic properties.[8,9] A full paper of C. J. Lewa, initially submitted in 1993 and published in 1995, detailed the first MRI method.[10] This early proposal was followed by a succession of exciting results on the application of improved viscoelastic NMR methods: these methods first used a synchronized mechanical wave requiring *a priori* knowledge.[11–13] Later, unsynchronized methods were also described.[14,15] They are more appropriate in case of unknown internal mechanical waves such as those resulting from cardiac motion. It was then shown that harmonic oscillations can be encoded by a radio-frequency field gradient,[16] providing a fully silent MRI method (no gradient noise) and opening the way to the study of the biological effect of acoustic waves.[17] The need of a better characterization of healthy or tumoural soft tissues can then converge with these NMR technological developments to provide clinical methods of quantitative and operator-independent 'virtual palpation' of embedded organs, as it has been initially called. These methods are still in progress but the clinical need of new *in vivo* approaches of tissue viscoelasticity might be considered as routinely satisfied in the near future. This constitutes a very important step for both tissue characterization (e.g., tumour heterogeneity) and tissue modelization (e.g., for computer assisted surgery, bio-implants design, coach building industry, etc...).

In this review, a brief account of physical backgrounds of viscoelasticity is given. Then the main spectroscopic and imaging methods to characterize or simply detect mechanical waves are described. As reconstruction of viscoelastic properties from NMR data sets is a challenging issue, several strategies that were proposed in the literature are cited here. Significant results, obtained *in vitro*, *ex vivo* (excised tissues) and *in vivo* in patients are given to emphasize the continuing improvements in MRE (Magnetic Resonance Elastography). NMR elastography is also compared to emerging complementary acoustic approaches based upon ultrasonic characterization of viscoelastic properties.

2. VISCOELASTIC PROPERTIES: THEORETICAL BACKGROUND

This section recalls several physical elements of mechanical wave propagation. It is by no way exhaustive and more detailed information can be found in Refs. 18–21. Moreover this theoretical part will be restricted to linear acoustics, first described in simple media and then extended to more complicated viscous anisotropic environments.

2.1. Acoustic waves in an elastic and isotropic medium

2.1.1. *Definitions*

In an elastic material medium a deformation (strain) caused by an external stress induces reactive forces that tend to recall the system to its initial state. When the medium is perturbed at a given time and place the perturbation propagates at a constant speed (or celerity) $\vec{c}$ that is characteristic of the medium. This propagating strain is called an elastic (or acoustic or mechanical) wave and corresponds to energy transport without matter transport. Under a periodic stress the particles of matter undergo a periodic motion around their equilibrium position and may be considered as harmonic oscillators.

The displacement of matter will be called $\vec{u}$ and their instantaneous velocity $\vec{v} = d\vec{u}/dt$.

A wave is described by a wave function: $y(\vec{r}, t)$, either scalar (as pressure p) or vector (as $\vec{u}$ or $\vec{v}$) at position $\vec{r}$ and time t. The wave function is the solution of a wave equation that describes the response of the medium to an external stress (see below).

Generally the wave function is a sine function: $y(\vec{r}, t) = A(\vec{r})e^{i(\omega t - \vec{k}\vec{r} + \varphi)}$ with $i^2 = -1$, $A(\vec{r})$ the wave magnitude, ω the angular frequency, $\vec{k}$ the wave vector and φ the phase. ω and $\vec{k}$ can be expressed as:

$$\omega = 2\pi\nu = 2\pi/T$$

where ν is the wave frequency and T the period,

$$||\vec{k}|| = k = \frac{2\pi}{\lambda}$$

where λ is the wavelength.

In planar waves the amplitude $A(\vec{r}) = A_0$ is a constant. All particles situated within a plane normal to the wave vector move at the same time. Longitudinal waves are planar waves where the displacements are parallel to the wave vector ($\vec{v}$ and $\vec{c}$ are colinear). Longitudinal waves can propagate in every material media. These are compression or dilatation waves. In transverse waves, $\vec{v}$ and $\vec{c}$ are orthogonal. Transverse waves do not propagate in fluids.

These are shear waves. Planar waves result from stress sources of infinite dimension. In practise planar waves are considered as the sum of spherical waves.

When the stress originates from a point-like source acoustic waves diverge from the source with a decreasing amplitude $A(\vec{r}) = A_0/r$.

2.1.2. *Energy, power, and intensity*

Assuming a volume element $V = S\lambda$ of density ρ where a periodic strain takes place the total energy is a constant:

$$E = 2\pi^2\nu^2A^2\rho S\lambda$$

The power is then: $P = (E/T) = 2\pi^2\nu^2A^2\rho Sc$.

The acoustic flux intensity is the power per unit area: $I = (P/S) = 2\pi^2\nu^2A^2\rho c$.

Relative acoustic intensity is often expressed in a logarithmic scale (decibel or dB):

$$I_{\mathrm{dB}} = 10\log\frac{I}{I_0}$$

where I_0 equals 10^{-12} W . m^{-2}.

2.1.3. *Wave equation*

A medium is called isotropic and homogeneous when its properties are the same everywhere in space and whatever the direction considered. Within such a medium the propagation velocity does not depend on the wave intensity. In a non-dispersive medium the wave velocity is no longer dependent on the wave frequency, i.e., no energy loss or decrease in amplitude occur during propagation. Let us call p the variation of pressure ($p = 0$ at equilibrium), and assuming mass and momentum conservation:

$$\frac{\partial\rho}{\partial t} + \vec{\nabla}(\rho\vec{v}) = 0 \quad \text{(mass conservation), and} \tag{1}$$

$$\frac{\partial(\rho\vec{v})}{\partial t} + \vec{\nabla}p = 0 \quad \text{(Euler's equation for momentum conservation)} \tag{2}$$

Moreover further developments will be restricted to linear acoustic. Therefore, space variations are small enough to approximate $\rho(\vec{r}) \approx \rho_0$. Regarding the velocity field $\vec{v}$ as the gradient of the velocity potential $\vec{v} = -\vec{\nabla}\Phi$ we can write $p = \rho_0(\partial\Phi/\partial t)$ and $(\partial\rho/\partial t) = \rho_0\vec{\nabla}^2\Phi$.

The wave equation is then:

$$\frac{\partial^2\Phi}{\partial t^2} = c^2\Delta\Phi$$

and the wave velocity is

$$c = \frac{1}{\sqrt{\chi \rho_0}}$$

where χ is the adiabatic compressibility coefficient of the medium, defined as:

$$\chi = -\frac{1}{V_0}\left(\frac{\partial V}{\partial p}\right)_T = \frac{1}{\rho_0}\left(\frac{\partial \rho}{\partial p}\right)_T.$$

The wave equation is also valid for p, $\vec{u}$, and $\vec{v}$.

2.1.4. *Interfaces and acoustic impedance*

The acoustic impedance Z is defined as the ratio of a variation of acoustic pressure to the induced velocity of matter:

$$Z = \frac{p}{v} = \frac{1}{\chi c} = \rho c$$

For instance in biological soft tissues $Z \approx 10^6$ kg . m^{-2} s$^{-1} \approx 10^6$ *Rayleigh*. From an acoustic point of view the propagating medium can be characterized by c and Z. Reflection and refraction processes occur in case of coexisting media with different acoustic impedances. For wave reaching with an incidence angle θ_i an acoustical diopter that separates two homogeneous media characterized by a celerity c_1 and an impedance Z_1 on one hand and a celerity c_2 and an impedance Z_2 on the other hand, part of the energy is reflected at a reflection angle $\theta_r = \theta_i$ and the remaining part is transmitted at a refraction angle θ_t. As in classical optics:

$$\theta_i = \theta_r \quad \text{and} \quad \frac{\sin\theta_t}{c_2} = \frac{\sin\theta_i}{c_1}$$

Defining $Z_1 = p_i/v_i = -p_r/v_r$ and $Z_2 = p_t/v_t$, it is possible to calculate transmission (t) and reflection (r) coefficients.

For acoustic pressure p:

$$r_p = \frac{Z_2\cos\theta_i - Z_1\cos\theta_t}{Z_2\cos\theta_i + Z_1\cos\theta_t}$$

$$t_p = \frac{2Z_2\cos\theta_i}{Z_2\cos\theta_i + Z_1\cos\theta_t}$$

For matter displacement u and matter velocity v:

$$r_v = r_u = -r_p,$$
$$t_v = t_u = \frac{2Z_1 \cos\theta_t}{Z_2 \cos\theta_i + Z_1 \cos\theta_t},$$
$$t_{u,v} = r_{u,v} + 1.$$

Finally, for energy E, power P, or intensity I:

$$I_{i,r} = \frac{p_{i,r}^2}{2Z_1} \quad \text{and} \quad I_t = \frac{p_t^2}{2Z_2}$$
$$R + T = 1$$
$$R = \left(\frac{Z_2 \cos\theta_i - Z_1 \cos\theta_t}{Z_2 \cos\theta_i + Z_1 \cos\theta_t}\right)^2$$
$$T = \frac{4Z_1 Z_2 \cos\theta_i \cos\theta_t}{(Z_2 \cos\theta_i + Z_1 \cos\theta_t)^2}$$

2.2. Elasticity and viscoelasticity

The analysis of propagating acoustic waves in an elastic medium allows its characterization by means of strain–stress relationships. The stress σ_{ij} is defined as the ratio of an external force F parallel to a direction i (x, y or z) to a surface S perpendicular to the direction j.

$$\sigma_{ij} = \frac{F_i}{S_j}$$

Examples of force and stress acting on a parallelepipedic element is shown in Fig. 1. A rank 2, real and symmetric stress tensor may thus be defined as:

$$\tilde{\sigma} = \sigma_{ij} = \begin{bmatrix} \sigma_{xx} & \sigma_{xy} & \sigma_{xz} \\ \sigma_{xy} & \sigma_{yy} & \sigma_{yz} \\ \sigma_{xz} & \sigma_{yz} & \sigma_{zz} \end{bmatrix}$$

Diagonal elements are traction or compression stress terms whereas non-diagonal elements are shear stress terms.

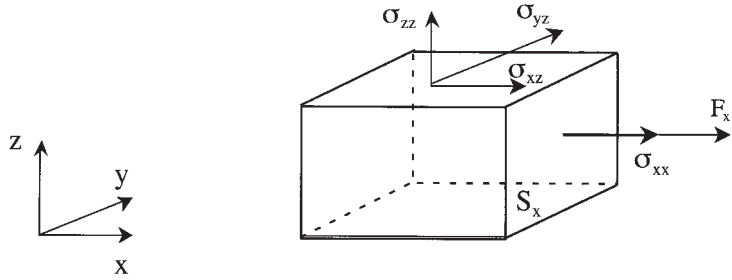

Fig. 1. Force and stress acting on a parallelepipedic element. S_x and F_x denote a surface element perpendicular to the x-axis and a force colinear to the x-axis, respectively. For stress tensor elements $\sigma_{.}$ the subscripts i and j (x, y or z) relate to the orientations of the force and the surface element, respectively.

In a similar fashion strain (deformation) ε_{ij} can be defined using a tensor notation:

$$\tilde{\varepsilon} = \varepsilon_{ij} = \begin{bmatrix} \varepsilon_{xx} & \varepsilon_{xy} & \varepsilon_{xz} \\ \varepsilon_{xy} & \varepsilon_{yy} & \varepsilon_{yz} \\ \varepsilon_{xz} & \varepsilon_{yz} & \varepsilon_{zz} \end{bmatrix} \quad \text{with } \varepsilon_{ij} = \frac{1}{2}\left(\frac{\partial u_i}{\partial j} + \frac{\partial u_j}{\partial i}\right)$$

where $i, j = (x, y \text{ or } z)$.

Diagonal terms are indeed relative elongation of the object in directions orthogonal to the surfaces. The trace of the tensor $\mathrm{tr}(\varepsilon)$ is thus the relative variation of volume. The non-diagonal elements are shear strains.

2.2.1. *Strain–stress relationship for small deformations*

Hooke's law is the relationship between strain and stress second rank tensors:

$$\sigma_{ij} = C_{ijkl}\varepsilon_{kl}$$

C_{ijkl} is a fourth order tensor that linearly relates σ and ε. It is sometimes called the elastic rigidity tensor and contains 81 elements that completely describe the elastic characteristics of the medium. Because of the symmetry of σ and ε, only 36 elements of C_{ijkl} are independent in general cases. Moreover only 2 independent rigidity constants are present in C_{ijkl} for linear homogeneous isotropic purely elastic medium: Lame coefficient λ and μ have a stress dimension, λ is related to longitudinal strain and μ to shear strain. For the purpose of clarity, a condensed notation is often used

for the symbols ij and kl: $xx=1$; $yy=2$; $zz=3$; $yz=zy=4$; $xz=zx=5$; $yx=xy=6$. Lame coefficients are defined from C_{ijkl} as follows:

$$C_{11} = C_{22} = C_{33} = \lambda + 2\mu$$
$$C_{12} = C_{13} = C_{23} = \lambda$$
$$C_{44} = C_{55} = C_{66} = \frac{C_{11} - C_{12}}{2} = \mu$$

The strain–stress relationship can be written as:

$$\varepsilon_{ij} = \frac{1}{2\mu}\sigma_{ij} + \frac{\lambda}{2\mu + 3\lambda}\mathrm{tr}(\sigma_{ij})\tilde{I}$$

with $\mathrm{tr}(\sigma)$ the trace of the stress tensor and $\tilde{I}$ the second rank metric tensor. Instead of Lame coefficients, Young's modulus E and Poisson's ratio ν are often used in the literature. E is the longitudinal elasticity modulus, i.e., the stress-to-strain ratio in the direction of the external force, while ν is the shear to longitudinal strain ratio ($\nu=0.5$ for a non-compressible medium). The adiabatic compressibility coefficient can thus be written as:

$$\chi = \frac{3(1-2\nu)}{E}$$

In Table 1 are listed conversions between Lame coefficients, Young's modulus, Poisson's ratio, χ, and C_{ijkl} for an isotropic elastic homogeneous medium.

Table 1. Elasticity and rigidity constants for a homogeneous isotropic elastic medium

	E, ν	λ, μ	C_{11}, C_{12}, C_{44}
E	E	$\frac{\mu(3\lambda+2\mu)}{\lambda+\mu}$	$C_{11} - 2\frac{C_{12}^2}{C_{11}+C_{12}}$
ν	ν	$\frac{\lambda}{2(\lambda+\mu)}$	$\frac{C_{12}}{C_{11}+C_{12}}$
λ	$\frac{E\nu}{(1+\nu)(1-2\nu)}$	λ	C_{12}
μ	$\frac{E}{2(1+\nu)}$	μ	C_{44}
C_{11}	$\frac{E(1-\nu)}{(1+\nu)(1-2\nu)}$	$\lambda + 2\mu$	C_{11}
C_{12}	$\frac{E\nu}{(1+\nu)(1-2\nu)}$	λ	C_{12}
C_{44}	$\frac{E}{2(1+\nu)}$	μ	C_{44}
$B=\chi^{-1}$	$\frac{E}{3(1-2\nu)}$	$\lambda+\frac{2}{3}\mu$	$\frac{C_{11}+2C_{12}}{3}$

2.2.2. *Propagation of small deformations in a linear elastic isotropic homogeneous medium*

From Euler's equation applied to σ_{ij}, and assuming a quasi-constant density, the displacement propagation can be expressed as:

$$\rho \frac{\partial^2 \vec{u}}{\partial t^2} = \vec{\nabla}\sigma_{ij} = (\lambda + \mu)\vec{\nabla}(\vec{\nabla} \cdot \vec{u}) + \mu \vec{\nabla}^2 \vec{u} \tag{3}$$

This equation can be simplified for purely longitudinal or transverse waves. In longitudinal waves (P waves) $\vec{\nabla} \times \vec{u} = \vec{0}$ and $\vec{\nabla} \cdot \vec{u} \neq 0$, so $\rho(\partial^2 \vec{u}/\partial t^2) = (\lambda + 2\mu)\vec{\nabla}^2 \vec{u}$, and in transverse waves $\vec{\nabla} \times \vec{u} \neq \vec{0}$, and $\vec{\nabla} \cdot \vec{u} = 0$, so $\rho(\partial^2 \vec{u}/\partial t^2) = \mu \vec{\nabla}^2 \vec{u}$ (Helmholtz equation). It can be deduced that the wave celerity is $c_L = \sqrt{(\lambda + 2\mu)/\rho}$ for longitudinal waves and $c_T = \sqrt{\mu/\rho}$ for transverse waves.

In a homogeneous isotropic elastic medium it is possible to split acoustic waves in independent longitudinal and transverse waves, each travelling at a speed c_L and c_T, respectively. As λ is greater than or equal to zero, c_T is lower than or equal to $c_L/\sqrt{2}$.

2.2.3. *Dispersion and attenuation: viscoelasticity*

The strain–stress relationship $\sigma_{ij} = C_{ijkl}\varepsilon_{kl}$ is valid when strain is instantaneously provoked by stress, i.e., no dephasing process occurs. In fact, it was observed that the magnitude of acoustic waves decreased as a function of the travelling distance. Introducing a damping term proportional to the time course of strain variations can solve this discrepancy:

$$\sigma_{ij} = C_{ijkl}\varepsilon_{kl} + \eta_{\text{ijkl}} \frac{\partial \varepsilon_{kl}}{\partial t} \tag{4}$$

where η_{ijkl} is the viscosity tensor. Under periodic stimulation ($\varepsilon_{kl} = \varepsilon_0 e^{i(\omega t - \vec{k}\vec{r})}$) the strain–stress relationship reads:

$$\sigma_{ij} = K_{ijkl}\varepsilon_{kl} \quad \text{with} \quad K_{ijkl} = C_{ijkl} + i\omega\eta_{ijkl}$$

K_{ijkl} is called the complex elastic rigidity tensor or viscoelasticity tensor. Note that η and K are fourth-rank tensors. Again, simplifications are possible for a homogeneous isotropic medium: K can be defined with 2 complex Lame constants λ_c and μ_c:

$$\begin{cases} \lambda_c = \lambda + i\omega\eta_\lambda \\ \mu_c = \mu + i\omega\eta_\mu \end{cases}$$

where η_λ is longitudinal viscosity and η_μ the shear viscosity.

In case of a transverse wave, the propagation equation becomes:

$$\rho\frac{\partial^2\vec{u}}{\partial t^2}=\mu\vec{\nabla}^2\vec{u}=(\mu+i\omega\eta_\mu)\vec{\nabla}^2\vec{u} \tag{5}$$

The shear wave celerity (c_T) is then:

$$c_T=\frac{\omega}{k}=\sqrt{\frac{2}{\rho}\left(\frac{\mu^2+\omega^2\eta_\mu^2}{\mu+\sqrt{\mu^2+\omega^2\eta_\mu^2}}\right)}=\sqrt{\frac{2}{\rho}\left(\frac{|\mu_c|^2}{\mu+|\mu_c|}\right)},$$

and the attenuation coefficient α_T:

$$\alpha_T=\sqrt{\frac{\rho\omega^2}{2}\left(\frac{\sqrt{\mu^2+\omega^2\eta_\mu^2}-\mu}{\mu^2+\omega^2\eta_\mu^2}\right)}=\sqrt{\frac{\rho\omega^2}{2}\left(\frac{|\mu_c|-\mu}{|\mu_c|^2}\right)}$$

Further approximations can be made assuming low viscosity, $\omega\eta_\mu \ll \mu$:

$$c_T\approx\sqrt{\frac{\mu}{\rho}}\quad\text{and}\quad\alpha_T\approx\frac{\omega^2\eta_\mu}{2\rho c_T^3}$$

For a longitudinal wave, the wave propagation reads:

$$\rho\frac{\partial^2\vec{u}}{\partial t^2}=(\lambda_c+2\mu_c)\vec{\nabla}^2\vec{u}=(\mu'+i\omega\eta')\vec{\nabla}^2\vec{u}$$

with $\mu'=\lambda+2\mu$, $\eta'=\eta_\lambda+2\eta_\mu$, and $\mu'_c=\mu'+i\omega\eta'$

$$c_L=\frac{\omega}{k}=\sqrt{\frac{2}{\rho}\left(\frac{(\lambda+2\mu)^2+\omega^2(\eta_\lambda+2\eta_\mu)^2}{\lambda+2\mu+\sqrt{(\lambda+2\mu)^2+\omega^2(\eta_\lambda+2\eta_\mu)^2}}\right)}=\sqrt{\frac{2}{\rho}\left(\frac{|\mu'_c|^2}{\mu'+|\mu'_c|}\right)}$$

$$\alpha_T=\sqrt{\frac{\rho\omega^2}{2}\left(\frac{\sqrt{(\lambda+2\mu)^2+\omega^2(\eta_\lambda+2\eta_\mu)^2}-(\lambda+2\mu)}{(\lambda+2\mu)^2+\omega^2(\eta_\lambda+2\eta_\mu)^2}\right)}=\sqrt{\frac{\rho\omega^2}{2}\left(\frac{|\mu'_c|-\mu'}{|\mu'_c|^2}\right)}$$

Note the presence of both viscosity coefficients in the expressions of the longitudinal amplitude attenuation and wave celerity. In case of low viscosity:

$$c_L \approx \sqrt{\frac{\lambda + 2\mu}{\rho}} \quad \text{and} \quad \alpha_L \approx \frac{\omega^2 \eta'}{2\rho c_L^3} = \frac{\omega^2(\eta_\lambda + 2\eta_\mu)}{2\rho c_L^3}$$

Note that attenuation of pressure wave follows $p = p_0 e^{-\alpha x}$ whereas attenuation of intensity is described by $I = I_0 e^{-2\alpha x}$. Attenuation is often expressed as $\alpha = \beta \nu$. For air, water and soft biological tissues, $\alpha = 10$, 2.10^{-3}, and 0.3 to 1.5 dB cm^{-1} MHz^{-1}, respectively.

2.2.4. *Propagation of acoustic waves in an anisotropic medium*

In an anisotropic medium the physical properties depend on the direction of observation. The equation of propagation now reads:

$$\rho \frac{\partial^2 u_i}{\partial t^2} = C_{ijkl} \frac{\partial^2 u_l}{\partial x_j \partial x_k} \quad \text{with } i, j, k, l = x, y, \text{or } z. \tag{6}$$

This is indeed a system of three second-order differential equations. The tensor elements C_{ijkl} may be complex-valued in case of viscoelasticity. Analysis shows that the propagation can be split into three orthogonally polarized planar waves propagating along a wave vector $\vec{k}$. Those three waves may have different propagating celerities. Phase celerity and polarization u_i^0 are connected through Christoffel equation:

$$\rho c^2 u_i^0 = C_{ijkl} n_j n_k u_l^0$$

with k_j and k_k the wave vectors along direction j and k.

The propagating wave in an anisotropic medium can then be described by two quasi-transverse (with respect to the direction of propagation) shear waves and one quasi-longitudinal wave, the latter being the faster. Thus the polarization may be no more strictly parallel or orthogonal to the wave vector. The acoustic energy propagates at an energy speed $\vec{V}^e$ with three components:

$$V_i^e = \frac{C_{ijkl} u_j^0 u_l^0 n_k}{\rho c (u_i^0)^2} \quad \text{and} \quad \vec{V}^e \vec{n} = c$$

This means that whenever V^e is parallel to $\vec{n}$, the wave is purely transverse or longitudinal.

3. NMR DETECTION AND CHARACTERIZATION OF MECHANICAL WAVES

Since the pioneering work of Lewa,[8,9] several methods have been developed in order to record mechanical waves by NMR. Most of the techniques dealt with conventional magnetic resonance imaging (MRI) procedures, mainly focused on the appraisal of viscoelastic parameters of living tissues or inert samples 'mimicking' biological materials. The advantage of MRI applied to elastography is obviously to map non-invasively spatial changes in compliance. Nevertheless, some low-cost spectroscopic approaches also exist and are still being developed.

3.1. Generation of mechanical and acoustic waves

Among the variety of published studies on NMR detection of mechanical waves one can distinguish several types of devices for generating vibrations into a sample.

Shear strain waves in the range of 10–1000 Hz were often generated by electromagnetic coils placed in the magnet and connected to a waveform generator. A sine wave current circulating in these coils induces a magnetic moment usually perpendicular to the static field B_0 thus creating a torque oscillating at the desired frequency (Fig. 2A). The coils are mechanically coupled to a shear stage or a surface plate, the latter connected to the sample. Such a device was successfully used on gels, *ex vivo* organs (skeletal muscle, liver, kidney...) as well as for *in vivo* studies (skeletal muscle, breast...).[11,13,22–27] An analog experimental setup was used by several authors[15,16] who used a vibrating table. This consisted in fact of an electric motor (placed outside the magnet) capable of alternating translations transmitted via a rigid rod to a surface plate (Fig. 2B). For measurements in the brain, external vibrations (100 Hz) were transmitted to the head of volunteers thanks to a thermoplastic bite held in their teeth.[28]

A device dedicated to low-frequency (20–200 Hz) acoustic longitudinal waves is described in Ref. 17. It was made of an audio amplifier supplying a high power bass loudspeaker. A waveguide ensured the propagation of the sound towards a gel sample.

The latter systems are obviously difficult to use with the aim of a routine clinical assessment of viscoelastic properties of tissues. The most convenient method for generating acoustic waves in a NMR system is to use a non-magnetic sound transducer. Focused ultrasounds (FUS) were mostly used because high acoustic pressures were needed to obtain NMR-detectable displacements. Either longitudinal waves are aimed to be visualized[29,30] or a sinusoidal modulation of the acoustic intensity was used to generate shear waves propagating radially from the US focus.[31,32] In the latter case the modulation frequency was also in the range of 100 Hz.

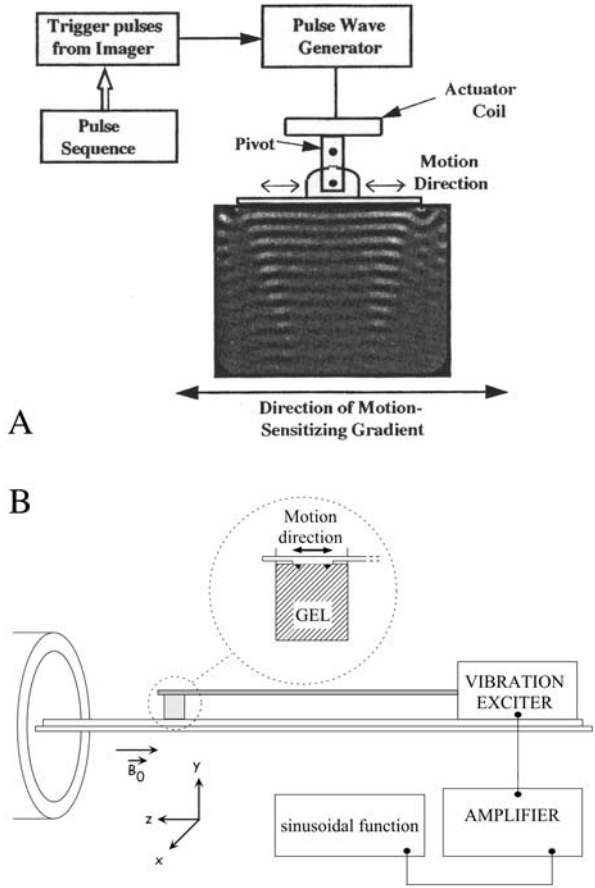

Fig. 2. Experimental setups for periodic shear wave generation. (A) The wave generator produces an alternating current into a coil with its field oriented perpendicularly to the MRI magnetic field (here horizontal). The alternating current thus creates an oscillating torque that moves horizontally a plate embedded in a gel phantom. Shear waves are then detected using a MRI sequence including a motion-encoding static magnetic field gradient. The detection of motions is optimized when this gradient is parallel to the spin displacement. (From Ref. 23 reprinted by permission of Wiley-Liss, Inc., a subsidiary of John Wiley & Sons, Inc.) (B) An alternative way uses a vibrational device similar to a loudspeaker connected to the plate by a rigid rod. Here the magnetic field produced by the magnet is horizontal (adapted from Ref. 15 reprinted by permission of Wiley-Liss, Inc., a subsidiary of John Wiley & Sons, Inc.)

3.2. MRI methods

Most of the methods are based upon the application of both a static magnetic field gradient and a mechanical wave in order to measure the consequence of the latter on a given NMR parameter. Indeed, the mechanically-induced

periodic displacement u of paramagnetic nuclei was expected to involve a change in their Larmor frequency ν_{NMR} when subjected to a constant field gradient G. Obviously, the scalar product $\vec{\xi} \cdot \vec{G}$ must be non-zero. Historically, Lewa[8,9] first demonstrated from a theoretical point of view the shape of the NMR spectrum $\nu_{NMR}(\Omega)$ as a function of the mechanical wave pulsation Ω:

$$\nu_{NMR} = \frac{\gamma}{2\pi} B_0 + n\frac{\Omega}{2\pi} \qquad \text{with } n = 0, 1, 2 \ldots, \tag{7}$$

where γ is the magnetogyric ratio, and B_0 the magnetic induction in the absence of gradient. A careful analysis showed that the amplitude of the nth sideband was roughly proportional to the square of the nth component of the Bessel function $J^2_n(\alpha)$. The argument α was then expressed as:

$$\alpha = \frac{\gamma}{2\pi} \frac{\chi p_0 \lambda G}{2\nu} \cos \Psi \tag{8}$$

where χ is the adiabatic compressibility of the medium, p_0 the acoustic pressure amplitude, λ the wavelength of the mechanical wave, ν its frequency, and Ψ the angle between the magnetic field gradient and the displacement. Lewa and de Certaines[10] confirmed later this theoretical approach by showing the existence of the first order side bands in ^{1}H NMR spectra and images of water phantoms subjected to a periodical mechanical excitation in the presence of a field gradient. Although preliminary and sometimes unrecognized, this piece of work opened the way to further developments in MRI of viscoelastic properties of tissues.

In 1995–1996 the MRI method for visualizing transverse waves was based upon the use of a bipolar field gradient to encode periodical spin motions.[11–13,22,23] Indeed the principle of detection was the same as the one originally proposed by Stejskal and Tanner for diffusion coefficient measurement.[33] Examples of experimental setups are represented in Fig. 2. A modified gradient-recalled echo sequence including motion sensitizing gradients and an illustration of the consequence of a bipolar gradient synchronized with the spin displacement are shown in Fig. 3. Briefly, after spin nutation induced by a slice–selective radiofrequency pulse, a first short pulsed gradient is applied when spins have reached the maximal displacement along a given direction. The phase of transverse magnetization is then spread over the sample. Before the transverse magnetization vanishes a second opposite gradient is applied when the spins are situated at the opposite maximal position. Then the phase of transverse magnetization adopts a constant value across the object (see below for details). The repetition of the bipolar gradient at the appropriate frequency (in this case the gradient

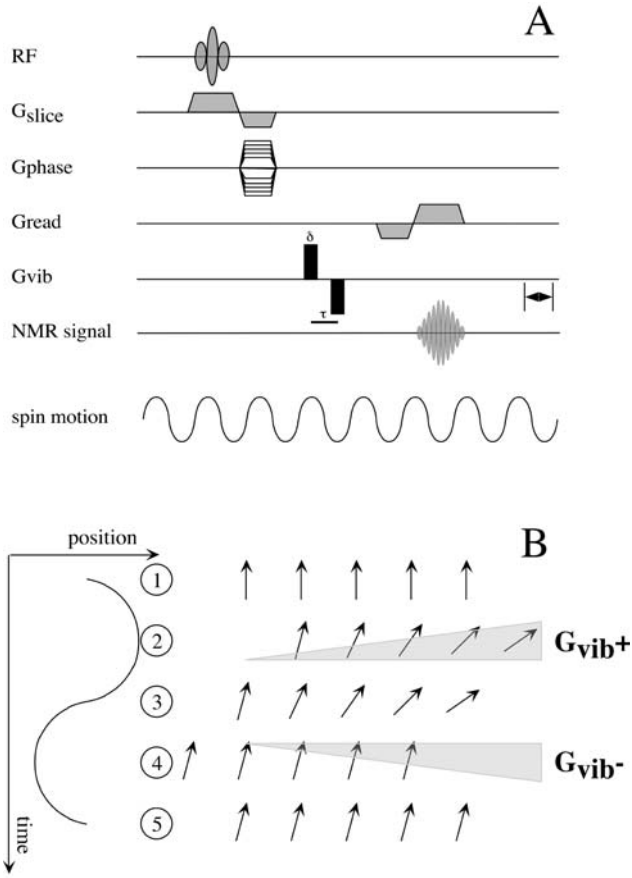

Fig. 3. Principle of detection of acoustic waves by conventional MRI. (A) Modified gradient-recalled echo sequence for 2D imaging. The application of the bipolar motion-sensitizing gradients G_{vib} (duration δ, interpulse delay τ) is synchronized with the displacement of matter. (B) Schematic view of motion encoding. Left: 1D sinusoidal displacement. Right: phase evolution of transverse magnetization of isochromat (arrows) undergoing the same cyclic motion. Step 1, no displacement occurs and no motion-sensitizing gradient is applied: transverse magnetization vectors are in phase. Step 2, the application of the positive lobe of G_{vib} and spin motion induces position-dependant phase shifts. Step 3, the magnetization vectors return to their original positions, but the phase shifts are conserved. Step 4, the application of the negative lobe of G_{vib} induces a constant phase shift. Step 5, at the end of a cycle, phase-shifted isochromats return to their initial position. The phase shift can be increase by repeating the synchronized application of G_{vib} during the mechanical waves.

interpulse period is half the motion period) gives rise to an accumulation of the phase of transverse magnetization.

Let us consider an unidirectional spin displacement (a very unlikely assumption in heterogeneous media such as living beings who bear a number

of different acoustic impedances). The equation of motion in case of longitudinal acoustic waves can be described as:

$$u(t, x) = u_0 \sin(2\pi\nu t - kx + \varphi) \tag{9}$$

where u is the instantaneous displacement, $u_0 = \chi p_0$ the maximal amplitude, $k = 2\pi/\lambda$ the wave vector, x the spin position and φ the initial phase of the propagating wave. Using a pulse sequence made of a single bipolar field gradient, we define the gradient pulse length as δ and the time interval between to opposite gradient pulses as τ (see Fig. 3). It was shown that the phase shift Φ of the transverse magnetization can be expressed as:[12]

$$\Phi = \frac{2G\gamma u_0}{\pi\nu} \sin(\pi\nu\delta) \sin(\pi\nu\tau) \cos(\varphi - kx) \cos\psi, \tag{10}$$

where ψ is the angle between the displacement vector and motion-encoding gradient.

This equation could be generalized for arbitrary cyclic motions:

$$\Phi = \frac{2\gamma\vec{G} \cdot \vec{u}_0}{\pi\nu} \sin(\pi\nu\delta) \sin(\pi\nu\tau) \cos(\varphi - \vec{k} \cdot \vec{r}) \tag{11}$$

By using the standard pulsed-field MRI protocols, such as spin-echo or gradient-recalled echo sequences, it was then possible to partially map the phase shift $\Phi(\mu, \mu')$ at a good planar resolution (μ and μ' are arbitrary spatial coordinates). The acquisition of $\Phi(\mu, \mu')$ theoretically allows to obtain $u_0(\mu, \mu')$ and then to map the wavelength and the celerity of the propagating wave. For low vibration frequencies the latter can be estimated independently by recording the time course of $u_0(\mu, \mu')$. However, care must be taken in extrapolating $u_0(\mu, \mu')$ from the raw data, because that cannot be done in a straightforward manner [see Eq. (11)]. Indeed calibration of the experimental setup (for instance by measuring displacements with laser optics[23]) is often needed.

Improvements in the MRI hardware, particularly the gradient pulse shape control, made it possible to vary sinusoidally the field gradient waveform to tune it properly to the mechanical wave.[23,24,29,30] The advantage of doing so is obviously to gain efficiency in detecting spin displacements as small as a few tens of nanometers. Such tiny motions may occur in case of marked attenuation of the propagating wave and/or at very high mechanical wave frequencies (for instance in ultrasound fields[29,30]).

Until now the mentioned approaches needed the NMR pulse sequence to be triggered with respect to the mechanical wave in order to avoid inappropriate wave detection due to the value of φ. Recently a method authorizing a proper detection of transverse waves without synchronization was

developed.[15] It was based on a derivative of the SPAMM sequence (SPAtial Modulation of Magnetization[34]). The SPAMM method consists in applying a strong magnetic field gradient prior to a standard imaging sequence. This strong gradient following a 90-degree RF pulse induces a sharp modulation of the phase of the transverse magnetization that is stored longitudinally by another 90-degree RF pulse. Such a preparation causes black and white stripes in the image, aligned perpendicularly to the SPAMM gradient direction. The modification of the SPAMM sequence is the following: during the preparation period the addition of a single gradient sine wave suffices to enable a correct encoding of cyclic motions. A single shot or a fast imaging sequence then allows to record distortions of the SPAMM stripes that can be converted into viscoelastic parameters. The main advantages of this method is its insensitivity to φ and its quickness.

3.3. Spectroscopic methods

Notwithstanding the significant progress brought by the continuously developed MRI methods to characterize mechanical waves, a drawback remains: an inaccurate determination of the vibration frequency. In Ref. 23, the authors showed that the MRI detection of the transverse waves was properly carried out when the motion sensitizing gradients oscillated at the same frequency. But a precise assessment of the vibration frequency strongly depends on the number of gradient oscillation periods.[15] A detailed study of the vibration frequency spectrum using MRI methods would be tedious and even inapplicable *in vivo*. This is why faster spectroscopic methods might be useful for this purpose. A possible approach using sinusoidal variation of a static field gradient could be derived from Ref. 14. In this work it was proposed to detect the phase variation Φ of the transverse magnetization following the application of an integer number n of oscillation periods $\tau = 1/\nu_G$ of a field gradient G when the sample is subjected to a vibration frequency ν. Defining α as ν/ν_G:

$$\frac{\Phi(r,t,\Psi)}{\gamma G_0 u_0 \cos\Psi} = \frac{1}{2\pi\nu(\alpha-1)}\cos\left\{2\pi\nu(\alpha-1)\left(t+\frac{n\tau}{2}\right)+\varphi-\vec{k}\cdot\vec{r}\right\}\cdot\sin\{\pi\nu(\alpha-1)n\tau\} \tag{12}$$

One should note that the phase shift becomes time-independent and maximal for $\alpha = 1$, i.e., at the resonance condition $\nu = \nu_G$. The frequency spectrum $\Phi(\alpha)$ bears a *sinc* shape with a bandwidth inversely proportional to the number of oscillations of the gradient field (Fig. 4). Such a behaviour was also predicted in Ref. 15. Recording in a systematic way the phase shift as a function of ν_G without space encoding would be a very fast and efficient method to scan in a whole object the possible frequencies of spin motions.

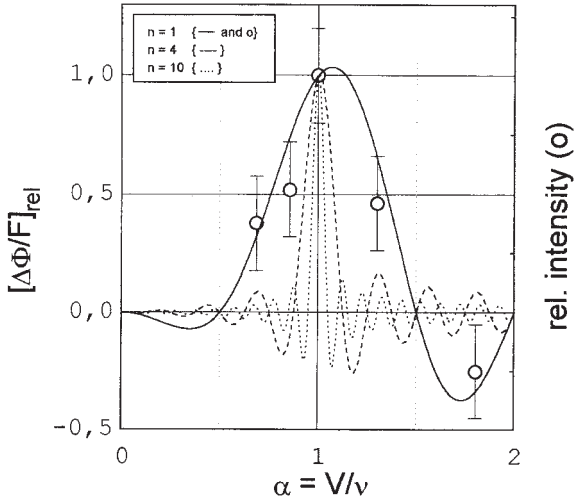

Fig. 4. Selectivity of detection of mechanical waves. The relative phase shift $\Delta\Phi/F$ (referred to as $(\Phi(r,t,\Psi))/\gamma G_0 u_0 \cos\Psi$ in Eq. (12)) is plotted versus the ratio α as ν/ν_G for $n=1$ (solid line), $n=4$ (dashed line) and $n=10$ (dotted line) cycles of motion-sensitizing gradient. Note that the selectivity increases according to the number of periods of motion encoding. The open symbols are experimental relative intensities measured on wave images obtained with a SPAMM sequence with $n=1$ (from Ref. 15, reprinted by permission of Wiley-Liss, Inc., a subsidiary of John Wiley & Sons, Inc.).

Yet such an approach would be hampered by self-cancellation due to phase averaging of the NMR signal by integration over r. A solution would then be the use a surface coil whose receptivity is confined to a limited number of propagation wavelengths, i.e., for low wave frequencies and/or high velocities.

A spectroscopic method using a radiofrequency field (RF or B_1) gradient[35] instead of a static field variation for motion encoding has been proposed recently.[16] The advantages of the RF gradients are their low sensitivity to magnetic susceptibility artifacts, the absence of Eddy currents and a low cost. The principle of detection of mechanical waves is based upon a distribution of nutation angles across the object. An example of pulse sequence using a series of binomial $1\bar{3}3\bar{1}$ rectangular pulses of length D separated by delays τ is shown in Fig. 5. The characteristic period $T_V = 4(D+\tau)$ enables the detection of periodic motions occurring at $\nu = 1/T_V$ and $\nu = 2/T_V$. Improved detection could be brought by increasing the number of $1\bar{3}3\bar{1}$ pulse cycles and by triggering the NMR sequence to the mechanical excitation. In order to selectively encode transverse spin motions in one direction with a limited influence of wave propagation in the orthogonal directions, a very asymmetric ladder-shaped surface coil was designed.[36] This shape enabled the existence of a quasi-constant B_1-gradient over 75% of the main axis of the coil. The same coil was proposed to detect low-frequency acoustic longitudinal waves by

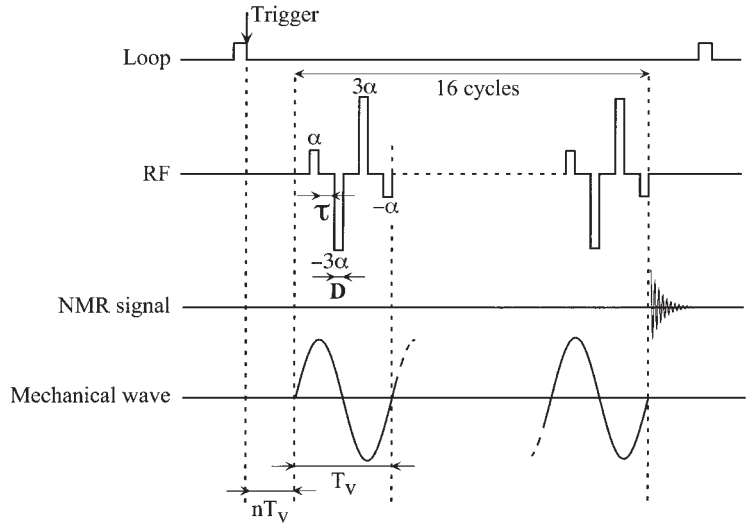

Fig. 5. Pulse sequence for MR detection of vibration using a radiofrequency field gradient. A binomial $1\bar{3}3\bar{1}$ radiofrequency pulse (pulse length D, interpulse delay τ) is applied in-phase with the mechanical wave. Thus the vibration period T_V is equal to $4(D+\tau)$. The number of cycles can be increased to ensure a better frequency selectivity. The constant RF field gradient generated by a dedicated RF coil allows space encoding without using conventional static field gradients (from Ref. 16 with permission from Elsevier).

assuming that for very high wavelengths (>1 m) the scalar product $\vec{k}\cdot\vec{r}$ is virtually constant for a coil length of 20 cm.

3.4. The reconstruction problem

Assuming that a number of NMR data sets (e.g., 2-D or 3-D maps of displacement vectors resulting from an external periodic excitation) from an object are acquired, the remaining difficulty is their reconstruction into viscoelastic parameters. As written in Section 2 the basic physical equation is a partial differential equation (PDE, Eq. (3)) relating the displacement vector to the density, the attenuation, Young's modulus and Poisson's ratio of the medium. The reconstruction problem is indeed two-fold:

- The forward problem is the calculation of displacement fields from input viscoelasticity parameters. The latter describe correctly the investigated object if the calculated and measured displacement images converge.
- The inverse problem is to evaluate the viscoelasticity pattern from the experimental (or simulated) strain data.

Both problems cannot be solved in a straightforward manner. Mathematical treatments can be ill-conditioned because of the large number of independent variables and noise. Approximations were often made in order to simplify the equation of motion. Examples of strategies of reconstruction are given in Ref. 28 and are briefly described below, in a decreasing order of approximations:

(i) The propagating medium is homogeneous, its Young's modulus is scalar (isotropic elasticity) and only one wave propagates. This simpler case correspond to *in vitro* studies in gels. The phase map obtained by MRI with only one motion encoding gradient applied parallel to the direction of the wave propagation suffices to derive the stiffness of the medium. This method is called the phase gradient method for elasticity reconstruction. It is noise-sensitive and is not valid for more than one propagating wave. Obviously this model is not applicable to heterogeneous media.

(ii) The isotropic viscoelastic parameters are not homogeneous throughout space but can be considered as locally homogeneous. The longitudinal Lame coefficient λ can be removed if the displacements due to the longitudinal wave vary slowly. Moreover if one assumes incompressibility, the complex-valued shear modulus μ can be derived from Helmholtz equation [Eq. (5)]. Then only one direction of the gradient sensitizing direction is required to determine μ from the wave image. Similar approximations were considered in calculating Young's modulus from quasi-static deformations.[37] Among more advanced data processing the local frequency estimation (LFE) method in fact can solve Helmholtz equation by calculating the local wave vector of the propagating wave from a combination of local estimates of instantaneous spatial frequency over several scales.[38–40] The method can be extended to 3D displacements, and handles reflected waves. Less assumptions are nevertheless needed with an other reconstruction method called AIDE (algebraic inversion of the differential equation). Complex-valued λ and μ are considered isotropic and locally homogeneous. Full inversion of the differential equation of motion requires all polarizations of motions, i.e., the 3-D displacement image.[41] AIDE can also be applied to solve Helmholtz equation. LFE and AIDE are more robust than the phase gradient method because they are less sensitive to noise and are valid for more than one propagating wave.[28]

(iii) The isotropic viscoelasticity parameters are not locally homogeneous. The general inhomogeneous partial differential equation [Eq. (5)] must be taken into account to extract the viscoelastic parameters from the wave images. Van Houten *et al.*[42–44] carefully studied this

problem. They used the finite element method (FEM) to reconstruct Young's modulus maps of simulated objects. The method indeed aims to minimize the difference between measured displacements and those calculated from a given elasticity map. The finite element model operates a geometrical discretization of the object through a mesh often made of triangles. The reconstruction works on small overlapping subzones with a limited amount of finite elements in order to minimize the number of fitting parameters (for instance all the elasticity parameters for every pixel of an MR image) that would be too high for the entire object. The refinement of the elasticity map of the subzone is achieved by iterative non-linear least-square minimization. This method is suited for analysis of MRI data because spatial discretization takes advantage of digital space resolution.

(iv) The viscoelasticity of the medium is neither homogeneous nor isotropic. This is the most general case: the only assumption is that the displacements are small enough to consider the strain–stress relationship as linear. Young's modulus and related quantities become tensor. Thus a very large number of independent parameters has to be evaluated in case of 3-D elasticity tensor imaging. Sinkus *et al.*[26] proposed a reconstruction method from complex-valued displacement data sets. The amplitude and phase of the displacement vector in each pixel can be obtained by recording successive MR wave images for different time delays between the excitation wave and the motion-sensitizing gradient. With reasonable assumptions of Poisson's ratio and density of the object, eigenvalues, and eigenvectors of the elasticity tensor can be derived. This would be of special interest to determine along which direction in the object the wave preferentially propagates.

3.5. Results

The goals of the different works listed below varied from methodological developments to attempts of determination of viscoelastic parameters in humans. Accordingly MR detection and/or characterization of mechanical waves has been carried out either on phantoms, excised biological tissues (*ex vivo* studies) or *in vivo* on a living organism. As a matter of fact most of the NMR procedures and reconstruction methods mentioned above still need to be developed to make them robust, reproducible and informative enough, especially when the goal is a clinical application.

Experimental confirmations of the theoretical predictions of Lewa and de Certaines[10] were independently published by Ehman's group[11,13,23] and by Plewes and *et al.*[22] The former authors used the vibrating system depicted

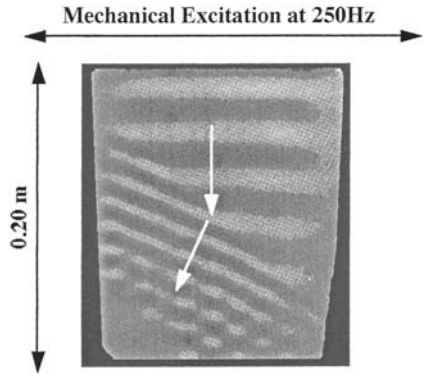

Fig. 6. MR wave image of acoustic refraction. Shear waves generated in the upper part of an agar gel phantom (horizontal motion) propagate vertically in the stiff part of the phantom ($\mu \sim 50$ kPa; $c_T \sim 7.5$ cm/s) and are refracted by the oblique lower part of soft gel ($\mu \sim 15$ kPa; $c_T \sim 4$ cm/s). Note the marked reduction of wavelength in the softer medium. From Ref. 23, reprinted by permission of Wiley-Liss, Inc., a subsidiary of John Wiley & Sons, Inc.

in Fig. 2 to create transverse waves in the range of 100–500 Hz and the MRI method using a series of bipolar static field gradients for spin motion encoding. Gradients were triggered synchroneously with the mechanical excitation. A spectacular result was the visualization of shear strain waves in a heterogeneous gel phantom (Fig. 6) with two distinct shear moduli. In the figure, one could easily estimate the wavelength and the direction of propagation. Displacements of 50 nm to 2 μm[23] or more[13] were typically measured. Moreover the change in wavelength and hence of speed due to the refraction was clearly visible. The phase celerity of the waves could be assessed simply by systematically varying the phase shift φ [Eq. (9)] between the stress and the motion sensitizing gradients. Then the propagation appeared clearly as moving wave crests. Plewes *et al.*[22] had a similar experimental approach to generate vibrations in a phantom but used a periodic compression–decompression paradigm in conjunction with a modified Stejskal-Tanner spin-echo sequence for MRI. Displacement magnitude in three directions were properly recorded on gel phantoms exhibiting different elastic moduli. More recently, Kruse *et al.*[25] shear moduli maps of an agar gel (10 kPa) with a stiffer (40 kPa) inclusion were derived from wave images (excitation frequency: 300 Hz). A spatial filtering was applied to estimate the local wavelength. In a recent work[45] a comparison between shear waves MRE and classical compression tests on various agar gels showed that shear moduli measured by the two methods were in good agreement. Simple media such as agar or silicon gels are favorable to explore the possibilities and the limits of MRE, as well as for developing dedicated pulse sequences. Thanks to the implementation of a derived SPAMM sequence, Lewa *et al.*[15] evaluated

without synchronization the frequency response of shear strain waves in a gel subject to mechanical vibrations. A similar goal was aimed by using radiofrequency field gradients instead of conventional gradients for motion encoding[16] using a similar experimental setup as in Fig. 2B. The authors carried out a careful analysis of the NMR response of a gel subject to periodic oscillations as a function of the vibration frequency, amplitude, and direction with respect to the RF gradient. The results confirmed that a spectroscopic approach could be useful in MRE. However, this method would be greatly improved if the collected data were defined both spectrally and spatially. The same method using exclusively RF gradients was successfully applied to the detection of small displacements (in the range of 100 nm) induced by low frequency (20–200 Hz) acoustic longitudinal strain waves.[17] In contrast other authors explored the feasibility of detecting high frequency acoustic waves in the range of ultrasounds. In studies published by Plewes and co-workers,[29,30] a specific magnetic field gradient insert operating at the sound wave frequency (515 kHz) enabled the detection of around 100 nm displacements (Fig. 7). As US-induced matter displacements could be very small focusing was required thus involving rather high acoustic pressures. In Ref. 32, authors detected shear waves displacements brought about by a sinusoidal modulation of the FUS intensity. As the modulation frequency was in the order of several hundreds of Hertz the calculated shear moduli of various phantoms using FUS was confirmed to be the same as those calculated from a mechanical excitation via a surface plate connected to a vibrating device. Shear moduli of silicon or bovine gel phantoms were around 3 and 8–9 kPa, respectively for an amplitude modulation of the FUS of 100 Hz. In this study acoustic powers greater than 170 dB were used, which need cautions to limit the increase in temperature.

A number of studies on simulated objects and gel phantoms were dedicated to validating reconstruction procedures. Simulated phantoms were for instance used by Van Houten *et al.*[42–44] in order to assess the performance of a subzone-based FEM non-linear inversion algorithm. Heterogeneous objects consisting of a soft matrix containing several inclusions of various stiffness were simulated. 3-D displacement fields and derived approximated 2-D motion fields were generated and 15% noise added. The subzone-based reconstruction algorithm proved to be efficient on corrupted data (Fig. 8) only from 3D data. Moreover, the authors showed that in order to extract 2D sets of viscoelastic parameters, the displacement fields must be measured in three dimensions, i.e., MR experiments must be performed using all the directions of the motion sensitizing gradients.[46] Sinkus *et al.*[26] designed a numerical breast-like shape with a Young's modulus of 2 kPa bearing a stiffer inclusion (15 kPa) simulating a carcinoma. Finite element model (FEM) calculations provided then a 2-D map of calculated complex-valued displacements occasioned by a given stress. The authors checked that their reconstruction method provided the correct anisotropic elasticity

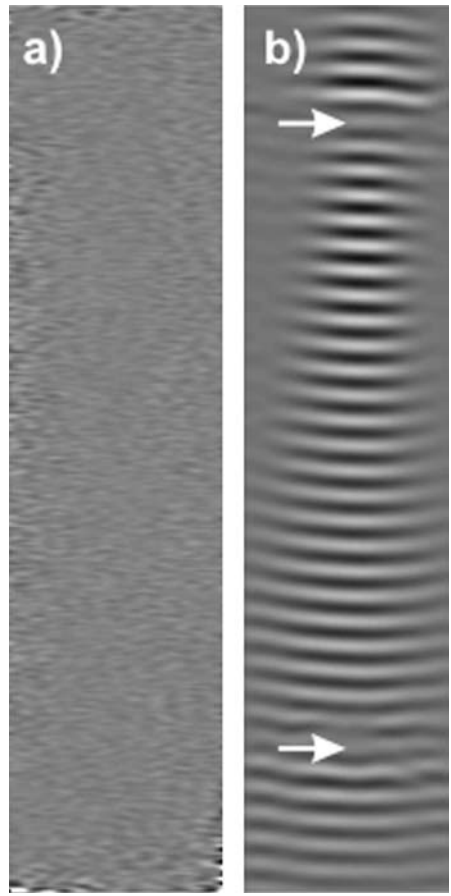

Fig. 7. MR detection of ultrasonic waves oscillating at 515 kHz. (a) Phase image of a phantom without insonation. (b) Phase image with 40 W peak power insonation. In the NMR sequence 50,000 cycles of synchronized sine-shaped motion-sensitizing gradient were applied. Arrows indicate the null-gradient positions of the dedicated gradient coil system. Wavelength is around 2.9 mm and peak matter displacement is around 120 nm. From Ref. 30, reprinted by permission of Wiley-Liss, Inc., a subsidiary of John Wiley & Sons, Inc.

values. The reconstruction method was then successfully applied to experimental MR images of mechanically-excited polyvinyl alcohol breast phantom with a stiff inclusion.[44] In another study, AIDE[41] was used to estimate shear speed and attenuation in agar gel phantoms containing one or two stiff inclusions, mechanically excited at 300 Hz. AIDE correctly evaluated shear speeds whereas the performance in assessing the attenuation was rather poor. Analysis using Helmholtz equation gave similar estimations. AIDE was thought to potentially reconstruct the full complex stiffness tensor.

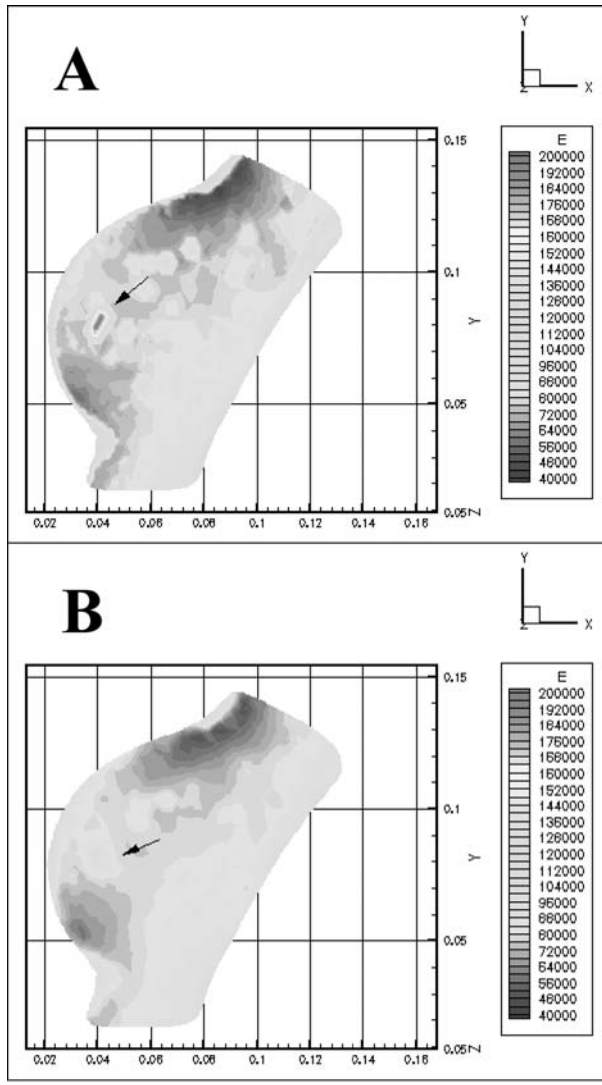

Fig. 8. Reconstruction of Young's modulus map in a simulated object. A 3D breast phantom was first designed *in silico* from MR anatomical images. Then a given 3D Young's modulus distribution was supposed with a 1 cm diameter stiff inclusion of 200 kPa (A). The forward problem was the computing of the 3D-displacement field using the partial differential equation [Eq. (5)]. The efficiency of the 3D reconstruction (inverse problem) of the mechanical properties from the 3D strain data corrupted with 15% added noise can be assessed in (B). The stiff inclusion is detected by the reconstruction algorithm, but its calculated Young's modulus is about 130 kPa instead of 200 kPa. From Ref. 44, reprinted by permission of Wiley-Liss, Inc., a subsidiary of John Wiley & Sons, Inc.

Another analysis method was based on the local wave vector estimation (LFE) approach applied on a field of coupled harmonic oscillators.[39] Propagating media were assumed to be homogeneous and incompressible. MRE images of an agar gel with two different stiffnesses excited at 200 Hz were successfully simulated and compared very well to the experimental data. Shear stiffnesses of 19.5 and 1.2 kPa were found for the two parts of the gel. LFE-derived wave patterns in two dimensions were also calculated on a simulated brain phantom bearing a tumour-like zone and virtually excited at 100–400 Hz. Shear-stiffnesses ranging from 5.8 to 16 kPa were assumed. The 'tumour' was better detected from the reconstructed elasticity images for an input excitation frequency of 0.4 kHz.

For several years application of MRE to biological tissues has been an active area of research. Strategies either turns towards excised tissues (*ex vivo*) or towards living animals or humans (*in vivo*). The former allows more detailed studies of strain–stress relationships and thus are important for the characterization of heterogeneous biological systems. From a biological point-of-view *in vivo* results might appear more relevant. However they are difficult to obtain and one must keep in mind biases that could arise from incomplete or noisy data.

Among the excised tissues investigated by MRE, muscle, kidney, and liver are frequently encountered. A shear modulus of around 25 kPa was estimated in a renal cortical specimen using shear wave excitation at 200–400 Hz.[11] Bishop *et al.*[24] measured shear waves in muscle and liver at 50–400 Hz excitation frequencies. In bovine muscle at 25°C the wave celerity was around 5 m s^{-1}, the wavelength was 20 mm and the attenuation coefficient was 60 m^{-1} for $\nu = 250$ Hz. Displacements were in the range of 100 μm. Lower celerity and higher attenuation were found in liver. Increasing temperature up to 37°C did not change parameters except in muscle where the velocity was only 3.5 m s^{-1}. The frequency dependence of both velocity and attenuation of shear waves in excised liver, muscle, and fat tissues was also investigated but no general trends could be derived from the results. Excised samples of muscles, liver, and kidney were also investigated by Kruse *et al.*[25] With an excitation frequency of 300 Hz shear stiffnesses of 25 kPa to 15 kPa were found in semi-tendinous muscle, depending on both polarization and propagation direction of the mechanical wave with respect to the fibre orientation. Even though well detected, the characterization of this anisotropic behaviour would have needed 3D MRE data sets and advanced reconstruction methods. The same authors showed on porcine liver and kidney specimen that the shear wave velocity increased with the wave frequency. This dependency was fitted to a simple viscoelastic model in which the real and imaginary parts of the shear modulus were taken into account. The calculated shear stiffness varied from 2.1 kPa at 100 Hz to 4.5 kPa at 300 Hz in kidney and from 3 kPa at 100 Hz to 5 kPa at 300 Hz in liver. Stiffness was also shown to increase by reducing temperature.

Additional data on *ex vivo* skeletal muscle were collected by Wu *et al.*[32,47] By generating shear waves either with a mechanical transducer or from amplitude-modulated focused ultrasounds, shear moduli of 20–25 kPa were found at 100 Hz in normal tissues. Again, it was shown in porcine muscle specimen that the shear modulus increased with shear wave frequency from 25 kPa at 200 Hz to 50 kPa at 500 Hz. Interestingly, much higher stiffness was recorded in thermo-coagulated tissues: μ varied between 100 and 250 kPa from 200 to 500 Hz excitation frequency (Fig. 9). MRE was then thought to be useful in monitoring ablathermy.[47] Dresner *et al.*[27] measured shear wave velocities on *ex vivo* bovine muscle specimen connected to a cable-and-pulley system loaded with different masses. Displacements of 700 μm were measured at the wave source location for an excitation frequency of 150 Hz. Assuming a Hookean isotropic material the calculated shear modulus was shown to increase linearly from 24 kPa without load up to 150–200 kPa with 8 kg loading.

In the fields of diagnostic and interventional imaging, virtual palpation using MRE has become a goal clearly displayed by several research groups. This is the reason why, although immature, the methodology is being applied *in vivo* in humans. Whereas the application of mechanical waves onto peripheral organs might be 'easily' carried out, production of controlled periodic motions in deeper parts of a body is a real challenge. Moreover, due to high complexity of living tissues data interpretation

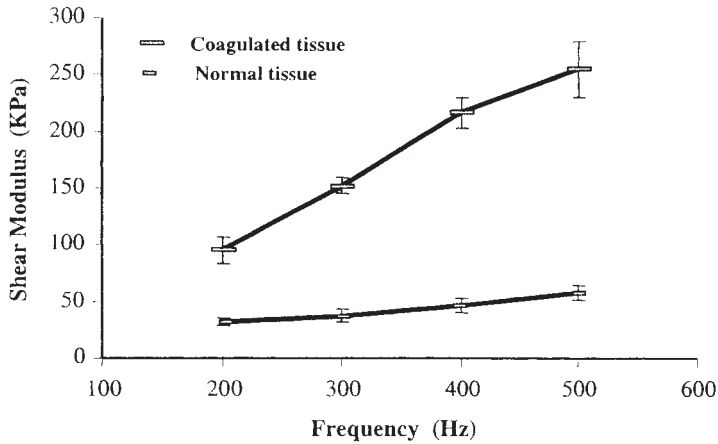

Fig. 9. Viscoelastic properties of ultrasound-treated *ex vivo* porcine muscle specimen. Muscle samples were coagulated with focused ultrasounds in selected regions. MRE using the method of Ref. 23 was carried out and shear moduli were calculated in normal and heated regions at different shear wave frequencies. Upper curve: FUS-treated tissue. Lower curve: normal tissue. Error bars are for standard deviations. (From Ref. 47, reprinted by permission of Wiley-Liss, Inc., a subsidiary of John Wiley & Sons, Inc.)

assuming too simple physical models might be erroneous. Nonetheless some encouraging results on humans have been published and are mentioned below.

As early as 1996[23] MR wave images were acquired *in vivo* on a human calf muscle for a vibration frequency of 125 Hz. This low frequency and the acoustic heterogeneity of muscle prevented an accurate determination of the strain wavelength. Using the same approach, Dresner *et al.*[27] investigated the elastic properties of human *biceps brachii* as a function of work loading. The authors considered only 1-D displacements along the muscle fibres and assumed a Hookean behaviour. As seen above in case of *ex vivo* bovine samples the calculated shear modulus increased linearly with load, but the slopes varied a lot between volunteers. A general trend would be that the elasticity dependence upon work load decreases as muscle size increases. One of the challenges of MRE is virtual palpation of deeply embedded carcinoma, as it could happen in breast cancer. MR wave images of breast bearing a tumoural inclusion were carried out with a mechanical frequency of 100 Hz.[25,28] Again using a simple physical model a shear modulus of up to 40 kPa was calculated within the tumour, a value 5–20 times higher than in normal soft breast tissue. In a very recent work Van Houten *et al.*[48] reported detailed Lame coefficient images (Fig. 10) obtained from normal human breasts *in vivo*. Moduli were computed using the subzone technique from 3D MR data sets of 3D motion field. Images of Fig. 10 clearly show the mechanical heterogeneity of breast tissue, with μ varying from 5 to 10 kPa and E from 15 to 30 kPa. Further work is needed to understand the poor correlation between anatomical and viscoelastic patterns. In a separate work Sinkus *et al.*[26] studied in detail the anisotropic elasticity tensor in breast. They measured 3-D complex-valued displacement fields ($\nu = 60$ Hz) and used an advanced reconstruction method to compute eigenvalues of the elasticity tensor (see Section 2.4). The main finding was the breast carcinoma was both stiffer and more anisotropic than the surrounding (Fig. 11). However, the measured cancer lesion appeared less stiff (3.5 kPa vs. 0.5–1 kPa in normal tissue) than in Kruse's work. Such a discrepancy may arise from tumoural variability as well as from the reconstruction procedure. The same group published recently that the elasticity of fibroglandular breast tissue varies along the menstrual cycle.[49]

4. CHARACTERIZATION OF VISCOELASTIC PROPERTIES: NMR VS. ULTRASOUND

Since NMR is at present an emerging method for the characterization of mechanical waves, it cannot as yet be considered as a gold standard in elastography. In the same way the use of ultrasounds (US) for characterizing crystalline, amorphous or biological materials is also an emerging research

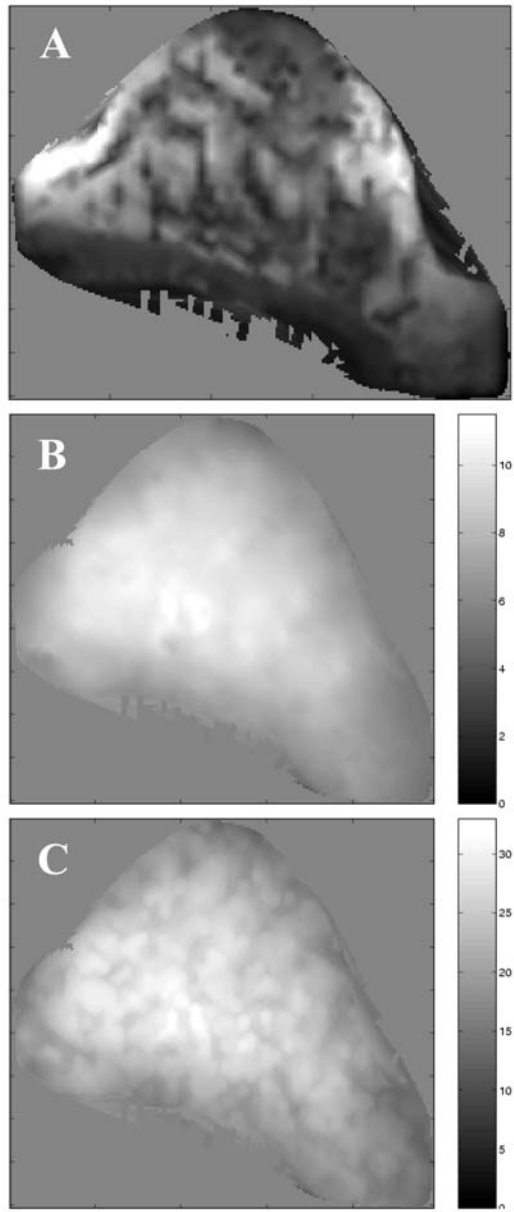

Fig. 10. Estimated viscoelatic properties in a normal human breast *in vivo*. (A) T_2* anatomical image. (B) Shear modulus image of the same slice. (C) Young's modulus image of the same slice. Grey scale bars are in kPa. Images B and C are extracted from 3D data sets of reconstructed elasticity parameters, obtained with the subzone based method used in Fig. 8. Note the good contrast in image C, even though the mechanical parameters are not obviously correlated to the structural properties depicted in image A (reprinted with permission from Ref. 48 © 2000 IOP Publishing Ltd.).

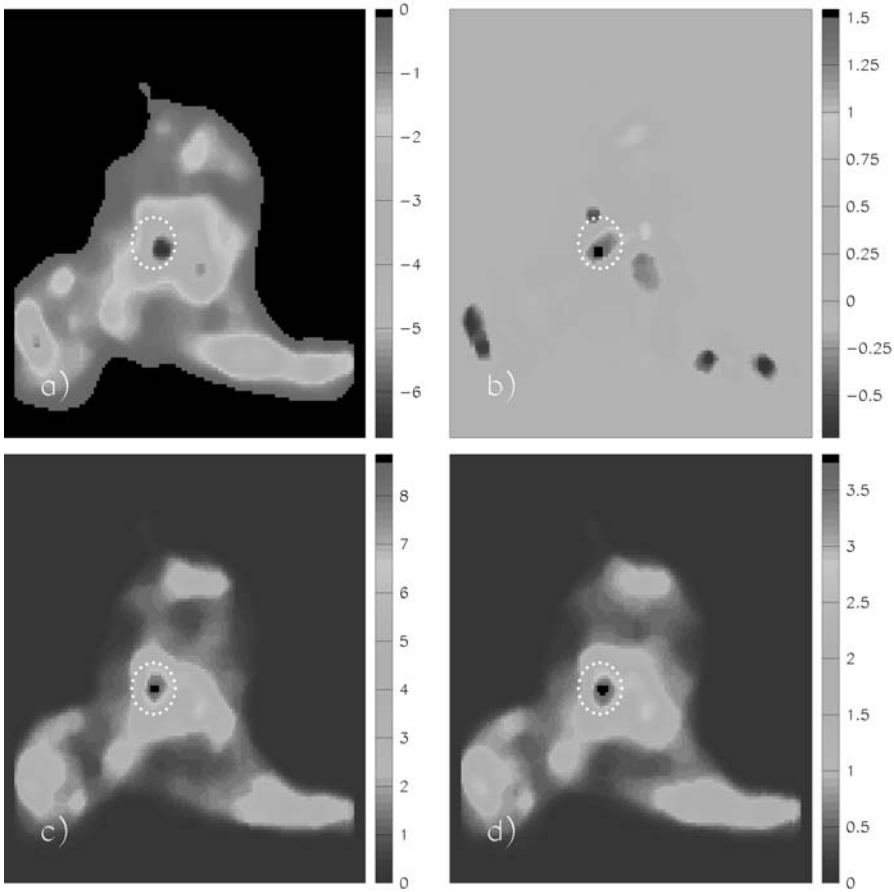

Fig. 11. Tensor-valued elasticity parameters in a human breast *in vivo*. A dotted circle symbolizes a carcinoma previously localized using gadolinium-enhanced T_1-weighted imaging. Eigenvalues E_1, E_2, and E_3 of the elasticity tensor are shown in (a), (b), and (c) respectively. Also shown in (d) is the isotropic elasticity $|E| = (1/3)\sqrt{E_1^2 + E_2^2 + E_3^2}$. All values are given in kPa. From (d), it can be seen that the lesion appears stiffer than normal tissue. The significant difference between E_1 and E_3 in carcinoma, together with their similar absolute value, is a strong argument in favour of anisotropy. From Ref. 26, reprinted by permission of Wiley-Liss, Inc., a subsidiary of John Wiley & Sons, Inc.

field. The goal of this section is not to recall the principles of the numerous US techniques but to present several significant results in the field of the so-called sonoelastography, especially in the case of biological tissues. Elasticity assessment using US can be achieved from either static or quasi-static compression tests or in a dynamic way with a periodic mechanical stress. The quasi-static approach will not be detailed as well because no real

mechanical waves are involved. Nevertheless numerous quasi-static US-elastographic studies have been published (see for instance Refs. 50–59) and may be regarded as complementary (rather than competing) elastography methods. At the frontier between quasi-static and dynamic approaches, intravascular elastography using cross-correlated US images of the vascular wall at different arterial pressures was used by Van der Steen's group (see Ref. 60 for a review). The authors used a 30-MHz intravascular catheter to image the vessel wall at high resolution (200 μm). The displacement was computed from local strain. The technique was validated *ex vivo* on diseased human arteries specimen using two intraluminal pressures.[61–65] Experiments on phantoms showed that this two pressure-level elastography was able to distinguish soft and hard tissues.[66] *In vivo* experiments in Yucatan pigs[67] and in humans[68] confirmed the clinical interest of intravascular ultrasound elastography. Indeed it was shown that it was possible to assess different kind of plaque in coronary diseases.

Surprisingly the first attempts to measure displacements originating from genuine periodic or quasi-periodic perturbations were carried out *in vivo*. Those studies took advantage of the internal pulsatile motions provided by heart beating. As soon as 1982 small displacements from aortic pulsations were visualized in liver on M-mode scans.[69] It was shown that such displacements could be calculated from correlated successive A-scans,[70] with an application on liver.[71,72] Correlation techniques were also applied on M-mode images to quantitatively estimate motions and deformations of fetal lung.[73,74]

Vibration amplitude sonoelastography (sonoelasticity imaging) is a US measurement of the vibration pattern of a given object submitted to low-frequency (20–1000 Hz) external periodic excitation. The first validation of the technique by pulsed range-gated Doppler on a phantom containing a stiff inclusion was published in 1988.[75] Further developments on phantoms or *ex vivo* soft tissues (prostate, liver, breast, kidney) were reported by the same group.[76–79] More informations about those studies can be found in Ref. 80. Parker's group remained involved in the development in sonoelasticity applied to diagnosis. The ability to detect lesions as a function of stiffness, external vibration amplitude, and lesion size was studied both theoretically and experimentally.[81] To discriminate normal/pathological tissues according to their shear moduli, a compromise must be found between high ability of detection and poor penetration depth of the periodic excitation, both occurring at high vibration frequencies (kHz). Sonoelastography and conventional MRI were compared to assess the quality of tumour delineation in three dimensions:[82] in US measurements sequential acquisitions of slices and image post-processing (segmentation) allowed similar visualization of stiff inclusions in phantoms as in MRE. Hardware developments are also in progress. In order to generate localized vibration field, Wu *et al.*[83] realized a device made of parallel bars vibrating against the surface of a phantom at

400–600 Hz. In this study, it was shown both theoretically and experimentally the presence of a shear wave focal zone that made possible a clear detection of the tumour-like inclusion of the phantom. Elastograms were computed from Doppler spectral variance and space resolution of elastography images was in the millimetre scale.

The determination of wave velocity and/or attenuation of mechanical waves induced by continuous low-frequency external vibrations is subject to diffraction biases because the theory of planar wave propagation in a linear elastic medium does not hold.[84,85] Then a frequency dependence of the elasticity parameters may occur. Such a drawback can be circumvented under transient excitation. It was shown that thanks to a pulsed compression perpendicular to the surface of a phantom, transient shear waves induced axial displacements in the material measured in the transmit mode with an US transducer placed at the opposite side.[84] Recent advances in transient elastography took advantage of ultra-fast ultrasonic imaging, a method that produces several thousand of frames per second thus making possible to record movies of propagating shear waves[86] (Fig. 12). This method is thought to be faster than classical Doppler or MRI and is in principle applicable to moving objects. In order to investigate the elastic properties of an object from one side (instead of two in the transmit mode), an integrated system with both the US transducer array and the vibrating device equipped with two parallel rods was designed.[87] With this apparatus 2D shear modulus images of different phantoms were acquired in the reflection mode. Spatial resolution was around 1 mm and detectable displacements were in the range of several micrometers. In a separate study the same group measured *in vivo* the velocity of shear waves in a human biceps as a function of its loading using 1D transient elastography and the same apparatus.[88] Measured wave velocities varied from 2 m/s (unloaded muscle) to 8 m/s (loaded).

NMR and US methods for characterizing mechanical waves have their respective qualities and drawbacks that are summarized in Table 2. A recent paper compared the efficiency of US-based vs. MR-based elastography. In this study[89] 2D images of displacements under external shear wave excitation (300 to 500 Hz) were measured by NMR as in[11,13,23] and in a phase-based US method using back-scattered signals. For displacements of around 1 mm, the signal-to-noise ratio and the spatial resolution of the wave images were comparable for both methods. However, one should keep in mind that space-resolved viscoelastic data of an object (for instance a Young's modulus map of a given organ) must be compared to the size and shape of the object itself. In that respect the high-quality anatomical images produced by conventional MRI are well suited for the regional attribution of physical parameters.

Until now matter displacements as small as several micrometres were observed using sonoelasticity.[87] More developments are needed to visualize periodic motions in the range of 100 nm as assessed in a few MRE studies.[17,29,30] Less anecdotic is the capability of MRE to obtain 3D images of

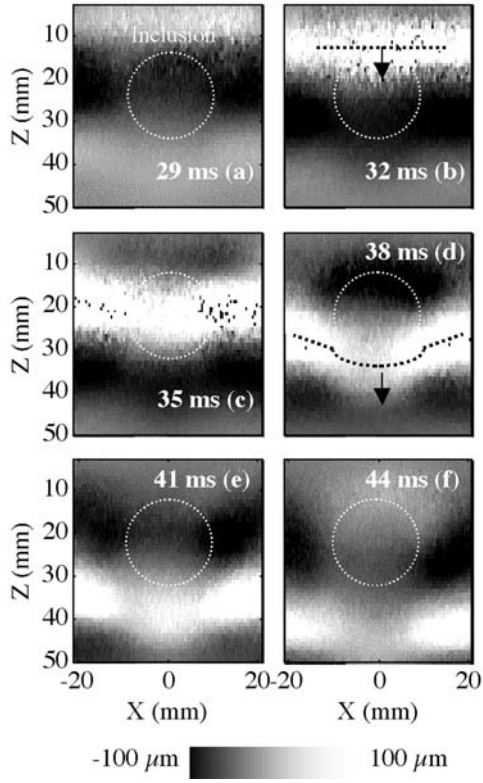

Fig. 12. Measurement of matter displacement during shear wave propagation using ultrafast ultrasonic imaging. An agar/gelatin phantom with an isoechoic stiff inclusion (white dotted circle) was excited at around 50 Hz. Shear wave propagation (from top to bottom) was imaged every millisecond and several frames are reported. The gray scale represents the axial displacement. As seen in (d) the stiff inclusion induces a significant distortion of the wave front (black dotted line). Inversion algorithm applied to spatio-temporal data allows 2D mapping of shear modulus ($\mu = 16$ kPa for the inclusion and $\mu = 4$ kPa for the softer surrounding). Reprinted with permission from Ref. 87, © 2002 IEEE.

Table 2. Qualitative comparison between NMR- and US-characterization of mechanical waves

	NMR	US
Small displacements	+ +	+
3D displacements	+ +	−
Spatial resolution	+ +	+ +
Anatomic localization	+ + +	+
Embedded organs	+ + +	−
Rapidity	−	+ +
Cost and handling	−	+ + +

3D motion vectors. This allows complete determination of the strain at any coordinate of the investigated object, a significant advantage of NMR over challenging methods.

A difficult issue is the measurement of mechanical waves in organs protected by bone walls, e.g., in brain. Due to the large difference in acoustic impedance between skull and brain, US do not penetrate efficiently across the bone barrier, making sonoelasticity difficult to achieve. MRE of the brain is not simple as well: for instance low-frequency shear waves have been produced by a dedicated vibrating device linked to the teeth of volunteers.[28] Even though useful, such a wave generation is likely uncomfortable for the patients and the stress pattern might not be completely known. However, the strain data in the brain can be acquired with all the advantages of the NMR methods.

Finally a big advantage of US-based methods is their cheapness when compared to NMR, as well as an easier handling. US probes are usually light and portable, two qualities not shared by the MRI systems, particularly those equipped with cylindrical magnets where the region of interest in often hardly accessible. To partly compensate this, cheaper open C-shaped low-field magnets might be considered since they allow accessibility to external equipments.

Everything considered, sonoelastography is a very challenging approach for characterization of mechanical waves. To become the gold standard in non-invasive elastography, US methods should provide good anatomic localization of the viscoelastic properties as well as the 3D assessment of the wave pattern. But such improvements would possibly make sonoelasticity methods slower and less convenient.

5. CONCLUSION

Despite the undeniable advantages of using MR to characterize mechanical waves (non-invasive method, high quality 3D images) a limited number of studies dealt with this subject. The reasons for this are two-fold: difficulty and expensiveness.

The production of mechanical waves can be readily achieved in inert soft materials thanks to simple vibrating devices. This is no longer true in case of living tissues, *a fortiori* in humans where the wave generation must take into account anatomic and physiological specificities. Low frequency longitudinal acoustic waves may not be an alternative to shear waves because they are less sensitive to viscoelastic variations and their amplitude are small. Mechanical waves are often refracted and reflected in biological systems, making the reconstruction of elasticity parameters more difficult than in homogeneous media. Accurate time-resolved measurement of amplitude of

displacement fields in three dimensions with a good spatial resolution using NMR is a wager because of the intrinsic low sensitivity of the technique. Most of the studies reported here were carried out in static fields in the range of 1–2 T. Higher fields of course give rise to better signal-to-noise ratio, but this is often associated with increased susceptibility to artifacts, RF power deposition problems and lower accessibility to external apparatus in narrow tunnel-shaped magnets. An additional drawback becomes obvious when switching to high-field MRI: the cost of such systems. MRI, mostly used by radiologists, is far from being attainable by anybody interested in virtual palpation (clinical routine) or in physical characterization of materials (industrial processes or applied research and development). In order to 'democratize' MRI for various applications one might think of low-field (below 0.5 T) MRI systems (often unfairly termed 'poor quality' imaging systems). Reasonably resolved 3D images can easily be obtained at 0.2 T with 1 mm pixel size with limited susceptibility artifacts. Open magnets allow accessibility to various vibrating systems. Imaging time is undoubtedly increased at low fields, a disadvantage counterbalanced by shorter T_1s and strongly reduced servicing costs.

Regarding the recent advances in MR elastography several developments might be expected. Most of the MRE studies were done using conventional MRI with very spectacular and enthusing results (see Figs. 10 and 11). The feasibility of virtual palpation in soft tissues is now clearly established even though further steps are required for MRE to become a standard clinical test. First the different contrasts observed in elastographic images of normal tissues must be interpreted upon an anatomic and/or functional basis. Systematic works could provide new data that would validate the power of MRE to discriminate normal and abnormal tissues. Second, the technique should allow detection of small abnormally stiff regions (e.g., not bigger than 5 mm). Even though increased stiffness may not be synonymous with abnormality, MRE might serve as an early test for tumour localization. Both contrast and resolution are needed to reach this goal, i.e., instrumental and post-processing problems remain to be solved. A possible development of NMR in measuring mechanical waves is the use of radiofrequency field gradients. At present the method[16,17] led to very preliminary results on phantoms and is still unable to space-encode viscoelastic properties in three dimensions as described in Ref. 26 or 48. Nevertheless nanometric displacements were detected with acceptable frequency selectivity. Combination of B_1-field by means of dedicated RF coils and conventional static field gradients would improve the quality of the raw data, a requisite for a robust reconstruction of elasticity images.

MRE has not been validated on hard materials, i.e., for shear moduli greater than 200 kPa. The reasons for this are obvious. In rigid matter, shortened T_2s will prevent accurate measurements, particularly when using MRI. Moreover, low flexibility induces small strain and an additional loss

of sensitivity. It is unlikely that such limitations will ever be overcome. In this respect the use of ultrasound appears more appropriate.

It is now well understood that NMR can contribute significantly to characterize mechanical waves. The reciprocal might be true, i.e., acoustic waves might be used to modulate the NMR signal of matter, depending on its structure. For instance, the spin–lattice relaxation rate R_1 can be modified by acoustic waves. Among a variety of relaxation mechanisms, spin–phonon interaction can be efficient in solids.[90] Kastler[91] and Al'tshuler[92] proposed the use of elastic waves oscillating at the Larmor frequency to modulate the spin–lattice relaxation rate (R_1) . Energy coupling between a given spin system with its surrounding in solids can be achieved by resonant absorption of a single phonon (quantum of vibration energy) or by inelastic phonon scattering (Raman effect). R_1 relaxation occurs via: (i) periodic magnetic field perturbation due to oscillation of distance between paramagnetic species; (ii) periodic changes in the lattice electric field; (iii) spin–orbit coupling when orbital levels are modified by an oscillating lattice field. In case of quadrupolar nuclei, spin–phonon relaxation occurs in a more efficient way because of the sensitivity of quadrupoles to electric field gradients. More details can be found in Refs. 93,94. Acoustic modes can induce transitions between the Zeeman quantum states. In this context, saturation of nuclear electric quadrupole levels of ^{35}Cl by ultrasound was first observed in solid-state sodium chlorate.[95,96] In liquids spin-phonon relaxation mechanisms were expected to be less effective because of intense molecular motions. However resonant acoustic saturation of water protons in a colloidal suspension of As_2S_3 was reported.[97] Alekseev and Kopvillem[98] measured the modulation of the ^1H NMR signal of Cu^{2+}-doped water by off resonance acoustic irradiation. In these studies ultrasounds induced fluctuations of the distance between water and paramagnetic species. Indeed, in pure liquid water, an acoustically driven decrease in T_1 is unlikely because of the dominant intramolecular dipolar relaxation mechanism. Nevertheless, acoustic resonance might be envisaged in heterogeneous media (both in the viewpoint of chemical composition and mechanical properties) e.g., living systems. Actually water in soft tissues cannot be considered as a true liquid since it interacts strongly with a variety of ions, macromolecules, and supramolecular structures. With the purpose of changing periodically the magnitude of these interactions at the Larmor frequency, T_1 of soft tissues would be decreased under on-resonance acoustic stimulation. This effect should depend on the acoustic transmittance and to a lesser extent on the mechanical properties of the tissue. Stiffer tissues like bone, well visible in low-field MR images would be concerned as well. Taking into account spin motion amplitude is inversely proportional to wave frequency, low-field imaging systems would be more appropriate to visualize acoustic resonance. In that way ultrasounds would become a new non-invasive T_1 contrast agent.

ACKNOWLEDGEMENTS

The authors are grateful to Mrs M. Legall for editorial assistance.

REFERENCES

1. S. M. Hanash, Global profiling of gene expression in cancer using genomics and proteomics, *Curr. Opin. Mol. Ther.*, 2001, **3**, 538–545.
2. S. M. Hanash, M. P. Bobek, D. S. Rickman, T. Williams, J. M. Rouillard and R. Kuick, Integrating cancer genomics and proteomics in the post-genome era, *Proteomics*, 2002, **2**, 69–75.
3. S. K. Hobbs, G. Shi, R. Homer, G. Harsh, S. W. Atlas and M. D. Bednarski, Magnetic resonance image-guided proteomics of human glioblastoma multiforme, *J. Magn. Reson. Imaging*, 2003, **18**, 530–536.
4. H. Delingette, S. Cotin and N. Ayache, Efficient linear elastic models of soft tissues for real-time surgery simulation, *Stud. Health Technol. Inform.*, 1999, **62**, 100–101.
5. J. A. Sidles, Non inductive detection of Single Proton Magnetic Resonance, *Appl. Phys. Lett.*, 1991, **58**, 2854.
6. D. Rugar, C. S. Yannoni and J. A. Sidles, Mechanical detection of Magnetic Resonance, *Nature*, 1992, **360**, 56.
7. C. J. Lewa and J. D. de Certaines, Selected States Magnetic Resonance Spectroscopy: a potential method for huge improvement in sensitivity, *Europhys. Lett.*, 1996, **35**, 73.
8. C. J. Lewa, Magnetic resonance imaging in presence of mechanical waves, *Spectrosc. Lett.*, 1991, **24**, 55–67.
9. C. J. Lewa, MRI response in the presence of mechanical waves, *Acoustica*, 1992, **77**, 43–45.
10. C. J. Lewa and J. D. de Certaines, MR imaging of viscoelastic properties, *J. Magn. Reson. Imaging*, 1995, **5**, 242–244.
11. R. Muthupillai, D. J. Lomas, P. J. Rossman, J. F. Greenleaf, A. Manduca and R. L. Ehman, Magnetic resonance elastography by direct visualization of propagating acoustic strain waves, *Science*, 1995, **269**, 1854–1857.
12. C. J. Lewa and J. D. De Certaines, Viscoelastic property detection by elastic displacement NMR measurements, *J. Magn. Reson. Imaging*, 1996, **6**, 652–656.
13. R. Muthupillai and R. L. Ehman, Magnetic resonance elastography, *Nature Med.*, 1996, **2**, 601–603.
14. C. J. Lewa, Elasto-magnetic resonance spectroscopy, *Europhys. Lett.*, 1996, **35**, 73–76.
15. C. J. Lewa, M. Roth, L. Nicol, J. M. Franconi and J. D. de Certaines, A new fast and unsynchronized method for MRI of viscoelastic properties of soft tissues, *J. Magn. Reson. Imaging*, 2000, **12**, 784–789.
16. N. Baril, C. J. Lewa, J. D. de Certaines, P. Canioni, J. M. Franconi and E. Thiaudiere, MR detection of mechanical vibrations using a radiofrequency field gradient, *J. Magn. Reson.*, 2002, **154**, 22–27.
17. G. Madelin, N. Baril, C. J. Lewa, J. M. Franconi, P. Canioni, E. Thiaudière and J. D. de Certaines, Detection of acoustic waves by NMR using a radiofrequency field gradient, *J. Magn. Reson.*, 2003, **161**, 108–111.
18. W. P. Mason, *Physical Acoustics. Principles and Methods*, Academic Press, New York, London, 1964.
19. R. T. Beyer and S. V. Letcher, *Physical Ultrasonics*, Academic Press, New York, London, 1969, 1–37.
20. J. D. Achenbach, *Wave Propagation in Elastic Solids*, North-Holland, Amsterdam, 1973.
21. B. A. Auld, *Acoustic Fields and Waves in Sozlids*, Wiley, New York, 1973.

22. D. B. Plewes, I. Betty, S. N. Urchuk and I. Soutar, Visualizing tissue compliance with MR imaging, *J. Magn. Reson. Imaging*, 1995, **5**, 733–738.
23. R. Muthupillai, P. J. Rossman, D. J. Lomas, J. F. Greenleaf, S. J. Riederer and R. L. Ehman, Magnetic resonance imaging of transverse acoustic strain waves, *Magn. Reson. Med.*, 1996, **36**, 266–274.
24. J. Bishop, G. Poole, M. Leitch and D. B. Plewes, Magnetic resonance imaging of shear wave propagation in excised tissue, *J. Magn. Reson. Imaging*, 1998, **8**, 1257–1265.
25. S. A. Kruse, J. A. Smith, A. J. Lawrence, M. A. Dresner, A. Manduca, J. F. Greenleaf and R. L. Ehman, Tissue characterization using magnetic resonance elastography: preliminary results, *Phys. Med. Biol.*, 2000, **45**, 1579–1590.
26. R. Sinkus, J. Lorenzen, D. Schrader, M. Lorenzen, M. Dargatz and D. Holz, High-resolution tensor MR elastography for breast tumour detection, *Phys. Med. Biol.*, 2000, **45**, 1649–1664.
27. M. A. Dresner, G. H. Rose, P. J. Rossman, R. Muthupillai, A. Manduca and R. L. Ehman, Magnetic resonance elastography of skeletal muscle, *J. Magn. Reson. Imaging*, 2001, **13**, 269–276.
28. A. Manduca, T. E. Oliphant, M. A. Dresner, J. L. Mahowald, S. A. Kruse, E. Amromin, J. P. Felmlee, J. F. Greenleaf and R. L. Ehman, Magnetic resonance elastography: non-invasive mapping of tissue elasticity, *Med. Image Anal.*, 2001, **5**, 237–254.
29. C. L. Walker, F. S. Foster and D. B. Plewes, Magnetic resonance imaging of ultrasonic fields, *Ultrasound Med. Biol.*, 1998, **24**, 137–142.
30. D. B. Plewes, S. Silver, B. Starkoski and C. L. Walker, Magnetic resonance imaging of ultrasound fields: gradient characteristics, *J. Magn. Reson. Imaging*, 2000, **11**, 452–457.
31. A. P. Sarvazyan, O. V. Rudenko, S. D. Swanson, J. B. Fowlkes and S. Y. Emelianov, Shear wave elasticity imaging: a new ultrasonic technology of medical diagnostics, *Ultrasound Med. Biol.*, 1998, **24**, 1419–1435.
32. T. Wu, J. P. Felmlee, J. F. Greenleaf, S. J. Riederer and R. L. Ehman, MR imaging of shear waves generated by focused ultrasound, *Magn. Reson. Med.*, 2000, **43**, 111–115.
33. E. O. Stejskal and J. E. Tanner, Spin diffusion measurements: spin echoes in the presence of a time-dependent field gradient, *J. Chem. Phys.*, 1965, **42**, 288–292.
34. L. Axel and L. Dougherty, MR imaging of motion with spatial modulation of magnetization, *Radiology*, 1989, **171**, 841–845.
35. D. Canet, Radiofrequency field gradient experiments, *Prog. NMR Spectroc.*, 1997, **30**, 101–135.
36. N. Baril, E. Thiaudiere, B. Quesson, C. Delalande, P. Canioni and J. M. Franconi, Single-coil surface imaging using a radiofrequency field gradient, *J. Magn. Reson.*, 2000, **146**, 223–227.
37. T. L. Chenevert, A. R. Skovoroda, M. O'Donnell and S. Y. Emelianov, Elasticity reconstructive imaging by means of stimulated echo MRI, *Magn. Reson. Med.*, 1998, **39**, 482–490.
38. H. Knutsson, C. J. Westin and G. Granlund, Local multiscale frequency and bandwidth estimation, *Proc. IEEE Int. Conf. Imag. Proc.*, 1994, **1**, 36–40.
39. J. Braun, G. Buntkowsky, J. Bernarding, T. Tolxdorff and I. Sack, Simulation and analysis of magnetic resonance elastography wave images using coupled harmonic oscillators and Gaussian local frequency estimation, *Magn. Reson. Imaging*, 2001, **19**, 703–713.
40. I. Sack, J. Bernarding and J. Braun, Analysis of wave patterns in MR elastography of skeletal muscle using coupled harmonic oscillator simulations, *Magn. reson. Imaging*, 2002, **20**, 95–104.
41. T. E. Oliphant, A. Manduca, R. L. Ehman and J. F. Greenleaf, Complex-valued stiffness reconstruction for magnetic resonance elastography by algebraic inversion of the differential equation, *Magn. Reson. Med.*, 2001, **45**, 299–310.
42. E. E. Van Houten, K. D. Paulsen, M. I. Miga, F. E. Kennedy and J. B. Weaver, An overlapping subzone technique for MR-based elastic property reconstruction, *Magn. Reson. Med.*, 1999, **42**, 779–786.
43. E. E. Van Houten, J. B. Weaver, M. I. Miga, F. E. Kennedy and K. D. Paulsen, Elasticity reconstruction from experimental MR displacement data: initial experience with an overlapping subzone finite element inversion process, *Med. Phys.*, 2000, **27**, 101–107.

44. E. E. Van Houten, M. I. Miga, J. B. Weaver, F. E. Kennedy and K. D. Paulsen, Three-dimensional subzone-based reconstruction algorithm for MR elastography, *Magn. Reson. Med.*, 2001, **45**, 827–837.
45. U. Hamhaber, F. A. Grieshaber, J. H. Nagel and U. Klose, Comparison of quantitative shear wave MR elastography with mechanical compression tests, *Magn. Reson. Med.*, 2003, **49**, 71–77.
46. J. B. Weaver, E. E. Van Houten, M. I. Miga, F. E. Kennedy and K. D. Paulsen, Magnetic resonance elastography using 3D gradient echo measurements of steady-state motion, *Med. Phys.*, 2001, **28**, 1620–1628.
47. T. Wu, J. P. Felmlee, J. F. Greenleaf, S. J. Riederer and R. L. Ehman, Assessment of thermal tissue ablation with MR elastography, *Magn. Reson. Med.*, 2001, **45**, 80–87.
48. E. E. Van Houten, M. M. Doyley, F. E. Kennedy, J. B. Weaver and K. D. Paulsen, Initial in vivo experience with steady-state subzone-based MR elastography of the human breast, *J. Magn. reson. Imag.*, 2003, **17**, 72–85.
49. J. Lorenzen, R. Sinkus, M. Biesterfeldt and G. Adam, Menstrual-cycle dependence of dreast parenchyma elasticity: estimation with magnetic resonance elastography of breast tissue during the menstrual cycle, *Invest. Radiol.*, 2003, **38**, 236–240.
50. J. Ophir, I. Cespedes, H. Ponnekanti, Y. Yazdi and X. Li, Elastography: a quantitative method for imaging the elasticity of biological tissues, *Ultrason. Imaging*, 1991, **13**, 111–134.
51. H. Ponnekanti, J. Ophir and I. Cespedes, Axial stress distributions between coaxial compressors in elastography: an analytical model, *Ultrasound Med. Biol.*, 1992, **18**, 667–673.
52. I. Cespedes and J. Ophir, Reduction of image noise in elastography, *Ultrason. Imaging*, 1993, **15**, 89–102.
53. I. Cespedes, J. Ophir, H. Ponnekanti and N. Maklad, Elastography: elasticity imaging using ultrasound with application to muscle and breast in vivo, *Ultrason. Imaging*, 1993, **15**, 73–88.
54. M. O'Donnell, A. R. Skovoroda, B. M. Shapo and S. Y. Emelianov, Internal displacement and strain imaging using ultrasonic speckle tracking, *IEEE Trans. Ultrason. Ferroelect. Freq. Control*, 1994, **41**, 314–325.
55. S. Diridollou, M. Berson, V. Vabre, D. Black, B. Karlsson, F. Auriol, J. M. Gregoire, C. Yvon, L. Vaillant, Y. Gall and F. Patat, An in vivo method for measuring the mechanical properties of the skin using ultrasound, *Ultrasound Med. Biol.*, 1998, **24**, 215–224.
56. E. Konofagou and J. Ophir, A new elastographic method for estimation and imaging of lateral displacements, lateral strains, corrected axial strains and Poisson's ratios in tissues, *Ultrasound Med. Biol.*, 1998, **24**, 1183–1199.
57. F. Kallel, R. J. Stafford, R. E. Price, R. Righetti, J. Ophir and J. D. Hazle, The feasibility of elastographic visualization of HIFU-induced thermal lesions in soft tissues. Image-guided high-intensity focused ultrasound, *Ultrasound Med. Biol.*, 1999, **25**, 641–647.
58. S. Y. Emelianov, M. A. Lubinski, A. R. Skovoroda, R. Q. Erkamp, S. F. Leavey, R. C. Wiggins and M. O'Donnell, Reconstructive ultrasound elasticity imaging for renal transplant diagnosis: kidney ex vivo results, *Ultrason. Imaging*, 2000, **22**, 178–194.
59. M. Fortin, M. D. Buschmann, M. J. Bertrand, F. S. Foster and J. Ophir, Dynamic measurement of internal solid displacement in articular cartilage using ultrasound backscatter, *J. Biomech.*, 2003, **36**, 443–447.
60. C. L. de Korte and A. F. van der Steen, Intravascular ultrasound elastography: an overview, *Ultrasonics*, 2002, **40**, 859–865.
61. C. L. de Korte, E. I. Cespedes, A. F. van der Steen, G. Pasterkamp and N. Bom, Intravascular ultrasound elastography: assessment and imaging of elastic properties of diseased arteries and vulnerable plaque, *Eur. J. Ultrasound*, 1998, **7**, 219–224.
62. C. L. de Korte, A. F. van der Steen, E. I. Cespedes and G. Pasterkamp, Intravascular ultrasound elastography in human arteries: initial experience in vitro, *Ultrasound Med. Biol.*, 1998, **24**, 401–408.
63. A. F. van der Steen, C. L. de Korte and E. I. Cespedes, Intravascular ultrasound elastography, *Ultraschall Med.*, 1998, **19**, 196–201.

64. C. L. de Korte, G. Pasterkamp, A. F. van der Steen, H. A. Woutman and N. Bom, Characterization of plaque components with intravascular ultrasound elastography in human femoral and coronary arteries in vitro, *Circulation*, 2000, **102**, 617–623.
65. C. L. de Korte, H. A. Woutman, A. F. van der Steen, G. Pasterkamp and E. I. Cespedes, Vascular tissue characterisation with IVUS elastography, *Ultrasonics*, 2000, **38**, 387–390.
66. C. L. de Korte, A. F. van der Steen, E. I. Cepedes, G. Pasterkamp, S. G. Carlier, F. Mastik, A. H. Schoneveld, P. W. Serruys and N. Bom, Characterization of plaque components and vulnerability with intravascular ultrasound elastography, *Phys. Med. Biol.*, 2000, **45**, 1465–1475.
67. C. L. de Korte, M. J. Sierevogel, F. Mastik, C. Strijder, J. A. Schaar, E. Velema, G. Pasterkamp, P. W. Serruys and A. F. van der Steen, Identification of atherosclerotic plaque components with intravascular ultrasound elastography in vivo: a Yucatan pig study, *Circulation*, 2002, **105**, 1627–1630.
68. C. L. de Korte, S. G. Carlier, F. Mastik, M. M. Doyley, A. F. van der Steen, P. W. Serruys and N. Bom, Morphological and mechanical information of coronary arteries obtained with intravascular elastography: feasibility study in vivo, *Eur. Heart J.*, 2002, **23**, 405–413.
69. L. S. Wilson and D. E. Robinson, Ultrasonic measurement of small displacements and deformations of tissue, *Ultrason. Imaging*, 1982, **4**, 71–82.
70. R. J. Dickinson and C. R. Hill, Measurement of soft tissue motion using correlation between A-scans, *Ultrasound Med. Biol.*, 1982, **8**, 263–271.
71. M. Tristam, D. C. Barbosa, D. O. Cosgrove, D. K. Nassiri, J. C. Bamber and C. R. Hill, Ultrasonic study of in vivo kinetic characteristics of human tissues, *Ultrasound Med. Biol.*, 1986, **12**, 927–937.
72. M. Tristam, D. C. Barbosa, D. O. Cosgrove, J. C. Bamber and C. R. Hill, Application of Fourier analysis to clinical study of patterns of tissue movement, *Ultrasound Med. Biol.*, 1988, **14**, 695–707.
73. R. Adler, J. M. Rubin, P. Bland and P. Carson, Characterization of transmitted motion in fetal lung: quantitative analysis, *Med. Phys.*, 1989, **16**, 333–337.
74. R. S. Adler, J. M. Rubin, P. H. Bland and P. L. Carson, Quantitative tissue motion analysis of digitized M-mode images: gestational differences of fetal lung, *Ultrasound Med. Biol.*, 1990, **16**, 561–569.
75. R. M. Lerner, K. J. Parker, J. Holen, R. Gramiak and R. C. Waag, Sono-elasticity: medical elasticity images derived from ultrasound signals in mechanically vibrating targets, *Acoust. Imaging*, 1988, **16**, 317–327.
76. R. M. Lerner, S. R. Huang and K. J. Parker, 'Sonoelasticity' images derived from ultrasound signals in mechanically vibrated tissues, *Ultrasound Med. Biol.*, 1990, **16**, 231–239.
77. K. J. Parker, S. R. Huang, R. A. Musulin and R. M. Lerner, Tissue response to mechanical vibrations for 'sonoelasticity imaging', *Ultrasound Med. Biol.*, 1990, **16**, 241–246.
78. F. Lee, J. P. BronsonJr., R. M. Lerner, K. J. Parker, S. R. Huang and D. J. Roach, Sonoelasticity imaging: results in in vitro tissue specimens, *Radiology*, 1991, **181**, 237–239.
79. K. J. Parker and R. M. Lerner, Sonoelasticity of organs: shear waves ring a bell, *J. Ultrasound Med.*, 1992, **11**, 387–392.
80. L. Gao, K. J. Parker, R. M. Lerner and S. F. Levinson, Imaging of the elastic properties of tissue-a review, *Ultrasound Med. Biol.*, 1996, **22**, 959–977.
81. K. J. Parker, D. Fu, S. M. Graceswki, F. Yeung and S. F. Levinson, Vibration sonoelastography and the detectability of lesions, *Ultrasound Med. Biol.*, 1998, **24**, 1437–1447.
82. L. S. Taylor, B. C. Porter, D. J. Rubens and K. J. Parker, Three-dimensional sonoelastography: principles and practices, *Phys. Med. Biol.*, 2000, **45**, 1477–1494.
83. Z. Wu, L. S. Taylor, D. J. Rubens and K. J. Parker, Shear wave focusing for three-dimensional sonoelastography, *J. Acoust. Soc. Am.*, 2002, **111**, 439–446.
84. S. Catheline, J. L. Thomas, F. Wu and M. Fink, Diffraction field of a low-frequency vibrator in soft tissues using transient elastography, *IEEE Trans. Ultrason. Ferroelect. Freq. Contr.*, 1999, **46**, 1013–1020.

85. S. Catheline, F. Wu and M. Fink, A solution to diffraction biases in sonoelasticity: the acoustic impulse technique, *J. Acoust. Soc. Am.*, 1999, **105**, 2941–2950.
86. L. Sandrin, S. Catheline, M. Tanter, X. Hennequin and M. Fink, Time-resolved pulsed elastography with ultrafast ultrasonic imaging, *Ultrason. Imaging*, 1999, **21**, 259–272.
87. L. Sandrin, M. Tanter, S. Catheline and M. Fink, Shear modulus imaging with 2-D transient elastography, *IEEE Trans. Ultrason. Ferroelectr. Freq. Control*, 2002, **49**, 426–435.
88. L. Sandrin, M. Tanter, J. L. Gennisson, S. Catheline and M. Fink, Shear elasticity probe for soft tissues with 1-D transient elastography, *IEEE Trans. Ultrason. Ferroelectr. Freq. Control*, 2002, **49**, 436–446.
89. V. Dutt, R. R. Kinnick, R. Muthupillai, T. E. Oliphant, R. L. Ehman and J. F. Greenleaf, Acoustic shear-wave imaging using echo ultrasound compared to magnetic resonance elastography, *Ultrasound Med. Biol.*, 2000, **26**, 397–403.
90. A. Abragam, *The Principles of Nuclear Magnetism*, Oxford Science Publications, Clarendon Press, 1986, 402–423.
91. A. Kastler, Quelques réflexions à propos des phénomènes de résonance magnétique dans le domaine des radiofréquences, *Experientia*, 1952, **8**, 1–44.
92. S. A. Al'tshuler, Resonant absorption of sound in paramagnetic materials, *Dokl. AN SSSR*, 1952, **85**, 1235.
93. V. A. Shutilov, Stimulation of nuclear magnetic resonance by ultrasound. Review, *Soviet Physics Acoustics*, 1963, **8**, 303–318.
94. D. I. Bolef, Interaction of acoustic waves with nuclear spins in solids, *Physical Acoustics*, Vol. 4, Academic Press, New York, 1966, 113–181.
95. G. W. Proctor and W. H. Tanttila, Saturation of nuclear electric quadrupole energy levels by ultrasonic excitation, *Phys. Rev.*, 1955, **98**, 1854.
96. G. W. Proctor and W. H. Tanttila, Influence of ultrasonic energy on the relaxation rate of chlorine nuclei in sodium chlorate, *Phys. Rev.*, 1956, **101**, 1757–1762.
97. L. O. Bowen, Nuclear magnetic acoustic resonance and Debye vibration potentials in non-viscous liquids, *Proc. Phys. Soc.*, 1966, **87**, 717–720.
98. A. V. Alekseev and U. K. Kopvillem, Pseudospin quantum acoustics in liquids, *Ultrasonics*, 1980, **18**, 76–80.

Aspects of Coherence Transfer in High Molecular Weight Proteins

PERTTU PERMI

Institute of Biotechnology, Structural Biology and Biophysics Program, NMR Laboratory, P.O. Box 65, FIN-00014, University of Helsinki, Helsinki, Finland; Tel: +358-9-19158940; Fax: +358-9-19159541; E-mail: Perttu.Permi@helsinki.fi

In order to understand the molecular mechanisms of life at atomic resolution, nuclear magnetic resonance (NMR) spectrocopy is among the most powerful biophysical methods available to study the structure and function of biological macromolecules. During the past 20 years, progress in NMR methodology together with instrumental development has pushed the protein size-limit amenable to solution state NMR studies from 10 kDa to 100–200 kDa. Thanks to the discovery of transverse relaxation optimized spectroscopy (TROSY), records on molecular size-limit were again broken and most likely new heights will soon be reached. In this chapter, we take a look into the performance of TROSY based triple-resonance experiments devised for the sequential assignment of high molecular weight proteins. In addition, a survey is made of basic building blocks for the coherence transfer under governing relaxation mechanisms during the course of triple-resonance experiments.

ANNUAL REPORTS ON NMR SPECTROSCOPY
VOLUME 53 ISSN 0066 4103
DOI 10.1016/S0066-4103(04)53005-3

1. INTRODUCTION

Nuclear magnetic resonance (NMR) spectroscopy with its many observables provides unique insight to structure of biological macromolecules, such as proteins, DNA/RNA molecules, and protein complexes.[1] NMR spectroscopy is not limited to solving protein three-dimensional structures at atomic-resolution but it enables the studies of structure–activity relationships of biomolecules in a surrounding close to their physiological conditions. Consequently, NMR spectroscopy is one of the key techniques in structural biology today and is expected to play a pivotal role in structural genomics and proteomics.[2–6] Until quite recently, NMR spectroscopy was judged, however, to be amenable for the structural studies of only smaller proteins (< 20–25 kDa). Innovative development of NMR methodology as well as methods in sample production and preparation concomitantly with instrumental breakthroughs has not only kept NMR in the race as an alternative to X-ray crystallography, but the progress has opened up new interesting biological questions that can be unravelled with NMR spectroscopy.[7,8] Most notably, design of experiments i.e., pulse sequences has played a decisive role in studies of biological macromolecules. During the last 15 years, extensive development and optimization of pulse sequences has provided the tools to study ever-larger proteins with higher sensitivity and with ever-finer details.[9–11] The latest achievements, in terms of molecular size, are astonishing from the historical point of view. The sequence-specific resonance assignment of 81.4 kDa, 723-residue Malate synthase G (MSG) from *Escherichia coli* as well as assignment of 110 kDa homo-octameric protein, 7,8-dihydroneopterin aldolase (DHNA) from *Staphylococcus aureus*, represent spectacular studies that seemed utterly infeasible not many years ago.[12,13] Recent studies with membrane proteins indicate that novel NMR techniques will open new avenues to meet the challenges which govern this class of molecules.[14–19]

The room for the long-term development in NMR stems from the fact that in NMR spectroscopy the magnetization can be transferred from one nucleus to another using different coherence transfer methods and routes. The sensitivity of an experiment depends on the properties of coherences along the chosen transfer path. Therefore it is not irrelevant which building blocks of transfer are used for constructing the optimal experiment for the particular task. In this chapter, we aim to shed light on NMR techniques devised for resonance assignment, and also point out remaining challenges. However, our objective in this chapter is not to elaborate on details of each and every experimental technique. Instead, the main goal is to provide the reader with intuition about the key elements which govern the efficiency of the experiment. For each experiment, together with coherence transfer throughput calculations, a short description of the main principle, advantages, and pitfalls are given. However, an interested reader is referred to the original literature for more details.

2. STRATEGIES FOR THE ASSIGNMENT OF POLYPEPTIDES BEYOND 30 kDa

The first step in structural studies of proteins by NMR spectroscopy is the resonance assignment, that is, signals are related to their sources in the chemical structure. So-called triple-resonance NMR experiments make use of proteins that are labelled with ^{15}N and ^{13}C isotopes to relay the magnetization or in general coherences from nucleus to nucleus. For instance, the magnetization originating from amide protons ($^{1}H^{N}$) can be transferred to directly bonded amide nitrogen (^{15}N) spin and further to alpha carbon ($^{13}C^{\alpha}$) or carbonyl carbon ($^{13}C'$) nuclei. In this process spins become correlated in multidimensional NMR spectra by labelling the nuclei specific resonance frequencies in two or more dimensions. The experiment in which $^{1}H^{N}(i)$ and $^{15}N(i)$ nuclei of the residue i is correlated with the $^{13}C^{\alpha}(i-1)$ spin of the preceding residue $i-1$, and the complementary experiment correlating $^{1}H^{N}(i)$ and $^{15}N(i)$ frequencies of the residue i with the $^{13}C^{\alpha}(i)$ frequency within the residue, establishes the resonance assignment in a sequential manner. Thus, the principal idea is to correlate frequencies of two equivalent spins in the sequential amino acid residues with a common frequency of another nucleus. Additional nuclei can be utilized for alleviating eventual resonance overlap.

The magnetization is transferred from one nucleus to another using scalar couplings. In the protein main chain, the sizes of different couplings vary. Figure 1a depicts typical values of one- and two-bond couplings found in polypeptides, which are used for magnetization transfer in $^{15}N/^{13}C/^{2}H$ labelled proteins. Figure 1b shows different strategies to obtain the sequential assignment of main chain nuclei in larger perdeuterated proteins. The efficiency of magnetization transfer on proteins depends mainly on two factors, namely the size of active coupling with respect to the transverse relaxation rate of the corresponding spin, and the size and number of passive couplings during the magnetization transfer step. In terms of transfer efficiency, the experiment yielding highest transfer amplitude will provide the highest *sensitivity*. This is of utmost importance, especially when working with large proteins and protein complexes, which normally require several days of spectrometer time per single experiment. Another salient feature of a good triple-resonance experiment is its *exclusivity*. It defines how ambiguous the information is that the particular experiment provides. Consider an experiment, which correlates solely $^{1}H^{N}$ and ^{15}N nuclei of the residue i with the $^{13}C^{\alpha}$ spin of the residue $i-1$ and compare it to an experiment correlating $^{1}H^{N}(i)$ and $^{15}N(i)$ nuclei with $^{13}C^{\alpha}$ spins of two sequential residues i and $i-1$. In the first experiment the number of cross peaks is 50% less than in the latter, thus incidental resonance overlap is diminished. Furthermore, there is no *explicit* way to distinguish between *intraresidual* and *sequential* connectivities in the latter

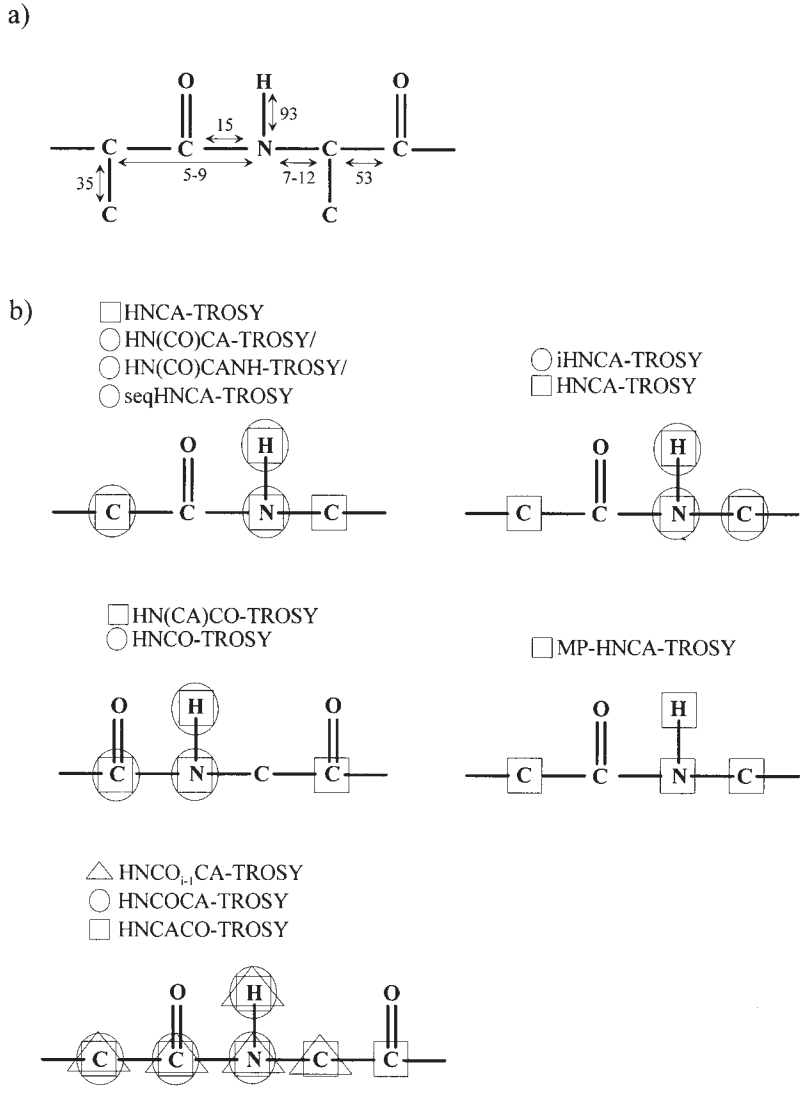

Fig. 1. Typical values for the scalar couplings in perdeuterated proteins, which can be used for the coherence transfer through the spin system (a). Strategies for obtaining resonance assignment in $^{15}N/^{13}C/^{2}H$ labelled proteins discussed in this chapter (b). The boxes, circles, and triangles indicate correlations established in the corresponding pulse scheme.

experiment, whereas solely sequential correlations are observed in the former experiment.

Let us first discuss common coherence transfer steps of triple-resonance experiments with the emphasis on relaxation mechanisms.

3. TRANSVERSE RELAXATION DURING THE MAGNETIZATION TRANSFER STEPS

Inspection of Fig. 1 reveals that there are a bewildering number of triple-resonance experiments that can be employed for the sequential assignment of large proteins. However, they all share certain common building blocks or magnetization transfer steps. The first step is the magnetization transfer from the amide proton ($^1H^N(i)$) to directly bound amide nitrogen ($^{15}N(i)$). The second step is the relay of coherence to the neighbouring carbon spins $^{13}C^{\alpha}(i/i-1)$ or $^{13}C'(i-1)$. The third phase is the coherence transfer from either $^{13}C^{\alpha}$ to $^{13}C'$ or vice versa. During these steps, the desired coherence will relax. The efficiency is primarily governed by the transverse relaxation of $^1H^N$, ^{15}N, and $^{13}C^{\alpha}$ or $^{13}C'$ spins. In the following pages, the emphasis will be on governing relaxation processes that take place during the magnetization transfer steps.

3.1. TROSY in $^1H^N$ detected experiments

Let us consider a $^1H^N$–^{15}N spin pair – the transverse relaxation T_2 for the ^{15}N spin (and $^1H^N$ as well) is mainly dictated by the dipole–dipole (DD) interaction between the $^1H^N$–^{15}N spin pair, and the chemical shift anisotropy (CSA) of ^{15}N (and $^1H^N$) spin.[20] The DD interaction is asymmetrical with respect to two single-quantum transitions of ^{15}N (and $^1H^N$) whereas the CSA mechanism is symmetrical. When there is interference, a cross-correlation, between these two relaxation mechanisms, the relaxation times for the individual single-quantum transitions can be very different; DD and CSA either add constructively or destructively to each other. Because the DD coupling is field independent and CSA depends on the strength of polarizing magnetic fields, there exists a 'magic' field strength where these two relaxation mechanisms, at least almost, compensate each other.[21] This 'magic' field strength for the ^{15}N–$^1H^N$ moiety is between 900 and 1100 ^1H MHz. The optimal field strength depends on the angle between the unique axis of ^{15}N–^1H dipolar and CSA tensors that varies, depending on the conformational variation of the polypeptide chain.[11] The practical outcome is that one of the transitions is very broad at this field strength whereas the other one is very narrow. By selecting the most slowly relaxing transition, significant improvement in sensitivity will be attained for larger proteins. This is the main principle of *t*ransverse *r*elaxation *o*ptimized *s*pectroscop*y* (TROSY).[11,21]

Exploitation of the TROSY effect is rather straightforward. In contrast to ^{15}N-HSQC (Heteronuclear Single Quantum Coherence) or standard triple-resonance experiments based on ^{15}N-HSQC, no radio frequency pulses or composite pulse decoupling should be applied on amide protons when $^1H^N$ spin is not in the transverse plane. Likewise the ^{15}N decoupling should be

omitted during the acquisition. The proton decoupling efficiently averages relaxation of α and β spin-states during the indirectly detected period, resulting in poor sensitivity if these two spin-states have very different relaxation times. Similarly the ^{15}N decoupling during the acquisition averages two spin-states, reducing the attainable sensitivity if considerable difference in relaxation rates occur. When decoupling is omitted in both ^{15}N and ^{1}H dimensions, a single ^{15}N–^{1}H cross peak is split into a multiplet with four transitions. The spin-state-selective TROSY element then selects for the most slowly relaxing transitions of the multiplet. Actually, in the absence of DD/CSA cross-correlation, TROSY experiments provide inherently 50% of the signal attainable with the sensitivity-enhanced HSQC experiment due to selection of only one multiplet component.[22,23] The TROSY selection is, however, warranted on large proteins at high field (>600 ^{1}H MHz), where the mutual cancellation of DD and CSA relaxation mechanisms provide spectacular sensitivity improvements in NH-detected experiments.[21–24] It is noteworthy that remote protons account for 95% of the residual transverse relaxation of amide protons and 75% of residual transverse relaxation of ^{15}N spin[21] (vide infra). Therefore, if the protein sample is simultaneously perdeuterated there are only a few relaxation pathways left for the TROSY component. It is then obvious that TROSY works optimally for large perdeuterated proteins at the highest magnetic fields. Several research groups have reported dramatic improvement in sensitivity for large proteins at the high field. Sequential assignment has now been accomplished for several proteins having a molecular mass far beyond the historical NMR size-limit.[12,13,15–18,25,26]

At this point, before going into the details of triple-resonance experiments, we shift the focus to the $^{1}H^{N}$–^{15}N polarization transfer step. Throughout this review, the emphasis will be on TROSY based triple-resonance experiments, but let us first take a look into different possibilities of transferring $^{1}H^{N}$ polarization to the directly bound ^{15}N spin. Figure 2 shows three different polarization transfer elements. The element in Fig. 2a is the familiar INEPT (Insensitive Nuclei-Enhanced Polarization Transfer) building block,[27] which is used in TROSY experiments as well as in their HSQC based counterparts. The INEPT element transfers the steady-state $^{1}H^{N}$ magnetization into an antiphase ^{15}N coherence, utilizing ~ 93 Hz scalar coupling between the amide proton and nitrogen. In the absence of cross-correlated relaxation, the INEPT element is able to transfer magnetization very efficiently. However, on larger proteins, INEPT becomes less and less sensitive since a significant amount of initial polarization is lost during the INEPT delay by the transverse relaxation. This is because the 180° pulse on ^{15}N efficiently removes the cross-correlation effect, analogously to the decoupling pulse in the TROSY experiments. The polarization transfer element in Fig. 2b is so-called CRIPT (Cross Relaxation-Induced Polarization Transfer) block.[28] It is basically analogous to INEPT except for the missing 180°(^{15}N) pulse. In contrast to

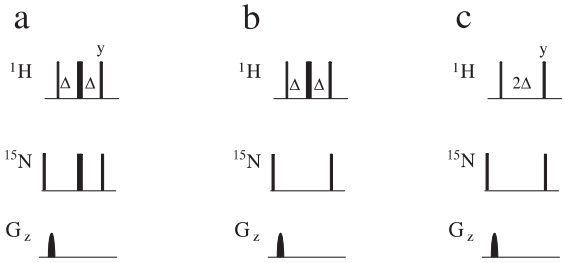

Fig. 2. Different polarization transfer elements for the $^1H^N$–^{15}N spin pair, INEPT (a), CRIPT (b), and CRINEPT (c) elements. Narrow and wide bars correspond to 90° and 180° flip angles, respectively, applied with phase x unless otherwise stated.

INEPT, the CRIPT element utilizes solely cross-correlated relaxation in order to transfer magnetization from $^1H^N$ to the ^{15}N spin. For this reason, CRIPT is very inefficient on smaller proteins since optimal transfer delay for CRIPT is inversely proportional to rotational correlation time, τ_c of the molecule.[28] The delay should then be set unreasonably long in smaller proteins, as the cross-correlation rate is very small. However, the CRIPT element becomes superior to INEPT on very high molecular weight systems (> 200 kDa) at the magnetic field close to 1000 ^{1}H MHz.[28]

The third polarization transfer element is depicted in Fig. 3c. This element, referred to as CRINEPT (Cross Relaxation-Enhanced Polarization Transfer), utilizes both scalar coupling and cross-correlated relaxation for the polarization transfer.[28] As it can be appreciated, the CRINEPT element lacks 180° pulses both on ^{15}N and ^1H. In this way, it is possible to transfer magnetization from $^1H^N$ to ^{15}N without removing the cross-correlation and without refocusing the scalar coupling between $^1H^N$ and ^{15}N spins. Obviously this polarization transfer mechanism is likely to be the most efficient on high molecular weight proteins and on smaller proteins as well since both the scalar coupling and cross-correlated relaxation can be utilized.[28] Unfortunately, half of the available $^1H^N$ magnetization is lost because the chemical shift of $^1H^N$ is not refocused at the end of the CRINEPT element, which somewhat reduces the attainable sensitivity enhancement. The CRINEPT and CRIPT experiments have recently been applied to studies of 900 kDa complex of tetradecamer protein GroEL from *E. coli* with GroES.[29,30] Unfortunately, on molecules where CRINEPT is efficient, the ^{15}N transverse relaxation times are probably too short in order to accomplish sequential assignment based on triple-resonance experiment equipped with the CRINEPT–TROSY $^1H^N$–^{15}N transfer steps.[31]

3.1.1. *TROSY in triple-resonance experiments*

Figure 3 depicts the famous triple-resonance experiment, HNCA (amide proton to nitrogen to alpha carbon experiment)[10,32–34] (Fig. 3a), and the

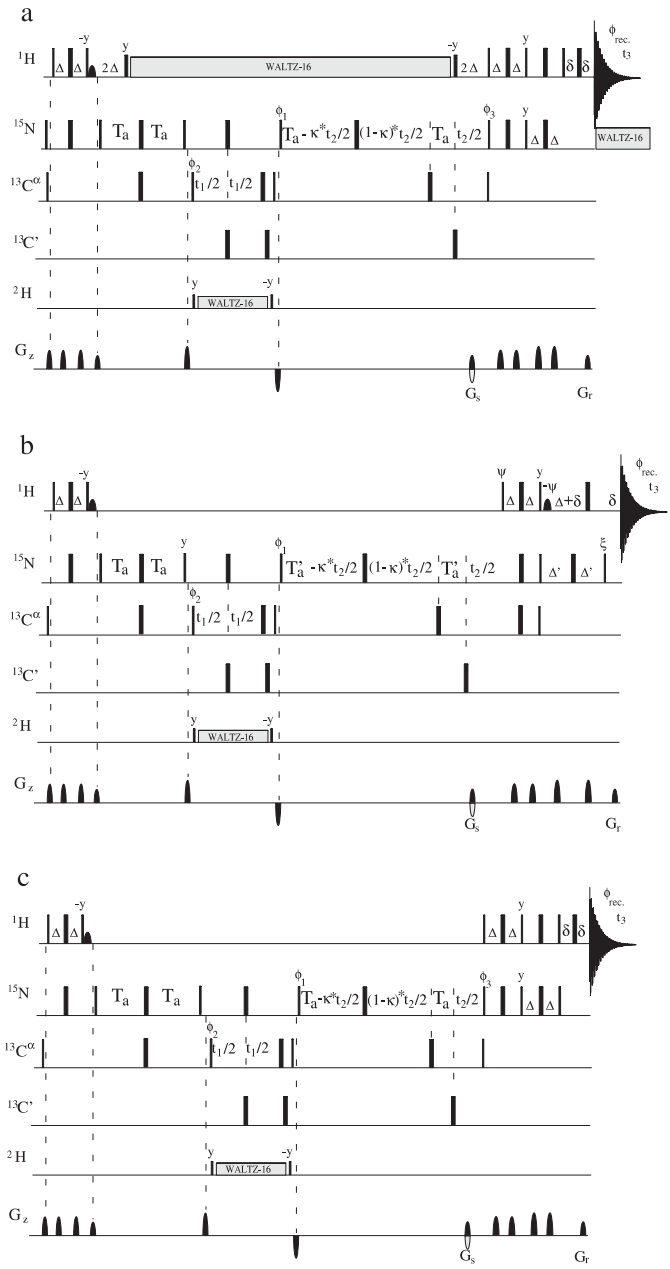

Fig. 3. HNCA (a) and two implementations of HNCA-TROSY (b–c) experiments for recording intraresidual $^{1}H^{N}(i)$, $^{15}N(i)$, $^{13}C^{\alpha}(i)$ and sequential $^{1}H^{N}(i)$, $^{15}N(i)$, $^{13}C^{\alpha}(i-1)$ correlations in $^{13}C/^{15}N/^{2}H$ labelled proteins. Narrow and wide bars correspond to 90° and 180° flip angles, respectively, applied with phase x unless otherwise indicated. Half-ellipse denotes water selective 90° pulse to obtain water-flip-back.[88,89] All 90°

corresponding implementations of HNCA-TROSY experiments[24,25,35,36] (Fig. 3b–c) utilizing the TROSY principle throughout the pulse sequences. All experiments correlate the $^{1}H^{N}(i)$ spin with its neighbouring intraresidual $^{13}C^{\alpha}(i)$ and sequential $^{13}C^{\alpha}(i-1)$ spins. In order to reduce spectral overlap, additional editing with respect to the $^{15}N(i)$ chemical shift is employed in the third dimension. Initially, the longitudinal $^{1}H^{N}$ magnetization is transferred to directly bound amide nitrogen (^{15}N) spin utilizing the $^{1}H^{N}$–^{15}N INEPT element (vide supra) and large one-bond coupling between the amide proton and nitrogen. Subsequently, the desired coherence is transferred to the intraresidual and sequential $^{13}C^{\alpha}$ nuclei. To this end, $^{15}N \rightarrow {}^{13}C^{\alpha}$ INEPT is tuned according to one-bond and two-bond scalar couplings between ^{15}N and intraresidual $^{13}C^{\alpha}$ spin, and sequential $^{13}C^{\alpha}$ spin, respectively. One-bond $^{1}J_{NC^{\alpha}}$ couplings and two-bond $^{2}J_{NC^{\alpha}}$ couplings have some dependence on protein secondary structure.[37,38] $^{1}J_{NC^{\alpha}}$ varies usually between 7 and 12 Hz, whereas $^{2}J_{NC^{\alpha}}$ typically varies between 5 and 9 Hz. The average values for $^{1}J_{NC^{\alpha}}$ and $^{2}J_{NC^{\alpha}}$ found in the α-helix are 9.6–9.9 and 6.3–6.4 Hz, respectively. The corresponding values found in β-sheet structures are somewhat larger, i.e., 10.9–11.2 and 8.3–8.4 Hz, respectively.[37,38] Therefore, the $^{15}N \rightarrow {}^{13}C^{\alpha}$ INEPT delay is set around 25 ms. After transferring the magnetization to $^{13}C^{\alpha}$, its chemical shift is labelled during the t_1 evolution period. Then the desired

(180°) pulses for the $^{13}C'$ and $^{13}C^{\alpha}$ spins are applied with a strength of $\Omega/\sqrt{15}$ ($\Omega/\sqrt{3}$), where Ω is the frequency difference between the centres of the $^{13}C'$ and $^{13}C^{\alpha}$ regions. Positions for the ^{1}H, ^{15}N, $^{13}C'$, and $^{13}C^{\alpha}$ transmitters are approximately 4.7 (water), 120 (centre of ^{15}N spectral region), 175 ppm (centre of $^{13}C'$ spectral region) and 56 ppm (centre of $^{13}C^{\alpha}$ spectral region), respectively. The $^{13}C'$ pulses are applied off-resonance with phase modulation by Ω. Frequency discrimination in ^{15}N dimension is attained using the PEP (Preservation of Equivalent Pathways) sensitivity-enhancement with gradient selection[40,41] in (a), whereas sensitivity-enhanced, gradient-selected 'clean' TROSY or PEP-TROSY elements is used in (b–c)[35,45,46] In (a) and (c) the echo and anti-echo signals are collected separately by inverting the sign of the Gs gradient pulse together with the inversion of ϕ_3. In (b) echo and anti-echo data sets are collected (I): $\psi = x$, $\xi = y$, (II): $\psi = -x$, $\xi = -y$, with simultaneous change in gradient G_S polarity. In addition to echo/anti-echo selection, ϕ_1 and ϕ_{rec} are incremented according to States-TPPI protocol[90] Shared or semi-constant time TROSY incrementation is employed for the ^{15}N chemical shift labelling in (b) and (c).[91–93] Quadrature detection in $^{13}C^{\alpha}$ dimension is obtained by States-TPPI applied to ϕ_2. Pulsed field gradients are inserted as indicated for coherence transfer pathway selection and residual water suppression. Delay durations: $\Delta = 1/(4J_{HN})$; $2T_a \sim 20$–28 ms; $2T'_a = 2T_a - 2\Delta$; δ = gradient + field recovery delay; $0 \le \kappa \le T'_a/t_{2,max}$ (b); $0 \le \kappa \le T_a/t_{2,max}$ (a) and (c). Phase cycling for HNCA (a): $\phi_1 = x$; $\phi_2 = x, -x$ + States-TPPI; $\phi_3 = x$; $\phi_{rec.} = x, -x$. Phase cycling for HNCA-TROSY (b–c): $\phi_1 = y$; $\phi_2 = x, -x$ + States-TPPI; $\phi_3 = x$; $\phi_{rec.} = x, -x$. Gradient strengths (durations): $G_s = 30$ G/cm (1.25 ms), $G_r = 29.6$ G/cm (0.125 ms). The last 90°($^{13}C^{\alpha}$) pulse removes the dispersive contribution from the lineshape.[47,48] The WALTZ-16 decoupling sequence[94] is used for decoupling of ^{1}H during $2T_a$ and t_1, and ^{15}N during acquisition in (a). Deuterium decoupling is applied during t_1 period using the WALTZ-16 sequence.

coherence is transferred back to ^{15}N, and the ^{15}N–$^{13}C^{\alpha}$ antiphase coherence is refocused during the latter $^{15}N \rightarrow {}^{13}C^{\alpha}$ INEPT step, simultaneously labelling the ^{15}N chemical shift during t_2. It can be realized that the ^{15}N spin remains in the transverse plane around 50 ms in both HNCA and HNCA-TROSY schemes. In the HNCA experiment (Fig. 3a), proton decoupling is applied during the $^{15}N \rightarrow {}^{13}C^{\alpha}$ INEPT step as well as during the t_1 period. Ultimately, the ^{15}N coherence is transferred back to $^{1}H^{N}$ single-quantum coherence using the gradient selected, sensitivity-enhanced PEP (Preservation of Equivalent Pathways) element,[39–41] and the ^{15}N composite pulse decoupling is applied during the acquisition.

In HNCA-TROSY experiments (Fig. 3b–c), no proton decoupling is applied during the $^{15}N \rightarrow {}^{13}C^{\alpha}$ INEPT periods. Consequently, α and β spin-states relax at their distinct rates during the $^{15}N \rightarrow {}^{13}C^{\alpha}$ INEPT steps. Subsequently, the ^{15}N coherence is transferred back to $^{1}H^{N}$ and no ^{15}N decoupling is applied during the acquisition. Although $^{1}H^{N}$–^{15}N scalar coupling is active during the t_2 period and also during the acquisition, only a single cross peak is observed for each $^{1}H^{N}$–^{15}N moiety because the TROSY element selects only the slowest relaxing multiplet component of the four single-quantum transitions.

There are a few additional features which will improve the performance of TROSY based triple-resonance experiments further. These are depicted in Fig. 3b–c, where various implementations of the HNCA-TROSY experiment are shown. The 90° pulse on ^{15}N prior to the first $^{1}H^{N} \rightarrow {}^{15}N$ INEPT element is removed in order to add ^{15}N Boltzmann magnetization to that originating from the amide proton[35,42] (Fig. 3b–c). Theoretically, this should lead to a 10% enhancement in signal amplitude, but in practice ca. 20% sensitivity gains have been obtained.[23,42] There are two reasons for this. First, the longitudinal relaxation time T_1 for the ^{15}N nucleus is significantly shorter than for the amide proton, especially in perdeuterated proteins.[23,42] Second, the magnetization originating in ^{15}N remains in the transverse plane for a shorter time period than the magnetization originating in $^{1}H^{N}$. The HNCA-TROSY experiment in Fig. 3b employs a gradient selected, sensitivity-enhanced 'clean' TROSY element[42–44] for the selection of desired TROSY multiplet with simultaneous concatenation of the $^{15}N \rightarrow {}^{13}C^{\alpha}$ back-INEPT step and the first spin-state-selective filter of the TROSY block.[36,45] As can be appreciated, the concatenation of the sequential delays shortens the overall length of the pulse scheme by 2Δ with an expense of additional 180°(^{13}C) pulse.[36,45] Although the transverse relaxation time for the ^{15}N TROSY component can be very long even on large proteins, the concatenation will improve the sensitivity significantly, especially on residues undergoing chemical exchange.[45] For example, on triosephosphate isomerase (TIM), a 54 kDa homodimer with 248 amino acid residues, the concatenation of delays improved sensitivity by 15% for the residues under the chemical exchange process in comparison to the original implementation.[45] Distinctively different

TROSY selection was recently introduced by Yang and Kay.[46] Their implementation of the TROSY element strongly resembles the conventional PEP element (vide infra) except for the additional 90° pulse on ^{15}N prior to the last ^{1}H spin-echo (Fig. 3c). In this scheme, part of the desired magnetization is transferred into the longitudinal ^{1}H and ^{15}N coherences during the TROSY element. These coherences relax more slowly in comparison to the heteronuclear multiple-quantum coherence, resulting in a similar gain in sensitivity as the concatenated 'clean' TROSY version. As a matter of fact, the PEP-TROSY element introduced by Yang and Kay operates as a 4π-rotation element for the longitudinal ^{1}H magnetization. Thus, no additional selective pulse(s) for the water resonance needs to be applied during the PEP-TROSY element. On the other hand, there is not a spin-state-selective filter in the ^{15}N dimension and the PEP-TROSY element transfers all ^{15}N transverse magnetization components into the $^{1}H^{N}$ coherence, forming an E.COSY like pattern between TROSY and antiTROSY transitions. Although it is possible to actively suppress the antiTROSY component,[46] this is not mandatory on larger proteins at high field. In typical triple-resonance experiments, the intensity of the undesired antiTROSY component is only 1/64 of the intensity of the desired TROSY component on a protein tumbling at 25 ns at 800 ^{1}H MHz.[46]

The last 90° pulse on ^{13}C acts as a purge pulse for the undesired dispersive magnetization.[47,48] The function of the pulse is to convert any magnetization remaining antiphase with respect to the ^{13}C spin into unobservable multiple-quantum coherence. This will provide cross peaks with pure lineshapes and with higher resolution, and consequently establishes reliable determination of coupling constants.[47,48]

A proper treatment of water magnetization throughout the TROSY experiments is required for optimal performance. It is a well-known fact that saturation transfer from solvent protons to labile amide protons results in loss of sensitivity in NH-detected experiments. Rance and co-workers showed that an additional 53% improvement in signal-to-noise ratio could be obtained by utilizing the water flip-back procedure in the TROSY experiment applied to the 54 kDa homodimer TIM at 800 ^{1}H MHz.[49] The key idea is to return bulk water magnetization back to the positive z-axis prior to detection. This can be obtained either 'actively', i.e., by arranging pulse phase and/or using selective water flip-back pulses in several ways[44,49–51] or 'passively' by utilizing radiation damping, at high field.[23] On very high molecular weight systems, the longitudinal relaxation time of amide protons can be reduced significantly by maintaining the water magnetization along the positive z-axis throughout the experiment. This can be accomplished most efficiently by adjusting each selective water flip-back pulse individually in order to avoid severe effects of radiation damping, especially at the highest magnetic field.[29]

Beside intra- and interresidue $^{13}C^{\alpha}$ nuclei, the magnetization can be transferred from the ^{15}N spin directly to the $^{13}C'$ nuclei of the preceding

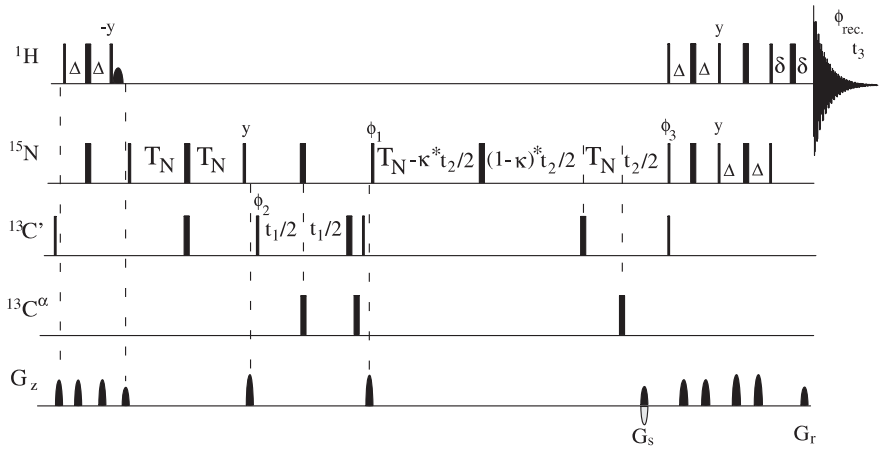

Fig. 4. The HNCO-TROSY experiment for recording solely interresidual $^1H^N$, ^{15}N, $^{13}C'$ correlations in $^{13}C/^{15}N/^2H$ labelled proteins. All 90° (180°) pulses for the $^{13}C'$ and $^{13}C^{\alpha}$ spins are applied with a strength of $\Omega/\sqrt{15}$ ($\Omega/\sqrt{3}$), where Ω is the frequency difference between the centres of the $^{13}C'$ and $^{13}C^{\alpha}$ regions. All $^{13}C^{\alpha}$ pulses are applied off-resonance with phase modulation by Ω. $\Delta = 1/(4J_{HN})$; $T_N = 1/(4J_{NC'})$; δ = gradient + field recovery delay; $0 \leq \kappa \leq T_N/t_{2,max}$. Phase cycling: $\phi_1 = y$; $\phi_2 = x$, $-x$ + States-TPPI; $\phi_3 = x$; $\phi_{rec.} = x, -x$.

residue by utilizing rather large one-bond scalar coupling, 15 Hz, between the $^{15}N(i)$ and $^{13}C'(i-1)$ spins. This experiment is HNCO-TROSY[24,46] (Fig. 4) and it is conceptually identical to the HNCA-TROSY except we have excitation of $^{13}C'$ spins instead of $^{13}C^{\alpha}$ spins. In contrast to HNCA-TROSY, where the amide proton magnetization is simultaneously transferred to both intra- and interresidual $^{13}C^{\alpha}$ spins, in the HNCO-TROSY experiment the magnetization is transferred exclusively to the sequential $^{13}C'(i-1)$ spin. This is because two-bond coupling between the $^{15}N(i)$ and $^{13}C'(i)$ spins is negligibly small. Transfer amplitude for the HNCO-TROSY experiment is very high – it is the most sensitive triple-resonance experiment (vide infra). The corresponding $^{15}N \rightarrow {}^{13}C'$ INEPT delay is set according to $1/(2J_{NC'})$ i.e., to ~25–33 ms, depending on the transverse relaxation rate of the ^{15}N spins (vide infra).

3.2. Deuteration

The magnetization has now been successfully transferred from the $^1H^N$ spin to the intraresidual and sequential $^{13}C^{\alpha}$ spins or alternatively to the interresidue $^{13}C'$ spin either using HNCA-TROSY or HNCO-TROSY schemes, respectively. It is inevitable that the HNCO-TROSY spectrum cannot be used for the sequential assignment alone because it does not bridge two sequential $^1H^N$–^{15}N shifts through common carbonyl carbon frequency. The

HNCA-TROSY experiment instead can be used for the sequential assignment but the resonance overlap can be too severe, especially on highly α-helical proteins, to distinguish unambiguously all cross peaks. In addition, the differentiation between the intraresidual and sequential correlations hinges on cross peak intensity. Because the ranges of $^{1}J_{NC^{\alpha}}$ (7–13 Hz) and $^{2}J_{NC^{\alpha}}$ (5–9 Hz) scalar couplings overlap and the transverse relaxation times of $^{13}C^{\alpha}$ spins can significantly differ from each other, it is not always obvious whether the cross peak represents the intraresidual or sequential pathway, especially in a crowded spectrum.

For these reasons, the magnetization has to be relayed either through the $^{13}C'(i-1)$ spin exclusively to the sequential $^{13}C^{\alpha}(i-1)$ nuclei in the HN(CO)CA-TROSY experiment (vide infra), or through the intraresidual $^{13}C^{\alpha}(i)$ spin to the $^{13}C'(i)$ nucleus in the HN(CA)CO-TROSY experiment (vide infra). Thus, we have either a complementary HNCA/HN(CO)CA or HNCO/HN(CA)CO TROSY experiment pair, which enables unambiguous resonance assignment in a sequential manner. Unfortunately, on high molecular weight proteins at the highest field, neither of these strategies is as efficient as TROSY based ^{15}N–^{13}C transfer. In the following, we elaborate on the transverse relaxation of $^{13}C^{\alpha}$ spin and coherence transfer through the $^{13}C^{\alpha}$ nuclei.

Consider a ^{1}H–^{13}C spin pair. Unlike the ^{15}N and $^{1}H^{N}$ spins, the $^{13}C^{\alpha}$ spin does not have large chemical shielding anisotropy ($\Delta\sigma = 34$ ppm) and consequently CSA accounts only fractionally for the $^{13}C^{\alpha}$ transverse relaxation.[52] The primary mechanism for the $^{13}C^{\alpha}$ spin–spin relaxation arises from the dipolar interaction with directly attached ^{1}H nucleus. The $^{13}C^{\alpha}$–$^{1}H^{\alpha}$ dipolar interaction is so strong on larger proteins that the transverse relaxation times found for the $^{13}C^{\alpha}$ carbons are on the order of 10–20 ms for the 25–30 kDa protein.[52] This was soon found to be the major bottleneck for the assignment and structure determination of proteins larger than ca. 25 kDa.

Although the first NMR spectra of deuterated proteins were published already in 1968, the deuteration was mainly employed for the purpose of simplifying one-dimensional proton spectra.[53,54] Later in the 1980s, LeMaster and co-workers employed random fractional deuteration for the assignment of thioredoxin using homonuclear two-dimensional spectroscopy.[55] However, it was realized that deuteration significantly improves the spectral quality of homonuclear multidimensional NMR experiments.

The effect of deuteration, for the needs of sequence-specific resonance assignments using triple-resonance experiments, was first demonstrated by Bax and co-workers on the 19.7 kDa protein calcineurin B in 1993.[56] By replacing the ^{1}H spin with deuterium, the transverse relaxation time of $^{13}C^{\alpha}$ spin is increased by nearly an order of magnitude due to the 6.5 times smaller gyromagnetic ratio of ^{2}H in comparison to ^{1}H.[52,56] Not surprisingly, deuteration was utilized for the aid of structure determination of several

proteins[57–61] and also novel pulse schemes were developed which exploited the fruits of deuteration. A panoply of triple-resonance experiments with a so-called *out-and-back* coherence transfer scheme were devised thanks to their aptness to deuterated protein samples.[62–68] In these experiments, the magnetization both originates and is detected on amide protons. Necessary modifications to the pulse sequences for deuterated samples are minimal. Basically, only additional decoupling of ^{2}H spins during periods that the magnetization resides on aliphatic carbons is needed owing to rapid T_1 of the ^{2}H spin with large quadropolar moment[56] (see for example Fig. 3). On proteins, which are only partially deuterated at aliphatic sites, it may be necessary to filter out protonated isotopomers[52] but on large proteins this is usually not an issue owing to the very rapid decay of these coherences.

Evidently it is vital that the otherwise deuterated protein contains protons at the amide position. In principle, deuterated protein samples are obtained by growing bacterial strains as for the $^{13}C/^{15}N$ labelled samples but in D_2O solution instead of H_2O.[69] For complete deuteration, the carbon source also has to be ^{2}H labelled.[69] The labile amide protons are then back-exchanged during purification in H_2O-based buffers, or by an unfolding/refolding procedure in H_2O-containing buffer. If the protein is thermostabile, it can be incubated at high temperature to catalyze NH back-exchange. Unfortunately, not all proteins are amenable to these procedures.

It has been observed for several proteins that, by deuteration, the transverse relaxation time of $^{13}C^{\alpha}$ nuclei increases from 10–20 ms to 100–140 ms.[52,69–71] In addition, transverse relaxation times of amide protons were increased substantially since the aliphatic protons contribute 40% to T_2 relaxation of $^{1}H^{N}$ spins.[69] When (per)deuteration is combined with the TROSY based triple-resonance experiments, dramatic gains in sensitivity are obtained. As residual protons account for the transverse relaxation of $^{1}H^{N}$ and ^{15}N spins by 95% and 75%, respectively, replacement of nonlabile protons suppress almost completely efficient relaxation mechanisms for the $^{1}H^{N}$–^{15}N spin pair at the highest field[21] (vide supra). Thus, deuteration increases concomitantly transverse relaxation times of aliphatic carbons and impacts constructively to the TROSY effect as well. In this way it is feasible to transfer magnetization efficiently from an amide proton via nitrogen to the $^{13}C^{\alpha}$ spin and record the $^{13}C^{\alpha}$ chemical shift using the constant-time approach with high resolution as in the CT-HNCA-TROSY experiment.[25,36] Alternatively, the desired coherence can be relayed further down to the neighbouring $^{13}C'$ or $^{13}C^{\beta}$ spins as in HN(CA)CO-TROSY[45,72] or HNCACB-TROSY experiments, respectively.[25,72] We have then two complementary experiments, HNCO-TROSY and HN(CA)CO-TROSY, which can be used concomitantly to resolve ambiguities during the assignment process.

Unfortunately, on perdeuterated high molecular weight proteins the decay of $^{13}C^{\alpha}$ coherence is much faster than it was first anticipated.

Yang and Kay observed that freely precessing $^{13}C^{\alpha}$ coherence relaxes more efficiently than the corresponding spin-locked coherence.[25] The $^{13}C^{\alpha}$ transverse relaxation times for the 42 kDa maltose binding protein (MBP) complexed with β-cyclodextrin tumbling at 23 ns at 25°C were around 38 ± 10 ms. These are clearly shorter values than the corresponding $T_{1,\rho}$ values (85 ± 20 ms) found in the MBP/β-cyclodextrin complex. The Reason for this discrepancy is not yet fully understood.[25] Therefore, despite deuteration, the transverse relaxation time of $^{13}C^{\alpha}$ nucleus remains an issue with high molecular weight proteins. The use of a long constant-time period of ~ 28 ms in order to achieve high resolution in $^{13}C^{\alpha}$ dimension for very large proteins becomes too costly in terms of sensitivity. Yang and Kay estimated that on a protein with a correlation time of 45 ns, use a of long constant-time period for $^{13}C^{\alpha}$ spin induces sensitivity loss by a factor of 3 in comparison with the real-time implementation of HNCA-TROSY ($t_{1,\max} = 7.4$ ms).[25] On larger systems, the loss will be much more pronounced. Hence, the transfer step from $^{13}C^{\alpha}$ spin to $^{13}C'$ nucleus becomes rather costly in high molecular weight proteins.

3.3. Chemical shift anisotropy of carbonyl carbon

In the alternative approach, the $^{1}H^{N}(i)$, $^{15}N(i)$, $^{13}C^{\alpha}(i/i-1)$ correlations in the HNCA-TROSY spectrum can be supplemented with the data from the HN(CO)CA-TROSY experiment[72,73] yielding solely $^{1}H^{N}(i)$, $^{15}N(i)$, $^{13}C^{\alpha}(i-1)$ correlations. To this end, the HNCO-TROSY experiment is extended with the $^{13}C' \rightarrow {}^{13}C^{\alpha}$ INEPT step, which utilizes rather large (ca. 51–55 Hz) one-bond scalar coupling between the $^{13}C'$ and $^{13}C^{\alpha}$ spins in order to transfer magnetization from the $^{13}C'(i-1)$ nucleus further to the $^{13}C^{\alpha}(i-1)$ spin.

Carbonyl carbon, which is not directly bonded to any proton, relaxes mainly through the chemical shift anisotropy (CSA) although some contribution arises from $^{13}C'$–$^{13}C^{\alpha}$, $^{13}C'$–$^{1}H^{N}$, $^{13}C'$–^{15}N dipolar interactions.[74] Thanks to its large couplings to adjacent $^{13}C^{\alpha}$ and ^{15}N spins and its distinct chemical shift range, the $^{13}C'$ spin is extremely useful for relaying magnetization efficiently on smaller proteins at lower magnetic field strengths. Actually, the HN(CO)CA experiment[32–34,63] is the second-most sensitive of the NH-detected triple-resonance experiments at lower magnetic field strengths. However, the chemical shift anisotropy of the $^{13}C'$ spin is very large.[45,75] Consequently, the performance of experiments, which relay the magnetization through the $^{13}C'$ spin becomes worse as the strength of the polarizing magnetic field increases, owing to the quadratic dependence of $T_{2,C'}$ on the field strength.[45,73,76] In addition, as CSA depends also on molecular size, i.e., on the rotational correlation time τ_c of a protein, this issue will get more serious at the highest fields on high molecular weight systems. It is unfortunate that under the conditions where

the TROSY effect is the most efficient, as well as when the amount of initial ^{1}H polarization is largest, the transverse relaxation of $^{13}C'$ spin is fastest. Thus, the $^{13}C'$ spin relaxation seriously compromises the overall sensitivity gain. Unlike in the case of aliphatic carbons or NH spins alongside the TROSY effect, the deuteration does not have significant impact on the transverse relaxation time of the $^{13}C'$ nucleus.[77] If we assume that the spin–spin relaxation of $^{13}C'$ spin is solely induced by the chemical shift anisotropy, the T_2 of $^{13}C'$ spin can be expressed according to Hu and Bax[78] as follows [Eq. (1)]:

$$T_{2,C'} \sim 1/[\tau_c(3/4 + B^2/150)] \tag{1}$$

where τ_c (ns) is the rotational correlation time of the protein, and B (T) is the strength of the polarizing magnetic field. Calculations of T_2 of $^{13}C'$, as a function of rotational correlation time against four different (800, 900, 1000, and 1100 ^{1}H MHz) magnetic fields, are shown in Fig. 5a. Similarly, the $T_{2,C'}$ values as a function of polarizing magnetic field strength with four different correlation times (35, 45, 60, and 75 ns) are shown in Fig. 5b. From this perspective, the transfer step from $^{13}C'(i-1)$ to $^{13}C^{\alpha}(i-1)$ will be heavily compromised owing to the rapid transverse relaxation of $^{13}C'$ at the highest magnetic field on high molecular weight proteins. Thus, the HNCA like coherence transfer pathway directly from $^{15}N(i)$ to $^{13}C^{\alpha}(i-1)$ becomes more efficient than the relay through carbonyl carbon in the HN(CO)CA-TROSY experiment[45,73,76] (vide infra).

In the last section, we will focus on the suite of novel triple-resonance TROSY experiments designed for accomplishing the sequence-specific assignment of backbone nuclei in high molecular weight proteins.

4. TROSY BASED TRIPLE-RESONANCE EXPERIMENTS

The compilation of triple-resonance experiments for the backbone resonance assignment is extensive. In order to provide the reader with practical insight in the applicability of experiments, we will emphasize the pros and cons of particular experiments. In addition, relative coherence transfer efficiency is evaluated for each experiment. All experiments transfer the magnetization initially from the amide proton to nitrogen using the conventional $^{1}H^{N}$–^{15}N INEPT step[27] and employ one of the several spin-state-selective filters for the TROSY selection.[22,35,42,46,49–51] Consequently, we will neglect these common steps from the transfer amplitude calculations. The same holds true also for the slowly relaxing longitudinal coherences that build up during the course of experiments. We also presume that (per)deuteration is a prerequisite for high molecular weight proteins. Thus, only the experiments equipped with the TROSY selection are

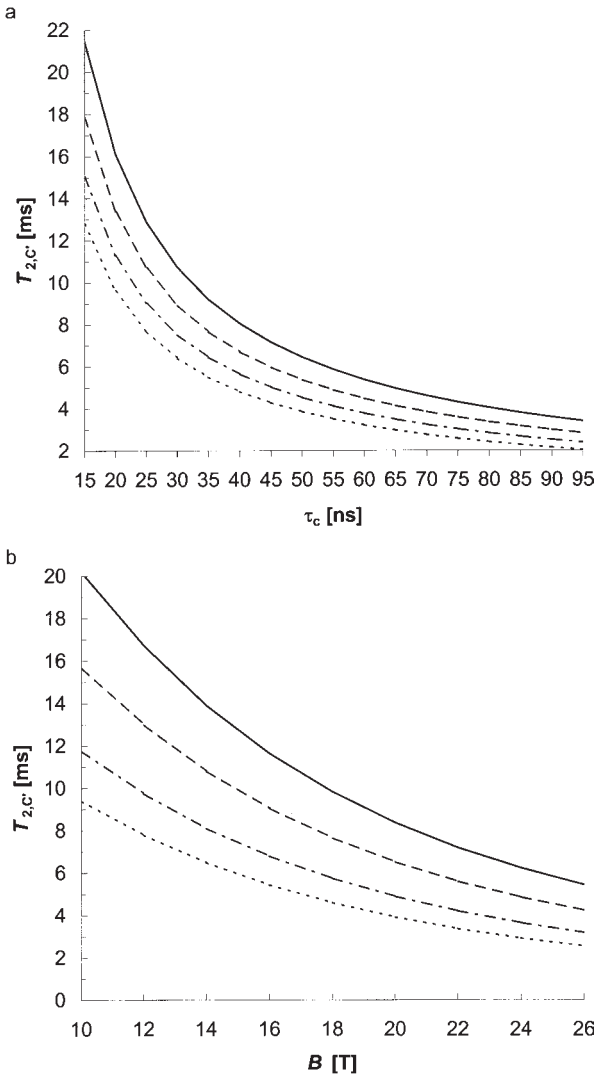

Fig. 5. Transverse relaxation times of carbonyl carbon as a function of rotational correlation time, τ_c (a), at four polarizing magnetic field strengths, and as a function of field strength, B_0, against four different correlation times (b), according to Eq. (1). Field strengths used in simulations are, 800 (——), 900 (– – –), 1000 (– – · – – · – –), 1100 (----) ^{1}H MHz (a). Correlation times used are $\tau_c = 35$ (——), 45 (– – –), 60 (– – · – – · – –), 75 (----) ns (b).

introduced. To this end, we assume that in a large, uniformly $^{15}N/^{13}C/^{2}H$ labelled protein ($\tau_c > 45$ ns) at the highest magnetic field, transverse relaxation times for the ^{15}N (TROSY component), $^{13}C'$, and $^{13}C^{\alpha}$ spins are 50, 6, and 25 ms, respectively.

4.1. Sequential assignment based on alpha carbon shifts

4.1.1. *HNCA-TROSY*

The HNCA scheme can be considered as the prototype of triple-resonance experiments. The corresponding HNCA-TROSY scheme depicted in Fig. 3c creates a $^{1}H^{N}(i)$, $^{15}N(i)$, $^{13}C^{\alpha}(i)/^{13}C^{\alpha}(i-1)$ correlation map. The magnetization is transferred from the $^{1}H^{N}(i)$ spin to the intraresidual $^{13}C^{\alpha}(i)$ and sequential $^{13}C^{\alpha}(i-1)$ spins via directly bound $^{15}N(i)$ spin, utilizing $^{1}J_{NC^{\alpha}}$ and $^{2}J_{NC^{\alpha}}$ scalar couplings, respectively (vide supra). The magnetization flows through the HNCA-TROSY experiment in the following way

$$^{1}H^{N}_{(i)} \xrightarrow{^{1}J_{NH}} {}^{15}N_{(i)} \xrightarrow{^{1}J_{NC^{\alpha}};J_{NC^{\alpha}}} {}^{13}C^{\alpha}_{(i/i-1)}(t_1)$$

$$\xrightarrow{^{1}J_{NC^{\alpha}};^{2}J_{NC^{\alpha}}} {}^{15}N_{(i)}(CT - t_2) \xrightarrow{^{1}J_{NH}} {}^{1}H^{N}_{(i)}(t_3)$$

In principle, for each residue, two correlations emerge. One is the strong intraresidual $^{1}H^{N}(i) \rightarrow {}^{13}C^{\alpha}(i)$ correlation and the other is the usually weaker sequential $^{1}H^{N}(i) \rightarrow {}^{13}C^{\alpha}(i-1)$ correlation. The coherence transfer amplitudes for the *intraresidual* and *sequential* correlations can be retrieved from Eqs. (2) and (3):

$$\sin^{2}(2\pi\,{}^{1}J_{NC^{\alpha}}T_a)\cos^{2}(2\pi\,{}^{2}J_{NC^{\alpha}}T_a)\exp(-4T_a/T_{2,N}) \tag{2}$$

$$\cos^{2}(2\pi\,{}^{1}J_{NC^{\alpha}}T_a)\sin^{2}(2\pi\,{}^{2}J_{NC^{\alpha}}T_a)\exp(-4T_a/T_{2,N}) \tag{3}$$

The overall performance is limited by the average $^{1}J_{NC^{\alpha}}$ and $^{2}J_{NC^{\alpha}}$ scalar coupling values that are 10.9 (9.6) Hz and 8.3 (6.4) Hz in the β-sheet structures (α-helical structures), respectively.[37] Consequently the delay $2T_a$ is routinely set to ~25 ms. Assuming that the ^{15}N spin–spin relaxation time for the TROSY component is 50 ms, the transfer efficiency for the *intraresidual* pathway, for the first t_1 increment ($t_1 = 0$), is 0.132, when we have optimized delays for the optimal *intraresidual* transfer in α-helices (Fig. 6). Throughputs for the *sequential* pathway then become 0.045 (0.058 β-sheet).

The sequential assignment could in principle be established using only the HNCA-TROSY experiment. However, as it was pointed out earlier, the intraresidual and sequential connectivities cannot always be distinguished from each other due to similar magnitudes of $^{1}J_{NC^{\alpha}}$ and $^{2}J_{NC^{\alpha}}$, increasing accidental overlap in the HNCA spectrum on larger proteins and discrepancy in the relaxation rates of $^{13}C^{\alpha}$ spins between amino acid residues. In practice, a number of complementary experiments are likely to be needed in order to obtain sequence-specific backbone resonance assignment on larger proteins.

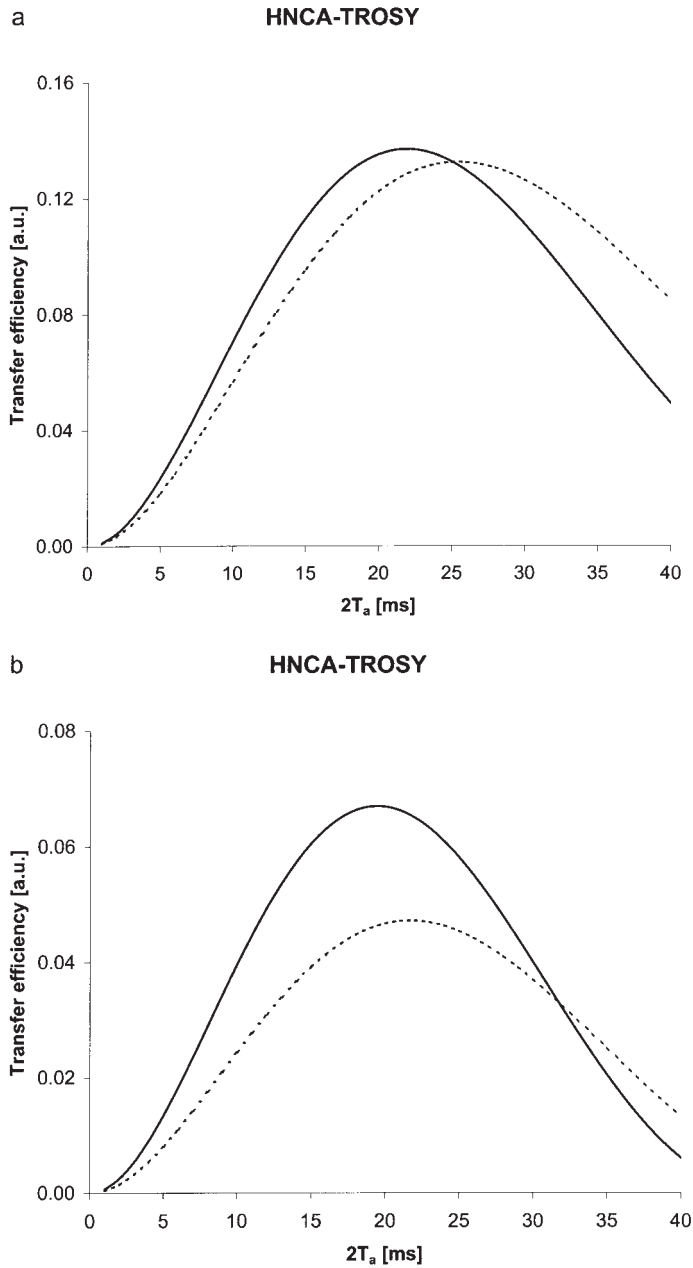

Fig. 6. The efficiency of the coherence transfer, for the first increment, as a function of delay $2T_a$ for the HNCA-TROSY. The transfer amplitudes for the intraresidual (a) and sequential (b) cross peaks were calculated with the following parameters, Eqs. (2–3): $T_{2,^{15}\text{N-TROSY}} = 50$ ms, $^1J_{\text{NC}^\alpha} = 10.9$ Hz and $^2J_{\text{NC}^\alpha} = 8.3$ Hz (——), $^1J_{\text{NC}^\alpha} = 9.6$ Hz and $^2J_{\text{NC}^\alpha} = 6.4$ Hz (- - - -).

4.1.2. *Four-dimensional extension of the HNCA-TROSY scheme*

The HNCA-TROSY experiment can be readily extended to correlate the $^{13}C'$ spin of the preceding residue with intraresidual $^{1}H^{N}(i)$, $^{15}N(i)$, and $^{13}C^{\alpha}(i)$ frequencies. This kind of four-dimensional $HNCO_{i-1}CA$-TROSY experiment (Fig. 7) was recently introduced by Konrat *et al.*[79] The coherence flows through the following pathway

$$^{1}H^{N}_{(i)} \xrightarrow{^{1}J_{NH}} {}^{15}N_{(i)} \xrightarrow{^{1}J_{NC^{\alpha}};{}^{1}J_{NC'};{}^{2}J_{NC^{\alpha}}} {}^{13}C'_{(i-1)}(t_2) \longrightarrow {}^{13}C^{\alpha}_{(i/i-1)}(t_1)$$

$$\xrightarrow{^{1}J_{NC^{\alpha}};{}^{1}J_{NC'};{}^{2}J_{NC^{\alpha}}} {}^{15}N_{(i)}(CT - t_3) \xrightarrow{^{1}J_{NH}} {}^{1}H^{N}_{(i)}(t_4)$$

Thus, the magnetization is transferred from the amide proton to the attached nitrogen and then simultaneously to the intra- and interresidual $^{13}C^{\alpha}$ spins and sequential $^{13}C'$ spin. The $^{13}C^{\alpha}$ chemical shift is labelled during t_1 and $^{13}C'$ frequency during t_2. The desired coherence is transferred back to the amide proton in the identical but reverse coherence transfer pathway. The ^{15}N chemical shift is frequency labelled during t_3, and implemented into the $^{13}C \rightarrow {}^{15}N$ back-INEPT step. The sensitivity of the $HNCO_{i-1}CA$-TROSY experiment is excellent and nearly similar to HNCA-TROSY except for the inherent sensitivity loss by a factor of $\sqrt{2}$, arising from additional quadrature detection needed for $^{13}C'$ frequency discrimination in the fourth dimension. The excellent sensitivity is due to a very efficient coherence transfer pathway,

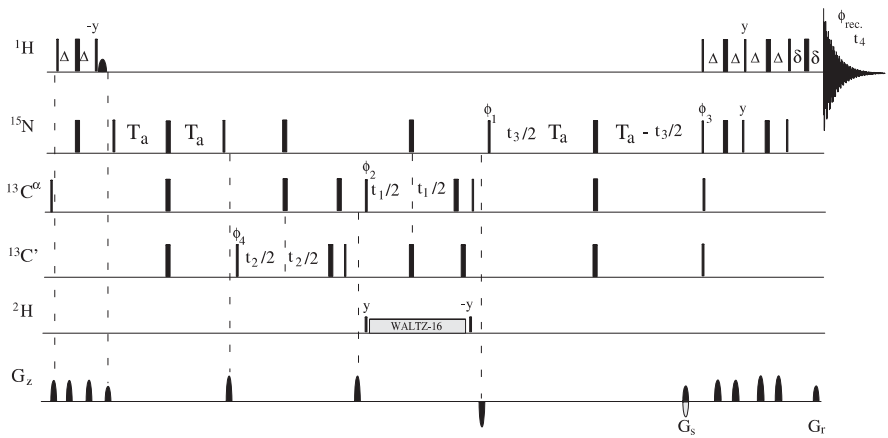

Fig. 7. Pulse scheme of four-dimensional $HNCO_{i-1}CA$-TROSY experiment for establishing intraresidual $^{13}C^{\alpha}(i)$, $^{13}C'(i-1)$, $^{15}N(i)$, $^{1}H^{N}(i)$ and sequential $^{13}C^{\alpha}(i-1)$, $^{13}C'(i-1)$, $^{15}N(i)$, $^{1}H^{N}(i)$ correlations in $^{13}C/^{15}N/^{2}H$ labelled proteins. Delay durations: $\Delta = 1/(4J_{HN})$; $2T_a = \sim 24$–29 ms; $\delta =$ gradient + field recovery delay. Phase cycling: $\phi_1 = x$; $\phi_2 = x$, $-x +$ States-TPPI; $\phi_3 = x$; $\phi_4 = 2(x)$, $2(-x) +$ States-TPPI; $\phi_{rec.} = x$, $2(-x)$, x.

i.e., the magnetization is not relayed through the efficiently relaxing $^{13}C'$ or $^{13}C^{\alpha}$ spins. The transfer amplitudes for the intraresidual and sequential correlations are calculated according to Eq. (4)

$$\cos^2(2\pi\,{}^2J_{NC^{\alpha}}T_a)\sin^2(2\pi\,{}^1J_{NC^{\alpha}}T_a)\sin^2(2\pi\,{}^1J_{NC'}T_a)\exp(-4T_a/T_{2,N}) \quad (4)$$

and Eq. (5)

$$\sin^2(2\pi\,{}^2J_{NC^{\alpha}}T_a)\cos^2(2\pi\,{}^1J_{NC^{\alpha}}T_a)\sin^2(2\pi\,{}^1J_{NC'}T_a)\exp(-4T_a/T_{2,N}), \quad (5)$$

respectively, and are plotted in Fig. 8. The $HNCO_{i-1}CA$-TROSY experiment together with the four-dimensional HNCOCA-TROSY/HNCACO-TROSY experiments[25] (vide infra) played a crucial role in this state-of-the-art work, which resulted in nearly complete (95% of ^{15}N, $^1H^N$, and 97% $^{13}C^{\alpha}$, $^{13}C'$, $^{13}C^{\beta}$) assignment of 723 residue Malate Synthase G.[12]

4.1.3. *HN(CO)CA-TROSY*

The complementary experiment to HNCA-TROSY is the HN(CO)CA-TROSY experiment[25,72,73] (Fig. 9a). The parallel use of the HN(CO)CA-TROSY and HNCA-TROSY experiments unravels most of the ambiguities arising from the intensity based differentiation of inter- and intraresidual cross peaks in the HNCA-TROSY spectrum. The HN(CO)CA-TROSY spectrum also contains only half the number of cross peaks found in the HNCA-TROSY spectrum, thanks to the unique coherence transfer route eliminating the intraresidual correlations. Because the chemical shift dispersion in the $^{13}C^{\alpha}$ region can be very modest, on partially folded or highly α-helical proteins, this exclusivity can be very advantageous for this kind of system, especially very large proteins. In order to transfer magnetization exclusively to the sequential $^{13}C^{\alpha}$ nucleus, an additional transfer step based on the $^{13}C' \rightarrow {}^{13}C^{\alpha}$ INEPT is warranted.

The flow of coherence in HN(CO)CA is as follows

$$\begin{aligned} &{}^1H^N_{(i)} \xrightarrow{{}^1J_{NH}} {}^{15}N_{(i)} \xrightarrow{{}^1J_{NC'}} {}^{13}C'_{(i-1)} \xrightarrow{{}^1J_{C'C^{\alpha}}} {}^{13}C^{\alpha}_{(i-1)}(t_1) \\ &\xrightarrow{{}^1J_{C'C^{\alpha}}} {}^{13}C'_{(i-1)} \xrightarrow{{}^1J_{NC'}} {}^{15}N_{(i)}(CT - t_2) \xrightarrow{{}^1J_{NH}} {}^1H^N_{(i)}(t_3) \end{aligned}$$

Magnetization is initially transferred from $^1H^N(i)$ to $^{15}N(i)$ spin. Unlike in the HNCA-TROSY scheme, the desired coherence is transferred from the $^{15}N(i)$ spin to the $^{13}C'(i-1)$ spin of the preceding residue. To this end, nearly uniform $^1J_{NC'}(\sim 15$ Hz) scalar coupling is used. As $^2J_{NC'}$ is negligibly small, the coherence is transferred exclusively to the $^{13}C'(i-1)$ nucleus. Finally, the $^{13}C' \rightarrow {}^{13}C^{\alpha}$ INEPT is used to transfer magnetization from $^{13}C'(i-1)$ to

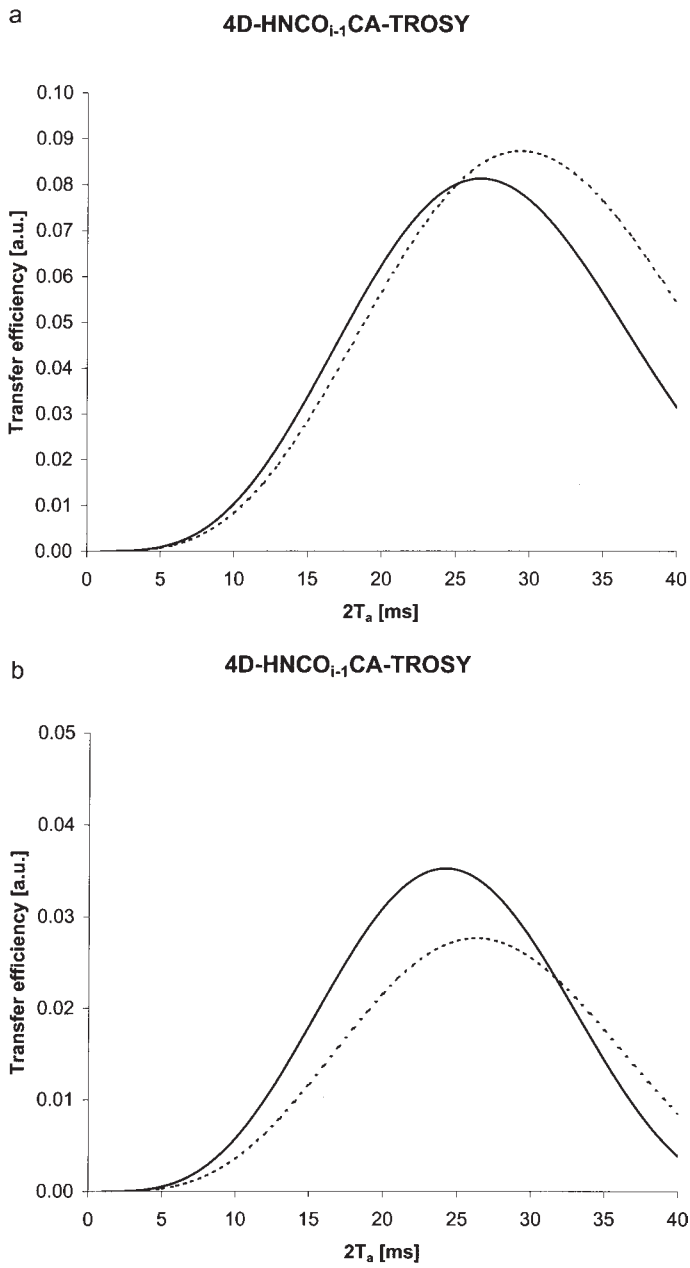

Fig. 8. Transfer amplitudes for the intraresidual $^{13}C^{\alpha}(i)$, $^{13}C'(i-1)$, $^{15}N(i)$, $^{1}H^{N}(i)$ (a) and interresidual $^{13}C^{\alpha}(i-1)$, $^{13}C'(i-1)$, $^{15}N(i)$, $^{1}H^{N}(i)$ (b) correlations as a function of ^{15}N–^{13}C transfer delay $2T_a$ in the HNCO$_{i-1}$CA-TROSY scheme. Functions in Eqs. (4)–(5) are plotted using the following parameters: $T_{2,^{15}N\text{-TROSY}} = 50$ ms, $^{1}J_{NC^{\alpha}} = 10.9$ Hz and $^{2}J_{NC^{\alpha}} = 8.3$ Hz (——), $^{1}J_{NC^{\alpha}} = 9.6$ Hz and $^{2}J_{NC^{\alpha}} = 6.4$ Hz (- - - -), $^{1}J_{NC'} = 15$ Hz.

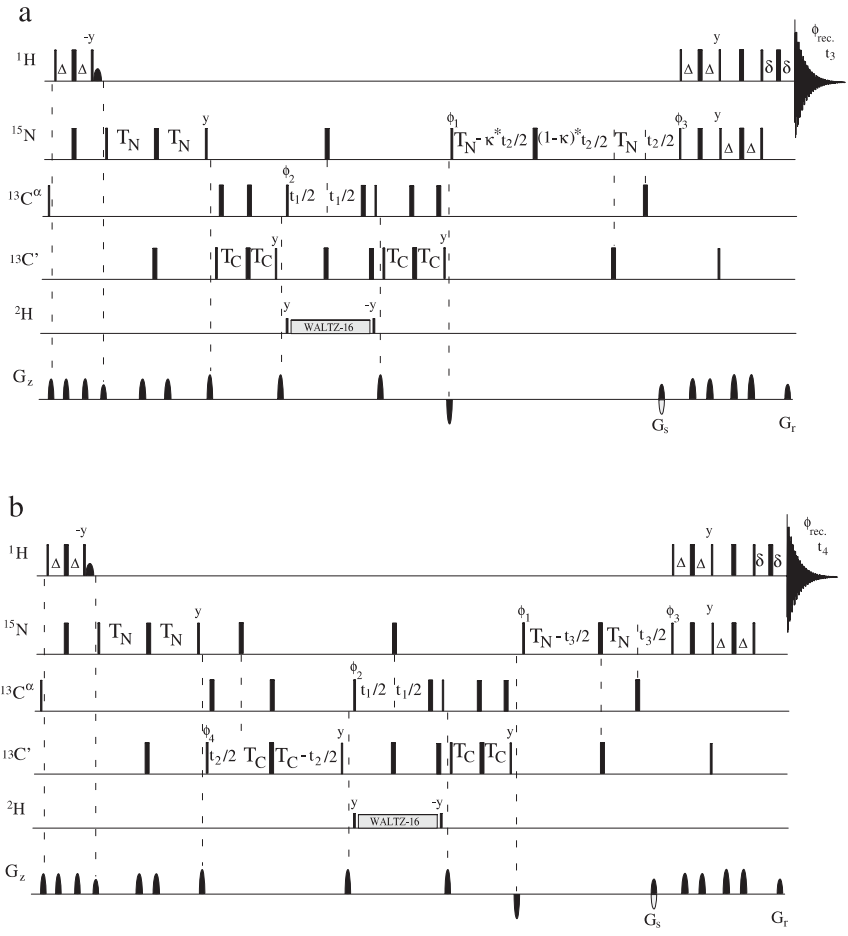

Fig. 9. HN(CO)CA-TROSY (a) and four-dimensional HNCOCA-TROSY (b) experiments for recording sequential $^1H^N$, ^{15}N, $^{13}C^\alpha$ (a) or $^1H^N$, ^{15}N, $^{13}C^\alpha$, $^{13}C'$(b) correlations in $^{13}C/^{15}N/^2H$ labelled proteins. Delay durations: $\Delta = 1/(4J_{HN})$; $T_N = 1/(4J_{NC'})$; $T_C = 1/(4J_{C'C^\alpha})$; δ = gradient + field recovery delay; $0 \le \kappa \le T_N/t_{2,max}$. Phase cycling for HN(CO)CA-TROSY (a): $\phi_1 = y$; $\phi_2 = x, -x$ + States-TPPI; $\phi_3 = x$; $\phi_{rec.} = x, -x$. Phase cycling for HNCOCA-TROSY (b): $\phi_1 = y$; $\phi_2 = x, -x$ + States-TPPI; $\phi_3 = x$; $\phi_4 = 2(x), 2(-x)$ + States-TPPI; $\phi_{rec.} = x, 2(-x), x$.

$^{13}C^\alpha(i-1)$, utilizing large $^1J_{C'C^\alpha}$ scalar coupling ($\sim$53 Hz). The coherence transfer amplitude for the interresidual pathway (Fig. 10) can be estimated using the Eq. (6):

$$\sin^2(2\pi\,{}^1J_{NC'}T_N)\sin^2(2\pi\,{}^1J_{C'C^\alpha}T_C)\exp(-4T_N/T_{2,N})\exp(-4T_C/T_{2,C'}). \quad (6)$$

The nominal values are: $^1J_{NC'} =$ 15 Hz, $^1J_{C'C^\alpha} = 53$ Hz, $2T_N \sim 33$ ms, and $2T_C \sim 9.1$ ms. The transfer efficiency in the HN(CO)CA-TROSY experiment

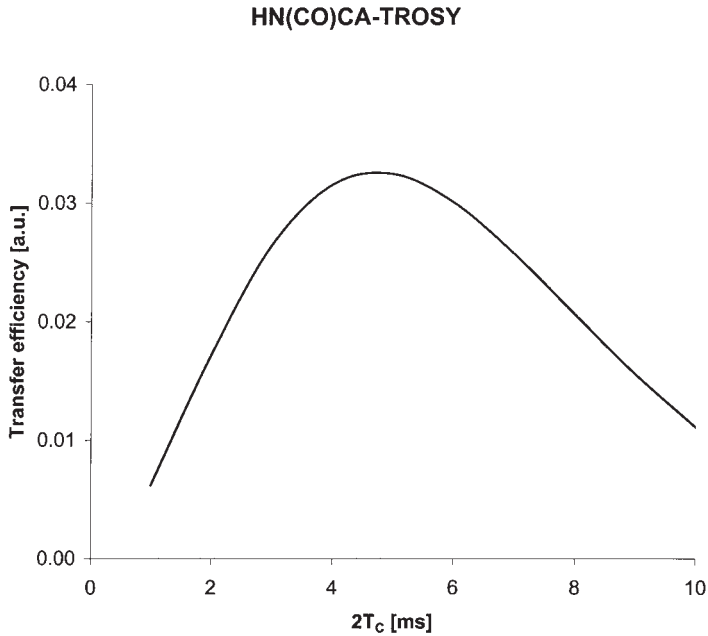

Fig. 10. Efficiency of the coherence transfer as a function of $^{13}C'$-$^{13}C^{\alpha}$ transfer delay $2T_C$ for the HN(CO)CA-TROSY scheme. The transfer function [Eq. (6)] is plotted using the following parameters: $2T_N = 25$ ms, $^1J_{NC'} = 15$ Hz, $^1J_{C'C^{\alpha}} = 53$ Hz, $T_{2,^{15}N\text{-TROSY}} = 50$ ms, $T_{2,C'} = 6$ ms.

becomes 0.032 when we assume that $T_2(^{13}C')$ at 900 MHz is around 6 ms for a protein with $\tau_c \sim 45$ ns (Fig. 5a). Although the HN(CO)CA experiment is clearly more sensitive than the HNCA-TROSY scheme on intermediate field strengths and on smaller proteins, its feasibility drops dramatically on high molecular weight proteins at field strengths optimal for the TROSY effect. In this case, the sequential pathway in the HNCA-TROSY experiment is more efficient than the corresponding route in the HN(CO)CA-TROSY scheme. This is particularly unfortunate since the HN(CO)CA-TROSY scheme plays a pivotal role in the sequence-specific assignment procedure, providing complementary and exclusively sequential data to supplement the HNCA-TROSY spectrum. Fortunately, there are also other possibilities to derive sequential connectivities using the experiments that minimize the time period during which the $^{13}C'$ spin is in the transverse plane (vide infra).

4.1.4. *Four-dimensional extension; HNCOCA-TROSY*

By frequency labelling the $^{13}C'(i-1)$ spin during additional incremented time delay, and implementing this into the $^{13}C' - ^{13}C^{\alpha}$ INEPT step in the HN(CO)CA-TROSY experiment, a four-dimensional HNCOCA-TROSY experiment[25] is obtained (Fig. 9b), which alleviates inevitable resonance

overlap in very large proteins. This can be accomplished without increasing the overall length of the pulse scheme, i.e., without sensitivity loss due to the spin–spin relaxation as no additional magnetization transfer steps are required. Thus, the coherence transfer throughput can be calculated using Eq. (6). However, as in the HNCO$_{i-1}$CA-TROSY scheme (vide supra), there is an inherent sensitivity loss by a factor of $\sqrt{2}$ in comparison to the three-dimensional HN(CO)CA-TROSY scheme owing to the additional frequency dimension. The HNCOCA-TROSY experiment performed well together with the HNCACO-TROSY scheme (vide infra) for the resonance-specific backbone assignment of 42 kDa maltose binding protein complexed with the β-cyclodextrin tumbling at 46 ns at 5°C on 600 MHz.[25] It also had a pivotal role in the assignment work of 81.4 kDa monomeric MSG although the 4D-HNCOCA-TROSY spectrum was recorded at 600 MHz due to significant drop of sensitivity at 800 MHz.[12]

4.1.5. *Sequential pathway revisited: HN(CO)CANH-TROSY*

As can be appreciated from Fig. 5, the time period during which the $^{13}C'$ spin remains in the transverse plane should be minimized. At the same time, intraresidual cross peaks should be able to be distinguished from the sequential correlations in the HNCA-TROSY experiment. Thus, pulse schemes providing solely sequential or intraresidual correlations in a complementary experiment as a substitute for the traditional HN(CO)CA-TROSY scheme are needed. There are several possibilities to reach this goal without sacrificing too much sensitivity due to the rapid transverse relaxation of carbonyl carbon. In the HN(CO)CANH-TROSY experiment[73] (Fig. 11), the $^{13}C'$ spin lingers in the transverse plane only half the time period in comparison to the HN(CO)CA-TROSY experiment while still offering exclusively sequential $^{1}H^{N}(i)$, $^{15}N(i)$, $^{13}C^{\alpha}(i-1)$ connectivities.

The flow of coherence can be described in the following way

$$^{1}H^{N}_{(i)} \xrightarrow{^{1}J_{NH}} {}^{15}N_{(i)} \xrightarrow{^{1}J_{NC'}} {}^{13}C'_{(i-1)} \xrightarrow{^{1}J_{C'C^{\alpha}}} {}^{13}C^{\alpha}_{(i-1)}(t_1)$$
$$\xrightarrow{^{1}J_{NC^{\alpha}};{}^{1}J_{NC'};{}^{2}J_{NC^{\alpha}}} {}^{15}N_{(i)}(CT - t_2) \xrightarrow{^{1}J_{NH}} {}^{1}H^{N}_{(i)}(t_3)$$

The first part, before the t_1 period, of the experiment is identical to the HN(CO)CA-TROSY scheme. This step chooses solely the sequential pathway in an HN(CO)CA-TROSY manner. The chemical shift of the $^{13}C^{\alpha}$ nucleus is recorded during the t_1 evolution period. The back-transfer route is, however, quite different. We transfer the desired coherence from $^{13}C^{\alpha}$ directly back to the ^{15}N nucleus and remove the second $^{13}C' \rightarrow {}^{13}C^{\alpha}$ INEPT step found in HN(CO)CA-TROSY and replace it with the HNCA like back-transfer step. The antiphase $^{2}J_{NC^{\alpha}}$ coupling then refocuses simultaneously with $^{1}J_{NC'}$ during the $^{13}C' \rightarrow {}^{15}N$ back-INEPT step. Thus, the HN(CO)CANH-TROSY

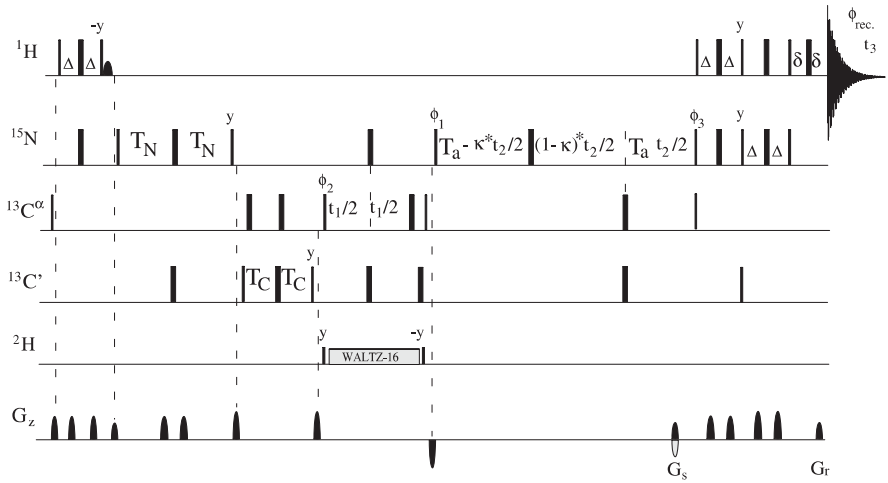

Fig. 11. HN(CO)CANH-TROSY experiment for establishing sequential $^{13}C^{\alpha}(i-1)$, $^{15}N(i)$, $^{1}H^{N}(i)$ connectivity in $^{13}C/^{15}N/^{2}H$ labelled proteins. Delay durations: $\Delta = 1/(4J_{HN})$; $2T_N = \sim 23$–33 ms, $2T_a = \sim 22$–28 ms, depending on rotational correlation time of the protein; $T_C = 1/(4J_{C'C^{\alpha}})$; δ = gradient + field recovery delay; $0 \leq \kappa \leq T_a/t_{2,max}$. Phase cycling: $\phi_1 = x$; $\phi_2 = x, -x$ + States-TPPI; $\phi_3 = x$; $\phi_{rec.} = x, -x$.

experiment utilizes so-called *out- and other way back* transfer scheme.[73] The coherence transfer efficiency for the α-helical and β-strand conformations can be calculated using Eq. (7).

$$\sin(2\pi {}^1J_{NC'}T_N)\sin(2\pi {}^1J_{C'C^{\alpha}}T_C)\sin(2\pi {}^1J_{NC'}T_a)\cos(2\pi {}^1J_{NC^{\alpha}}T_a)$$
$$\sin(2\pi {}^2J_{NC^{\alpha}}T_a)\exp(-2(T_N+T_a)/T_{2,N})\exp(-2T_C/T_{2,C'}). \quad (7)$$

The transfer efficiencies (Fig. 12) for the α-helical and β-strand substructures are 0.036 and 0.04, respectively. Therefore, calculations suggest that the HN(CO)CANH-TROSY experiment becomes superior to the HN(CO)CA-TROSY scheme, especially on β-sheet substructures of high molecular weight proteins at the highest magnetic field currently available.

Figure 13 shows expansion of the HN(CO)CANH (panel a) and HN(CO)CA (panel b) spectra, recorded from a 30.4 kDa (286 amino acid residues), uniformly ^{15}N, ^{13}C, and ^{2}H labelled, protein Cel6A from the thermophilic soil bacterium *Thermobifida fusca*[80] at 800 ^{1}H MHz at 4°C. Both spectra were recorded under identical conditions. As can be observed, several sequential cross peaks are missing in the HN(CO)CA-TROSY spectrum whereas they are clearly visible in the HN(CO)CANH-TROSY spectrum. On the contrary, some of the correlations are more intense in the HN(CO)CA-TROSY spectrum than in the HN(CO)CANH-TROSY spectrum.

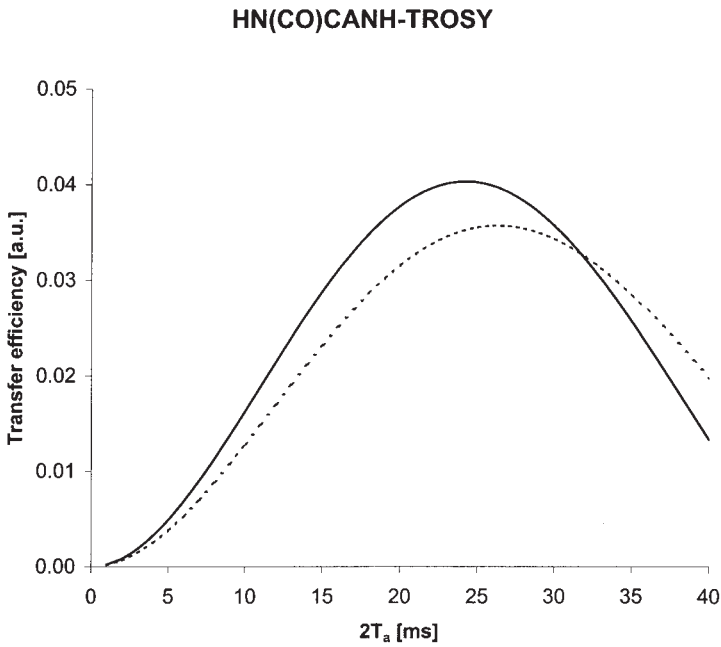

Fig. 12. Coherence transfer amplitudes for residues in α-helical and β-sheet substructures as a function of delay $2T_a$ for the HN(CO)CANH-TROSY experiment. The transfer functions according to Eq. (7) are plotted with the following parameters: $T_{2,^{15}\mathrm{N}\text{-TROSY}} = 50$ ms, $T_{2,C'} = 6$ ms, $2T_N = 25$ ms, $2T_C = 4.7$ ms, $^1J_{NC^\alpha} = 10.9$ Hz and $^2J_{NC^\alpha} = 8.3$ Hz (——), $^1J_{NC^\alpha} = 9.6$ Hz and $^2J_{NC^\alpha} = 6.4$ Hz (- - - -), $^1J_{NC'} = 15$ Hz, $^1J_{C'C^\alpha} = 53$ Hz.

Nevertheless, for the backbone assignment of a high molecular weight protein, several supporting triple-resonance experiments are usually needed. In that respect, these two experiments are mutually complementary to each other. On the other hand, when going into higher magnetic field or ever-larger proteins, a balance in overall sensitivity is shifted further towards the HN(CO)CANH-TROSY like experiments that reduce the time period that the $^{13}C'$ spin stays in the transverse plane to avoid sensitivity losses due to the rapid T_2 of the carbonyl carbon nucleus.

As in the case of the HN(CO)CA-TROSY scheme, the HN(CO)CANH-TROSY experiment can be readily expanded to a four-dimensional HN(CO)CANH-TROSY experiment without increasing the overall length of the pulse sequence. This can be accomplished by labelling the $^{13}C'(i)$ chemical shift during additional incremented time delay, implemented into the $^{13}C' \rightarrow {}^{13}C^\alpha$ INEPT delay. As a result, a well-dispersed $^{13}C^\alpha(i-1)$, $^{13}C'(i-1)$, $^{15}N(i)$, $^1H^N(i)$ correlation map is obtained with minimal resonance overlap *albeit* with the inherent sensitivity loss by a factor of $\sqrt{2}$.

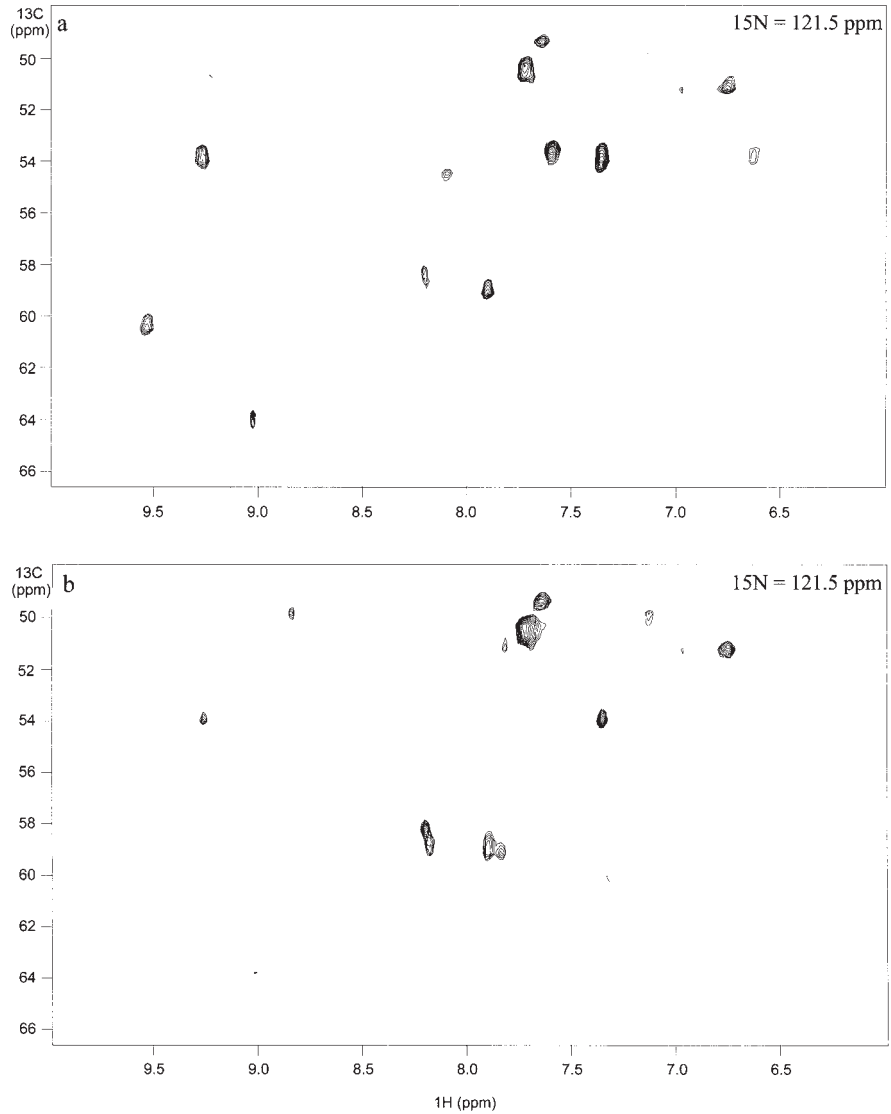

Fig. 13. $^{13}C^{\alpha}$–$^{1}H^{N}$ planes from the HN(CO)CANH-TROSY (a) and HN(CO)CA-TROSY (b) spectra. Spectra were recorded on uniformly ^{15}N, ^{13}C, ^{2}H enriched, 30.4 kDa protein Cel6A at 800 ^{1}H MHz at 277 K. The data were measured using identical parameters and conditions, using 8 transients per FID, 48, 32, 704 complex points corresponding acquisition times of 8, 12, and 64 ms in t_1, t_2, and t_3, respectively. A total acquisition time was 24 h per spectrum. The data were zero-filled to $128 \times 128 \times 2048$ points before Fourier transform and phase-shifted squared sine-bell window functions were applied in all three dimensions.

4.1.6. *Sequential HNCA*

Another alternative pulse scheme for generating only sequential $^{13}C^{\alpha}$ connectivities is dubbed as seqHNCA-TROSY[81] (Fig. 14).

The $^{1}H^{N}$ and ^{15}N steady-state polarizations are initially transferred to both intra- and interresidual $^{13}C^{\alpha}$ spins and simultaneously also to the sequential $^{13}C'$ nucleus. The sequential pathway is subsequently selected by refocusing one-bond coupling between the sequential $^{13}C^{\alpha}(i-1)$ and $^{13}C'(i-1)$ nuclei during the delay $2T_C$. The chemical shift of $^{13}C^{\alpha}$ spin is recorded during the t_1 period, which is implemented into the constant-time period $2T_C$. The undesired intraresidual pathway is converted into the double antiphase form with respect to the $^{13}C'(i-1)$ and $^{13}C'(i)$ spins. This magnetization becomes unobservable by applying composite pulse decoupling to the $^{13}C'$ region during the subsequent t_2 period. After labelling the $^{13}C^{\alpha}$ chemical shift, the coherence of interest is transferred back to the $^{1}H^{N}$ nucleus in the usual HNCA-TROSY manner.

The coherence flows through the experiment as follows:

$$^{1}H^{N}_{(i)} \xrightarrow{^{1}J_{NH}} {}^{15}N_{(i)} \xrightarrow{^{1}J_{NC^{\alpha}};{}^{1}J_{NC'};{}^{2}J_{NC^{\alpha}}} {}^{13}C^{\alpha}_{(i-1)}(CT - t_1) \xrightarrow{^{1}J_{C'C^{\alpha}}}$$
$$^{15}N_{(i)}(CT - t_2) \xrightarrow{^{1}J_{NC^{\alpha}};{}^{2}J_{NC^{\alpha}}} \xrightarrow{^{1}J_{NH}} {}^{1}H^{N}_{(i)}(t_3)$$

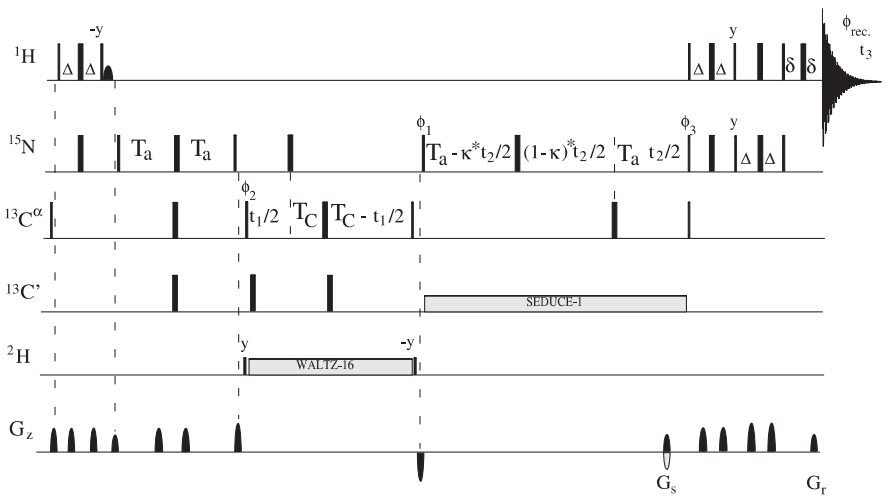

Fig. 14. SeqHNCA-TROSY experiment for establishing sequential $^{1}H^{N}(i)$, $^{15}N(i)$, $^{13}C^{\alpha}(i-1)$ correlations in $^{13}C/^{15}N/^{2}H$ enriched proteins. Durations of transfer delays: $\Delta = 1/(4J_{HN})$; $2T_a = \sim 20$–27 ms, depending on rotational correlation time of protein; $2T_C = 5$–7 ms; $\delta =$ gradient + field recovery delay; $0 \le \kappa \le T_a/t_{2,max}$. Phase cycling: $\phi_1 = y$; $\phi_2 = y, -y +$ States-TPPI; $\phi_3 = x$; $\phi_{rec.} = x, -x$. Semi-selective decoupling of $^{13}C'$ spins is attained using a SEDUCE-1 decoupling sequence.[95]

The sequential correlation can be obtained without converting the magnetization into the fast decaying transverse $^{13}C'$ coherence at any point of the pulse scheme. However, in order to select a sequential pathway, the magnetization has to be transformed into the $^{13}C^{\alpha}$ transverse magnetization for the $2T_C$ period. The transverse relaxation of $^{13}C^{\alpha}$ spin can be very effective on very large proteins despite deuteration (vide supra). Consequently, the sequential HNCA-TROSY experiment is susceptible to the rapid $^{13}C^{\alpha}$ transverse relaxation during the $2T_C$ period. In addition, the delay $2T_C$ is a compromise between the homonuclear $^{13}C^{\alpha}$–$^{13}C^{\beta}$ coupling and $^{13}C^{\alpha}$–$^{13}C'$ coupling modulations. The coherence transfer efficiencies for the residues in α-helix and β-strand are plotted in Fig. 15 according to Eq. (8)

$$\sin^2(2\pi\,{}^2J_{NC^{\alpha}}T_a)\cos^2(2\pi\,{}^1J_{NC^{\alpha}}T_a)\sin(2\pi\,{}^1J_{NC'}T_a)\cos(2\pi\,{}^1J_{C^{\alpha}C^{\beta}}T_C)$$
$$\sin(2\pi\,{}^1J_{C^{\alpha}C'}T_C)\exp(-2T_C/T_{2,C^{\alpha}})\exp(-4(T_a)/T_{2,N}), \quad (8)$$

using the value of 25 ms for the $^{13}C^{\alpha}$ transverse relaxation time ($T_{2,C^{\alpha}}$) in a high molecular weight protein. As can be seen from the plots in Fig. 15, the

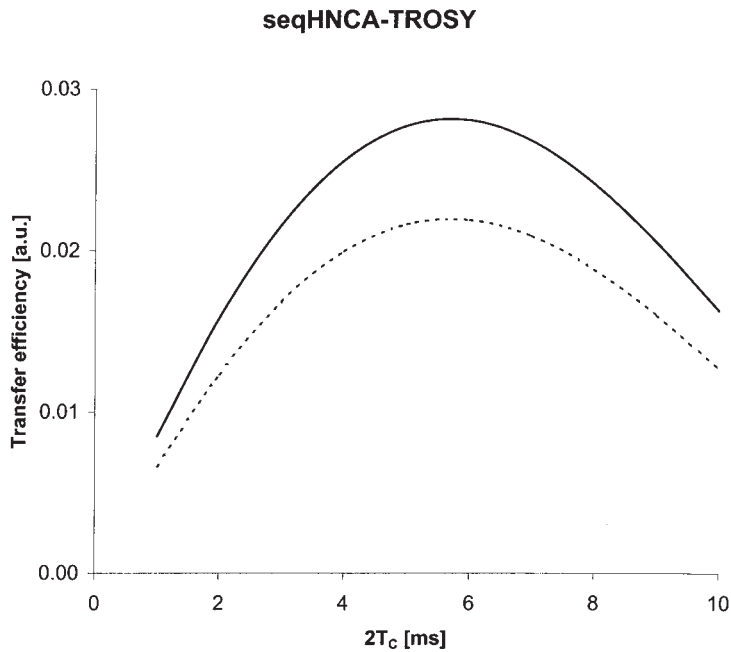

Fig. 15. Coherence transfer efficiencies as a function of delay $2T_C$ for the residues in α-helix and β-sheet in the sequential HNCA-TROSY scheme. Equation (8) is plotted using the following parameters: $T_{2,^{15}N\text{-TROSY}} = 50$ ms, $T_{2,C^{\alpha}} = 25$ ms, $2T_a = 25$ ms, ${}^1J_{NC^{\alpha}} = 10.9$ Hz and ${}^2J_{NC^{\alpha}} = 8.3$ Hz (——), ${}^1J_{NC^{\alpha}} = 9.6$ Hz and ${}^2J_{NC^{\alpha}} = 6.4$ Hz (- - - -), ${}^1J_{NC'} = 15$ Hz, ${}^1J_{C^{\alpha}C^{\beta}} = 35$ Hz, ${}^1J_{C'C^{\alpha}} = 53$ Hz.

performance of the sequential HNCA-TROSY experiment is dictated by the $^{13}C^{\alpha}$ transverse relaxation and $^{1}J_{C^{\alpha}C^{\beta}}$ modulation, which are effective during the delay $2T_C$. Calculations predict that overall performance is not as good as with the HN(CO)CA-TROSY or HN(CO)CANH-TROSY experiments.

4.1.7. *Route to the intraresidual correlation: iHNCA-TROSY*

So far we have concentrated on the set of TROSY experiments that provide solely sequential connectivities as a supplement to the sensitive HNCA-TROSY experiment. Thus, ambiguities in the assignment arising from overlapping cross peaks or equivocal difference in intensity of intra- and interresidual cross peaks can often be unravelled with concomitant use of assisting *sequential* experiment(s). It is of interest that we can also resolve these ambiguities with an alternative approach in which solely intraresidual connectivities are present in a complementary experiment.[82] In other words, we use the familiar HNCA-TROSY to record both intraresidual and sequential connectivities and employ an *intraresidual* HNCA-TROSY experiment (iHNCA-TROSY), yielding exclusively intraresidual cross peaks, for disentangling existing uncertainties in the assignment procedure.[82] This strategy is conceptually similar to the traditional use of the HNCA-TROSY/HN(CO)CA-TROSY experiment pair. However, solely *intraresidual* cross peaks are displayed in the complementary experiment instead of *sequential* correlations. Whether this approach is more efficient than the use of the HNCA-TROSY/HN(CO)CA-TROSY pair, depends mainly on the transverse relaxation time of the ^{15}N TROSY component. Thus, the main objective is to retrieve the intraresidual connectivities with better sensitivity than the corresponding sequential connectivities are obtained in the HN(CO)CA-TROSY experiment.[82] There are basically two different routes to obtain solely intraresidual connectivities. One can use either *out and back* style coherence transfer[82,83] or *out and other way back* scheme.[82,84] The *out and other way back* version of the *intraresidual* HNCA-TROSY experiment[82,84] is more efficient for the very large proteins at the highest field, and is presented in Fig. 16a.

The magnetization is first transferred from $^{1}H^{N}(i)$ to the directly bound $^{15}N(i)$ spin by the INEPT step and the ^{15}N Boltzmann magnetization is included in the usual way. The following delays $4T_a$ and $2T_N$, which are concatenated, are used for converting the ^{15}N transverse coherence into the triple antiphase form with respect to the $^{13}C^{\alpha}(i)$, $^{13}C^{\alpha}(i-1)$, and $^{13}C'(i-1)$ spins. To this end, $^{1}J_{NC^{\alpha}}$, $^{2}J_{NC^{\alpha}}$, and $^{1}J_{NC'}$ scalar couplings are utilized. It should be noted that the delay $4T_a$ is set to ~ 50 ms in order to create antiphase magnetization with respect to both $^{13}C^{\alpha}(i)$ and $^{13}C^{\alpha}(i-1)$ spins. This means that the ^{15}N spin remains in the transverse plane for a time period, that is approximately 2 times longer than in the conventional HNCA scheme during the first ^{15}N–^{13}C transfer step. For the intraresidual selection, the

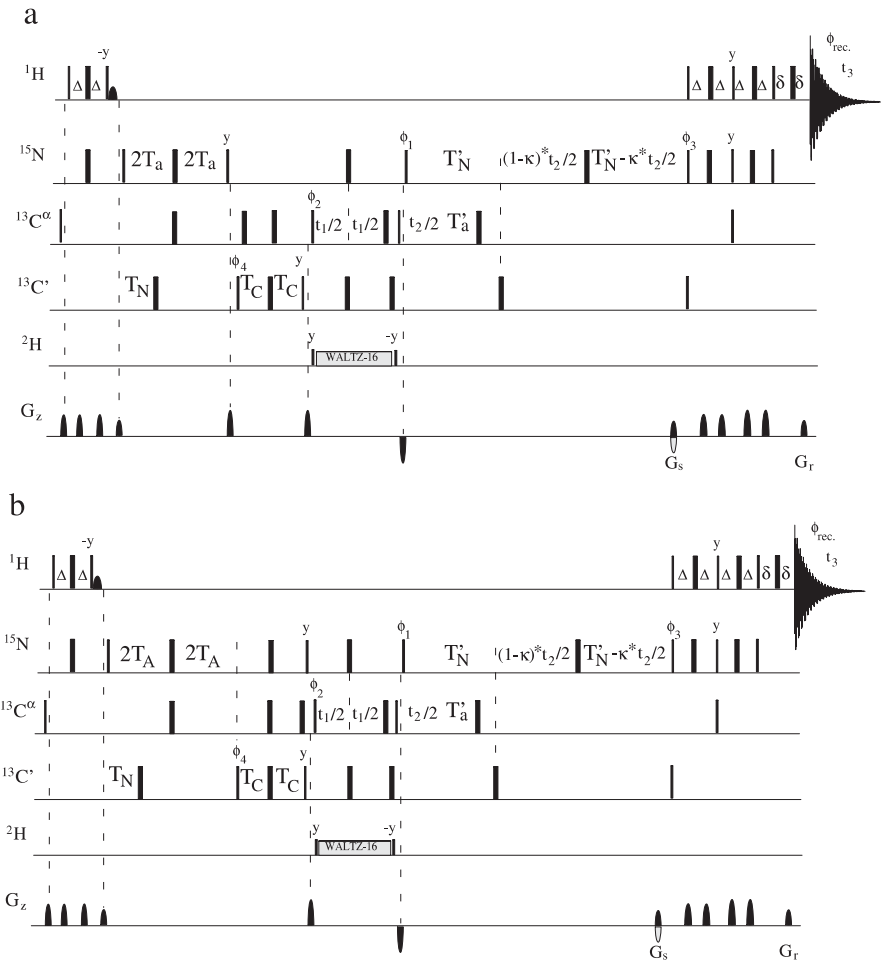

Fig. 16. The iHNCA-TROSY scheme (a) and a novel streamlined version of the iHNCA-TROSY experiment (b), for correlating solely $^{1}H^{N}(i)$, $^{15}N(i)$, $^{13}C^{\alpha}(i)$ shifts in $^{13}C/^{15}N/^{2}H$ labelled proteins. $\Delta = 1/(4J_{HN})$; $T_N = 1/(4J_{NC'})$; $1/(J_{NC'}) \geq T'_N \geq T'_a$; $2T_a \sim 25$ ms; $2T_A = 2T_a - T_C$; $T_C = 1/(4J_{C'C\alpha})$; δ = gradient + field recovery delay; $0 \leq \kappa \leq T'_N/t_{2,max}$. Phase cycling: $\phi_1 = x$; $\phi_2 = x$, $-x$ + States-TPPI; $\phi_3 = x$; $\phi_4 = 2(x)$, $2(-x)$; $\phi_{rec.} = x, 2(-x), x$.

$^{13}C' \rightarrow {}^{13}C^{\alpha}$ INEPT scheme is employed. During $^{13}C' \rightarrow {}^{13}C^{\alpha}$ INEPT, the antiphase $^{13}C'(i-1)$ coherence is refocused with respect to the *sequential* $^{13}C^{\alpha}(i-1)$ nucleus thanks to ~ 53 Hz $^{1}J_{C'C^{\alpha}}$ coupling. Instead, the coherence remains virtually intact with respect to the *intraresidual* $^{13}C^{\alpha}(i)$ spin since the small $^{2}J_{C'C^{\alpha}}$ coupling is not refocused during the short INEPT delay. The chemical shift of the intraresidual $^{13}C^{\alpha}(i)$ spin is then recorded during the indirect detection period. The magnetization is subsequently converted

directly back to the ^{15}N coherence in a way identical to the HN(CO)CANH-TROSY experiment (vide supra). Thus, the $^{13}C'$–$^{13}C^{\alpha}$ back transfer step is removed from the pulse scheme and the double antiphase coherence with respect to both $^{13}C'(i-1)$ and $^{13}C^{\alpha}(i)$ spins is refocused during the $^{13}C \rightarrow {}^{15}N$ back-INEPT. In the end, the desired coherence is converted back into the $^{1}H^{N}(i)$ coherence.

The magnetization floats through the iHNCA-TROSY experiment in the following way

$$^{1}H^{N}_{(i)} \xrightarrow{^{1}J_{NH}} {}^{15}N_{(i)} \xrightarrow{^{1}J_{NC^{\alpha}};{}^{1}J_{NC'};{}^{2}J_{NC^{\alpha}}} {}^{13}C'_{(i-1)} \xrightarrow{^{1}J_{C'C^{\alpha}}} {}^{13}C^{\alpha}_{(i)}(CT - t_1)$$
$$\xrightarrow{^{1}J_{NC^{\alpha}};{}^{1}J_{NC'};{}^{2}J_{NC^{\alpha}}} {}^{15}N_{(i)}(CT - t_2) \xrightarrow{^{1}J_{NH}} {}^{1}H^{N}_{(i)}(t_3)$$

The coherence transfer amplitude for the intraresidual pathway is described as in Eq. (9)

$$\begin{aligned}&\sin(2\pi\,{}^{1}J_{NC'}T_N)\sin(2\pi\,{}^{1}J_{NC'}T'_N)\sin(4\pi\,{}^{1}J_{NC^{\alpha}}T_a)\sin(4\pi\,{}^{2}J_{NC^{\alpha}}T_a)\\&\sin(2\pi\,{}^{1}J_{C'C^{\alpha}}T_C)\sin(2\pi\,{}^{1}J_{NC^{\alpha}}T'_a)\cos(2\pi\,{}^{2}J_{NC^{\alpha}}T'_a)\\&\exp(-2(T'_N+2T_a)/T_{2N})\exp(-2T_C/T_{2C'}).\end{aligned} \tag{9}$$

As can be seen from the plots in Fig. 17, the transfer efficiency is higher for residues in β-sheet than in α-helical substructures.

The coherence transfer efficiency computations suggest that whenever T_2 of the ^{15}N TROSY component is sufficiently long (> 50–60 ms), the coherence transfer efficiency is comparable or superior to the HN(CO)CA-TROSY, HN(CO)CANH-TROSY or sequential HNCA-TROSY experiments introduced above. Recently, Laue's group demonstrated efficiency of the iHNCA-TROSY on a ^{15}N, ^{13}C, ^{2}H (Ile, Leu, Val)-methyl-protonated H-Ras (1–171)-GDP protein at 4°C.[84] The iHNCA-TROSY experiment showed superior performance in comparison to the HN(CO)CA-TROSY and sequential HNCA-TROSY experiments on the protein with a correlation time of 28 ns at 800 ^{1}H MHz. The average signal-to-noise ratios (S/N) for the intraresidual HNCA-TROSY and HN(CO)CA-TROSY experiments were 41 and 28, respectively.[84] More importantly, the intensities of the weakest correlations (S/N < 15 in HN(CO)CA-TROSY) were significantly higher in the intraresidual HNCA-TROSY experiment. As expected, at lower magnetic field (600 ^{1}H MHz), the sensitivities of the intraresidual HNCA-TROSY and conventional HN(CO)CA-TROSY experiments were comparable, with an average S/N of approximately 33.[84] The sensitivity of the intraresidual HNCA-TROSY experiment is mainly dictated by the improved $J_{NC^{\alpha}}$ transfer versus the spin–spin relaxation rate of the ^{15}N TROSY component. This is because the ^{15}N spin is susceptible to the transverse relaxation for a longer time period than in the conventional HNCA-TROSY scheme, owing

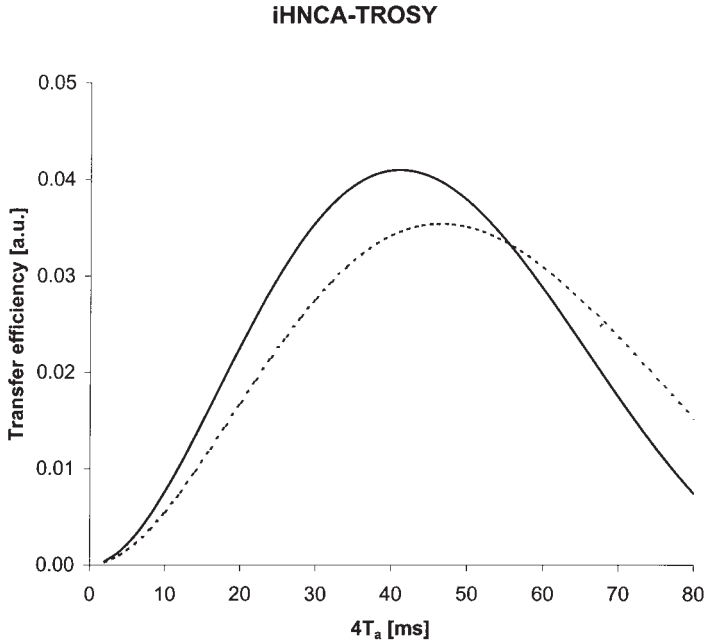

Fig. 17. Efficiencies of coherence transfer for the residues in α-helix and β-sheet, as a function of delay $4T_a$ in the iHNCA-TROSY experiment. Equation (9) is plotted with the following parameters: $T_{2,^{15}N} = 50$ ms, $T_{2,C'} = 6$ ms, $2T_N = 33$ ms, $2T'_N = 2T'_a = 29$ ms, $2T_C = 4.7$ ms, $^1J_{NC^\alpha} = 10.9$ Hz and $^2J_{NC^\alpha} = 8.3$ Hz (——), $^1J_{NC^\alpha} = 9.6$ Hz and $^2J_{NC^\alpha} = 6.4$ Hz (- - - -), $^1J_NC' = 15$ Hz, $^1J_{C'C^\alpha} = 53$ Hz.

to the extended dephasing delay needed to create triple antiphase coherence with respect to the $^{13}C^\alpha(i)$, $^{13}C^\alpha(i-1)$ and $^{13}C'(i-1)$ spins. On proteins where the ^{15}N TROSY relaxation is shorter than 50 ms, the improved J_{NC^α} transfer is not able to compensate for the relaxation losses during the ^{15}N–^{13}C dephasing delay. On a 30.4 kDa protein Cel6a at 4°C at 800 ^1H MHz, the sensitivity of the iHNCA-TROSY experiment was clearly inferior to the sensitivity of the HN(CO)CANH-TROSY or HN(CO)CA-TROSY experiments (Fig. 18a).

It should be noted that the selection of the intraresidual pathway is not perfectly exclusive. The suppression of sequential pathway depends on the range of $^1J_{NC^\alpha}$ and $^2J_{NC^\alpha}$ scalar couplings. The suppression is very good when these couplings sample in the range of 7–13 and 6–9 Hz, respectively. For this reason, the ^{15}N–$^{13}C^\alpha$ dephasing delay should be set to ~48–52 ms in order to maximize the amplitude for the intraresidual pathway and to minimize/suppress the sequential pathway. Under these circumstances, the intraresidual cross peak will be at least ~15 times more intense than the sequential correlation.[82,83] Although this holds true for the great majority of residues, in some cases where the $^1J_{NC^\alpha}$ is large and $^2J_{NC^\alpha}$ is very small,

the intensity of sequential correlation could compete with the weakest intraresidual correlations. It is also possible to annihilate the sequential pathway completely. To this end, two data sets are recorded. In one experiment, the last 90°($^{13}C^{\alpha}$) pulse after t_1 evolution period is applied whereas it is omitted in the second experiment while the receiver phase is inverted between two data sets. Unfortunately, this will reduce the sensitivity by a factor of $\sqrt{2}$.[82]

Figure 16b depicts a new variant of the iHNCA-TROSY experiment. In this pulse scheme, the magnetization is transferred to the intraresidual $^{13}C^{\alpha}$ spin in a manner related to the intraresidual HNCA scheme devised by Brutscher,[83] i.e., by converting ^{15}N single-quantum coherence into the ^{15}N–$^{13}C'$ multiple-quantum coherence during the transfer. However, unlike in the scheme described by Brutscher, we implement the RF pulses and the corresponding interpulse delays in such a way that modulation periods for the $^{1}J_{NC^{\alpha}}$, $^{2}J_{NC^{\alpha}}$, $^{1}J_{NC'}$, and $^{1}J_{C'C^{\alpha}}$ couplings can be arranged independently from each other (see caption of Fig. 16 for details). Thus, this novel implementation both concatenates ^{15}N–^{13}C and $^{13}C'$–$^{13}C^{\alpha}$ transfers steps and also allows unrestricted tuning of delays – that is, it merges advantages of the iHNCA-TROSY (Fig. 16a) and intra-HNCA-TROSY[83] experiments. Considering that the ^{15}N spin relaxation is slow whereas the T_2 of $^{13}C'$ is fast, the efficiency of the ^{15}N–$^{13}C^{\alpha}$ transfer can be kept high by setting the ^{15}N–$^{13}C^{\alpha}$ J transfer delay to approximately 50 ms while the $^{13}C'$–$^{13}C^{\alpha}$ transfer delay can be shortened significantly in order to avoid relaxation losses at the highest magnetic field. Figure 18b illustrates the $^{13}C^{\alpha}$–$^{1}H^{N}$ plane from the iHNCA-TROSY data set of Cel6A at ^{1}H 800 MHz at elevated temperature (40°C) recorded with the novel pulse scheme in Fig. 16b.

4.1.8. *A new breed: MP-HNCA-TROSY*

A completely different philosophy for accomplishing sequence-specific assignment lies behind a TROSY experiment dubbed as MP-CT-HNCA-TROSY[76] and its real time variant MP-HNCA-TROSY scheme.[73] The acronym MP stands for *multipurpose* because the experiment contains information on resonance type in various forms, which can be utilized for the sequential assignment in several ways. At first glance, the MP-HNCA-TROSY experiment (Fig. 19) has the appearance of the HNCA-TROSY experiment. However, there are two fundamental differences between the MP-HNCA-TROSY and HNCA-TROSY experiments. Firstly, the $^{13}C'$ decoupling is not applied during the t_1 evolution period in MP-HNCA-TROSY. Secondly, in the MP-HNCA-TROSY experiment, two data sets, referred here to as *in-phase* and *antiphase* spectra, are recorded. In order to briefly outline the key idea behind the MP-HNCA-TROSY experiment, let us first describe the course of the experiment. The familiar $^{1}H^{N}$–^{15}N INEPT step is used to transfer the magnetization from an amide proton to a neighbouring amide nitrogen, and ^{15}N steady-state magnetization is constructively

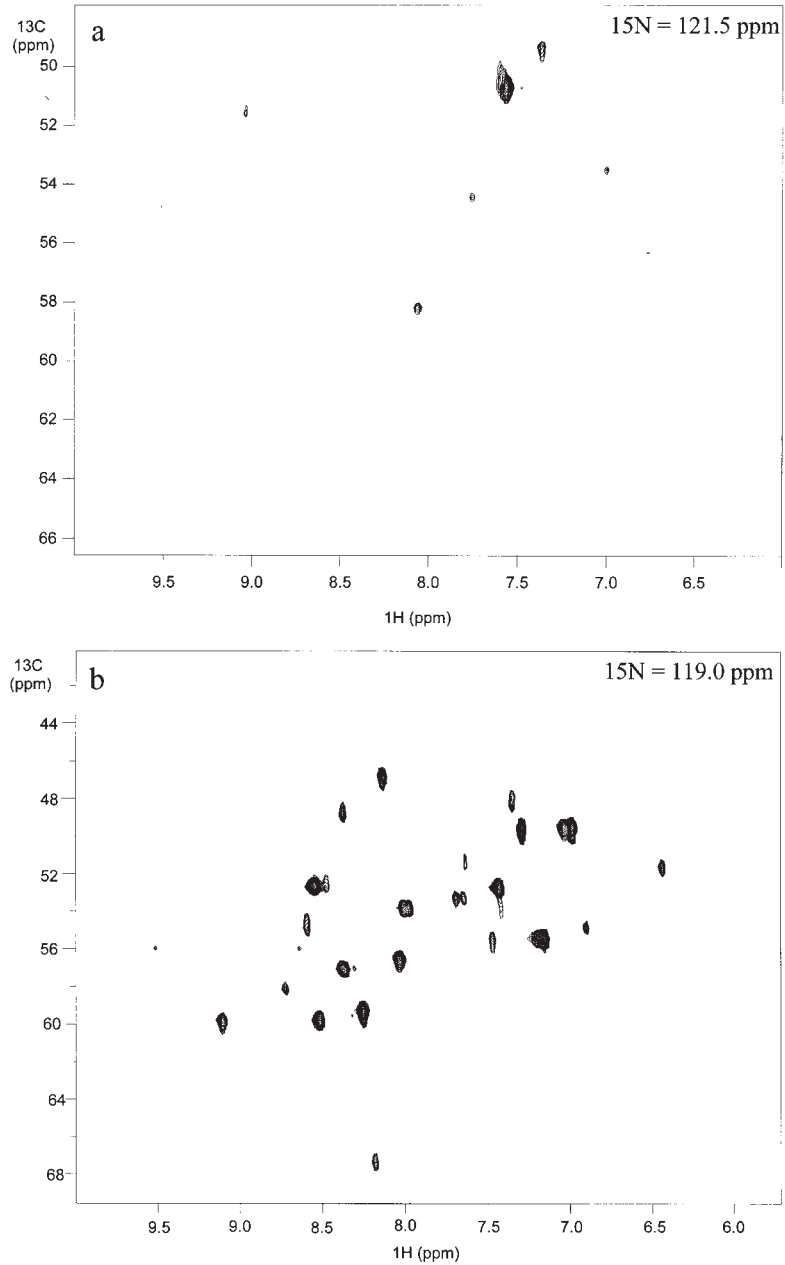

Fig. 18. Enlargement of the $^{13}C^{\alpha}$–$^{1}H^{N}$ plane in the intraresidual iHNCA-TROSY spectrum (a), recorded on uniformly ^{15}N, ^{13}C, ^{2}H enriched, 30.4 kDa Cel6a at 800 ^{1}H MHz at 277 K. The iHNCA-TROSY spectrum was measured and processed with identical parameters to the corresponding HN(CO)CA-TROSY and HN(CO)CANH spectra shown in Fig. 13 i.e., using 8 transients, 48, 32, 704 complex points F_1, F_2

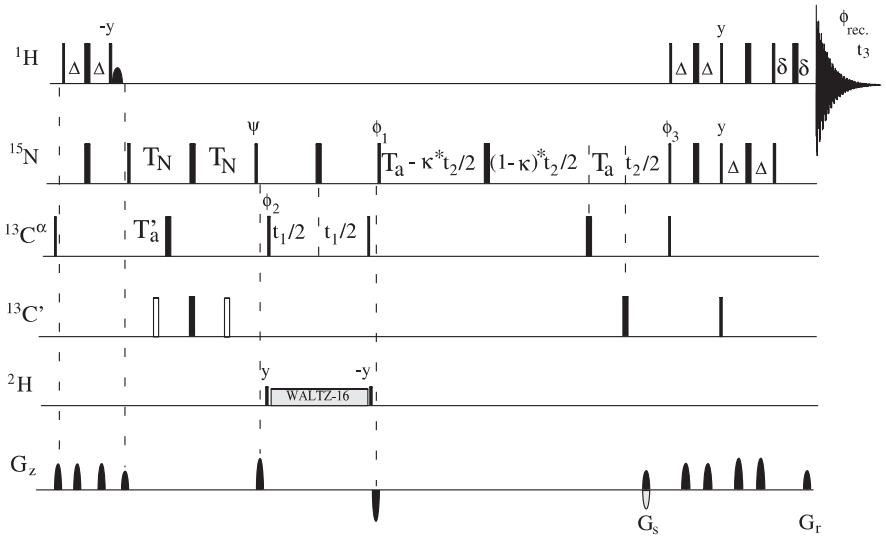

Fig. 19. Pulse scheme of the MP-HNCA-TROSY experiment. Delay durations: $\Delta = 1/(4J_{HN})$; $2T'_a = 27$ ms; $2T_a = 18$–27 ms; $2T_N = 1/(2J_{NC'})$; δ = gradient + field recovery delay; $0 \le \kappa \le T_a/t_{2,max}$. Phase cycling scheme for the in-phase spectrum is $\phi_1 = y$; $\phi_2 = x, -x$ + States-TPPI; $\phi_3 = x$; $\phi_{rec.} = x, -x$; $\psi = y$. For the antiphase spectrum, ψ is incremented by 90°. The intraresidual and sequential connectivities are distinguished from each other by recording the antiphase and in-phase data sets in an interleaved manner and subsequently adding and subtracting two data sets to yield two subspectra.

added to the magnetization originating on $^1H^N$ as in a typical TROSY experiment. Subsequently, the magnetization is transferred from the ^{15}N spin to the $^{13}C^\alpha$ spins of two consecutive residues as in the familiar HNCA-TROSY scheme. During t_1, the chemical shift of the $^{13}C^\alpha$ spin is labelled and the magnetization is transferred to the ^{15}N spin whose chemical shift is recorded during t_2. Ultimately the magnetization is transferred back to the amide proton. The function of 180°($^{13}C'$) pulses is to create *in-phase* or *antiphase* coherence with respect to the preceding $^{13}C'$ spin prior to the t_1 period. Thus, two experiments are recorded in an interleaved manner. In the first experiment, the $^{13}C^\alpha$ coherence is antiphase with respect to the $^{13}C'(i-1)$ spin prior

and F_3, respectively. (b) Representative $^{13}C^\alpha$–$^1H^N$ plane from the iHNCA-TROSY data set of the ~1 mM $^{15}N/^{13}C/^2H$ labeled Cel6a at 800 ^1H MHz recorded with the novel intraresidual iHNCA-TROSY scheme shown in Fig. 16b. The spectrum was measured at 313 K, using 4 transients per FID, 48, 32 and 704 complex points in ^{13}C, ^{15}N and ^1H dimensions, corresponding to acquisition times of 8, 12 and 64 ms in t_1, t_2, and t_3, respectively. The data were zero-filled to $128 \times 128 \times 2048$ matrix prior to Fourier transform and shifted sine-bell weighting functions were applied in both dimensions.

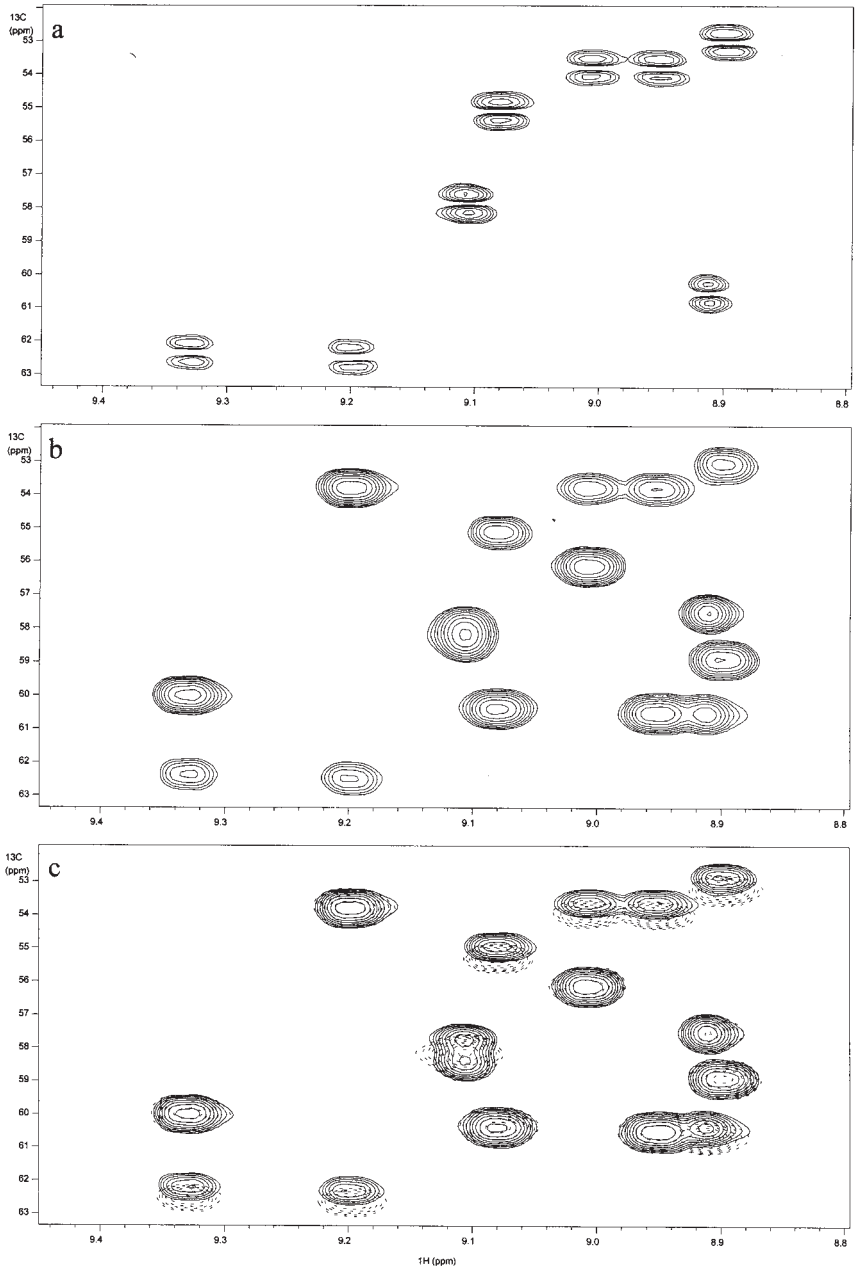

Fig. 20. Enlargement of the $^{13}C^{\alpha}$–$^{1}H^{N}$ region from the MP-HNCA-TROSY spectrum. The antiphase and in-phase data sets are shown in (a) and (b). In (c), two subspectra are overlaid (indicated as solid and dashed line contours) and the corresponding intra- and interresidual connectivities can be distinguished by the $\sim$53 Hz offset of α and β states of the sequential cross peaks, whereas the intraresidual cross peaks

to the t_1 period. In the second experiment, the in-phase $^{13}C^{\alpha}$ coherence is created prior to the t_1 period. Because there is no $^{13}C'$ decoupling during the t_1 period, the $^{13}C^{\alpha}$ resonances split into doublets, which are separated by ~ 53 Hz one-bond coupling between the $^{13}C^{\alpha}$ and $^{13}C'$ spins. By inspecting the first data set i.e., the *antiphase* spectrum, we can perceive that the sequential $^{13}C^{\alpha}(i-1)$ cross peaks are doublets with antiphase character with respect to $^{1}J_{C'C^{\alpha}}$. The intraresidual $^{13}C^{\alpha}$ cross peaks are also antiphase with respect to the sequential $^{13}C'(i-1)$ spin, however, this splitting is due to the small $^{2}J_{C'C^{\alpha}}$. Consequently, the intraresidual cross peaks are almost entirely suppressed from the *antiphase* spectrum as shown for the 8.6 kDa human ubiquitin protein, labelled uniformly with $^{15}N/^{13}C$ isotopes, in Fig. 20a. The second data set, i.e., the *in-phase* experiment exhibits both the sequential and intraresidual correlations in-phase with respect to the $^{13}C'(i-1)$ spin and it superficially has the appearance of the HNCA-TROSY spectrum if the acquisition time in t_1 is not long enough to resolve the $^{1}J_{C'C^{\alpha}}$ splitting (Fig. 20b). This *in-phase* data set can then be used to distinguish between intra- and interresidual connectivities based on differential cross peak intensities in an identical way to the HNCA-TROSY experiment. On the contrary, the *antiphase* spectrum reveals solely sequential correlations and it can be used to verify the origin of cross peaks.

Now, let us consider the outcome when the antiphase and in-phase data sets are added to or subtracted from each other. This is schematically illustrated in Fig. 21. By adding (or subtracting) the antiphase (Fig. 21a) and in-phase (Fig. 21b) data sets, we obtain two subspectra in which the sequential cross peaks appear as singlets with ~ 53 Hz offset between the corresponding cross peaks in two subspectra (Fig. 21c–d). This is because the spin-state-selective filtering selects either the α or β spin-state of the $^{1}J_{C'C^{\alpha}}$ doublet for the one subspectrum. The intraresidual correlations appear as doublets, provided that acquisition time in t_1 is sufficiently long to resolve the $^{1}J_{C'C^{\alpha}}$ splitting, because the spin-state-selection is made between the α and β states of the $^{2}J_{C'C^{\alpha}}$ splitting. As the $^{2}J_{C'C^{\alpha}}$ splitting is at least one order of magnitude smaller than $^{1}J_{C'C^{\alpha}}$, the offset between the emerging intraresidual cross peaks between two subspectra seem virtually invariable. Thus, it is possible to differentiate between the sequential and intraresidual connectivities based on cross peak multiplicity (long $t_{1,\max}$) or frequency offset between the

---

are virtually superimposed in two subspectra. The MP-HNCA-TROSY spectrum was recorded on ~ 1.9 mM, uniformly ^{15}N, ^{13}C labelled human ubiquitin at 600 ^{1}H MHz at 303 K. Spectrum was recorded as a two-dimensional $^{13}C^{\alpha}$–$^{1}H^{N}$ correlation experiment using 192 transients. Number of complex points in F_1 and F_3 dimensions were 56 and 896, respectively, corresponding to acquisition times of 14 ms and 128 ms. The data were zero-filled to 1024×2048 points before Fourier transform and shifted squared sine-bell window functions were applied in both dimensions.

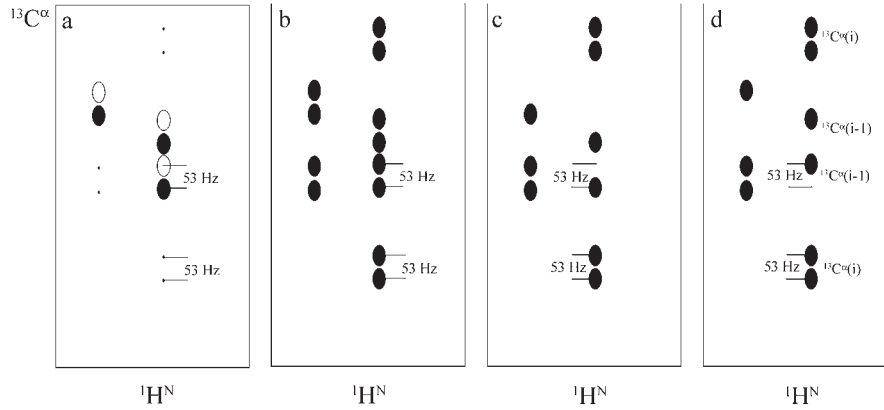

Fig. 21. Schematic illustration of MP-HNCA-TROSY antiphase (a) and in-phase (b) spectra with long acquisition time in t_1. The corresponding subspectra are shown after addition of the antiphase and in-phase data sets (c) and after subtraction of the antiphase and in-phase data sets (d). Due to very small $^{2}J_{C'C^{\alpha}}$, the intraresidual cross peaks are almost entirely cancelled out from the antiphase spectrum (a). In the subspectra, the intraresidual cross peaks are shown as doublets, separated by $\sim$53 Hz splitting in F_1-dimension, whereas sequential cross peaks are shown as singlets, and they exhibit $\sim$53 Hz offset for the upfield and downfield components between the subspectra.

corresponding correlations in two subspectra (short $t_{1,\max}$). The example of the latter approach is demonstrated in Fig. 20c, where two subspectra, retrieved from the antiphase (Fig. 20a) and in-phase (Fig. 20b) data sets by addition and subtraction, are shown overlaid. As can be seen, the intraresidual cross peaks are virtually superimposed in two subspectra, whereas the sequential connectivities show clear frequency offset ($\sim$53 Hz) between two subspectra.

Although, the MP-HNCA-TROSY experiment alone can yield sequential assignment, it can be also used concomitantly with the HNCA-TROSY experiment. This strategy is explained later, but let us first focus on the coherence transfer efficiency of the MP-HNCA-TROSY experiment. The transfer functions for the antiphase experiment (the efficiency for the in-phase experiment is practically the same) are calculated according to Eqs. (10) and (11) for the intraresidual

$$\cos(2\pi\,{}^{2}J_{NC^{\alpha}}T_a)\sin(2\pi\,{}^{1}J_{NC^{\alpha}}T_a)\cos(2\pi\,{}^{2}J_{NC^{\alpha}}T'_a)\sin(2\pi\,{}^{1}J_{NC^{\alpha}}T'_a)$$
$$\sin(2\pi\,{}^{1}J_{NC'}T_N)\cos(2\pi\,{}^{1}J_{C^{\alpha}C^{\beta}}T_C)\exp(-2T_C/T_{2,C^{\alpha}})\exp(-2T_N/T_{2,N})$$
$$\exp(-2T_a/T_{2,N}) \qquad (10)$$

and sequential cross peaks

$$\sin(2\pi\,{}^{2}J_{\mathrm{NC}^{\alpha}}\mathrm{T_a})\cos(2\pi\,{}^{1}J_{\mathrm{NC}^{\alpha}}\mathrm{T_a})\sin(2\pi\,{}^{2}J_{\mathrm{NC}^{\alpha}}\mathrm{T'_a})\cos(2\pi\,{}^{1}J_{\mathrm{NC}^{\alpha}}\mathrm{T'_a})$$
$$\sin(2\pi\,{}^{1}J_{\mathrm{NC}'}\mathrm{T_N})\cos(2\pi\,{}^{1}J_{\mathrm{C}^{\alpha}\mathrm{C}^{\beta}}\mathrm{T_C})\exp(-2\mathrm{T_C}/\mathrm{T_{2,C^{\alpha}}})\exp(-2\mathrm{T_N}/\mathrm{T_{2,N}})$$
$$\exp(-2\mathrm{T_a}/\mathrm{T_{2,N}}) \qquad (11)$$

respectively (Fig. 22). As the first $^{15}\mathrm{N}$–$^{13}\mathrm{C}$ dephasing delay consists of the $^{1}J_{\mathrm{NC}'}$ pin-state-selective filter[85] in which the $^{15}\mathrm{N} \rightarrow {}^{13}\mathrm{C}^{\alpha}$ INEPT is implemented into, the two concatenated delays $2\mathrm{T_N}$ and $2\mathrm{T'_a}$ are set to 33 and 27 ms. It should be realized that the sensitivity of the in- or antiphase spectrum is inherently $\sqrt{2}$ times lower than for the HNCA-TROSY spectrum because the experimental time is divided between the in- and antiphase data sets. In other words, only half the number of transients can be used per unit time for the MP-HNCA-TROSY experiment. Typically the HNCA-TROSY and any complementary experiment yielding solely sequential or intraresidual connectivities are run in pairs in order to distinguish explicitly between intra- and interresidual correlations. However, the MP-HNCA-TROSY experiment contains the same information itself, and consequently the experimental time used for the MP-HNCA-TROSY experiment is equal to the HNCA/HN(CO)CA-TROSY pair, compensating for the factor of $\sqrt{2}$ sensitivity loss.

The sensitivity of both antiphase and in-phase data sets of the MP-HNCA-TROSY experiment will be reduced by a factor of 2 if the acquisition time in the $^{13}\mathrm{C}^{\alpha}$-dimension is long enough to resolve $^{1}J_{\mathrm{C'C}^{\alpha}}$ splitting ($t_{1,\max} > 12$ ms). In that case the sensitivity of the *sequential* cross peak in two subspectra is higher, by a factor of $\sqrt{2}$, than in the in-phase and antiphase spectra. On the contrary, the sensitivity of the *intraresidual* cross peak is reduced by a factor of $\sqrt{2}$.[73] Additional loss in sensitivity arises from the $^{13}\mathrm{C}^{\alpha}$–$^{13}\mathrm{C}^{\beta}$ coupling modulation if the $t_{1,\max}$ is long enough (> 15 ms) as in the case of the traditional HNCA-TROSY experiment. If the transverse relaxation time of $^{13}\mathrm{C}^{\alpha}$ spin is sufficient, it may be advantageous to implement the t_1 evolution period in a constant-time manner, i.e., use the MP-CT-HNCA-TROSY experiment,[76] which removes the homonuclear one-bond $^{13}\mathrm{C}^{\alpha}$–$^{13}\mathrm{C}^{\beta}$ coupling evolution during t_1. In the real-time implementation, a semi-selective $^{13}\mathrm{C}^{\beta}$–decoupling can also be employed during t_1. However, due to overlapping $^{13}\mathrm{C}^{\alpha}$ and $^{13}\mathrm{C}^{\beta}$ spectral regions in serines, and partly with threonines and leucines, these amino acid residues will show reduced sensitivity. Although the resolution in $^{13}\mathrm{C}^{\alpha}$-dimension is improved together with the longer acquisition time, the signal dispersion will become worse owing to the doublet nature of intraresidual cross peaks in the subspectra.

If $t_{1,\max}$ is kept rather short (i.e., < 10–12 ms), *both* the intra- and interresidual correlations exhibit ca. $\sqrt{2}$ times higher intensity in the in-phase spectrum than in the subspectra because the $^{1}J_{\mathrm{C'C}^{\alpha}}$ coupling is not resolved.

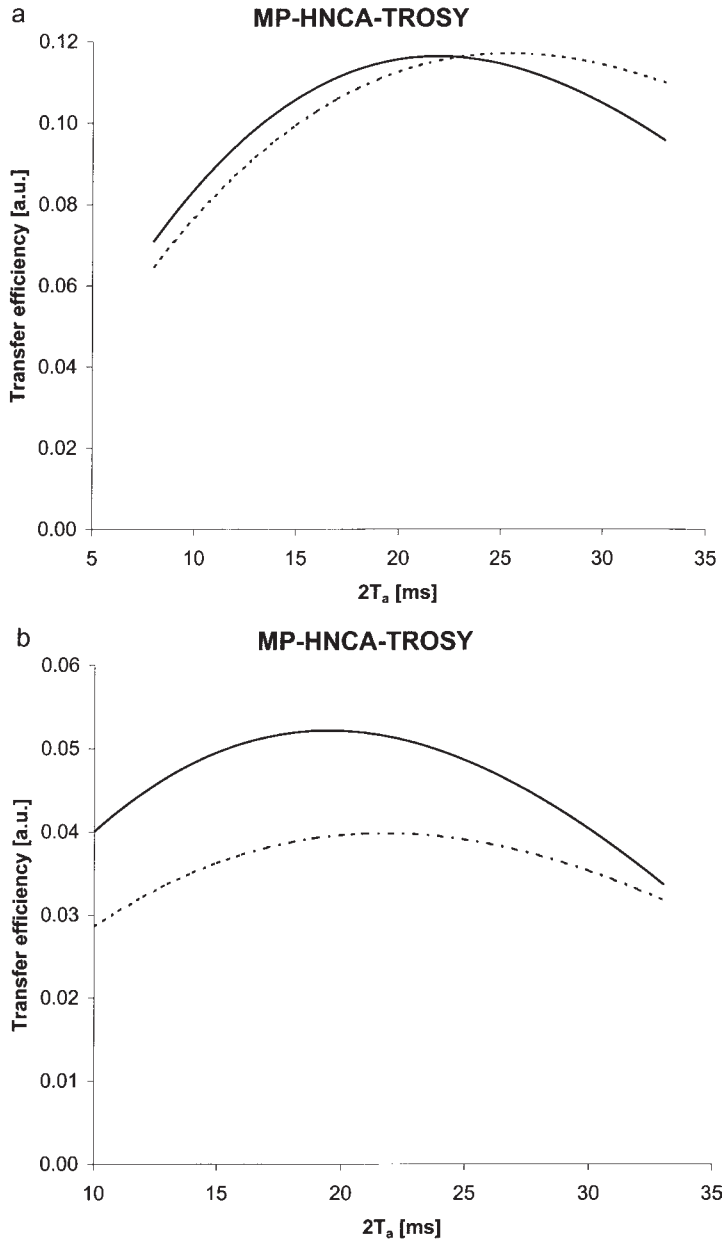

Fig. 22. Efficiency of coherence transfer for the intraresidual (a) and sequential (b) cross peaks in the antiphase experiment (the first increment, optimised for sequential transfer) as a function of the delay $2T_a$ in the MP-HNCA experiment. Transfer functions, according to Eqs. (10) and (11) are plotted using the following parameters: $T_{2,^{15}\text{N-TROSY}} = 50$ ms, $2T_N = 33$ ms, $2T'_a = 27$ ms $^1J_{NC'} = 15$ Hz, $^1J_{NC^\alpha} = 10.9$ Hz and $^2J_{NC^\alpha} = 8.3$ Hz (——), $^1J_{NC^\alpha} = 9.6$ Hz and $^2J_{NC^\alpha} = 6.4$ Hz (- - - -).

From these viewpoints, it is advantageous to use the in-phase spectrum for assigning the resonances in the usual HNCA manner in the first place, thanks to its higher intensity when short $t_{1,\max}$ is used. The subspectra can then be used to distinguish between the intra- and interresidual correlations in an ambiguous case.[73,76]

As mentioned above, the MP-HNCA-TROSY scheme can be used concomitantly with the conventional HNCA-TROSY experiment. This strategy relies on the following principles. The conventional HNCA-TROSY experiment is optimized for the sequential connectivities, i.e., ^{15}N–^{13}C delays are shortened in order to maximize sequential transfer (see Fig. 6). The MP-HNCA-TROSY experiment is then optimized for the intraresidual correlations. The subspectra of the MP-HNCA-TROSY experiment can then be used to unravel any ambiguities involving the sequential and intraresidual cross peaks. Hence, the intraresidual cross peaks can easily be recognized, as they do not show ~ 53 Hz offset between the two MP-HNCA-TROSY subspectra (vide supra). As noted earlier, the sensitivity loss by a factor of $\sqrt{2}$ results in the MP-HNCA-TROSY experiment since both the in-phase and antiphase data sets have to be recorded in the same experimental time as the HNCA-TROSY spectrum, i.e., only half the number of transients can be used in comparison to HNCA-TROSY. Additional sensitivity loss by a factor of $\sqrt{2}$ originates on subspectral editing (vide supra). Although sensitivities of the MP-HNCA-TROSY subspectra are inherently two times lower than the HNCA-TROSY spectrum, the *intraresidual* cross peaks in the MP-HNCA-TROSY subspectra display equal or better sensitivity than the sequential correlations in the HNCA-TROSY spectrum. In this respect, the concomitant usage of MP-HNCA-TROSY and conventional HNCA-TROSY experiments can offer an interesting approach to assign high molecular weight proteins.

4.2. Sequential assignment based on carbonyl carbon shifts

4.2.1. *HNCO-TROSY*

So far we have been emphasizing TROSY experiments in which the $^{13}C^{\alpha}$ spins are used for establishing resonance assignment in the sequential manner. We have seen that performance of the HNCA-TROSY prevails at the highest magnetic field available today and holds the promise also for the future. What about the experiments relying on $^{13}C'$ chemical shifts? The well-known and most sensitive triple-resonance experiment, HNCO-TROSY[24,46] is depicted in Fig. 4. In this scheme, the $^{1}H^{N}$ and ^{15}N steady-state magnetizations are exclusively transferred to the $^{13}C'$ spin of the preceding residue using $^{15}N \rightarrow {}^{13}C'$ INEPT. The chemical shift labelling of $^{13}C'$ spins takes place during the t_1 period and the desired coherence is converted back to the

^{15}N single quantum coherence. The chemical shift of ^{15}N is recorded in a (semi-)constant-time manner during t_2 and ultimately the ^{15}N–^{1}H^{N} PEP-TROSY element selects the most slowly relaxing ^{15}N–^{1}H^{N} multiplet component prior the acquisition. The coherence flow can thus be described as

$$^{1}H^{N}_{(i)} \xrightarrow{^{1}J_{NH}} {}^{15}N_{(i)} \xrightarrow{^{1}J_{NC'}} {}^{13}C'_{(i-1)}(t_1)$$
$$\xrightarrow{^{1}J_{NC'}} {}^{15}N_{(i)}(CT - t_2) \xrightarrow{^{1}J_{NH}} {}^{1}H^{N}_{(i)}(t_3)$$

The transfer amplitude for the sequential ^{13}C′, ^{15}N, ^{1}H^{N} correlation can be calculated using Eq. (12)

$$\sin^2(2\pi\,{}^{1}J_{NC'}T_N)\exp(-4T_N/T_{2,N}) \tag{12}$$

As can be seen by inspecting Figure 23, the coherence transfer efficiency is overwhelmingly good thanks to the very efficient $^{15}\text{N} \rightarrow {}^{13}\text{C}'$ INEPT step employed for transferring magnetization exclusively from ^{15}N to the sequential ^{13}C′ nucleus. In addition, the possibility of an accidental resonance

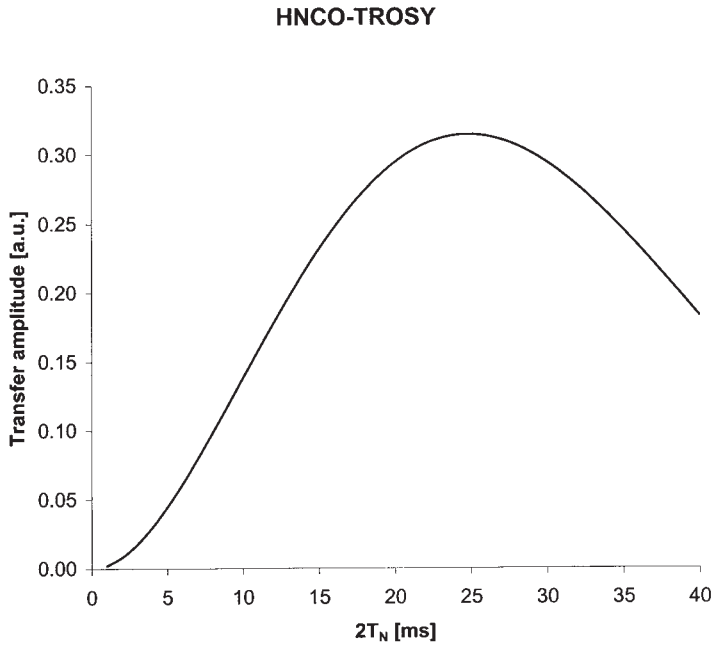

Fig. 23. Coherence transfer efficiency as a function of delay $2T_N$ for the HNCO-TROSY scheme. Following parameters were used [Eq. (12)]: $T_{2,^{15}N} = 50$ ms, $^{1}J_{NC'} = 15$ Hz.

overlap is minimized due to the emergence of a single cross peak per residue. However, in order to establish sequential connectivities, additional experiment(s) is needed to provide the intraresidual $^{13}C'$ connectivities. To this end, the HN(CA)CO-TROSY experiment shown in Fig. 24a can be employed.

4.2.2. *HN(CA)CO-TROSY*

The coherence transfer route is basically identical to the HNCA-TROSY scheme (vide supra) except that additional transfer step from $^{13}C^{\alpha}$ to $^{13}C'$ is needed. First, as in the HNCA-TROSY scheme, the initial $^{1}H^{N}$ magnetization is transferred to the intraresidual as well as to the sequential $^{13}C^{\alpha}$ spin. In order to transfer magnetization further to the intraresidual and sequential $^{13}C'$ nuclei, either the $^{13}C^{\alpha}$–$^{13}C'$ INEPT or HMQC transfer can be utilized.[10,45,72] In very large, perdeuterated proteins, the most efficient transfer utilizes the $^{13}C^{\alpha} \rightarrow {}^{13}C'$ INEPT in which the 180°($^{13}C^{\alpha}$) pulse in the middle of the delay $2T_C$ is replaced by the selective $^{13}C^{\alpha}$ refocusing pulse.[25,66] Subsequently, the chemical shift of $^{13}C'$ nucleus is recorded during t_1 and the magnetization is transferred back to the amide proton in an identical but reverse coherence transfer pathway. Thus, the coherence flows through the following pathway

$$^{1}H^{N}_{(i)} \xrightarrow{^{1}J_{NH}} {}^{15}N_{(i)} \xrightarrow{^{1}J_{NC^{\alpha}};{}^{2}J_{NC^{\alpha}}} {}^{13}C^{\alpha}_{(i/i-1)} \xrightarrow{^{1}J_{C'C^{\alpha}}} {}^{13}C'_{(i/i-1)}(t_1)$$
$$\xrightarrow{^{1}J_{C'C^{\alpha}}} {}^{13}C^{\alpha}_{(i/i-1)} \xrightarrow{^{1}J_{NC^{\alpha}};{}^{2}J_{NC^{\alpha}}} {}^{15}N_{(i)}(CT - t_2) \xrightarrow{^{1}J_{NH}} {}^{1}H^{N}_{(i)}(t_3)$$

and the corresponding transfer amplitudes for the intra- and interresidual pathways are given by Eq. (13)

$$\sin^2(2\pi\,{}^{1}J_{NC^{\alpha}}T_a)\cos^2(2\pi\,{}^{2}J_{NC^{\alpha}}T_a)\sin^2(2\pi\,{}^{1}J_{C'C^{\alpha}}T_C)$$
$$\exp(-4T_a/T_{2,N})\exp(-4T_C/T_{2,C^{\alpha}}), \tag{13}$$

and Eq. (14)

$$\cos^2(2\pi\,{}^{1}J_{NC^{\alpha}}T_a)\sin^2(2\pi\,{}^{2}J_{NC^{\alpha}}T_a)\sin^2(2\pi\,{}^{1}J_{C'C^{\alpha}}T_C)$$
$$\exp(-4T_a/T_{2,N})\exp(-4T_C/T_{2,C^{\alpha}}). \tag{14}$$

As can be appreciated from the curve in Fig. 25, the amplitudes vary more for the sequential cross peaks than for the intraresidual pathway, depending on the secondary structure. This is because we have intentionally optimized the ^{15}N–$^{13}C^{\alpha}$ transfer step for the intraresidual correlations. Although the sequential connectivities also appear in the HN(CA)CO-TROSY

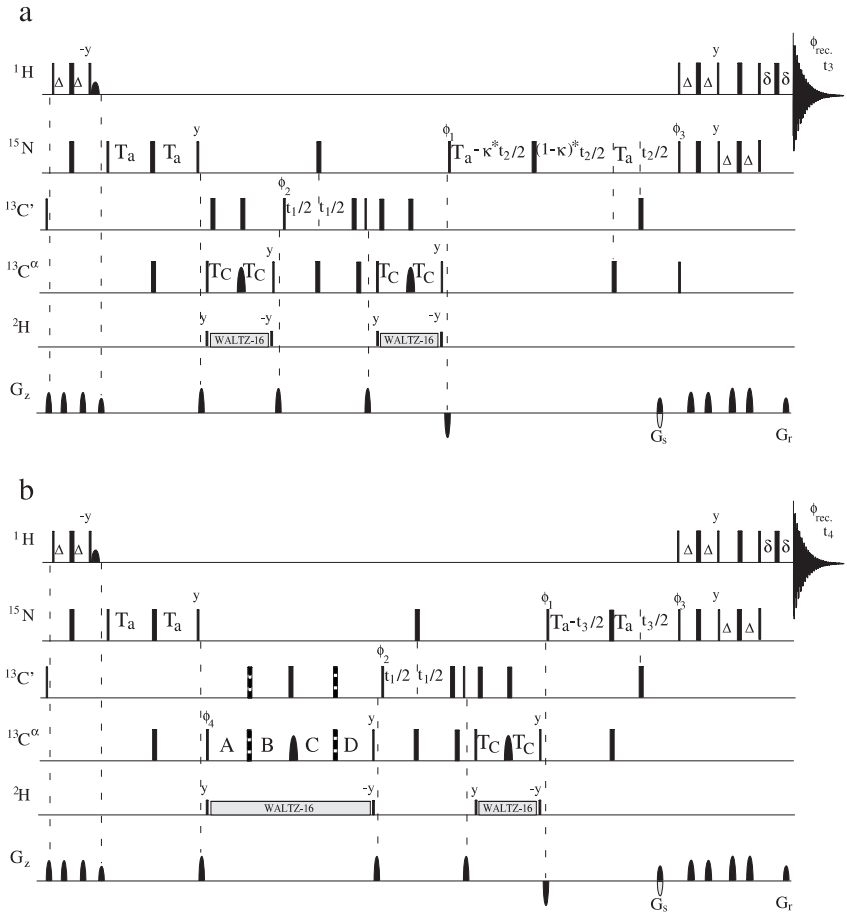

Fig. 24. The HN(CA)CO-TROSY (a) and four-dimensional HNCACO-TROSY (b) experiments for establishing $^{13}C'(i/i-1)$, $^{15}N(i)$, $^{1}H^{N}(i)$ and $^{13}C'(i/i-1)$, $^{13}C^{\alpha}(i/i-1)$, $^{15}N(i)$, $^{1}H^{N}(i)$ correlations, respectively, in $^{13}C/^{15}N/^{2}H$ labelled proteins. $\Delta = 1/(4J_{HN})$; $2T_a = \sim 25$ ms; $2T_C = 1/(2J_{C'C^{\alpha}})$; $A = C = (2T_C - t_1)/4$; $B = D = (2T_C + t_1)/4$; δ = gradient + field recovery delay; $0 \leq \kappa \leq T_a/t_{2,max}$. The band-selective RE-BURP refocusing pulse[96] applied in the middle of $^{13}C^{\alpha}$-$^{13}C'$ transfer delay is denoted by a half-ellipsoid. The simultaneous $^{13}C^{\alpha}$ and $^{13}C'$ pulses (indicated as shaded pulses in (b)) are applied as single composite $90°_x 180°_y 90°_x$ pulses, centred at 55 ppm, with a field strength of 20.8 kHz $\times$ y/600, where y is the spectrometers ^{1}H frequency in MHz.[25] Phase cycling for the HN(CA)CO-TROSY: $\phi_1 = y$; $\phi_2 = x, -x$ + States-TPPI; $\phi_3 = x$; $\phi_{rec.} = x, -x$. Phase cycling for the HNCACO-TROSY: $\phi_1 = y$; $\phi_2 = x, -x$ + States-TPPI; $\phi_3 = x$; $\phi_4 = 2(x), 2(-x)$ + States-TPPI; $\phi_{rec.} = x, 2(-x), x$.

spectrum, they can be collected from the HNCO-TROSY spectrum with enormously higher intensity, making these correlations redundant. Thus, in the assignment strategy based on $^{13}C'$ shifts on perdeuterated proteins, it is the *intraresidual* pathway that constitutes the bottleneck of the assignment process.

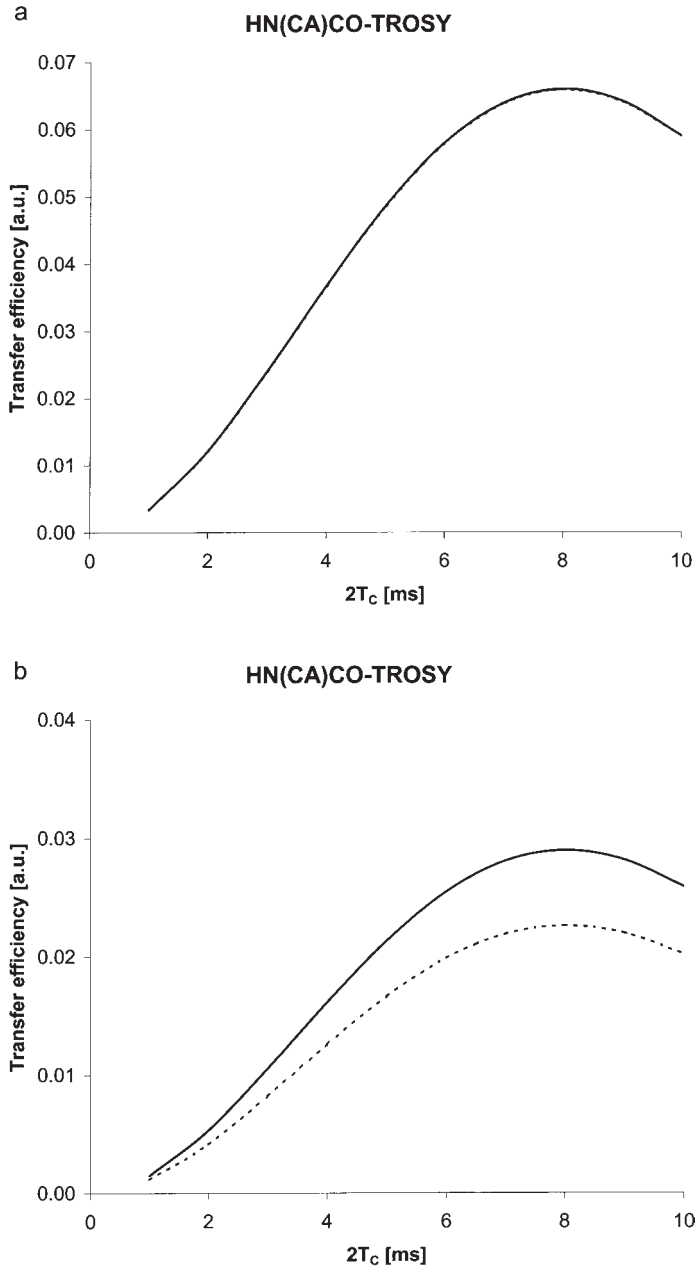

Fig. 25. The transfer efficiency for the intraresidual (a) and sequential (b) pathway as a function of $^{13}C^{\alpha}$–$^{13}C'$ transfer delay $2T_C$ in the HN(CA)CO-TROSY scheme. Equations (13)–(14) are plotted with the following parameters: $T_{2,^{15}N} = 50$ ms, $T_{2,C^{\alpha}} = 25$ ms, $2T_a = 25$ ms, $^1J_{NC^{\alpha}} = 10.9$ Hz and $^2J_{NC^{\alpha}} = 8.3$ Hz (——), $^1J_{NC^{\alpha}} = 9.6$ Hz and $^2J_{NC^{\alpha}} = 6.4$ Hz (- - - -), $^1J_{C'C^{\alpha}} = 53$ Hz.

The sensitivity of the experiment is governed by two factors, the rapid transverse relaxation of the $^{13}C^{\alpha}$ spin, and the homonuclear $^{1}J_{C^{\alpha}C^{\beta}}$ modulation during the $^{13}C^{\alpha}$–$^{13}C'$ transfer steps. The latter issue can be taken out of the equation thanks to the selective $^{13}C^{\alpha}$ refocusing pulse. Unfortunately, the $^{13}C^{\beta}$ spins of serine, and partly threonine and leucine residues resonate on frequencies, that partly overlap with the $^{13}C^{\alpha}$ chemical shift range. Consequently, the selective $^{13}C^{\alpha}$ pulse fully or partly inverts $^{13}C^{\beta}$ resonances of these residues and the $^{1}J_{C^{\alpha}C^{\beta}}$ modulation cannot be fully refocused. Thus, these residues display reduced sensitivity. On the other hand, the $^{13}C^{\alpha}$ nuclei of glycines resonate on the far edge of the refocusing bandwidth and can also show reduced intensity due to incomplete refocusing by the selective pulse.[66] Consequently, additional experiments are needed to gather supporting data for the HN(CA)CO-TROSY. The sensitivity of the residues with overlapping $^{13}C^{\alpha}/^{13}C^{\beta}$ shifts can be somewhat improved by inserting additional delay ($1/2(J_{C^{\alpha}C'})$ between two consecutive 90°($^{13}C^{\alpha}$) and 90°($^{13}C'$) pulses prior to t_1.[12]

In contrast to the $^{13}C^{\alpha}$ shifts, the $^{13}C'$ resonance frequencies are not indicative of residue type, which makes the assignment more demanding in comparison to the $^{13}C^{\alpha}$, ^{15}N, $^{1}H^{N}$ correlation map. Nevertheless, the HN(CA)CO-TROSY scheme equipped with the selective $^{13}C^{\alpha}$ refocusing pulses during the $^{13}C^{\alpha}$–$^{13}C'$ transfer steps is able to provide $^{13}C'$ (i), $^{15}N(i)$, $^{1}H^{N}(i)$ connectivities with good sensitivity, excluding serines, threonines, leucines, and glycines (and probably valines and prolines). Thus, the use of HNCO-TROSY/HN(CA)CO-TROSY experiment pair can be very useful in assigning high molecular weight proteins.

4.2.3. *Four-dimensional extension; HNCACO-TROSY*

The three-dimensional HN(CA)CO-TROSY scheme can be converted into the four-dimensional HNCACO-TROSY experiment without prolonging the pulse scheme. The HNCACO-TROSY pulse sequence[25] developed by Yang and Kay is depicted in Fig. 24b. In addition to the HN(CA)CO-TROSY experiment, the $^{13}C^{\alpha}$ chemical shift labelling takes place during the t_2 period, and is implemented into the $^{13}C^{\alpha}$–$^{13}C'$ INEPT step. From the relaxation point of view, the sensitivity of the HNCACO-TROSY is then identical to its three-dimensional counterpart. However, the inherent sensitivity loss by a factor of $\sqrt{2}$ occurs owing to the additional frequency discrimination needed in the $^{13}C^{\alpha}$-dimension. As in the case of HN(CA)CO-TROSY experiment, the selective refocusing pulse applied during $^{13}C^{\alpha}$–$^{13}C'$ INEPT partly inverts Ser, Thr, and Leu residues, and only partly refocuses Gly (and possibly Val and Pro) residues.[25]

The set of four-dimensional ($HNCO_{i-1}CA$, HNCOCA and HNCACO) TROSY experiments has been successfully applied in the assignment of several large proteins.[12,25,26] These three experiments are able to resolve

most of the ambiguities arising during the assignment process. For instance, if there are several degenerated $^{1}H^{N}$, ^{15}N spin pairs, the $HNCO_{i-1}CA$-TROSY spectrum can be employed for directly connecting the $^{13}C^{\alpha}$ and $^{13}C'$ frequencies to these amide frequencies in ambiguous HNCACO-TROSY and HNCOCA-TROSY spectra.[12] On the other hand, degeneracies of $^{13}C'/^{13}C^{\alpha}$ pairs of chemical shifts cannot be disentangled using these experiments alone.[12]

5. CONCLUDING REMARKS

The sequence-specific assignment of the protein main-chain is the first step in the determination of a protein's three-dimensional structure. The sequence-specific assignment is also imperative for detailed studies of protein dynamics or interaction with other molecules. The design of pulse schemes for the purposes of sequential assignment is basically an optimization problem to maximize sensitivity, resonance dispersion, and resolution. These are constrained by the relaxation, signal dispersion as well as by isotopic labelling. Consequently, there is no concise all-purpose set of experiments. In this chapter we have outlined several TROSY based triple-resonance experiments devised for the backbone assignment of high molecular weight proteins. There are two experiments which are clearly superior to others in terms of sensitivity on very large proteins at the highest magnetic field, HNCO-TROSY and HNCA-TROSY. Only the latter can potentially be used for the sequential assignment without complementary experiments, but it is not very likely that complete sequence-specific backbone assignment could be established using the HNCA-TROSY experiment alone. In practice, a number of complementary experiments are required. Several supplementary experiments are available, but their overall performance hinges heavily on the protein's rotational correlation time, the strength of the polarizing magnetic field and level of deuteration, which all affect to the transverse relaxation rates of different nuclei in the protein main-chain. In addition, beside the transverse relaxation, also the resonance overlap becomes a more serious problem on large monomeric proteins constituting hundreds of amino acids. These kinds of systems clearly benefit from the pulse schemes that give rise to a minimal number of cross peaks per residue in order to prevent coincidental signal overlap. On the contrary, for segmentally labelled[86–88] high molecular weight proteins, oligomers or protein complexes, the resonance overlap is not necessarily the primary issue and these systems profit most from the highest coherence transfer efficiency. For these reasons, we have only been able to provide the reader with basic guidelines for the selection of optimal TROSY experiments for the particular case. However, the evolution goes on.

ACKNOWLEDGEMENTS

I am indebted to Dr. Outi Salminen for preparing Cel6A sample and to Dr. Arto Annila for his comments and suggestions concerning the manuscript. This work was supported by the Academy of Finland.

REFERENCES

1. K. Wüthrich, *NMR of Proteins and Nucleic Acids*, John Wiley and Sons, New York, 1986, 1–292.
2. G. T. Montelione, D. Zheng, Y. Huang, C. Gunsalus and T. Szyperski, *Nat. Struct. Biol.*, 2000, **7**, 982.
3. G. Wider and K. Wüthrich, *Curr. Opin. Struct. Biol.*, 1999, **9**, 594.
4. A. Yee, X. Chang, A. Pineda-Lucena, B. Wu, A. Semesi, B. Le, T. Ramelot, G. M. Lee, S. Bhattacharyya, P. Gutierrez, A. Denisov, C.-H. Lee, J. R. Kozlov, G. Cort, J. Liao, G. Finak, L. Chen, D. Wishart, W. Lee, L. P. McIntosh, K. Gehring, M. A. Kennedy, A. M. Edwards and C. H. Arrowsmith, *Proc. Natl. Acad. Sci. USA*, 2002, **99**, 1825.
5. K. Wüthrich, *Nat. Struct. Biol.*, 1998, **5**, 492.
6. A. Ferentz and G. Wagner, *Q. Rev. Biophys.*, 2000, **33**, 29.
7. M. A. Kennedy, G. T. Montelione, C. H. Arrowsmith and J. L. Markley, *J. Struct. Funct. Genom.*, 2002, **2**, 155.
8. J. H. Prestegard, H. Valafar, J. Glushka and F. Tian, *Biochemistry*, 2001, **40**, 8677.
9. A. Bax and S. Grzesiek, *Acc. Chem. Res.*, 1993, **26**, 131.
10. M. Sattler, J. Schleucher and C. Griesinger, *Prog. Nuc. Magn. Reson. Spectr.*, 1999, **34**, 93.
11. K. Pervushin, *Q. Rev. Biophys.*, 2000, **33**, 161.
12. V. Tugarinov, D. R. Muhandiram, A. Ayed and L. E. Kay, *J. Am. Chem. Soc.*, 2003, **124**, 10025.
13. M. Salzmann, K. Pervushin, G. Wider, H. Senn and K. Wüthrich, *J. Am. Chem. Soc.*, 2000, **122**, 7543.
14. A. Arora and L. K. Tamm, *Curr. Opin. Struct. Biol.*, 2001, **11**, 540.
15. C. Fernandez, K. Adeishvili and K. Wüthrich, *Proc. Natl. Acad. Sci. U.S.A.*, 2001, **98**, 2358.
16. M. Schubert, M. Kolbe, B. Kessler, D. Oesterhelt and P. Schmieder, *ChemBioChem*, 2002, **10**, 1019.
17. C. Fernandez, C. Hilty, S. Bonjour, K. Adeishvili, K. Pervushin and K. Wüthrich, *FEBS Lett.*, 2001, **504**, 173.
18. A. Arora, F. Abildgaard, J. H. Bushweller and L. K. Tamm, *Nat. Struct. Biol.*, 2001, **8**, 334.
19. P. M. Hwang, W.-Y. Choy, E. I. Lo, L. Chen, J. D. Forman-Kay, C. R. H. Raetz, G. G. Prive, R. E. Bishop and L. E. Kay, *Proc. Natl. Acad. Sci. U.S.A.*, 2002, **99**, 13560.
20. J. Cavanagh, W. J. Fairbrother, A. G. Palmer III and N. J. Skelton, *Protein NMR Spectroscopy*, Academic Press, San Diego, 1996, 243–299.
21. K. V. Pervushin, R. Riek, G. Wider and K. Wüthrich, *Proc. Natl. Acad. Sci. U.S.A.*, 1997, **94**, 12366.
22. P. Andersson, A. Annila and G. Otting, *J. Magn. Reson.*, 1998, **133**, 364.
23. G. Kontaxis, G. M. Clore and A. Bax, *J. Magn. Reson.*, 2000, **143**, 184.
24. M. Salzmann, K. Pervushin, G. Wider, H. Senn and K. Wüthrich, *Proc. Natl. Acad. Sci. U.S.A.*, 1998, **95**, 13585.
25. D. Yang and L. E. Kay, *J. Am. Chem. Soc.*, 1999, **121**, 2571.
26. F. A. Mulder, A. Ayed, D. Yang, C. H. Arrowsmith and L. E. Kay, *J. Biomol. NMR*, 2000, **18**, 173.

27. G. A. Morris and R. Freeman, *J. Am. Chem. Soc*., 1979, **101**, 760.
28. R. Riek, G. Wider, K. Pervushin and K. Wüthrich, *Proc. Natl. Acad. Sci. U.S.A*., 1999, **96**, 4918.
29. R. Riek, J. Fiaux, E. B. Bertelsen, A. L. Horwich and K. Wüthrich, *J. Am. Chem. Soc*., 2002, **124**, 12144.
30. J. Fiaux, E. B. Bertelsen, A. L. Horwich and K. Wüthrich, *Nature*, 2002, **418**, 207.
31. J. Chung and G. Kroon, *J. Magn. Reson*., 2003, **163**, 360.
32. L. E. Kay, M. Ikura, R. Tschudin and A. Bax, *J. Magn. Reson*., 1990, **89**, 496.
33. M. Ikura, L. E. Kay and A. Bax, *Biochemistry*, 1990, **29**, 4659.
34. S. Grzesiek and A. Bax, *J. Magn. Reson*., 1992, **96**, 432.
35. J. Weigelt, *J. Am. Chem. Soc*., 1998, **120**, 10778.
36. M. Salzmann, G. Wider, K. Pervushin and K. Wüthrich, *J. Biomol. NMR*, 1999, **15**, 181.
37. F. Delaglio, D. A. Torchia and A. Bax, *J. Biomol. NMR*, 1991, **1**, 439.
38. J. Wirmer and H. Schwalbe, *J. Biomol. NMR*, 2002, **23**, 47.
39. J. Cavanagh, A. G. Palmer III, P. E. Wright and M. Rance, *J. Magn. Reson*., 1991, **91**, 429.
40. L. E. Kay, P. Keifer and T. Saarinen, *J. Am. Chem. Soc*., 1992, **114**, 10663.
41. J. Schleucher, M. Sattler and C. Griesinger, *Angew. Chem. Int. Ed. Engl*., 1993, **32**, 1489.
42. K. V. Pervushin, G. Wider and K. Wüthrich, *J. Biomol. NMR*, 1998, **12**, 345.
43. C. Kojima and M. Kainosho, *J. Magn. Reson*., 2000, **143**, 417.
44. T. Schulte-Herbrüggen and O. W. Sorensen, *J. Magn. Reson*., 2000, **144**, 123.
45. J. P. Loria, M. Rance and A. G. Palmer III, *J. Magn. Reson*., 1999, **141**, 180.
46. D. Yang and L. E. Kay, *J. Biomol. NMR*, 1999, **13**, 3.
47. P. Permi, T. Sorsa, I. Kilpeläinen and A. Annila, *J. Magn. Reson*., 1999, **141**, 44.
48. D. Yang and L. E. Kay, *J. Biomol. NMR*, 1999, **14**, 273.
49. M. Rance, P. Loria and A. G. Palmer III, *J. Magn. Reson*., 1999, **136**, 92.
50. M. Czisch and R. Boelens, *J. Magn. Reson*., 1998, **134**, 158.
51. G. Zhu, X. M. Kong and K. H. Sze, *J. Biomol. NMR*, 1999, **13**, 77.
52. K. H. Gardner and L. E. Kay, *Annu. Rev. Biophys. Biomol. Struct*., 1998, **27**, 357.
53. H. L. Crespi, R. M. Rosenberg and J. J. Katz, *Science*, 1968, **161**, 795.
54. J. L. Markley, I. Putter and O. Jardetzky, *Science*, 1968, **161**, 1249.
55. D. M. LeMaster and F. M. Richards, *Biochemistry*, 1988, **27**, 142–150.
56. S. Grzesiek, J. Anglister, H. Ren and A. Bax, *J. Am. Chem. Soc*., 1993, **115**, 4369.
57. D. S. Garrett, Y.-J Seok, D.-I. Liao, A. Peterkofsky, A. M. Gronenborn and G. M. Clore, *Biochemistry*, 1997, **36**, 2517.
58. H. Matsuo, H. Li, A. M. McGuire, C. M. Fletcher, A. C. Gingras, N. Sonenberg and G. Wagner, *Nat. Struct. Biol*., 1997, **4**, 717.
59. M. Caffrey, M. Cai, J. Kaufman, S. J. Stahl, P. T. Wingfield, D. G. Covell, A. M. Gronenborn and G. M. Clore, *EMBO J*., 1998, **17**, 4572.
60. A. Jasanoff, G. Wagner and D. C. Wiley, *EMBO J*., 1998, **17**, 6812.
61. D. S. Garrett, Y.-J. Seok, A. Peterkofsky, A. M. Gronenborn and G. M. Clore, *Nat. Struct. Biol*., 1999, **36**, 2517.
62. T. Yamazaki, W. Lee, M. Revington, D. L. Mattiello, F. W. Dahlquist, C. H. Arrowsmith and L. E. Kay, *J. Am. Chem. Soc*., 1994, **116**, 6464.
63. T. Yamazaki, W. Lee, C. H. Arrowsmith, D. R. Muhandiram and L. E. Kay, *J. Am. Chem. Soc*., 1994, **116**, 11655.
64. X. Shan, K. H. Gardner, D. R. Muhandiram, N. S. Rao, C. H. Arrowsmith and L. E. Kay, *J. Am. Chem. Soc*., 1996, **118**, 6570.
65. H. Matsuo, H. Li and G. Wagner, *J. Magn. Reson*., 1996, **110B**, 112.
66. H. Matsuo, E. Kupce, H. Li and G. Wagner, *J. Magn. Reson*., 1996, **111B**, 194.
67. T. Ikegami, S. Sato, M. Wälchli, Y. Kyogoku and M. Shirakawa, *J. Magn. Reson*., 1997, **134**, 214.
68. H. Matsuo, E. Kupce, H. Li and G. Wagner, *J. Magn. Reson*., 1996, **111B**, 194.

69. M. A. Markus, K. T. Dayie, P. Matsudaira and G. Wagner, *J. Magn. Reson.*, 1994, **105B**, 192.
70. R. A. Venters, B. T. Farmer, C. A. Fuerke and L. D. Spicer, *J. Mol. Biol.*, 1996, **264**, 1101.
71. T. Yamazaki, H. Tochio, J. Furui, S. Aimoto and Y. Kyogoku, *J. Am. Chem. Soc.*, 1997, **120**, 872.
72. M. Salzmann, G. Wider, K. Pervushin, H. Senn and K. Wüthrich, *J. Am. Chem. Soc.*, 1999, **121**, 844.
73. P. Permi and A. Annila, *J. Magn. Reson.*, 2002, **155**, 123.
74. M. Fischer, A. Majumdar and E. R. P. Zuiderweg, *Prog. Nucl. Magn. Reson. Spectr.*, 1998, **33**, 207.
75. G. Cornilescu and A. Bax, *J. Am. Chem. Soc.*, 2000, **122**, 10143.
76. P. Permi and A. Annila, *J. Biomol. NMR*, 2001, **20**, 127.
77. B. T. Farmer II and R. A. Venters, *Biological Magnetic Resonance*, Vol. 16, Kluwer Academic Press/Plenum Press, Dordrecht/New York, 1998, 75.
78. J.-S. Hu and A. Bax, *J. Am. Chem. Soc.*, 1997, **119**, 6360.
79. R. Konrat, D. Yang and L. E. Kay, *J. Biomol. NMR*, 1999, **15**, 309.
80. M. Spezio, D. B. Wilson and P. A. Karplus, *Biochemistry*, 1993, **32**, 9906.
81. A. Meissner and O. W. Sørensen, *J. Magn. Reson.*, 2001, **150**, 100.
82. P. Permi, *J. Biomol. NMR*, 2002, **23**, 201.
83. B. Brutscher, *J. Magn. Reson.*, 2002, **156**, 155.
84. D. Nietlispach, Y. Ito and E. D. Laue, *J. Am. Chem. Soc.*, 2002, **124**, 11199.
85. P. Permi, S. Heikkinen, I. Kilpeläinen and A. Annila, *J. Magn. Reson.*, 1999, **140**, 32.
86. T. Yamazaki, T. Otomo, N. Oda, Y. Kyogoku, K. Uegaki, N. Ito, Y. Ishino and H. Nakamura, *J. Am. Chem. Soc.*, 1998, **120**, 5591.
87. T. Otomo, K. Teruya, K. Uegaki, T. Yamazaki and Y. Kyogoku, *J. Biomol. NMR*, 1999, **14**, 105.
88. M. Piotto, V. Sauder and V. J. Sklenar, *J. Biomol. NMR*, 1992, **2**, 661.
89. S. Grzesiek and A. Bax, *J. Am. Chem. Soc.*, 1993, **115**, 12593.
90. D. Marion, M. Ikura, R. Tschudin and A. Bax, *J. Magn. Reson.*, 1989, **85**, 393.
91. T. M. Logan, E. T. Olejniczak, R. X. Xu and S. W. Fesik, *J. Biomol. NMR*, 1993, **3**, 225.
92. S. Grzesiek and A. Bax, *J. Biomol. NMR*, 1993, **3**, 185.
93. P. Permi and A. Annila, *J. Biomol. NMR*, 2000, **16**, 221.
94. A. J. Shaka, P. B. Parker and R. Freeman, *J. Magn. Reson.*, 1985, **64**, 547.
95. M. McCoy and L. Mueller, *J. Am. Chem. Soc.*, 1992, **114**, 2108.
96. H. Geen and R. Freeman, *J. Magn. Reson.*, 1991, **93**, 93.

Local Dynamics in Polypeptides Studied by Solid State ^{2}H NMR: Side Chain Dynamics of Poly(γ-benzyl L-glutamate) and Racemic Poly(γ-benzyl glutamate)

T. HIRAOKI*, S. KITAZAWA AND A. TSUTSUMI*

Department of Applied Physics, Graduate School of Engineering, Hokkaido University, N13W8, Kita-Ku, Sapporo 060-8628, Japan
**Tel.: +81-11-706-6640; Fax: +81-11-716-6175;*
E-mail: hiraoki@eng.hokudai.ac.jp [TH]

Side chain dynamics of right-handed α-helical poly(γ-benzyl L-glutamate) (PBLG) was investigated by solid state ^{2}H NMR. Two main motional modes composed of the large amplitude motions and the rapid and small-amplitude librations along the side chain were extracted from line shapes and T_1 data above the glass-like transition temperature. The motional correlation times and amplitudes of the former are widely distributed, showing the heterogeneity of the side chain region. The phenyl rings at the end of the side chain also undergoes π-flipping. This reorientation is slightly restricted in the racemic complex of PBLG and its enantiomer, left-handed α-helical poly(γ-benzyl D-glutamate), in which phenyl rings from each L and D

ANNUAL REPORTS ON NMR SPECTROSCOPY
VOLUME 53 ISSN 0066 4103
DOI 10.1016/S0066-4103(04)53006-5

polymer are considered to stack regularly. The large amplitude motions and the librations are rather restricted in the stack state. About 75% of the side chain participate in the stacking. It is noted that the stacking structure is very flexible on the NMR time scale and the model for the 'static' stacks of the phenyl rings should be modified.

1. INTRODUCTION

Solid state ^{2}H NMR parameters are almost exclusively governed by the quadrupole interaction with the electric field gradient (EFG) tensor at the deuteron site.[1–8] The EFG is entirely intramolecular in nature. Thus molecular order and mobility are monitored through the orientation of individual C–^{2}H bond directions. Therefore, ^{2}H NMR is a powerful technique for studying local molecular motions. It enables us to discriminate different types of motions and their correlation times over a wide frequency range. Dynamics of numerous polymers has been examined by solid state ^{2}H NMR.[1–3,7,9] Dynamic information on polypeptides by NMR is however limited,[10–26] although the main-chain secondary structures of polypeptides in the solid have been extensively evaluated by ^{13}C and ^{15}N CP/MAS NMR.[27,28]

The long side chains of a homopolypeptide have remarkable motional freedom about multiple bonds, while the main chain forms the secondary regular conformation such as α-helix, β-sheet, and turn, which are rigid structures. The macroscopic properties of the rigid α-helical polypeptide, therefore, highly depends on the dynamic structure of the side chains so that a lot of studies on the side chain dynamics of the α-helical polypeptides have been carried out in the solid and solution states.[12,14,29–66]

Poly(γ-benzyl L-glutamate) (PBLG) is a typical right-handed α-helical polypeptide, and has been characterized by various techniques.[29–64] The side chains are located between the pseudo-hexagonally packed α-helical rods.[45–49] The side chain structure of PBLG is displayed in Fig. 1. Various physicochemical studies revealed that rapid and large amplitude motions are prominent above room temperature,[30–33,37,41–43,47,48] and that the relaxation process is well described by the WLF equation.[32,38] These phenomena show behaviour like the glass transition of the PBLG side chains at around room temperature, which is refered to as the glass-like transition, T_g'. Local internal motions along the side chain investigated by ^{13}C CP/MAS showed the presence of motions of the order of 70 kHz at the side chain around 70–90°C.[11]

Racemic complex (racemic PBG), composed of PBLG and its enantiomer poly(γ-benzyl D-glutamate) (PBDG), takes an α-helical conformation in the solid state and has different physical properties from those of PBLG or

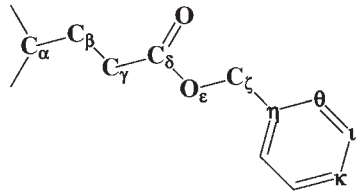

Fig. 1. Skeletal structure of the PBLG side chain.

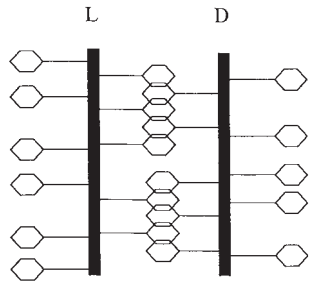

Fig. 2. Stacking model.[69] Phenyl rings form the regular stacking structure between L and D molecules. Bold lines show the α-helical axes. Reproduced with permissions from Elsevier Science.

PBDG.[26,67–78] These results were ascribed to the interactions between the side chains of adjacent PBLG and PBDG molecules which have an opposite helical sense to each other. Squire and Elliott proposed the 'stacking model' that phenyl rings at the end of side chains stack regularly, as schematically shown in Fig. 2.[69] According to this model, a regular stack of phenyl groups comprises five side chains and the side chains of PBLG molecules interdigitate with the side chains of the adjacent PBDG molecules having an opposite screw sense. Physicochemical measurements showed the presence of the reversible first order transition at about 90°C.[71,72,74,75] This transition was deduced to be due to the collapse of the stacking structure. Though phenomenological effects arising from the stacking structure have been studied by various techniques, the dynamic structure of the stacking has scarcely been investigated. It was shown that NMR relaxation times of racemic PBG are longer than those for PBLG at room temperature and gradually decrease with increasing temperature and that at around 100°C they decrease suddenly to similar values to those for PBLG.[26,76–78] These results suggest the presence of the restriction of the side chain motion due to stacking below the transition temperature.

In this review we focus on the detailed side chain dynamic of PBLG and racemic PBG deuterated at several positions in a side chain by means of solid state ^{2}H NMR. The brief description of the ^{2}H NMR parameters used

is presented in Section 2. Sections 3 and 4 deal with the results for PBLG and racemic PBG, respectively.

2. INTRODUCTORY SOLID STATE ^{2}H NMR

2.1. Line shape

It will be useful to outline the basic features of solid state ^{2}H NMR spectra. Deuteron is a spin $I=1$ nucleus possessing an electric quadrupole moment. The EFG interacts with the electric quadrupole moment to produce a frequency shift. Frequencies of the symmetric line shape centred around the Larmor frequency ω_0, which depend on the relative orientation of an external magnetic field B_0 and the EFG tensor, are given by[1–7]

$$\omega = \omega_0 \pm \frac{8}{3}\omega_Q(3\cos^2\beta - 1 - \eta\sin^2\beta\cos 2\alpha) \tag{1}$$

where ω_0 is the Larmor frequency, ω_Q is the quadrupole coupling constant (QCC) $e^2qQ/\hbar$, η is the asymmetry parameter of the EFG tensor, and (α, β) are the spherical polar angles defining the orientation of B_0 in the EFG tensor principal axis system. It was reported that $\omega_Q/2\pi = 170$ kHz and $\eta = 0.0$ for aliphatic deuterons, and that $\omega_Q/2\pi = 180$ kHz and $\eta = 0.05$ for aromatic deuterons.[79] If η is taken as zero, the NMR frequencies are given by

$$\omega = \omega_0 \pm \frac{8}{3}\omega_Q(3\cos^2\beta - 1) \tag{2}$$

This means that the frequencies of signals depend only on the angle β that the C–^{2}H bond makes with B_0. For a powder sample (with C–^{2}H bonds at various orientations β), the spectrum will be given by a properly weighted superposition of the signal corresponding to the each orientation, resulting in a typical pattern illustrated in Fig. 3 (bottom) in rigid state. The spectrum is symmetric about ω_0 and the dominant characters of this line shape are two strong peaks disposed symmetrically about ω_0 and separated by $(3/4)\omega_Q$ and two extreme shoulders separated by $(3/2)\omega_Q$. The former corresponds to $\beta = 90^\circ$ orientation which is referred as the 'perpendicular components' and the latter to $\beta = 0^\circ$ orientation referred as the 'parallel components'. The separation of perpendicular components $\nu_Q = (3/4)\omega_Q/2\pi$ is called as the 'quadrupolar splitting'.

^{2}H NMR spectra are profoundly influenced by motions.[1–7] It is possible to calculate the powder spectra in the presence of any type of motion by taking into account the geometry, and amplitudes and rates of motions involved.[80,81] Consider a C–^{2}H bond which can jump between three equivalent sites,

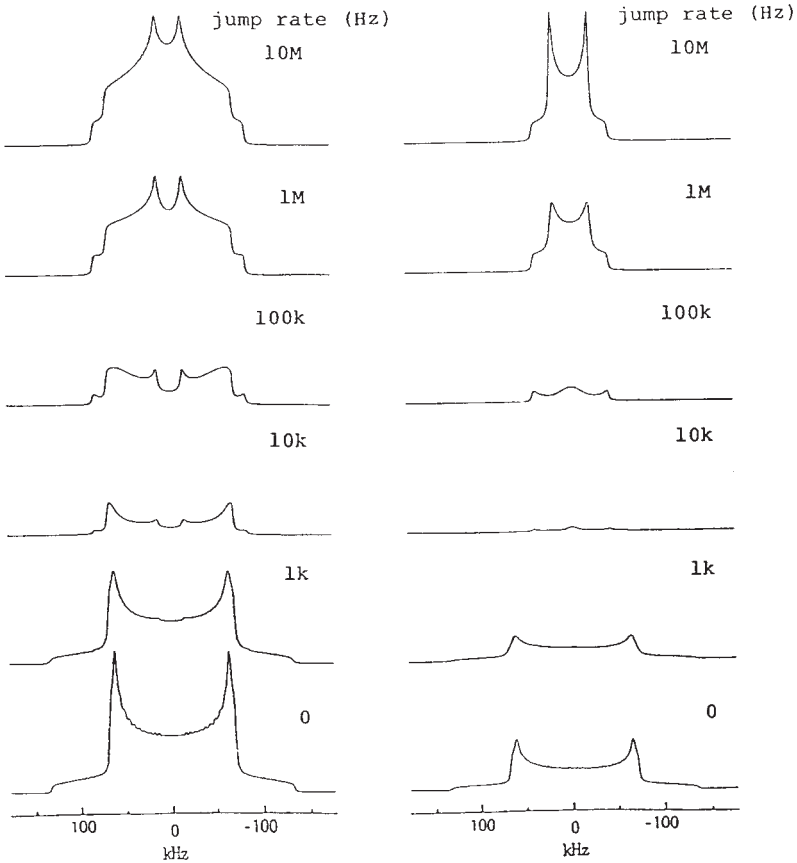

Fig. 3. Calculated ^{2}H NMR spectra for a phenyl ring (left) and a methyl group (right) as a function of jump rate.

as a model of a rapidly rotating methyl group. The C–^{2}H bond makes an angle θ with respect to the Zc axis, which indicates z-axis in the molecular frame, and the asymmetry parameter $\eta = 0$ for simplicity. The averaged NMR frequency is given by[1,2]

$$\omega = \omega_0 \pm \frac{3}{4}\omega_Q \left(\frac{3\cos^2\theta - 1}{2}\right)\left(\frac{3\cos^2\Theta - 1}{2}\right) \tag{3}$$

where θ is the spherical polar angle defining the EFG tensor in the molecular frame, which is 109.5° for a methyl group. With a powder sample one would therefore expect a pattern (top right) analogous to the static (rigid state) powder pattern at bottom in Fig. 3, but reduced along the frequency axis by a factor of $(3\cos^2\theta - 1)/2$.

Figure 3 (top left) also shows the line shape which arises when deuterated phenyl rings undergo a fast 180° flipping motion. In this case a C–^{2}H bond jumps between two equivalent positions separated by 180°. The angle between the C–^{2}H bond and the flipping axis is 60°. The component of the EFG tensor perpendicular to the phenyl ring is unaffected by the motion, and remains at $\pm\nu_Q/2$. Another component of the tensor is averaged by 120°, and thus occurs at $\pm\nu_Q/8$. Because the tensor must remain traceless, the third component occurs at $\overline{+}5\nu_Q/8$. $\overline{\eta}$ of this motion is 0.6. Suppose the phenyl rings undergoes a free rotation. In this situation the averaged NMR frequency is given by Eq. (3) with $\theta = 60°$. The entire pattern is therefore averaged by a factor of 1/8, which is definitely different from the line shape with a 180° flipping motion.

If a C–^{2}H bond diffuses uniformly over the surface of a cone having semiangle θ_C, we have

$$\omega = \omega_0 \pm \frac{3}{4}\omega_Q\left(\frac{\cos\theta_C(1+\cos\theta_C)}{2}\right)\left(\frac{3\cos^2\Theta - 1}{2}\right) \tag{4}$$

Then averaged quadrupolar splitting $\overline{\nu_Q}$ is given by[82]

$$\overline{\nu_Q} = \nu_Q\frac{\cos\theta_C(1+\cos\theta_C)}{2} \tag{5}$$

where ν_Q is a rigid lattice value of 128 kHz for aliphatic C–^{2}H bond.

The line shape alters considerably when the motional rate is comparable to ω_Q, which is called as the 'intermediate exchange regime'.[1,2,6] For such a case, exchange-modified Bloch equation theory is needed in which the angular dependent resonance frequency is modulated by the rotational motion. Remarkable line shape distortions arise when the motional rate is in the intermediate exchange regime, as shown in Figs. 3 and 5 for the methyl and ring motions. The general theory for calculating line shapes has been discussed.[1,2,6,80,81] The molecular motion not only leads to a reduction of the echo amplitude, but also causes characteristic line shape changes.[80,81] The integrated intensities of spectra for the three-site jump of a methyl group are shown in Fig. 4 as a function of jump rate k. In the intermediate exchange regime the loss of intensity is most remarkable. The signal intensity thus provides additional information about the time scale of the motion. The effect of different pulse spacings τ_1 of the quadrupole echo on the line shape for a phenyl ring flipping motion is shown in Fig. 5 as a function of the jump rate. For slow ($k = 10^3$ Hz) or fast ($k = 10^7$ Hz) jumps, little change occurs in the line shapes as a function of τ_1. For $k = 10^4$ to 10^6 Hz, the line shapes apparently change with an increase in τ_1. Thus additional information about the motional time scales can also be obtained by using the quadrupole echo pulse sequence.

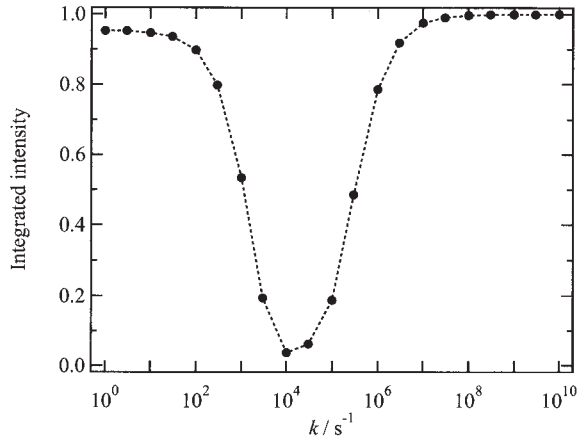

Fig. 4. Integrated intensity of spectra for a methyl rotation with the three site jump as a function of jump rate k.

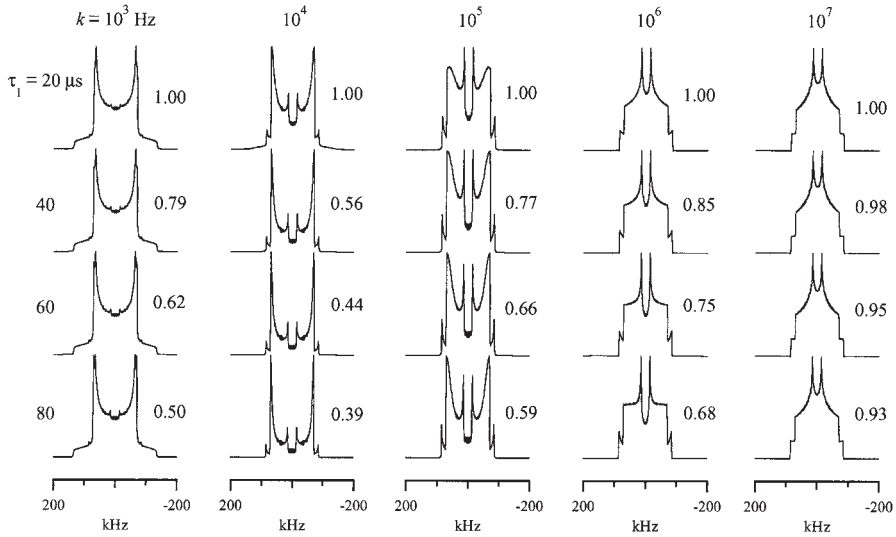

Fig. 5. Line shapes for the 180° flipping jump of a phenyl ring as a function of pulse spacing τ_1 and jump rate k. The figures on the right-hand side of the spectra indicate the relative intensities.

2.2. Spin-lattice relaxation

Although ^{2}H NMR line shapes provide information about the type of motions, it contains no further information about the rates when the motion is faster than QCC. However, T_1 enables us to evaluate the correlation times

of such motions. Explicit expressions for solid state ^{2}H NMR T_1 values have been obtained by Torchia and Szabo,[83] and their T_1s are exclusively governed by the quadrupole interaction.

In the case of jumps between two equivalent sites with a jump rate k, T_1 is given by

$$\frac{1}{T_1} = \frac{1}{8}\left(\frac{3\omega_Q}{4}\right)^2 A_1 \left\{ \begin{array}{c} g(\tau,\omega)[B_4 - (0.75B_1 - B_2)\cos 2\Phi] \\ +g(\tau,2\omega)[4B_5 - 4B_2\cos 2\Phi] \end{array} \right\} \tag{6}$$

where $g(\tau,\omega) = \tau/(1+\tau^2\omega^2)$, $\tau = (2k)^{-1}$, and A_j, B_j are given in Table II of Ref. 83.

In the case of jumps between three equivalent sites, such as a methyl group, with a jump rate k, T_1 is given by

$$\frac{1}{T_1} = \frac{1}{8}\left(\frac{3\omega_Q}{4}\right)^2 \left\{ \begin{array}{c} g(\tau,\omega)[A_1B_4 + A_2B_5 - 8A_3B_3\cos 3\Phi] \\ +g(\tau,2\omega)[4A_1B_5 + A_2B_6 - 8A_3B_3\cos 3\Phi] \end{array} \right\} \tag{7}$$

where $\tau = (3k)^{-1}$, and g, A_j, B_j are defined after Eq. (6).

If a C–^{2}H bond diffuses freely with the diffusion coefficient D_W in a cone of semiangle θ_C, then T_1 is given by[84]

$$\frac{1}{T_1} = \frac{1}{3}\left(\frac{3\omega_Q}{4}\right)^2 [J_1(\omega_0) + 4J_2(2\omega_0)]. \tag{8}$$

The spectral density functions in Eq. (8) are defined as

$$J_m(\omega) = 2\int_0^\infty C_m(t)\cos(\omega t)\,dt. \tag{9}$$

The autocorrelation function $C_m(t)$ in Eq. (9) is given by

$$C_m(t) = \sum_{aa'=-2}^{2} d^{(2)}_{ma}(\Theta) d^{(2)}_{ma'}(\Theta) e^{i(a-a')\Phi} C_{aa'}(t) \tag{10}$$

$$C_{aa'}(t) = \delta_{aa'}\left[G_a(\infty) + \{G_a(0) - G_a(\infty)\}e^{-t/\tau^{(a)}_{eff}}\right], \tag{11}$$

with the approximation of $\eta = 0$. $d^{(2)}_{ma}(\Theta)$ are the reduced Wigner rotation matrix elements.[85,86] $G_a(\infty)$, $G_a(0)$, and $\tau^{(a)}_{eff}$ are given as functions of θ_C and D_W.

2.3. Solid state ^{2}H NMR measurements

Solid state ^{2}H NMR measurements were performed on a Bruker MSL-200 spectrometer at 30.7 MHz with a home-made 5-mm horizontal solenoid coil. The spectra were obtained by the quadrupole echo pulse sequence with a 90° pulse of 1.7 μs or less and a pulse spacing of 25 μs, unless otherwise states. The spectral width was 2.5 MHz with 2 k data points zero-filled to 8 k. The time domain data were left-shifted to the echo maximum prior to the Fourier transformation and the Lorentzian line broadening of 2 kHz being applied to the spectrum. T_1 was measured with an inversion-recovery quadrupole echo pulse sequence. Amorphous selection quadrupole echo pulse sequence[87] is used to detect selectively the deuterons having shorter T_1 values in the case that there are two kinds of deuterons having longer and shorter T_1s. This sequence consists of three parts: (1) a 90° pulse train to saturate the entire spin system, (2) a delay time to allow the deuterons having shorter T_1 to relax, and (3) the quadrupole echo pulse sequence. The optimum delay time is generally three times longer than the shorter T_1. Deuterons having considerably long T_1 values undergo negligible relaxation during the delay time. The following quadrupole echo pulse sequence is then used to read out the signal from the deuterons having shorter T_1 values. Calculations of line shapes are carried out with a program described by Greenfield *et al.*[80]

3. MATERIALS

The samples used are PBLG deuterated at γ(PBLG-γd_2), ζ(PBLG-ζd_2), phenyl ring(PBLG-d_5) and κ(PBLG-κd_1) positions, respectively, which were prepared as described previously.[13,15,16,26,88] The racemic complex was obtained by casting the solution in chloroform of an equi-weight mixture of PBLG deuterated at each position and PBDG. Racemic complex of PBDG and PBLG-γd2, PBLG-ζd2, and PBLG-d5 are refered to PBG-γd_2, PBG-ζd_2, and PBG-d_5, respectively.[78,88]

4. PBLG

4.1. PBLG-d_5[15,78,88]

The phenyl ring motion for peptides and various synthetic polymers have been studied with the solid state ^{2}H NMR by many workers,[89–93] undergoing a 180° flipping motion in a two-fold potential. The reported activation energies of the flipping motion reflect the degree of crystallinity, the crystal

structure and the degree of molecular packing. The activation energies for the tyrosine-ring flipping motion in crystalline tyrosine-containing peptides are 88 and 27 kJ mol^{-1}.[91] The activation energy of the ring flipping motion in polystyrene were reported to be 233 kJ/mol in the glass transition region.[93] The motion of the phenyl ring at the end of a relatively long chain such as the PBLG side chain has been scarcely reported so far. Because of the flexibility of the side chain, the phenyl ring of PBLG is expected to undergo additional motions in addition to the flipping motion.

4.1.1. *Spectra of PBLG-d_5*

The temperature dependent spectra of PBLG-d_5 is shown in Fig. 6. Line shapes below $-76°C$ are similar to the rigid state pattern, indicating the absence of fast and large-amplitude motions. They are, however, different in

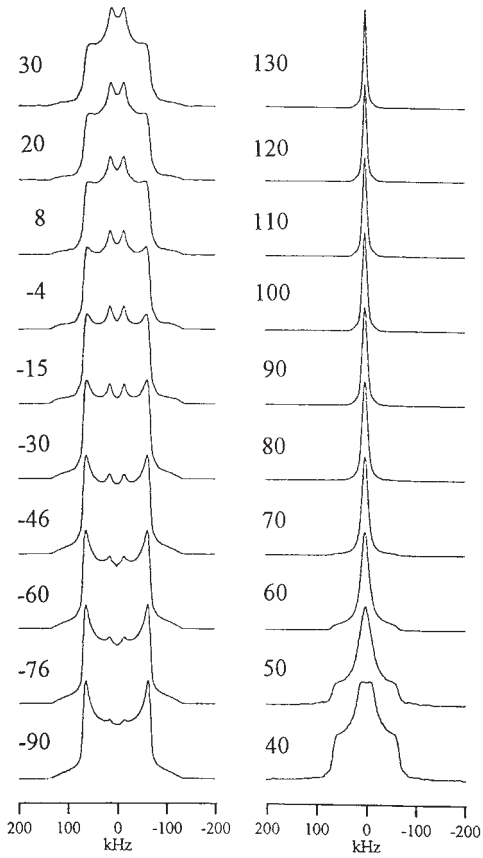

Fig. 6. ^2H NMR spectra of PBLG-d_5 as a function of temperature.

a few points: the parallel components are obscure, and the centre of the spectrum is more filled-in than the rigid state pattern and a narrow quadrupolar splitting of 30 kHz exists in the centre of the spectrum, which is refered as 'inner $\overline{\nu_Q}$', in addition to a wide outer one of 126 kHz corresponding to perpendicular components, which is refered to as 'outer $\overline{\nu_Q}$'. The temperature dependence of the inner and outer $\overline{\nu_Q}$ are shown in Fig. 7. The outer $\overline{\nu_Q}$ values are slightly smaller than the rigid state value of 128 kHz[79] and decrease gradually with increasing temperature. The inner $\overline{\nu_Q}$ decrease with raising temperature as well. These facts imply the presence of rapid and small-amplitude librations at the phenyl ring and the increase in its amplitude with raising temperature.[10,20,93,94] The amplitude of the librations was estimated with the diffusion in a cone model. The cone semiangle θ_C is given by from Eq. (6) from the outer $\overline{\nu_Q}$. The θ_C values are 8° and 17°C at -105 and -4°C, respectively.

The intensity in the centre of the spectrum increases with an increase in temperature, showing that the phenyl ring at the end of the PBLG side chain undergoes a rapid 180° flipping motion about the C_ζ–C_η axis. The typical line shape for the rapid flipping motion of a phenyl ring appears at room temperature. The spectrum at 30°C has value for the $\overline{\nu_Q}$ of 24 kHz which is smaller by 6 kHz than the rigid state value, indicating the presence of the libration as the outer $\overline{\nu_Q}$ at low temperatures. The θ_C value obtained is 28° at 30°C.

The line shape remarkably changes with a further increase in temperature and a motionally-averaged singlet spectrum with the half-width of 10 kHz at 130°C. These results show that the flipping axis itself undergoes rapid and large-amplitude motions in addition to the flipping motion and the small-amplitude librations. This flipping-axis motion definitely results

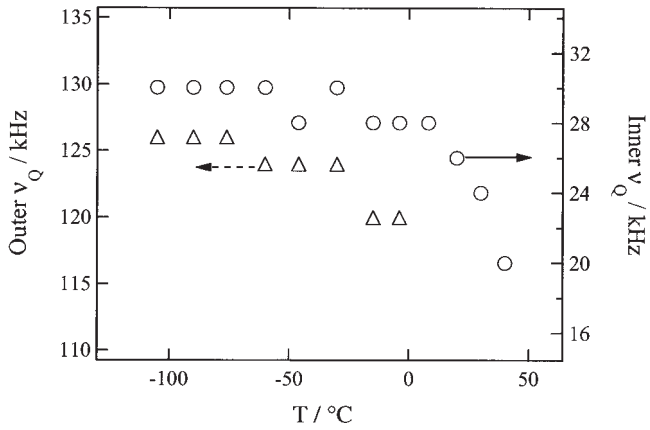

Fig. 7. Temperature dependence of the quadrupole splitting for the inner (circle) and the outer (triangle) of PBLG-d_5.

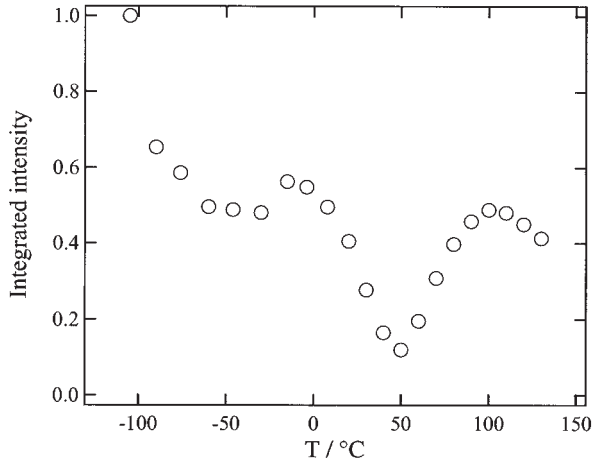

Fig. 8. Integrated intensity of PBLG-d_5 as a function of temperature.

from the multiple internal rotations along the side chain above the glass-like transition temperature, T_g'.

The temperature dependence of the integrated intensities of the spectra is shown in Fig. 8. The intensity decreases with an increase in temperature and achieves a broad minimum at -30°C. After rising a little, it decreases again and exhibits the deep minimum at 50°C. The temperature regions where the intensity takes a minimum correspond to the intermediate exchange regime as shown in Section 2. Therefore, the rate of the motion is as high as the QCC of 180 kHz in these temperature regions. Taking account of the line shape changes, the minima at the lower and higher temperatures are expected to correspond to the flipping motion of a phenyl ring and the motion of the flipping axis itself, respectively.

4.1.2. *T_1 of PBLG-d_5*

The temperature dependent T_1 data are shown in Fig. 9. T_1 values decrease from 28 ms at 21°C with increasing temperature, and show a minimum of 6.4 ms at 80°C. These results indicate the presence of the motion with a Larmor frequency of 30 MHz at this temperature. This minimum was found to be attributed to the flipping motion of a phenyl ring from the result of our other experiments discussed in later section.[13] The jump rates of the flipping motion were estimated with a two-site jump model that a C–^{2}H bond jumps between two equivalent sites separated by 180°, and that the angle made by the C–^{2}H bond and the rotational axis is 60°. The quadrupole coupling constant of 180 kHz and the asymmetry parameter approximated to zero were used in the calculation. The calculated values for fitting with the

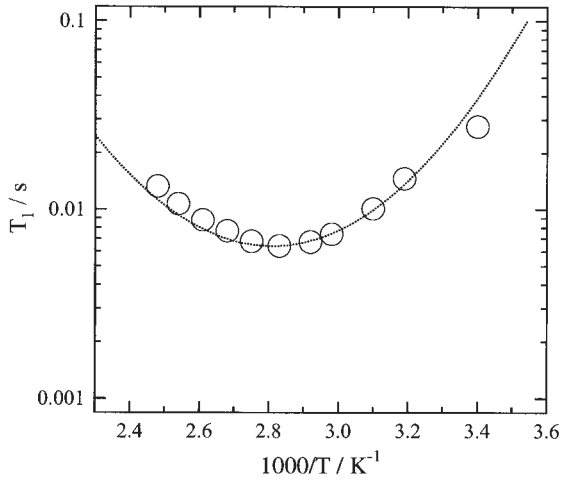

Fig. 9. Temperature dependence of the observed (circle) and calculated (line) T_1 values of PBLG-d_5.

experimental ones are shown in Fig. 9. The temperature dependence of the jump rate follows the Arrhenius relationship:

$$k = k_0 \exp\left(-\frac{\Delta E_a}{RT}\right) \tag{12}$$

where ΔE_a and R are the apparent activation energy and the gas constant, respectively, and k_0 is a constant. The following log-Gaussian distribution was assumed for the jump rate.

$$\phi(k) = \frac{1}{\sqrt{2\pi}\sigma} \exp\left\{-\frac{1}{2\sigma^2}\left\{\log(k/k_{av})\right\}^2\right\}, \tag{13}$$

where σ and k_{av} are the standard deviation and the average jump rate, respectively. The average jump rates k_{av} are 7.6×10^5 and 1.2×10^8 s^{-1} at 30 and 80°C, respectively, as shown in Fig. 10. An apparent activation energy of 90 kJ mol^{-1} and a standard deviation of 1.3 in a log scale were obtained above T_g'.

The line shapes were calculated for the flipping motion with the two-site jump model described above, and the calculated spectra are shown in Fig. 11 for the higher temperature region. The experimental line shapes at 20 and 30°C are well reproduced showing the motional mode and rates obtained by T_1 analysis are reasonable at least around these temperatures. Above 40°C the calculated line shapes are invariable and remain in the powder pattern undergoing a rapid flipping motion, while the experimental ones

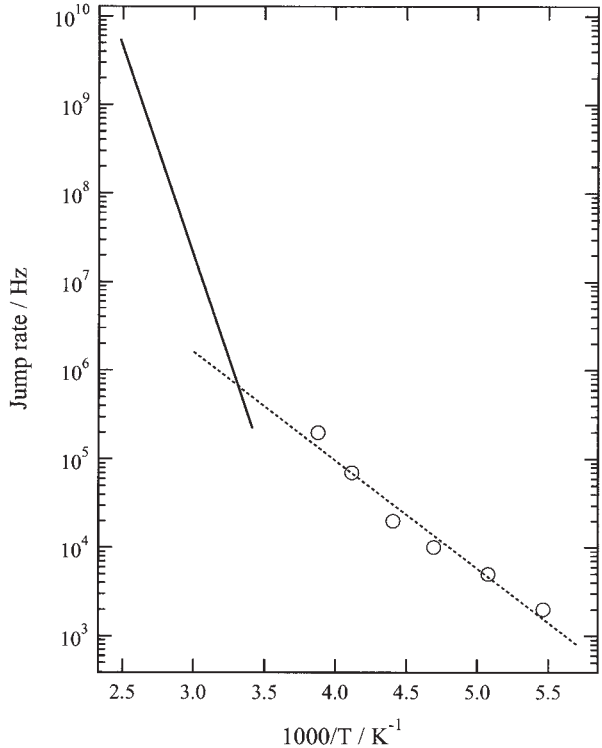

Fig. 10. Jump rates of the phenyl ring as a function of temperature obtained from T_1 values (solid line) and line shape calculation (circle). The dashed line is the least-square line for the jump rates.

are further motionally averaged and become sharp singlet spectra as shown in Fig. 6. This is because the large amplitude motions of the flipping axis itself becomes faster above T_g' and averages further the line shape of the flipping motion. The calculated spectra fitted with the experimental ones below $-15°C$ are shown in Fig. 12. The experimental spectra cannot be explained with a single jump rate, so that we assumed the log-Gaussian distribution[13] for the jump rate. The distribution width of the jump rate is 2.0 in log scale for all temperatures below $-15°C$. The obtained average jump rate is 7×10^4 Hz at $-30°C$. This result is compatible with the fact that the observed integrated intensity achieves a minimum originating from the exchange broadening at $-30°C$. The average jump rate at each temperature is plotted in Fig. 10. Temperature dependence of these average jump rates shows an Arrhenius type whose ΔE_a value is 23 kJ mol^{-1}, while the obtained value above room temperature is 90 kJ mol^{-1} described above. The distribution widths of the flipping jump rate are 1.3 and 2.0 in log scale above and below T_g', respectively, suggesting that the degree of the

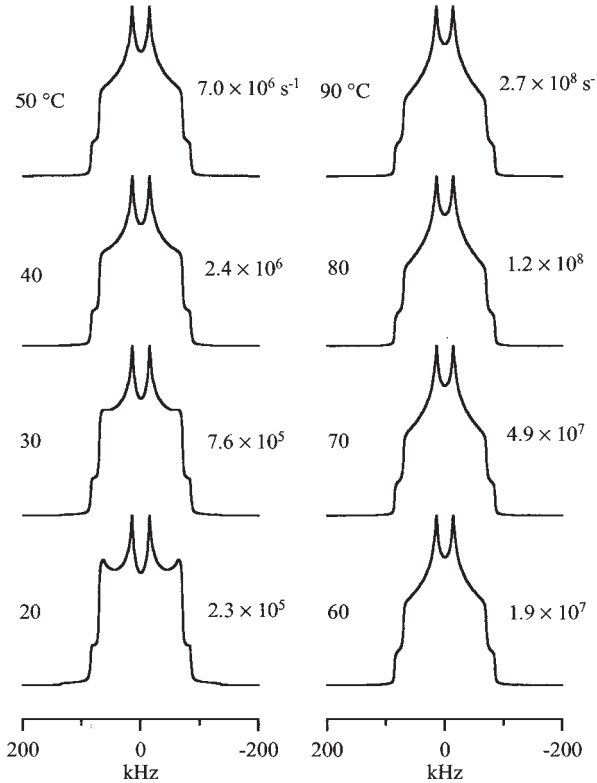

Fig. 11. Calculated spectra of PBLG-d_5 for the phenyl ring flipping as a function of temperature. Figures on the left- and right-hand side of the spectra indicate temperature and jump rate obtained from T_1, respectively.

heterogeneity of the side chain region in the glassy state is larger than that above T_g'. Similar results of ΔE_a and the distribution of the jump rate were obtained for the ring motion of poly(L-phenylalanine), although there is no flipping axis motion.[14]

4.2. PBLG-ζd_2 and PBLG-κd_1[13,78,88]

The previous section has shown that the phenyl ring undergoes a rapid 180° flipping motion about the C_ζ–C_η axis and fast and small-amplitude librations, and that the flipping axis itself undergoes a large amplitude motion originating from multiple internal rotations along the side chain. The κ position of the side chain is unaffected by the flipping motion about the C_ζ–C_η axis. The ^{2}H NMR spectra of PBLG-κd_1 will, therefore, give us direct information about the motion of the flipping axis itself. The flipping axis

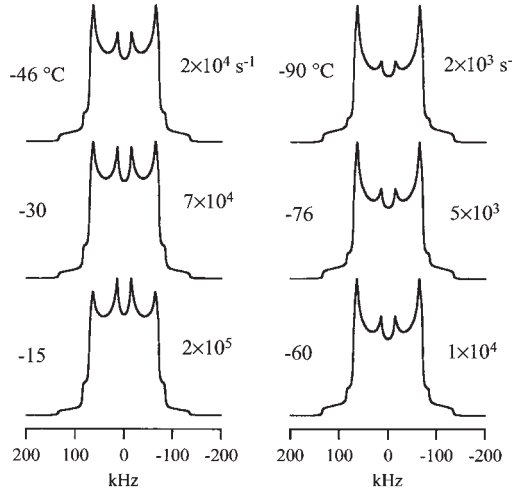

Fig. 12. Calculated spectra of PBLG-d_5 for the phenyl ring flipping as a function of temperature below −15°C. Figures on the left- and right-hand side of the spectra indicate temperature and jump rate, respectively.

motion is expected to be detected in PBLG-ζd_2 as well, because the C_ζ–^2H bonds and the C_ζ–C_η bond have a common motional axis.

4.2.1. *Spectra of PBLG-κd_1 and PBLG-ζd_2*

The temperature dependent ^2H NMR spectra of PBLG-κd_1 and PBLG-ζd_2 are shown in Figs. 13 and 14, respectively. The line shapes of both samples appear to be the static powder pattern below room temperature, indicating the absence of a large amplitude motion. These line shapes, however, are slightly different from completely static ones. The parallel components of the spectrum are not clear and the centre of the spectrum is more filled-in than the static one. The $\overline{\nu_Q}$ values for both samples are slightly smaller than the rigid state value of 128 kHz, and decreases gradually with increasing temperature as shown in Fig. 15. These results suggest that there is a rapid and small-amplitude libration at both the κ and ζ positions, and that its amplitude increases with rising temperatures.

The temperature dependent integrated intensities of the spectra of PBLG-κd_1 and PBLG-ζd_2 are shown in Fig. 16. The integrated intensities start to decrease gradually from the lowest temperature to room temperature at which the glass-like transition occurs and decrease steeply above room temperature. A remarkable intensity loss is observed around 50°C corresponding to the intermediate exchange regime of the ^2H NMR spectra. With a further increase in temperature, the spectrum recovers its intensity. Above 80°C the motionally averaged singlet-like spectra are observed for

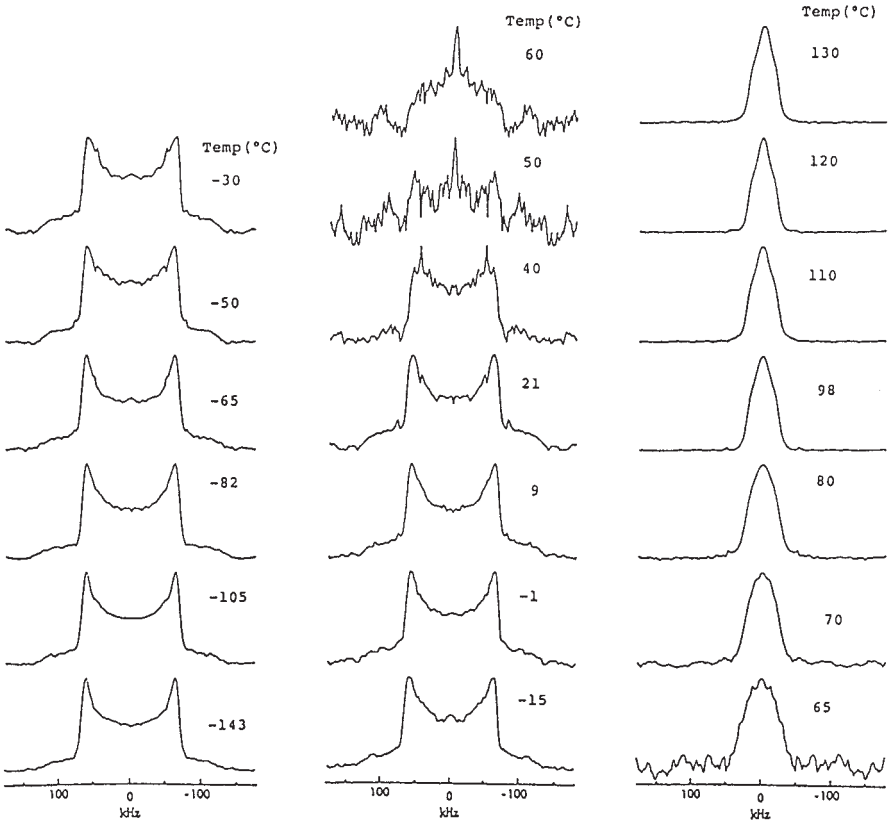

Fig. 13. ^{2}H NMR spectra of PBLG-κd$_1$ as a function of temperature.

both PBLG-κd$_1$ and PBLG-ζd$_2$, showing that the presence of rapid and large amplitude motions of which the frequency is as high as 100 kHz around 50°C and becomes far higher above 80°C.

The τ-dependence of the spectra of PBLG-ζd$_2$ is shown in Fig. 17. An increase in the pulse spacing τ leads to a reduction of the spectral intensity and characteristic line shape changes. The remarkable τ-dependence is observed around 40–60°C for both samples. These results show the presence of motions with rates as high as the QCC at the κ and ζ positions in this temperature region, and are consistent with the remarkable signal intensity loss around 50°C.

4.2.2. *T_1 of PBLG-κd$_1$ and PBLG-ζd$_2$*

The temperature dependent T_1 data of both samples are shown in Fig. 18. There is little difference between the T_1 values of PBLG-κd$_1$ and PBLG-ζd$_2$ over all the temperature range of the measurements. T_1s of both samples

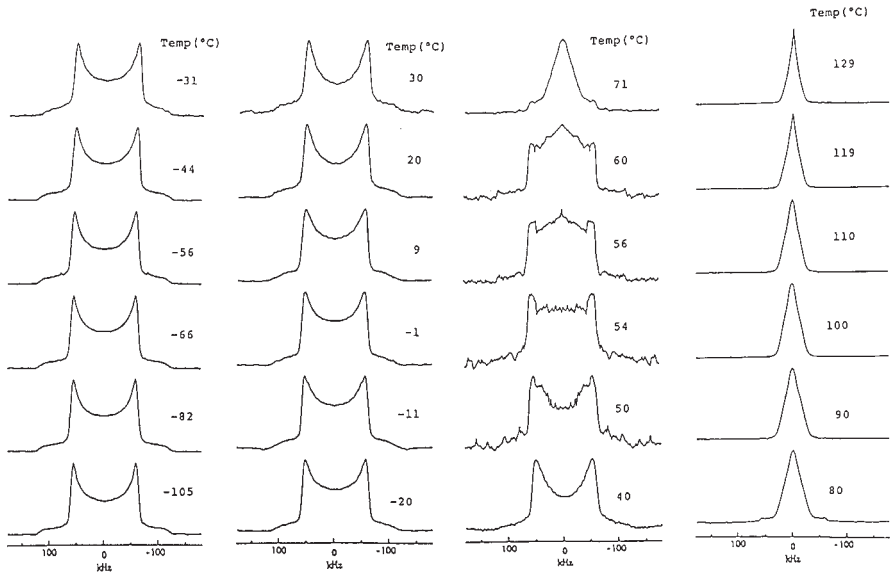

Fig. 14. ^{2}H NMR spectra of PBLG-ζd_2 as a function of temperature.

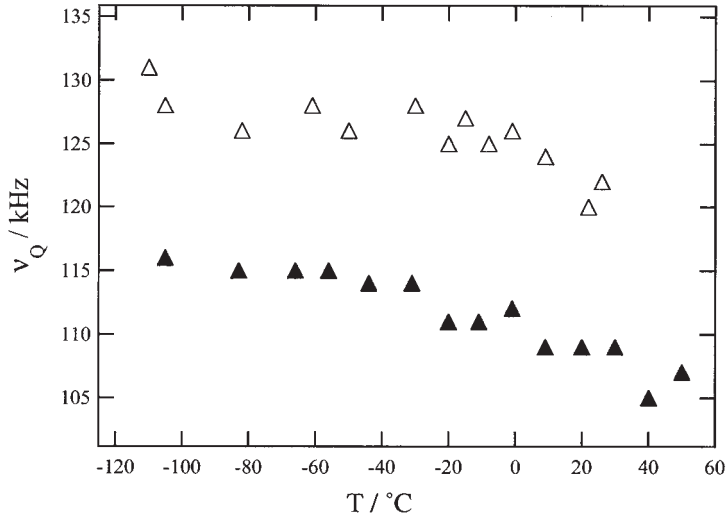

Fig. 15. Temperature dependent quadrupole splitting of PBLG-κd_1 (open triangle) and PBLG-ζd_2 (filled triangle). Reproduced with permission from the Society of polymer Science, Japan.

decrease gradually with an increase in temperature and start to decrease steeply from room temperature at which the glass-like transition occurs. T_1s of both samples take minimum values at 110°C, showing the presence of the large amplitude motion of the side chain whose rate is as high as the

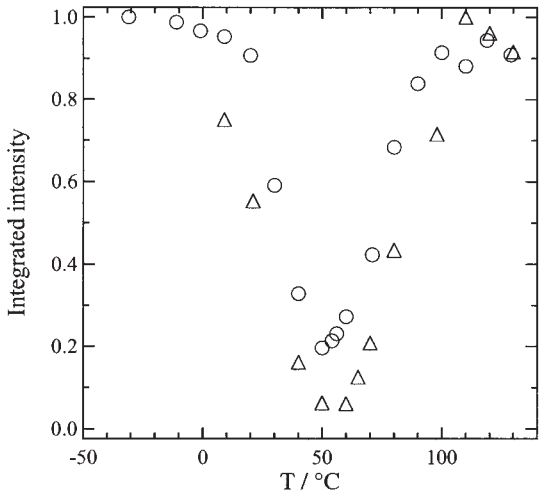

Fig. 16. Temperature dependent integrated intensity of PBLG-κd$_1$ (triangle) and PBLG-ζd$_2$ (circle).

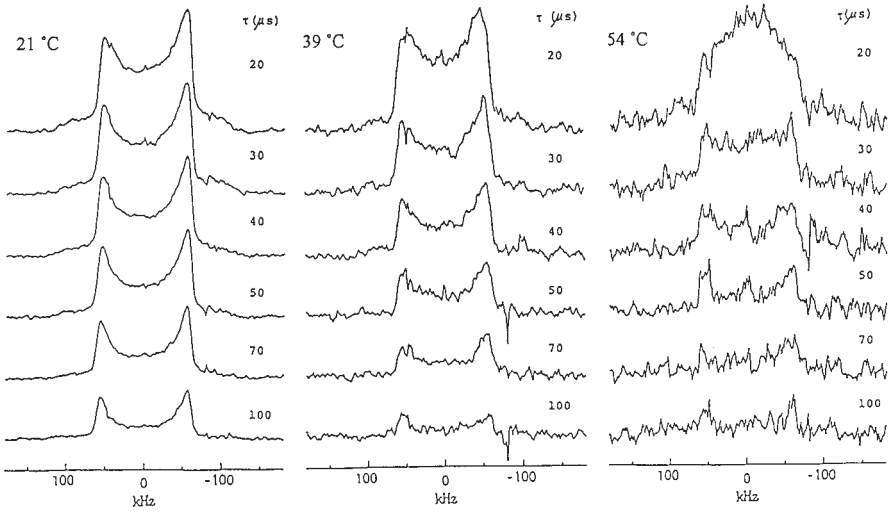

Fig. 17. τ-dependence of the ^{2}H NMR spectra of PBLG-ζd$_2$.

observed frequency of 30 MHz at this temperature. The temperature dependent T_1 data can be apparently divided into two regions by room temperature. Therefore, T_1 will be assumed to be governed by different motional modes of the side chain, that is, the libration and the large amplitude motion below and above room temperature, respectively, taking the temperature dependence of the line shapes into account.

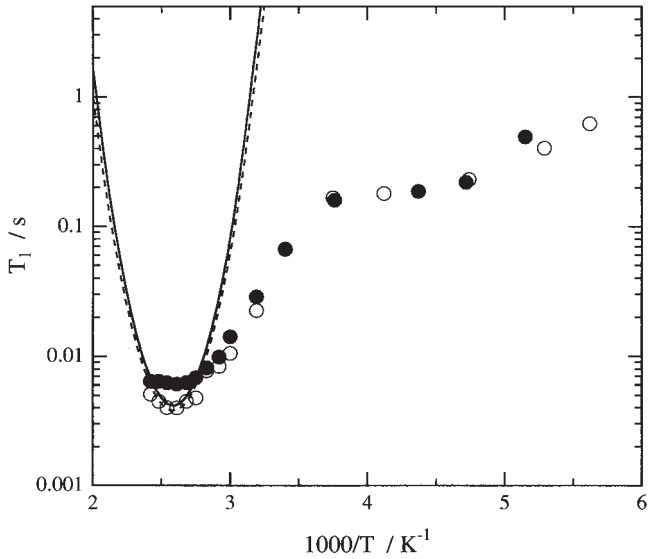

Fig. 18. Temperature dependence of observed (symbols) and calculated (lines) values of T_1. Observed (open circle) and calculated (dotted line) for PBLG-κd_1, and observed (filled circle) and calculated (solid line) for PBLG-ζd_2. Reproduced with permission from the society of Polymer Science, Japan.

Subsequently, librational effects on line-shape and T_1 are examined. The amplitude of the libration with the diffusion in a cone model, the cone semiangle θ_C is given by Eq. (6) with the $\overline{\nu_Q}$. The θ_C obtained are from 10° at −110°C to 25° at 22°C for both PBLG-κd_1 and PBLG-ζd_2 and is almost proportional to temperature as expected. In order to estimate the rate of the libration, T_1 below room temperature was calculated with the following three models: a two-site jump, a three-site jump, and diffusion in a cone. The correlation times obtained are the order of 10^{-11} s from −75°C to 25°C, independent of the models, and almost equivalent for both samples. These values are short enough to be in the fast motion limit for line shapes. Line shapes were calculated to confirm the effects of the libration. The libration was approximated by the equi-populated three-site jump model for simplicity. The polar angles used in the calculation are assumed to be the Gaussian distribution of the root mean square of θ_C. The results for PBLG-ζd_2 are shown in Fig. 19. They are in fairly good agreement with the observed.

4.2.3. *Large amplitude motion*

In order to understand the large amplitude motion, the allowed conformations brought about the multiple internal rotations were calculated for a single

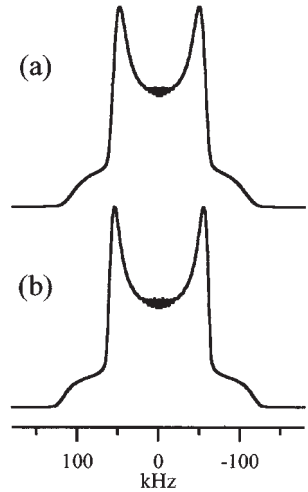

Fig. 19. Calculated spectra for PBLG-ζd_2 with the three site-jump for the libration. (a) and (b) corresponds to the observed ones at 40°C and −105°C, respectively.

side chain. This calculation was carried out under the following two assumptions: (1) each of the six internal rotation angles (χ_1, χ_2, χ_3, χ_4, χ_5, χ_6) can take only three rotational isomeric states of t, g^+, and g^- and (2) any atom of a side chain cannot approach within the van der Waals radius of each atom.

The projections of a single side chain on the plane perpendicular to the helix axis are shown in Fig. 20(a), and the directions of a C_κ–^{2}H bond are shown in Fig. 20(b). The C–^{2}H bond vectors are distributed nearly symmetrically around the average direction. The same result was obtained for a C_ζ–^{2}H bond. Therefore, jumps among multiple sites which are axially symmetric about the average direction are a good approximation for the large amplitude motion.

If the jump rate of the large amplitude motion k_{LAM} is high enough, the line shapes for such multi-site jumps could be emulated with the equi-populated three-site jumps as described in Fig. 20(c). The k_{LAM} at higher temperatures is obviously high enough to be the fast motion limit for line shapes, because the line shapes no longer change above about 80°C and the T_1s take the minimum values around 110°C for both samples.

In addition to the large amplitude motion, the libration is expected to exist at higher temperatures as well as at lower temperatures, so that the libration was taken into account as small angle three-site jumps. As a result, the C–^{2}H bond undergoes motions superimposed with two independent three-site jumps. In the calculations, a θ_{rms} value of 14° at room temperature was used as the polar angle of the libration, and its distribution was not

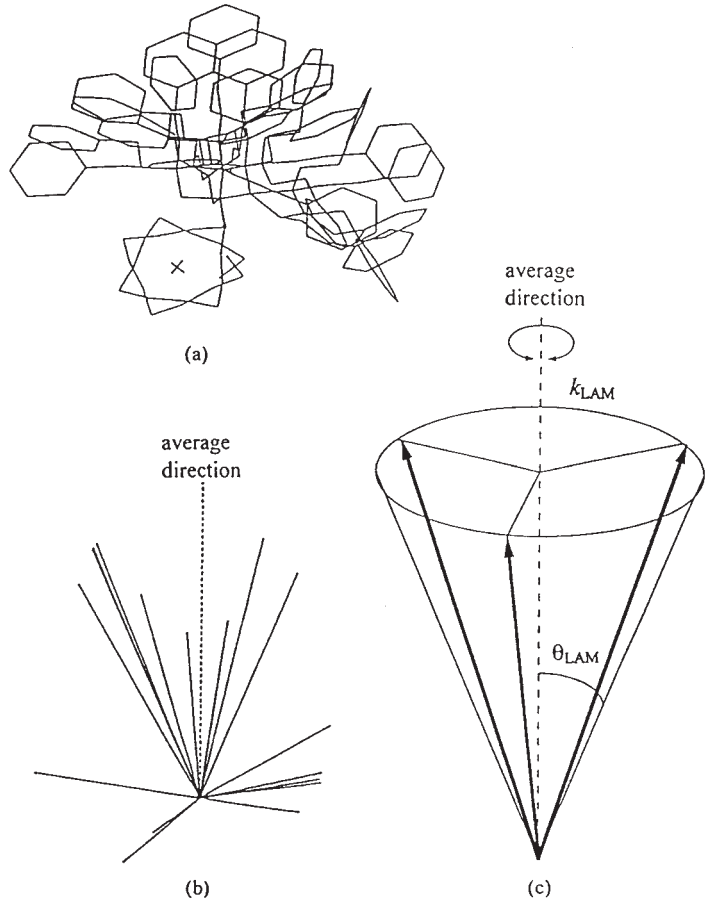

Fig. 20. (a) Allowed side chain conformations. (b) Distribution of C_κ–^2H bond vectors. (c) Three-site jump model as an approximation of multi-site jumps. Reproduced with permission from the Society of Polymer Science, Japan.

considered for simplicity. The jump rate of the libration is 10^{11} Hz. For the large amplitude motion, a log-Gaussian and Gaussian distribution were assumed for k_{LAM}, and the polar angle θ_{LAM}, respectively. The average k_{LAM} of 64 MHz was used in the calculation at 110°C which is the temperature T_1 takes a minimum value, because the k_{LAM} at the T_1 minimum is given as $k_{LAM} = 1/(3\tau_c) \approx \omega_0/3$, where τ_c is the correlation time of the large amplitude motion. The calculated spectra of PBLG-κd_1 and PBLG-ζd_2 at 110°C are shown in Fig. 21(a), respectively. These spectra are in good agreement with the observed ones in Fig. 21(b). The average θ_{LAM} is 49° for PBLG-ζd_2, and the standard deviation of θ_{LAM} is 3.8° for both samples. These parameters are the same as those of PBLG-κd_1.[13] This result is reasonable because the

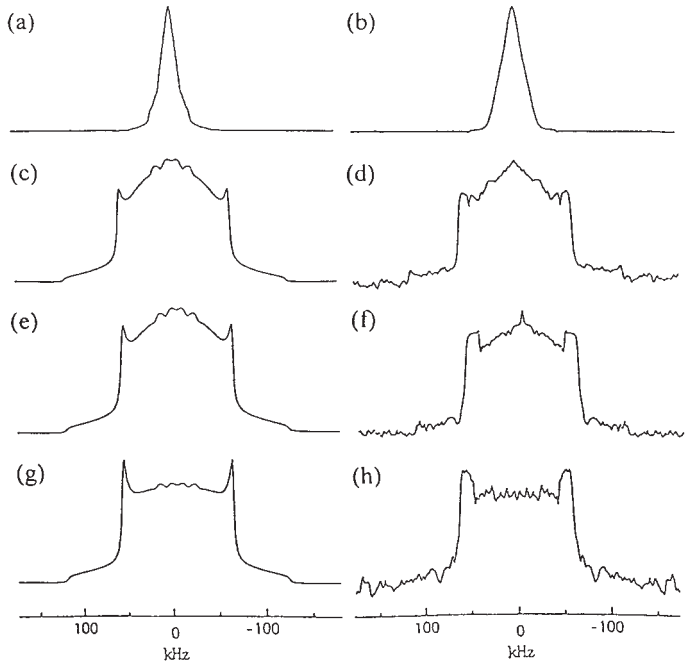

Fig. 21. Observed and calculated line shapes of PBLG-ζd_2. (a), (c), (e), and (g) are calculated line shapes corresponding to the observed ones at (b) 110°C, (d) 60°C, (f) 56°C, and (h) 54°C, respectively. Reproduced with permission from the Society of Polymer Science, Japan.

C_κ–^{2}H and C_ζ–^{2}H bonds attach to a common motional axis, i.e., the O_ε–C_ζ bond. The distribution width of k_{LAM} is estimated to be 1.3 on a log scale. The results for several other temperatures are shown in Fig. 21(c)–(h). The parameters obtained are summarized in Table 1.

At temperatures around 50–60°C the three-site jump model is not a good approximation to the multi-site jump model, because the motion is not sufficiently rapid to be in the fast motion limit. However, the calculated spectra are fairly fitted with the observed ones. This is because the calculated spectrum is a superposition of constituent spectra whose rates are spread over several orders, so that the resultant spectrum is governed by the constituent spectra in the fast and slow motion limits having greater intensity than that in the intermediate exchange regime.

The temperature dependent T_1 for both samples was calculated by the three-site jump model with the parameters derived from the line shape and the result is shown in Fig. 18. The calculated T_1 values for both samples are in good agreement with the experimental ones around the minimum, showing the validity of the parameters concerning with the jump rates and polar

Table 1. Parameters of large amplitude motions for PBLG-ζd_2

Temp (°C)	θ_{LAM} (deg)	Standard deviation of θ_{LAM} (deg)	k_{LAM} (kHz)	Standard deviation of log k_{LAM} (kHz)
110	49	3.8	64,000	1.3
60	38	13	20	1.3
56	38	13	15	1.3
54	38	13	8	1.3

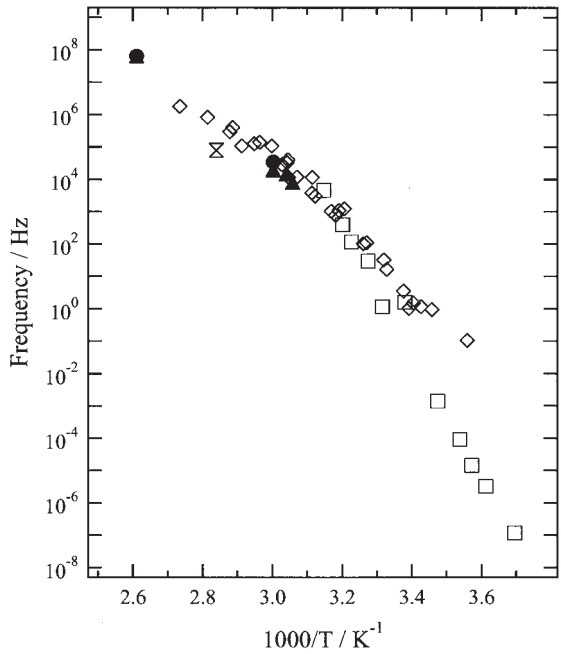

Fig. 22. Relaxation map for PBLG side chain motion. Experiments except ^{2}H NMR measurements are open symbols, and PBLG-κd_1 (filled circle) and PBLG-ζd_2 (filled triangle).

angles at least around 110°C and the presence of large amplitude motions caused by the multiple internal rotations along a side chain.

The jump rates obtained by the line shape simulations are plotted on the relaxation map in Fig. 22 together with values obtained by other experimental methods. The points of the mechanical and dielectric relaxations correspond to the process of the large-scale side chain motions refered to as the 'β-process' and follow the WLF equation very well above T_g'.[11] It should be noted that the present ^{2}H NMR results are located on the curve obtained by other relaxation experiments. This fact shows that

the motional mechanism of the end of the PBLG side chain follows the WLF type.

4.3. PBLG-γd_2

4.3.1. *Spectra of PBLG-γd_2*

The temperature dependent ^{2}H NMR spectrum of PBLG-γd_2 and its integrated intensity are shown in Figs. 23 and 24, respectively. The line shapes below about 30°C appear to be an axially symmetric powder pattern, showing the absence of large amplitude motions. The $\overline{\nu_Q}$ of 121 kHz at -81°C is slightly smaller than the rigid state value of 128 kHz, showing the presence of the rapid and small-amplitude libration at the γ position as observed at the phenyl ring and ζ position of the side chain. It decreases to 115 kHz at 60°C. The integrated intensity starts to decrease gradually and reaches a minimum value at 55°C with an increase in temperature. Line shapes remarkably changes from about 30°C and the characteristic line-shape change is also

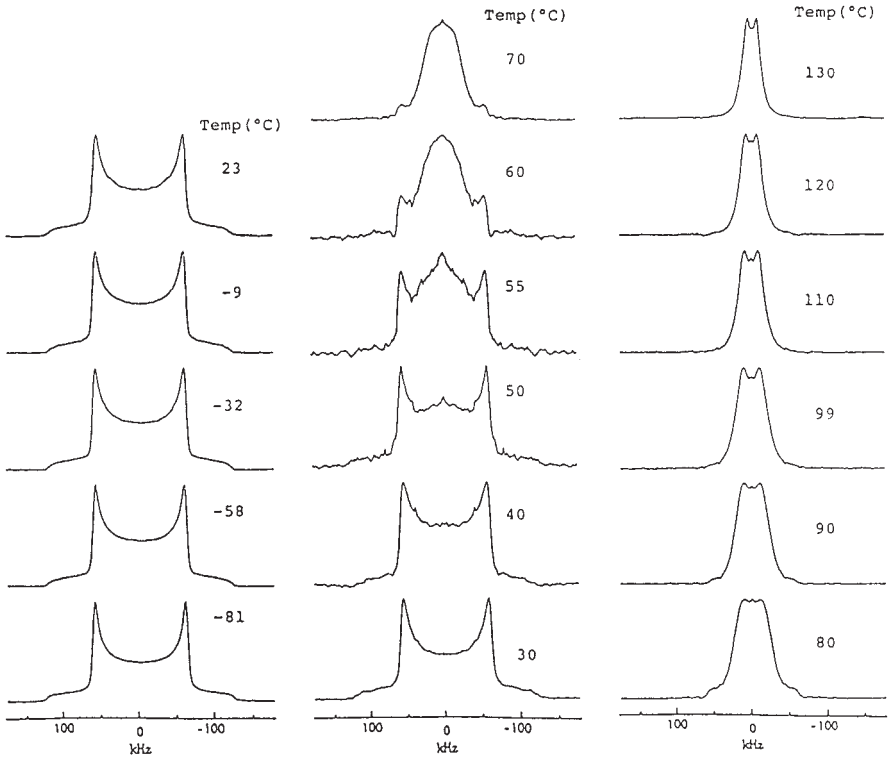

Fig. 23. ^{2}H NMR spectra of PBLG-γd_2 as a function of temperature.

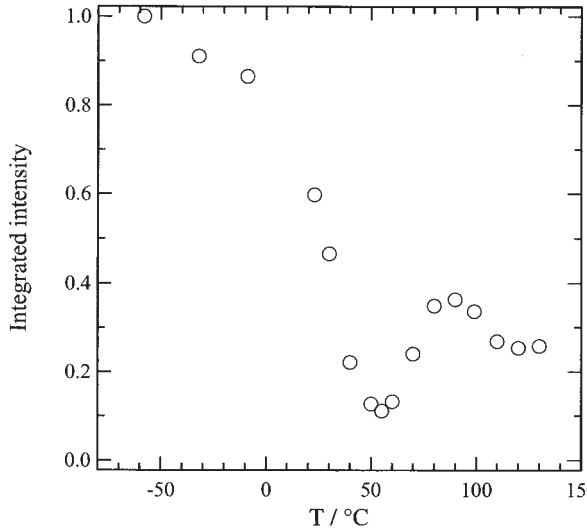

Fig. 24. Temperature dependent integrated intensity of PBLG-γd_2.

observed around 55°C. This intensity loss and the remarkable line shape change result from increasing the mobility, indicating the presence of a motion of which the rate is the order of 10^5 Hz at the γ position. With a further increase in temperature, the spectrum recovers its intensity and gradually changes into the motionally-averaged narrow doublet one whose splitting and half width are 12 and 27 kHz at 130°C, respectively. These results show the presence of the rapid and large-amplitude motion at the γ position. The temperature dependence of the integrated intensity of PBLG-γd_2 is quite similar to that of PBLG-κd_1 and PBLG-ζd_2. In particular the integrated intensities of all these three samples take a minimum at the same temperature of around 55°C, implying that the motions effective in the line shape changes of PBLG-γd_2 are also effective in the line shape changes of PBLG-κd_1 and PBLG-ζd_2.

The τ-dependence of the spectra of PBLG-γd_2 is shown in Fig. 25, a remarkable τ-dependence is observed at 55°C. This result is comparable to the integrated intensity loss around 55°C.

4.3.2. *T_1 of PBLG-γd_2*

The temperature dependent T_1 data of PBLG-γd_2 are shown in Fig. 26. With increasing temperature, T_1 decreases from 630 ms at -80°C and drops above room temperature. T_1 takes the minimum value of 5 ms at 120°C, showing the presence of a motion of which the rate is as high as the Larmor frequency of 30 MHz at this temperature. Temperature dependent T_1 results can be apparently divided into two regions by T_g'. These facts suggest that

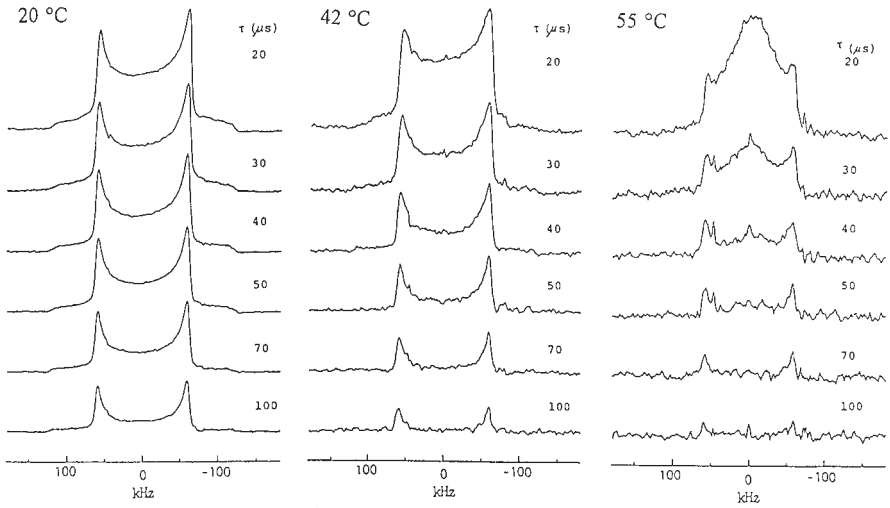

Fig. 25. τ-dependence of the ^{2}H NMR spectra of PBLG-γd_2.

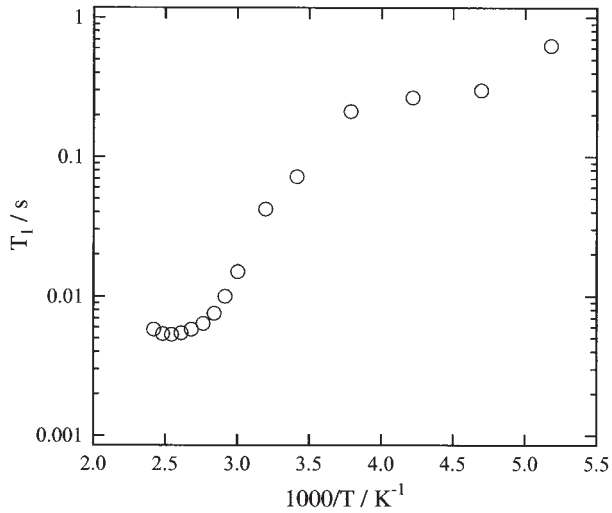

Fig. 26. Temperature dependent T_1 values of PBLG-γd_2.

the T_1 of PBLG-γd_2 is governed by the libration and the large amplitude motion below and above room temperature, respectively, as well as for those of PBLG-κd_1 and PBLG-ζd_2. The T_1 profile of PBLG-γd_2 is very similar to that of PBLG-κd_1 or PBLG-ζd_2. Especially in the high temperature region, T_1 results of all three samples achieve a minimum at 110 to 120°C, revealing that the common motional modes contributes to the T_1 values of three different positions in a side chain and/or that the motions at three

different positions have a common motional rate. In the low temperature region, the T_1 values of PBLG-γd_2 are a little longer than those of PBLG-κd_1 and PBLG-ζd_2, suggesting that the libration at the γ position is more restricted than that at the κ and ζ positions.

4.3.3. *Large amplitude motion*

The line shapes and T_1 results show the presence of the rapid and large-amplitude motion above room temperature. In order to understand the large amplitude motion at the γ position quantitatively, the spectral simulation was carried out. The methodology is the same as that used for PBLG-κd_1 and PBLG-ζd_2. The line shapes for multi-site jumps were emulated with the equi-populated three-site jumps. The averaging effect of the libration was neglected for simplicity. As for PBLG-κd_1 and PBLG-ζd_2, the observed spectra could not be explained with a single jump rate, k_{LAM} and/or a single polar angle, θ_{LAM}, so that log-Gaussian and Gaussian distributions were assumed for k_{LAM} and θ_{LAM}, respectively. The calculated spectra of PBLG-γd_2 are shown in Fig. 27, being in good agreement with the observed ones. The parameters obtained in this calculation are shown in Table 2. The k_{LAM} remarkably increases with increasing temperature. This result suggests that the movable range of the γ position is almost independent of temperature and only the jump rate increases with increasing temperature.

The k_{LAM} of PBLG-γd_2 obtained are located on the WLF curve obtained by other relaxation experiments, showing that the motional mechanism of the

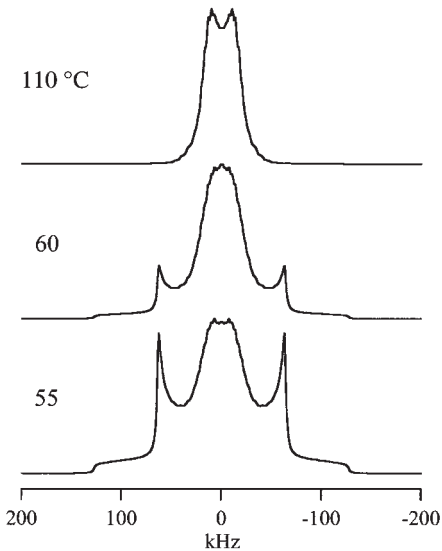

Fig. 27. Calculated spectra of PBLG-γd_2.

Table 2. Parameters of large amplitude motions for PBLG-γd_2

Temp (°C)	θ_{LAM} (deg)	Standard deviation of θ_{LAM} (deg)	k_{LAM} (kHz)	Standard deviation of log k_{LAM} (kHz)
110	45	3	64,000	1.5
60	45	5	50	2.0
55	45	5	5	2.0

γ position of the PBLG side chain follows the WLF type. We have already shown in the previous section that the k_{LAM}s of PBLG-κd_1 and PBLG-ζd_2 are also located on the WLF curve, suggesting that the segmental motion including at least the γ to κ positions participate in the glass-like transition phenomenon.

5. RACEMIC PBG

5.1. Racemic PBG-d_5[77,78,88]

It is shown in Section 4 that the phenyl rings of the side chains undergo a rapid 180° flipping motion. In addition to this motion, there are a large amplitude motion along a side chain and rapid and small-amplitude librations. According to the stacking model proposed by Squire and Elliott,[69] the flipping motion and the large amplitude motions of the phenyl ring are expected to be highly restricted by regular stacking below the transition temperature of 90°C.

5.1.1. *Spectra of racemic PBG-d_5*

The temperature dependent spectra of racemic PBG-d_5 are shown in Fig. 28 together with those of PBLG-d_5. If the phenyl ring motions are highly restricted, the ^{2}H NMR spectra will show a rigid state powder pattern. The spectrum of racemic PBG-d_5 at room temperature surprisingly shows the characteristic line shape of a rapid 180° flipping motion with an inner quadrupolar splitting of 28 kHz in the centre. The integrated intensities start to decrease with increasing temperature. Remarkable intensity loss is observed at 60°C for racemic PBG-d_5, corresponding to the intermediate exchange regime of the large amplitude motion. With a further increase in temperature, the spectrum of racemic PBG-d_5 recovers its intensity and a motionally averaged line shape is observed. No remarkable change in line shape was observed at the transition temperature. The line shapes of racemic PBG-d_5 are shifted to high temperature by 10–20°C as compared with those of PBLG-d_5. These results show the presence of the large amplitude motions

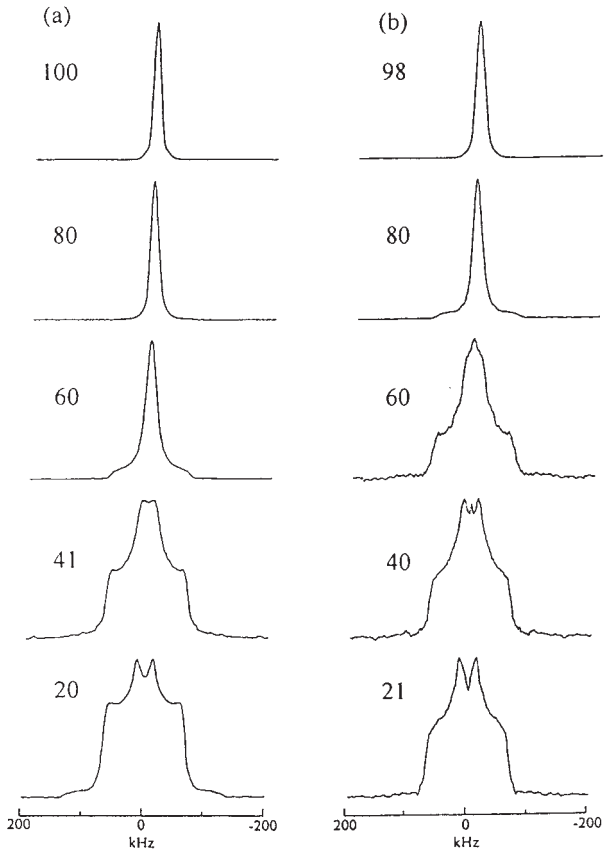

Fig. 28. ^{2}H NMR spectra of PBLG-d_5 (a) and PBG-d_5 (b) as a function of temperature. Reproduced with permission from Elsevier Science.

originated from the multiple internal rotations even in the stacking structure as well as the rapid flipping motion, however, the reorientation of the phenyl ring seems to be restricted by the stacking structure to some extent.

5.1.2. *T_1 of racemic PBG-d_5*

The temperature dependent T_1 results of racemic PBG-d_5 are shown in Fig. 29. As shown in Section 4, T_1 of PBLG-d_5 achieves a broad minimum at 80°C, showing that the rate of the flipping motion is as high as the Larmor frequency of 30 MHz at this temperature. The T_1 value of racemic PBG-d_5 decreases more slowly than that of PBLG-d_5 as temperature is raised, and drops steeply around 60°C. The T_1 value of racemic PBG-d_5 was found to be same as that for PBLG-d_5 above 80°C. There is little difference in the T_1 values of both samples even below the transition temperature of 90°C. These differences in

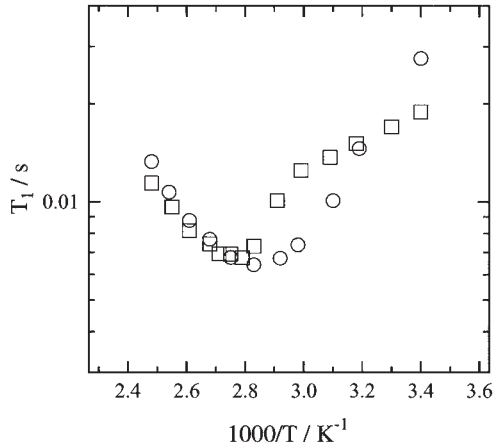

Fig. 29. Temperature dependent T_1 of PBLG-d_5 (circle) and racemic PBG-d_5 (square). Reproduced with permission from Elsevier Science.

T_1 reveal that the reorientation of the phenyl ring is restricted, but that most of the phenyl rings undergo the flipping motion even in the stacked state. This agrees with the result of the temperature dependence of the line shapes and ^{13}C CP/MAS measurements.[76]

According to the stacking model, the stacked and free side chains co-exist in the racemic complex. The T_1 value of racemic PBG-d_5 is supposed to consist of both contributions below the transition temperature. The single component of T_1 could be virtually obtained from the inversion-recovery measurement. However, we could not separate these contributions, because the correlation times of the flipping motion in both states, which are very close in this case, are considered to be distributed over a wide frequency range and cross over each other. Therefore, it is reasonable to assume that the distribution width of the correlation time of the flipping motion in racemic PBG is expected to be broader than that in PBLG below the transition temperature. In general, when the distribution of the correlation time becomes broader, the T_1 value increases and the T_1 profile becomes less sharp. The T_1 profile below 80°C is such a case. Unfortunately, the dynamic NMR parameters for the distribution were not determined, since the T_1 minimum of racemic PBG-d_5 in the stacked state was not observed.

5.2. Racemic PBG-ζd_2[77,78,88]

5.2.1. *Spectra of racemic PBG-ζd_2*

The temperature dependent line-shapes of racemic PBG-ζd_2 are shown in Fig. 30, together with those of PBLG-ζd_2. The line shape at room temperature

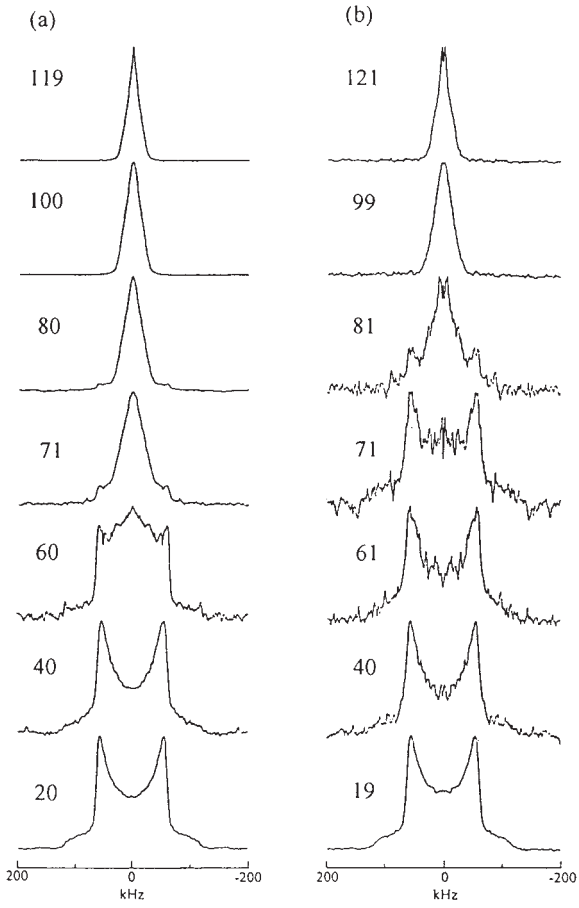

Fig. 30. ^{2}H NMR spectra of PBLG-ζd_2 (a) and racemic PBG-ζd_2 (b) as a function of temperature. Reproduced with permission from Elsevier Science.

appears to be the rigid state powder pattern, showing the absence of the large amplitude motion in the benzyl methylene deuterons. The signal intensity of the spectrum decreases gradually with an increase in temperature. A remarkable intensity loss is observed at around 80°C for racemic PBG-ζd_2, which is higher by about 20° than that for PBLG-ζd_2. This intensity loss corresponds to the intermediate exchange regime for the large amplitude motion. With a further increase in temperature, the spectrum recovers its intensity and a motionally averaged line shape is observed. These line shape changes are due to the large amplitude motions caused by the multiple internal rotations along the side chains. If the large amplitude motion is highly restricted due to the stacking structure, the ^{2}H NMR spectra would have the component of the rigid state powder pattern below the transition

temperature of 90°C. However, the line shape change remarkably occurs below the transition temperature. This temperature dependence of racemic PBG-ζd_2 appears to shift to higher temperature by 10–20°C compared with that of PBLG-ζd_2, as in the case of racemic PBG-d_5. No remarkable change is observed around the transition temperature of 90°C. These data suggest that the restriction of the large amplitude motions exists, but that it is not so strong. According to the stacking model, not every side chain participates in the stacked state below the transition temperature in the racemic PBG. Stacked and free side chains simultaneously exist in the racemic sample. Both contributions have, therefore, to be separated, in order to investigate the dynamic structure of the stacked side chains in detail.

5.2.2. *T_1 of racemic PBG-ζd_2*

The temperature dependent T_1 results of racemic PBG-ζd_2 is shown in Fig. 31. The T_1 data obtained are found to comprises two components: a short component T_{1S} and a long component T_{1L}. T_{1S} is an order of magnitude shorter than T_{1L}, and is in good agreement with the T_1 of PBLG-ζd_2 which is governed by the large amplitude motion and libration above and below room temperature, respectively. Both T_{1S} and T_{1L} decrease gradually with an increase in temperature. Above 80°C the T_{1L} component disappears and both components reduce to one. These results imply that T_{1S} and T_{1L} correspond to the contributions from the side chains in the free and stacked states, respectively.

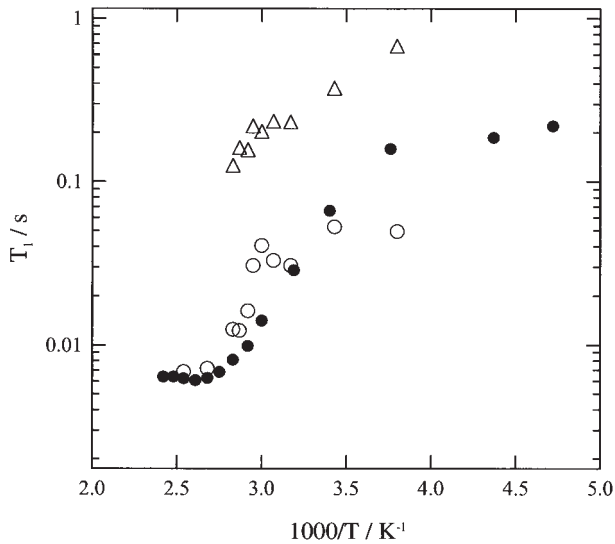

Fig. 31. Temperature dependent T_1 of PBLG-ζd_2 (filled circle) and racemic PBG-ζd_2; T_{1L} (triangle) and T_{1S} (circle). Reproduced with permission from Elsevier Science.

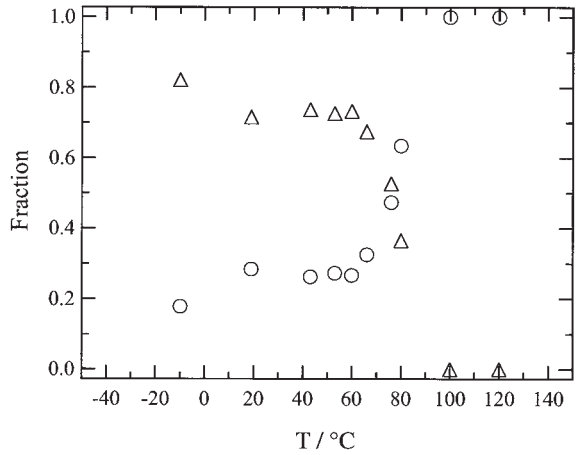

Fig. 32. Fractions of T_{1L} (triangle) and T_{1S} (circle) components of racemic PBG-ζd_2.

Figure 32 shows each fraction of the T_{1S} and T_{1L} components of racemic PBG-ζd_2 as a function of temperature. The average fraction of the stacked side chains was estimated to be 75% below 60°C. An L-molecule is surrounded by six nearest neighbour D-molecules according to the stacking model, and 73% benzyl groups of an L-molecule interact with those of neighbouring D-molecules to form the stacking structure. This is an ideal case by which a maximum amount of stacks occurs. The same degree of stacking was reported by other experiments.[71,72,74] The fraction of the stacked side chains estimated in this experiment also agrees well with the value calculated with the stacking model.

5.2.3. *Libration in stacking structure*

The side chains participating in the stacking structure are deduced to be not rigid, because the T_{1L} value is several hundred ms, being considerably short and having mobility. It was shown that the T_1 at the ζ position of PBLG side chain below room temperature is governed by the rapid and small-amplitude libration. The libration is expected to exist in the stacked state as well as the free state. Accordingly, T_{1L} is considered to be governed by the libration in the stacked state. In order to estimate the amplitude of the libration in the stacked state, we extracted the T_{1L} component of the spectrum by using the amorphous quadrupole echo pulse sequence described in Section 2.3. This pulse sequence provides an effective way to obtain the T_{1S} component of a spectrum, because the longer T_1 component is suppressed when two T_1 values in the system are quite different. The T_{1L} component can be extracted by subtracting the spectrum obtained with the amorphous quadrupole echo from that obtained with the quadrupole echo. The T_{1L}

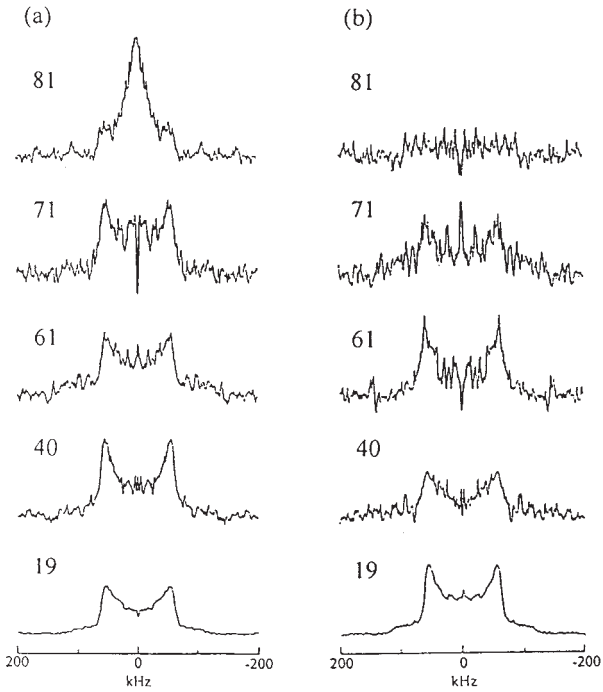

Fig. 33. ^{2}H NMR spectra of racemic PBG-ζd_2 with T_{1S} (a) and T_{1L} (b) components as a function of temperature. Reproduced with permission from Elsevier Science.

component spectrum corresponds to the signal from the side chains in the stacked state.

The T_{1L} and T_{1S} components of the spectra obtained are shown in Fig. 33. The $\overline{\nu_Q}$ of the T_{1L} component is 114 kHz and is larger by 5 kHz than that of PBLG-ζd_2 at 19°C. This suggests that the amplitude of the libration in the stacked state is smaller than that in the free state. The $\overline{\nu_Q}$ value of the T_{1S} component is 109 kHz and is similar to that of PBLG-ζd_2. This is compatible with the assumption that the T_{1S} component corresponds to the side chains in the free state. The fraction of the T_{1L} component is estimated to be about 60% from the integrated intensity of the spectrum at 19°C, which is comparable with the value estimated from T_1.

The amplitude and correlation time τ_c of the libration in the stacked state were estimated by using the diffusion in a cone model. The semiangle of the cone θ_C at 20°C were obtained to be 22° and 26° for the T_{1L} component and PBG-ζd_2 and PBLG-ζd_2, respectively. The τ_c values were obtained to be about 10^{-12} s at 19°C in both states. The θ_C of T_{1L} component is 4° smaller than that of PBLG-ζd_2, showing that the amplitude of the libration in the stacked state is smaller than that in the free state due to the steric hindrance between the adjacent side chains forming the stacking

structure. There is little difference in the τ_c values between the stacked and free states.

5.3. Racemic PBG-γd$_2$[88]

5.3.1. *Spectra of racemic PBG-γd$_2$*

The temperature dependent line shape of racemic PBG-γd$_2$ is shown in Fig. 34 together with those of PBLG-γd$_2$. The line shapes at room temperature appear to be the rigid state powder pattern, showing the absence of the large amplitude motion in the γ position. The signal intensity of the

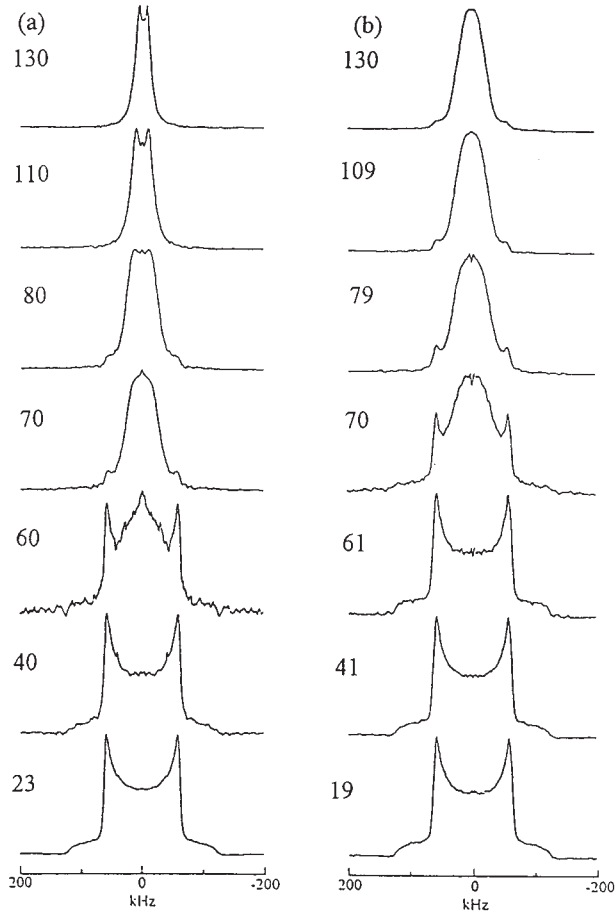

Fig. 34. ^{2}H NMR spectra of PBLG-γd$_2$ (a) and racemic PBG-γd$_2$ (b) as a function of temperature.

spectrum decreases gradually with increasing temperature. A remarkable intensity loss is observed at around 70°C for racemic PBG-γd_2, which is higher by about 15° than that for PBLG-γd_2. With a further increase in temperature, the spectrum recovers its intensity and a motionally averaged line shape is observed. These line shape changes are due to the large amplitude motion caused by the multiple internal rotations around the C_α–C_β and C_β–C_γ bonds. If the large amplitude motion is highly restricted due to the stacking structure, the rigid state powder pattern would appear in a spectrum below the transition temperature of 90°C. However, the line shape change already occurs below the transition temperature. The temperature dependence of the line shape of racemic PBG-γd_2 appears to shift to higher temperature by 10–20°C compared with that of PBLG-γd_2. No remarkable change was observed around the transition temperature of 90°C. These results suggest that the large amplitude motions may be restricted.

5.3.2. *T_1 of racemic PBG-γd_2*

The temperature dependent T_1 results of racemic PBG-γd_2 are shown in Fig. 35. The T_1 value of racemic PBG-γd_2 comprises two components of T_{1S} and T_{1L} as well as T_1 of racemic PBG-ζd_2. T_{1S} is an order of magnitude shorter than T_{1L}, and in fairly good agreement with the T_1 data of PBLG-γd_2 which are governed by the large amplitude motion and the libration above and below room temperature, respectively. Both T_{1S} and T_{1L} decrease gradually with an increase in temperature. Above the transition temperature

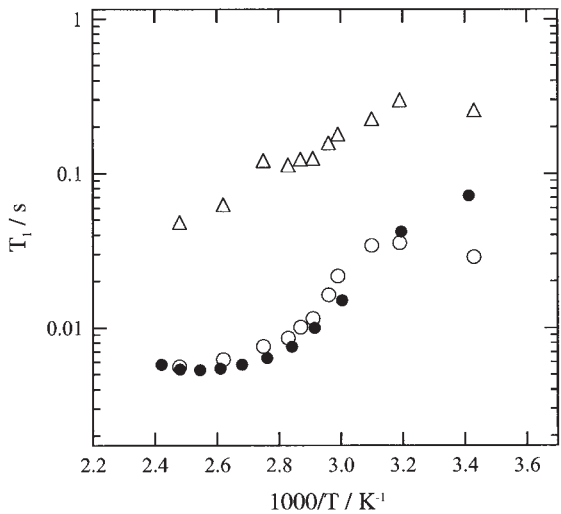

Fig. 35. Temperature dependent T_1 of PBLG-γd_2 (filled circle) racemic PBG-γd_2 with T_{1L} (triangle) and T_{1S} (circle).

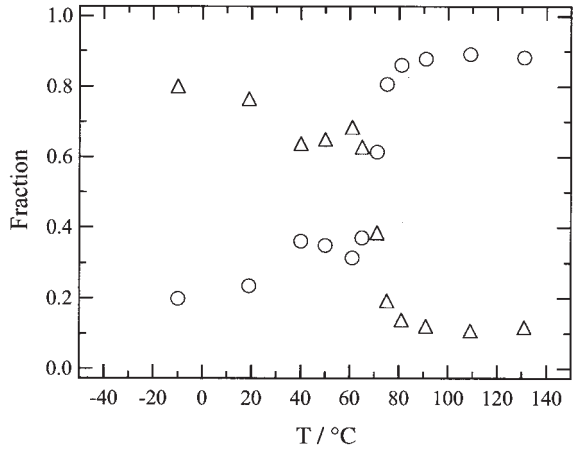

Fig. 36. Fractions of T_{1L} (triangle) and T_{1S} (circle) components of racemic PBG-γd_2.

of 90°C, the T_{1L} component dose not disappear and goes on decreasing gradually with an increase in temperature.

Figure 36 shows each fraction of the T_{1S} and T_{1L} components of racemic PBG-γd_2 as a function of temperature. The average fraction of the stacked side chains was estimated to be 70% by using the values below 60°C. According to the stacking model, 73% benzyl groups participate in the stacking structure as mentioned above. The degree of the stacking estimated in this experiment agrees well with the value obtained by the ^{2}H NMR experiment of racemic PBG-ζd_2 and the value calculated with the stacking model. The fraction of the T_{1L} component drops to about 10% at 60 to 70°C. The average fraction of the T_{1L} component above 80°C is 12%. These results suggest that T_{1S} and T_{1L} correspond to the side chains in the free and stacked states, respectively, and that some restriction remains even after the collapse of the stacking structure at 90°C. In the stacking model, a regular stack of phenyl groups comprises five side chains and the side chains of one molecule interdigitate with the side chains of the adjacent molecules. The most restrained side chain is probably the centre one out of five stacked side chains. According to the stacking model, the fraction of the side chain in the centre of the stacking structure is 16%. This fraction is in good agreement with the experimental value. Although the T_{1L} fraction of racemic PBG-ζd_2 is zero above the transition temperature, that of racemic PBG-γd_2 takes a non-zero value. These results mean that the large amplitude motion caused by the rotations about the C_α–C_β and C_β–C_γ bonds is restricted in the centre of the stacking structure above the transition temperature, however a large-amplitude internal rotations about exterior bonds such as the C_γ–C_δ, C_δ–O_ε, and O_ε–C_ζ bonds will be allowed.

5.3.3. *Libration in stacking structure*

The T_{1L} value of racemic PBG-γd_2 is several hundred ms and decreases gradually as temperature increases. These results show that the side chains participating in the stacking structure are not rigid. T_1 at the γ position below room temperature is governed by the rapid and small-amplitude libration as shown in Section 4.3. The libration is expected to exist in the stacked state as well as the free state. T_{1L} is considered to be governed by libration in the stacked state. In order to estimate the amplitude of the libration in the stacked state, we extracted the T_{1L} component of the spectrum in the same way as that used for racemic PBG-ζd_2. The spectra of the T_{1L} and T_{1S} components are shown in Fig. 37. The $\overline{\nu_Q}$ value of the T_{1L} component is

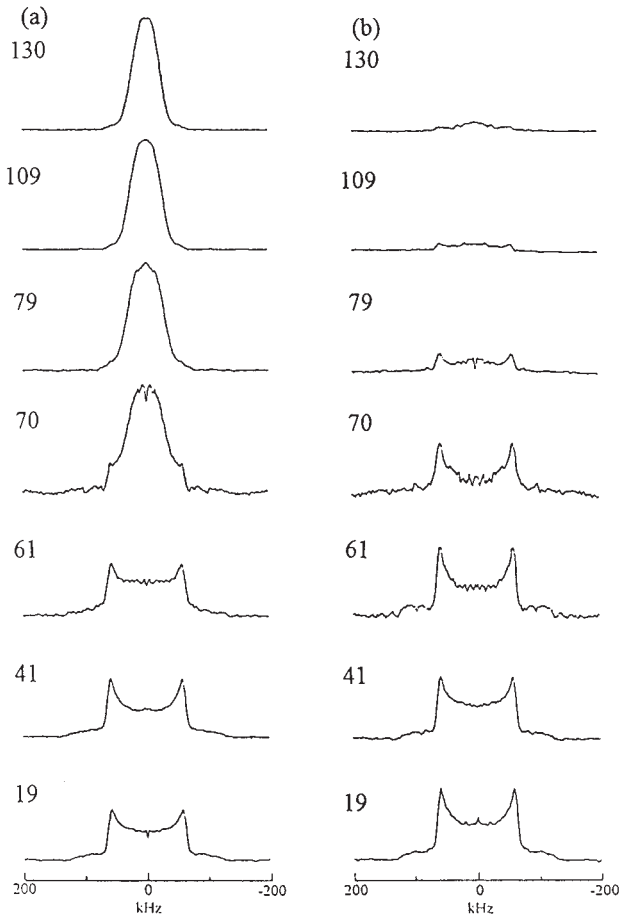

Fig. 37. ^{2}H NMR spectra of racemic PBG-γd_2 with T_{1S} (a) and T_{1L} (b) components as a function of temperature.

larger by 5 kHz than that of PBLG-γd_2. This suggests that the amplitude of the libration in the stacked state is smaller than that in the free state. The $\overline{\nu_Q}$ value of the T_{1S} component is almost equal to that of PBLG-γd_2. This is compatible with the assumption that the T_{1S} component corresponds to the side chains in the free state. The fraction of each component is obtained from the integrated intensity and the fraction of the T_{1L} component is about 60% at 20°C. This is comparable with the value estimated by the T_1 procedure.

The amplitude and correlation time τ_c of the libration in the stacked state are estimated by using the diffusion in a cone model. The semiangles of the cone θ_C are obtained to be 17°, 18°, and 19° for the T_{1L} component at 20, 40, and 60°C, respectively, while 20°, 22°, and 22° for the PBLG-γd_2 at 23, 40, and, 55°C, respectively. The θ_C in the stacking structure is smaller by 3° to 4° than that in the free state at the γ position. Comparing the θ_C value at the γ position with that at the ζ position in the stacked state, the θ_C value at the γ position is 5° smaller than that at the ζ position at 20°C. This is because the C_ζ–^2H bond is located at a more terminal part of the side chain than is the C_γ–^2H bond. The τ_c values were obtained to be about 10^{-11} s for both stacked and free states in this temperature range. There is little difference in the correlation time between the stacked and free states.

6. CONCLUSION

We have investigated the dynamic structures of the side chain in PBLG and racemic PBG by using solid state ^2H NMR. The motional modes of the PBLG side chain were elucidated by ^2H NMR line shapes and T_1 data. Two main motional modes such as the large amplitude motion and the rapid and small-amplitude libration contribute. The large amplitude motion of the side chain was detected in all samples of PBLG-d_5, PBLG-κd_1, PBLG-ζd_2, PBLG-γd_2, especially above T_g'. The large amplitude motion arises from of the multiple internal rotations about chemical bonds along the side chain. Their motional correlation times and amplitudes are widely distributed, characterizing the heterogeneity of the side chain region. It was shown that segmental motions including at least the γ to κ positions are involved in the glass-like transition phenomenon. Because the large amplitude motion below T_g' is too slow to be effective on the ^2H NMR line shape, it could not be detected clearly below room temperature. Thus, the change in the motional correlation time for the large amplitude motion around T_g' was not elucidated. The libration on a 10 ps time scale exists in the PBLG side chain. Its amplitude gradually increases with rising temperature and is distributed to some extent.

The reorientation of the phenyl rings at the end of the side chain is slightly restricted in racemic PBG, but most of the phenyl rings undergo the

180° flipping motion even in the stacked state. The large amplitude motion along the side chain due to the multiple internal rotations is loosely restricted in the stacking structure and allowed after the transition. However, extra large amplitude motions caused by the rotations around the C_α–C_β and C_β–C_γ bonds are partly restrained even after the collapse of the stacked state. About 10% of the side chains are involved in this restriction. The libration along the side chain is present in the stacked state as well as in the free state. The amplitude of the libration in the regular structure is several degrees smaller than that in the free state, and the correlation time is almost equal to that in the free state. It was found that about 75% of the PBLG side chains participate in the stacking structure. This is in good agreement with the stacking model proposed.[69] It should be noted that the stacking structure is very flexible in terms of NMR and the model for the 'static' stacks of the phenyl rings should be modified at least above room temperature.

ACKNOWLEDGEMENTS

We are indebted to Professor T. Hamada for preparing deuterated reagents, and Professors R. L. Vold and the late R. R. Vold for providing a copy of MXQET. We also offer thanks to Professors I. Ando and G. A. Webb for the chance to write this Report.

REFERENCES

1. H. W. Spiess, *Colloid Polym. Sci.*, 1983, **261**, 193.
2. H. W. Spiess, *Adv. Polym. Sci.*, 1985, **66**, 23.
3. L. W. Jelinski, in *High-Resolution NMR Spectroscopy of Synthetic Polymers in Bulk*, R. A. Komoroski, ed., VCH, Deerfield Beach, 1986, ch. 10.
4. D. A. Torchia, *Ann. Rev. Biophys. Bioeng.*, 1984, **13**, 125.
5. S. J. Opella, *Methods Enzymol.*, 1986, **131**, 327.
6. R. R. Vold and R. L. Vold, *Adv. Magn. Opt. Reson.*, 1991, **16**, 85.
7. K. Schmidt-Rohr and H. W. Spiess, *Multidimensional Solid-State NMR and Polymers*, Academic Press, London, 1994, chs. 2 and 7.
8. D. M. Grant, R. K. Harris, eds., *Encylopedia of Nuclear Magnetic Resonance*, John Wiley and Sons, Chichester, 1996, 1574.
9. I. Ando and T. Asakura, *Solid State NMR of Polymers*, Elsevier, Amsterdam, 1998.
10. M. G. Usha, W. L. Peticolas and R. J. Wittebort, *Biochemistry*, 1991, **30**, 3955.
11. M. Yamaguchi and A. Tsutsumi, *Polym. J.*, 1993, **25**, 131.
12. T. Hiraoki, K. Tomita, A. Kogame and A. Tsutsumi, *Polym. J.*, 1994, **26**, 766.
13. S. Kitazawa, T. Hiraoki, T. Hamada and A. Tsutsumi, *Polym. J.*, 1994, **26**, 1213.
14. T. Hiraoki, A. Kogame, N. Nishi and A. Tsutsumi, *J. Mol. Struc.*, 1998, **441**, 243.
15. K. Matsuo, T. Hiraoki and A. Tsutsumi, *Rep. Prog. Polym. Phys. Jpn.*, 1989, **32**, 495.
16. T. Hiraoki, A. Kogame, K. Matsuo and A. Tsutsumi, *Rep. Prog. Polym. Phys. Jpn.*, 1990, **33**, 541.

17. M. Yamaguchi Karasawa, S. Shimokawa, T. Hiraoki and A. Tsutsumi, *Rep. Prog. Polym. Phys. Jpn.*, 1991, **34**, 423.
18. S. Kitazawa, T. Hiraoki, T. Hamada and A. Tsustumi, *Rep. Prog. Polym. Phys. Jpn.*, 1992, **35**, 543.
19. S. Kitazawa, T. Hiraoki, S. Okamoto, H. Furuya, A. Abe and A. Tsutsumi, *Rep. Prog. Polym. Phys. Jpn.*, 1995, **38**, 467.
20. T. Hirayama, S. Kitazawa, T. Hiraoki and A. Tsutsumi, *Rep. Prog. Polym. Phys. Jpn.*, 1995, **38**, 469.
21. Y. Kawase, T. Hiraoki and A. Tsutsumi, *Rep. Prog. Polym. Phys. Jpn.*, 1996, **39**, 519.
22. Y. Kawase, T. Hiraoki and A. Tsutsumi, *Rep. Prog. Polym. Phys. Jpn.*, 1997, **40**, 491.
23. S. Kubota, T. Izumikawa, T. Hiraoki and A. Tsutsumi, *Rep. Prog. Polym. Phys. Jpn.*, 1998, **41**, 527.
24. Y. Kawase, T. Hiraoki and A. Tsutsumi, *Rep. Prog. Polym. Phys. Jpn.*, 1998, **41**, 573.
25. N. Morikoshi, T. Hiraoki and A. Tsutsumi, *Rep. Prog. Polym. Phys. Jpn.*, 1999, **42**, 477.
26. A. Tsutsumi, *Prog. Polym. Sci.*, 1993, **18**, 651.
27. H. Saito and I. Ando, *Ann. Rep. NMR Spectrosc.*, 1989, **22**, 209.
28. A. Shoji, S. Ando, S. Kuroki, I. Ando and G. A. Webb, *Ann. Rep. NMR Spectrosc.*, 1993, **24**, 55.
29. M. Tsuboi, *J. Polym. Sci.*, 1962, **59**, 139.
30. K. Hikichi, *J. Phys. Soc. Jpn.*, 1964, **19**, 2169.
31. A. Tsutsumi, *Japan. J. Appl. Phys.*, 1970, **9**, 1125.
32. A. Tsutsumi, K. Hikichi, T. Takahashi, Y. Yamashita, N. Matsushima, M. Kanke and M. Kaneko, *J. Macromol. Sci., Phys.*, 1973, **B8**, 413.
33. A. Tsutsumi, T. Suzuki, K. Hikichi and M. Kaneko, *Rep. Prog. Polym. Phys. Jpn.*, 1974, **17**, 579.
34. S. Makino, K. Kamashima, S. Kubota and S. Sugai, *Japan. J. Appl. Phys.*, 1964, **3**, 55.
35. K. Hikichi, K. Saito, M. Kaneko and J. Furuichi, *J. Phys. Soc. Jpn.*, 1964, **19**, 577.
36. N. Sasaki, A. Tsutsumi, K. Hikichi, Y. Konishi and M. Hatano, *Polym. J.*, 1979, **11**, 583.
37. K. Hikichi, S. Yamashita and A. Tsutsumi, *Polym. J.*, 1985, **17**, 1241.
38. Y. Yamashita, A. Tsutsumi, K. Hikichi and M. Kaneko, *Polym. J.*, 1979, **11**, 241.
39. A. Hiltner, J. M. Anderson and E. Borkowski, *Macromolecules*, 1972, **5**, 446.
40. Y. Yamashita, A. Tsutsumi, K. Hikichi and M. Kaneko, *Polym. J.*, 1976, **8**, 114.
41. J. A. E. Kail, J. A. Sauer and A. E. Woodward, *J. Phys. Chem.*, 1962, **66**, 1292.
42. A. Tsutsumi, S. Anzai and K. Hikichi, *Polym. J.*, 1983, **15**, 355.
43. K. Hikichi, A. Tsutsumi, S. Isozaki and M. Kaneko, *Polym. J.*, 1975, **7**, 646.
44. A. Tsutsumi, K. Hikichi and M. Kaneko, *Polym. J.*, 1976, **8**, 511.
45. N. Matsushima, K. Hikichi, A. Tsutsumi and M. Kaneko, *Polym. J.*, 1975, **7**, 44.
46. N. Matsushima, K. Hikichi, A. Tsutsumi and M. Kaneko, *Polym. J.*, 1976, **8**, 88.
47. A. J. McKinnon and A. V. Tobolsky, *J. Phys. Chem.*, 1968, **72**, 1157.
48. A. J. McKinnon and A. V. Tobolsky, *J. Phys. Chem.*, 1966, **70**, 1453.
49. N. Matsushima and K. Hikichi, *Polym. J.*, 1978, **10**, 437.
50. K. Hikichi, *Rep. Prog. Polym. Phys. Jpn.*, 1978, **21**, 509.
51. A. Allerhand and E. Oldfield, *Biochemistry*, 1973, **12**, 3428.
52. H. Pivcová, D. Doskocilová and E. M. Bradbury, *Polymer*, 1979, **20**, 139.
53. F. Heatley, T. J. Holton and C. Price, *J. Chem. Soc., Faraday Trans. 2*, 1981, **77**, 689.
54. P. M. Budd, F. Heatley, T. J. Holton and C. Price, *J. Chem. Soc., Faraday Trans. 1*, 1981, **77**, 759.
55. S. Noji, T. Nomura and K. Yamaoka, *Macromolecules*, 1980, **13**, 1114.
56. T. Hiraoki and A. Tsutsumi, unpublished data.
57. A. Shoji, T. Ozaki, H. Saito, R. Tabeta and I. Ando, *Macromolecules*, 1984, **17**, 1472.
58. Y. Tsujita, Y. Murafuji, K. Yano and A. Takizawa, *J. Macromol. Sci. Phys.*, 1984, **B23**, 311.
59. H. Pivcová, V. Saudek, P. Schmidt, D. Hlavata, J. Plestil and F. Laupretre, *Polymer*, 1987, **28**, 991.
60. F. R. Colomer and J. L. G. Ribelles, *Polymer*, 1989, **30**, 849.

61. A. Abe and T. Yamazaki, *Macromolecules*, 1989, **22**, 2138.
62. A. Abe and T. Yamazaki, *Macromolecules*, 1989, **22**, 2145.
63. J. J. Breen and G. W. Flynn, *J. Phys. Chem.*, 1992, **96**, 6825.
64. J. Helfrich, R. Hentschke and U. M. Apel, *Macromolecules*, 1994, **27**, 472.
65. A. Schmidt, S. Lehmann, M. Georgelin, G. Katana, K. Mathauer, F. Kremer, K. Schmidt-Rohr, C. Boeffel, G. Wegner and W. Knoll, *Macromolecules*, 1995, **28**, 5487.
66. V. Copié, Ann E. McDermott, K. Beshah, J. C. Williams, M. S. Assink, R. Gebhard, J. Lugtenburg, J. Herzfeld and R. G. Griffin, *Biochemistry*, 1994, **33**, 3280.
67. M. Tsuboi, A. Wada and N. Nagashima, *J. Mol. Biol.*, 1961, **3**, 705.
68. Y. Mitsui, Y. Iitaka and M. Tsuboi, *J. Mol. Biol.*, 1967, **24**, 15.
69. J. M. Squire and A. Elliott, *J. Mol. Biol.*, 1972, **65**, 291.
70. T. Fukuzawa, I. Uematsu and Y. Uematsu, *Polym. J.*, 1974, **6**, 537.
71. T. Takahashi, A. Tsutsumi, K. Hikichi and M. Kaneko, *Macromolecules*, 1974, **7**, 806.
72. N. Matsushima, K. Hikichi, A. Tsutsumi and M. Kaneko, *Polym. J.*, 1975, **7**, 382.
73. J. Watanabe, K. Imai and I. Uematsu, *Rep. Prog. Polym. Phys. Jpn*, 1980, **23**, 671.
74. M. Tokita, Y. Yamashita and K. Hikichi, *Polym. J.*, 1981, **13**, 569.
75. A. Tsutsumi, M. Uchida and K. Hikichi, *Polym. J.*, 1986, **18**, 625.
76. M. Yamaguchi and A. Tsutsumi, *Polym. J.*, 1993, **25**, 427.
77. S. Kitazawa, T. Hiraoki and A. Tsutsumi, *Rep. Prog. Polym. Phys. Jpn*, 1994, **37**, 561.
78. S. Kitazawa, T. Hiraoki and A. Tsutsumi, *J. Mol. Struct.*, 1995, **355**, 87.
79. C. M. Gall, J. A. DiVerdi and S. J. Opella, *J. Am. Chem. Soc.*, 1981, **103**, 5039.
80. M. S. Greenfield, A. D. Ronemus, R. L. Vold and R. R. Vold, *J. Magn. Reson.*, 1987, **72**, 89.
81. R. J. Wittebort, E. T. Olejniczak and R. G. Griffin, *J. Chem. Phys.*, 1987, **86**, 5411.
82. L. S. Batchelder, C. H. Niu and D. A. Torchia, *J. Am. Chem. Soc.*, 1983, **105**, 2228.
83. D. A. Torchia and A. Szabo, *J. Magn. Reson.*, 1982, **49**, 107.
84. G. Lipari and A. Szabo, *J. Chem. Phys.*, 1981, **75**, 2971.
85. M. Mehring, in *High Resolution NMR Spectroscopy in Solids*, 2nd ed., Springer, Berlin, 1983, ch. 10.
86. R. J. Wittebort and A. Szabo, *J. Chem. Phys.*, 1978, **69**, 1722.
87. A. L. Cholli, J. J. Dumais, A. K. Engel and L. W. Jelinski, *Macromolecules*, 1984, **17**, 2399.
88. S. Kitazawa, *Ph. D. Thesis*, Hokkaido University, 1996.
89. C. M. Gall, J. A. DiVerdi and S. J. Opella, *J. Am. Chem. Soc.*, 1981, **103**, 5039.
90. D. M. Rice, R. J. Wittebort, R. G. Griffin, E. Meirovitch, E. R. Stimson, Y. C. Meinwald, J. H. Freed and H. A. Scheraga, *J. Am. Chem. Soc.*, 1981, **103**, 7707.
91. D. M. Rice, Y. C. Meinwald, H. A. Scheraga and R. G. Griffin, *J. Am. Chem. Soc.*, 1987, **109**, 1636.
92. R. J. Schadt, E. J. Cain, K. H. Gardner, V. Gabara, S. R. Allen and A. D. English, *Macromolecules*, 1993, **26**, 6503.
93. R. J. Schadt, K. H. Gardner, V. Gabara, S. R. Allen, D. B. Chase and A. D. English, *Macromolecules*, 1993, **26**, 6509.
94. A. S. Kulik and K. O. Prins, *Polymer*, 1993, **34**, 4635.
95. H. Shindo, Y. Hiyama, S. Roy, J. S. Cohen and D. A. Torchia, *Bull. Chem. Soc. Jpn.*, 1987, **60**, 1631.
96. A. Kintanar, T. M. Alam, W. Huang, D. C. Schindele, D. E. Wemmer and G. Drobny, *J. Am. Chem. Soc.*, 1988, **110**, 6367.

Index

Note – Page numbers in *italic* type refer to figures and tables.